



QA: QA

MDL-NBS-HS-000001 REV 05

September 2007

Drift-Scale THC Seepage Model

Prepared for:
U.S. Department of Energy
Office of Civilian Radioactive Waste Management
Office of Repository Development
1551 Hillshire Drive
Las Vegas, Nevada 89134-6321

Prepared by:
Sandia National Laboratories
OCRWM Lead Laboratory for Repository Systems
1180 Town Center Drive
Las Vegas, Nevada 89144

Under Contract Number
DE-AC04-94AL85000

DISCLAIMER

This report was prepared as an account of work sponsored by an agency of the United States Government. Neither the United States Government nor any agency thereof, nor any of their employees, nor any of their contractors, subcontractors or their employees, makes any warranty, express or implied, or assumes any legal liability or responsibility for the accuracy, completeness, or any third party's use or the results of such use of any information, apparatus, product, or process disclosed, or represents that its use would not infringe privately owned rights. Reference herein to any specific commercial product, process, or service by trade name, trademark, manufacturer, or otherwise, does not necessarily constitute or imply its endorsement, recommendation, or favoring by the United States Government or any agency thereof or its contractors or subcontractors. The views and opinions of authors expressed herein do not necessarily state or reflect those of the United States Government or any agency thereof.

QA: QA

Drift-Scale THC Seepage Model

MDL-NBS-HS-000001 REV 05

September 2007



Model Signature Page/Change History

Complete only applicable items.

Page iii

1. Total Pages: 490

2. Type of Mathematical Model <input checked="" type="checkbox"/> Process Model <input type="checkbox"/> Abstraction Model <input type="checkbox"/> System Model Describe Intended Use of Model <p>The purpose of this report is to document predictive simulations of the thermal-hydrologic-chemical behavior in the repository host rock, evaluating the effect of water/rock interactions at elevated temperature on potential seepage water compositions.</p>			
3. Title Drift-Scale THC Seepage Model			
4. DI (including Rev. No.): MDL-NBS-HS-000001 REV 05			
	Printed Name	Signature	Date
5. Originator	Nicolas Spycher	<i>[Signature]</i>	9/28/07
6. Independent Technical Reviewer	David Sassani	<i>[Signature]</i>	10/01/07
7. Checker	Mark Sutton	<i>[Signature]</i>	10/01/07
8. QCS/Lead Lab QA Reviewer	Charles Beach	<i>[Signature]</i>	10-01-07
9. Responsible Manager/Lead	Ernest Hardin	<i>[Signature]</i>	10/1/07
10. Responsible Manager	Geoff Freeze	<i>[Signature]</i>	10/5/07
11. Remarks			
Change History			
12. Revision No.	13. Description of Change		
REV 00	Initial Issue		
REV 01	Incorporated additional data from DST for model validation. Incorporated sensitivity studies, including effect of backfill versus no backfill. Additional Models/Updates: REV01 DST THC Model; Tptpmn THC No-Backfill Model; Tptpmn THC Heterogeneous Model; Tptpll THC Model; Plug-Flow Reactor Model Validation		
REV 01 ICN 01	Incorporated minor editorial changes to text and references. Incorporated additional figure (Figure 32b). Incorporated auditor's recommendations (Audit M&O-APR-01-02). All changes are marked by a black vertical line on the margin of the affected page.		

<p>REV 01 ICN 02</p>	<p>Removed incorrect reference DTN: MO0008THRMODYN.000 [DIRS 153742], inserted correct reference DTN: MO0009THRMODYN.001 [DIRS 152576] (this impacted sections 4, 8.3 and attachments V and VI). Made editorial correction in section 5.A.7. Added assumption 20 to section 5.A, to identify DTN: LA0008SC12213N.001 [DIRS 153386] as data that augments DTN: MO0009THRMODYN.001 [DIRS 152576]. Revised three assumptions to indicate no further confirmation is required as the assumptions were adequately justified (C-1, C-4, and C-6). Revision of assumptions resulted in the removal of TBVs 5028, 5029, and 5030 in the Document Input Reference System (DIRS). Updated section 8.3 to remove URNs where appropriate. Changes to the data status made in DIRS. The following sections were revised in REV 01 ICN 02: Section 1 (p. 23), 2 (p. 27), 3 (p. 30), 4 (pp. 33, 37-38, 42), 5 (pp. 50, 53, 55), 6 (p. 107), 7 (p. 225), 8 (pp. 228-229, 235-240), Att V (p. V-3), and VI (p. VI-3).</p>
<p>REV 02</p>	<p>Entire model documentation was revised. Side bars are not used because the changes were too extensive to use Step 5.9d)1) per AP-SIII.10Q/REV.1/ICN 2.</p>
<p>REV 03</p>	<p>Entire model documentation was revised. Side bars are not used because the changes were too extensive to use Step 5.8f)1), AP-SIII.10Q/REV 02/ICN 5. All Revision 01 THC Seepage Model simulations (Sections 6.5, 6.6, 6.7 of REV 02) and Revision 01 DST THC model simulations (in Section 7.1 of REV 02) and associated inputs that are not used by the current revision were removed. In Section 4.1, superseded or historical inputs to the current model were justified for intended use. Section 5 was expanded to include more assumptions. Several subsections of Section 6 were removed, and a new section, documenting a sensitivity analysis relating to host rock thermal properties has been added. Section 7.1 was rewritten to more explicitly address procedural requirements. Sections 7.2 and 7.3 were reduced to short descriptions. The errata associated with the previous revision were fixed. Regulatory Integration Team review items were addressed through more thorough descriptions of the process model, justification of assumptions, evaluation of the model validation, and discussion of propagation of model uncertainty to downstream models. The report also addresses Condition Reports CR79, CR168, CR821, CR938, CR1805, CR1821, CR2049, CR2050, and CR2104.</p>
<p>REV 04</p>	<p>Revisions to the validation section (Section 7) of the document, to address CR99 and CR4888. Specifically, changes were made to Sections 1.1, 1.3, 4.2, 7.1.7, 7.1.7.2, and 7.1.11.3. Side bars are not used because the changes were too extensive to use Step 5.7.2c)1) per LP-SIII.10Q-BSC REV. 0/ICN 0.</p>
<p>REV 05</p>	<p>This is a major revision and addresses the following CRs: 5154, 5383, 6334, 6342, 6344, 6489, 6491, 6492, 6691, 7037, 7187, 7193, 7697, 7811, 8009, 8032, and 8316. Side bars are not used because the changes were too extensive. Compared to previous versions, main changes to the model inputs include new thermodynamic and mineral data, an updated set of rock properties consistent with those used in other Near-Field Environment models, and new infiltration rates. A new set of pore-water compositions is used in the model runs to represent variability and uncertainty. The calculations use a new version of the TOUGHREACT software. The sampled output waters are shifted from those at the boiling/wetting front around the drift, to those in zones of higher liquid flux further away than the boiling/wetting front.</p>

ACKNOWLEDGMENTS

This study was carried out by Nicolas Spycher, Eric Sonnenthal, Guoxiang Zhang, and Sumit Mukhopadhyay (of Lawrence Berkeley National Laboratory, Earth Sciences Division), who developed the THC seepage model and are responsible for the technical content of this document.

We would like to acknowledge contributions by John Apps to the thermodynamic data, technical data coordination by Carol Valladao, technical review by David Sassani, and help in tracking and checking technical inputs by Mark Sutton, Emma Thomas, Jim Nowak, Wendy Mitcheltree, and David Shields. Production assistance by Krys Avina, Lisa Feedar, Dan Hawkes, and Tom Breene is also duly acknowledged.

INTENTIONALLY LEFT BLANK

CONTENTS

	Page
ACKNOWLEDGMENTS	v
ACRONYMS AND ABBREVIATIONS	xix
1. PURPOSE	1-1
1.1 BACKGROUND	1-1
1.2 OVERVIEW OF MODELS	1-2
1.3 MODEL LIMITATIONS	1-3
2. QUALITY ASSURANCE	2-1
3. USE OF SOFTWARE	3-1
3.1 QUALIFIED SOFTWARE	3-1
3.2 EXEMPT SOFTWARE	3-1
4. INPUTS	4-1
4.1 DIRECT INPUTS	4-1
4.1.1 Hydrologic and Thermal Properties	4-1
4.1.1.1 Transport Properties	4-3
4.1.1.2 Thermal Properties	4-4
4.1.1.3 Effective Thermal Conductivities for In-Drift Open Spaces	4-4
4.1.2 THC Model Grid	4-6
4.1.3 Model Boundary Conditions	4-6
4.1.4 Mean Infiltration Rates	4-7
4.1.5 Thermal Load and Ventilation Efficiency	4-8
4.1.6 Mineral Abundance, Composition, and Reactive Surface Area Data	4-8
4.1.7 Kinetic Data	4-9
4.1.8 Thermodynamic Data	4-10
4.1.9 Water and Gas Chemistry	4-11
4.1.10 Drift Design Information	4-11
4.2 CRITERIA	4-15
4.3 CODES, STANDARDS, AND REGULATIONS	4-20
5. ASSUMPTIONS	5-1
6. MODEL DISCUSSION	6-1
6.1 RELEVANT FEATURES, EVENTS, AND PROCESSES	6-5
6.2 CONCEPTUAL MODEL	6-6
6.2.1 Conceptualization of Coupled THC Processes	6-6
6.2.1.1 TH Processes	6-7
6.2.1.2 THC Processes	6-8
6.2.1.3 Effects of Infiltration and Climate Changes on THC Processes	6-11
6.2.1.4 Hydrologic Property Changes in Fractures and Matrix	6-11
6.2.1.5 Dual-Permeability Model for THC Processes	6-12

CONTENTS (Continued)

	Page
6.2.2	Conceptualization of the Geochemical System 6-12
6.2.2.1	Initial Pore-Water and Pore-Gas Chemistry 6-13
6.2.2.2	Geochemical Systems 6-19
6.2.2.3	Mineral Volume Fractions 6-21
6.2.2.4	Mineral Compositions 6-23
6.2.3	Conceptualization of the Model Domain 6-25
6.3	ALTERNATIVE CONCEPTUAL MODELS 6-26
6.4	MATHEMATICAL MODEL 6-27
6.4.1	General Numerical Model for Coupled THC Processes 6-27
6.4.2	Kinetic Rate Laws 6-30
6.4.3	Mineral Reactive Surface Areas 6-31
6.4.3.1	Fracture Mineral Reactive Surface Areas 6-31
6.4.3.2	Matrix Mineral Reactive Surface Areas 6-33
6.4.4	Effects of Mineral Precipitation/Dissolution on Hydrologic Properties 6-37
6.4.4.1	Porosity Changes 6-37
6.4.4.2	Fracture Permeability Changes 6-37
6.4.4.3	Matrix Permeability Changes 6-39
6.4.4.4	Effects of Permeability and Porosity Changes on Capillary Pressure 6-39
6.4.5	Mineral Precipitation in Dry Gridblocks 6-39
6.4.6	Principal Model Approximations and Approaches 6-41
6.4.7	Summary of Hydrologic and Thermal Properties 6-46
6.4.8	Post-Processing Methodology for Predicted Water Compositions 6-48
6.5	THC SEEPAGE MODEL 6-52
6.5.1	Numerical Mesh 6-52
6.5.2	Boundary Conditions 6-56
6.5.3	Summary of Inputs and Modeling Procedure 6-57
6.5.4	Model Simulations 6-58
6.5.5	Simulation Results 6-59
6.5.5.1	THC Simulations of Ambient Conditions 6-61
6.5.5.2	General Thermal and Hydrological Effects 6-63
6.5.5.3	Mineral Precipitation and Fracture Permeability 6-70
6.5.5.4	Water Chemistry Trends 6-73
6.6	MODEL SENSITIVITY ANALYSES 6-95
6.6.1	Sensitivity to Time Discretization 6-97
6.6.2	Sensitivity to Model Revisions 6-102
6.6.3	Sensitivity to CO ₂ Transport Properties 6-107
6.6.4	Sensitivity to Dryout Mineral Assemblage 6-111
6.6.5	Sensitivity to Reaction Rates 6-119
6.7	MODEL UNCERTAINTY 6-124
6.7.1	Potential Sources of Uncertainty 6-124
6.7.2	Evaluation of Model Result Uncertainty 6-130

CONTENTS (Continued)

	Page
7. VALIDATION.....	7-1
7.1 THE DRIFT SCALE TEST THC SUBMODEL.....	7-4
7.1.1 Modeling Approach.....	7-5
7.1.2 Drift Scale Test Two-Dimensional Numerical Grid.....	7-5
7.1.3 Heater Power.....	7-6
7.1.4 Hydrologic and Geochemical Input Data.....	7-10
7.1.5 Initial and Boundary Conditions: Hydrologic and Thermal.....	7-10
7.1.6 Initial and Boundary Conditions: Geochemical.....	7-11
7.1.7 Model Validation Methods, Criteria, and Limitations.....	7-11
7.1.7.1 Corroboration with Experimental Data.....	7-11
7.1.7.2 Publication in a Refereed Technical Journal.....	7-14
7.1.8 THC Simulations.....	7-15
7.1.9 Simulation Results: Thermal and Hydrologic Evolution.....	7-16
7.1.10 Gas-Phase CO ₂ Evolution: Measured Compositions and Simulation Results.....	7-20
7.1.10.1 Gas Sampling and CO ₂ Measurements.....	7-20
7.1.10.2 Modeled Spatial Distribution of CO ₂	7-21
7.1.10.3 Modeled and Measured CO ₂ Concentrations over Time.....	7-24
7.1.11 Aqueous Species Evolution.....	7-28
7.1.11.1 Chemistry of Waters Sampled during the Drift Scale Test.....	7-28
7.1.11.2 Evolution in the pH of Waters from the DST.....	7-38
7.1.11.3 Evolution of Anion and Cation Concentrations.....	7-44
7.1.12 Mineralogical Changes.....	7-61
7.1.13 Porosity and Permeability Changes.....	7-64
7.1.14 Isotopic Compositions of Gases and Water: Model Corroboration Using ¹⁴ C in CO ₂	7-67
7.1.15 Summary of Model–Data Comparisons Using the Drift Scale Test.....	7-69
7.2 SIMULATION OF THE PLUG-FLOW REACTOR EXPERIMENT.....	7-70
7.3 SIMULATION OF THE FRACTURE SEALING EXPERIMENT.....	7-71
7.4 VALIDATION SUMMARY.....	7-72
8. CONCLUSIONS.....	8-1
8.1 MODELED COUPLED PROCESSES AND UNCERTAINTY.....	8-3
8.2 THC SEEPAGE MODEL RESULTS.....	8-5
8.3 DST THC SUBMODEL RESULTS (VALIDATION).....	8-7
8.4 UNCERTAINTIES AND RESTRICTIONS FOR DOWNSTREAM USE.....	8-9
8.5 CRITERIA.....	8-10
9. INPUTS AND REFERENCES.....	9-1
9.1 DOCUMENTS CITED.....	9-1
9.2 CODES, STANDARDS, REGULATIONS, AND PROCEDURES.....	9-15
9.3 SOURCE DATA, LISTED BY DATA TRACKING NUMBER.....	9-15
9.4 SOFTWARE CODES.....	9-20

CONTENTS (Continued)

	Page
APPENDIX A: MINERAL INITIAL VOLUME FRACTIONS	A-1
APPENDIX B: MINERAL REACTIVE SURFACE AREAS	B-1
APPENDIX C: THERMODYNAMIC DATABASE	C-1
APPENDIX D: WASTE PACKAGE AVERAGE HEAT TRANSFER.....	D-1
APPENDIX E: EFFECTIVE THERMAL CONDUCTIVITY FOR IN-DRIFT OPEN SPACES	E-1
APPENDIX F: PARAMETERS FOR FRACTURE PERMEABILITY MODIFICATION	F-1
APPENDIX G: LIST OF MODEL INPUT AND OUTPUT FILES.....	G-1
APPENDIX H: QUALIFICATION OF MINERAL DISSOLUTION/PRECIPITATION KINETICS DATA FOR USE IN THC COUPLED PROCESS MODELING	H-1
APPENDIX I: DESIGN INFORMATION FOR ASSUMPTIONS 7, 8, AND 9.....	I-1
APPENDIX J: ORIGINAL NUMERICAL GRID DEVELOPMENT	J-1
APPENDIX K: MESH MODIFICATIONS CALCULATIONS	K-1
APPENDIX L: STATISTICAL CALCULATIONS.....	L-1
APPENDIX M: DRIFT SCALE TEST CO2 CONCENTRATIONS	M-1
APPENDIX N: QUALIFICATION PLANS FOR INTENDED USE OF UNQUALIFIED DATA	N-1
APPENDIX O: QUALIFICATION FOR INTENDED USE OF HYDROLOGIC AND MINERALOGICAL DATA	O-1
APPENDIX P: RESOLUTIONS OF CONDITION REPORTS	P-1
APPENDIX Q: TOUGHREACT V3.1.1 AND CUTCHEM V2.0 EXECUTABLES INSTALLATION INFORMATION	Q-1

FIGURES

		Page
4.1-1.	Sketch Showing Modeled In-Drift Dimensions.....	4-14
6.2-1.	Schematic Diagram of THC Processes around a Heated Drift.....	6-8
6.2-2.	Schematic Diagram of Fracture–Matrix Interface Showing the Relation between TH Processes and Geochemical Processes	6-9
6.2-3.	Conceptual Model (schematic) for Reaction–Transport Processes in Dual-Permeability Media.....	6-12
6.2-4.	Piper Plot of Water Compositions (meq/L) from Repository Units	6-15
6.4-1.	Quadrant Designations for Data Selection from the THC Seepage Model	6-49
6.5-1.	THC Model Mesh with Hydrogeologic Units Shown in the Vicinity of the Drift: Topopah Spring Tuff Middle Nonlithophysal (tsw34: triangles), Lower Lithophysal (tsw35: dots), and Lower Nonlithophysal (tsw36: diamonds) Units	6-54
6.5-2.	Discretization of the Repository Drift in the THC Model	6-55
6.5-3.	Time Profiles of Predicted Temperature and Relative Humidity in Fractures (similar in matrix) at the Drift Crown.....	6-66
6.5-4.	Contour Plot of Predicted Temperature (°C) and Liquid Saturation in Fractures at Times near Maximum Dryout.....	6-67
6.5-5.	Time Profiles of Predicted Liquid Saturation in Fractures at the Drift Crown.....	6-68
6.5-6.	Time Profiles of Predicted Liquid Saturation in the Matrix at the Drift Crown.....	6-69
6.5-7.	Time Profiles of Predicted Liquid Flux in Fractures at the Drift Crown.....	6-70
6.5-8.	Contour Plot of Modeled Change in Fracture Permeability for Repository-Center and -Edge Conditions	6-72
6.5-9.	Fracture Permeability as a Function of Porosity Decrease for Various Values of Initial Fracture Permeability	6-73
6.5-10.	Location of Model Gridblocks for Data Shown on Figures 6.5-11 through 6.5-22.....	6-80
6.5-11.	Time Profiles of Modeled Temperatures in Fracture Water above the Drift.....	6-81
6.5-12.	Time Profiles of Modeled Liquid Saturations in Fracture Water above the Drift.....	6-82
6.5-13.	Time Profiles of Modeled Total Aqueous Chloride Concentrations in Fracture Water above the Drift.....	6-83
6.5-14.	Time Profiles of Modeled CO ₂ Gas Concentrations in Fractures above the Drift.....	6-84
6.5-15.	Time Profiles of Modeled CO ₂ Gas Concentrations at the Drift Wall	6-85
6.5-16.	Time Profiles of Modeled pH in Fracture Water above the Drift.....	6-86
6.5-17.	Time Profiles of Modeled Total Aqueous Carbonate Concentrations in Fracture Water above the Drift.....	6-87
6.5-18.	Time Profiles of Modeled Total Aqueous Calcium Concentrations in Fracture Water above the Drift.....	6-88
6.5-19.	Time Profiles of Modeled Total Aqueous Calcium to Total Aqueous Carbonate Ratios in Fracture Water above the Drift.....	6-89
6.5-20.	Time Profiles of Modeled Total Aqueous Calcium to Total Aqueous Chloride Ratios in Fracture Water above the Drift.....	6-90
6.5-21.	Time Profiles of Modeled Total Aqueous Magnesium Concentrations in Fracture Water above the Drift	6-91

FIGURES (Continued)

	Page
6.5-22. Time Profiles of Modeled Total Aqueous Magnesium to Total Aqueous Chloride Ratios in Fracture Water above the Drift.....	6-92
6.5-23. Time Profiles of Modeled Total Aqueous Sodium Concentrations in Fracture Water above the Drift.....	6-93
6.5-24. Time Profiles of Modeled Total Aqueous Sodium to Total Aqueous Chloride Ratios in Fracture Water above the Drift.....	6-94
6.6-1. Time Discretization Analysis: Time Profiles of Modeled CO ₂ Gas Concentrations, Total Aqueous Carbonate Concentrations, and pH	6-99
6.6-2. Time Discretization Analysis: Time Profiles of Modeled Aqueous Chloride Concentrations, Sulfate to Chloride Ratios, and Nitrate to Chloride Ratios	6-100
6.6-3. Time Discretization Analysis: Time Profiles of Modeled Aqueous Calcium and Sodium Concentrations, and Calcium to Total Aqueous Carbonate Ratios	6-101
6.6-4. Sensitivity to Model Revisions: Time Profiles of Modeled Distance above Drift Center, and Aqueous Chloride and Sodium Concentrations	6-104
6.6-5. Sensitivity to Model Revisions: Time Profiles of Modeled CO ₂ Gas Concentrations, Total Aqueous Carbonate Concentrations, and pH	6-105
6.6-6. Sensitivity to Model Revisions: Time Profiles of Modeled Calcium and Magnesium Concentrations, and Calcium to Total Aqueous Carbonate Ratios.....	6-106
6.6-7. Sensitivity to CO ₂ Transport: Time Profiles of Modeled CO ₂ Gas Concentrations, Total Aqueous Carbonate Concentrations, and pH	6-109
6.6-8. Sensitivity to CO ₂ Transport: Time Profiles of Modeled Calcium and Magnesium Concentrations, and Calcium to Total Aqueous Carbonate Ratios.....	6-110
6.6-9. Sensitivity to Dryout Mineral Assemblage: Time Profiles of Modeled CO ₂ Gas Concentrations, Total Aqueous Carbonate Concentrations, and pH	6-114
6.6-10. Sensitivity to Dryout Mineral Assemblage: Time Profiles of Modeled Chloride Concentrations, Sulfate to Chloride Ratios and Nitrate to Chloride Ratios	6-115
6.6-11. Sensitivity to Dryout Mineral Assemblage: Time Profiles of Modeled Sodium, Calcium and Magnesium Concentrations	6-116
6.6-12. Sensitivity to Dryout Mineral Assemblage: Time Profiles of Modeled Sodium to Chloride, Calcium to Chloride, and Nitrate to Chloride Ratios.....	6-117
6.6-13. Sensitivity to Dryout Mineral Assemblage: Time Profiles of Modeled Potassium and Fluoride Concentrations, and Potassium to Chloride Ratios	6-118
6.6-14. Sensitivity to Mineral Reaction Rates: Time Profiles of Modeled CO ₂ Gas Concentrations, Total Aqueous Carbonate Concentrations, and pH	6-121
6.6-15. Sensitivity to Mineral Reaction Rates: Time Profiles of Modeled Sodium, Potassium, and Silica Concentrations	6-122
6.6-16. Sensitivity to Mineral Reaction Rates: Time Profiles of Modeled Chloride, Calcium, and Magnesium Concentrations	6-123
6.7-1. Standard Deviations in Predicted Concentrations.....	6-132
7.1-1. Three-Dimensional Schematic Diagram of the DST Showing Perspective View of Numerical Mesh for DST THC Submodel Simulations.....	7-7
7.1-2. Numerical Mesh for DST THC Submodel Simulations	7-7

FIGURES (Continued)

	Page
7.1-3. Enlarged View of the Numerical Grid Showing the Locations of Gridblocks Representing the Heated Drift, Wing Heaters, and Concrete Invert.....	7-8
7.1-4. Locations of Hydrology Boreholes, Sampling Intervals (numbered), and Temperature Sensors.....	7-13
7.1-5. Drift Center Modeled Temperatures over the Preheating, Heating, and Cooling Periods of the DST.....	7-17
7.1-6. Comparison of Modeled and Measured Temperatures over Time (infiltration rates of about 14 and 1.4 mm/yr) for the Sensor Located at Hydrology Borehole Packer 60-4.....	7-18
7.1-7. Modeled Liquid Saturation (colors) and Temperature (contour lines) in the DST at One, Four, and Eight Years (matrix: a, c, and e; fracture: b, d, and f).....	7-19
7.1-8. Measured Concentrations of CO ₂ (log vol. fraction) in Gas Phase around the DST at 1 Year and at 15 Months.....	7-21
7.1-9. Modeled Gas Phase CO ₂ Concentrations (log ppmv) in Fractures, and Matrix Temperatures (contour lines) during the Heating Phase of the DST at 1, 2, 3, and 4 Years.....	7-22
7.1-10. Modeled Gas Phase CO ₂ Concentrations (log ppmv) in Fractures, and Matrix Temperatures (contour lines) during the Cooling Phase of the DST at 5, 6, 7, and 8 Years.....	7-23
7.1-11. Close-Up of DST Grid, Showing Nodes Used to Extract Model Data for Comparison to Concentrations Measured in Gas Samples.....	7-24
7.1-12. Comparison of Measured and Corrected Model CO ₂ Concentrations for Borehole Interval 75-3 for Simulations dst_thc_r5_01 (high infiltration rate) and dst_thc_r5_03 (low infiltration rate).....	7-26
7.1-13. Comparison of Modeled CO ₂ Concentrations (corrected to different NCG fractions) in Fractures to Measured Concentrations in Boreholes: (a) Borehole Interval 74-3 (average of bounding gridblocks); (b) Borehole Interval 74-3 (average of bounding gridblocks); (c) Borehole Interval 75-3; (d) Borehole Interval 76-3; (e) Borehole Interval 78-3 (interval center).....	7-27
7.1-14. Zones Where Water Was Collected from Hydrology Boreholes Superimposed (thick shading in blue) on the Model Grid.....	7-37
7.1-15. Modeled Distribution of pH in Fractures at Various Times When Water Was Sampled from Hydrology Borehole Intervals (months): (a) 6, (b) 8, (c) 11, (d) 11, (e) 14, (f) 14, (g) 16, (h) 20, (i) 23, (j) 23, (k) 24, (l) 24, (m) 26, (n) 30, (o) 30, (p) 31, (q) 38, (r) 40.....	7-40
7.1-16. Comparison of Measured pH in Water Samples Collected from Borehole Intervals (a) 60-3, (b) 59-2, and (c) 76-3 to the Modeled Fracture Water pH at Representative Model Gridblocks.....	7-43
7.1-17. Modeled Distribution of Cl ⁻ in Fractures and Matrix at One and Four Years during the Heating Phase of the DST, and at the End of the Cooling Phase (eight years): (a) Fracture (1Y), (b) Matrix (1Y), (c) Fracture (4Y), (d) Matrix (4Y), (e) Fracture (8Y), and (f) Matrix (8Y).....	7-45

FIGURES (Continued)

	Page
7.1-18. Cl ⁻ Concentrations (mg/L) in Water Samples and Condensates Collected from Borehole Intervals (a) 60-3, (b) 59-2, and (c) 76-3 Compared to the Modeled Fracture Water Cl ⁻ and Fracture Liquid Saturations	7-47
7.1-19. SO ₄ ²⁻ Concentrations (mg/L) in Water Samples and Condensates Collected from Borehole Intervals (a) 60-3, (b) 59-2, and (c) 76-3 Compared to the Modeled Fracture Water SO ₄ ²⁻	7-48
7.1-20. Na ⁺ Concentrations (mg/L) in Water Samples and Condensates Collected from Borehole Intervals (a) 60-3, (b) 59-2, and (c) 76-3 Compared to Modeled Na ⁺ Concentrations in Fractures	7-49
7.1-21. Ca ²⁺ Concentrations (mg/L) in Water Samples and Condensates Collected from Borehole Intervals (a) 60-3, (b) 59-2, and (c) 76-3 Compared to Modeled Ca ²⁺ in Fracture Water and Fracture Liquid Saturations.....	7-50
7.1-22. SiO ₂ (aq) Concentrations (mg/L) in Water Samples and Condensates Collected from Borehole Intervals (a) 60-3, (b) 59-2, and (c) 76-3 Compared to Modeled Fracture Water SiO ₂ (aq) Concentrations	7-52
7.1-23. K ⁺ Concentrations (mg/L) in Water Samples and Condensates Collected from Borehole Intervals (a) 60-3, (b) 59-2, and (c) 76-3 Compared to Modeled Fracture Water K ⁺ Concentrations and Fracture Liquid Saturations.....	7-53
7.1-24. HCO ₃ ⁻ Concentrations (mg/L) in Water Samples and Condensates Collected from Borehole Intervals (a) 60-3, (b) 59-2, and (c) 76-3 Compared to Modeled Fracture Water HCO ₃ ⁻ Concentrations	7-54
7.1-25. Mg ²⁺ Concentrations (mg/L) in Water Samples and Condensates Collected from Borehole Intervals (a) 60-3, (b) 59-2, and (c) 76-3 Compared to Modeled Fracture Water Mg ²⁺ Concentrations.....	7-58
7.1-26. NO ₃ ⁻ Concentrations (mg/L) in Water Samples Collected from Borehole Intervals (a) 60-3, (b) 59-2, and (c) 76-3 Compared to Modeled Fracture Water NO ₃ ⁻ Concentrations.....	7-59
7.1-27. F ⁻ Concentrations (mg/L) in Water Samples Collected from Borehole Intervals (a) 60-3, (b) 59-2, and (c) 76-3 Compared to Modeled Fracture Water F ⁻ Concentrations	7-60
7.1-28. Modeled Volume Percent Change in Calcite in Fractures Compared to Observed Calcite Location in Borehole 54: (a) November 2000 (35 months of heating) and (b) 8 Years.....	7-63
7.1-29. Modeled Volume Percent Amorphous Silica in Fractures Compared to Observed Amorphous Silica Locations in Borehole 54: (a) November 2000 (35 months of heating) and (b) 8 Years	7-63
7.1-30. Modeled Volume Percent Anhydrite in Fractures Compared to Observed Gypsum Locations in Borehole 54: (a) November 2000 (35 months of heating) and (b) 8 Years.....	7-64
7.1-31. Change in Fracture Porosity after Four Years of Heating and at the End of the Cooling Period (8 years) for Simulations Using the Initial Conditions at the 14.4 mm/yr Infiltration Rate (a, b) and for the 1.446 mm/yr Rate (c, d).....	7-65

FIGURES (Continued)

	Page
7.1-32. Change in Matrix Porosity after (a) Four Years of Heating and (b) End of the Cooling Phase (eight years)	7-66
7.1-33. Measured Activities of ¹⁴ C (expressed as a fraction of modern carbon) in CO ₂ from Gas Collected in Several Hydrology Boreholes over Most of the Heating Phase of the DST	7-68
7.1-34. Measured Activities of ¹⁴ C (expressed as a fraction of modern carbon) Compared to Measured CO ₂ (corrected for water vapor removal) from Gas Collected in Some Hydrology Boreholes over Most of the Heating Phase of the DST	7-69
8-1. Key Findings of the THC Seepage Model	8-2
C.4-1. α-Cristobalite Solubility	C-15
C.4-2. β-Cristobalite solubility	C-18
C.6-1. Plot of YMP Pore-Water Analyses Relative to the Albite-Stellerite Equilibrium Boundary	C-25
I-1. Design Information for Drift Geometry	I-1
I-2. Design Information for Drip Shield Dimensions	I-2
I-3. Design Information for Waste Package Dimensions	I-3
M-1. Standardization Curve for CO ₂ Data	M-12
Q-1. Folders of CUTCHEM on the LBNL PC DOE # 6574913	Q-12
Q-2. List of Source Files and the Executable File in Subfolder \Code	Q-13
Q-3. List of the ReadMe File of CUTCHEM V2.0 Installation Tests	Q-13
Q-4. List of Files in Subfolder \Installation Test\ITC1\input	Q-13
Q-5. List of Files in Subfolder \Installation Test\ITC1\output	Q-13
Q-6. List of Files in Subfolder \Installation Test\ITC2\input	Q-14
Q-7. List of Files in Subfolder \Installation Test\ITC2\output	Q-14
Q-8. List of Files in Subfolder \Installation Test\ITC3\input	Q-14
Q-9. List of Files in Subfolder \Installation Test\ITC3\output	Q-15
Q-10. List of Source Files and the Executable File in Subfolder \Code	Q-15
Q-11. List of Files in Subfolder \Installation Test\ITC1\input	Q-15
Q-12. List of Files in Subfolder \Installation Test\ITC1\output	Q-16
Q-13. List of Files in Subfolder \Installation Test\ITC2\input	Q-16
Q-14. List of Files in Subfolder \Installation Test\ITC2\output	Q-16
Q-15. List of Files in Subfolder \Installation Test\ITC3\input	Q-17
Q-16. List of Files in Subfolder \Installation Test\ITC3\output	Q-17

INTENTIONALLY LEFT BLANK

TABLES

	Page
3-1. Qualified Software Used.....	3-2
4.1-1. DTNs Used as Sources of Hydrologic, Thermal, and Geochemical Data for Direct Input to the THC Seepage Model	4-1
4.1-2. Summary of Invert Hydrological and Thermal Properties	4-5
4.1-3. Top and Bottom Boundary Conditions for the THC Model.....	4-6
4.1-4. Average Infiltration Fluxes (in mm/yr) for Different Climate Periods.....	4-7
4.1-5. Drift and Committed Materials Model Parameters.....	4-13
4.2-1. Applicable Project Requirements and YMRP Acceptance Criteria	4-15
6-1. Summary of the Development of the THC Seepage Model	6-2
6.1-1. Included Features, Events, and Processes Addressed in This Report.....	6-5
6.2-1. Input Pore-Water Compositions for the THC Seepage Model	6-16
6.2-2. Mineral, Aqueous, and Gaseous Species Used in the THC Seepage Model	6-20
6.2-3. Smectite Composition (wt %) from Bish et al. (1996 [DIRS 101430], Table 1)	6-22
6.2-4. Repository Unit Bulk Rock Composition (TSw), Measured Biotite and Plagioclase Phenocryst Compositions, and Calculated Ideal Endmember Compositions for Other Primary Minerals	6-24
6.4-1. Dryout Mineral Assemblages and Sequences Considered in This Study	6-40
6.4-2. Summary of Hydrologic and Thermal Properties of Repository Units	6-47
6.5-1. Vertical Mesh Dimensions and Geologic Contacts in the THC Seepage Model (Tptpll Unit).....	6-52
6.5-2. Effective Drift Spacings Considered for the THC Seepage Model	6-53
6.5-3. THC Seepage Model Boundary Conditions	6-56
6.5-4. THC Seepage Model Predictive Simulations	6-59
6.5-5. Summary Output Data Files and DTNs Showing Predicted Water Composition and Plots for THC Seepage Model Simulations	6-60
6.5-6. Predicted Times at Which Boiling Ceases in Fractures and Drift Wall Rewets.....	6-65
6.6-1. Summary Output Data Files and DTNs for Sensitivity Analyses.....	6-96
6.6-2. Time Discretization Analysis.....	6-98
6.6-3. Total Residuals at near 2,000 Years for Three Dryout Mineral Assemblages	6-113
6.6-4. Sensitivity to Reaction Rates	6-120
6.7-1. Summary of Uncertainties Affecting Chemical Processes in the THC Seepage Model.....	6-126
7-1. Sources of Data Used for Model Validation or Corroboration.....	7-3
7.1-1. Input DTNs Used for Estimating Times/Dates of Power Reductions and Outages for DST THC Submodel Simulations.....	7-8
7.1-2. Step-Wise Averaged Power Data for the DST THC Simulations	7-9
7.1-3. Measured Concentrations in Tptpmn Pore Water from Alcove 5 and Chemistry of Water Samples from Hydrology Boreholes.....	7-29
A-1. Mineral Initial Volume Fractions (1).....	A-1
A-2. Mineral Initial Volume Fractions (2).....	A-3
B-1. Primary Mineral Initial Reactive Surface Areas (1)	B-1
B-2. Primary Mineral Initial Reactive Surface Areas (2)	B-3
C.1-1. Thermodynamic Data: Minerals and Gases.....	C-2

TABLES (Continued)

	Page
C.1-2. Thermodynamic Data: Aqueous Species	C-6
C.2-1. Values of Effective Ionic Radii ($r_{e,j}$)	C-9
C.3-1. Verification of Suitability for Intended Use of the Mordenite Molar Volume from Chipera and Apps (2001 [DIRS 171017], Table 3)	C-11
C.4-1. Amorphous Silica Equilibrium Constants and Solubility	C-12
C.4-2. α -Cristobalite Equilibrium Constants and Solubility	C-15
C.4-3. Equilibrium Constants and Solubility for “ β -cristobalite”	C-17
C.4-4. Equilibrium Constants of Tridymite and Quartz	C-19
C.8-5. Oxide and Hydroxide Dissociation Reactions Used for Glass Log(K) Calculation	C-30
D-1. Waste Package Average Heat Transfer	D-1
E-1. Effective Thermal Conductivity for In-Drift Open Spaces during Preclosure	E-1
E-2. Effective Thermal Conductivity for In-Drift Open Spaces during Postclosure (no backfill)	E-2
F-1. Parameters for Fracture Permeability Modification	F-1
G-1. List of Model Output DTNs	G-1
H.2-1. Mineral Dissolution/Precipitation Reaction Rate Constants ($k_{+/-}$) and Activation Energies (E_a) to Be Qualified	H-2
J.2-1. Two-Dimensional Subgrid Development: Input and Output files	J-2
J.5-1. Comparison of Adopted and Revised Values of Elevation and Thickness of Hydrostratigraphic Units for the THC Seepage Model	J-8
M-1. Standardization of CO ₂ Concentrations	M-1
O.3.3-1. YMP Zeolite Formulas and Molar Volume Qualified for Use	O-3
O.3.4-1. Comparison of Glass Compositions	O-5

ACRONYMS AND ABBREVIATIONS

BET	Brunauer, Emmet, Teller (static volume method)
CR	condition report
DST	Drift Scale Test
DTN	data tracking number
ECRB	Enhanced Characterization of the Repository Block
ESF	Exploratory Studies Facility
FEPs	features, events, and processes
$K_{th_{max}}$	maximum thermal conductivity
LA	license application
LBNL	Lawrence Berkeley National Laboratory
MSA	Mineralogical Society of America
MSTHM	multiscale thermohydrologic model
NCG	noncondensable gas
TDMS	Technical Data Management System
TH	thermal-hydrologic
THC	thermal-hydrologic-chemical
TSPA	total system performance assessment
TWP	technical work plan
UZ	unsaturated zone
YMP	Yucca Mountain Project
YMRP	<i>Yucca Mountain Review Plan, Final Report</i>
1-D	one-dimensional
2-D	two-dimensional
3-D	three-dimensional

Major Hydrogeologic Units

PTn	Paintbrush Tuff nonwelded hydrogeologic unit
TSw	Topopah Spring welded hydrogeologic unit
TCw	Tiva Canyon welded hydrogeologic unit
Tptpul	Topopah Spring Tuff upper lithophysal zone
Tptpmn	Topopah Spring Tuff middle nonlithophysal zone
Tptpll	Topopah Spring Tuff lower lithophysal zone
Tptpln	Topopah Spring Tuff lower nonlithophysal zone

Geologic and Model Layer Abbreviations

Stratigraphic Unit ^a					Abbreviation ^a	UZ Model Layer ^b
Group	Formation	Member	Zone	Subzone		
	Alluvium and Colluvium				Qal, Qc	
	Timber Mountain Group				Tm	
	Rainier Mesa Tuff				Tmr	
	Paintbrush Group				Tp	
				Post-tuff unit "x" bedded tuff	Tpbt6	
				Tuff unit "x"	Tpki (informal)	
				Pre-tuff unit "x" bedded tuff	Tpbt5	
	Tiva Canyon Tuff				Tpc	
		Crystal-Rich Member			Tpcr	
			Vitric zone		Tpcrv	
			Nonwelded subzone		Tpcrv3	
			Moderately welded subzone		Tpcrv2	
			Densely welded subzone		Tpcrv1	
			Nonlithophysal subzone		Tpcrn	tcw11
			Subvitrophyre transition subzone		Tpcrn4	
			Pumice-poor subzone		Tpcrn3	
			Mixed pumice subzone		Tpcrn2	
			Crystal transition subzone		Tpcrn1	
			Lithophysal zone		Tpcrl	
			Crystal transition subzone		Tpcrl1	
		Crystal-Poor Member			Tpcp	
			Upper lithophysal zone		Tpcpul	
			Spherulite-rich subzone		Tpcpul1	
			Middle nonlithophysal zone		Tpcpmn	
			Upper subzone		Tpcpmn3	
			Lithophysal subzone		Tpcpmn2	tcw12
			Lower subzone		Tpcpmn1	
			Lower lithophysal zone		Tpcpll	
			Hackly-fractured subzone		Tpcpllh	
			Lower nonlithophysal zone		Tpcpln	

Geologic and Model Layer Abbreviations (Continued)

Stratigraphic Unit ^a				Abbreviation ^a	UZ Model Layer ^b
Group	Formation	Member	Zone	Subzone	
				Hackly subzone	Tpcplnh
				Columnar subzone	Tpcplnc
				Vitric zone	Tpcpv
				Densely welded subzone	Tpcpv3
				Moderately welded subzone	Tpcpv2
				Nonwelded subzone	Tpcpv1
				Pre-Tiva Canyon bedded tuff	Tpbt4
				Yucca Mountain Tuff	Tpy
				Pre-Yucca Mountain bedded tuff	Tpbt3
				Pah Canyon Tuff	Tpp
				Pre-Pah Canyon bedded tuff	Tpbt2
				Topopah Spring Tuff	Tpt
				Crystal-Rich Member	Tptr
				Vitric zone	Tptrv
				Nonwelded subzone	Tptrv3
				Moderately welded subzone	Tptrv2
				Densely welded subzone	Tptrv1
				Nonlithophysal zone	Tptrn
				Dense subzone	Tptrn3
				Vapor-phase corroded subzone	Tptrn2
				Crystal transition subzone	Tptrn1
				Lithophysal zone	Tptrl
				Crystal transition subzone	Tptrl1
				Crystal-Poor Member	Tptp
				Lithic-rich zone	Tptpf or Tptrf
				Upper lithophysal zone	Tptpul
				Middle nonlithophysal zone	Tptpmn
				Nonlithophysal subzone	Tptpmn3
				Lithophysal bearing subzone	Tptpmn2
				Nonlithophysal subzone	Tptpmn1
				Lower lithophysal zone	Tptpll
				Lower nonlithophysal zone	Tptpln

Geologic and Model Layer Abbreviations (Continued)

Stratigraphic Unit ^a					Abbreviation ^a	UZ Model Layer ^b
Group	Formation	Member	Zone	Subzone		
			Vitric zone		Ttpv	tsw38
			Densely welded subzone		Ttpv3	
			Moderately welded subzone		Ttpv2	tsw39
			Nonwelded subzone		Ttpv1	ch1
		Pre-Topopah Spring bedded tuff			Tpbt1	
	Calico Hills Formation				Ta	ch2, ch3, ch4, ch5
		Bedded tuff			Tacbt	ch6
	Crater Flat Group				Tc	pp4
	Prow Pass Tuff				Tcp	
			Prow Pass Tuff upper vitric nonwelded zone		Tcpuv	pp3
			Prow Pass Tuff upper crystalline nonwelded zone		Tcpuc	
			Prow Pass Tuff moderately-densely welded zone		Tcpmd	pp2
			Prow Pass Tuff lower crystalline nonwelded zone		Tcplc	
			Prow Pass Tuff lower vitric nonwelded zone		Tcplv	pp1
		Pre-Prow Pass Tuff bedded tuff			Tcpbt	
	Bullfrog Tuff				Tcb	bf3
			Bullfrog Tuff upper vitric nonwelded zone		Tcbuv	
			Bullfrog Tuff upper crystalline nonwelded zone		Tcbuc	bf2
			Bullfrog Tuff welded zone		Tcbmd	
			Bullfrog Tuff lower crystalline nonwelded zone		Tcblc	bf2
			Bullfrog Tuff lower vitric nonwelded zone		Tcblv	
		Pre-Bullfrog Tuff bedded tuff			Tcbbt	
	Tram Tuff				Tct	
			Tram Tuff upper vitric nonwelded zone		Tctuv	

Geologic and Model Layer Abbreviations (Continued)

Stratigraphic Unit ^a					Abbreviation ^a	UZ Model Layer ^b
Group	Formation	Member	Zone	Subzone		
				Tram Tuff upper crystalline nonwelded zone	Tctuc	tr3
				Tram Tuff moderately-densely welded zone	Tctmd	
				Tram Tuff lower crystalline nonwelded zone	Tctlc	
				Tram Tuff lower vitric nonwelded zone	Tctlv	tr2
				Pre-Tram Tuff bedded tuff	Tctbt	
				Lava and flow breccia (informal)	Tll	
				Bedded tuff	Tllbt	
				Lithic Ridge Tuff	Tr	
				Bedded tuff	Tlrbt	
				Lava and flow breccia (informal)	Tll2	
				Bedded tuff	Tllbt	
				Lava and flow breccia (informal)	Tll3	
				Bedded tuff	Tll3bt	
				Older tuffs (informal)	Tt	
				Unit a (informal)	Tta	
				Unit b (informal)	Ttb	
				Unit c (informal)	Ttc	
				Sedimentary rocks and calcified tuff (informal)	Tca	
				Tuff of Yucca Flat (informal)	Tyf	
				Pre-Tertiary sedimentary rock		
				Lone Mountain Dolomite	Slm	
				Roberts Mountain Formation	Srm	

Sources: ^a BSC 2004 [DIRS 170029], Table 6-2.

^b BSC 2004 [DIRS 169855], Table 6-5.

CHEMICAL ABBREVIATIONS**Elements**

Al	aluminum
C	carbon
Ca	calcium
Cl	chlorine
F	fluorine
Fe	iron
H	hydrogen
K	potassium
Mg	magnesium
N	nitrogen
Na	sodium
O	oxygen
S	sulfur
Si	silicon

Chemical Compounds, Aqueous Species, and Gases

AlO_2^-	aluminum primary aqueous species (essentially same as $\text{Al}(\text{OH})_4^-$); used here to describe total aqueous aluminum concentrations as AlO_2^-
CO_2	carbon dioxide gas
H_2O	water
HCO_3^-	bicarbonate aqueous species; used here to describe total aqueous carbon concentration
HFeO_2^0	iron primary aqueous species (essentially same as $\text{Fe}(\text{OH})_3^0$); used here to describe total aqueous iron concentrations as HFeO_2^0
K_2SO_4	potassium sulfate (solid; mineral name: arcanite)
MgSO_4	magnesium sulfate (solid)
Na_2SO_4	sodium sulfate (solid; mineral name: thenardite)
NaCl	sodium chloride (solid; mineral name: halite)
NaNO_3	sodium nitrate (solid)
NO_3^-	nitrate aqueous species

CHEMICAL ABBREVIATIONS (Continued)

O ₂	oxygen gas
pCO ₂	carbon dioxide partial pressure (in bars)
pH	negative logarithm of the hydrogen ion activity
SiO ₂	silica
SO ₄ ⁻²	sulfate aqueous species

Chemical Units

meq	milliequivalent ($\text{mol} \times 10^3 \times \text{ionic charge}$)
meq/L	milliequivalent per liter of solution
mg/L	milligram per liter of solution
mol	moles
mol/kg	moles per kilogram water (molality)
ppm	parts per million
ppmv	parts per million volume

INTENTIONALLY LEFT BLANK

1. PURPOSE

1.1 BACKGROUND

The purpose of this report is to document the thermal-hydrologic-chemical (THC) seepage model and model simulations. The simulations predict the composition of fracture water that could potentially seep into repository emplacement drifts and the composition of the associated gas phase. The THC seepage model is not used to feed the total system performance assessment (TSPA) for the license application (LA). However, results of this model are intended to provide confidence in the results of simpler models discussed in *Engineered Barrier System: Physical and Chemical Environment* (SNL 2007 [DIRS 177412]), which directly feed TSPA-LA. Specifically, simulation results from the THC seepage model are used for validation of the near-field chemistry model component of the physical and chemical environment model (SNL 2007 [DIRS 177412], Section 7.1.3). The THC seepage model is also intended for use in the bases of screening discussions on features, events, and processes (FEPs) regarding drift-scale coupled THC processes (as described in Section 6.1).

This report has been developed in accordance with SCI-PRO-006, *Models*, and with *Technical Work Plan for: Revision of Model Reports for Near-Field and In-Drift Water Chemistry* (SNL 2007 [DIRS 179287]). The technical work plan (TWP) describes planning information pertaining to the technical scope, content, and management of this report. The plan for validation of the models documented in this report is given in Section 2.2.1 of the TWP (SNL 2007 [DIRS 179287]). Section 3.2 of the TWP (SNL 2007 [DIRS 179287]) identifies Acceptance Criteria 1 to 5 for “Quantity and Chemistry of Water Contacting Engineered Barriers and Waste Forms” (NRC 2003 [DIRS 163274]) as being applicable to this report, and the criteria are addressed in Section 4.2.

This report documents the THC seepage model and a submodel used for validation, the Drift Scale Test (DST) THC submodel. The THC seepage model is a drift-scale process model for predicting the composition of gas and water that could enter waste emplacement drifts and the effects of mineral alteration on flow in rocks surrounding drifts. The DST THC submodel uses a drift-scale process model relying on the same conceptual model and many of the same input data (i.e., physical, hydrologic, thermodynamic, and kinetic) as the THC seepage model. The DST THC submodel is the primary means for validating the THC seepage model. The DST THC submodel compares predicted water and gas compositions, and mineral alteration patterns, with observed data from the DST. The DST THC submodel is used solely for the validation of the THC seepage model and is not used for calibration to measured data. These models provide the framework to evaluate THC coupled processes at the drift scale, predict flow and transport behavior for specified thermal-loading conditions, and predict the evolution of mineral alteration and fluid chemistry around potential waste emplacement drifts.

The work scope for this report is summarized as follows: document the development of the THC seepage model; use sensitivity analyses and model–data comparisons to evaluate model, data, and parameter uncertainties; validate the THC seepage model with the DST THC submodel, by comparison of model results with field data collected during the DST; perform simulations to predict the composition of fracture water that could potentially seep into repository emplacement drifts; submit modeling results to the Technical Data Management System (TDMS) and

document the models; and evaluate model uncertainty and the propagation of uncertainty to other models.

This report (Revision 05) is a major revision of the previous versions, with changes driven primarily by the following condition reports (CRs): 5154, 5383, 6334, 6342, 6344, 6489, 6491, 6492, 6691, 7037, 7187, 7193, 7697, 7811, 8009, 8032, and 8316. A brief description of these CRs is provided in Section 4.2. Approaches followed to address these CRs are described in Section 1.2.1 of *Technical Work Plan for: Revision of Model Reports for Near-Field and In-Drift Water Chemistry* (SNL 2007 [DIRS 179287]), and in Appendix P of this report.

Compared to previous versions, main changes to the model inputs include new thermodynamic and mineral data, an updated set of rock properties consistent with those used in other Near-Field Environment models, and new representative infiltration rates. A new set of four input pore-water compositions are used in the model to represent variability and uncertainty. In addition, simulations are run using a new version of the TOUGHREACT software (see Section 3.1). Sampled output waters from the THC seepage model simulations have been shifted from those at the boiling/wetting front around the drift, to those in zones of highest flux above the modeled waste emplacement tunnel (drift), which closely correspond to areas of highest liquid saturations but essentially discard areas of elevated liquid saturations resulting from a decrease in porosity and permeability. Sensitivity analyses have been conducted to evaluate potential seepage water compositions at cooler locations near the repository edge. The THC seepage model has been revalidated against the DST based on new simulations with updated inputs, and including cooling-phase data, although the validation methodology and criteria did not change from previous versions. This model is intended for use as a process-level corroborative model developed for understanding of DST results and postclosure conditions.

Specific work activities are described in Section 1.2.1 of the TWP (SNL 2007 [DIRS 179287]). This report deviates from the TWP as follows: simulations of the plug-flow and crushed-tuff column experiments were not carried out. The model sensitivity to space discretization (gridding) was not specifically evaluated, although the model sensitivity to time discretization (for a given numerical grid) was evaluated, such that confidence was still gained about the appropriateness of the time/space discretization for simulations presented in this report. In this revision, one-dimensional simulations were carried to 10^5 years instead of 10^6 years.

Previous revisions of this model investigated model sensitivity to other parameters. Those results may be discussed, as applicable, in this document, but not presented in detail. Those developmental model simulations are discussed for comparative purposes to evaluate model uncertainty and sensitivity to model parameters and are not direct inputs to TSPA-LA.

1.2 OVERVIEW OF MODELS

The THC seepage model provides an analysis of the effects of THC processes on percolation water chemistry and gas-phase composition in the near-field host rock around the emplacement drifts. This analysis includes a complete description of the relevant mineral–water interactions in the host rock. Sensitivity studies document the effect of varying certain input parameters, most notably input water compositions and reaction rates.

The DST THC submodel, constructed for the DST, is used to investigate THC processes during the DST and validate the THC modeling approach. The spatial scale and temperatures for the DST are similar to those for current designs of the repository. This similarity, combined with the extended period of operation (four years of heating, ending in January 2002, and continued monitoring during cooling), makes the DST the best available experiment for validating drift-scale THC coupled process models (such as the THC seepage model). Measured data from the DST are used to evaluate and validate the conceptual and numerical models presented here.

The following designations are assigned for description of the work presented in this report:

- THC seepage model (Section 6.5): Developed as a corroborative model to other near-field water–rock interaction models that feed TSPA. In this model, the repository is located in the Tptpll lithostratigraphic unit. Eight simulations, using four different starting pore waters, each at two repository locations (center and edge), provide potential feeds or complementary data for downstream models. Several sensitivity analyses using the current model are also documented here.
- DST THC submodel: DST THC submodel simulations developed for the current revision of this report (Section 7.1). This model is derived from the THC seepage model and used for validation of the THC seepage model. The DST is located in the middle nonlithophysal unit (Tptpmn), but the results are applicable to all the host rock lithostratigraphic units as discussed below.

As discussed later in this report, the THC seepage model is located in the Tptpll lithostratigraphic unit, but is run using a range of input water compositions from various host rock lithostratigraphic units (including the Tptpmn, Tptpll, and Tptpul units) that express the natural variability in pore-water compositions. The range of model results from the use of these different water compositions is expected to cover most of the variability associated with other factors such as host rock unit, infiltration rate, and other model conceptualizations discussed in Section 6.3. Also, all the host rock lithostratigraphic units are mineralogically similar (DTN: GS000308313211.001 [DIRS 162015]; Peterman and Cloke 2002 [DIRS 162576]). Therefore, it is assumed (Section 5) that the THC model results calculated for the Tptpll unit (taking into account the variability introduced by the different input water compositions) are applicable to the other repository host rock units.

1.3 MODEL LIMITATIONS

The THC seepage model has stated limitations associated with its mathematical formulation, certain assumptions (Section 5), and approximations in model development (Section 6.4.6).

The THC seepage model is designed for simulation of speciation and mineral precipitation for evaporatively concentrated waters with ionic strength < 4 molal. At ionic strengths > 4 molal, the model uses specific approximations to represent the behavior of soluble salts. While the method is consistent with the activity model implemented here and ensures numerical stability, it introduces uncertainty with respect to the relative concentrations of soluble species (e.g., NO_3^- and Cl^-) when the salts are first redissolved. The sensitivity of model results to approximations regarding salt precipitation at ionic strengths > 4 molal (Section 6.4.1) indicate that water

compositions at the initial rewetting stage are not highly sensitive to these approximations. In addition, during this initial rewetting stage, the liquid saturation is low and the associated volume of water is small, immobile, and unlikely to contribute to seepage. This limitation and others affecting the uncertainty of model results, such as the use of average properties to describe thermal, hydrologic, and chemical characteristics of the host rock, are discussed in Section 6.7.1.

Another limitation of the THC seepage model is that it is computationally intensive; hence, the number of sensitivity analyses is limited. These limitations are addressed by evaluating the model sensitivity to key input parameters (Section 6.6), and by comparing model results against data from the DST (Section 7) and laboratory experiments (Dobson et al. 2003 [DIRS 165949]). Also, the model conceptualization and mathematical formulation (Sections 6.2 through 6.4) have been improved, through the successive revisions of this report, to achieve reasonably good agreement (generally to within an order of magnitude) between calculated and measured data.

Although the THC seepage model provides aqueous Fe concentrations as output, these values are not used by downstream models. Because of the paucity of measured Fe values in DST waters, and the large uncertainty in these values due to the low solubility of Fe³⁺ (Section 7.1.11.3), Fe model predictions are not validated, and are presented in THC seepage model results for information only.

The THC seepage model represents a two-dimensional slice across a repository drift, at two representative locations: repository center and repository edge. This approach is expected to closely bound conditions throughout much of the repository. For these reasons, results presented here can be used to reasonably represent potential effects of THC processes on the composition of seepage at all waste package locations.

2. QUALITY ASSURANCE

Development of this report and supporting modeling activities has been determined to be subject to the Yucca Mountain Project (YMP) quality assurance program as indicated in *Technical Work Plan for: Revision of Model Reports for Near-Field and In-Drift Water Chemistry* (SNL 2007 [DIRS 179287]). Approved quality assurance implementing procedures identified in Section 4 of the TWP have been used to conduct and document the activities described in this report. An evaluation in accordance with IM-PRO-002, *Control of the Electronic Management of Information*, has been conducted, and this work is subject to requirements to manage and control electronic data. The evaluation was submitted to the Records Processing Center as part of the TWP records package.

The methods used to control the electronic management of information are described in IM-PRO-002. The model and its associated documentation were developed in accordance with SCI-PRO-006.

This report investigates the effect of drift-scale THC processes on the following safety category barriers that are important to the demonstration of compliance with the postclosure performance objective prescribed in 10 CFR 63.113 [DIRS 180319]:

- Unsaturated zone above the repository
- Unsaturated zone below the repository.

The barriers are classified as “Safety Category” with regard to importance to waste isolation as defined in LS-PRO-0203, *Preparation and Maintenance of the Q-List*. The report contributes to the analyses and modeling data used to support TSPA, but is not directly used by TSPA. The conclusions from this report do not directly impact the engineered features important to pre-closure safety as defined in LS-PRO-0203.

INTENTIONALLY LEFT BLANK

3. USE OF SOFTWARE

3.1 QUALIFIED SOFTWARE

The qualified software used in this study is listed in Table 3-1. The software has been qualified, and meets the requirements of IM-PRO-003, *Software Management*. The software is adequate and appropriate for the intended use, and it is used strictly within the range of validation. The software performs the functions described in Table 3-1 in the qualified environment described. Input limitations are discussed in table column “Range of Use.” Unless specifically listed in Table 3-1, there are no limitations on the software output, provided that the appropriate input limitations are observed.

TOUGHREACT Version 3.1.1 (TOUGHREACT V3.1.1 [DIRS 180937], STN: 10396-3.1.1-00) is the primary code used for the DST THC submodel and THC seepage model. AMESH Version 1.0 (AMESH V.1.0 [DIRS 147561], STN: 10045-1.0-00) is used to generate grids for the models. Other routines listed in Table 3-1 are used for various data pre- and post-processing tasks. Note that TOUGHREACT V3.1.1 and CUTCHEM Version 2.0 (CUTCHEM V.2.0 [DIRS 181352], STN: 10898-2.0-00) were used prior to qualification. The baselined executable files are identical to the versions used to conduct the modeling, as documented in Appendix Q.

This report documents the DST THC submodel and the THC seepage model as described in Section 1. The input and output files for the model runs presented in this report are listed in Appendix G.

3.2 EXEMPT SOFTWARE

The commercial, off-the-shelf software code Microsoft Excel has been used in the preparation of this report in an exempt manner to do basic calculations and statistical operations based on the internal functions of the code. TOUGHREACT V3.1.1 model output is also exported to Excel for graphing and data presentation, and the primary output DTNs for this model (Appendix G) contain data summarized in Excel spreadsheets. The individual spreadsheets are called out in the DTNs where they are used and are summarized in Appendix G. As discussed in Appendix G, *readme.doc* files in each data tracking number (DTN) contain a general description of the spreadsheets contained therein, and worksheets in the Excel spreadsheets document in detail the calculations that are performed in each spreadsheet. Plots in Section 7.1 were produced using the scientific plotting software programs Generic Mapping Tools and Abcissa.

Table 3-1. Qualified Software Used

Software Name and Version	Software Tracking Number	Platform	Operating System	Range of Use	Brief Description
TOUGHREACT V3.1.1 [DIRS 180937]	10396-3.1.1-00	Alpha System	OSF1 V5.1	Porous and fractured media in a pressure-temperature-composition (P-T-X) range defined by the P-T-X range of the thermodynamic database. Ionic strength limit of ~4 molal (NaCl-dominant solutions).	Used to calculate coupled thermal-hydrologic and chemical processes for kinetic and/or equilibrium mineral-water reactions and equilibrium gas-water reactions.
		Linux Custer	CAOS Linux	Porous and fractured media in a pressure-temperature-composition (P-T-X) range defined by the P-T-X range of the thermodynamic database. Ionic strength limit of ~4 molal (NaCl-dominant solutions).	Used to calculate coupled thermal-hydrologic and chemical processes for kinetic and/or equilibrium mineral-water reactions and equilibrium gas-water reactions.
SUPCRT92 V1.0 [DIRS 153218]	10058-1.0-00	PC	PC Windows	Pressure-temperature-composition (P-T-X) range defined by the P-T-X range of the input reference thermodynamic data and equation of state parameters (1 to 5,000 bar and 0°C to 1,000°C)	Used to calculate the standard molal thermodynamic properties of minerals, gases, aqueous species, and reactions from 1 to 5,000 bars and 0°C to 1,000°C
AMESH V1.0 [DIRS 147561]	10045-1.0-00	Sun UltraSparc	SUNOS 5.5.1	1-D, 2-D, or 3-D grids of any size	Generates discrete 1-D, 2-D, or 3-D grids for numerical modeling of flow and transport problems in which the formulation is based on the integral finite difference method
KREG V1.1 [DIRS 161258]	10318-1.1-00	PC	DOS Emulation	Input database must be in TOUGHREACT V3.1.1 database format. Pressure-temperature-composition (P-T-X) range defined by the P-T-X range of the thermodynamic database.	Used to calculate regression coefficients of log(K) data as a function of temperature for the thermodynamic database of TOUGHREACT V3.1.1
KSWITCH V1.1 [DIRS 161259]	10319-1.1-00	PC	DOS Emulation	Input database must be in TOUGHREACT V3.1.1 database format. Pressure-temperature-composition (P-T-X) range defined by the P-T-X range of the thermodynamic database.	Used to switch component species in the thermodynamic database of TOUGHREACT V3.1.1 and above
THERMOCHK V1.1 [DIRS 161262]	10895-1.1-00	PC	DOS Emulation	Input database must be in TOUGHREACT V3.1.1 (and above) database format, and molecular weights must be provided for all species listed (aqueous, solid, and gas).	Used to check the consistency (mass balance and charge balance) of reactions in the thermodynamic database of the reactive transport code TOUGHREACT V3.1.1 and above

Table 3-1. Qualified Software Used (Continued)

Software Name and Version	Software Tracking Number	Platform	Operating System	Range of Use	Brief Description
DBCONV V1.0 [DIRS 161263]	10893-1.0-00	PC	DOS Emulation	Input database must be in EQ3/6 database format, with pressure-temperature-composition (P-T-X) range defined by the P-T-X range of the thermodynamic database.	Used to convert the YMP EQ3/6 thermodynamic database to a format suitable for input into the reactive transport model TOUGHREACT V3.1.1
CUTCHEM V2.0 [DIRS 181352]	10898-2.0-0.0	PC	DOS Emulation	Only for use with TOUGHREACT output files <i>TEC_nnn.dat</i> . Limit of 30 extracted points per general location per point in time.	Used to extract automatically data from large output data files created by the reactive transport model TOUGHREACT V3.1.1
exclude.f V1.0 [DIRS 153089]	10316-1.0-00	Sun UltraSparc	SUNOS 5.5.1	Only for use with output files from <i>mk_circ2 V1.0</i> and <i>mk_rect2 V1.0</i>	Used to exclude points outside a specified radius so that points will not overlap when output is merged using <i>mergrid.f V1.0</i> for 2-D THC seepage model
assign.f V1.0 [DIRS 153090]	10315-1.0-00	Sun UltraSparc	SUNOS 5.5.1	2-D grids in TOUGH2 MESH format	Used to assign a geologic name to all TOUGH2 elements according to their location in the Z-direction for 2-D THC seepage model
mergrid2.f V1.0 [DIRS 153091]	10314-1.0-00	Sun UltraSparc	SUNOS 5.5.1	Only for use with output files from <i>mk_circ2 V1.0</i> , <i>mk_rect2 V1.0</i> , and <i>exclude V1.0</i>	Used to merge input files into one file for input into AMESH V1.0 for 2-D THC seepage model
<i>mk_circ2 V1.0</i> [DIRS 153092]	10312-1.0-00	Sun UltraSparc	SUNOS 5.5.1	1-D or 2-D grids only	Used to create a radial grid for 2-D THC seepage model
<i>mk_rect2 V1.0</i> [DIRS 153093]	10313-1.0-00	Sun UltraSparc	SUNOS 5.5.1	1-D or 2-D grids only	Used to create orthogonal grid for 2-D THC seepage model
<i>2kgridv1a.for V1.0</i> [DIRS 153067]	10382-1.0-00	PC	DOS Emulation	Only for use with 2-D grids in TOUGH2 format	Generates dual-permeability grids for the TOUGH2 family of codes
<i>mk_grav2.f V1.0</i> [DIRS 153068]	10379-1.0-00	Sun UltraSparc	SUNOS 5.5.1	Only for use with 2-D grids generated by AMESH	Reads AMESH V1.0 output files and creates TOUGH2 V1.4 mesh input file data, namely the gravity vector data and gridblock labeling data
<i>sav1d_dst2d.f V1.0</i> [DIRS 153083]	10381-1.0-00	Sun UltraSparc	SUNOS 5.5.1	Limited to 1-D column for input, and 2-D mesh for output	Creates an INCON file for TOUGH2 input for a 2-D mesh from existing INCON and MESH data for a 1-D column

Table 3-1. Qualified Software Used (Continued)

Software Name and Version	Software Tracking Number	Platform	Operating System	Range of Use	Brief Description
Mrgdrift.f V1.0 [DIRS 153082]	10380-1.0-00	Sun UltraSparc	SUNOS 5.5.1	Limited for use only with a TOUGH2 and TOUGHREACT numerical mesh. The connecting boundaries of the drift and geologic meshes must exactly overlap.	Merges the geologic mesh with the drift mesh for TOUGH2 and TOUGHREACT simulations
EQ3/6 V8.0 [DIRS 162228]	10813-8.0-00	PC	WINDOWS 2000, WIN NT 4.0, WIN 98, WIN 95	Pressure-temperature-composition (P-T-X) range defined by the P-T-X range of the thermodynamic database. Ionic strength limit of typically 1 molal.	Reaction path and equilibrium speciation calculations

NOTE: 1-D = one-dimensional; 2-D = two-dimensional; 3-D = three-dimensional.

4. INPUTS

4.1 DIRECT INPUTS

This section presents all input data used for the THC seepage model (i.e., for the simulations presented in Section 6.5). Source DTNs for these data are listed in Table 4.1-1. The qualified status of all direct inputs is shown in the Document Input Reference System database. Because this report documents models of coupled phenomena, a wide variety of input data is required. The appropriateness of technical product outputs directly used by this model is discussed in the following sections, and they are justified for intended use in this model. Input data and parameter uncertainties are further addressed in Sections 6 and 7. Section 7 documents model inputs that are related to model validation.

4.1.1 Hydrologic and Thermal Properties

All sources of direct inputs for hydrologic and thermal parameters are listed in Table 4.1-1; other DTNs and data sources discussed in this section are presented for corroborative or informational purposes only. Specific values of hydrologic and thermal properties for the repository hydrogeologic model units tsw33, tsw34, and tsw35 (Topopah Spring Tuff upper-lithophysal, middle-nonlithophysal, and lower-lithophysal units, respectively), including calculated data, are summarized in Table 6.4-2.

Modeling analyses utilized data from the “mean-calibrated” hydrologic property sets for the present-day climate. The data sets include properties that are calibrated, such as fracture and matrix permeabilities and van Genuchten parameters, and properties that are obtained from field measurements, such as porosity, heat capacity, and thermal conductivity. DTNs for model-boundary temperatures are also included in Table 4.1-1.

Table 4.1-1. DTNs Used as Sources of Hydrologic, Thermal, and Geochemical Data for Direct Input to the THC Seepage Model

Source DTN	Data/Parameter Description ^a
Hydrologic and Thermal Rock Properties	
LB0205REVUZPRP.001 [DIRS 159525] (file: <i>FRACTURE_PROPERTY.xls</i>)	Fracture parameters: permeability, porosity, frequency, and fracture/matrix interface area
LB0208UZDSCPMI.002 [DIRS 161243] (file: <i>drift-scale calibrated properties for mean infiltration2.xls</i>)	Matrix porosity, and matrix and fracture residual saturation
LB0610UZDSCP30.001 [DIRS 179180] (file: <i>Calibrated Parameter_R113_30%.doc</i> in <i>lb0610uzdscp30_001.zip</i>)	Matrix permeability, fracture and matrix van Genuchten α and m ; active fracture parameter γ
LB0704THRMLPRP.001 [DIRS 181318] (file: <i>LB0704THRMLPRP.001.xls</i> in <i>LB0704THRMLPRP.001.zip</i>)	Thermal properties: dry- and wet-rock thermal conductivity, grain specific heat capacity, and grain density
LB06123DPDUZFF.001 [DIRS 178587] (file: <i>pd_30.dat</i>)	30th percentile infiltration rates: average infiltration rate for present-day climatic conditions
LB07013DMOUZFF.001 [DIRS 179064] (file: <i>mo_30.dat</i>)	30th percentile infiltration rates: average infiltration rate for monsoon climatic conditions

Table 4.1-1. DTNs Used as Sources of Hydrologic, Thermal, and Geochemical Data for Direct Input to the THC Seepage Model (Continued)

Source DTN	Data/Parameter Description ^a
LB07013DGTUZZFF.001 [DIRS 179066] (file: <i>gt_30.dat</i>)	30th percentile infiltration rates: average infiltration rate for glacial transition climatic conditions
SN0002T0872799.009 [DIRS 153364] (file: <i>tough2-input_noBF.txt</i> in <i>effKth_noBF.ZIP</i>)	Effective thermal conductivities for in-drift open spaces (see Appendix E)
MO0703PAHYTHRM.000 [DIRS 182093] (files: <i>Kozeny Rev01 13Jul07.xls</i> and <i>thermalk_vc.xls</i> ; and files: <i>arya_original data interpretation 4 13Jul07.xls</i> and <i>Genuchten Properties 13Jul07.xls</i> in <i>rev01.zip/Residual Saturation of_15.zip</i>)	Invert properties (see Table 4.1-2)
Heat Load	
MO0701VENTCALC.000 [DIRS 179085] (file: <i>Base Case Analysis Rev01.xls</i> , worksheet: "Ventilation Efficiency")	Ventilation efficiency
MO0702PASTREAM.001 [DIRS 179925] (file: <i>DTN-Inventory-Rev00.xls</i> , worksheet: "decay curves")	Line thermal load
Mineralogical Data	
SN0307T0510902.003 [DIRS 164196] (file: <i>rock_grain_heat_capacity (edited).xls</i> , worksheet: "Mineralogy_abundances")	Average Yucca Mountain mineral abundances
LA0009SL831151.001 [DIRS 153485] (Table S00413_002)	Fracture mineral abundances (Single Heater Test)
LA9912SL831151.001 [DIRS 146447] (Table S00013_001)	Fracture mineral abundances (Drift Scale Test)
LA9912SL831151.002 [DIRS 146449] (Table S00014_001)	Fracture mineral abundances (Drift Scale Test)
GS000308313211.001 [DIRS 162015] (Table S00224_001)	Bulk rock compositions for derivation of sanidine groundmass composition
LB02081DKMGRID.001 [DIRS 160108] (file: <i>boreholes.mck</i>)	Model layer elevations for assignment of mineralogy
LA9908JC831321.001 [DIRS 113495] (file: <i>SD9_well</i>)	Model layer geologic designations for assignment of mineralogy
Thermodynamic Data	
SN0612T0502404.014 [DIRS 178850] (file: <i>data0.ymp.R5</i>)	Thermodynamic data for aqueous species, gases and minerals: equilibrium constants, molecular weights, molar volumes (see Appendix C)
SN0609T0502404.012 [DIRS 179067] (file: <i>data0.ypf.R2</i>)	Thermodynamic data for solid salts: equilibrium constants, molecular weights, molar volumes (see Appendix C)
MO0009THRMODYN.001 [DIRS 152576] (file: <i>data0.YMP.R0</i>)	Thermodynamic data for α -cristobalite and opal-CT (see Appendix C)

Table 4.1-1. DTNs Used as Sources of Hydrologic, Thermal, and Geochemical Data for Direct Input to the THC Seepage Model (Continued)

Source DTN	Data/Parameter Description ^a
Analytical Water and Gas Chemistry Data	
MO0005PORWATER.000 [DIRS 150930] (file: <i>S00281_00</i>)	Analysis of pore-water sample ESF-HD-PERM-3/34.8-35.1
GS060908312272.004 [DIRS 179065] (file: <i>GS060908312272_004.xls</i>)	Analysis of pore-water sample HD-PERM-3/56.7-57.1
GS030408312272.002 [DIRS 165226] (file: <i>PoreWater.xls</i>)	Analysis of pore-water sample SD-9/1184.7-1184.8
GS031008312272.008 [DIRS 166570] (file: <i>PW Data Package.xls</i>)	Analysis of pore water sample ESF-THERMALK-017/26.5-26.9
LB0208ISODSTHP.001 [DIRS 161638] (file: <i>TTMR_T6342-1-mc_Rev_02.doc</i> in <i>lb0208isodsth_001.zip</i>)	Analysis of pore gas CO ₂ content in repository rock units
THC Model Grid Data	
LB990501233129.004 [DIRS 111475] ^b (file: <i>3d2kcalib_pc1.mesh</i>)	Stratigraphy (Z coordinates of hydrogeologic units) for central location (column j34) Tptpll THC model
LB0701UZMTHCAL.001 [DIRS 179286] (file: <i>Mesh_thn.v1</i>)	
LB0205REVUZPRP.001 [DIRS 159525] (file: <i>FRACTURE_PROPERTY.xls</i>)	Fracture parameters: permeability, porosity, frequency, and fracture/matrix interface area
LB0701UZMTHCAL.001 [DIRS 179286] (folder: \Output files, file: <i>TH_30% GAS CALIBRATED.OUT</i>)	Top and bottom boundary temperatures, pressure and liquid/gas saturations; extracted for Column "c82," the nearest column to the location of the THC model grid

^a Values of thermal and hydrologic properties used in the THC model are summarized in Table 6.4-2.

^b Qualified for intended use in Appendix J (Section J.5).

4.1.1.1 Transport Properties

Transport parameters considered in the model are diffusion coefficients for aqueous and gaseous species and tortuosities of the fracture, matrix, and engineered system components.

Diffusion coefficients for all aqueous species are direct inputs to the model and entered as the tracer diffusion coefficient of the chloride anion (Cl⁻) at infinite dilution. The aqueous diffusion coefficient of Cl⁻ at infinite dilution is 2.03×10^{-9} m²/s at 25°C (Lide 1993 [DIRS 123032], p. 5-111), which in the model input is rounded to 2.0×10^{-9} m²/s. This handbook source is Established Fact, and requires no further justification for use. This is roughly an intermediate value for the aqueous species considered in the model, some of which have larger diffusion coefficients (such as H⁺), and others of which have smaller values (e.g., Ca²⁺) (Lasaga 1998 [DIRS 117091], p. 315).

These same sources provide inputs for approximating the CO₂ diffusion coefficient from ideal gas behavior as described in Section 6.4.6(7), using direct inputs for molecular diameter (d_m) and molecular weight (M) as follows (unless specified otherwise in Section 6.6.3):

$$d_m = 3.23 \times 10^{-10} \text{ m (Lide 1993 [DIRS 123032], p. 14-19)}$$
$$M = .04401 \text{ kg/mol (Lide 1993 [DIRS 123032], p. 4-50).}$$

Inputs from Lide (1993 [DIRS 123032]) are considered Established Fact and are widely accepted and referenced throughout the scientific community.

The diffusion coefficient for CO₂ is calculated using Equation 6.4-39 (Lasaga 1998 [DIRS 117091], p. 322). This is a standard method of calculating the diffusion coefficient (see, for instance, Bird et al. 1960 [DIRS 103524], Equations 16.4 to 16.9), is quite common, and is justified for use in this document.

Tortuosities are set to 0.7 for fractures, based upon theoretical calculations and experimental measurements given by Penman (1940 [DIRS 109941], p. 441, Equation 5), who estimated that an isotropic porous medium has a tortuosity of $\sqrt{2}^{-1}$ or ~ 0.707 . Penman (1940 [DIRS 109941], p. 461) also obtained an experimentally measured tortuosity value 0.66 based on steady-state vapor diffusion through soil material having porosities of up to 0.7, thus corroborating his own theoretical value. The tortuosity data of Penman (1940 [DIRS 109941]) are qualified for intended use in Appendix O (Section O.2), following the qualification plan in Appendix N (Section N.1). The matrix tortuosity is set at 0.2, with rationale provided, in Section 6.4.6(19).

4.1.1.2 Thermal Properties

The source for the thermal properties data are listed in Table 4.1-1.

4.1.1.3 Effective Thermal Conductivities for In-Drift Open Spaces

The effective thermal conductivities for in-drift open spaces that are used in the THC seepage model are listed in Appendix E. These effective conductivities include the effect of heat radiation. The source for these numbers is an historical DTN: SN0002T0872799.009 [DIRS 153364]. Because the effective thermal conductivity of the rock is much lower than that of the in-drift atmosphere, the rock properties dominate in terms of thermal-hydrologic effects, and the model is not very sensitive to the range of these data.

More recent estimates of thermal conductivities of the in-drift space are available in DTN: SN0407T0507803.026 [DIRS 170939]. These latest calculations of thermal conductivities of the in-drift air space are based on an assumption of heat transport by convection only within the drift and can be found in *In-Drift Natural Convection and Condensation* (SNL 2007 [DIRS 181648], Equations 6.4-10 and 6.4-15). In other words, these calculations do not include the contribution of radiation heat transfer in the calculated effective thermal conductivities. However, for simulations with TOUGHREACT V3.1.1, an effective thermal conductivity inclusive of both convective and radiative heat transfer is more appropriate. As a result, the effective thermal conductivities from DTN: SN0002T0872799.009 [DIRS 153364] are used.

4.1.1.4 Invert Hydrological and Thermal Properties

The invert at the bottom of the drift, to be made of crushed tuff rock material, is treated as a single continuum domain in the THC model. More complex conceptualizations like a dual-continuum approach are possible, as adopted for example in *Multiscale Thermohydrologic Model* (SNL 2007 [DIRS 181383]), but not necessary for the purpose of this report (remember that the THC model deals with flow of water into the emplacement drifts but not flow within them). Most of the hydrological and thermal properties of the invert at the bottom of the drift are obtained from DTN: MO0703PAHYTHRM.000 [DIRS 182093], except as follows. The grain density of the invert materials is adopted from DTN: MO9808RIB00041.000 [DIRS 104850]. The specific heat capacity of the invert material is adopted from DTN: LB0704THRMLPRP.001 [DIRS 181318]. A more detailed discussion of how these properties were obtained can be found in *Multiscale Thermohydrologic Model* (SNL 2007 [DIRS 181383], Appendix X[a]). Table 4.1-2 tabulates the invert hydrological and thermal properties used in the THC model simulations.

Table 4.1-2. Summary of Invert Hydrological and Thermal Properties

Parameter Name	Parameter Value	Source Information
Intrinsic permeability	$4.19 \times 10^{-12} \text{ m}^2$	MO0703PAHYTHRM.000 [DIRS 182093] (file: <i>Kozeny Rev01 13Jul07.xls</i> (method 2) in <i>Rev01.zip</i>)
Porosity	0.224	MO0703PAHYTHRM.000 [DIRS 182093] (file: <i>arya_original data interpretation 4 13Jul07.xls</i> , worksheet: "LTBM-2, Average, revised," in file <i>rev01.zip/Residual Saturation of _15.zip</i>)
Grain density	2,550 kg/m ³	MO9808RIB00041.000 [DIRS 104850] (file: <i>s04175_001_001.pdf</i>)
Specific heat	930 J/kg K	LB0704THRMLPRP.001 [DIRS 181318] (file: <i>LB0704THRMLPRP.001.xls</i> , specific heat capacity of 'tsw35')
Thermal conductivity	0.22 W/m-K	MO0703PAHYTHRM.000 [DIRS 182093] (file <i>thermalk_vc.xls</i> in file <i>rev01.zip</i> , value corresponding to porosity =0.22, particle size 1mm, and temperature 50°C)
van Genuchten ($1/\alpha$)	1,780.59 Pa	MO0703PAHYTHRM.000 [DIRS 182093] (file: <i>Van Genuchten Properties 13Jul07.xls</i> in <i>rev01.zip/Residual Saturation of _15.zip</i>)
van Genuchten 'm'	0.283	MO0703PAHYTHRM.000 [DIRS 182093] (file: <i>Van Genuchten Properties 13Jul07.xls</i> in <i>rev01.zip/Residual Saturation of _15.zip</i>)
Residual saturation	0.15	MO0703PAHYTHRM.000 [DIRS 182093] (taking residual moisture content from file <i>arya_original data interpretation 4 13Jul07.xls</i> , worksheet "LTBM-2, Average, revised," in file <i>rev01.zip/Residual Saturation of _15.zip</i> , and then dividing it by porosity)

4.1.2 THC Model Grid

Direct input sources of the THC model grid data are provided in Table 4.1-1. Stratigraphy is provided by DTN: LB99051233129.004 [DIRS 111475] and fracture properties by DTN: LB0205REVUZPRP.001 [DIRS 159525]. The THC model mesh was developed from these inputs as described in Appendix J.

DTN: LB99051233129.004 [DIRS 111475] is an historical DTN representing the unsaturated zone (UZ) model grid that was current at the time the THC seepage modeling first began. This DTN is qualified for intended use in Appendix J (Section J.5) using data from the most current UZ model grid (DTN: LB0701UZMTHCAL.001 [DIRS 179286]).

4.1.3 Model Boundary Conditions

The THC model grid extends from the land surface at the top to the water table at the bottom. The grid is located at approximately Nevada State Plane coordinates E170604.2 m, N233255.7 m. The location closest to the THC model grid location is Column “c82” in the updated UZ model grid in DTN: LB0701UZMTHCAL.001 [DIRS 179286] (file: *MESH_THN.VI*). This DTN also contains the input and output files for 3-D ambient thermal model and calibration results for the present-day climate of 10th, 30th, 50th, and 90th percentile infiltration maps. For obtaining the top and bottom boundary conditions for the THC model grid, conditions (pressure, temperature, and gas saturation) at the top and bottom, respectively, of Column “c82” were extracted. The calibration results for the 30th percentile infiltration map can be found in file *INFILE_TH_30%_GAS_CALIBRATED.OUT* of DTN: LB0701UZMTHCAL.001 [DIRS 179286]. The top and bottom boundary conditions of the THC model grid are thus those of gridblocks “TP TPc82” (top of Column “c82”) and “BT BTc82” (bottom of Column “c82”), respectively. The top and bottom boundary conditions so obtained are listed in Table 4.1-3.

Table 4.1-3. Top and Bottom Boundary Conditions for the THC Model

Boundary	Boundary Condition
Top boundary for THC model (ground surface)	T = 16.02°C Sg = 1.000 P = 84,610 Pa
Bottom boundary for THC model (water table)	T = 32.0°C Sg = 0.000 P = 91,762 Pa

Source: DTNs: LB0701UZMTHCAL.001 [DIRS 179286],
file: *TH_30%_GAS_CALIBRATED.OUT*.

NOTE: The gas saturation (Sg) in element “TP TPc82” and “BT BTc82” in file *TH_30%_GAS_CALIBRATED.OUT* are 0.98791 and 0.001, respectively. These values have been rounded to 1.0 (only air present) and 0.0 (only water present) for input to the THC model.

4.1.4 Mean Infiltration Rates

The infiltration fluxes applied at the top boundary of the THC model grid are 7.96, 12.89, and 20.45 mm/yr, respectively, for present-day, monsoon, and glacial climatic conditions. These input infiltration fluxes correspond to the mean 30th percentile infiltration and represent the averages over the entire 3-D UZ model domain as described in *UZ Flow Models and Submodels* (SNL 2007 [DIRS 175177]). For present-day climatic conditions, the mean infiltration flux (7.96 mm/yr) can be found in the file *pd_30.dat* in DTN: LB06123DPDUZFF.001 [DIRS 178587]. Similarly, for the monsoon climate conditions, the mean infiltration flux can be found in file *mo_30.dat* in DTN: LB07013DMOUZFF.001 [DIRS 179064]. Finally, the mean infiltration flux (20.45 mm/yr) for the glacial transition can be found in file *gt_30.dat* in DTN: LB07013DGTUZZFF.001 [DIRS 179066]. For all these cases, the mean infiltration can be found next to the keyword “GENER” in the cited files (*pd_30.dat*, *mo_30.dat*, and *gt_30.dat*).

Various mean (averaged over the entire 3-D UZ model domain) infiltration fluxes are reported in *UZ Flow Models and Submodels* (SNL 2007 [DIRS 175177]) for different climate conditions and corresponding to the 10th, 30th, 50th, and 90th percentile mapping of the infiltration fluxes. For convenience, these different mean infiltration fluxes are reproduced in Table 4.1-4, which is taken from from *UZ Flow Models and Submodels* (SNL 2007 [DIRS 175177]). Of these, the 30th percentile infiltration scenario is chosen as the base case (or reference) for the simulations in this report. The primary justification for this selection is that a conservative approach on seepage is required. The mean infiltration fluxes (with mean values of 3.03, 6.74, and 11.03 mm/yr, respectively, for present-day, monsoon, and glacial-transition climates) for the 10th percentile scenario was thought to be not conservative enough as far as seepage is concerned. This is a reasonable approach, as it is unlikely that seepage will happen for the 10th percentile scenario if no seepage is observed in the 30th percentile case. Sensitivity to infiltration fluxes (with respect to seepage) is determined in *THC Sensitivity Study of Heterogeneous Permeability and Capillarity Effects* (SNL 2007 [DIRS 177413]) by performing simulations with infiltration fluxes ten times as large as the base-case infiltration fluxes (the 30th percentile case). The higher end of the infiltration fluxes (the 50th and 90th percentile scenarios) is, thus, covered through sensitivity runs presented in the THC sensitivity study (SNL 2007 [DIRS 177413]).

Table 4.1-4. Average Infiltration Fluxes (in mm/yr) for Different Climate Periods

Scenario	Present-Day	Monsoonal	Glacial-Transition
10th percentile	3.03	6.74	11.03
30th percentile	7.96	12.89	20.45
50th percentile	12.28	15.37	25.99
90th percentile	26.78	73.26	46.68

Source: SNL 2007 [DIRS 175177].

4.1.5 Thermal Load and Ventilation Efficiency

The thermal output of individual waste canisters placed into drifts is represented by an average thermal line load of 1.45 kW/m, according to the current design. This value and corresponding heat decay curve (Appendix C) were taken from DTN: MO0702PASTREAM.001 [DIRS 179925] (worksheet: “decay curves”).

Ventilation efficiency denotes the fraction of heat removed from the repository as a result of ventilation during the 50-year preclosure period. The ventilation efficiency was taken from DTN: MO0701VENTCALC.000 [DIRS 179085] (file: *Base Case Analysis Rev01.xls*) for the 600-m drift. For the THC model, the ventilation efficiency from this DTN (87.5%) was rounded to 88%.

4.1.6 Mineral Abundance, Composition, and Reactive Surface Area Data

The THC seepage model is assumed to represent a typical column through the repository. Therefore, mineralogical abundances were chosen from the average values reported in DTN: SN0307T0510902.003 [DIRS 164196]. Where data were not available for individual layers (e.g., PTn) or for minor mineral phases, they were derived from measurements made on samples from borehole SD-9 (Bish et al. 2003 [DIRS 169638], Supplementary Data Table 1), which is near the center of the repository footprint, and also the closest surface-based borehole to the DST. Typically, there are a few or more measurements made for samples within a given hydrogeological unit, and there the SD-9 values were in most cases averaged. Fracture mineralogical data are based on fracture mineral abundances in core from underground boreholes in the Exploratory Studies Facility (ESF), in the regions of the Single Heater Test (DTN: LA0009SL831151.001 [DIRS 153485]) and the Drift Scale Test (DTNs: LA9912SL831151.001 [DIRS 146447] and LA9912SL831151.002 [DIRS 146449]). Section 6.4.3 details the sources and methods for obtaining these data.

The compositions of mixed solid phases (solid solutions) were derived either from specific measurements, calculated from bulk rock compositions and mineral abundances, or directly from the project database *data0.ymp.R5* (DTN: SN0612T0502404.014 [DIRS 178850]). Other minerals were taken as pure phases with ideal composition from the project database *data0.ymp.R5* (DTN: SN0612T0502404.014 [DIRS 178850]) (e.g., hematite, quartz, and other silica polymorphs). Data and calculations of mixed mineral compositions are discussed in Section 6.2.2.4 and Appendix C. Sources used as direct inputs include:

- Bulk rock chemical analyses (for calculation of groundmass sanidine composition): DTN: GS000308313211.001 [DIRS 162015] (as published by Peterman and Cloke 2002 [DIRS 162576])
- Plagioclase: Johnson et al. (1998 [DIRS 101630], Table 6)
- Biotite phenocrysts analyses (used in calculation of groundmass sanidine composition): Flood et al. (1989 [DIRS 182723], Table 2); Biotite formula: Johnson et al. (1998 [DIRS 101630], Table 6)

- Smectite: Bish et al. (1996 [DIRS 101430], Table 1) (with endmember compositions for Na-, K-, Mg, and Ca-beidellite given in *data0.ymp.R5* (DTN: SN0612T0502404.014 [DIRS 178850]))
- Zeolites: mordenite from *data0.ymp.R5* (DTN: SN0612T0502404.014 [DIRS 178850]); stellerite and clinoptilolite from Chipera and Apps (2001 [DIRS 171017], Table 3, phases listed for the diagenetic alteration of volcanic tuff), with endmember compositions for Na-, K-, and Ca-clinoptilolite taken from *data0.ymp.R5* (DTN: SN0612T0502404.014 [DIRS 178850])
- Rhyolitic glass: Bish et al. (1996 [DIRS 101430], Table 1) (sample GU-3 1195C)
- Illite fraction of smectite: Carey et al. (1998 [DIRS 109051], p. 18).

Unqualified sources are qualified for intended use in this report in Appendix O (Section O.3), following the qualification plan listed in Appendix N (Section N.5).

Reactive surface areas are used to characterize minerals either in the matrix of the rock ($\text{cm}^2/\text{g}_{\text{mineral}}$) or those on the surface of fractures ($\text{m}^2_{\text{fracture surface}}/\text{m}^3_{\text{fracture medium solids}}$), respectively (see Section 6.4.3). For convenience, these data are shown in Appendix A (volume fractions) and Appendix B (reactive surface areas), respectively. Although these data are input into simulations, they are intermediate results calculated from fracture properties and mineral abundances as listed in Table 4.1-1, and as discussed in Section 6.4.3. These include stratigraphic and mineralogical data, as well as fracture properties, as discussed below.

4.1.7 Kinetic Data

Kinetic data refer to the reaction-rate constants (k_o), activation energies (E_a), and related data required to describe the rates of dissolution and precipitation of minerals as a function of temperatures and fluid chemistry, as defined in Section 6.4.2 and used in Equations 6.4-5 through 6.4-8. The data are shown in Table H.3-1 of Appendix H. External data sources were used as direct inputs as follows:

- Quartz reaction rate constant (dissolution only) and activation energy from Tester et al. (1994 [DIRS 101732], p. 2415)
- Alpha-cristobalite reaction rate constant (dissolution only) and activation energy from Renders et al. (1995 [DIRS 107088], pp. 77 and 81)
- Amorphous silica reaction rate constant (precipitation only) and activation energy from Carroll et al. (1998 [DIRS 124275], pp. 1379 and 1389)
- Amorphous silica kinetic reaction rate constant (dissolution only) and activation energy from Rimstidt and Barnes (1980 [DIRS 101708], pp. 1683 and 1690)
- Clinoptilolite reaction rate constant and activation energy from Murphy et al. (1996 [DIRS 142167], p. 160)

- Heulandite dissolution rates from Ragnarsdottir (1993 [DIRS 126601], pp. 2442 and 2447)
- Oligoclase activation energy from Blum and Stillings (1995 [DIRS 126590], p. 313, Table 2)
- Sanidine activation energy from Berger et al. (2002 [DIRS 181221], p. 669)
- Biotite reaction rate constant and activation energy from Malmstrom et al. (1996 [DIRS 181209], p. 208)
- Muscovite and illite reaction rate constant from Knauss and Wolery (1989 [DIRS 124300], p. 1500)
- Kaolinite reaction rate constant from Brady and Walther (1989 [DIRS 110748], p. 2826, Figure 6)
- Kaolinite activation energy from Carroll and Walther (1990 [DIRS 160681], p. 806, Table 2)
- Calcite dissolution rate constant from Svensson and Dreybrodt (1992 [DIRS 127978], p. 129)
- Calcite activation energy from Inskip and Bloom (1985 [DIRS 128129], p. 2165)
- Fluorite reaction rate constant from Knowles-van Capellan et al. (1997 [DIRS 124306], p. 1873)
- Hematite reaction rate constant from Bruno et al. (1992 [DIRS 160189])
- Rhyolite glass reaction rate constant from Mazer et al. (1992 [DIRS 124354], p. 574)
- Hematite dissolution rate constant from Hersman et al. (1995 [DIRS 160190], pp. 3327 and 3330)
- Reaction rate constants for feldspars (oligoclase, sanidine) from White and Brantley (1995 [DIRS 168088], p. 313, Table 2).

These unqualified sources are qualified for intended use in this report in Appendix H, following the qualification plans listed in Appendix N (Sections N.3 and N.4).

4.1.8 Thermodynamic Data

These data consist of chemical equilibrium constants in logarithmic form, $\log(K)$, as a function of temperature (for reactions describing the dissociation of secondary aqueous species, minerals, and gases involved in the model; see Section 6.4.1), molecular weight, molar volume, and ion size data for the calculation of aqueous activity coefficients. These data and their sources are listed in Appendix C, which is considered an integral part of this section.

Except for a few minerals, the source of the log(K), molecular weight, and molar volume data was the project databases *data0.ypf.R2* in DTN: SN0609T0502404.012 [DIRS 179067], and *data0.ymp.R5* in DTN: SN0610T0502404.013 [DIRS 178113], which has been superseded by DTN: SN0612T0502404.014 [DIRS 178850]. Changes from DTN: SN0610T0502404.013 [DIRS 178113] to DTN: SN0612T0502404.014 [DIRS 178850] were evaluated and determined to be inconsequential (Appendix C). External data sources were also used as direct inputs as follows:

- Free energies of silicated oxides used for log(K) calculations from Chermak and Rimstidt (1989 [DIRS 105073], Table 2)
- Input effective ionic radii for activity coefficient calculations from Helgeson et al. (1981 [DIRS 106024], Table 3)
- Development of input plagioclase log(K) values using regression coefficients from Arnórsson and Stefansson (1999 [DIRS 153329], p. 173, Tables 4 and 6)
- Amorphous silica log(K) values from Gunnarson and Arnórsson (2000 [DIRS 160465], p. 2295)
- Stellerite log(K) revised from data of Fridriksson et al. (2001 [DIRS 160460], Table 4)
- Solubility of silica phase resembling beta-cristobalite from Fournier (1973 [DIRS 153464], Figure 1), used for opal-CT solubility
- Alpha-cristobalite solubility from Fournier and Rowe (1962 [DIRS 124282], Table 1)
- Heat capacity of Al(OH)₃ calculated using regressing heat capacities of Barin and Platski (1995 [DIRS 157865], p. 55).

These unqualified sources are qualified for intended use in this report in Appendix C, following the qualification plans listed in Appendix N (Section N.2).

4.1.9 Water and Gas Chemistry

Sources of water- and gas-chemistry input data are provided in Table 4.1-1. The pore-water compositions used as inputs to the model simulations involved the calculations of concentration for some components as discussed in Section 6.2.2.1. Both original and recalculated data are presented in Table 6.2-1.

4.1.10 Drift Design Information

Design information is specified in contrast to data resulting from measurements. Design information has evolved continuously as the THC seepage model has been developed, and current design-related parameters may vary slightly from the values used in this report to generate the THC model output used by TSPA. These differences between design information used in this report and the current design are not expected to significantly affect model results, because these results are primarily dependent on the initial water compositions, mineralogy, and

applied heat load, and not on the specifics of in-drift engineered features. All direct input design parameters used in the THC model are summarized in Table 4.1-5, under the column “Model Direct Inputs.” Current values are also presented in the table, for corroborative or informational purposes only. The parameters used in the model vary little from the currently accepted values, and these inputs are adequate and justified for the intended use in this model. Some design parameters are from DTN: SN9908T0872799.004 [DIRS 108437]; because the calculations summarized in that DTN were not verified, these data, specifically, have been justified and qualified for use in Appendix I of this document, in accordance with SCI-PRO-001, *Qualification of Unqualified Data*, and SCI-PRO-006, and with qualification plans in Appendix N.

Two time periods are considered in the THC seepage model:

- A 50-year preclosure period during which a large amount of the heat released by the waste packages is removed by ventilation (see below)
- A postclosure simulation period following the initial 50-year preclosure period to 100,000 years, beyond which there are no thermal effects to be considered, and during which a drip shield is located above the waste packages and no heat is removed by ventilation.

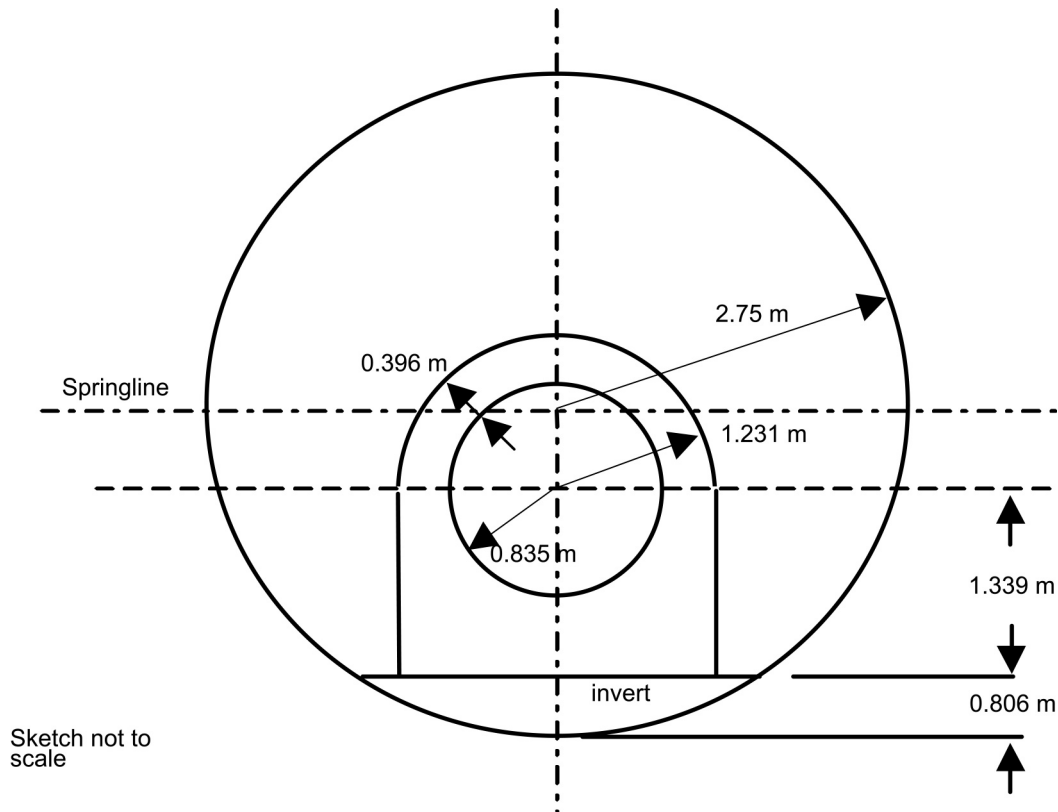
Accordingly, some of the drift-specific model-input design information is not the same for the preclosure and postclosure time periods. The model drift geometry and thermophysical properties of design elements are shown in Table 4.1-5 and Figure 4.1-1. This design information is the same as that used for the Site Recommendation. Because the drift is modeled as open to both advective and diffusive fluxes of liquid and gas, hydrologic properties had to be assigned to open in-drift areas. These properties are included in Table 4.1-5. The discretization of the drift is consistent with the dimensions shown in Figure 4.1-1, within the limits imposed by the resolution of the model mesh.

The drip shield is not explicitly modeled as a barrier to gas transport, but its thickness and thermal conductivity have been considered in the width and thermal properties, respectively, of the open zone between the waste package and drip shield during the postclosure period. This has no effect on predicted THC model water compositions, because the effective thermal conductivity of the in-drift open spaces is much greater than that of the host rock. Thus, heat loss and predicted temperatures are controlled by the host rock thermal properties, and in-drift components have no significant effect. In addition, because of the high permeability of the invert, and the relative ease with which gas-phase diffusion and equilibration occur, a pathway for equilibration of in-drift atmosphere above and below the drip shield exists through the invert, and little difference in gas-phase composition would be expected.

Table 4.1-5. Drift and Committed Materials Model Parameters

Parameter	Value	Source
Drift spacing	81m	SNL 2007 [DIRS 179466], Table 4-1, parameter 01-13
Drift diameter	5.5 m	SNL 2007 [DIRS 179354], Table 4-1, parameter 01-10
Location of waste package center above bottom of drift	1.945 m	DTN: SN9908T0872799.004 [DIRS 108437], file: <i>indrifgeom_rev01.doc</i>
Location of waste package center below the drift springline	0.805 m	DTN: SN9908T0872799.004 [DIRS 108437], file: <i>indrifgeom_rev01.doc</i>
Air gap between waste package surface and the inside of drip shield	0.396 m	DTN: SN9908T0872799.004 [DIRS 108437], file: <i>indrifgeom_rev01.doc</i>
Inside radius of drip shield	1.231 m	DTN: SN9908T0872799.004 [DIRS 108437], file: <i>indrifgeom_rev01.doc</i>
Waste package nominal diameter	1.67 m	Assumed ^(a)
Top of invert as measured from bottom of drift (invert thickness)	0.8 m	Assumed ^(a)
Drip shield thickness	0.02 m	Assumed ^(a)
Waste package thermal conductivity	13.965 W/m-K	Average of lowest and highest values in the 20°C to 300°C range taken from BSC 2001 [DIRS 156276], Table 5-11 (10.1 W/m-K for Alloy 22 at 48°C) and Table 5-13 (17.83 W/m-K for 316NG stainless steel at 287.78°C)
Waste package density	8,690 kg/m ³	DTN: MO0003RIB00071.000 [DIRS 148850], file: <i>s04196_001_001.pdf</i>
Waste package specific heat	554.5 J/kg-K average of 378 and 731 (see source)	SNL 2007 [DIRS 179567], Table 4-1, parameter 03-11 (homogeneous thermal properties for waste package internal cylinder)
Open drift areas (linear capillary pressure and relative permeability functions): – Permeability – Residual saturation (drift wall/all other areas) – Porosity – Capillary pressure	$1 \times 10^{-9} \text{ m}^2$ 0.01 / 0.0 1.0 0.0 Pa	Model setup (Section 6.4.6(17))
Effective Kthermal for drift open space (maximum values and multiplication factors as a function of time)	Preclosure max: 10.568 W/m K Postclosure max: – Inner 2.298 W/m K (up to drip shield) – Outer 14.407 W/m K (outside drip shield)	DTN: SN0002T0872799.009 [DIRS 153364], file: <i>tough2-input_noBF.txt</i> in <i>effKth_noBF.ZIP</i>

^(a) These data are considered assumed as discussed in Section 5 (Assumptions 7, 8, and 9).



Source: See Table 4.1-5, and Assumptions 7, 8, and 9 in Section 5.

Figure 4.1-1. Sketch Showing Modeled In-Drift Dimensions

Heat transfer from the waste package to the drift wall is implemented in the model by using time-varying effective thermal conductivities (for open spaces within the drift) that have been calculated to account for radiative and convective heat transport. These time-varying variables are input into the model as coefficients (values between 0 and 1) for each open zone within the drift. Each zone is also assigned a constant maximum thermal conductivity (Kth_{max}), which is then multiplied by the corresponding time-varying coefficients to obtain effective conductivities as a function of time (DTN: SN0002T0872799.009 [DIRS 153364]; Appendix E).

The effective thermal conductivities (Section 4.1.1.3) and corresponding open zones of the drift prior to closure are not the same as those following closure. Only one open space between the waste package and the drift wall is considered for the preclosure period. For postclosure, two zones are considered: (1) the open space between the waste package and the drip shield (Inner Zone, drip shield included) and (2) the open space between the drip shield and the drift wall (Outer Zone) (Figure 4.1-1). Kth_{max} values are listed in DTN: SN0002T0872799.009 [DIRS 153364]. For preclosure, $Kth_{max} = 10.568$ W/m-K for the zone between the waste package and the drift wall. For postclosure, $Kth_{max} = 2.298$ W/m-K for the Inner Zone (between the waste package and the drip shield), and $Kth_{max} = 14.407$ W/m-K for the Outer Zone (between the drip shield and the drift wall). Accordingly, model runs are started with the preclosure thermal conductivities, then stopped after 50 years and restarted with the corresponding postclosure data.

A summary of the hydrologic and thermal properties of repository units used in the current model is given in Table 6.4-2.

4.2 CRITERIA

The applicable federal regulations and technical requirements related to the work activities associated with this model report have been identified in *Technical Work Plan for: Revision of Model Reports for Near-Field and In-Drift Water Chemistry* (SNL 2007 [DIRS 179287], Section 3). The pertinent requirements and acceptance criteria for this report are summarized in Table 4.2-1.

Table 4.2-1. Applicable Project Requirements and YMRP Acceptance Criteria

Requirement	YMRP Acceptance Criteria ^a
10 CFR 63.114 (a)–(c) and (e)–(g) [DIRS 180319]	Criteria 1 to 5 for <i>Quantity and Chemistry of Water Contacting Waste Packages and Waste Forms</i>

^a From NRC 2003 [DIRS 163274], Section 2.2.1.3.3.3.

The acceptance criteria identified in Section 2.2.1.3.3.3 of *Yucca Mountain Review Plan, Final Report* (YMRP) (NRC 2003 [DIRS 163274]) are given below, along with the subcriteria applicable to the present report:

- Acceptance Criterion 1, *System Description and Model Integration Are Adequate*
 - (1) Total system performance assessment adequately incorporates important design features, physical phenomena, and couplings, and uses consistent and appropriate assumptions throughout the quantity and chemistry of water contacting engineered barriers and waste forms abstraction process.
 - (2) The abstraction of the quantity and chemistry of water contacting engineered barriers and waste forms uses assumptions, technical bases, data, and models, that are appropriate and consistent with other related U.S. Department of Energy abstractions.
 - (3) Important design features, such as waste package design and material selection, backfill, drip shield, ground support, thermal loading strategy, and degradation processes, are adequate to determine the initial and boundary conditions for calculations of the quantity and chemistry of water contacting engineered barriers and waste forms.
 - (5) Sufficient technical bases and justification are provided for total system performance assessment assumptions and approximations for modeling coupled thermal-hydrologic-mechanical-chemical effects on seepage and flow, the waste package chemical environment, and the chemical environment for radionuclide release. The effects of distribution of flow on the amount of water contacting the engineered barriers and waste forms are consistently addressed, in all relevant abstractions.

- (8) Adequate technical bases are provided, including activities such as independent modeling, laboratory or field data, or sensitivity studies, for inclusion of any thermal-hydrologic-mechanical-chemical couplings and features, events, and processes.
 - (9) Performance-affecting processes that have been observed in thermal-hydrologic tests and experiments are included into the performance assessment.
 - (10) Likely modes for container corrosion (Section 2.2.1.3.1 of the Yucca Mountain Review Plan) are identified and considered in determining the quantity and chemistry of water entering the engineered barriers and contacting waste forms. For example, the model abstractions consistently address the role of parameters, such as pH, carbonate concentration, and the effect of corrosion on the quantity and chemistry of water contacting engineered barriers and waste forms.
 - (12) Guidance in NUREG-1297 (Altman et al. 1988 [DIRS 103597]) and NUREG-1298 (Altman et al. 1988 [DIRS 103750]), or other acceptable approaches, is followed.
- Acceptance Criterion 2, *Data Are Sufficient for Model Justification*
 - (1) Geological, hydrological, and geochemical values used in the license application are adequately justified. Adequate description of how the data were used, interpreted, and appropriately synthesized into the parameters is provided.
 - (2) Sufficient data were collected on the characteristics of the natural system and engineered materials to establish initial and boundary conditions for conceptual models of thermal-hydrological-mechanical-chemical coupled processes, that affect seepage and flow and the engineered barrier chemical environment.
 - (3) Thermo-hydrologic tests were designed and conducted with the explicit objectives of observing thermal-hydrologic processes for the temperature ranges expected for repository conditions and making measurements for mathematical models. Data are sufficient to verify that thermal-hydrologic conceptual models address important thermal-hydrologic phenomena.
 - (4) Sufficient information to formulate the conceptual approach(es) for analyzing water contact with the drip shield, engineered barriers, and waste forms is provided.
 - Acceptance Criterion 3, *Data Uncertainty Is Characterized and Propagated Through the Model Abstraction*
 - (1) Models use parameter values, assumed ranges, probability distributions, and bounding assumptions that are technically defensible, reasonably account for uncertainties and variabilities, and do not result in an under-representation of the risk estimate.
 - (2) Parameter values, assumed ranges, probability distributions, and bounding assumptions used in the total system performance assessment calculations of quantity and chemistry of water contacting engineered barriers and waste forms are technically defensible and reasonable, based on data from the Yucca Mountain region (e.g., results from large

block and drift-scale heater and niche tests), and a combination of techniques that may include laboratory experiments, field measurements, natural analog research, and process-level modeling studies.

- (3) Input values used in the total system performance assessment calculations of quantity and chemistry of water contacting engineered barriers (e.g., drip shield and waste package) are consistent with the initial and boundary conditions and the assumptions of the conceptual models and design concepts for the Yucca Mountain site. Correlations between input values are appropriately established in the U.S. Department of Energy total system performance assessment. Parameters used to define initial conditions, boundary conditions, and computational domain in sensitivity analyses involving coupled thermal-hydrologic-mechanical-chemical effects on seepage and flow, the waste package chemical environment, and the chemical environment for radionuclide release, are consistent with available data. Reasonable or conservative ranges of parameters or functional relations are established.
 - (4) Adequate representation of uncertainties in the characteristics of the natural system and engineered materials is provided in parameter development for conceptual models, process-level models, and alternative conceptual models. The U.S. Department of Energy may constrain these uncertainties using sensitivity analyses or conservative limits. For example, the U.S. Department of Energy demonstrates how parameters used to describe flow through the engineered barrier system bound the effects of backfill and excavation-induced changes.
- Acceptance Criterion 4, *Model Uncertainty Is Characterized and Propagated Through the Model Abstraction*
 - (1) Alternative modeling approaches of features, events, and processes are considered and are consistent with available data and current scientific understanding, and the results and limitations are appropriately considered in the abstraction.
 - (2) Alternative modeling approaches are considered and the selected modeling approach is consistent with available data and current scientific understanding. A description that includes a discussion of alternative modeling approaches not considered in the final analysis and the limitations and uncertainties of the chosen model is provided.
 - (3) Consideration of conceptual-model uncertainty is consistent with available site characterization data, laboratory experiments, field measurements, natural analog information and process-level modeling studies; and the treatment of conceptual-model uncertainty does not result in an under-representation of the risk estimate.
 - (4) Adequate consideration is given to effects of thermal-hydrologic-mechanical-chemical coupled processes in the assessment of alternative conceptual models.

- (5) If the U.S. Department of Energy uses an equivalent continuum model for the total system performance assessment abstraction, the models produce conservative estimates of the effects of coupled thermal-hydrologic-mechanical-chemical processes on calculated compliance with the postclosure public health and environmental standards.
- Acceptance Criterion 5, *Model Abstraction Output is Supported by Objective Comparisons*
 - (3) Accepted and well-documented procedures are used to construct and test the numerical models that simulate coupled thermal-hydrologic-mechanical-chemical effects on seepage and flow, engineered barrier chemical environment, and the chemical environment for radionuclide release. Analytical and numerical models are appropriately supported. Abstracted model results are compared with different mathematical models, to judge robustness of results.

This revision of the THC seepage model is primarily CR-driven and includes: changes in model inputs such as water chemistry, analysis of repository edge conditions, use of an updated revision of the TOUGHREACT software, re-evaluation of model uncertainties, and revalidation of the updated model by comparison to DST water and gas compositions.

The representativeness of input water compositions is discussed in Section 6.2.2.1. The selection of input water compositions from various repository-level lithostratigraphic units has been made to take into account the natural variability in pore-water compositions. In this way, the model results are sufficiently representative for locations throughout the repository footprint. Uncertainties in output parameters for downstream users of the THC seepage model are discussed in Section 6.7. Boundary conditions used in the THC seepage model are established in other documents and are presented and justified for intended use in Section 4.1.

The report addresses the following CRs, as discussed in Appendix P (with planned approaches to address these CRs in this report and in other Near-Field Environment reports in preparation described in Section 1.2.1 of SNL 2007 [DIRS 179287]):

- CR-5154: *Use of invert thermal and hydrologic properties that are not based on the ballast material description on the IED.*
- CR-5383: *Use of DST waters affected by introduced materials in validation of the THC seepage model.*
- CR-6334: *Errors and inconsistencies in simulation of new infiltration.*
- CR-6342: *Errors and traceability for reactive surface area in THC models.*
- CR-6344: *Database file not captured for SOLVEQ/CHILLER calculations.*
- CR-6489: *Sensitivity studies on the form of sepiolite used in ANL-EBS-MD-000074, Rev. 00.*
- CR 6491: *Scientific Notebooks do not meet requirements.*

- CR-6492: *Technical issues with Rev. 04 of Drift-Scale THC Seepage Model*
- CR-6691: *Failure to maintain mass balance in THC normative salt precipitation calculations.*
- CR-7037: *New information available from THC sensitivity analyses (ANL-NBS-HS-000047 Rev. 00).*
- CR-7187: *Opportunity to improve THC model validation.*
- CR-7193: *RIT action items associated with MDL-NBS-HS-000001, Drift Scale Coupled Process Model.*
- CR-7697: *Minor transparency and traceability issues in the THC model.*
- CR-7811: *Discrepancy between MDL-NBS-HS-000001 Rev. 04 [DIRS 172862], Section 6.4.1, and the TOUGHREACT V3.0 description of activity coefficients for neutral species.*
- CR-8009: *Capillary pressure function flag of 10 and Leverett scaling function in TOUGHREACT.*
- CR-8032: *THC time stepping effect unresolved (MDL-NBS-HS-000001 Rev. 04).*
- CR-8316: *Pore-water chemistry analyses lack charge balance.*

The THC seepage report will also address Independent Validation Review Team comments documented by Booth (2006 [DIRS 176638]):

- IDC-1: Sensitivity to reaction rate constants—the sensitivity of the THC seepage model results to reaction-rate constants must be evaluated. The sensitivity study described above for CRs 6342 and 6492 will provide a response to this comment. It is anticipated that predicted water compositions will only be slightly sensitive to order-of-magnitude variation in the product of the intrinsic rate constant and the reactive surface area. If necessary, the THC seepage model uncertainty estimates will be modified to reflect additional uncertainty due to reaction rate constants.
- IDC-2: Equal weighting of all five pore waters—the probability of a given starting water should be tied to the probability of occurrence of that water type. This comment will be addressed during reevaluation of the currently available pore-water data, in revision of the physical and chemical environment report discussed in Section 2.1.2.3 of the TWP.
- IDC-10: Drift variability of water chemistries—use of time histories developed for repository-center THC simulations to represent repository edge water compositions is not appropriate. This comment will be addressed by the planned repository-edge sensitivity study, and by the near-field chemistry model described in Section 1.2.3 of the TWP.

Section 6.6 describes sensitivity analyses conducted in large part for the evaluation of CRs. Approaches followed in this report have been as specified in the TWP (SNL 2007 [DIRS 179287]).

4.3 CODES, STANDARDS, AND REGULATIONS

No specific, formally established codes, standards, or regulations, other than those discussed in Section 4.2, have been identified as applying to this modeling activity.

5. ASSUMPTIONS

The development of the methodology and process models applied to simulate heat and fluid flow in unsaturated fractured porous media, mineral–water reactions, and transport of aqueous and gaseous species is discussed in Sections 6.2 through 6.4. Many simplifications and approximations underlie this methodology, yet other simplifications and approximations are inherent in data that describe repository designs and associated parameters on which model simulations rely. In this section, only cases in which an assumption is made where there is an absence of data or information for the parameter or concept are described. These are listed below. Approximations and simplifications related to the development and implementation of the mathematical model applied for this study are presented as part of the model documentation in Section 6.4.6.

1. **The THC model results, calculated for a repository in the Tptpll lithologic unit, are applicable to all lithologies intersected by the repository drifts**—Analysis and results of this model are assumed to apply across the lithology of the entire repository drift, although the current THC seepage model results only provide output from the Tptpll lithologic unit. This assumption has several bases:

- Model simulations carried out in a previous revision of this report (Table 6-1) were run in both the Tptpmn and Tptpll lithologic units, and showed that the lithology had little effect on predicted water chemistries. Although the Tptpmn simulations have not been repeated with the current THC model, which uses different input parameters and differs conceptually in some ways from the earlier model, these developmental simulations provide confidence that the current model results are applicable over the stratigraphic section intersected by the repository.
- The repository horizon within the Topopah Spring Tuff (including the Tptpln, Tptpll, Tptpmn, and Tptpul units) is relatively uniform in composition. Peterman and Cloke (2002 [DIRS 162576]), as reported in DTN: GS000308313211.001 [DIRS 162015], analyzed twenty core samples, in duplicate, from the cross-drift within the four lithologic units constituting the repository level. All samples were compositionally similar with respect to major oxides and trace elements (Peterman and Cloke 2002 [DIRS 162576], Table 4), and normative mineral compositions (Peterman and Cloke 2002 [DIRS 162576], Figure 4, Table 5, p. 692). Samples vary by only 2% in SiO₂ concentration, and plot as a tight cluster in the rhyolite field on the chemical rock classification diagram for igneous rocks (SiO₂ plotted against Na₂O + K₂O) (Peterman and Cloke 2002 [DIRS 162576], Figure 3, Table 4, p. 687). The tight clustering also indicates that the effect of localized mineral heterogeneity on large-scale rock compositions, due to the presence of minerals that precipitated from the vapor phase during cooling of the tuff, and low-temperature minerals, such as calcite and amorphous SiO₂ (opal), is likely very small (Peterman and Cloke 2002 [DIRS 162576], pp. 695 to 696).

- The four starting waters used in the current THC seepage model simulations have been chosen to represent a range of available pore-water compositions, and include pore waters from three of the four repository-level lithologic units (Ttptll, Ttptmn, and Ttptul) (Section 6.2.2.1).
2. **THC model runs using the four starting waters represent a suitable range of possible seepage water compositions**—The four starting waters (Section 6.2.2.1) have been chosen from available measured pore-water compositions for repository-level lithologic units. These waters are plotted on Figure 6.2-4, and cover a range of measured compositions. However, pore-water samples are not available from all possible locations in the repository, and available data are assumed to be representative of all water chemistries actually present in the repository units. This assumption is supported in part by the similar chemical compositions of the four TSw lithostratigraphic units that will host the repository, as described in the previous assumption. Reaction with these rocks should homogenize water compositions, and variations in the concentrations of aqueous species are largely a function of evaporation or dilution (i.e., the proportions of many constituents do not vary as much as their concentrations). This assumption is borne out by the available data (Figure 6.2-4).

Support that these four waters represent a suitable range of pore-water compositions is presented in *Engineered Barrier System: Physical and Chemical Environment* (BSC 2007 [DIRS 177412], Section 6.6).

3. **Water compositions in the fractures and matrix are identical, and the same water is present in all hydrogeologic units**—The infiltrating water and initial fracture-water chemical compositions are set to be the same as the initial matrix pore-water compositions, with minor adjustments for temperature at the upper boundary of the model. The basis for this assumption is that the pore waters must, at any given point in time, constitute the vast majority of the water in the rock column, because the total porosity and liquid saturation in the rock matrix are much greater than in fractures.

Also, the same initial water compositions are used in all hydrogeologic units. This model simplification is justified because the THC model provides, as output, near-field water compositions derived from gridblocks within 10 m of the drift center (water compositions from greater distances are of no interest).

4. **Aqueous species are unreactive at solution concentrations greater than 4 molal**—Upon boiling or evaporation, the aqueous phase is treated as unreactive and is not concentrated further, once its ionic strength reaches an input upper limit of 4 or if the liquid saturation drops below an input lower limit of 10^{-5} . This ensures that the calculated ionic strength does not exceed the range of applicability of the activity coefficient model used (Section 6.4.1). Thus, reaction of aqueous components in concentrated solutions (ionic strength greater than 4 molal) does not occur. Transport is neglected if the liquid saturation drops below an input lower limit of 10^{-5} , which is also below the residual saturation, but takes place at all values of the ionic strength. At liquid saturations this low, the total amount of dissolved mass present in any given model gridblock is exceedingly small. Thus, ignoring chemical reaction for such small mass amounts (and over a limited time period) does not significantly affect the general computed trends of aqueous phase concentrations and precipitated mineral amounts

over long periods of time and a wide range of liquid saturations. The salt phases that are formed during dryout are described in Section 6.4.5. These phases are available for dissolution upon rewetting (using a relatively fast dissolution rate constant of $10^{-6} \text{ mol m}^{-2} \text{ s}^{-1} \text{ kg}_{\text{H}_2\text{O}}^{-1}$).

5. **Axial transport effects would not significantly impact THC Seepage Model results**—The THC seepage model is a two-dimensional slice through an emplacement drift at the center of the repository. Transport of heat and mass (liquid/vapor) in the third dimension, paralleling the drift, is not incorporated into the model. The effect of such transport on water chemistry is assumed to be negligible. Confidence in this assumption is gained by comparing the two-dimensional THC model results (with water–rock interactions turned off) and the three-dimensional multiscale thermohydrologic model (MSTHM) results (SNL 2007 [DIRS 181383]) for a repository-center location. The two models predict similar drift wall temperatures for given waste package temperatures.
6. **In the event of complete drift collapse, the composition of potential seepage is assumed to be the same as seepage for uncollapsed drifts**—In the low-probability-seismic collapsed-drift scenario, the drift opening collapses, and the resulting host-rock rubble completely fills the modified drift opening, from the outer surface of the drip shield out to the modified “drift wall.” It is assumed that drift collapse will have no effect on potential seepage water compositions. Thermal-hydrologic simulation results for a complete drift-collapse scenario are presented in *Multiscale Thermohydrologic Model* (SNL 2007 [DIRS 181383], Section 6.3.17[a]) and show that the main effect of the rubble is to thermally insulate the waste package, resulting in higher temperatures and extended boiling duration in the drift (relative to the no-collapse scenario).
7. **Top of invert as measured from bottom of drift (invert thickness)**—The top of invert as measured from the bottom of the drift (invert thickness) used in the modeling was assumed to be 0.8 m, based on values shown in Appendix I, Figure I-1, which reflect typical design values. This value differs from the current project value of 1.321 m (4 feet 4 inches; see SNL 2007 [DIRS 179354], Figure 4-1). The difference is not anticipated to significantly impact the results of simulations because heat loss and predicted temperatures are controlled primarily by the host rock thermal properties, and in-drift components have much less effect.
8. **Nominal Waste Package Diameter**—The nominal waste package diameter used in the modeling was assumed to be 1.67 m, based on values shown in Appendix I, Figure I-3. This value was based on the 44-BWR waste package diameter at the time the modeling effort was started. The current diameter is 1.963 m for the transportation, aging, and disposal canister (formerly the 44-BWR waste package) (SNL 2007 [DIRS 179394], Table 4-3). The difference is not anticipated to significantly impact the results of simulations because heat loss and predicted temperatures are controlled primarily by the host rock thermal properties, and in-drift components have much less effect.

9. **Drip shield thickness**—A thickness of 0.02 m was assumed, based on values shown in Appendix I, Figure I-2, which reflects typical design values. This thickness was not explicitly modeled, but was considered in the width of the open zone between the waste package and drip shield during the postclosure period. The exact thickness value is not anticipated to significantly impact the results of simulations because heat loss and predicted temperatures are controlled primarily by the host rock thermal properties, and in-drift components have much less effect.

6. MODEL DISCUSSION

This section presents the conceptual and mathematical models implemented for the development of the drift-scale thermal-hydrologic-chemical (THC) seepage model. Relevant features, events, and processes (FEPs) are also briefly discussed in Section 6.1. Details on the conceptualization and mathematical treatment of the various coupled processes considered in the THC seepage model follow in Sections 6.2 through 6.4, including the methodology for post-processing predicted water chemistries in Section 6.4.8. The results of the THC seepage model are presented in Section 6.5, where coupled THC processes are evaluated for 100,000 years under boundary conditions that are varied to represent the effects of potential climatic change, four input water compositions, and two repository locations (center and edge). The model sensitivity to various input parameters is discussed in Section 6.6. Model uncertainty is discussed in Section 6.7. The validation of the THC seepage model is presented in Section 7. The post-development model validation consists of simulating the water, gas, and mineral evolution in the Drift Scale Test (DST) using the DST THC submodel (Section 7.1). The model validation simulations rely on the same conceptualizations and mathematical formulations presented in the current model.

The development history of the THC seepage model is summarized in Table 6-1, which shows main changes between model revisions and provides a summary of the various conceptualizations and sensitivities that have been considered over the course of model development.

The results of developmental (pre-Revision 05) models will be discussed in context throughout Section 6 as alternative model conceptualizations (Section 6.3) and also to provide information on model sensitivities and uncertainties (Sections 6.6 and 6.7). The current THC model implements many improvements relative to these earlier models, as shown in Table 6-1. Results of the current simulations are presented in Section 6.5, and sensitivity studies in Section 6.6. A separate detailed study looking at the effect of fracture permeability heterogeneity on water chemistry and flow is reported in *THC Sensitivity Study of Heterogeneous Permeability and Capillarity Effects* (SNL 2007 [DIRS 177413]).

Table 6-1. Summary of the Development of the THC Seepage Model

	THC Model REV 01 ^a Homogeneous Tptpmn Unit	THC Model REV 01 ^a Heterogeneous Tptpmn Unit	THC Model REV 01 ^a Homogeneous Tptpl Unit	THC Model REV 02 ^b Homogeneous Tptpl Unit	THC Model REV 05 Homogeneous Tptpl Unit (current report)
Completion year	2001	2001	2001	2003	2007
Chronological order of model development	1	2	3	4	5
Information provided by this model	Compare with the Tptpl model (REV01) to evaluate the effect of host hydrogeologic unit and stratigraphic location	Compare with the homogeneous Tptpmn model (REV01) to evaluate the effect of fracture permeability heterogeneity	Compare with the Tptpmn model (REV01) to evaluate the effect of host hydrogeologic unit and stratigraphic location	Evaluates sensitivities to various model parameters and conceptualizations	Provides confidence in alternative models feeding TSPA-LA and evaluates sensitivities to various model parameters and conceptualizations
TOUGHREACT version	2.3	2.3	2.3	3.0	3.1.1
Model dimensions: Thermal loading Ambient conditions (baseline)	Two-dimensional Two-dimensional	Two-dimensional Two-dimensional	Two-dimensional Two-dimensional	Two-dimensional One-dimensional ^c	Two-dimensional One-dimensional ^c
Heat load areal location	Repository center	Repository center	Repository center	Repository center	Repository center and edge
Stratigraphic column location	SD-9	SD-9	Center of repository	Center of repository	Center of repository
Host lithostratigraphic unit	Tptpmn	Tptpmn	Tptpl	Tptpl	Tptpl
Heterogeneous permeability	No	Yes	No	No	No
Geochemical system (Table 6.2-2 for the current "Extended" geochemical system)	Base ^d Extended ^e	Base ^d Extended ^e	Base ^d Extended ^e	Extended	Extended
Thermodynamic data	original	original	original	minor revisions	more significant revisions

Table 6-1. Summary of the Development of the THC Seepage Model (Continued)

	THC Model REV 01 ^a Homogeneous Tptpmn Unit	THC Model REV 01 ^a Heterogeneous Tptpmn Unit	THC Model REV 01 ^a Homogeneous Tptpl Unit	THC Model REV 02 ^b Homogeneous Tptpl Unit	THC Model REV 05 Homogeneous Tptpl Unit (current report)
Kinetic data	Original	Original	Original	Minor revisions	Rate constants for primary minerals reduced by 2 to 3 orders of magnitude
Input pore-water composition (Table 6.2-1)	ESF Alcove 5	ESF Alcove 5	ESF Alcove 5	ESF Alcove 5 ECRB, 500 m ECRB, 1,000 m ECRB, 2,000 m SD-9, 990 ft	ESF Alcove 5 (2 samples) SD-9, 1,184.5 ft ESF Thermal K borehole 17, 26.5 ft
Infiltration rates (mm/yr)	Stepped up 6, 16, 25	Stepped up 6, 16, 25	Stepped up 6, 16, 25	Stepped up 6, 16, 25 (Sensitivities: constant 6 and 25)	Stepped up 7.96, 12.89, 20.45
Heat load (kW/m)	1.45	1.45	1.45	1.45	1.45
Effective drift spacing (m)	81	81	81	81	81 and 162
Ventilation period (years)	50	50	50	50	50
Ventilation efficiency (% heat removal)	70	70	70	86.3	88
Drift wall conceptualization	Closed to advective fluid flow	Closed to advective fluid flow	Closed to advective fluid flow	Open	Open
Invert thickness	0.6	0.6	0.8	0.8	0.8
Vapor-pressure lowering due to capillary pressure	No	No	No	Yes No (sensitivity)	Yes
Leverett Scaling	No	No	No	Intended but not operational	Yes
CO ₂ diffusion coefficient	Original	Original	Original	6× increase from original (Sensitivity using original value)	2.5× decrease from original (Sensitivities: 3× and 10× selected value)

Table 6-1. Summary of the Development of the THC Seepage Model (Continued)

	THC Model REV 01 ^a Homogeneous Ttpm Unit	THC Model REV 01 ^a Heterogeneous Ttpm Unit	THC Model REV 01 ^a Homogeneous Ttpm Unit	THC Model REV 02 ^b Homogeneous Ttpm Unit	THC Model REV 05 Homogeneous Ttpm Unit (current report)
Maximum time-step for transport:	Step (run period) 180 d (0–50 y) 1 y (50–600 y) 2 y (0.6–2 ky) 5 y (2–20 ky) 10 y (20–100 ky) No	Step (run period) 180 d (0–50 y) 1 y (50–600 y) 2 y (0.6–2 ky) 5 y (2–20 ky) 10 y (20–100 ky) No	Step (run period) 180 d (0–50 y) 1 y (50–600 y) 2 y (0.6–2 ky) 5 y (2–20 ky) 10 y (20–100 ky) No	Step (run period) 15 d (0–50 y) 30 d (50–600 y) 60 d (0.6–2 ky) 1 y (2–20 ky) 5 y (20–100 ky) Yes	Step (run period) 15 d (0–2 ky) 100 d (2–10 ky) 300 d (10–30 ky) 1,000 d (30–20 ky) Yes (Sensitivities: two alternative dryout salt assemblages)
Improved treatment of mineral precipitation at boiling front	No	No	No	Yes	(Sensitivities: two alternative dryout salt assemblages)
Chronological changes in Mineralogy (Table 6.2-2 and Appendix A for current values)	Initial data ^d	No change	Added fluorite and opal as primary minerals in host rock	Added sepiolite and removed goethite as possible secondary minerals	Amorphous antigorite instead of sepiolite; biotite; primary feldspar solid solutions; no secondary feldspars; goethite back in
Main chronological changes in thermal properties (Table 6.4-2 for current values)	Initial data ^d	No change	In Ttpm versus Ttpm: 23% and 13% decrease in effective K_{dry} and K_{wet} , respectively	For Ttpm, 6% increase in K_{dry} and 6% decrease in K_{wet} (effective values)	Minor changes: about same as previous in Ttpm
Main chronological changes in hydrologic properties (Table 6.4-2 for current values)	Initial data ^d	In Ttpm fractures: heterogeneous, four-order-of-magnitude spread in fracture permeability in Ttpm (three different realizations)	In Ttpm fractures: higher permeability, 80% increase in porosity, and six times higher capillarity (1/alpha)	In Ttpm fractures: 62% decrease in permeability, 47% decrease in porosity and 20% decrease in capillarity (1/alpha)	In Ttpm fractures: no change in fracture porosity and permeability, 5x less capillarity. In Ttpm matrix: 2.5x more permeable, 3x more capillarity

^a CRWMS M&O 2001 [DIRS 154426].

^b BSC 2004 [DIRS 168848].

^c One-dimensional simulations of ambient conditions without a drift opening.

^d See BSC 2004 [DIRS 168848], Table 6.2-2, for a summary of these values.

^e The REV01 “Extended” geochemical system varies slightly from that in REV02–REV04.

NOTE: ECRB = Enhanced Characterization of the Repository Block; ESF = Exploratory Studies Facility; REV = Revision. Sources of model input data and technical information shown here are discussed in Section 4.1.

6.1 RELEVANT FEATURES, EVENTS, AND PROCESSES

The results of this model are part of the basis for the treatment of FEPs as discussed in *Technical Work Plan for: Revision of Model Reports for Near-Field and In-Drift Water Chemistry* (BSC 2007 [DIRS 179287]), Section 2.1.3). FEPs that are relevant to the subject matter of this report and that are included in TSPA-LA are summarized in Table 6.1-1.

These FEPs have been taken from the LA FEP list (DTN: MO0706SPAFEPLA.001 [DIRS 181613]). Each FEP is cross-referenced to the relevant section (or sections) in this report in Table 6.1-1. The discussions provided in this and other model and analysis reports form the technical basis for evaluating these FEPs for TSPA-LA.

Table 6.1-1. Included Features, Events, and Processes Addressed in This Report

LA FEP Number	FEP Name	Location Discussing FEPs-Related Items
1.1.02.02.0A	Preclosure ventilation	4.1.5 4.1.10
1.2.02.01.0A	Fractures	4.1.1 6.2.1 6.4.3 6.4.4 6.5.5.3 Tables 4.1-1, 6.4-2
1.3.01.00.0A	Climate change	4.1.4 6.2.1.3 6.5.2
1.4.01.01.0A	Climate modification increases recharge	4.1.4 6.2.1.3 6.5.2
2.1.08.01.0A	Water influx at the repository	6.5.2 (infiltration) 6.5.5.1 (ambient) 6.5.5.2 (thermal)
2.2.03.01.0A	Stratigraphy	4.1.1 4.1.2 4.1.6 6.5.1 Table 4.1-3
2.2.03.02.0A	Rock properties of host rock and other units	4.1.1 6.2.1 6.3 6.4.4 6.4.6 6.5.5.3 Table 6.4-2
2.2.07.02.0A	Unsaturated groundwater flow in the geosphere	6.2.1 6.5.5.2
2.2.07.04.0A	Focusing of unsaturated flow (fingers, weeps)	6.2.1
2.2.07.08.0A	Fracture flow in the UZ	6.2.1 6.4.3 6.4.4
2.2.07.09.0A	Matrix imbibition in the UZ	6.2.1

Table 6.1-1. Relevant Features, Events, and Processes Included in TSPA-LA (Continued)

LA FEP Number	FEP Name	Location Discussing FEPs-Related Items
2.2.07.10.0A	Condensation zone forms around drifts	6.2.1 6.5.5.3
2.2.07.11.0A	Resaturation of geosphere dryout zone	6.2.1 6.5.5.2 6.5.5.3
2.2.07.20.0A	Flow diversion around repository drifts	6.2.1 6.5.5.1 6.5.5.3
2.2.08.01.0B	Chemical characteristics of groundwater in the UZ	4.1.1 6.2.2 6.5.5.2 Tables 4.1-1, 6.2-1
2.2.08.12.0A	Chemistry of water flowing into the drift	4.1.1 6.2.1.2 6.2.2 6.5.5.2 6.5.5.4 Tables 4.1-1, 6.2-1
2.2.10.03.0B	Natural geothermal effects on flow in the UZ	6.5.2
2.2.10.10.0A	Two-phase buoyant flow/heat pipes	6.2.1
2.2.10.12.0A	Geosphere dry-out due to waste heat	6.2.1 6.4.5

Source: DTN: MO0706SPAFEPLA.001 [DIRS 181613].

6.2 CONCEPTUAL MODEL

This section describes the conceptual model underlying the drift-scale THC seepage model. The THC seepage model conceptualization is presented in several parts. The first part deals with the conceptualization of the coupled processes that need to be taken into account to model water–gas–rock interactions in a heated, unsaturated, and fractured rock environment. In the second part, the conceptualization of the chemical system is presented and a rationale is laid out for selecting input water compositions, mineral phases, and chemical constituents included within the model. Finally, the conceptualization of the physical domain being modeled is discussed.

6.2.1 Conceptualization of Coupled THC Processes

The THC conceptual model underlies the numerical simulations of THC processes in the DST THC submodel and THC seepage model. The thermal-hydrologic (TH) conceptual model must be able to describe processes involving liquid and vapor flow, heat transport, and thermal effects resulting from boiling and condensation. The THC conceptual model must treat the transport of aqueous and gaseous species, mineralogical characteristics and changes, and aqueous and gaseous chemistry. A conceptual model of reaction-transport processes in the fractured welded tuffs of the repository host rock must also account for different rates of transport in highly permeable fractures compared to the much less permeable rock matrix (Steefel and Lichtner 1998 [DIRS 144878], pp. 186 and 187).

In addition to the unsaturated hydrologic properties required to simulate THC processes in the unsaturated zone (UZ), the data necessary for the evaluation of THC processes include the initial and boundary water and gas chemistry, initial mineralogy, mineral volume fractions, reactive surface areas, equilibrium thermodynamic data for minerals, aqueous and gaseous species, kinetic data for mineral–water reactions, and diffusion coefficients for aqueous and gaseous species. The following subsections describe the conceptual model for TH, geochemical, and coupled THC processes in the fractured tuffs.

6.2.1.1 TH Processes

TH processes in the fractured welded tuffs at Yucca Mountain have been examined theoretically and experimentally since the early 1980s (Pruess et al. 1984 [DIRS 144801]; Pruess et al. 1990 [DIRS 100818]; Buscheck and Nitao 1993 [DIRS 100617]; Pruess 1997 [DIRS 144794]; Tsang and Birkholzer 1999 [DIRS 137577]; Kneafsey and Pruess 1998 [DIRS 145636]). A conceptual model showing the important TH processes occurring around a drift (as derived through these studies and through observations of the Single Heater Test and the DST) is shown in Figure 6.2-1. This diagram also indicates (in boxes) the important parameters and issues addressed in the THC seepage model simulations. To summarize the processes as depicted in the figure, heat conduction from the drift wall into the rock matrix results in vaporization and boiling, with vapor migration out of matrix blocks into fractures. The vapor moves away from the drift through the permeable fracture network by buoyancy, by the increased vapor pressure caused by heating and boiling, and through local convection. In cooler regions, the vapor condenses on fracture walls, where it drains through the fracture network either down toward the heat source from above or away from the drift into the zone underlying the heat source. Slow imbibition of water from fractures into the matrix gradually leads to increases in the liquid saturation in the rock matrix. Under conditions of continuous heat loading, a dryout zone may develop closest to the heat source separated from the condensation zone by a nearly isothermal zone maintained at about the boiling temperature. Where this nearly isothermal zone is characterized by a continuous process of boiling, vapor transport, condensation, and migration of water back to the heat source (either by capillary forces or gravity drainage), this zone may be termed a heat pipe (Pruess et al. 1990 [DIRS 100818], p. 1235).

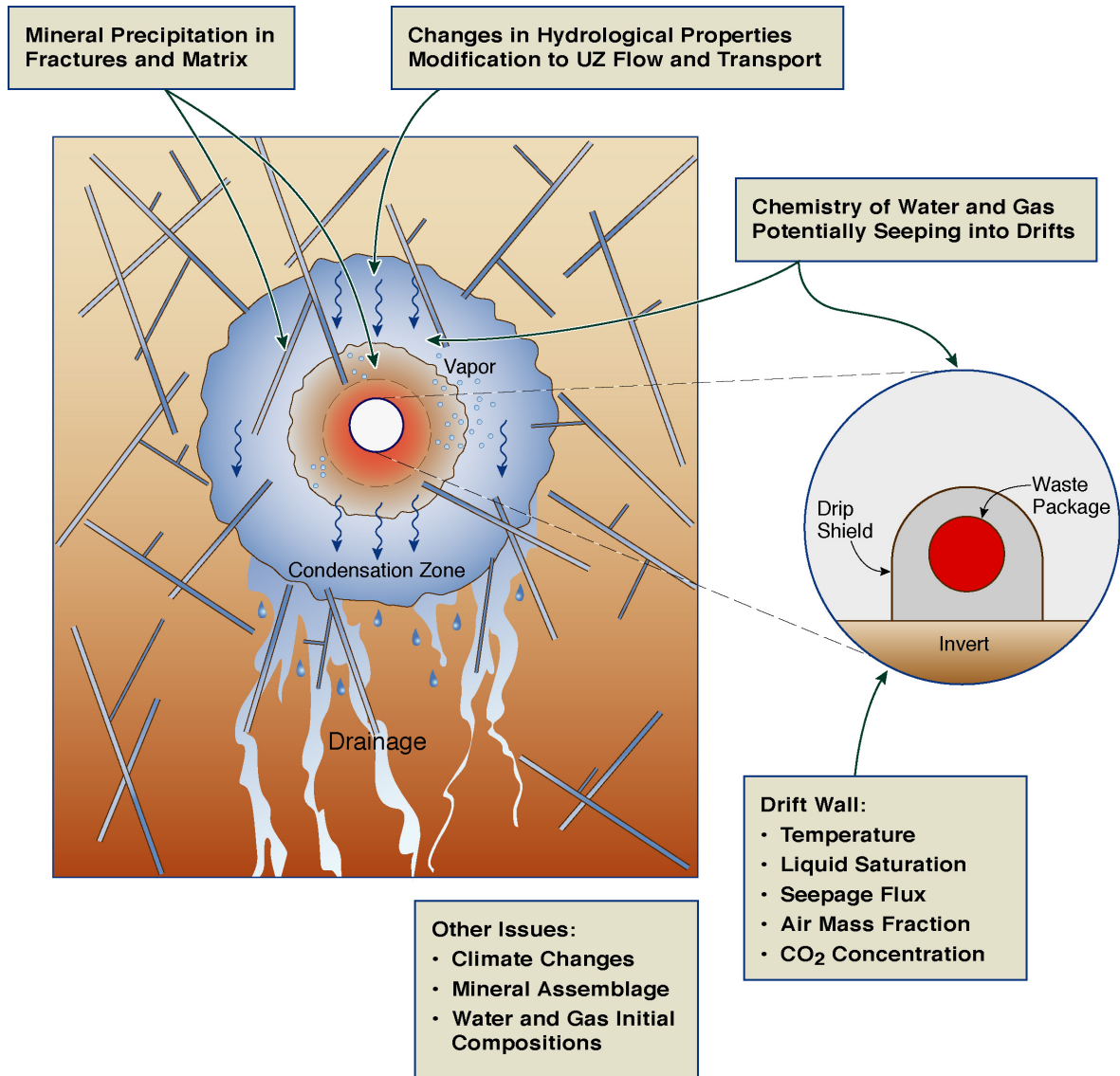


Figure 6.2-1. Schematic Diagram of THC Processes around a Heated Drift

6.2.1.2 THC Processes

The chemical evolution of waters, gases, and minerals is intimately coupled to the TH processes (boiling, condensation, and drainage) discussed in the previous section. The distribution of condensate in the fracture system determines where mineral dissolution and precipitation can occur in the fractures and where there can be direct interaction (via diffusion) between matrix pore waters and fracture waters. Figure 6.2-2 shows schematically the relationships between TH and geochemical processes in the zones of boiling, condensation, and drainage in the rock mass at the fracture–matrix interface outside of the drift and above the heat source.

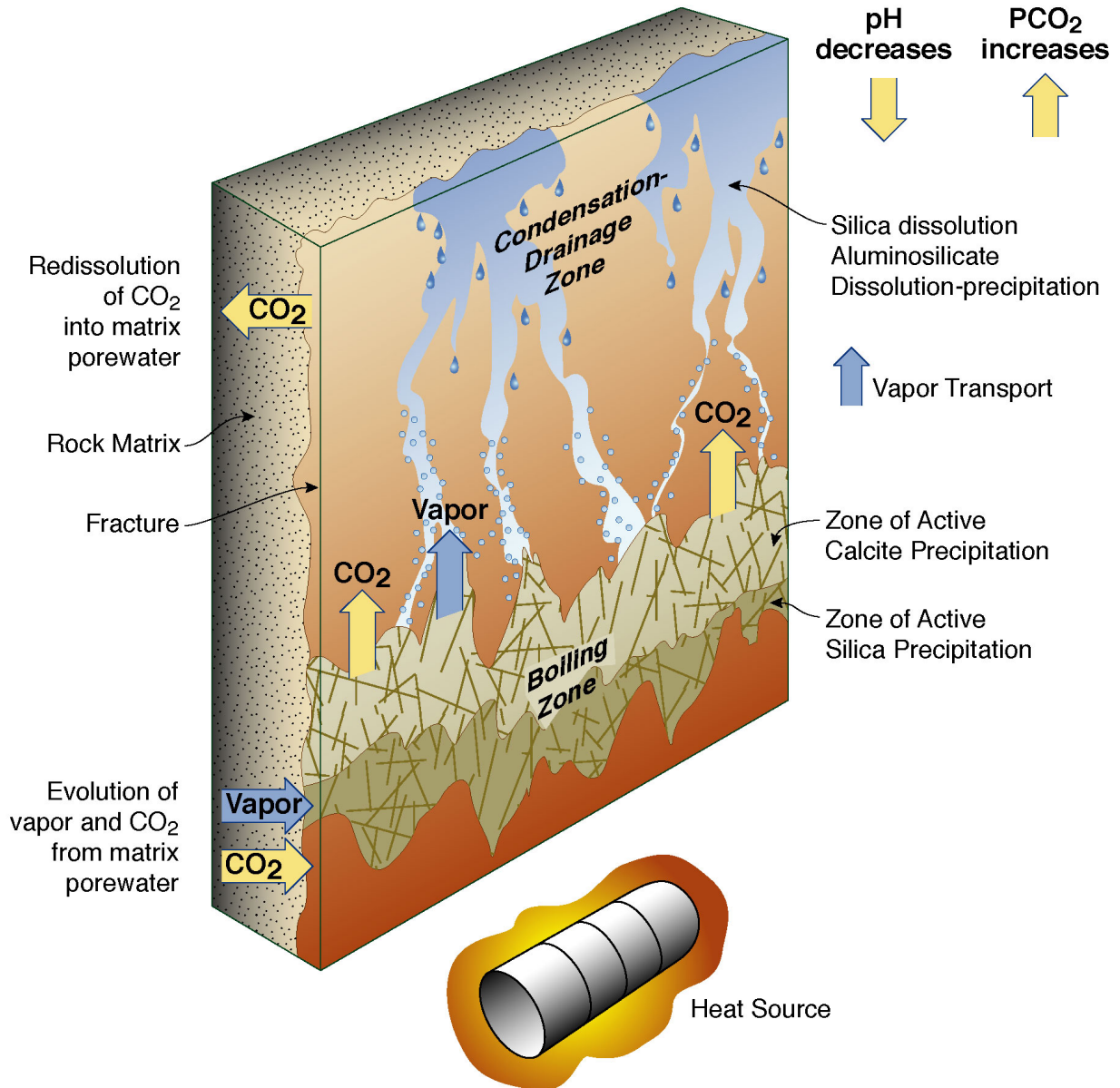


Figure 6.2-2. Schematic Diagram of Fracture–Matrix Interface Showing the Relation between TH Processes and Geochemical Processes

One important aspect of the system is the exsolution of CO_2 from the liquid phase as the temperature increases. The exsolution of CO_2 in the boiling zone results in a local increase in pH, and a decrease in pH in the condensation zone into which the vapor enriched in CO_2 is transported and condensed. The extent to which the pH is shifted depends strongly on the rates of mineral–water reactions, which can buffer the change in pH. Because the diffusivities of gaseous species are several orders of magnitude greater than those of aqueous species, and because the advective transport of gases can be more rapid than that of liquids, the region where CO_2 degassing affects water and gas chemistry could be much larger than the region affected by the transport of aqueous species.

The effects of TH processes on water chemistry are varied and depend on the behavior of the dissolved species and their relation to mineral–water reactions. Conservative species (i.e., those that are unreactive and nonvolatile), such as chloride (Cl^-) and nitrate (NO_3^-), become concentrated in waters undergoing vaporization or boiling, but are essentially absent from the vapor condensing in the fractures. Therefore, the concentration of conservative species in the draining condensate waters is determined by mixing with fracture waters and diffusive mixing with matrix pore waters.

More reactive aqueous species are affected by mineral precipitation/dissolution and ion exchange reactions, in addition to dilution and evaporative concentration as described above. Calcium concentrations are affected by calcite dissolution or precipitation, by feldspar dissolution, and by ion exchange reactions involving Ca-bearing zeolites and clays. Ion exchange is not explicitly included in the THC seepage model, but is represented by dissolution/precipitation of solid solutions for smectites, and of pure end-member compositions for other clays and zeolites. Similarly, magnesium concentrations are affected by ion exchange (the THC seepage model does not contain a magnesium zeolite, but magnesium-bearing clay phases are included), and by precipitation/dissolution of amorphous antigorite (Gunnarsson et al. 2005 [DIRS 176844]).

Sodium (Na^+) and potassium (K^+) are more conservative than the divalent ions, and concentrations are mainly controlled by evaporation (and salt precipitation at dryout conditions) and dilution, and, to a lesser degree, by feldspar dissolution reactions and ion exchange with clays and zeolites.

Aqueous silica ($\text{SiO}_2(\text{aq})$) concentrations are controlled by precipitation of amorphous silica, as well as by dissolution and precipitation of other silicates.

Zonation in the distribution of mineral phases can occur as a result of differences in mineral solubility as a function of temperature. The inverse relation between temperature and calcite solubility (as opposed to the silica phases, which are more soluble at higher temperatures) can cause zonation in the distribution of calcite and silica phases in both the condensation and boiling zones (Figure 6.2-2). Precipitation of amorphous silica or another silica phase is likely to be confined to a narrower zone where evaporative concentration from boiling exceeds its solubility. In contrast, calcite could precipitate in fractures over a broad zone of elevated temperature and where CO_2 has exsolved because of temperature increases or boiling. Alteration of feldspars to clays and zeolites is likely to be most rapid in the boiling zone because of their increased solubility (as well as having higher dissolution and precipitation rates) at higher temperatures (Lasaga 1998 [DIRS 117091], p. 66). In drainage zones, mineral alteration could be zoned within the rock matrix adjacent to a fracture, in a similar manner to that observed as a function of distance along the transport path (Steefel and Lichtner 1998 [DIRS 144878], p. 186).

In the THC seepage model, most precipitation and dissolution reactions are modeled as being kinetically limited (Section 6.4.2), with dissolution–precipitation rates that are a function of both temperature and the degree of saturation–undersaturation (the saturation index). Hence, species concentrations in solution at any given time and location are not controlled by the equilibrium thermodynamic condition, but rather by the influx rate, the rate of evaporation, and the rate of mineral dissolution in the grid cell of interest as countered by the rates of precipitation and

outflow. For this reason, predicted solution compositions at any given location can be supersaturated with respect to a given mineral and remain so for extended periods of time.

When chemical species are transported in fracture waters at rates greater than the rate of equilibration with the rock matrix, disequilibrium will exist between waters in fractures and matrix, potentially leading to different precipitating mineral assemblages and differences in reaction rates. Because the system is unsaturated and undergoes boiling, the transport of gaseous species between matrix and fractures is also important. The separate yet interacting geochemical, hydrologic, and thermal processes in the fractures and the rock matrix are incorporated into a dual-permeability modeling approach. In this approach, each location in the model is represented by both matrix and fracture gridblocks, each with its own pressure and temperature, liquid saturation, water and gas chemistry, and mineralogy. Communication between the coinciding matrix and fracture gridblocks is implemented by advective and diffusive transport of aqueous and gaseous species (Section 6.2.1.5).

6.2.1.3 Effects of Infiltration and Climate Changes on THC Processes

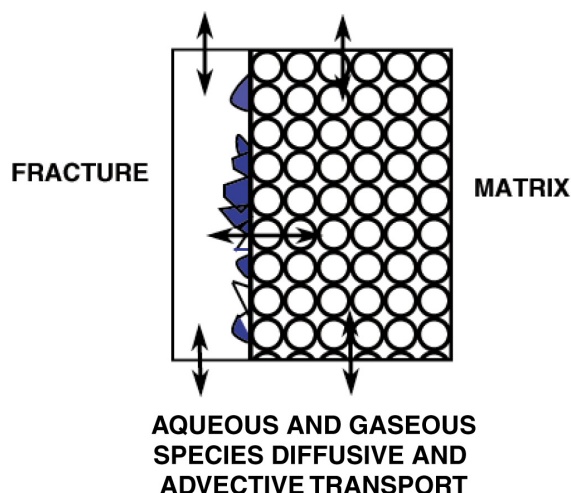
Early in the thermal period of the repository, much of the chemistry of the UZ around drifts will be constrained by the chemistry of ambient fracture and matrix pore water, which could change as a result of boiling, dilution with condensate water, or mineral–water–gas reactions. Once the peak thermal period has subsided, percolating water will mix with the condensate above the repository and eventually rewet the dryout zone. The composition of the percolating waters (before mixing) could be similar to that presently found above the repository as matrix pore water, or it could be more dilute, reflecting wetter climate conditions. Changes in the percolation flux also affect the extent of mineral deposition and dissolution, because of the changes in the flux of dissolved species to the region around drifts. For example, the greater the flux of calcium, the more calcite would precipitate for a given initial calcium concentration in percolating water. Higher percolation fluxes could increase the dissolution rates of minerals that are undersaturated in the fluid, because it could increase the degree to which the mineral is undersaturated.

6.2.1.4 Hydrologic Property Changes in Fractures and Matrix

Mineral precipitation and dissolution in fractures and the matrix have the potential for modifying the porosity, permeability, and unsaturated hydrologic properties of the system. Because the molar volumes of minerals created by hydrolysis reactions (i.e., anhydrous phases, such as feldspars, reacting with aqueous fluids to form hydrous minerals, such as zeolites or clays) are commonly larger than the molar volumes of the primary reactant minerals, dissolution–precipitation reactions commonly lead to porosity reductions. The extent of mineral–water reaction is controlled by the surface areas of the mineral phases in contact with the aqueous fluid, and heterogeneity in the distribution of minerals in the fractures. Therefore, changes in porosity and permeability caused by these processes may also be heterogeneously distributed. Other factors that could lead to heterogeneity in property changes are the distribution of liquid saturation in fractures, proportion of fractures having actively flowing water, and rates of evaporative concentration due to boiling, which could change the dominant mechanisms of crystal growth and nucleation.

6.2.1.5 Dual-Permeability Model for THC Processes

Transport rates by fluid flow in fractures greater than the rate of equilibration via diffusion necessarily leads to disequilibrium between waters in fractures and matrix. This disequilibrium can lead to differences in the prevailing mineral assemblage and to differences in reaction rates. Because the system is unsaturated and undergoes boiling, the transport of gaseous species is an important consideration. The model must also capture the differences between the initial mineralogy in fractures and matrix and their evolution. These separate yet interacting processes in fractures and matrix have been treated by adapting the dual-permeability model to include geochemical as well as hydrologic and thermal processes. In the dual-permeability model, each gridblock is partitioned into matrix and fracture continua, each characterized by its own pressure, temperature, liquid saturation, water and gas chemistry, and mineralogy. Figure 6.2-3 illustrates the dual-permeability conceptual model used for THC processes in the drift-scale THC seepage model and the DST THC submodel. Note that the permeability of each continuum is coupled to mineral precipitation and dissolution in each continuum (through volume changes) (Section 6.4.4), but the fracture–matrix interface area is not modified (see model approximations 1 and 8 in Section 6.4.6).



NOTE: Arrows refer to aqueous and gaseous species transport pathways. Angular objects in the fracture are minerals coating the fracture surface.

Figure 6.2-3. Conceptual Model (schematic) for Reaction–Transport Processes in Dual-Permeability Media

As summarized in the Section 6.2.1, the conceptual model for THC processes incorporates a wide range of coupled physical and chemical processes. Section 6.2.2 describes the implementation of this conceptual framework into a numerical model.

6.2.2 Conceptualization of the Geochemical System

The rationale used for defining the types and concentrations of chemical constituents (aqueous, solid, and gaseous) included in the THC seepage model is presented below. This section also includes discussions on the initial pore-water and pore-gas compositions used in the model, as

well as a description of the geochemical system. Note that the rationale for the selection of specific input water compositions for the model is described in *Engineered Barrier System: Physical and Chemical Environment* (SNL 2007 [DIRS 177412], Section 6.6). The geochemical system includes the aqueous components used in the model, the types and initial abundances of “primary” minerals (those already present in the rock), and “secondary” minerals that may precipitate as the result of water–gas–rock interactions.

6.2.2.1 Initial Pore-Water and Pore-Gas Chemistry

The initial water composition input into the model could be chosen from either the pore-water chemistry in the UZ at or above the repository horizon, or from the perched water or saturated zone. The perched waters are generally much more dilute than UZ pore waters. Isotopic compositions ($^{36}\text{Cl}/\text{Cl}$, $^{18}\text{O}/^{16}\text{O}$, D/H, ^{14}C) and chloride concentrations suggest that the perched waters have a large proportion of late Pleistocene/early Holocene water (Levy et al. 1997 [DIRS 126599], p. 906; Sonnenthal and Bodvarsson 1999 [DIRS 117127], pp. 107 and 108). The saturated zone water is also more dilute than pore waters, and neither saturated nor perched water reflects calculated CO_2 partial pressures consistent with CO_2 concentrations in gas measured in the unsaturated zone in repository units. The saturated zone and perched-water compositions are, therefore, deemed poor candidates as initial input water compositions for the THC seepage model. Preference is given instead to actual pore waters from unsaturated regions within or above the repository units.

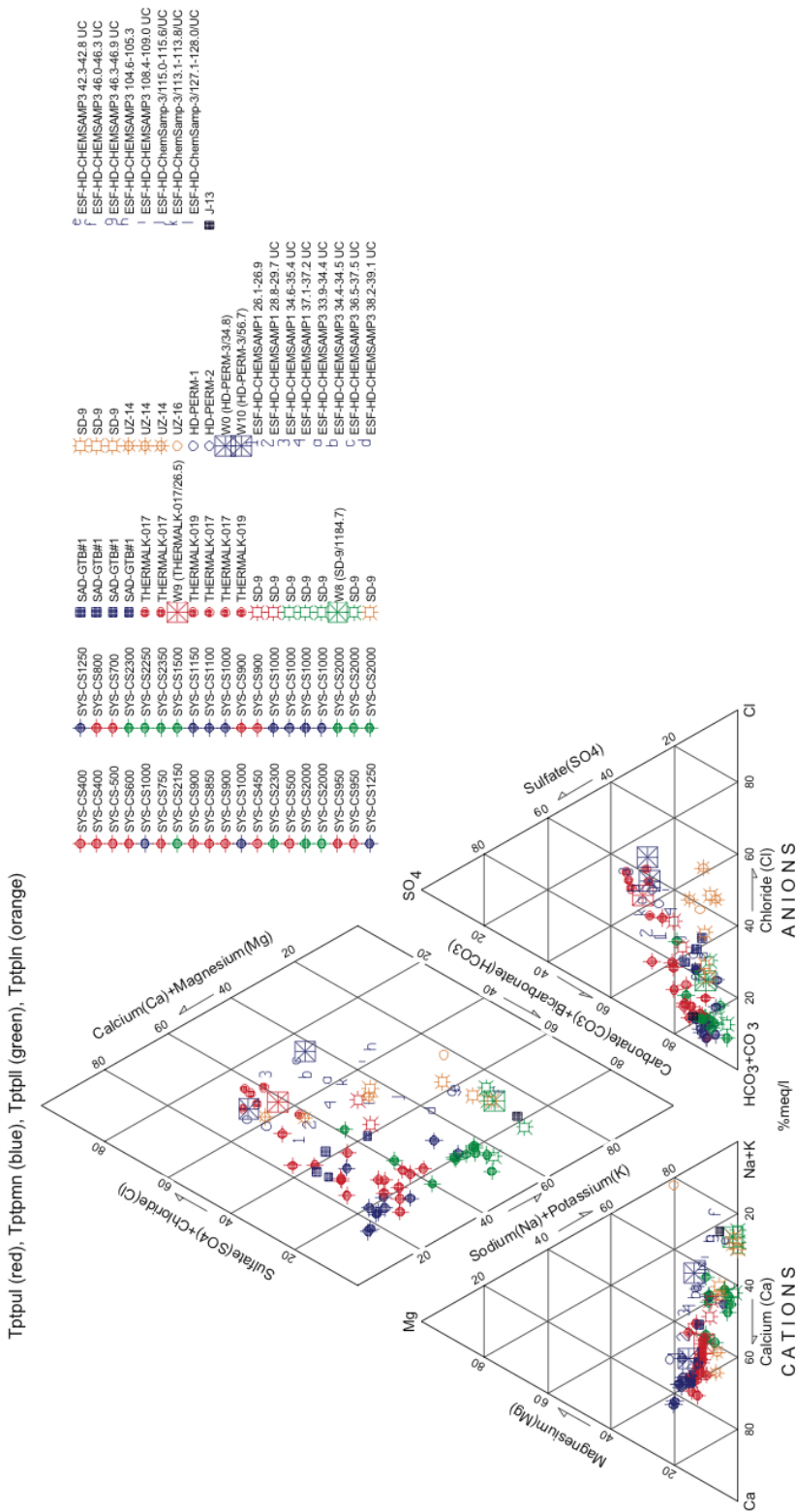
A conceptual model that explains the aqueous chemistry and background $^{36}\text{Cl}/\text{Cl}$ isotopic ratios in the ESF holds that percolating water must pass mostly through the Paintbrush nonwelded hydrogeologic unit (PTn) matrix (because of its high permeability and low fracture density) before reverting to predominantly fracture flow in the Topopah Spring welded hydrogeologic unit (TSw). As discussed by Levy et al. (1997 [DIRS 126599], pp. 907 and 908), this seems to be true everywhere except near large structural discontinuities in the PTn (i.e., faults). Hence, percolating water in the TSw ultimately had come predominantly through the PTn matrix. Analyses of PTn pore waters (and some at the top of the TSw) and many chloride analyses of TSw pore waters are consistent with this interpretation (Sonnenthal and Bodvarsson 1999 [DIRS 117127], pp. 140 and 141). The relatively higher concentrations of anions and cations in pore waters (compared to perched water) from the TSw, similar to PTn waters, are consistent with the premise that the waters had flowed through the PTn matrix.

The initial composition of water in fractures is taken to be the same as in the rock matrix throughout the model domain, using the same initial composition in all hydrogeologic units. The composition of water infiltrating the top of the model domain (in the Tiva Canyon welded hydrogeologic unit – TCw) is also set to be the same as the initial fracture and matrix pore-water composition, with the exception of minor changes related to a pH adjustment, reflecting a higher CO_2 partial pressure and a lower temperature at the top model boundary than deeper into the model domain (see below). Setting nearly identical compositions for infiltration at the top model boundary and initial fracture–matrix waters is a simplification of the natural system to avoid having to consider complex near-surface hydrological, geochemical, biological, and transport processes, such as evapotranspiration, weathering and calcite formation, and biologically mediated reactions.

In the early stages of development of the THC seepage model, only a few nearly complete pore-water analyses from a repository unit were available. These were water ultracentrifuged from core samples collected from the Tptpmn geologic unit in Alcove 5 near the DST. Three water samples were analyzed (HD-PERM-1, HD-PERM-2, and HD-PERM-3) from the same suite of cores and yielded similar compositions. Two of these analyses with nearly identical compositions were averaged for use as an input water composition in earlier model revisions. Since then, a series of pore-water samples from repository host units has been analyzed. Representative compositions of these waters are shown on a Piper diagram in Figure 6.2-4. This figure also shows the hydrogeologic units from which the water samples were extracted. It is evident from Figure 6.2-4 that the span of potential initial water compositions for use in the THC seepage model is large. This figure also shows a tendency for samples from deeper hydrogeologic units to exhibit higher sodium (plus potassium) concentrations relative to calcium (plus magnesium) concentrations, and a higher proportion of aqueous carbonate (relative to chloride and sulfate) compared to shallower waters. The sodium increase relative to calcium with depth has been noted previously in pore waters from hydrogeologic units above and below the repository units (Yang et al. 1996 [DIRS 100194], p.13). It is likely caused by the hydrolysis of volcanic glass and feldspars and, mostly below the repository units, exchange reactions with zeolites (Vaniman et al. 2001 [DIRS 157427]). The precipitation of calcite in fractures under the ambient geothermal gradient would also exacerbate the decrease in calcium relative to sodium concentrations with depth. Trends in carbonate concentrations relative to chloride and sulfate concentrations are subject to large uncertainties as a result of the determination of total aqueous carbonate concentrations. An increase in aqueous carbonate concentration with depth could be attributed to the pH increase expected to accompany glass and feldspar hydrolysis reactions.

Selected initial water compositions for simulations presented in this report are shown in Table 6.2-1 and plotted in Figure 6.2-4. These waters were selected as described in *Engineered Barrier System: Physical and Chemical Environment* (SNL 2007 [DIRS 177412], Section 6.6), and input into the current THC seepage model. The selection criteria for these waters included reliability of analytical data (mainly on the basis of charge balance), potential end-brine compositions upon evaporation, span of natural variability, and other less critical factors discussed in *Engineered Barrier System: Physical and Chemical Environment* (SNL 2007 [DIRS 177412], Section 6.6). These waters are designated as W0, W8, W9, and W10 in this report, and span a range of compositions (Table 6.2-1). Table 6.2-1 also includes calculated concentrations used for input into the THC seepage model, as discussed further below, and distinguishes between the compositions used for initial fracture and matrix waters within the model domain and at its top boundary.

Topopah Spring Tuff Pore Waters



Source DTNs: GS030408312272.002 [DIRS 165226], GS020408312272.003 [DIRS 160899], GS020808312272.004 [DIRS 166569], GS031008312272.008 [DIRS 166570], MO0005PORWATER.000 [DIRS 150930], GS060908312272.004 [DIRS 179065].

NOTE: Samples labeled HD-PERM are pore waters from the Tptpmn unit in Alcove 5 of the ESF. Sample IDs starting with SYS-CS represent pore waters from the ECRB Cross-Drift and are listed in order of increasing distance (m) into the drift (down stratigraphy). Additional borehole interval information after each SYS-CS sample labeling is sample interval distances from borehole collar given in feet. CS is the abbreviation for Construction Station, indicating distance along the ECRB Cross-Drift in meters. THERMALK pore waters are from near the south bend of the ESF drift. SAD-GTB pore water samples are from the Alcove 7 area of the ESF. CHEMSAMP pore waters represent samples collected in the heated rock block of the Drift Scale Test. Sample IDs starting with SD-9, UZ-14, and UZ-16 represent pore waters from surface boreholes with the same names. The four starting waters (Table 6.2-1) are also indicated (see text). DTN: GS020808312272.004 [DIRS 166569] is unqualified due to missing closing calibrations for electronic balances and weights traceable by the National Institute of Standards and Technology. These data are included here to show the full spread of measured waters.

Figure 6.2-4. Piper Plot of Water Compositions (meq/L) from Repository Units

Table 6.2-1. Input Pore-Water Compositions for the THC Seepage Model

Sample ID:	ESF-HD-PERM-3/34.8-35.1 (Alcove 5)	ESF-HD-PERM-3/56.7-57.1 (Alcove 5)	SD-9/1184.7-1184.8 (Borehole SD-9)	ESF-THERMAL-K-017/26.5-26.9
Lithostratigraphic Unit:	Tptpmn HDPERM3	Tptpmn ESPERM4	Tptpll SD9-3	Tptpul ESFTHER1
Internal Reference Name:	MO005PORWATER.000 [DIRS 150930]	GS060908312272.004 [DIRS 179065]	GS030408312272.002 [DIRS 165226]	GS031008312272.008 [DIRS 166570]
DTN:	W0	W10	W8	W9
Simulation Water ID:	Fract/Matrix	Fract/Matrix	Fract/Matrix	Fract/Matrix
Water Input Type:	Boundary ^a	Boundary ^a	Boundary ^a	Boundary ^a
Units				
Temperature	20	20	20	20
pH (measured)	8.31	—	8.2	7.7
pH (calc) ^b	7.86	7.93	8.10	7.87
Na ⁺	62	123	59	45
K ⁺	9	13.8	4.8	14.4
Ca ²⁺ (measured)	97	59.9	19	62
Ca ²⁺ (calc) ^b	64.1	46.6	18.1	56.5
Mg ²⁺	17.4	16.7	0.7	7.9
SiO ₂ (measured)	75	—	42	52
SiO ₂ (calc) ^c	49.3	49.4	(d)	49.3
Cl ⁻	123	146	23	67
SO ₄ ²⁻	120	126	16	82
HCO ₃ ⁻ (measured)	—	149	142	126
HCO ₃ ⁻ (calc) ^b	85.8	102.3	140.5	87.4
NO ₃ ⁻	10	57.4	16	44
F ⁻	0.76	1.3	2.2	1.4

Table 6.2-1. Input Pore-Water Compositions for the THC Seepage Model (Continued)

Sample ID:	ESF-HD-PERM-3/34.8-35.1 (Alcove 5)	ESF-HD-PERM-3/56.7-57.1 (Alcove 5)	SD-9/1184.7-1184.8 (Borehole SD-9)	ESF-THERMALK-017/26.5-26.9
Lithostratigraphic Unit:	Tptpmn	Tptpmn	Tptpll	Tptpul
Internal Reference Name:	HDPERM3	ESPERM4	SD9-3	ESFTHER1
DTN:	MO005PORWATER.000 [DIRS 150930]	GS060908312272.004 [DIRS 179065]	GS030408312272.002 [DIRS 165226]	GS031008312272.008 [DIRS 166570]
Simulation Water ID:	W0	W10	W8	W9
Water Input Type:	Fract/Matrix	Fract/Matrix	Fract/Matrix	Fract/Matrix
Units	Boundary ^a	Boundary ^a	Boundary ^a	Boundary ^a
Al ³⁺ (calc) ^e	2.30 × 10 ⁻⁹	1.75 × 10 ⁻⁹	6.03 × 10 ⁻⁹	2.20 × 10 ⁻⁹
Fe ³⁺ (calc) ^e	2.06 × 10 ⁻¹²	1.35 × 10 ⁻¹²	2.04 × 10 ⁻¹²	2.06 × 10 ⁻¹²
log(pCO ₂) ^f	-3.0	-3.0	-3.0	-3.0
CO ₂ (approx) ^g	1,136	1,136	1,136	1,136

Output DTNs (calculated values): LB0705DSTHC001.001, LB0705DSTHC002.001, LB0705DSTHC003.001, LB0705DSTHC004.001.

^a Same data as for fracture/matrix except for calculated values.

^b pH, total aqueous carbonate as HCO₃⁻, and total aqueous calcium as Ca²⁺ calculated by speciation with TOUGHACT V3.1.1 at the temperatures and log(pCO₂) shown, forcing charge balance as well as equilibration with calcite.

^c Total aqueous silica as SiO₂(aq) calculated by equilibration of the solution with opal-CT (using TOUGHACT V3.1.1) at the temperatures shown (measured values, if any, yield solutions supersaturated with respect to opal-CT).

^d The measured total silica concentration yields solutions near equilibrium with opal-CT (saturation indices of -0.07 and -0.002 at 20 and 16 °C, respectively) and is not recalculated.

^e Total aqueous aluminum and iron calculated by equilibration of the solution with illite and goethite, respectively, at the temperatures shown.

^f CO₂ partial pressures were set at values shown, which are representative of field conditions.

^g Conversion from CO₂ partial pressure shown using approximate total pressure of 0.88 bar at the repository level.

NOTE: Compositions shown are those used for initial fracture and matrix water (column labeled "Fract/Matrix") and infiltration water at the model top boundary (column labeled "Boundary"). Calculated concentrations, where shown, were used in simulations.

The set of analyzed species for the selected input water composition does not include iron and aluminum. Because these components are needed to include aluminum silicates and iron minerals in the simulations, their concentrations have been calculated assuming equilibrium with goethite and illite, respectively. Illite was chosen to set the initial aluminum concentration because it is a common alteration mineral, and Yucca Mountain pore waters typically plot near the theoretical illite-K-feldspar boundary. Goethite is more soluble and metastable with respect to hematite, which is the most abundant iron oxide mineral found in the tuffs at Yucca Mountain. Goethite is therefore a reasonable candidate to use for setting the initial iron concentration in solution.

Calcite is a fast-reacting mineral and is commonly observed in fractures at Yucca Mountain (e.g., Whelan et al. 2002 [DIRS 160442]). However, measured pH values (if available) for most of the TSw pore-water samples yield CO₂ gas partial pressures much larger than observed values when these waters are assumed to be at equilibrium with calcite. Conversely, when trying to adjust the measured pH values and/or bicarbonate content of these waters such that charge balance and reasonable CO₂ gas partial pressures are obtained, most of the TSw waters are computed to be significantly supersaturated with respect to calcite (typically by around 1 saturation index unit). This may be caused, at least in part, by sampling artifacts as well as bacteriological effects on the measured alkalinity and calcium concentrations, as further discussed in *Engineered Barrier System: Physical and Chemical Environment* (SNL 2007 [DIRS 177412], Section 6.6). For these reasons, the pH, total aqueous carbonate concentration, and total calcium concentrations (reported here as HCO₃⁻ and Ca²⁺) in analyses used as input to the current THC seepage model were recomputed by forcing charge balance and equilibrium with calcite at a given CO₂ gas partial pressure (10⁻³ bar, assumed equal to fugacity)¹ (Table 6.2-1). This was accomplished using TOUGHREACT V3.1.1 and full speciation calculations at temperatures of 20°C (corresponding to the model domain near the repository horizon) and 16.02°C (corresponding to the model upper boundary). A CO₂ partial pressure of 10⁻³ bar was selected because it is consistent with CO₂ concentrations near 1,000 ppmv measured in repository units in the ESF (DTN: LB0208ISODSTHP.001 [DIRS 161638]) and in borehole UZ-1 (Yang et al. 1996 [DIRS 100194], p. 42). It should be noted that the equilibration with calcite results in a significant (up to ~30%) drop of the calcium concentration in waters W0 and W10, only a slight drop (~10%) in water W9, and essentially no drop in water W8, the latter being initially close to saturation with respect to calcite.

Opal-CT is one of the most common fracture- and cavity-lining minerals in Yucca Mountain besides calcite (e.g., Whelan et al. 2002 [DIRS 160442]). The silica concentration in water W8 essentially reflects equilibrium with opal-CT (saturation indices of -0.07 and -0.002 at 20 and 16°C, respectively). Water W9 is also nearly saturated with respect to this mineral (saturation indices of 0.02 and 0.09 at 20°C and 16°C, respectively). Water W0 is somewhat more strongly supersaturated (saturation indices of 0.18 and 0.25 at 20°C and 16°C, respectively), possibly the result of storage for several years in a glass jar before the silica analysis was completed. The concentration of silica in water W10 was not measured. For these reasons, it was decided to

¹ In the present case, this was established by simultaneous initial constraints of: total hydrogen ion concentration set by charge balance, total calcium concentration set by forced equilibration with calcite, and total aqueous carbonate concentration set by forced equilibration with CO₂(gas) at a fugacity of 10⁻³ bar. The numerical solution being unique, any combination of these three constraints and three parameters (i.e., total concentrations of H⁺, Ca²⁺, and HCO₃⁻ primary species) would yield the same results.

calculate the silica concentrations in all input waters to reflect equilibrium with opal-CT, except for water W8, which is initially essentially at equilibrium with this mineral. In doing so, the initial silica concentration of water W0 dropped by about 30%, and that of W9 by about 5%.

6.2.2.2 Geochemical Systems

Minerals and chemical-aqueous components considered in this study are shown in Table 6.2-2. Primary mineral types and abundances are derived from averages of x-ray diffraction measurements on cores reported in the Yucca Mountain mineralogical model (DTN: LA9908JC831321.001 [DIRS 113495]) and analyses of fracture surfaces (Carlos et al. 1993 [DIRS 105210], p. 47; DTNs: LA9912SL831151.001 [DIRS 146447] and LA9912SL831151.002 [DIRS 146449]), as well as literature data on bulk rock compositions (DTN: GS000308313211.001 [DIRS 162015]; Peterman and Cloke 2002 [DIRS 162576]). Amounts of minerals observed, but present in quantities below the detection limit (typically around 1% for x-ray diffraction), have been estimated. Potential secondary minerals (i.e., those allowed to precipitate but which may not necessarily form) have been determined from field observations of thermal alteration or ambient weathering (e.g., Vaniman et al. 2001 [DIRS 157427]). Initial mineral amounts used in simulations were calculated as described in Section 6.2.2.3, with results shown in Appendix A.

The bases for selection of aqueous species included in this study are: (1) use the major components of pore water, (2) use all components in major rock-forming minerals considered in the model, and (3) use additional components specifically requested by downstream users (nitrate, iron, and fluoride). Thus, the modeled geochemical system (Table 6.2-2) includes the major solid phases (minerals and glass) encountered in geologic units at Yucca Mountain, a range of possible reaction product minerals, CO₂ gas, and the aqueous species necessary to describe this system. Additional high solubility “salt” phases are included which typically only form under conditions of complete dryout. These “salt” phases, and the methods in which they are considered to form, are described in Section 6.4.5.

The treatment of mixed phases (feldspars, clays, and zeolites), as far as the number and compositions of endmembers to consider, the nature of the phases (primary or secondary), and whether a solid-solution model should be implemented, is based in large part on simulations of ambient conditions as described in Section 6.5.5.1. An ideal solid-solution model is implemented for beidellite (Na, K, Ca, and Mg end-members), with each end-member’s activity equaling its mole fraction. Treating these clays as a solid solution results in individual smectite end-members either all dissolving or all precipitating, providing a better physical representation of dissolution/precipitation processes. Note that the potassium end-member in beidellite was included only as a potential secondary phase. Illite was assumed to be the primary potassium-bearing clay, and K-beidellite was included to provide an additional degree of freedom for potentially precipitating potassium-bearing clays. Other solid-solution primary minerals are considered as solid solutions with thermodynamic data corresponding to their respective fixed compositions (Appendix C). These minerals include: plagioclase, sanidine, and ymp-clinoptilolite, which are only allowed to dissolve; and stellerite, mordenite, and secondary Ca-, K-, and Na-clinoptilolite, which can precipitate or dissolve. Sources of inputs for the determination of mixed phase compositions are given in Section 4.1.6 and discussed in Appendix C.

Table 6.2-2. Mineral, Aqueous, and Gaseous Species Used in the THC Seepage Model

Minerals	Mineral Name in Simulations	Mineral Formula in Simulations ^a	Mineral Type ^b
Cristobalite- α	cristoba-a	SiO ₂	P
Biotite	biotite-ox	K(Fe _{0.57} Mg _{0.43}) ₃ AlSi ₃ O ₁₀ (OH) ₂	P
Clinoptilolite (solid sol.)	clinpt-ym/10 ^c	K _{0.0408} Na _{0.0203} Ca _{0.1428} Al _{0.3467} Si _{1.4533} O _{3.6} 1.0922H ₂ O	P
Hematite	hematite	Fe ₂ O ₃	P
Plagioclase	plagio-ym	Na _{0.76} K _{0.07} Ca _{0.17} Al _{1.17} Si _{2.83} O ₈	P
Quartz	quartz	SiO ₂	P
Rhyolitic glass	glass-rhyol	Si _{0.8016} Al _{0.1581} Na _{0.0745} K _{0.0796} Ca _{0.0022} Mg _{0.0003} Fe _{0.0074} H _{0.2166} O _{2.0393}	P
Sanidine	sanidi-ym	Na _{0.47} K _{0.48} Ca _{0.05} Al _{1.05} Si _{2.95} O ₈	P
Tridymite	tridymite	SiO ₂	P
Beidellite-Ca	beidel-ca	Ca _{0.165} Al ₂ Al _{0.33} Si _{3.67} O ₁₀ (OH) ₂	P, S
Beidellite-Mg	beidel-mg	Mg _{0.165} Al ₂ Al _{0.33} Si _{3.67} O ₁₀ (OH) ₂	P, S
Beidellite-Na	beidel-na	Na _{0.33} Al ₂ Al _{0.33} Si _{3.67} O ₁₀ (OH) ₂	P, S
Calcite	calcite	CaCO ₃	P, S
Fluorite	fluorite	CaF ₂	P, S
Illite	illite	K _{0.6} Mg _{0.25} Al _{2.3} Si _{3.5} O ₁₀ (OH) ₂	P, S
Mordenite	mordenit/10 ^c	Ca _{0.08685} Na _{0.1083} Al _{0.282} Si _{1.518} O _{3.6} 1.0404H ₂ O	P, S
Opal-CT	opal_CT	SiO ₂	P, S
Stellerite	stell-ym/10 ^c	Ca _{0.195} Na _{0.005} Al _{0.395} Si _{1.405} O _{3.6} 28H ₂ O	P, S
Amorphous antigorite	antigo_am	Mg ₃ Si ₂ O ₅ (OH) ₄	S
Amorphous silica	sio2(am)	SiO ₂	S
Anhydrite	anhydrite	CaSO ₄	S
Beidellite-K	beidel-k	K _{0.33} Al ₂ Al _{0.33} Si _{3.67} O ₁₀ (OH) ₂	S
Clinoptilolite-Ca	clinpt-ca/10 ^c	Ca _{0.17335} Al _{0.3467} Si _{1.4533} O _{3.6} 1.0922H ₂ O	S
Clinoptilolite-K	clinpt-k/10 ^c	K _{0.3467} Al _{0.3467} Si _{1.4533} O _{3.6} 1.0922H ₂ O	S
Clinoptilolite-Na	clinpt-na/10 ^c	Na _{0.3467} Al _{0.3467} Si _{1.4533} O _{3.6} 1.0922H ₂ O	S
Goethite	goethite	FeOOH	S
Kaolinite	kaolinite	Al ₂ Si ₂ O ₅ (OH) ₄	S
Aqueous Primary Species: H ₂ O, H ⁺ , Na ⁺ , K ⁺ , Ca ²⁺ , Mg ²⁺ , SiO ₂ , AlO ₂ ⁻ , HFeO ₂ ²⁻ , HCO ₃ ⁻ , Cl ⁻ , SO ₄ ²⁻ , F ⁻ , NO ₃ ⁻			
Gases: CO ₂ , H ₂ O, Air			

^a Data sources listed in Appendix C.

^b Primary (P) and secondary (S) minerals.

^c The formulae of these minerals with large structural units were divided by 10 (and therefore their equilibrium constants, log(K), were also divided by 10) to avoid the use of large log(K) values in simulations, which could potentially result in numerical problems.

It should be noted that the model was initially set up (Section 6.2.2.3) using Ca- and Na-montmorillonite (in addition to illite) as the representative primary clay minerals (using thermodynamic data and compositions from the project database *data0.ymp.R5*; DTN: SN0612T0502404.014 [DIRS 178850]). The magnesium endmember did not have an elevated calcium content as observed in clays at Yucca Mountain (Bish et al 1996 [DIRS 101430], Table 1). However, using the available montmorillonite compositions in *data0.ymp.R5*, the observed elevated calcium content in clays could not quite be reproduced, even after discarding the Mg endmember. Furthermore, all initial pore-water compositions (Table 6.2-1) are strongly supersaturated with respect to montmorillonite, even when taken as separate endmembers instead of a solid solution. As a result, trial simulations of ambient conditions (Section 6.5.5.1) did not yield realistic results when using montmorillonite. For this reason, primary clay minerals were switched from Ca- and Na-montmorillonite to Ca-, Na-, and Mg-beidellite (using thermodynamic data and compositions from the project database

data0.ymp.R5; DTN: SN0612T0502404.014 [DIRS 178850]), yielding much better results (Section 6.5.5.1).

6.2.2.3 Mineral Volume Fractions

This section describes the methodology for calculating mineral volume fractions from various measured data on mineral abundances (usually in terms of weight percent) for the THC seepage model. As discussed briefly in Section 4.1.6, the THC seepage model is assumed to represent a typical column through the repository. Therefore, mineralogical abundances (in weight percent) were chosen from the average values reported in DTN: SN0307T0510902.003 [DIRS 164196]. Where data were not available for individual layers (e.g., PTn) or for minor mineral phases, they were derived from measurements (also in weight percent) made on samples from Borehole SD-9 (Bish et al. 2003 [DIRS 169638], Supplementary Data Table 1), which is near the center of the current repository footprint, and also the closest surface-based borehole to the DST. Typically, there are a few or more measurements made for samples within a given hydrogeological unit, and there the SD-9 values were in most cases averaged. Fracture mineralogical data are based on fracture mineral abundances in core from underground boreholes in the ESF, in the regions of the Single Heater Test (DTN: LA0009SL831151.001 [DIRS 153485]) and the Drift Scale Test (DTNs: LA9912SL831151.001 [DIRS 146447] and LA9912SL831151.002 [DIRS 146449]).

The steps involved in calculating mineral volume fractions in the rock matrix are described below. Calculations were implemented in Excel spreadsheets with names listed below, and submitted to the TDMS under Output DTN: LB0707DSTHC006.003:

1. Obtained measured mineral abundances (in weight percent) from Bish et al. (2003 [DIRS 169638], Supplementary Data Table 1) for borehole SD-9.
2. Calculated average values of mineral abundances (in weight percent) for hydrogeological units (spreadsheet: *sd9_minabund_rev05_c1.xls*²), using model layer elevations from DTN: LB02081DKMGRID.001 [DIRS 160108] and geological designations from DTN: LA9908JC831321.001 [DIRS 113495].
3. Calculated proportions of average clinoptilolite and mordenite abundances to total abundance (spreadsheet: *sd9_minabund_rev05_c1.xls*).
4. Calculated proportions of average cristobalite and opal-CT abundances to total abundance (spreadsheet: *sd9_minabund_rev05_c1.xls*).
5. Obtained average mineral abundances for the entire site (in weight percent) from DTN: SN0307T0510902.003 [DIRS 164196] (listed in spreadsheet *Avg_mineralogy_MM3.0_rev05_c1.xls*).
6. Assigned values based on lithologic units to model hydrogeological units (spreadsheet: *Avg_mineralogy_MM3.0_rev05_c1.xls*).

² Note: minor errors have been found in this spreadsheet during the checking process after completion of this work. These errors are documented in the spreadsheet and are inconsequential.

7. Supplemented average mineral abundances with SD-9 data (spreadsheet: *Avg_mineralogy_MM3.0_rev05_c1.xls*).
8. Separated feldspar abundances into 1% plagioclase plus remaining feldspar as sanidine (spreadsheet: *Avg_mineralogy_MM3.0_rev05_c1.xls*).
9. Used ratios of average mordenite and clinoptilolite abundances in borehole SD-9 to recalculate those mineral abundances from average zeolite abundances (spreadsheet: *Avg_mineralogy_MM3.0_rev05_c1.xls*).
10. Used ratios of average cristobalite and opal-CT abundances in borehole SD-9 to recalculate those mineral abundances from average cristobalite abundances (spreadsheet: *Avg_mineralogy_MM3.0_rev05_c1.xls*).
11. Calculated moles of minerals per 100 grams of rock (Mol_{min}) from unrenormalized weight percent abundances (W_{min}) and molecular weight (MW in g/mol), as follows (spreadsheet: *minabund_areas_rev05_final_c1.xls*³):

$$Mol_{min} = \frac{W_{min}}{MW_{min}} \quad (\text{Eq. 6.2-1})$$

12. Calculate mineral mole fractions by normalizing moles to 1 (spreadsheet: *minabund_areas_rev05_final_c1.xls*).
13. Used composition of smectite from Bish et al. (1996 [DIRS 101430], Table 1) (Table 6.2-3) and fraction of illite (0.1) based on the study by Carey et al. (1998 [DIRS 109051], p. 18) to recalculate smectite into illite, Ca-montmorillonite and Na-montmorillonite. Calculated cation mole fractions (excluding Fe) are 0.06 (Na), 0.04 (K), 0.60 (Ca), and 0.30 (Mg) (spreadsheet: *minabund_areas_rev05_final_c1.xls*).

Table 6.2-3. Smectite Composition (wt %) from Bish et al. (1996 [DIRS 101430], Table 1)

Oxide	wt %
SiO ₂	43.20
Al ₂ O ₃	21.40
Na ₂ O	0.14
K ₂ O	0.15
CaO	2.48
MgO	0.89
FeO	1.57
H ₂ O	30
Total	99.83

³ Note: minor errors have been found in this spreadsheet during the checking process after completion of this work. These errors are documented in the spreadsheet and are inconsequential.

The montmorillonite-Ca composition in the project database *data0.ymp.R5* (DTN: SN0612T0502404.014 [DIRS 178850]) contains much more magnesium than calcium, and for this reason the montmorillonite-Mg endmember in this database was not considered (there would be too much magnesium in the smectite if this endmember was included). Because the sodium mole fraction is approximately 10% of the calcium mole fraction in the smectite analysis of Bish et al. (1996 [DIRS 101430], Table 1), montmorillonite-Na was included with an estimated (rough) amount equal to 10% of the smectite mole fraction in the rock. Therefore, the proportions were approximated as follows ($X_{smectite}$ is the mole fraction of smectite in the rock):

$$\begin{aligned} \text{illite} &= 0.1 * X_{smectite} \\ \text{montmorillonite-Ca} &= 0.9 * 0.9 * X_{smectite} \\ \text{montmorillonite-Na} &= 0.1 * 0.9 * X_{smectite} \end{aligned}$$

As discussed in Section 6.2.2.2, the use of montmorillonite as a primary clay mineral did not yield satisfactory results, and it was decided to switch the type of clays from montmorillonite to beidellite. Because of schedule constraints, the switch was made directly in the TOUGHREACT input files (rather than revising the calculations in spreadsheet *minabund_areas_rev05_final_c1.xls*)⁴ by assigning the originally calculated amount of Na-montmorillonite to Na-beidellite, then assigning 2/3 of the originally calculated amount of Ca-montmorillonite to Ca-beidellite, and 1/3 of the originally calculated amount of Ca-montmorillonite to Mg-beidellite. This effectively resulted in the following calculated proportions:

$$\begin{aligned} \text{illite} &= 0.1 * X_{smectite} \\ \text{beidellite-Ca} &= 0.6 * 0.9 * X_{smectite} \\ \text{beidellite-Mg} &= 0.3 * 0.9 * X_{smectite} \\ \text{beidellite-Ca} &= 0.1 * 0.9 * X_{smectite} \end{aligned}$$

14. Mineral volumes (V_{min} in cc/mole rock) were calculated (spreadsheet: *minabund_areas_rev05_final_c1.xls*) from mole fractions (X_{min}) and molar volumes (v_{min}) as follows:

$$V_{min} = X_{min} v_{min} \quad (\text{Eq. 6.2-2})$$

15. Volume fractions were calculated by normalizing volumes to 1.0 (spreadsheet: *minabund_areas_rev05_final_c1.xls*).

6.2.2.4 Mineral Compositions

The compositions of mixed solid phases (solid solutions) were derived either from specific measurements, calculated from bulk rock compositions and mineral abundances, or taken directly from the project database *data0.ymp.R5* (DTN: SN0612T0502404.014 [DIRS 178850]), as discussed below. Other minerals were taken as pure phases with ideal composition from the project database *data0.ymp.R5* (DTN: SN0612T0502404.014 [DIRS 178850]) (e.g., hematite,

⁴ Note: All calculations were later redone using beidellite instead of montmorillonite and are reported in DTN: LB0707DSTHC006.003 in addition to the original calculations described here.

quartz and other silica polymorphs). Resulting mineral formulae used in the simulations are shown in Table 6.2-2.

The composition of the sanidine groundmass was calculated from bulk rock analyses and mineral compositions given in Table 6.2-4, as presented in spreadsheet *tsw_plag_bulk_rev05_c1.xls*.

Table 6.2-4. Repository Unit Bulk Rock Composition (TSw), Measured Biotite and Plagioclase Phenocryst Compositions, and Calculated Ideal Endmember Compositions for Other Primary Minerals

Oxide	TSw	Biotite	Plag Pheno	Anorthite	Albite	Orthoclase	Quartz	Calcite	Hematite
SiO ₂	76.290	36.49	63.90	43.19	68.74	64.76	100.00	0.00	0.00
TiO ₂	0.109	4.50	0.00	0.00	0.00	0.00	0.00	0.00	0.00
Al ₂ O ₃	12.550	13.79	22.13	36.65	19.44	18.32	0.00	0.00	0.00
Fe ₂ O ₃	0.970	0.00	0.00	0.00	0.00	0.00	0.00	0.00	100.00
FeO	0.130	22.34	0.00	0.00	0.00	0.00	0.00	0.00	0.00
MnO	0.068	0.54	0.00	0.00	0.00	0.00	0.00	0.00	0.00
MgO	0.120	9.93	0.00	0.00	0.00	0.00	0.00	0.00	0.00
CaO	0.500	0.00	3.53	20.16	0.00	0.00	0.00	56.03	0.00
Na ₂ O	3.520	0.52	8.65	0.00	11.82	0.00	0.00	0.00	0.00
K ₂ O	4.830	9.22	1.24	0.00	0.00	16.92	0.00	0.00	0.00
P ₂ O ₅	0.010	0.00	0.00	0.00	0.00	0.00	0.00	0.00	0.00
CO ₂	0.011	0.00	0.00	0.00	0.00	0.00	0.00	43.97	0.00
F	0.038	0.00	0.00	0.00	0.00	0.00	0.00	0.00	0.00
Total	99.146	97.330	99.450	100.00	100.00	100.00	100.00	100.00	100.00

Sources: Bulk rock chemical analyses (for calculation of groundmass sanidine composition): DTN: GS000308313211.001 [DIRS 162015] and Peterman and Cloke 2002 [DIRS 162576].
Biotite phenocrysts: Flood et al. 1989 [DIRS 182723], Table 2.

Plagioclase phenocrysts (plag pheno): calculated from plagioclase formula (Or_{0.07}Ab_{0.76}An_{0.17}) reported in Johnson et al. 1998 [DIRS 101630], as shown in spreadsheet *tsw_plag_bulk_rev05_c1.xls*.

NOTE: MgO was incorrectly typed as 0.13 instead of 0.12 in spreadsheet *tsw_plag_bulk_rev05_c1.xls*, and has been noted there. This has no effect on the results because MgO is not a component in the ideal feldspar compositions and is too small in abundance to affect the renormalization of the oxides.

Calculation of the sanidine groundmass composition was performed by first removing the calcium attributed to plagioclase and calcite in the bulk rock analysis. An estimated 1% (by mass) of the plagioclase phenocryst composition was removed. The amount of calcite to remove was determined by assuming that calcite accounts for all the CO₂ content in the rock. Mass fractions of the mineral endmembers were then calculated by performing a least squares fit using the mineral compositions and the bulk rock composition (as given in spreadsheet *tsw_plag_bulk_rev05_c1.xls*). The final sanidine groundmass, recalculated as mole fractions of the endmembers, is An_{0.049}Ab_{0.474}Or_{0.477}.

The plagioclase composition, Or_{0.07}Ab_{0.76}An_{0.17}, and biotite formula were taken directly from Johnson et al. (1998 [DIRS 101630], Table 6).

The rhyolitic glass composition was calculated from analyses reported by Bish et al. (1996 [DIRS 101430], Table 1) (sample GU-3 1195C) as described in Appendix C (Section C.8.1).

Formulae for clay endmembers (illite, Na-, K-, Mg, and Ca-beidellite), mordenite (mixed phase), and Na-, K-, and Ca-clinoptilolite endmembers were taken from project database *data0.ymp.R5* (DTN: SN0612T0502404.014 [DIRS 178850]). Formulae for stellerite (mixed phase) and primary clinoptilolite (mixed phase) were taken from Chipera and Apps (2001 [DIRS 171017], Table 3, phases listed for the diagenetic alteration of volcanic tuff). Note that the formulae of all zeolites were recalculated on the basis of 36 oxygen atoms for internal consistency (see Appendix C, Section C.6).

6.2.3 Conceptualization of the Model Domain

The current repository design includes a planar series of parallel, equidistant, and horizontal waste emplacement drifts that are laid out over a large surface area. As such, encompassing all areas of the repository would require a large and detailed three-dimensional model. However, the scope of this report covers THC processes at the drift scale. Therefore, the model has been reduced and simplified to focus on areas surrounding a typical waste emplacement drift. Because the number of gridblocks directly affects the simulation time, the model domain is reduced as much as possible without losing important information. Based on the geologic framework model (BSC 2002 [DIRS 170029]), the dip of repository host units is subhorizontal. Assuming that the rock properties are laterally homogeneous between drifts (Section 6.4.6(15)), a planar and parallel drift layout can be conceptualized, in two dimensions, as a series of symmetrical, identical half-drift X-Z models (X representing the horizontal distance in a direction perpendicular to the length of the drifts, and Z the vertical distance) with no-flux (heat, fluid, chemical) vertical boundaries between them. Note that this half-drift simplification based on symmetry is theoretically applicable only for homogeneous properties, but is also a good approximation for heterogeneous fracture permeability fields if they display only weak spatial correlation.

Accordingly, the THC seepage model has been reduced to a half-drift model with a width corresponding to the midpoint between drifts. Because temperatures at edge locations are different from the interior, and do not follow the same trend with time as at the repository center (which may affect predicted water compositions), two cases of drift spacing are considered:

- 81 m: This case (model width of 40.5 m) represents the designed drift spacing and corresponds to a heat load located near the center of the repository.
- 162 m: This case (model width of 81 m) represents an “effective” drift spacing corresponding to a heat load located near the edge of the repository.

The model is refined in the vicinity of the drift and extends in a progressively coarser fashion to the TCw (near the ground surface) above the drift and to the water table below the drift. Such a symmetrical “chimney” model represents coupled THC processes at the drift scale in areas that are unaffected (81-m case) and affected (162-m case) by repository-edge effects (i.e., effects resulting from the cooler temperatures at the repository edge).

In addition to the thermal loading and temperature history, another major contributor to variations in potential seepage chemistry is the initial water chemistry. For this reason, water compositions were selected from available data (Section 6.2.2.1) to include samples collected from a range of repository locations. The repository host rock mineralogy, however, is relatively uniform throughout the repository block (DTN: GS000308313211.001 [DIRS 162015]; Peterman and Cloke 2002 [DIRS 162576], p. 683; see Assumption 1 for a more complete description), and simulations for previous revisions of this model (Table 6-1) have shown that predicted water chemistries are not sensitive to the considered repository rock unit (Ttptmn versus Ttptll). As such, the THC seepage model results can be viewed as representing a range of potential effects of THC processes covering a reasonably wide range of waste package locations.

In the THC seepage model, perched-water effects are ignored. Perched-water conditions are confined mainly to the lower units of the Topopah Spring welded (TSw) hydrogeological unit and on top of the Calico Hills nonwelded unit (CHn). Over the repository domain, perched-water locations are typically 100 to 150 m below the repository horizon (Wu et al. 1999 [DIRS 117167]). Because the dominant heat-transfer mechanism at these locations is heat conduction and boiling conditions are not attained, the effect of repository thermal load on perched-water bodies can be ignored (BSC 2005 [DIRS 174101], Section 6.1.2).

6.3 ALTERNATIVE CONCEPTUAL MODELS

Developmental versions of the THC seepage model included alternative conceptualizations of drift location, drift representation, modeled stratigraphic column, geochemical systems, and boiling/evaporation mathematical models (Table 6-1). These conceptualizations were implemented in various model revisions discussed in previous versions of this report (BSC 2004 [DIRS 168848]; BSC 2005 [DIRS 172862], Sections 6.5), in Sections 6.5 to 6.7 of the present report, as well as in the recent THC sensitivity study (SNL 2007 [DIRS 177413]). Although the model has been significantly revised between the earlier revisions and the current one (Table 6-1), the early results are adequate and sufficient for their intended use in this report, which is to evaluate model sensitivity and uncertainty, and they do not provide feeds to TSPA. These historical simulations are discussed in this report where relevant.

Earlier model revisions (Table 6-1) provided an assessment of the sensitivity of model results to the drift geologic host unit (Ttptmn versus Ttptll). The THC models in the Ttptll and Ttptmn units do not show significantly different water chemistry in either space or time, indicating that the THC seepage model is relatively insensitive to the choice of repository host rock, and provide the basis for extrapolation of the results of the current THC seepage model (in the Ttptll unit) to other lithostratigraphic units (Section 5).

The recent study *THC Sensitivity Study of Heterogeneous Permeability and Capillarity Effects* (SNL 2007 [DIRS 177413]), as well as earlier revisions of the THC seepage model (Table 6-1), considered the observed natural heterogeneity in fracture permeability (four orders of magnitude). These studies did not predict significantly different water chemistries when compared to the homogeneous models, justifying the use of homogeneous properties in the current model (Section 6.4.6(15)).

Alternative conceptualizations not treated here could yield differences in model results. Examples of such alternative models include the use of more than two porous media continua (to better represent lithophysae or better capture gradients between fractures and matrix, or both), heterogeneous fracture porosity (in addition to heterogeneous permeability), or other sets of potential secondary minerals. These alternatives have not been considered because they are expected to result in smaller differences in model results than the alternatives considered here. This is in part because the range of input water compositions considered in the model (Section 6.2.2.1), by itself, already introduces a significant spread in model results (Sections 6.5.5.4 and 6.7.2).

6.4 MATHEMATICAL MODEL

This section describes the mathematical formulations that underlie the THC seepage model (and the DST THC submodel presented in Section 7). The model is implemented using the TOUGHREACT V3.1.1 reactive transport code (see Section 3.1). Other reactive transport simulators, using various formulations, were considered by the project, including OS3D/GIMRT (Steefel and Yabusaki 1996 [DIRS 100827]) and MULTIFLO (Lichtner and Seth 1996 [DIRS 151989]). However, these simulators either have limitations that make them unsuitable for use in this study or have drawbacks in terms of availability, technical support, and qualification status. For instance, OS3D/GIMRT (Steefel and Yabusaki 1996 [DIRS 100827]) deals only with fully liquid-saturated conditions. When development of the THC seepage model was initiated in 1997, TOUGHREACT was the only code that could perform coupled thermal-hydrologic-chemical calculations in unsaturated rock, with phase changes (boiling), gaseous species transport (e.g., water vapor, CO₂, air), multicomponent transport, and kinetic and equilibrium reactions, in multicontinuum and multidimensional domains with unstructured grids. TOUGHREACT is the only software of its type qualified for Yucca Mountain work. Also, the developers of the THC seepage model have contributed to the development of TOUGHREACT for applications to the repository at Yucca Mountain. They are also familiar with other thermal hydrology and transport codes used by the Yucca Mountain Project, and have repeatedly updated and requalified TOUGHREACT with new features to maintain consistency with the other hydrologic codes used by the project. For these reasons, TOUGHREACT and its formulation have been selected for this study. As stated in Section 3, the software is adequate and appropriate for the intended use in this model, and is used strictly within the range of validation.

For brevity, unless a formulation is used that is specific to a particular version of TOUGHREACT, hereafter the code version is not cited.

6.4.1 General Numerical Model for Coupled THC Processes

Thermal and hydrologic processes modeled using TOUGHREACT (all versions) are equivalent to those using TOUGH2 version 1.6 (TOUGH2 V. 1.6 [DIRS 161491], STN: 10007-1.6-01), and are described in detail in *Drift-Scale Coupled Processes (DST and TH Seepage) Models* (BSC 2005 [DIRS 172232], Section 6.2.1.1) and in the User's Manual for TOUGHREACT V3.1.1 (DOE 2007 [DIRS 182183]).

The geochemical module incorporated in TOUGHREACT simultaneously solves a set of chemical mass-action, kinetic-rate expressions for mineral dissolution/precipitation and mass-balance equations. This provides the extent of reaction and mass transfer between a set of given aqueous species, minerals, and gases at each gridblock of the flow model. Equations for heat, liquid and gas flow, aqueous and gaseous species transport, and chemical reactions are summarized by Xu and Pruess (1998 [DIRS 117170]; 2001 [DIRS 156280], p. 30, Tables A and B), and by Xu et al. (1998 [DIRS 101751]; 2001 [DIRS 161864]). Flow, transport, and reaction equations are solved sequentially (Steefel and Lasaga 1994 [DIRS 101480], p. 550). Equations for mineral–chemical equilibrium, kinetic rates, and permeability–porosity changes are given further below.

The setup of mass-action and mass-balance equations in TOUGHREACT is similar to the formulation implemented by Reed (1982 [DIRS 117901], pp. 514 to 516). Additional provisions are made for mineral dissolution and precipitation under kinetic constraints and a volume-dependent formulation for gas equilibrium, as described below. The chemical system is described in terms of primary aqueous species (the independent variables). Minerals, gases, and secondary aqueous species are defined in terms of reactions involving only the primary species. It has been shown that if the diffusivities of all aqueous species are equal, only the transport of primary species (in terms of total dissolved concentrations) needs to be considered to solve the entire reactive flow/transport problem (Steefel and Lasaga 1994 [DIRS 101480], p. 546).

The system of nonlinear equations describing chemical mass-balance, mass-action, and kinetic-rate expressions is solved by a Newton-Raphson iterative procedure. Except in very early (retired) versions of TOUGHREACT, activity coefficients of aqueous species are calculated with the extended Debye-Hückel formulation of Helgeson et al. (1981 [DIRS 106024], Equations 298, 190, and 106, and Tables 1, 3, 29, and 30). Because the near-field water–rock interactions simulated by the THC seepage model occur primarily under dilute conditions, the use of an extended Debye-Hückel equation is appropriate. A Pitzer approach would be an advantage only directly at the boiling/rewetting front, where liquid saturations are very small and the ionic strength becomes elevated. Nevertheless, using the Helgeson et al. extended Debye-Hückel equation, activities of water and activity coefficients of single electrolytes such as NaCl, CaCl₂, Mg₂SO₄, and Ca₂SO₄ are fairly well reproduced up to ionic strengths of 6 molal. For salt mixtures, the ionic strength limit for applicability of the activity coefficient model is typically between 2 and 4 molal (see Section A.H.1 of DOE 2007 [DIRS 182183]). Activity coefficients of aqueous CO₂ are computed using correlations derived from Drummond (1981 [DIRS 157903]), as described in Section A.H.3 of the User Information Document for TOUGHREACT V3.1.1 (DOE 2007 [DIRS 182183]). Activity coefficients of other neutral species are assumed equal to 1 in the present study.

Equilibration with mineral phases is computed by adding a mass-action equation, for each saturated mineral, into the system of nonlinear equations as follows:

$$\log(K_i) = \log(Q_i) \tag{Eq. 6.4-1}$$

where K_i denotes the equilibrium constant and Q_i the product of the ion activities in the reaction that expresses mineral i in terms of the primary aqueous species. A term representing the amount of primary aqueous species consumed or produced by equilibration of minerals is added

to the mass-balance equation for each primary species involved in mineral reactions, and this term is solved simultaneously with the concentrations of all primary species. Minerals thus dissolve if $\log(Q_i/K_i) < 0$ and precipitate if $\log(Q_i/K_i) > 0$. For some minerals (e.g., calcite in Section 6.6.2), a “supersaturation gap” can be specified by which the mineral is not allowed to precipitate if $\log(Q_i/K_i)$ is greater than zero but less than a specified “gap” value (positive). This gap can be set to decrease exponentially with temperature, as described in Section A.B.3 of the User Information Document for TOUGHREACT (DOE 2007 [DIRS 182183]).

Gas species, such as CO_2 , are treated as ideal mixtures of gases in equilibrium with the aqueous solution. A mass-action equation is added to the system of simultaneous equations for each saturated gas present, except for H_2O vapor and air, which are handled separately through the flow module in TOUGHREACT. The gas mass-action equation takes the form:

$$\log(K_i) = \log(Q_i) - \log(P_i) \quad (\text{Eq. 6.4-2})$$

where P_i is the partial pressure of gaseous species i . P_i is first calculated from the advective-diffusive gas transport equation in TOUGHREACT. Then P_i is replaced with the ideal gas law:

$$P_i = \frac{n_i RT}{V_g} \quad (\text{Eq. 6.4-3})$$

where n_i denotes the number of moles of gas species i , R is the gas constant, T is the absolute temperature, and V_g is the gas total volume. By expressing V_g in terms of the gas saturation S_g , the porosity of the medium ϕ , and the volume of each gridblock in the flow model V_{block} , Equation 6.4-3 is rewritten as:

$$P_i = \frac{n_i RT}{V_{block} \phi S_g} \quad (\text{Eq. 6.4-4})$$

The gas saturation is computed in the flow module of the code (reflecting H_2O and air partial pressures computed in this module). The amount of trace gas species (n_i/V_{block}) is then obtained by substitution of Equation 6.4-4 into Equation 6.4-2 and solving together with the concentrations of all primary species.

The partial pressures of trace gas species are not fed back to the multiphase flow module for solving the water and gas flow equations. Therefore, this method should only be applied to gases (excluding H_2O and air) with partial pressures significantly lower than the total gas pressure. No absolute cutoff exists at which this approximation breaks down, and therefore it is validated by comparison to DST-measured CO_2 concentrations (Section 7). For cases where the partial pressures of a trace gas become closer to the total pressure, chemical equilibrium with the aqueous phase is computed correctly, but the gas pressure will be underestimated in the mass-balance equation solved for gas flow. Because CO_2 concentrations encountered in the DST and model simulations are generally less than a few percent, and rarely over 10%, this model for the gas species is a reasonable approximation for this particular system (Section 6.4.6(4)).

6.4.2 Kinetic Rate Laws

Rates of mineral dissolution and precipitation close to equilibrium can be described via a relationship of the rate to the saturation index (Q/K) as follows (transition state theory-derived equation such as in Steefel and Lasaga 1994 [DIRS 101480], p. 540, or in Oelkers et al. 1994 [DIRS 111051], p. 2012):

$$\text{Rate}(\text{mol s}^{-1}\text{kg}_{\text{water}}^{-1}) = \pm k A_e \prod_i a_i^p \left[1 - \left(\frac{Q}{K} \right)^m \right]^n \quad (\text{Eq. 6.4-5})$$

where k is the rate constant (in $\text{mol m}^{-2} \text{s}^{-1}$), A_e is the effective reactive surface area (in $\text{m}^2_{\text{mineral}} / \text{kg}_{\text{water}}$), a_i is the activity of each inhibiting or catalyzing species, and p , m , and n are empirically determined exponents. For cases where values of n are not available, these are set to 1 (see Appendix H for values used). For cases where values of m are not available, these are set to $1/\sigma$, where σ is the Temkin's average stoichiometric number (e.g., Oelkers et al. 1994 [DIRS 111051], p. 2012) (see Appendix H for values used). Following Steefel and Lasaga (1994 [DIRS 101480], p. 568), the effect of pH or other aqueous species activities on reaction rates is neglected by setting $p=0$ for each species, so that the product $\prod_i a_i^p = 1$ is eliminated from Equation 6.4-5.

The ratio of the species activity product (Q) and the equilibrium constant (K) in Equation 6.4-5 describes the extent to which a mineral is in disequilibrium with a given solution composition. For Q/K equal to one, the mineral is at equilibrium, and thus the net rate of reaction becomes zero. For Q/K less than one, the solution is undersaturated with respect to the mineral, and the rate takes a positive value. For Q/K greater than one, the solution is supersaturated with respect to the mineral and the rate takes a negative value. Because the exponent n can affect the sign of the bracketed expression in Equation 6.4-5, the rate sign is always forced to take a positive value for dissolution and a negative value for precipitation (by convention). In the case of ideal solutions, the saturation index of the solid solution is calculated as the sum of the saturation indices of the individual endmembers, and the reaction rate of the solid solution is calculated as described in Section A.I of the User Information Document for TOUGHREACT V3.1.1 (DOE 2007 [DIRS 182183]).

The rate constant k (in Equation 6.4-5) is given by (e.g., Steefel and Lasaga 1994 [DIRS 101480], p. 541):

$$k = k_0 \exp \left[\frac{-E_a}{R} \left(\frac{1}{T} - \frac{1}{298.15} \right) \right] \quad (\text{Eq. 6.4-6})$$

where k_0 is the rate constant (in $\text{mol m}^{-2} \text{s}^{-1}$) at 25°C, and the temperature dependence of the reaction rate is related to the activation energy (E_a) in units of kJ/mol, and T is the temperature in Kelvin units.

Carroll et al. (1998 [DIRS 124275], p. 1379) noted that the calculated rates of amorphous silica precipitation, based on research by Rimstidt and Barnes (1980 [DIRS 101708], p. 1683), are

about three orders of magnitude lower than those observed in geothermal systems. Carroll et al. (1998 [DIRS 124275], p. 1379) presented experimental data on amorphous silica precipitation for more complex geothermal fluids at higher degrees of supersaturation, and also for a near-saturation simple fluid chemistry. Under far from equilibrium conditions, the rate law for amorphous silica precipitation has been expressed as (Carroll et al. 1998 [DIRS 124275], p. 1382):

$$\text{Rate (mol s}^{-1}\text{kg}_{\text{water}}^{-1}\text{)} = kA_e \left(\frac{Q}{K} \right)^m \quad (\text{Eq. 6.4-7})$$

This rate does not tend to zero as Q/K goes to one; therefore, a modification has been made to this law so that it tends to zero as Q/K approaches one, as follows:

$$\text{Rate (mol s}^{-1}\text{kg}_{\text{water}}^{-1}\text{)} = kA_e \left[\left(\frac{Q}{K} \right)^m - \frac{1}{\left(\frac{Q}{K} \right)^{2m}} \right] \quad (\text{Eq. 6.4-8})$$

This rate law applies only to silica precipitation (and is also implemented for amorphous antigorite precipitation in this report). For silica dissolution, the rate law expressed in Equation 6.4-8 is used. Rate constants for the two cases are different (Appendix H).

Over a finite time step (Δt), the change in the concentration of each primary species j on account of mineral precipitation or dissolution under kinetic constraints is computed from the sum of the rates, r_i , of all j -containing minerals i as follows:

$$\Delta C_j = - \sum r_i v_{ij} \Delta t \quad (\text{Eq. 6.4-9})$$

where v_{ij} is the stoichiometric coefficient of component j in mineral i . These concentration changes are incorporated into the mass-balance equation of each primary species involved in mineral reactions, using Equations 6.4-5 through 6.4-7, and solved simultaneously with the concentrations of all primary species.

6.4.3 Mineral Reactive Surface Areas

This section describes the conceptual model and calculation methodology for fracture and matrix mineral reactive surface areas (the fracture-matrix conceptualization is illustrated in Figure 6.2-3).

6.4.3.1 Fracture Mineral Reactive Surface Areas

Reactive surface areas of minerals on fracture walls are calculated from the fracture-matrix interface area/volume ratio, the fracture porosity, and the derived mineral volume fractions. These areas can be calculated based on the fracture densities, fracture porosities, and mean fracture diameter.

The wall of the fracture is treated as a nearly flat surface covered by mineral grains. The geometric surface area of the fracture wall can be approximated by:

$$A_r = \frac{\pi A_{f-m}}{2\phi_f} \quad (\text{Eq. 6.4-10})$$

where A_r is the reactive surface area ($\text{m}^2/\text{m}^3_{\text{fracture medium}}$), A_{f-m} is the fracture–matrix interface area/volume ratio ($\text{m}^2/\text{m}^3_{\text{fracture medium}}$), and ϕ_f is the true fracture porosity of the rock. The factor of $\pi/2$ is a roughness factor equal to the actual surface area of solid grain on the fracture plane divided by the fracture plane surface, given by cubic packing of spherical grains. The grain diameter and spatial density are not included in this calculation, so that the area is actually only marginally greater than the fracture geometric surface area.

With TOUGHREACT V3.1.1, the surface area A' entered in simulations is $A' = A_{f-m}/[(1-\phi_{fmed})\phi_f]$, where ϕ_{fmed} is the assumed porosity of the fracture medium (0.5 in this study, not the true fracture porosity ϕ_f). In the dual permeability method, the porosity of the fracture medium can be taken as 1.0. However, for modeling of mineral dissolution and precipitation, some rock needs to be included in the fracture medium, otherwise there would then be no rock to dissolve. As noted above, the fracture medium is assumed to be half rock and half void, and therefore ϕ_{fmed} is 0.5 initially (by volume; see Section 6.4.6(11) and Figure 6.2-3). Correspondingly, input A' values take the units of $\text{m}^2_{\text{fracture surface}}/\text{m}^3_{\text{fracture medium solids}}$. Using this convention, and assuming that the fracture areal coverage for each mineral is approximately equivalent to the mineral volume fraction in solids, the effective reactive surface area of each mineral (in units of $\text{m}^2_{\text{mineral}}/\text{kg}_{\text{water}}$) is then computed by:

$$A_e (\text{m}^2_{\text{mineral}}/\text{kg}_{\text{water}}) = 1.5 \frac{A' f_m}{\rho_w \phi_{fmed}} (1 - \phi_{fmed}) \quad (\text{Eq. 6.4-11})$$

where factor of 1.5 is an approximation of the factor $\pi/2$ in Equation 6.4-11, f_m is the volume fraction of the mineral in the mineral assemblage, ρ_w is the density of water (in kg/m^3), and ϕ_{fmed} is the porosity of the fracture medium, as opposed to the fracture porosity of the rock. This is the surface area/water mass ratio for a mineral in a liquid-saturated system. To provide the correct rock/water ratio in an unsaturated system, the form of this surface area would be:

$$A_e (\text{m}^2_{\text{mineral}}/\text{kg}_{\text{water}}) = 1.5 \frac{A' f_m}{\rho_w \phi_{fmed} S_w} (1 - \phi_{fmed}) \quad (\text{Eq. 6.4-12})$$

where S_w is the water saturation. However, as S_w goes to zero, the reactive surface area would tend to infinity. Clearly, at a very low liquid saturation, the surface area of the rock in contact with water is likely much smaller than the total area. Two methods are considered to address this phenomenon. The first method considers that the area of the surface in contact with water diminishes proportionately to the liquid saturation. In this case, Equation 6.4-12 is multiplied by S_w , effectively canceling out this term and reverting to the saturated surface area given by Equation 6.4-11. This method is not implemented in this study, because for consistency

with the unsaturated hydrological model parameters, the active fracture model is adapted as discussed below.

The second method, implemented here, employs the active-fracture-model concept (Liu et al. 1998 [DIRS 105729]) modified to consider water–rock reactions taking place below the residual saturation. The form of the active fracture parameter for reaction is then given by the following set of equations:

$$S_{ar} = (S_w - S_m)/(1 - S_m) \quad (\text{Eq. 6.4-13})$$

$$a_{fmr} = S_{ar}^{(1+\gamma)} \quad (\text{Eq. 6.4-14})$$

where S_m is the minimum liquid saturation for which water–rock reactions are considered (see Section 6.4.6(14)) and S_{ar} is the effective saturation for reaction. The active fracture parameter, γ (Liu et al. 1998 [DIRS 105729], p. 2636), is obtained from the calibrated hydrological properties. The factor that reduces the surface area contacted by the water phase is given by a_{fmr} . S_m is generally set to a small saturation (10^{-5} in the current study), to ensure that reactions take place until virtually no water is left (e.g., during dryout via evaporation or boiling). Finally, the reactive surface area, using this modified form of the active fracture model, is given by:

$$A_e (\text{m}^2_{\text{mineral}}/\text{kg}_{\text{water}}) = 1.5 \frac{A' f_m a_{fmr}}{\rho_w \phi_{fmed} S_w} (1 - \phi_{fmed}) \quad (\text{Eq. 6.4-15})$$

Note that values of A_e are not the input surface areas that are listed in Appendix B, as these are calculated by TOUGHREACT from input values of A' .

The surface areas calculated in this way are applicable only to reactions taking place in the fracture medium and are used directly in Equations 6.4-5 and 6.4-8.

6.4.3.2 Matrix Mineral Reactive Surface Areas

The conceptual model and calculations of rock-matrix mineral reactive surface areas are discussed in this section (the fracture-matrix conceptualization is illustrated in Figure 6.2-3). Tabulated results used as input to the THC seepage model are given in Appendix B. Calculations are presented in spreadsheet *minabund_areas_rev05_final_c1.xls*.

The conceptual model is based on the premise that the geometric surface area of mineral grain surfaces in contact with the pore fluid is a good first approximation to the reactive surface area. The grains forming the framework of this rock are considered to be the primary high-temperature phases of the tuff (i.e., quartz, cristobalite, tridymite, feldspars, and biotite). The abundance of secondary phases (i.e., those that formed as alteration products or low-temperature coatings on the primary assemblage), such as clay minerals, calcite, opal, and zeolites, are used to reduce the free surface area of the framework grains.

The surface areas of primary minerals potentially in contact with pore fluid were estimated using the geometric area of a cubic array of truncated spheres, which make up the framework of the

rock. The mineral surface areas of framework grains (truncated spheres) in contact with the open pore space are calculated using an initial grain diameter, followed by successive truncation of the grains in the vertical direction, until the porosity of this system is close to the measured porosity of the rock. In the welded tuff, crystals are often tightly intergrown with little or no pore space within the aggregate. Thus, a check is made so that the resultant mean pore throat size and spacing yields a permeability (from a modified Hagen-Poiseuille relation) (Ehrlich et al. 1991 [DIRS 117799], p. 1582, Equation 11) that is relatively close to the measured saturated permeability. The surface areas of the primary minerals are then reduced by the volume fractions of the secondary minerals, assuming that they only coat an equivalent fraction of the exposed area. The specifics of the calculations are described below, which are performed in spreadsheet *minabund_areas_rev05_final_c1.xls*.

The volume of truncated sphere (V_g) in a cubic array is given as follows (Dewers and Ortoleva 1990 [DIRS 181454], p. 1624):

$$V_g = L_f^3(-8\pi/3) + \pi L_z(L_f^2 - L_z^2/12) + 2\pi L_x(L_f^2 - L_x^2/12) \quad (\text{Eq. 6.4-16})$$

where L_f is free-face grain radius (this is the radius given by the distance from the grain center to the curved surface in contact with the pore fluid), L_x is the X-dimension (horizontal truncated length) grain width, and L_z is the Z-dimension (vertical truncated length) grain height (Dewers and Ortoleva 1990 [DIRS 181454], Figure 1, p. 1610). The porosity (ϕ_{calc}) can then be calculated as follows:

$$\phi_{calc} = 1 - \frac{V_g}{L_x^2 L_z} \quad (\text{Eq. 6.4-17})$$

If the amount of truncation is the same for all faces (i.e., $L_x = L_z$), and L_f is known, then L_x and L_z can be found by finding a value for L_z that yields a calculated porosity close to the measured value. The calculated porosity is actually only a function of the degree of truncation of the sphere, not the actual grain size, so that the unknown is a truncation factor, given as follows:

$$f_t = \frac{L_x}{L_f} \quad (\text{Eq. 6.4-18})$$

which for a perfect sphere gives a value of 2.0 (because L_x is the horizontal diameter and L_f is the diagonal radius). Assuming that the permeability can be related to the same grain packing geometry, resulting pore throat diameter (d_{pt}), and areal density (N_{pt}), L_f can be estimated. Here permeability is calculated with a modified form of the Hagen-Poiseuille equation (modified from Ehrlich et al. 1991 [DIRS 117799], p. 1582, Equation 11), as follows:

$$k_{calc} (m^2) = \frac{N_{pt} \pi d_{pt}^4 10^{-12}}{128} \quad (\text{Eq. 6.4-19})$$

where d_{pt} is in μm , and N_{pt} is in the number of pore throats per μm^2 . Compared to that presented in the original source, all pore throats are assumed to have the same diameter, and the factor of 10^{-12} converts the permeability in μm^2 to m^2 .

The truncated sphere array yields a pore throat diameter given by the following relation:

$$d_{pt} = 1000 \left[(L_x^2 + L_z^2)^{0.5} - 2L_f \right] \quad (\text{Eq. 6.4-20})$$

where the grain dimensions L_f , L_x , and L_z are in millimeters. The number of pore throats per unit area (μm^2) is obtained from:

$$N_{pt} = 10^{-6} \left(\frac{N_{eff}}{L_x L_z} \right) \quad (\text{Eq. 6.4-21})$$

where N_{eff} is the number of pore throats per pore that are effective in the fluid flow, and the factor of 10^{-6} converts the area in mm^2 to μm^2 . For many granular materials the number of effective throats per pore would be between 2 and 3. However, because the devitrification during welding of the tuff resulted in small-scale mineral intergrowths, with fewer pores and pore throats than a granular material, the effective throats per pore, N_{eff} , is assumed to be at the lower end (2).

Therefore, L_f can be obtained by trial and error until the calculated permeability is close to the measured permeability (a match within ~20% was deemed acceptable, a reasonably small value in comparison to natural variations in permeability spreading over several orders of magnitude).

Having all of the textural parameters allows the free face surface area (A_f in mm^2) for the rock to be calculated, assuming no alteration, as follows (Dewers and Ortoleva 1990 [DIRS 181454], p. 1624):

$$A_f = 4\pi L_f (0.5L_z + L_x - 2L_f) \quad (\text{Eq. 6.4-22})$$

The free face surface area per unit volume (mm^2/mm^3) is:

$$A_{fv} = \frac{A_f}{L_z L_x^2} \quad (\text{Eq. 6.4-23})$$

The free face surface area per unit volume converted to m^2/m^3 is:

$$A_{fv}(\text{m}^2/\text{m}^3) = 10^3 A_{fv} \quad (\text{Eq. 6.4-24})$$

Now the effect of alteration on the surface areas is included. The volume fraction of alteration minerals, V_{f-alt} , is the sum of the volume fractions of the alteration minerals, as follows:

Volume fraction alteration (V_{f-alt}) = Ca-montmorillonite Na-montmorillonite + illite + clinoptilolite + mordenite + opal-CT + hematite + calcite

Note that the final mineral assemblage has beidellites replacing the montmorillonites. However, for the consideration of volume changes for calculation of surface areas, this difference is

negligible since their densities are nearly the same. The alteration contribution to porosity (ϕ_{alt}) decrease is then given by:

$$\phi_{alt} = V_{f-alt}(1 - \phi_{meas}) \quad (\text{Eq. 6.4-25})$$

For the calculations presented in this report, ϕ_{alt} was further decreased by an estimated factor of 0.2 to approximate the proportion of alteration that occludes pore space rather than just replaces minerals. The framework porosity ϕ_{fr} is then adjusted by increasing the measured porosity by ϕ_{alt} , up to close to the limit of spherical grains in cubic packing (the true limit is 0.4764, but a slightly smaller value was chosen such that contact areas do not go to zero), as follows:

$$\phi_{fr} = \text{MIN}(\phi_{meas} + \phi_{alt}, 0.4756) \quad (\text{Eq. 6.4-26})$$

The change in pore throat diameter owing to alteration can be approximated by:

$$\Delta d_{alt} \approx V_{alt} 2000 / A_f \quad (\text{Eq. 6.4-27})$$

where 2,000 is derived from a conversion factor of 1,000 to convert from millimeters to micrometers, and a factor of 2 to account for the thickness reduction on each face of the pore throat on opposite grains (each side of the pore throat). The volume of alteration V_{alt} (in mm^3) is calculated by multiplication of V_{f-alt} by the volume of the cube enclosing the grain ($L_x^2 L_z$).⁵

Calculation of the permeability (m^2), considering alteration effects is:

$$k_{calc}(\text{m}^2) = \frac{N_{pt} \pi (d_{pt} - \Delta d_{alt})^4 10^{-12}}{128} \quad (\text{Eq. 6.4-28})$$

The free face surface area of the mineral framework grains (A_m in cm^2/g) is finally given by:

$$A_m = \frac{10 A_f}{2.65 V_g} \quad (\text{Eq. 6.4-29})$$

where the density of the mineral grains is assumed to be that of quartz (2.65 g/cm^3), and “10” is a conversion factor from 1/mm to 1/cm. Because the resulting surface area of alteration minerals was only several hundred cm^2/g , and these minerals typically have very high surface areas, the surface areas were increased by a factor of 10. However, as described in footnote “4” above, an inadvertent error resulted in the areas being about an order of magnitude too low. Therefore, the

⁵ Note: In DTN: LB0707DSTHC006.003, spreadsheet: *minabund_areas_rev05_final_c1.xls*, worksheet 2, column Y37:Y67, the factor of L_x was inadvertently left out. The effect of this error on the final reactive surface areas is documented in spreadsheet *minabund_areas_rev05_jul07.xls* in the same sheet and column locations. The corrected areas are about an order of magnitude greater for the framework grains in the repository units and are about 50% higher for the alteration minerals (because the corrected alteration mineral areas are not multiplied by an extra factor of 10). Because the rate constants were modified to capture the ambient system evolution using the uncorrected areas (a rough calibration), the overall rate is little affected by this error (i.e., the modification factors for the minerals would have been different given a different reactive surface area).

modification of the alteration mineral areas by the factor of 10 made the areas closer to the values calculated correctly (both sets of calculations in Output DTN: LB0707DSTHC006.003).

For the rock matrix, effective reactive surface areas, A_e ($\text{m}^2_{\text{mineral}}/\text{kg}_{\text{water}}$) are computed dynamically in TOUGHREACT V3.1.1 from the input mineral surface areas A_m (determined as described above) as:

$$A_e = 100 A_m \frac{M}{V} \frac{f_m(1-\phi)}{\rho_w \phi S_l} S_l \quad (\text{Eq. 6.4-30})$$

Here, A_m is input in $\text{cm}^2_{\text{mineral}}/\text{g}_{\text{mineral}}$, M is molecular weight (g/mol), V is molar volume (cm^3/mol), f_m is the mineral volume fraction of solid, ϕ is porosity, S_l is liquid saturation, ρ_w is the water density (kg/m^3), and the factor of 100 is for unit conversion. Note that the multiplication by liquid saturation on the right side of Equation 6.4-30 is added to take account of the proportionality of the wetted surface area with liquid saturation, and effectively cancels out this parameter from the equation (as discussed previously for Equation 6.4-12).

6.4.4 Effects of Mineral Precipitation/Dissolution on Hydrologic Properties

6.4.4.1 Porosity Changes

Changes in porosity and permeability resulting from mineral dissolution and precipitation have the potential to modify percolation fluxes and seepage fluxes at the drift wall. In this analysis, porosity changes in matrix and fractures are directly tied to the volume changes that result from mineral precipitation and dissolution. The molar volumes of hydrous minerals, such as zeolites and clays, created by hydrolysis reactions with anhydrous phases, such as feldspars, are commonly larger than those of the primary reactant minerals. Therefore, constant molar precipitation/dissolution reactions can lead to porosity reductions. These changes are taken into account in this analysis. The porosity of the medium (fracture or matrix) is given by:

$$\phi = 1 - \sum_{m=1}^{nm} fr_m - fr_u \quad (\text{Eq. 6.4-31})$$

where nm is the number of minerals, fr_m is the volume fraction of mineral m in the rock ($V_{\text{mineral}}/V_{\text{medium}}$, including porosity), and fr_u is the volume fraction of nonreactive rock. As the fr_m of each mineral changes, the porosity is recalculated at each time step. The porosity is not allowed to go below zero.

6.4.4.2 Fracture Permeability Changes

Fracture permeability changes can be approximated using the porosity change and considering plane parallel fractures of uniform aperture (cubic law) (Steeffel and Lasaga 1994 [DIRS 101480], p. 556). Details on the cubic law itself can be found in Konzuk and Kueper (2004 [DIRS 181363], and references therein). If the fracture spacing and density remain constant, the updated permeability, k , is given by:

$$k = k_i \left(\frac{\phi}{\phi_i} \right)^3 \quad (\text{Eq. 6.4-32})$$

where k_i and ϕ_i are the initial permeability and porosity, respectively. This law yields zero permeability only under the condition of zero fracture porosity.

In most experimental and natural systems, permeability reductions to values near zero occur at porosities significantly greater than zero. This generally is the result of mineral precipitation preferentially closing the narrower interconnecting apertures. The hydraulic aperture, as calculated from the fracture spacing and permeability (as determined through air-permeability measurements) using a cubic law relation, is a closer measure of the smaller apertures in the flow system. Using the hydraulic aperture, a much stronger relationship between permeability and porosity can be developed. This relationship can be approximated as follows:

The initial hydraulic aperture $b_{0,h}$ (in meters) is calculated using the following cubic law relation:

$$b_{0,h} = [12k_0s]^{1/3} \quad (\text{Eq. 6.4-33})$$

where k_0 is the initial fracture permeability (m^2) and s is the fracture spacing (in meters) for a single fracture set. The permeability (k) resulting from a change in the hydraulic aperture is given by:

$$k' = \frac{(b_{0,h} + \Delta b)^3}{12s} \quad (\text{Eq. 6.4-34})$$

where Δb is the aperture change resulting from mineral precipitation/dissolution. The aperture change resulting from a calculated volume change can be approximated by assuming precipitation of a uniform layer over the entire geometric surface area of the fracture, assuming also that this area (as well as the fracture spacing) remains constant. In geologic systems, the actual distribution of mineral alteration is much more heterogeneous and depends on many factors that are active at scales much smaller than the resolution of the model. The combined effect of the initial heterogeneities and localized precipitation processes can only be treated through model sensitivity studies and experiments. The initial aperture available for precipitation (b_g , the geometric, rather than the hydraulic, aperture) can be approximated (Appendix F) from the ratio of the initial fracture porosity ($\phi_{f,0}$) to the fracture surface area (A_{frac} in m^2 fracture surface/ m^3 total rock volume), as follows:

$$b_g = \frac{\phi_{f,0}}{A_{frac}} \quad (\text{Eq. 6.4-35})$$

For a dual-permeability model, changes in the fracture porosity are calculated based on the porosity of the fracture medium, so that Δb can be approximated by:

$$\Delta b = \frac{(\phi_{fm} - \phi_{fm,0})}{\phi_{fm,0}} b_g \quad (\text{Eq. 6.4-36})$$

where ϕ_{fm} and $\phi_{fm,0}$ are the current and initial porosity of the fracture medium (not the fracture porosity). Equations 6.4-33, 6.4-34, and 6.4-36 were implemented in TOUGHREACT, and for the THC seepage model the input parameters b_g and s were calculated for each model layer (Appendix F).

6.4.4.3 Matrix Permeability Changes

Matrix permeability changes are calculated from changes in porosity using ratios of permeabilities calculated from the Carman-Kozeny relation (Bear 1988 [DIRS 101379], p. 166, Equation 5.10.18, symbolically replacing n by ϕ), and neglecting changes in grain size, tortuosity, and specific surface area as follows:

$$k = k_i \frac{(1 - \phi_i)^2}{(1 - \phi)^2} \left(\frac{\phi}{\phi_i} \right)^3 \quad (\text{Eq. 6.4-37})$$

6.4.4.4 Effects of Permeability and Porosity Changes on Capillary Pressure

Changing permeability and porosity also results in changes in the unsaturated flow properties of the rock. These effects are treated by modifying the calculated capillary pressure (P_c) using the Leverett scaling relation (Slider 1976 [DIRS 128146], p. 280) to obtain a scaled P_c' as follows:

$$P_c' = P_c \sqrt{\frac{k_i \phi}{k \phi_i}} \quad (\text{Eq. 6.4-38})$$

6.4.5 Mineral Precipitation in Dry Gridblocks

In certain cases of evaporation or boiling, a gridblock may experience an influx of water that evaporates completely during the solution of the flow equations. After the flow equations are solved, TOUGHREACT solves the transport equations followed by the speciation and reaction equations. The speciation and reaction equations require that a certain amount of water be present in the gridblock to compute mineral precipitation; that is, mineral precipitation cannot be computed through the mass-action/mass-balance scheme described in Section 6.4.1 unless the liquid saturation is greater than zero (or a small value). For cases when the liquid saturation is below a prescribed small value (10^{-5} for simulations in this report, Section 6.1.4(14)), a method has been developed for forming minerals by “storing” the dissolved content of the drying solution in a solid assemblage, referred to hereafter as the “dryout mineral assemblage.”

The amount of solute “stored” is simply the product of the concentration in the upstream gridblock and the flux of water into the gridblock that dries out. Also, any water that is initially present in the gridblock, and dries out, gives rise to some solute mass that is transformed into solid phases. For these cases, the mass of each primary solute species is saved and may be assigned to minerals in a prescribed order in the chemical input file. This approximation is performed so that solute mass loss is minimized, and most of the solute mass can be accounted for in a solid mineral phase.

In the simulations presented in this report, for the specific cases when water flows into gridblocks that dry out in the flow calculation (by boiling or evaporation), the solid phases were formed as shown in Table 6.4-1, stoichiometrically, and in the same order as shown in column “Selected” of this table. The table also shows two alternative dryout mineral sequences used for sensitivities discussed in Section 6.6.

Note that processes associated with extreme dryout and salt precipitation in the drift, including salt separation, deliquescence, and acid degassing, are treated with a model able to deal with very high ionic strength in *In-Drift Precipitates/Salts Model* (SNL 2007 [DIRS 177411]). These processes are currently not included in the THC seepage model and are shown by *In-Drift Precipitates/Salts Model* (SNL 2007 [DIRS 177411]) to be of secondary importance.

Table 6.4-1. Dryout Mineral Assemblages and Sequences Considered in This Study

Mineral	Formula ^a	Precipitation Order ^b		
		Selected	Sensitivity "Salt1"	Sensitivity "Salt0"
Amorphous Antigorite	Mg ₃ Si ₂ O ₅ (OH) ₄	1	1	4
Silica	SiO ₂	2	2	5
Hematite	Fe ₂ O ₃	3	7	6
Fluorite	CaF ₂	4	3	2
Villiumite	NaF	5	4	
Halite	NaCl	6	8	7
Hydrophilite	CaCl ₂	7	10	
Niter	KNO ₃	8	11	
Soda niter	NaNO ₃	9	12	
Ca(NO ₃) ₂	Ca(NO ₃) ₂	10	13	
Arcanite	K ₂ SO ₄	11	14	
Anhydrite	CaSO ₄	12	6	3
Thenardite	Na ₂ SO ₄	13	15	
Calcite	CaCO ₃	14	5	1
Natrite	Na ₂ CO ₃	15	16	
K ₂ CO ₃	K ₂ CO ₃	16	17	
Sylvite	KCl		9	8

^a Mineral formulas from project databases *data0.ymp.R5* (DTN: SN0612T0502404.014 [DIRS 178850]) and *data0.ypf.R2* (DTN: SN0609T0502404.012 [DIRS 179067]).

^b No value means the mineral is not included in the assemblage.

The selected precipitated order was predetermined to ensure minimal mass loss in cases when an insufficient amount of some component remains to form a given mineral. The goal here was not to model evaporation accurately, but to save as much mass of the dissolved constituents as possible for gridblocks that completely dry out. The list “Salt1” was tested as an alternative with minimal loss, whereas the list “Salt0” was tested as a case with elevated loss of components, most notably nitrate.

Minerals other than amorphous antigorite, silica, hematite, anhydrite, and calcite in Table 6.4-1 represent salts having a solubility that exceeds the ionic strength limit of the speciation calculations (set to 4 molal in this study). Upon rewetting, these minerals are assumed to dissolve kinetically with a relatively fast rate constant (set here at 10^{-6} mol/m²/s) and a dissolution rate limited by their solubility product (Equation 6.4-5), thus capturing the general behavior of salt dissolution as the boiling front recedes. However, the predicted major ion concentrations during the short time when these salts dissolve are more qualitative than quantitative, because the identity of the salt phases is not based on a thermodynamic speciation/precipitation model, and their dissolution rates are only approximate.

6.4.6 Principal Model Approximations and Approaches

The following modeling approximations and simplifications are used in the THC seepage model.

1. The rock is described by a dual-permeability model (Section 6.2.1.5), which considers separate but interacting fracture and matrix continua, each with specified permeabilities. In the dual-permeability model, the fracture continuum is considered as co-located but interacting with the matrix continuum, in terms of the flow of heat, water, and vapor through advection, diffusion, and conduction (for heat). The aqueous and gaseous species are transported via advection and molecular diffusion between the fractures and matrix. Each continuum has its own well-defined initial physical and chemical properties. The dual-permeability approach for modeling physical processes in fractured porous media is discussed in detail by Doughty (1999 [DIRS 135997], pp. 76 and 77). In addition, the active-fracture-model concept (Liu et al. 1998 [DIRS 105729]) used in these simulations employs an active-fracture parameter that considers the wetted portion of the fracture–matrix interface area and the proportion of flowing fractures. This approach is validated by comparing geochemical data obtained from the DST to the results of simulations of the DST (Section 7.1), and further validated in *Drift-Scale Coupled Processes (DST and TH Seepage) Models* (BSC 2005 [DIRS 172232], Section 7).
2. The mass of minerals precipitated is small and its thermal properties are similar to those of the host rock. Therefore, the thermal properties are not modified to account for precipitated minerals. However, the bulk heat capacity is modified to account for changes in porosity.
3. The infiltrating water and water in the fractures are set to the same chemical composition as the chemical analysis of the matrix pore-water samples that were collected (Table 6.2-1). The rationale for this modeling approach is given in Section 6.2.2.2. This is also an assumption in Section 5.
4. Effects of changes in the partial pressure of CO₂ (resulting from heating, water reaction with calcite, and gas-phase transport) on the density of the gas phase are neglected. This is justified because, in this study, CO₂ generally accounts for less than 5% and always less than 10% of the gas-phase volume (air, water, and CO₂). Although the molecular weight of CO₂ is greater than that of air (approximately 44 g/mol versus 29 g/mol), the density is only increased proportionally to the volume fraction of CO₂ and the ratio of the molecular weights. This would result in a density increase of about 5% for a gas with a CO₂ volume fraction of 10%. These conditions make the effect of evolved CO₂ on the physical

properties of the gas phase negligibly small and justify the use of this approximation. The effect of CO₂ on the density of steam (molecular weight approximately 18 g/mol) would be somewhat greater; however, increases in the steam fraction accompanying boiling would tend to dilute the CO₂ fraction.

5. The effects of changes in water chemistry on the water density, viscosity, and boiling point are neglected. This approximation is justified because aqueous-species concentrations are low in waters at most values of the liquid saturation (in the rock matrix or fractures). In cases where concentrations are significantly higher, the liquid saturation is generally much less than 1%. Therefore, the liquid is nearly immobile because of the very small relative permeability for the liquid phase under such conditions. Boiling point elevation due to salts could result in liquid saturations remaining at non-zero values at temperatures significantly higher than the boiling point of pure water. However, the elevated dissolved salt concentrations required to significantly raise the boiling point would require very high evaporative concentration, which would typically result in very small liquid saturations (much less than 1%) at which the total amount of liquid water present would be too small to impact the general thermal and hydrological processes around the modeled drift.
6. Diffusion coefficients of all aqueous species are set to the same value (the value for the chloride anion; Section 4.1.1.1). This is justified because the tracer diffusion coefficients of aqueous species differ by, at most, about one order of magnitude, with many differing by less than a factor of 2 (Lasaga 1998 [DIRS 117091], p. 315). The strong effects of water–rock interaction, boiling condensation, and rapid fracture drainage typically overwhelm effects of aqueous species diffusion.
7. Diffusion coefficients for gases are calculated. In the gas phase, CO₂ is the only transported reactive species (other than H₂O vapor). For an ideal gas, the tracer diffusion coefficient of a gaseous species can be expressed as a function of temperature and pressure in the following form (Lasaga 1998 [DIRS 117091], p. 322):

$$D = \frac{RT}{3\sqrt{2}\pi P N_A d_m^2} \sqrt{\frac{8RT}{\pi M}} \quad (\text{Eq. 6.4-39})$$

where

- D = diffusion coefficient (m²/s)
- R = gas constant (8.31451 m² kg s⁻² mol⁻¹ K⁻¹)
- T = temperature in Kelvin units
- P = pressure (kg m⁻¹ s⁻²)
- N_A = Avogadro's number (6.0221367 × 10²³ mol⁻¹)
- d_m = molecular diameter (m)
- M = molecular weight (kg/mol).

The CO₂ diffusion coefficient is calculated using input values of d_m and M (Section 4.1.1.1).

8. Mineral precipitation or dissolution is modeled to occur uniformly over the smooth plane-parallel fracture walls (Section 6.4.4.2). However, mineral precipitation could be non-uniform, leading to a different relationship between changes in permeability and porosity. This approximation can be justified by the use of bulk permeabilities and porosities that initially account for the net effect of variability in fracture aperture at a macroscopic scale. Furthermore, effective (hydraulic) apertures are used instead of true apertures, the latter being much larger (Section 6.4.4.2). As a result, the permeability change is quite sensitive to porosity changes (in this study, a 10% to 14% drop in fracture porosity leads to zero permeability in fractures in the modeled repository units).

The permeability of the fracture and matrix continua are coupled to mineral precipitation and dissolution in each continuum as discussed in Section 6.4.4. However, the properties of the fracture–matrix interfacial area, including the active-fracture parameter (Liu et al. 1998 [DIRS 105729]), are not coupled to mineral precipitation or dissolution (see Section 6.2.1.5 and model approximation 1 for the conceptualization of the dual-permeability model). Mineral precipitation on the fracture wall could further restrict flow across the fracture–matrix interfacial area, and thus further affect matrix imbibition after dryout. However, in the present model, the bulk of mineral precipitation in fractures is predicted to occur hundreds of years after the matrix has rewetted. For this reason, this approximation is not expected to significantly affect model results.

9. CO₂ gas is treated as an ideal gas (i.e., obeys the ideal gas law and its partial pressure equals its fugacity). This approximation is valid for the low ambient pressures (near atmospheric) considered in this study (Langmuir 1997 [DIRS 100051], p. 15).
10. An ideal solid-solution model is implemented for beidellites (Na, Ca, and Mg endmembers), with each endmember's activity equaling its mole fraction. Treating these clays as a solid solution results in individual smectite end-members either all dissolving or all precipitating, providing a better physical representation of dissolution/precipitation processes. Other solid-solution primary minerals are considered as solid solutions with thermodynamic data corresponding to their respective fixed compositions. These minerals include: plagioclase, sanidine, and ymp-clinoptilolite, which are only allowed to dissolve; and stellerite, mordenite and secondary Ca-, K-, and Na-clinoptilolite, which can precipitate or dissolve.
11. The simulation of water–rock interaction in fractures can only be performed if the modeled fracture medium contains some rock, in addition to the void representing the fracture. For this reason, the fracture medium must be modeled with gridblocks having an initial fraction of void space less than one, and thus an initial rock fraction larger than zero. In the current THC seepage model, this rock fraction is set at 0.5 (50% rock and 50% void by volume). The exact value used has no bearing on model results, as long as the fracture medium always contains solids that can react with fluids in fractures. It is verified that there is always enough solid initially present in the fracture continuum to avoid the possibility that some of the primary rock-forming minerals become exhausted (through dissolution). Note that the volume of each gridblock assigned to the fracture medium is calculated in such a way that the true fracture porosity (i.e., the fraction of the bulk rock occupied by fracture void space) is always reproduced.

12. The thermal conductivities of fracture and matrix gridblocks are calculated assuming a linear interpolation between dry and wet conductivities as a function of liquid saturation. These are the thermal conductivities for the solid + fluid system. For fractures, thermal conductivities are multiplied by the fracture porosity to account for the correct fracture-to-fracture connection area in calculations of heat conduction (i.e., this is needed because full gridblock areas are input into the model). The volume of the fracture continuum is, however, only a small fraction of the matrix continuum. Therefore, heat conduction occurs primarily through the matrix continuum and, as a result, the model is not sensitive to the amount of heat conduction in fractures.
13. Vapor-pressure lowering due to capillary pressure (the Kelvin effect) is implemented in simulations carried out for this current model revision (Sections 6.5 and 7.1). The impact of including or neglecting this effect was evaluated in *Drift-Scale Coupled Processes (DST and THC Seepage) Models* (BSC 2004 [DIRS 168848], Section 6.8.5.3).
14. Upon boiling or evaporation, the aqueous phase is treated as unreactive and is not concentrated further, once its ionic strength reaches an input upper limit of 4 molal or if the liquid saturation drops below an input lower limit of 10^{-5} . This ensures that the calculated ionic strength remains within the range of applicability of activity coefficient models (Section 6.4.1). Past these limits, solid phases (mostly salts) are formed as described in Section 6.4.5 and evaluated in Section 6.6-4. These solid phases are then available for dissolution upon rewetting (using a fast dissolution rate constant arbitrarily set at $10^{-6} \text{ mol m}^{-2}\text{s}^{-1} \text{ kg}_{\text{H}_2\text{O}}^{-1}$).

At liquid saturations as small as 10^{-5} , the total amount of dissolved mass present in any given model gridblock is exceedingly small. Thus, ignoring chemical reactions for such small mass amounts (and over a limited time period) does not significantly affect the general computed trends of aqueous phase concentrations and precipitated mineral amounts over long time periods and a wide range of liquid saturations.
15. Hydrogeologic rock properties in each hydrogeologic unit of the model are approximated as being laterally homogeneous. The effect of natural heterogeneity in fracture permeability (four orders of magnitude) on both flow and water chemistry was presented in *THC Sensitivity Study of Heterogeneous Permeability and Capillarity Effects* (SNL 2007 [DIRS 177413]), as well as in previous model revisions (Table 6-1). These results did not show significantly different water chemistry in either space or time when compared to the homogeneous model. Furthermore, good comparisons are obtained between modeled and measured water and gas chemistry for the DST, assuming homogeneous properties (Section 7.1). Local effects of heterogeneity on seepage have been reported in *THC Sensitivity Study of Heterogeneous Permeability and Capillarity Effects* (SNL 2007 [DIRS 177413]), but do not affect the conclusions of this report regarding water chemistry.
16. The capillary pressure in both fractures and matrix must reach some maximum, finite value upon complete dryout (zero liquid saturation). Without a limit, the capillary-pressure/liquid-saturation function implemented in the simulations (van Genuchten model, e.g., Pruess et al. 1999 [DIRS 160778], Appendix G) would require capillary pressure to go to infinity as the liquid saturation reaches zero. However, liquid water can only be stretched (i.e., remain metastable) up to a certain (negative) pressure,

beyond which spontaneous cavitation occurs (e.g., Lassin et al. 2005 [DIRS 182921], Figure 2). This limit depends on temperature, and is between about 1,000 and 2,000 bar in the 0°C to 100°C temperature interval (e.g., Lassin et al. 2005 [DIRS 182921], Figure 2). The default capillary pressure limit in the THC seepage model and the DST THC submodel is set to 10^8 Pa (1,000 bar). For fractures and matrix in the Ttpmn, Ttpml, and Ttpln lithostratigraphic units (model units tsw34, tsw35, and tsw36, respectively), the limit is set, as previously, by the calculated slope of the capillary pressure (P_{cap}) versus liquid saturation curve at a liquid saturation value equal to $S_r + \epsilon$. For these units, ϵ values for the matrix yield maximum P_{cap} values of 10^8 Pa; for fractures, ϵ is set to 0.01, equal to the residual saturation (corresponding to maximum P_{cap} values around 10^3 to 10^4 Pa).

17. Open spaces in the drift are approximated as a porous medium with a high permeability (10^{-9} m²) greater than in surrounding rocks, but not so large as to create numerical difficulties when computing flow. In addition, these open spaces are modeled with no capillarity, unit porosity, and no residual saturation except directly against the drift wall (arbitrary small value of 0.01 to account for some water condensation, if any, against the drift wall). These approximations are made because the mathematical model is not formulated to accurately treat fluid flow in non-porous media. The sensitivity to the chosen nonporous permeability value for the porous medium has been evaluated for in-drift RH and temperature in *Multiscale Thermohydrologic Model* (SNL 2007 [DIRS 181383]) and found to be insignificant.
18. The fracture tortuosity value of 0.7 (Section 4.1.1.1) has been adopted for use with thermal and diffusive transport parameters of lithologic units. This value is based on experimental determinations of tortuosity in soils having various porosities (Penman 1940 [DIRS 109941], pp. 441 to 461), and also corresponds to the highest tortuosity value given by de Marsily (1986 [DIRS 100439], p. 233). The rationale for this value is that fracture tortuosity should be high compared to matrix tortuosity (i.e., less tortuous path in fractures than in the matrix). This fracture tortuosity is modified for fracture–fracture connections by multiplication of the tortuosity by the fracture porosity of the bulk rock. This operation yields a better approximation for the fracture-to-fracture interconnection area (only for calculation of diffusive fluxes; the entire gridblock connection area is used for calculating advective fluxes, because the bulk fracture permeability of the entire gridblock is entered into the model).
19. An estimated matrix tortuosity of 0.2 is assumed to be applicable to the tuff matrix at Yucca Mountain. This is in the lower part of the parameter range given by de Marsily (1986 [DIRS 100439], p. 233), consistent with the much finer pore size in the matrix. The tortuosity is a factor applied along with the porosity and the saturation to the diffusion coefficient. Common matrix tortuosity values only cover a span of about one order of magnitude, so this value has a very limited effect on reaction-transport processes. A tortuosity of 0.7 is assumed for the invert for similar reasons as described for the matrix fracture permeability above. The invert is coarse granular material, and its tortuosity would be expected to be between 0.7 and 1.0. The tortuosity of sand is about 0.7 (de Marsily 1986 [DIRS 100439], p. 233). These values only slightly affect diffusive transport of CO₂ in the drift. Because reactions involving CO₂ are minimal in the drift, the diffusivity of

CO₂ within in-drift components has a negligible effect on THC processes outside of the drift.

20. The saturated saturation is the maximum liquid saturation before saturated flow conditions are reached (i.e., at which the capillary pressure reaches zero). It is typically given the value of 1 (fully saturated conditions).
21. The drift wall is open to all fluid fluxes. No specific boundary conditions of pressure, relative humidity, or gas compositions are applied inside the drift (i.e., as if the repository is sealed off, and neglecting sources or sinks of CO₂ due to microbial activity or atmospheric CO₂). Computing fluid flow through open spaces of the drift using a model designed to calculate flow through porous media is by itself a very coarse approximation. Thus, modeling the drift wall as either open or closed to advective fluid flow yields equally coarse approximations. However, the scope of this report is to model THC processes in the near-field outside the drift and not in the drift itself.
22. The molar volume of salts used in the mineral dryout assemblage (Section 6.4.4), when not readily available, was set to 50 cm³/g with justification provided in Section C.3 (within the range of known volumes for other salts).
23. The fracture permeability was determined from air-permeability measurements. The use of air-permeability data for simulations of water flow is considered appropriate, given the fact that other hydrologic properties such as capillary properties and active-fracture parameter were calibrated to matrix liquid saturation using these data. This approach is also validated by comparing geochemical data obtained from the DST to the results of simulations of the DST (Section 7.1).

6.4.7 Summary of Hydrologic and Thermal Properties

The hydrologic and thermal properties of repository units used in simulations presented in Section 6.5 (and 6.6.2 through 6.6.5) are summarized in Table 6.4-2. Sources of properties used for all modeled hydrogeological units and other input data are listed in Section 4.1.

Table 6.4-2. Summary of Hydrologic and Thermal Properties of Repository Units

Geological Unit >		30th Percentile Parameter Set			
		<i>Ttpul</i> (tsw33)	<i>Ttpmn</i> (tsw34)	<i>Ttpll</i> (tsw35)	Source
MATRIX DATA					
Permeability	k_m (m ²)	1.86E-17	3.16E-18	1.11E-17	DTN: LB0610UZDSCP30.002 [DIRS 179180]
Porosity	f_m (-)	0.155	0.111	0.131	DTN: LB0208UZDSCPMI.002 [DIRS 161243] ^a
van Genuchten α	α_m (1/Pa)	6.56E-6	1.71E-6	3.38E-6	DTN: LB0610UZDSCP30.002 [DIRS 179180]
van Genuchten m (or λ)	m_m (-)	0.283	0.317	0.216	DTN: LB0610UZDSCP30.002 [DIRS 179180]
Residual saturation	S_{irm} (-)	0.12	0.19	0.12	DTN: LB0208UZDSCPMI.002 [DIRS 161243] ^a
Epsilon (for maximum P_{cap})	ϵ	0.136	0.166	0.291	Calculated to Yield maximum $P_{cap} = 10^8$ Pa (Section 6.4.6(16))
Rock grain density	ρ (kg/m ³)	2,520	2,520	2,540	DTN: LB0704THRMLPRP.001 [DIRS 181318]
Rock grain specific heat capacity	C_p (J/kg K)	930	930	930	DTN: LB0704THRMLPRP.001 [DIRS 181318]
Dry thermal conductivity	λ_{dry} (W/m/K)	1.22	1.39	1.24	DTN: LB0704THRMLPRP.001 [DIRS 181318]
Wet thermal conductivity	λ_{wet} (W/m/K)	1.78	2.06	1.87	DTN: LB0704THRMLPRP.001 [DIRS 181318]
Tortuosity	τ (-)	0.20	0.20	0.20	After Penman 1940 [DIRS 109941], pp. 441 and 461
FRACTURE DATA^b					
Permeability	k_f (m ²)	7.8E-13	3.3E-13	9.1E-13	DTN: LB0610UZDSCP30.002 [DIRS 179180]
Porosity	f_f (-)	5.8E-3	8.5E-3	9.6E-3	DTN: LB0205REVUZPRP.001 [DIRS 159525]
van Genuchten α	α_f (1/Pa)	1.58E-3	3.16E-4	5.75E-4	DTN: LB0610UZDSCP30.002 [DIRS 179180]
van Genuchten m (or λ)	m_f (-)	0.633	0.633	0.633	DTN: LB0610UZDSCP30.002 [DIRS 179180]
Residual saturation	S_{irf} (-)	0.01	0.01	0.01	DTN: LB0208UZDSCPMI.002 [DIRS 161243] ^c
Epsilon (for maximum P_{cap})	ϵ	0.01	0.01	0.01	Model setup (Section 6.4.6(16))
Effective tortuosity	τ (-)	0.0041 ^d	0.0060 ^d	0.0067 ^d	Model setup (Section 6.4.6(18))
AFM coefficient	γ (-)	0.400	0.400	0.400	DTN: LB0610UZDSCP30.002 [DIRS 179180]

^a The matrix of tsw33, tsw34, and tsw35 units are referred to in the source (DTN: LB0208UZDSCPMI.002 [DIRS 161243]) as tswM3, tswM4, and tswM5, respectively.

^b Fracture thermal properties are calculated from matrix thermal properties as discussed in Section 6.4.6(12)

^c The fractures of tsw33, tsw34, and tsw35 units are referred to in the source document (DTN: LB0208UZDSCPMI.002 [DIRS 161243]) as tswF3, tswF4, and tswF5, respectively.

^d Fracture tortuosity of 0.7 is multiplied by fracture porosity to arrive at effective tortuosity factor for the fracture continuum.

6.4.8 Post-Processing Methodology for Predicted Water Compositions

The conceptualization of drift-scale coupled processes underlying the THC seepage model is presented in Section 6.2. Multi-dimensional output data are available for various input water compositions and two repository locations (center and edge). In order to extract the data appropriately from THC model results, the conceptualization and principles of the data selection are examined. The intention of the THC seepage model is to represent the effect of THC processes in the rock around waste emplacement drifts, including:

- Composition of waters and gases that could enter the drifts
- The effect of THC processes on seepage into drifts.

However, the THC seepage model does not simulate actual seepage of water into drifts because the range of simulated infiltration rates (including rates for future climate conditions of high infiltration) remains well below the theoretical seepage threshold for rocks around the drift. Note that in-drift seepage is quantified using another model (SNL 2007 [DIRS 177413]). Also, the predicted chemistry of actual in-drift seepage waters is examined in *THC Sensitivity Study of Heterogeneous Permeability and Capillarity Effects* (SNL 2007 [DIRS 177413]).

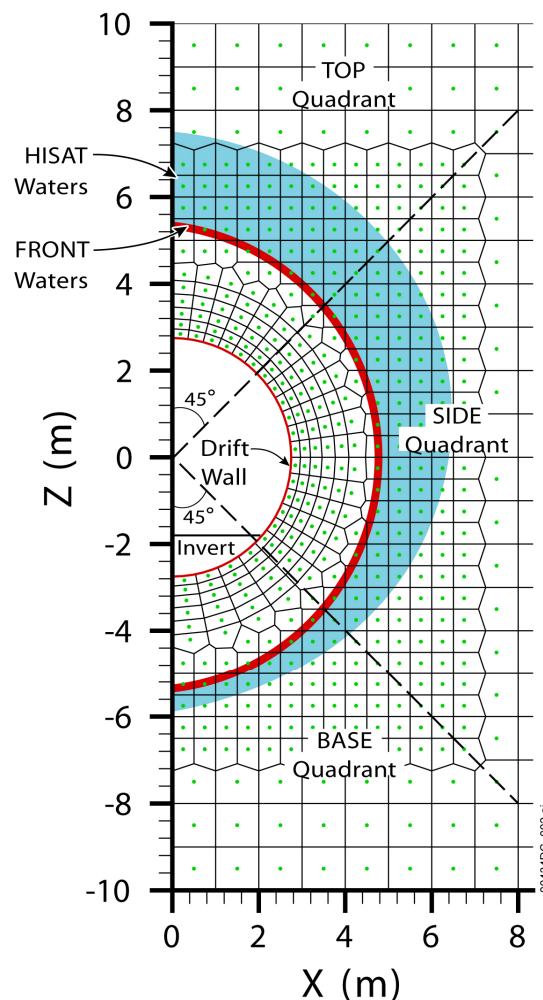
Here, the model is used to compute the compositions of pore water and gas in the repository host rock (matrix and fractures) around a typical drift (Figure 6.4-1). Predicted compositions for seepage and the associated gas-phase compositions are obtained from locations (around the modeled drift) that would best represent the composition of potential seepage. Water compositions predicted at the drift wall could be considered; however, composition data are not available during the time that the drift wall remains dry.

Predicted concentration gradients near the drift are steep, resulting from sharp temperature and liquid saturation gradients. Therefore, selected water compositions depend strongly on the location (around the drift) chosen for selection. Because of the transient nature of the thermal pulse, predicted water compositions also change significantly through time. Therefore, the selection of THC model results is based on extracting time profiles of modeled data for locations evolving in space around the modeled drift. Data are extracted in both the fracture and matrix continua, using criteria relying primarily on water fluxes, as further examined below. This is done using CUTCHEM V2.0 (see Section 3.1), which was designed specifically for this purpose.

Using CUTCHEM, data are extracted from THC model results for three cross-sectional quadrants (TOP, SIDE, and BASE; see Figure 6.4-1) and within a certain specified radial distance from drift center (15 m in the present study). The extraction procedure considers both fracture and matrix waters in these cross-sectional quadrants, and data for these two continua at these locations are provided in files accompanying this report (see Section 6.5.5 and Table 6.5-5). However, priority is given here to the predicted composition of water in fractures above the drift. The permeability of fractures around the drift is several orders of magnitude higher than the permeability of the matrix. Also, fractures have much lower capillarity than the matrix. Therefore, any water potentially seeping into the drift by gravity is likely to be fracture water above the drift, and for this reason the composition of that water is taken as best representing potential seepage.

The three quadrants corresponding to the crown, side, and base of the drift are defined with the following spatial characteristics and assigned attributes (Figure 6.4-1):

- TOP Quadrant: The first quadrant encompassing the area above the drift, defined by model gridblocks having a ratio of their vertical (Z) to their horizontal (X) coordinate greater or equal to 1 (45° arc from crown)
- SIDE Quadrant: The second quadrant encompassing the area to the side of the drift, defined by model gridblocks having their Z/X ratio ranging from -1 to +1 (45° arc above and 45° below the drift spring line)
- BASE Quadrant: The third quadrant encompassing the area below the drift, defined by model gridblocks having their Z/X ratio less than -1 (45° arc from base).



Grid source: Appendix J.

NOTE: The areas delineating high saturation zones (HISAT and FLUX) and FRONT waters are for illustrative purposes only. The extent of these areas varies through time and is different for fracture and matrix waters. Since only half-symmetry is modeled, both TOP and BASE represent a half quadrant.

Figure 6.4-1. Quadrant Designations for Data Selection from the THC Seepage Model

Waters from three types of locations are then defined:

- HISAT: Waters in zones around the drift where liquid saturations are higher than in surrounding host rock (e.g., condensation zones).
- FLUX: Waters in zones around the drift where liquid mobility is higher than in surrounding host rock (e.g., condensation and reflux zones). These waters essentially correspond to HISAT waters, except that they mostly exclude waters from zones of high liquid saturations caused by reduced permeability and porosity (Leverett scaling; Section 6.4.4.4).
- FRONT: Waters from zones closest to the drift, where non-zero liquid saturations occur.

CUTCHEM V2.0 applies the following methodology for identifying these locations:

FRONT waters (boiling/wetting front)—At each time interval, model results are extracted for gridblocks according to the following criteria (in order of preference):

1. Distance from drift center is within search radius (15 m in the present case, to cover the dryout and rewetting zone)
2. Nonzero liquid saturation (in matrix or fractures depending on which is selected)
3. First six gridblocks with smallest radial distance from drift center—these are ranked with attribute INDX=1 through 6 from the closest to the farthest from the drift center. However, if ties occur (same radial distance), the gridblocks and corresponding indexes INDX are selected and ranked in order of decreasing liquid saturation, then decreasing absolute values of Z coordinates (Figure 6.4-1).

HISAT waters (zone of increased liquid saturation)—At each time interval, model results are extracted for gridblocks according to the following criteria (in order of preference):

1. Distance from drift center is within search radius (15 m in the present case, to cover the dryout and re-wetting zone)
2. First six gridblocks with highest liquid saturation (in matrix or fractures depending on the selected medium)—these are ranked with attribute INDX=1 through 6 from most to least liquid saturated. However, if ties occur (same liquid saturation), then gridblocks and corresponding indexes INDX are selected and ranked in order of increasing radial distance from drift center, then decreasing absolute values of Z coordinates (Figure 6.4-1).

FLUX waters (zone of increased liquid mobility)—At each time interval, model results are extracted for gridblocks according to the following criteria (in order of preference):

1. Distance from drift center is within search radius (15 m in the present case, to cover the dryout and re-wetting zone)

2. First six gridblocks with highest liquid mobility (in matrix or fractures depending on the selected medium)—these are ranked with attribute INDX=1 through 6 from highest to lowest flux. However, if ties occur (same flux), then gridblocks and corresponding indexes INDX are selected and ranked in order of increasing radial distance from drift center, then decreasing absolute values of Z coordinates (Figure 6.4-1).

The liquid mobility for a given gridblock is calculated from the computed water flow (kg/s) at each connection. The connection-based water flow is converted into a water mass flux (kg/m²/s) by:

$$f_i = \frac{f_i^w}{A_i} \quad (\text{Eq. 6.4-40})$$

where f_i is the water mass flux of the i^{th} connection (kg/m²/s), f_i^w is the water flow (kg/s) of i^{th} connection, and A_i is the interface area of i^{th} connection (m²). The connection-based water mass flux of the i^{th} connection is then converted to gridblock-based water mass-flux components, using:

$$f_x = \sum_{i=1}^{N_c} f_i \cos \theta \quad (\text{Eq. 6.4-41})$$

$$f_z = \sum_{i=1}^{N_c} f_i \sin \theta \quad (\text{Eq. 6.4-42})$$

where f_x and f_z are water mass flux components in the X- and Z-direction, respectively, θ is the angle between the connection direction and the x-direction, and N_c is the number of connections for the given gridblock. The total water mass flux, f , for each gridblock is then calculated as:

$$f = (f_x^2 + f_z^2)^{0.5} \quad (\text{Eq. 6.4-43})$$

and taken as representing the liquid mobility.

The selection of six gridblocks for each water at each time step stems from the configuration of the numerical grid (Figure 6.4-1). In this grid, each successive radially distributed row of gridblocks in the TOP quadrant, from the drift wall outwards, contains approximately six gridblocks (Figure 6.4-1; see also Section 6.5.1). The number of sampling points is dependent on the grid resolution. By limiting the number of selected gridblocks, extraction of data over a wide area is avoided, and the potential for overlapping HISAT/FLUX and FRONT waters is limited. Note that extracted fracture and matrix data following the procedure described above do not necessarily correspond to the same gridblocks.

In this report, the described selection method is used to extract simulated water and CO₂ concentrations for six points (gridblocks) per time interval for each run, for extracted type FLUX in each quadrant (TOP, SIDE, and BASE). In this way, the method captures the spatial variability of model results around the drift for each given model run. It also captures the

predicted compositions of most “mobile” waters, which, above the drift, are most likely to represent in-drift seepage. The large quantity of data extracted in this way is then narrowed down to consider only waters deemed most susceptible to seep into drifts, namely TOP FLUX waters in fractures, for six points (gridblocks) per time interval for each run. The data from the SIDE and BASE quadrants, as well as matrix waters, are not considered further in this report, because most in-drift seepage is expected to occur by gravity drainage in fractures above the drift.

6.5 THC SEEPAGE MODEL

6.5.1 Numerical Mesh

The conceptualization of the model domain is described in Section 6.2.3. Simulations are performed on a vertical two-dimensional mesh reduced to a half-drift model with laterally homogeneous rock properties (Figure 6.5-1). The stratigraphy of the modeled grid is shown in Table 6.5-1, and corresponds to a location near the center of the repository, as discussed in Section 4.1.2.

Table 6.5-1. Vertical Mesh Dimensions and Geologic Contacts in the THC Seepage Model (Tptpl unit)

Model Layer	Top of Layer Elevation (m)	Mesh Top of Layer Z Coordinate (m)
Top	1446.6	363.8
tcw11	1446.6	363.8
tcw12	1419.2	336.4
tcw13	1342.1	259.3
ptn21	1326.5	243.7
ptn22	1323.1	240.3
ptn23	1321.0	238.2
ptn24	1318.2	235.4
ptn25	1312.7	229.9
ptn26	1303.6	220.8
tsw31	1294.1	211.3
tsw32	1279.7	196.9
tsw33	1249.3	166.5
tsw34	1169.2	86.4
tsw35	1132.0	49.2
Drift center	1082.8	0.0
tsw36	1030.6	-52.2
tsw37	997.4	-85.4
tsw38	980.8	-102.0
tsw39	967.0	-115.8
ch1v	956.9	-125.9
ch2v	945.2	-137.6
ch3v	931.9	-150.9
ch4z	919.2	-163.6
ch5z	906.4	-176.4
ch6	892.4	-190.4
pp4	878.5	-204.3
pp3	865.9	-216.9
pp2	833.2	-249.5

Table 6.5-1. Vertical Mesh Dimensions and Geologic Contacts in the THC Seepage Model (Tptpl Unit) (Continued)

Model Layer	Top of Layer Elevation (m)	Mesh Top of Layer Z Coordinate (m)
pp1	818.2	-264.6
bf3	756.7	-326.1
Bottom	730.0	-352.8

Source: Developed as specified in Appendix J, after DTN: LB990501233129.004 [DIRS 111475] (geologic column).

Thermal histories at both center and edge locations are taken into account by considering two cases of drift spacing:

- 81 m: The designed drift spacing, corresponding to a center location (half-drift model width of 40.5 m)
- 162 m: An “effective” drift spacing corresponding to an edge location (half-drift model width of 81 m).

Both these cases make use of the same design heat load, ventilation period, and ventilation efficiency (Section 4.1.5 and Appendix D). In doing so, the heat loss at the edge of the repository is simulated through the use of the increased “effective” drift spacing, and the peak temperatures in the drift remain approximately the same in both cases (Section 6.5.5.2). Note that the two values of drift spacing yield boiling periods (i.e., periods when drift-wall temperatures are $\geq 96^{\circ}\text{C}$) in the high-range (~100th percentile) and low-range (~5th percentile) of lengths predicted with the multiscale thermohydrologic model (MSTHM) with 30th percentile infiltration (SNL 2007 [DIRS 181383], Section 6.3) (Table 6.5-2).

Table 6.5-2. Effective Drift Spacings Considered for the THC Seepage Model

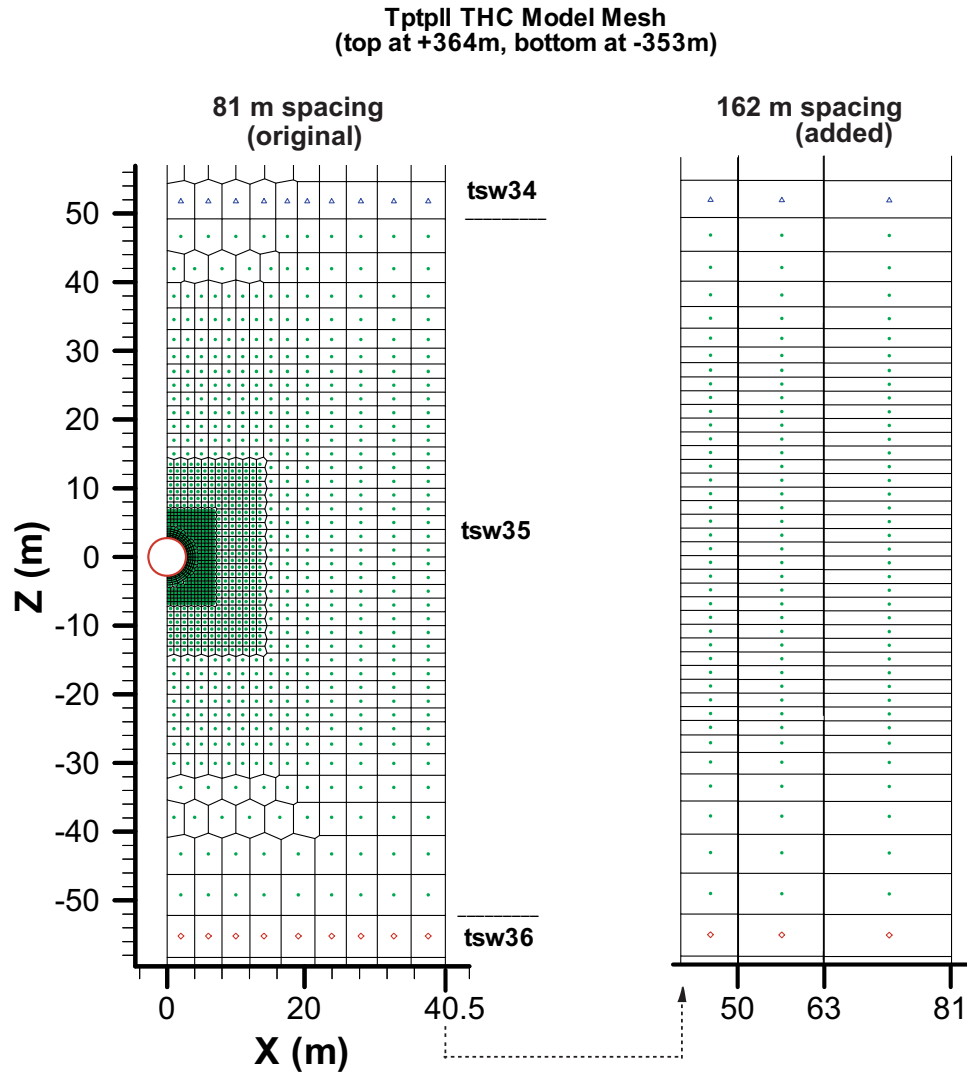
Drift Spacing	Case Type	Areal Mass Loading (MTU/Acre)	Time When Boiling Ceases at Drift Wall
81 m	Design spacing, repository center	55 ^a	~1,270 years ^b
162 m	Effective spacing, repository edge	27 ^c	~ 180 years ^b

^a Value corresponding to the effective drift spacing of 81 m, as calculated in SNL 2007 [DIRS 181383], Section 6.2.4. The calculation was conducted based upon the most updated design parameters, and is qualified as a source in this report.

^b Time at which the drift crown temperature falls below 96°C (see Section 6.5.5.2).

^c Derived from the one-to-one equivalence between effective drift spacing and areal mass loading, based on the mass loading for the drift spacing of 81 m (i.e., $27 = 55 \times 81/162$).

The model grid was developed in two stages, as described in Appendix J. The mesh for the designed 81-m drift spacing was produced first. The second stage involved the addition of three model columns to the right of the original mesh to extend the effective drift spacing (Figure 6.5-1).



Source: DTN: LB990501233129.004 [DIRS 111475].

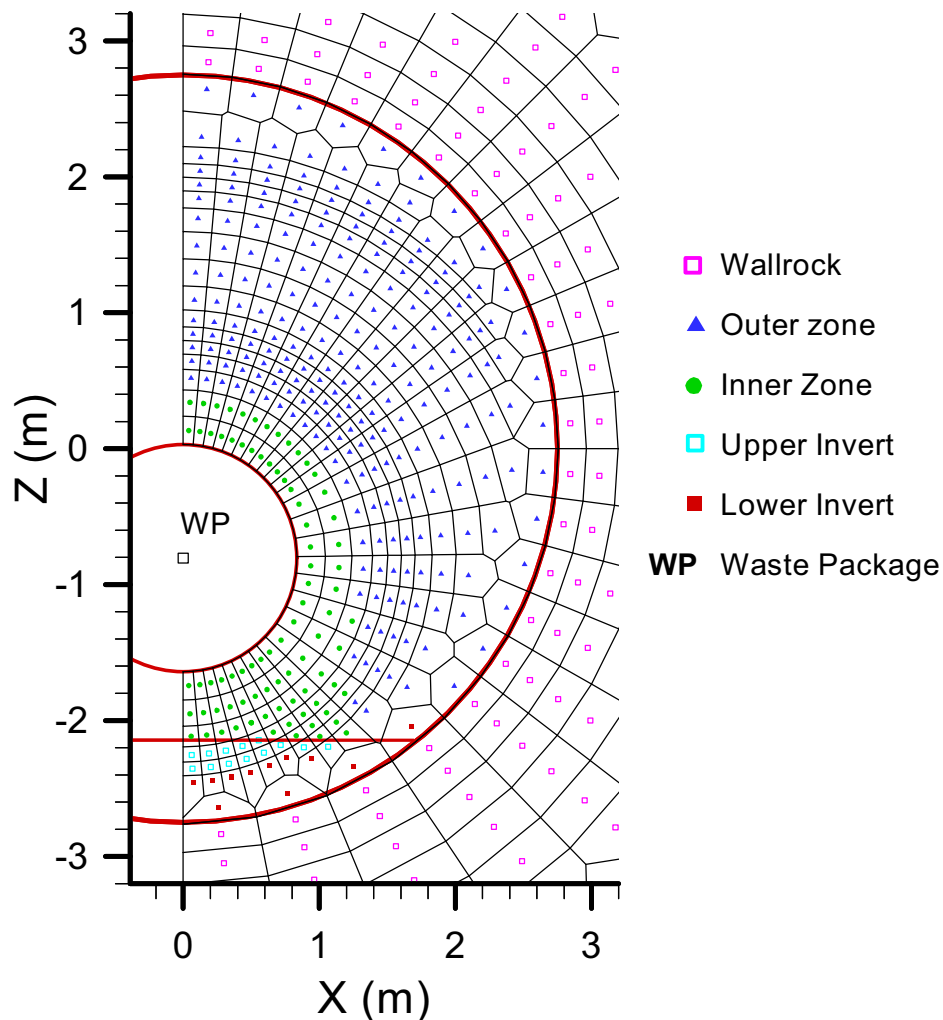
NOTE: Grid detail around (0, 0) is shown in Figure 6.5-2.

Figure 6.5-1. THC Model Mesh with Hydrogeologic Units Shown in the Vicinity of the Drift: Topopah Spring Tuff Middle Nonlithophysal (tsw34: triangles), Lower Lithophysal (tsw35: dots), and Lower Nonlithophysal (tsw36: diamonds) Units

To limit grid orientation effects, the mesh design is mostly orthogonal, with a small radially gridded area in the immediate vicinity of the drift (Figures 6.5-1 and 6.5-2). The area extending approximately 40 m above the drift is more finely gridded than other areas to capture THC effects potentially affecting seepage into the drift. Outside the drift, the smallest grid spacing is specified at the drift wall (20 cm) and increased outward. A constant square cell size of 50 cm is used from approximately 5 to 7 m above drift center, increased to a 1-m size until 15 m above drift center, then a 2-m size from 15 to 30 m above drift center. All geologic layers down to the water table below the modeled drift are incorporated into the numerical mesh (Table 6.5-1). Gridblock sizes increase significantly 100 m above and below the drift to increase computing efficiency. The mesh consists of 3,202 gridblocks, including those representing matrix, fracture, and in-drift design elements.

The drift discretization is shown in Figure 6.5-2. The drift is discretized to include the design elements and dimensions shown on Figure 4.1-1 (338 gridblocks total). The invert, 0.8 m thick, is divided into an “upper invert” and “lower invert” for assignment of different thermal conductivities in these zones (Section 4.1.10). The drip shield is not explicitly modeled (Section 4.1.10). The gridblock size inside the drift is chosen to be small enough to provide a realistic drift model (compare Figure 6.5-2 to Figure 4.1-1). Two in-drift configurations are considered in this model:

- Preclosure configuration (during the first 50 years): waste package, upper invert, lower invert, and open space between the waste package and drift wall
- Postclosure configuration (after 50 years): waste package, upper invert, lower invert, drip shield, and two open zones (inner zone, between the waste package and drip shield; and outer zone, between the drip shield and drift wall).



Source: See Section 4.1.10.

Figure 6.5-2. Discretization of the Repository Drift in the THC Model

The discretization of the drift is kept the same for the two configurations. As such, the preclosure period is simulated by assigning identical open-space properties to gridblocks representing the inner zone and outer zone.

THC simulations of ambient conditions (no thermal load) are run with a one-dimensional (vertical column) grid representing the same stratigraphy as the two-dimensional mesh. This one-dimensional model does not have a drift opening and uses uniform vertical gridding through the area cutting across the drift on Figure 6.5-2, with a grid spacing of 2 m between $Z = -14$ and $Z = +14$ m. The spacing follows the same discretization as the two-dimensional mesh (at $X = 0$ m) beyond that point. One-dimensional columns are used to speed up the computational effort. Because of the no-flow boundary conditions existing on each side of the model mesh, the horizontal geologic contacts and laterally continuous rock properties, two-dimensional simulations under ambient conditions are essentially the same as one-dimensional simulations (vertical flow only). Close to the drift, however, flow is diverted around the drift opening because of the capillary barrier created by this opening. Therefore, the only differences between one- and two-dimensional ambient simulations result from the effect of the drift opening.

6.5.2 Boundary Conditions

The boundary conditions are set as shown in Table 6.5-3. The pressure and temperature are constant at the top and bottom boundaries, with temperature values reflecting the natural geothermal gradient. The use of a constant temperature boundary at the water table is not expected to have much effect on the predicted thermal history or water chemistry in the repository drifts, because the boundary is so far (more than 350 m) from the repository horizon (BSC 2005 [DIRS 174101], Section 6.1.3). The initial CO_2 partial pressure in the drift is set to the same CO_2 partial pressure assumed in the adjacent wall rock at the start of simulations (fugacity \approx partial pressure of 10^{-3} bar; see Section 6.2.2.1). Three stepped-up values of infiltration rate are considered, as described in Section 4.1.4. One-dimensional simulations of ambient conditions are run with the same boundary conditions as shown in Table 6.5-3, except that these simulations do not include a drift opening.

Table 6.5-3. THC Seepage Model Boundary Conditions

Boundary	Boundary Condition	Reference
Top	T = 16.02°C S _g = 1.0 P = 84,610 Pa pCO ₂ = 10 ⁻³ bar Time-varying infiltration rate (30th percentile, stepped up from 7.96 to 12.89 mm/yr at 600 years, then to 20.45 mm/yr at 2,000 years) Constant composition of infiltration (W0, W8, W9 or W10) and pCO ₂ = 10 ⁻³ bar ^a	Table 4.1-4 Table 4.1-4 Table 4.1-4 Section 6.2.2.1 Table 4.1-5 Table 6.2-1
Bottom	T = 32.00°C S _L = 0.0 P = 91,762 Pa Constant water composition (W0, W8, W9 or W10) and pCO ₂ = 10 ⁻³ bar ^a	Table 4.1-1 Table 4.1-1 Table 4.1-1 Table 6.2-1
Sides	No flux for water, gas, heat, and chemical species	Not applicable
Drift Wall ^b	Open to gas and liquid fluxes (advective and diffusive); conduction only for heat	Not applicable

Table 6.5-3. THC Seepage Model Boundary Conditions (Continued)

Boundary	Boundary Condition	Reference
Waste Package ^b	Initial full heat load of 1.45 kW/m decreasing with time (due to radioactive decay), and reduced by 88% during the first 50 years (due to heat removal by ventilation)	Appendix D and Table 4.1-6

^a Does not apply to TH simulations (i.e., simulations that do not include chemical interactions).

^b Does not apply to simulations of ambient conditions (without drift opening).

NOTES: T = temperature; S_g = gas saturation; S_L = liquid saturation; P = pressure.

6.5.3 Summary of Inputs and Modeling Procedure

Simulations are run using TOUGHREACT V3.1.1 and the EOS4 module (vapor pressure lowering option; see Section 6.4.6(13)). Simulations are carried out for:

- Two different spatial locations (center and edge) (Section 6.5.1)
- Four different input water compositions (Section 6.2.2.1, Table 6.2-1)
- Ambient (no heat load) and heat load conditions (Section 4.1.5)
- Various sensitivity analyses as described in Section 6.6.

Main inputs to these simulations are summarized in the following tables or appendices:

- Rock properties: Table 6.4-2
- Initial water compositions: Table 6.2-1
- Geochemical system: Tables 6.2-2
- Thermodynamic data: Appendix C
- Kinetic data: Appendix H
- Mineral abundance and surface areas: Appendices A and B, respectively
- Heat load: Appendix D.

In all simulations, minerals are set to react under kinetic constraints (Appendix H), except for the following minerals that react at equilibrium: calcite, anhydrite, and goethite. Assuming equilibrium with these minerals is reasonable because their reaction rates are quite rapid. Furthermore, very similar results in simulations of the DST are obtained when using local equilibrium for calcite and assuming a kinetically controlled reaction rate (BSC 2005 [DIRS 172862], Section 7.1). Also, assuming equilibrium for these minerals has the advantage of allowing simulations with larger time steps than would be required with a kinetically controlled fast reaction rate.

Before any predictive modeling work, simulations with both the one- and two-dimensional grids (Section 6.5.1) are run with a constant infiltration rate of 7.96 mm/yr (and other top and bottom boundary conditions as shown in Table 6.5.3), without a drift opening, and without water-rock chemical interactions, until steady conditions of pressure, temperature, and liquid saturations are obtained throughout the modeled columns. These conditions are considered steady once these parameters remain constant for simulated periods of at least 1 million years, and once the sum of fluxes (liquid and vapor) at the top model boundary matches the sum of fluxes at the bottom

boundary with differences not exceeding 0.001%. These conditions are then used as initial thermal and hydrological conditions for all other TH and THC simulations.

Before modeling water–rock interactions under thermal loading conditions, THC simulations under ambient conditions (i.e., without thermal loading, under natural geothermal gradient, and without drift opening) are run using a one-dimensional grid (Section 6.5.1) and the same inputs as described above. These simulations are used in part to help bound reaction rates and refine the geochemical system being modeled, as discussed in Section 6.5.5.1. Results of these simulations also provide a baseline against which the effects of thermal loading can be compared.

THC simulations are then run for an initial period of 50 years, using the preclosure drift configuration and thermal properties. The simulations are then restarted using the postclosure drift configuration and properties from 50 years to a total simulation time of 100,000 years. At times corresponding to changes in infiltration rates (at 600 and 2,000 years; Table 4.1-5), the simulations are stopped and then restarted with the new infiltration rate, resulting in a stepwise change in infiltration.

The time discretization is defined using the following maximum time step sizes, which are further evaluated in Section 6.6.1:

- Ambient simulations:
 - ~35 to 53 days for the entire simulated period of 0 to 100,000 years (set by limiting the time step to values less than half the residence time in any one gridblock).
- Heat-load simulations:
 - 15 days for simulated period 0 to 2,000 years
 - 100 days for simulated period 2,000 to 10,000 years
 - 300 days for simulated period 10,000 to 30,000 years
 - 1,000 days for simulated period 30,000 to 100,000 years.

Note that time-step size restrictions related to flow (not transport) are built into TOUGHREACT and yield time-step values that are often smaller than the prescribed input maximum time-step sizes shown above, particularly in areas undergoing boiling and/or rewetting.

6.5.4 Model Simulations

A number of predictive simulations have been performed, as summarized in Table 6.5-4. These do not include sensitivity analyses discussed in Section 6.6. Boundary conditions were those given in Table 6.5.3.

Table 6.5-4. THC Seepage Model Predictive Simulations

Input Water Composition (Table 6.5-3)	Drift Spacing (Section 6.5.1)	Simulation Type	Thermal Loading	Domain Type	Simulation ID
Not Applicable	81 m	TH ambient ^a	No	2-D	2dflow_81m
Not Applicable	81 m	TH	Yes	2-D	th7_81
W0	81 m	THC	Yes	2-D	thc7_81_w0
W8	81 m	THC	Yes	2-D	thc7_81_w8
W9	81 m	THC	Yes	2-D	thc7_81_w9
W10	81 m	THC	Yes	2-D	thc7_81_w10
Not Applicable	81 m	TH ambient ^a	No	2-D	2dflow_162m
Not Applicable	162 m	TH	Yes	2-D	th7_162
W0	162 m	THC	Yes	2-D	thc7_162_w0
W8	162 m	THC	Yes	2-D	thc7_162_w8
W9	162 m	THC	Yes	2-D	thc7_162_w9
W10	162 m	THC	Yes	2-D	thc7_162_w10
Not Applicable	None	TH ambient ^a	No	1-D	1dflow
W0	None	THC ambient	No	1-D	thc7_amb_w0
W8	None	THC ambient	No	1-D	thc7_amb_w8
W9	None	THC ambient	No	1-D	thc7_amb_w9
W10	None	THC ambient	No	1-D	thc7_amb_w10

^a Initial simulations to steady TH state (no chemistry).

NOTE: 1-D = one-dimensional; 2-D = two-dimensional.

6.5.5 Simulation Results

The model results are presented below. One-dimensional THC simulations of ambient conditions (without thermal loading) are discussed first in Section 6.5.5.1, as these helped define the modeled geochemical system (Section 6.2.2.2) and bound some input thermodynamic and kinetic parameters. Thermal and hydrological effects resulting from the heat generated by waste packages are then presented in Section 6.5.5.2, and compared for cases excluding and including water–rock chemical interactions. The effect of mineral alteration on permeability around the drift is discussed in Section 6.5.5.3. Predicted water-chemistry trends above the drift are discussed in Section 6.5.5.4.

All model input and output files have been submitted to the TDMS under DTNs as listed in Table 6.5-5 and Section 8.5. For each simulation, Excel tables and plots summarizing the predicted chemistry of fracture and matrix waters around the simulated drift have also been generated. These summary tables have been submitted to the TDMS with file names and DTNs as summarized in Table 6.5-5. These files contain many more results and plots than shown in this report.

Table 6.5-5. Summary Output Data Files and DTNs Showing Predicted Water Composition and Plots for THC Seepage Model Simulations

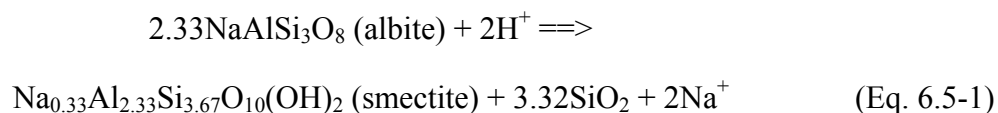
Description	Location in Model ^a	Medium	File Name	DTN	Run ID (Table 6.5-4)	DTN for TOUGHREACT I/O Files
Water W0	Zones of high liquid fluxes around drift	Fractures	<i>frac_81_162_w0.xls</i>	LB0705DSTHC001.001	thc7_amb_w0	LB0705DSTHC001.002
		Matrix	<i>mat_81_162_w0.xls</i>		thc7_81_w0	
	Crown, side, and base of drift	Fractures	<i>frac_81_162_dr_w0.xls</i>		thc7_162_w0	
		Matrix	<i>mat_81_162_dr_w0.xls</i>			
Water W8	Zones of high liquid fluxes around drift	Fractures	<i>frac_81_162_w8.xls</i>	LB0705DSTHC002.001	thc7_amb_w8	LB0705DSTHC002.002
		Matrix	<i>mat_81_162_w8.xls</i>		thc7_81_w8	
	Crown, side, and base of drift	Fractures	<i>frac_81_162_dr_w8.xls</i>		thc7_162_w8	
		Matrix	<i>mat_81_162_dr_w8.xls</i>			
Water W9	Zones of high liquid fluxes around drift	Fractures	<i>frac_81_162_w9.xls</i>	LB0705DSTHC003.001	thc7_amb_w9	LB0705DSTHC003.002
		Matrix	<i>mat_81_162_w9.xls</i>		thc7_81_w9	
	Crown, side, and base of drift	Fractures	<i>frac_81_162_dr_w9.xls</i>		thc7_162_w9	
		Matrix	<i>mat_81_162_dr_w9.xls</i>			
Water W10	Zones of high liquid fluxes around drift	Fractures	<i>frac_81_162_w10.xls</i>	LB0705DSTHC004.001	thc7_amb_w10	LB0705DSTHC004.002
		Matrix	<i>mat_81_162_w10.xls</i>		thc7_81_w10	
	Crown, side, and base of drift	Fractures	<i>frac_81_162_dr_w10.xls</i>		thc7_162_w10	
		Matrix	<i>mat_81_162_dr_w10.xls</i>			

^a All data files also include results of ambient 1-D THC simulations at the repository elevation (grid nodes F43 and M43).

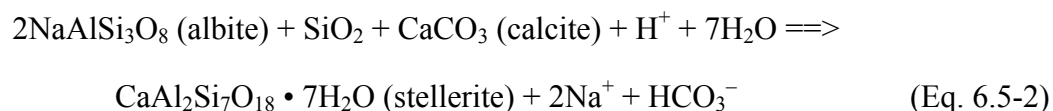
6.5.5.1 THC Simulations of Ambient Conditions

THC simulations of ambient conditions (no thermal loading) were first run to test and refine the modeled geochemical system (Section 6.2.2.2), and bound some uncertain input thermodynamic and kinetic parameters. These simulations were then used to provide a baseline against which to compare results of thermal loading simulations.

THC simulations of ambient conditions should predict relatively steady water composition trends over the time period considered (100,000 years, which is short compared to the geologic history of Yucca Mountain), as well as mineral deposition patterns consistent with field observations. Obtaining an initial “steady-state” hydrochemical system yielding aqueous species concentrations consistent with measured concentrations in pore water is difficult. This is because the stability of the modeled geochemical system depends on reaction rates and relative mineral thermodynamic stability, as well as infiltration rates and rock properties. The difficulty in reaching a chemical steady state increases with the number of reactive minerals included in the system, because each additional mineral adds its own uncertainty in reaction rate to the total model uncertainty. In the present case, obtaining a reasonably “steady” ambient hydrochemical state required reducing the dissolution rates of primary aluminum silicates (plagioclase, sanidine, rhyolitic glass, and biotite), as well as the reaction rate of clays (beidellite and illite), by several orders of magnitude compared to measured data, as discussed in Appendix H. This is consistent with the common observation that field reaction rates are typically much lower than rates measured in the laboratory (e.g., White and Brantley 2003 [DIRS 168088]). Model simulations are quite sensitive to the effective reaction rates of aluminum silicates, particularly clays and calcium zeolites. For example, the dissolution of albite (a sodium feldspar) to form sodium smectite (a clay) results in an increase in pH (decrease in H^+ activity), as follows:



The alteration of albite to stellerite (a calcium zeolite) can also drive pH to higher values if the calcium necessary to form stellerite originates from calcite dissolution, as in the following reaction:



In addition, the consumption of calcium to form calcium-bearing zeolites or clays inhibits calcite precipitation as a means of controlling the increase of pH and total aqueous carbonate concentrations.

Lowering the rates of these reactions, however, was not sufficient to yield chemical trends consistent with field data. Ambient CO_2 partial pressures as well as the observed trend of calcite precipitation in fractures could not be reproduced without slightly destabilizing stellerite. Increasing the Gibbs free energy of stellerite by $\sim 0.2\%$, well within the range of uncertainty of this thermodynamic parameter, was sufficient to produce reasonable trends and bring the compositions of all repository pore waters close to the albite-stellerite boundary, as discussed in

Appendix C. Without this adjustment, modeled results predicted significant calcite dissolution in fractures (Equation 6.5-2) as well as the formation of stellerite in amounts that are not substantiated by field data.

The type of clay minerals included in the model also significantly affected ambient trends of pH and water chemistry (Equation 6.5-1). Good trends could only be obtained by using beidellites (Na, Ca, and Mg endmembers) rather than montmorillonites, and by treating these minerals as an ideal solid solution. It should be noted that the source of thermodynamic data for clays used in this study (the project database *data0.ymp.R5*; see Appendix C) does not include calcium-rich clays representative of compositions at Yucca Mountain. For these reasons, and the fact that the simulations do not incorporate ion exchange or complex solid solution models, the model is quite approximate as far as the treatment of clay minerals.

The same is true for zeolites, which are treated as fixed-composition phases in the current report. However, to account for potentially variable clinoptilolite compositions, ambient simulations were used to test various representations of this mineral. Initial efforts to treat clinoptilolite as an ideal solution of the Na, K, and Ca endmembers provided in the project thermodynamic database *data0.ymp.R5* did not yield satisfactory results. Better results were obtained by using these data to create and incorporate into the geochemical system a primary clinoptilolite phase with a fixed, mixed, Ca-Na-K composition representative of Yucca Mountain tuffs, which was only allowed to dissolve, then by adding into the system three separate secondary Ca, Na, and K endmembers phases allowed to precipitate or dissolve independently (Appendix C).

This “fine tuning” of the modeled geochemical system was achieved by running a large number of test ambient THC simulations, using the composition of water W0 as initial input and a constant infiltration rate of 7.96 mm/yr. Once the modeled geochemical system and input kinetic and thermodynamic data were finalized (as shown in Table 6.2-2, Appendix C, and Appendix H, respectively), “final” ambient simulations were run using stepped-up infiltration rates (Table 6.5-3) and all selected input water compositions (W0, W8, W9, and W10). Relatively steady and consistent trends were obtained with all input water compositions over the range of infiltration rates considered, thus providing some confidence in the modeled geochemical system and its inputs. Additional confidence was then provided with the model validation simulations (Section 7), which make use of the same geochemical system and input parameters.

It must be recognized that the model adjustments carried out using ambient THC simulations may not be unique, because many degrees of freedom exist in such complex simulations. In the present case, the adjustments made were those that seemed the most obvious, although it cannot be ruled out that the adjustment of other model parameters could have a similar effect. It should also be emphasized that, under “undisturbed” temperature and pressure conditions, as well as slow infiltration rates such as at Yucca Mountain, a delicate balance exists between various reactive-transport processes. When modeling such a system, this balance can be easily offset as the result of model simplifications (Section 6.4.6), or variations in input kinetic and thermodynamic data that are well within their range of uncertainty. Under heavily disturbed conditions, however, such as the thermal loading from waste packages, the modeled system is drawn so far from its initial state that model results become much less sensitive to some of these model simplifications and/or adjustments (see Section 6.6.5).

The results of final ambient simulations for a location at repository level are included in Excel spreadsheets and plots submitted with this report (Table 6.5-5) and also shown in figures presented later in this report (Section 6.5.5.4) that depict the effects of thermal loading.

6.5.5.2 General Thermal and Hydrological Effects

Predicted effects of the heat load on temperatures and liquid saturations around the modeled drift, as well as on vertical liquid fluxes directly above the drift crown, are presented in this section. Results of simulations carried out with and without the effects of water–rock interactions are compared for both a central and edge repository location, and initial water compositions W0, W8, and W9. Model results using water W10 are not shown here because this water has almost the same composition as water W0 (Table 6.2-1) and yields essentially the same model results as water W0, as far as thermal and hydrological effects. Further details on the effects of water–rock interactions on permeability around the drift are discussed in Section 6.5.5.3. Additional results and plots can be found in files accompanying this report, which are listed in Table 6.5-5.

Results of TH and THC simulations for the center and edge locations (81-m and 162-m drift-spacing cases, respectively) are shown in Figures 6.5-3 through 6.5-7. Comparing the results of TH and THC simulations shown in these figures indicates very little effect of water–rock interactions on the general thermal and hydrological behavior around the drift. The times at which boiling is predicted to cease (defined as the time when average drift wall temperatures drop below 96°C) and times when fractures at the drift crown are predicted to rewet are summarized in Table 6.5-6. The increase in drift spacing (thus heat loss) reduces the length of the boiling period without significantly affecting peak temperatures at the drift wall (Figure 6.5-3). These peak temperatures at the drift crown are around 140°C, and are reached fairly quickly (at 75 to 100 years; Figure 6.5-3), at which time the relative humidity in the drift is lowest (~0.37; Figure 6.5-3). Accordingly, the time at which the boiling front starts to recede towards the drift is significantly shorter for repository-edge conditions, although the maximum extent of dryout in fractures decreases only slightly (Figure 6.5-4). Predicted temperatures and rewetting times are similar to the results of the MSTHM (SNL 2007 [DIRS 181383]; see footnote in Table 6.5-6).

Above the drift, the maximum predicted extent of dryout in fractures is around 6 m (from drift center) for repository-edge conditions, and close to 7 m for center conditions (Figure 6.5-4). In the latter case, the boiling front in fractures is observed to recede by ~1 m between 100 and 200 years, and then remains at a nearly constant location (between 5 and 6 m from drift center) until ~550 years, before steadily collapsing further towards the drift crown. This behavior is observed with both TH and THC simulations, showing no significant differences in the predicted trends of dryout extent whether the effects of water–rock interactions are considered or not.

The rock matrix dries out for much shorter periods of time than fractures (Figures 6.5-5 and 6.5-6) because of the vapor-pressure lowering effect caused by the rock capillarity. Dryout in the rock matrix extends to a maximum of ~5 m from drift center, for both repository-center and edge conditions. Rewetting at the drift crown in the rock matrix occurs at 100 to 150 years for edge locations, and 200 to 250 years for center locations (Figure 6.5-6).

Liquid saturation profiles for fractures at the drift crown (Figure 6.5-5) show jumps related to the effect of infiltration rate increases (climate change) from 7.96 mm/yr to 12.89 mm/yr at 600 years, and to 20.45 mm/yr at 2,000 years. Slight differences in long-term predicted liquid saturations between the TH and THC simulations reflect the effect of mineral precipitation, which is further discussed in Section 6.5.5.3. Long-term increases in liquid saturations are the result of increased capillarity caused by the reduction in porosity accompanying mineral precipitation. These effects, however, are quite small and within the range of the model uncertainty (Section 6.7). Peaks in liquid saturations following the boiling period correspond to increased liquid fluxes at the time the drift crown rewets. These peaks are not fully resolved, as discussed further below.

For all cases considered, the vertical liquid fluxes in fractures at the drift crown are predicted to be on the same order as ambient values (Figure 6.5-7). Note that the predicted ambient water flux in the model is for a one-dimensional column without a drift opening. The diverting effect of a drift opening is not taken into account (i.e., the diversion of percolating water around the drift capillary barrier) and, for this reason, the ambient flux remains slightly higher than for cases with a drift opening. No liquid flux is predicted to enter the drift. Vertical fluxes in the rock matrix above the drift are much lower than in fractures (by a factor > 20 compared to Figure 6.5-7). Some condensation is predicted to occur inside the drift on the drift wall during the cooling period, resulting in small (negligible) liquid fluxes from the drift to the rock matrix (through capillary suction).

The magnitude of reflux in fractures after the boiling period is sensitive to the length of the boiling period and the infiltration rate in effect. This reflux is shown in Figure 6.5-7 as flux peaks following the boiling period, and is a direct result of downward percolation of condensation/reflux waters previously mobilized during boiling. The general trend is that the shorter the boiling period is, the smaller this reflux, with the added effect of lower infiltration (pre-climate change) for the 162-m case. Note, however, that the flux peaks on Figure 6.5-7 are not fully resolved because they are plotted from points at predetermined printout time intervals. The flux peaks at 50 years (Figure 6.5-7) are not fully resolved either, and result from reflux of evaporated water following the temperature decrease (related to the decay of short-lived radionuclides) at the end of the preclosure period.

Not much weight should be given to the preclosure flux and liquid saturation data because the model ignores drying of the rock caused by drift ventilation during preclosure. This drying could reduce the amount of water available for mobilization by boiling during postclosure, although previous studies have shown that preclosure dryout due to ventilation has little effect on TH conditions around the drift during the postclosure period. Therefore, inclusion of preclosure dryout is not expected to have a large effect on thermal seepage. The effect of evaporative concentration on pore-water compositions would be more pronounced during preclosure than predicted here. However, the small effect of preclosure dryout on postclosure TH conditions is not expected to significantly affect water compositions during postclosure.

Table 6.5-6. Predicted Times at Which Boiling Ceases in Fractures and Drift Wall Rewets

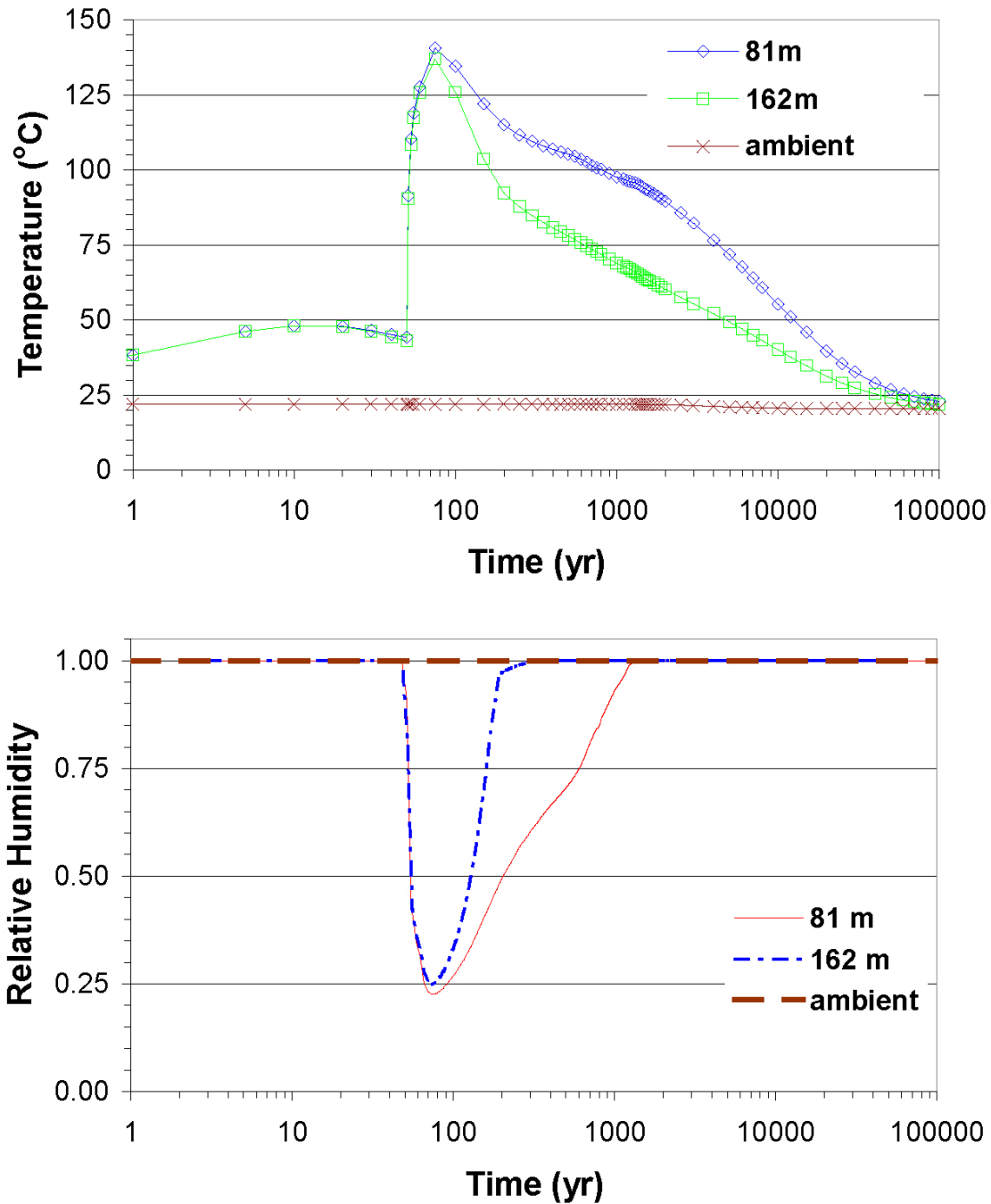
Simulation Type	Initial Water Composition	End of Boiling Period ^a (years)	Percentile of Boiling Duration ^b	Time of Fracture Rewetting at Crown ^c (years)	Temperature When Fractures Rewet at Crown ^d (°C)
Repository center (designed drift spacing of 81 m)					
TH	N/A	1270 (1,250–1,300)	100%	1,200–1,250	95.9–95.8
THC	W0	1278 (1,200–1,300)	100%	1,208	96.1
THC	W8	1279 (1,200–1,300)	100%	1,215	96.0
THC	W9	1273 (1,250–1,300)	100%	1,212	96.0
THC	W10	1267 (1,250–1,300)	100%	1,205	96.1
Repository edge (effective drift spacing of 162 m)					
TH	N/A	183 (150–200)	3%	150–200	104–92.4
THC	W0	183 (150–200)	3%	189	94.0
THC	W8	183 (150–200)	3%	189	93.9
THC	W9	183 (150–200)	3%	188	94.2
THC	W10	183 (150–200)	3%	189	93.9

^a Time at which the average temperature around the drift wall falls below 96°C, linearly extrapolated between the two nearest times for which simulation results were available (shown in parentheses). Note that the maximum boiling duration (1,250 to 1,300 years) is about 100 years longer than computed with the MSTHM (SNL 2007 [DIRS 181383]). A combination of differences in model treatments of heat flow within the drift and model dimensionality (two- versus three-dimensional) is likely responsible for this model result uncertainty.

^b Estimated from Figure 6.3-4a in SNL 2007 [DIRS 181383], mean infiltration case, and end of boiling periods shown, for simulations without considering the effects of mineral precipitation and dissolution.

^c Time at which model gridblock at drift crown (F 121) shows liquid saturation returning to a non-zero value (a better time resolution is obtained for THC runs by using time values for gridblock F 121 in output file *time.dat*, which is not available for the TH runs).

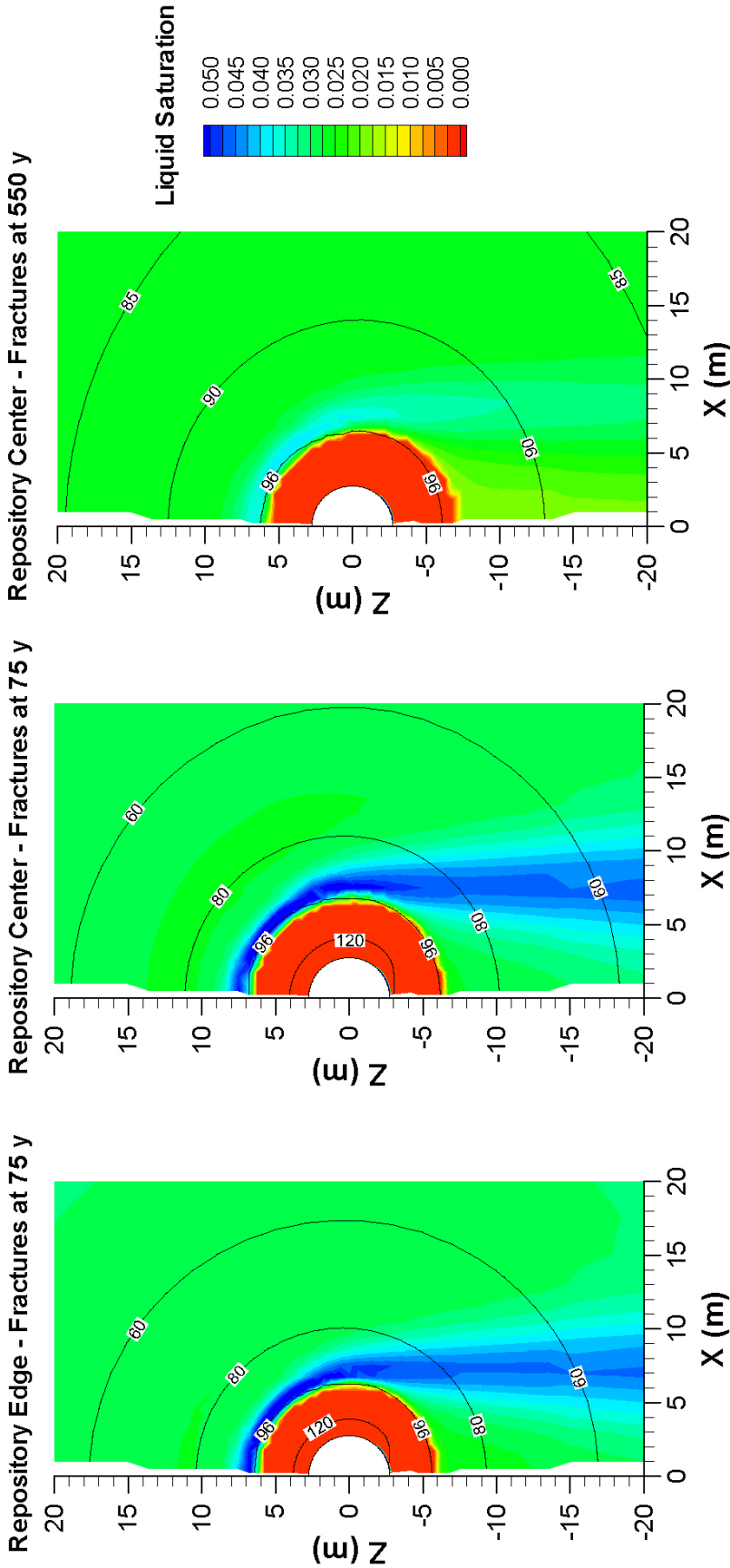
^d Temperature range corresponding to time range in previous column.



Source: Output DTN: LB0704DSTHONLY.001.

NOTE: Predictions of conditions under thermal loading are shown with curve labels starting with the modeled drift spacing (81 or 162 m for repository-center and edge locations, respectively). Predictions under ambient conditions (no thermal load) are shown with curves labeled "ambient." Results are shown for simulations that do not consider the effect of water-rock interactions and are essentially identical (for the parameters shown) to the results of simulations that consider the effect of water-rock interactions.

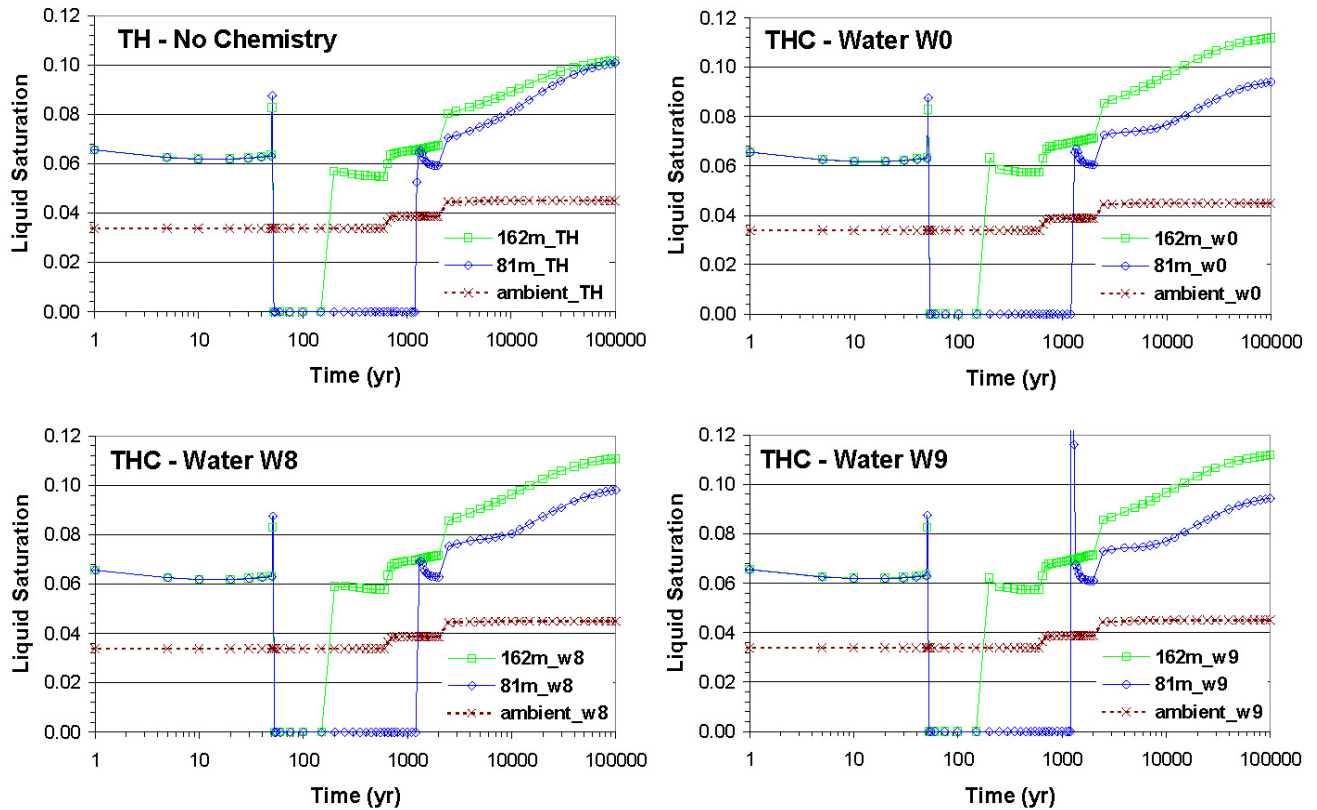
Figure 6.5-3. Time Profiles of Predicted Temperature and Relative Humidity in Fractures (similar in matrix) at the Drift Crown



Output DTN: LB0704DSTHONLY.002.

NOTE: TH simulation (without water-rock interactions). THC simulations (including the effects of water-rock interactions) yield similar results.

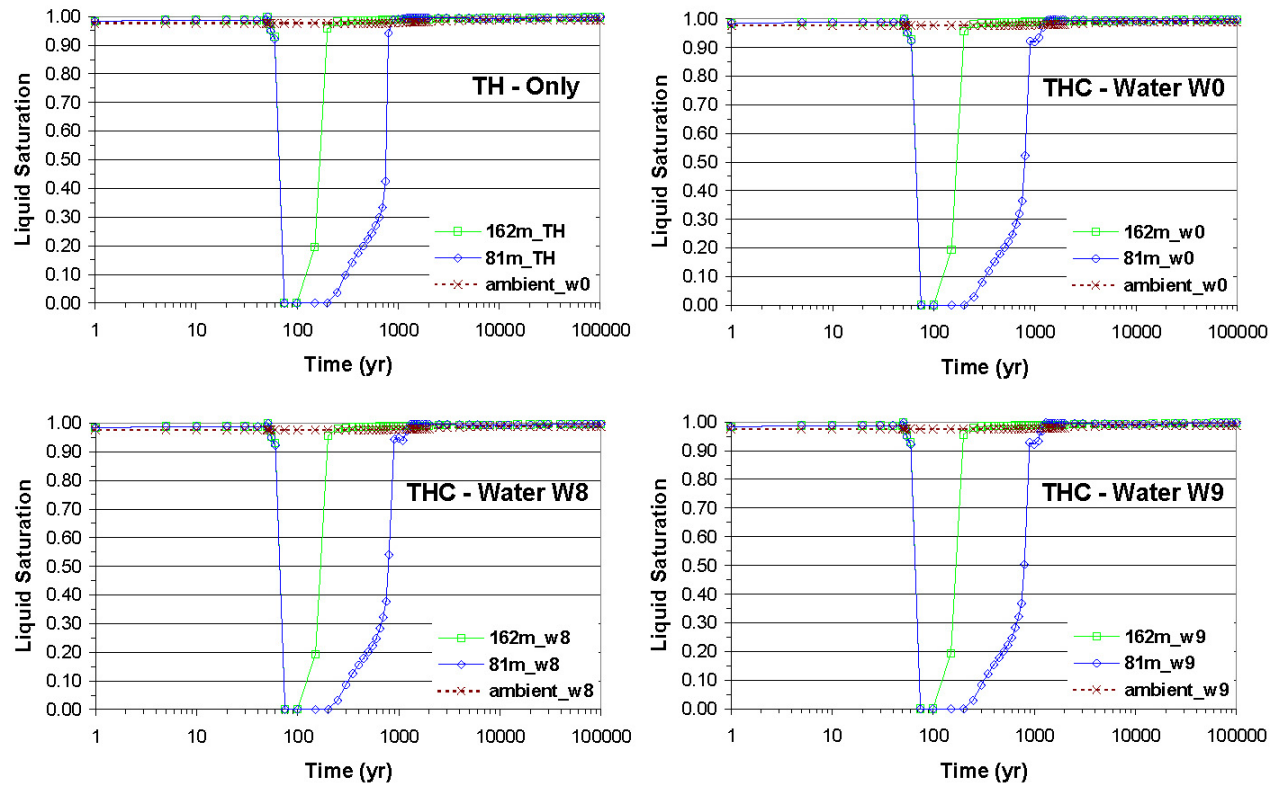
Figure 6.5-4. Contour Plot of Predicted Temperature ($^{\circ}C$) and Liquid Saturation in Fractures at Times near Maximum Dryout



Output DTNs: LB0704DSTHONLY.001, LB0705DSTHC001.001, LB0705DSTHC002.001, LB0705DSTHC003.001, LB0705DSTHC004.001.

NOTE: Predictions of conditions under thermal loading are shown with curve labels starting with the modeled drift spacing (81 or 162 m for repository-center and edge locations, respectively). Predictions under ambient conditions (no thermal load) are shown with curve labels starting with “ambient.” The second part of the curve labels shows the initial water composition (W0, W8, or W9) used in the THC simulations, or “TH” for simulations that do not consider the effect of water–rock interactions.

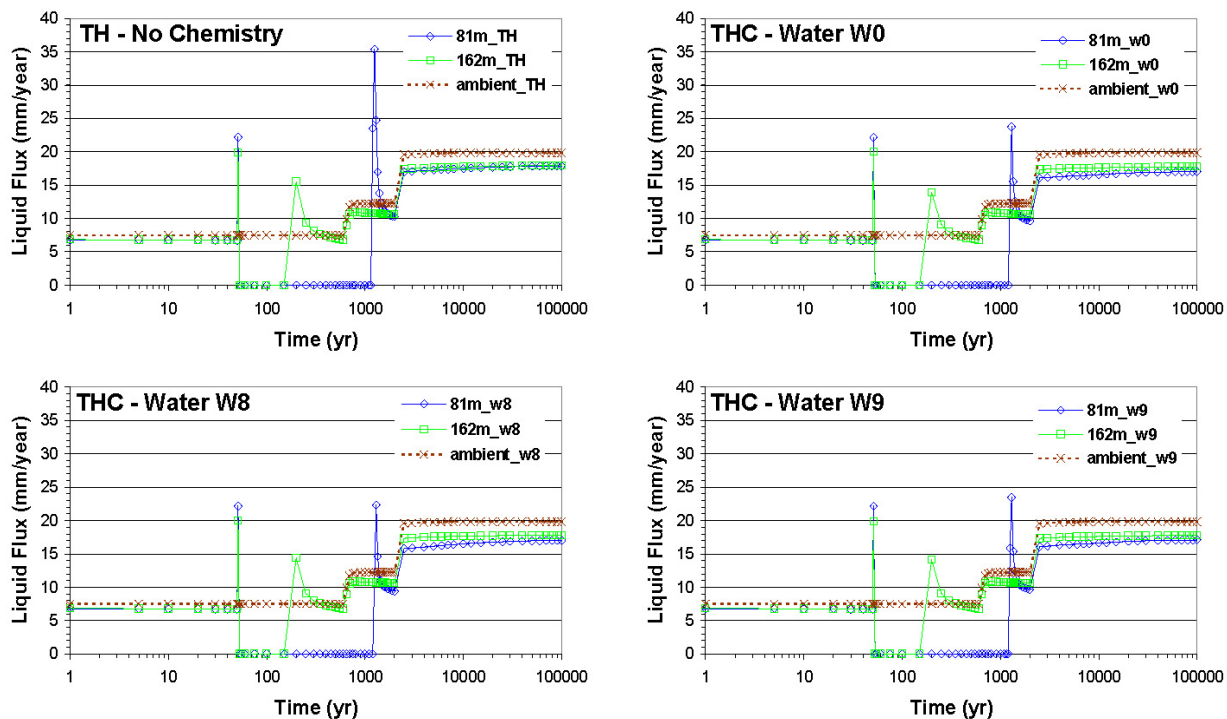
Figure 6.5-5. Time Profiles of Predicted Liquid Saturation in Fractures at the Drift Crown



Output DTNs: LB0704DSTHONLY.001, LB0705DSTHC001.001, LB0705DSTHC002.001, LB0705DSTHC003.001, LB0705DSTHC004.001.

NOTE: Predictions of conditions under thermal loading are shown with curve labels starting with the modeled drift spacing (81 or 162 m for repository-center and edge locations, respectively). Predictions under ambient conditions (no thermal load) are shown with curve labels starting with “ambient.” The second part of the curve labels shows the initial water composition (W0, W8, or W9) used in the THC simulations, or “TH” for simulations that do not consider the effect of water–rock interactions.

Figure 6.5-6. Time Profiles of Predicted Liquid Saturation in the Matrix at the Drift Crown



Output DTNs: LB0704DSTHONLY.001, LB0705DSTHC001.001, LB0705DSTHC002.001, LB0705DSTHC003.001, LB0705DSTHC004.001.

NOTE: Predictions of conditions under thermal loading are shown with curve labels starting with the modeled drift spacing (81 or 162 m for repository-center and edge locations, respectively). Predictions under ambient conditions (no thermal load) are shown with curve labels starting with “ambient.” The second part of the curve labels shows the initial water composition (W0, W8, or W9) used in the THC simulations, or “TH” for simulations that do not consider the effect of water–rock interactions.

Figure 6.5-7. Time Profiles of Predicted Liquid Flux in Fractures at the Drift Crown

6.5.5.3 Mineral Precipitation and Fracture Permeability

As shown previously (Figure 6.5-7), the effect of mineral precipitation/dissolution on the vertical liquid flux above the drift is negligible. These results are in contrast with findings of earlier work, which showed that mineral precipitation above the drift resulted in somewhat decreased fluxes and a significant delay in rewetting of fractures at the drift crown (BSC 2005 [DIRS 172862], Section 6.5.5.3). The difference, here, is attributed to revisions in hydrologic properties, as well as the implementation of porosity-permeability-capillary pressure coupling (Leverett scaling; Section 6.4.4.4), which cause an increase in capillarity when the porosity and permeability decrease as a result of mineral precipitation. Hydrologic properties of repository units have changed significantly since Revision 04 of this report, including a $\sim 5\times$ decrease in the capillarity of fractures, and a $\sim 3\times$ increase in the capillarity and a $\sim 2.5\times$ increase in permeability of the rock matrix in the Tptpl (Table 6-1). The Leverett-scaling option was (unintentionally) not operational in previous (Revision 04) simulations, and was then enabled in the version of TOUGHREACT (V3.1.1) used for the present study.

The effect of mineral precipitation at the boiling front above the drift results in a decrease in permeability (Figure 6.5-8), which is similar in magnitude for all cases of input water

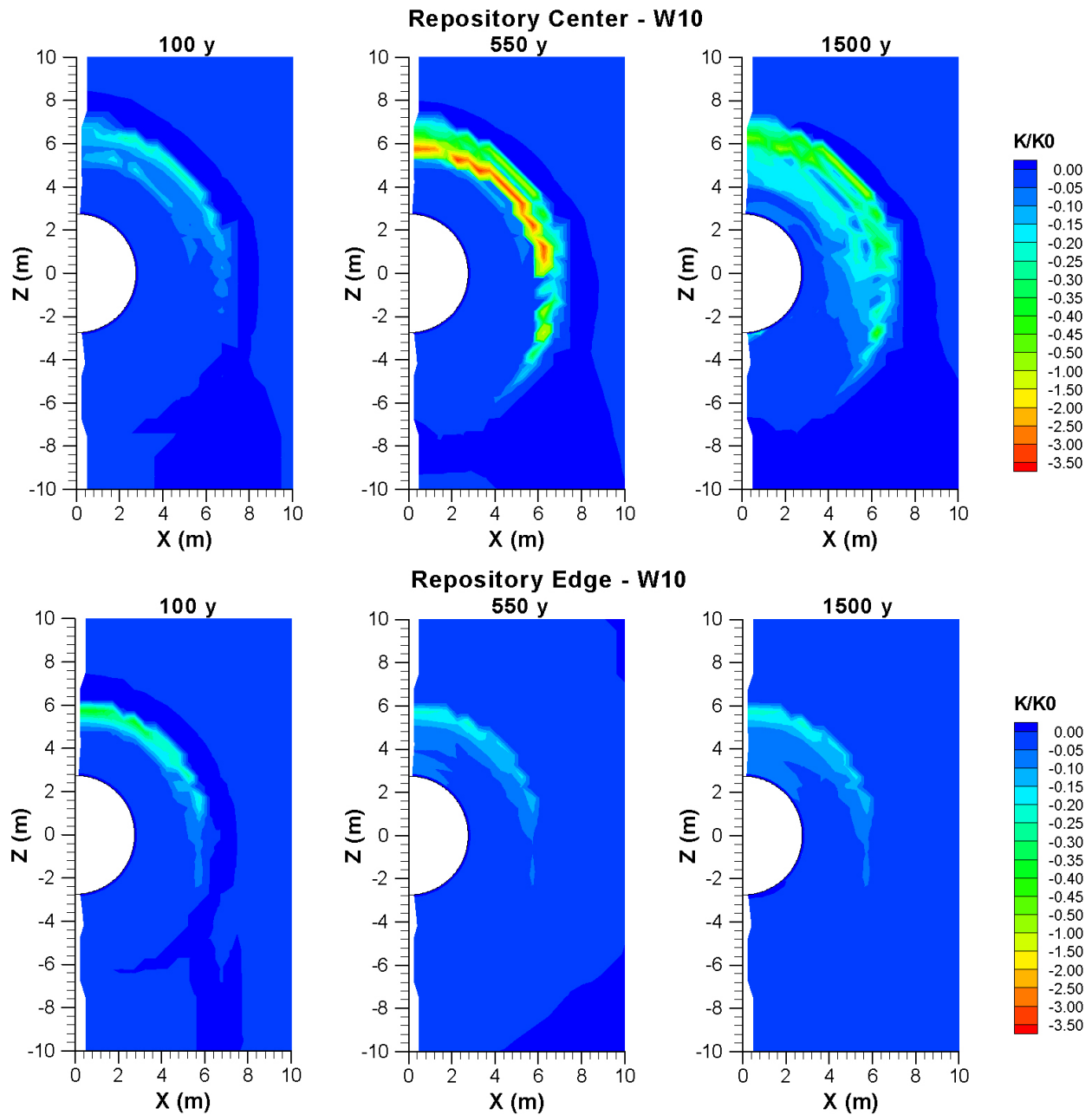
compositions considered. The decrease is most important for repository-center conditions, with a maximum permeability decrease of ~3.5 orders of magnitude reached at ~550 years, and a long-term decrease less than an order of magnitude (Figure 6.5-8, top). For repository edge conditions, the maximum permeability decrease is ~0.4 orders of magnitude, reached at about 100 years, dropping to less than ~0.2 orders of magnitude over the long term (Figure 6.5-8, bottom). Thus, as would be expected, the longer boiling period at the repository center results in more mineral precipitation and permeability decrease than at the edge of the repository.

In all cases, the long-term permeability decrease is caused primarily by the deposition of silica from evaporative concentration at the boiling front (4% to 7% of the fracture porosity), as well as minor calcite precipitation (<1% of the fracture porosity) caused by the increased temperatures (retrograde solubility) and CO₂ degassing (Equation 6.5-4). Clays (beidellites and illite) are the principal secondary aluminum silicates to form, although the predicted amounts of these minerals are extremely small and thus insignificant.

The short-term permeability decrease is caused by the precipitation of salts upon dryout at the boiling front. These salts readily dissolve as the boiling front collapses back towards the drift wall, and have dissolved entirely once rewetting of the drift wall has occurred. These salts consist primarily of halite, which accounts for up to ~4% in additional fracture porosity decrease in simulations with highest initial chloride concentrations (water W10), and ~1 % in additional fracture porosity decrease in simulations with lowest initial chloride concentrations (water W8). The other salts in amounts of 0.2% to 2% of the fracture porosity include CaSO₄, K₂SO₄, K₂CO₃, and KNO₃. The sulfate salts dominate the nitrate salts in simulations with waters W0 and W10 because of the elevated sulfate concentrations in these waters (Table 6.2-1). All other salts form in amounts <0.2% of the fracture porosity. Note that the calculation method for salt precipitation upon dryout is very approximate and relies on a predetermined normative list of salt minerals that is not based on thermodynamics (Sections 6.4.5 and 6.6.4). For this reason, not much significance should be given to the formation of salts other than anhydrite and halite, which thermodynamically would be expected to be the first salts to form.

The permeability decrease is a strong function of the permeability-porosity coupling relationship used in the model (Section 6.4.4.2), which relies on parameters including fracture spacing, surface area, and initial fracture permeability. Because the relationship is based on a reduction in hydraulic aperture, the permeability decreases slowly upon initial precipitation of minerals, but after some point decreases drastically when only a small amount of mineral precipitation is sufficient to block the flow almost entirely (Figure 6.5-9). In the present work, which uses a mean initial fracture permeability of $9.1 \times 10^{-13} \text{ m}^2$, the long-term fracture porosity decrease is not more than ~7% (by precipitation of amorphous silica and calcite), thus affecting permeability by less than one order of magnitude (Figure 6.5-9). The additional temporary fracture porosity decrease (bringing the porosity drop up to ~14%) brings a much larger decrease in permeability (up to 3.5 orders of magnitude) even though the added amount of precipitated minerals (salts) is half or less the volume of previously deposited minerals (silica and calcite). Also, at ~14% decrease, the porosity-permeability curve for the mean initial permeability case (Figure 6.5-9) becomes quite steep, such that small differences in precipitated mineral amounts could yield large differences in computed permeability. For example, previous work using the same initial fracture permeability and porosity as in this report, but otherwise different rock properties, showed a temporary permeability decrease by up to 6 orders of magnitude (BSC 2006

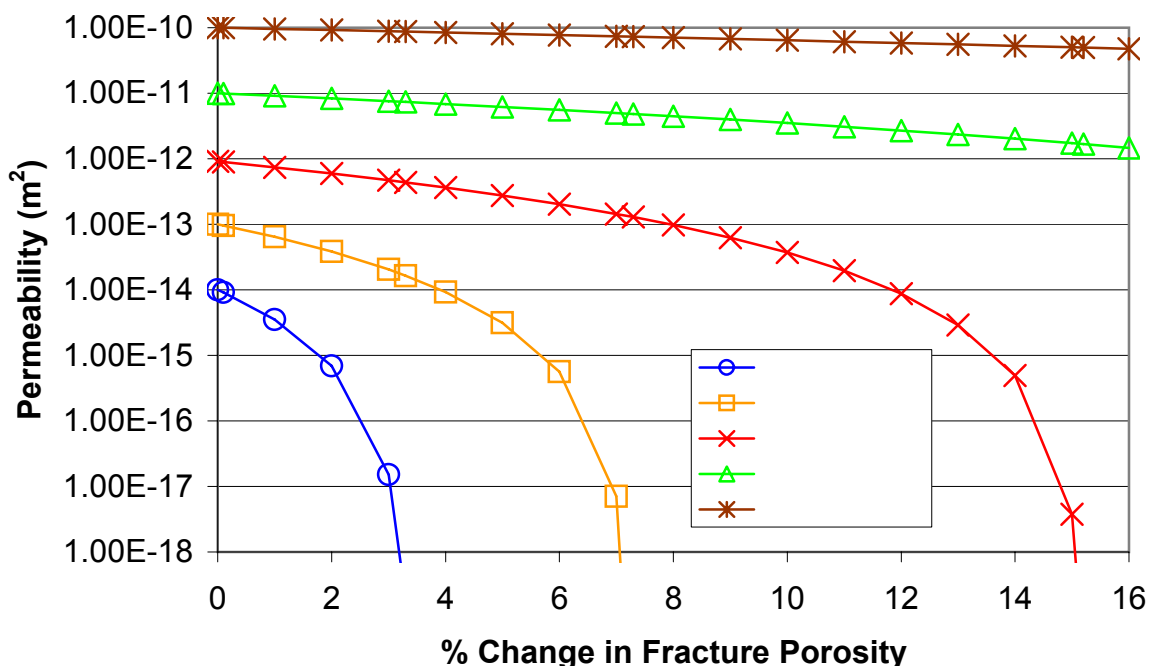
[DIRS 174104]). In that work, however, the effects of Leverett scaling were not accounted for, impeding the dissolution of porosity-plugging salts in fractures during the collapse of the boiling front, and thus likely overestimating the effects of mineral precipitation on flow.



Output DTNs: LB0705DSTHC001.002, LB0705DSTHC002.002, LB0705DSTHC003.002, LB0705DSTHC004.002.

NOTE: Simulation using initial water W10 (similar results are obtained using water W0, W8, or W9). The long-term drop in permeability results from the precipitation of primarily amorphous silica and calcite (up to 7% decrease in the fracture porosity). The short-term drop in permeability (up to 14% decrease in the fracture porosity) results from the precipitation of primarily halite, which dissolves upon collapse of the boiling front.

Figure 6.5-8. Contour Plot of Modeled Change in Fracture Permeability for Repository-Center and -Edge Conditions



Output DTN: LB0705DSTHC006.007.

NOTE: Calculated using Equations 6.4-18 through 6.4-21, Section 6.4.4.2, and fracture property values given in Table 6.4-2, for the Tptll lithostratigraphic unit.

Figure 6.5-9. Fracture Permeability as a Function of Porosity Decrease for Various Values of Initial Fracture Permeability

6.5.5.4 Water Chemistry Trends

The THC seepage model does not simulate actual seepage of water into drifts, because the range of simulated infiltration rates produces liquid saturations below the theoretical seepage threshold for rocks around the emplacement drift (see Section 6.4.8). Instead, the model computes the compositions of pore water and gas throughout the host rock around an emplacement drift (i.e., in the matrix and fractures). The THC seepage model provides, for each gridblock at each printout time interval, parameter values for thermal-hydrologic variables such as temperature, pressure, and gas and liquid saturation; concentrations of aqueous species; mineral volume fractions; and the CO₂ volume fraction in matrix and fractures.

Results relating to water compositions and CO₂ gas concentrations have been summarized in Excel tables, including plots, which were submitted to the TDMS with names and DTNs listed in Table 6.5-5. These results cover two general areas around the drift:

- (1) Three fixed locations to provide information on CO₂ concentrations, each representing one model gridblock adjacent to the drift wall at the crown, springline, and base of the drift

- (2) A dynamic zone comprising a series of (non-dry) gridblocks that follows the expansion, and contraction of the condensation/reflux zone around the drift as explained in Section 6.4.8.

No information regarding the evolution of water chemistry at the drift wall is available during the boiling period (Table 6.5-6) because the drift wall remains dry during this period. In addition, examining the evolution of water compositions at single points around the drift provides only limited information on the spatial variability of model results around the drift. For this reason, results from item (1) are only used here to provide information on CO₂ gas concentrations at the drift wall, which are fairly spatially uniform.

Results from item (2) for fracture waters above the drift are considered to best represent the composition (and spatial variability) of potential in-drift seepage during the entire postclosure period, including the boiling period. The methodology for extracting predicted water compositions in this case is discussed in Section 6.4.8. The methodology involves selecting gridblocks with non-zero liquid saturations on the basis of mobility (FLUX waters), where mobility is assessed as the vectorial sum of liquid Darcy fluxes over the connections of any given gridblock to adjacent gridblocks. Above the drift, in fractures, the location of FLUX and HISAT waters generally closely coincide. Exceptions occur where high liquid saturations result from increased capillarity owing to permeability reduction caused by mineral precipitation and implementation of the Leverett-scaling effect (Section 6.4.4.4). Waters in such gridblocks are mostly excluded from FLUX waters. Therefore, when the Leverett-scaling formulation is implemented, as is the case here, potential in-drift seepage is considered better represented by FLUX waters than by HISAT waters. As explained in Section 6.4.8, model results are extracted for six gridblocks within a 45-degree quadrant from the drift crown (TOP quadrant, Figure 6.4-1) for each point in time, and each simulation, thus capturing the spatial variability above the drift. Various time profiles for data extracted in this manner are discussed below.

Results are presented for simulations including:

- The four different input initial water compositions described in Section 6.2.2.1 (waters W0, W8, W9, and W10; see Table 6.2-1 and Figure 6.2-4)
- Two repository locations: center (modeled with a drift spacing of 81 m) and edge (modeled with a drift spacing of 162 m), as discussed in Section 6.5.1
- Ambient conditions of temperature and pressure for a location at repository level (1-D simulations without drift opening), as discussed in Section 6.5.5.1.

Waters W0 and W10 come from the same general location and are quite similar in composition. These waters are distinct from waters W8 and W9 by their elevated chloride, sulfate, magnesium, and calcium concentrations. The main difference between waters W0 and W10 is the elevated nitrate concentration in water W10 relative to water W0. Water W8 contains much less chloride, sulfate, magnesium, and calcium than the other waters. The composition of water W9 ranges between that of W0 (or W10) and W8, and also displays a relatively high nitrate concentration. All waters are initially equilibrated with calcite at a CO₂ partial pressure of 10⁻³ bar (Section 6.2.2.1).

The time-profiles of distance of gridblocks from drift center, temperature, and liquid saturation for model gridblocks representing TOP FLUX waters (Section 6.4.8) are shown in Figures 6.5-10, 6.5-11, and 6.5-12, respectively. These profiles provide a context for the chemistry profiles discussed below. For simulated times up to 50 years, TOP FLUX waters represent gridblocks directly above, and adjacent to, the drift crown (i.e., at a distance ~ 2.8 m from drift center) (Figure 6.5-10). From the onset of boiling at approximately 50 years, the TOP FLUX waters correspond to the condensation/reflux zone in fractures directly above the boiling front, and thus their distance from drift center (Figure 6.5-10) corresponds approximately to the extent of dryout in fractures. These distances drop down to ~ 2.8 m at the same time temperature drops down below $\sim 96^\circ\text{C}$ (Figure 6.5-11), the boiling point for the modeled elevation. This behavior indicates that the rewetting front in fractures around the drift more or less coincides with the collapse of the boiling front, reaching the drift wall at times shown in Table 6.5-6. As mentioned earlier (Section 6.5.5.2), no significant differences in drift-wall rewetting times are observed between simulations using different initial water compositions.

The spatial variability in liquid saturation for gridblocks located in the condensation/reflux zone typically translates directly to the variability of predicted concentrations of dissolved species in that zone. This is because variations in liquid saturation caused by dilution and evaporation directly affect concentrations. The spatial variability of liquid saturations at TOP FLUX locations is smaller than at the boiling front, where liquid saturations are very small and somewhat erratic. Therefore, examining the variability of predicted water compositions in TOP FLUX zones provides a better means of evaluating the model sensitivity to various input data or model conceptualizations than would examination of predicted water compositions directly at the boiling front. For each model run, at any given time, predicted liquid saturations at TOP FLUX locations show relatively small variations (Figure 6.5-12) because these data typically represent areas of highest liquid saturation in a locally homogeneous model. Except for a few gridblocks, liquid saturations in fractures at TOP FLUX locations remain between ambient (~ 0.004) and $\sim 3\times$ ambient values. As would be expected, the variability is highest during the boiling period under repository-center conditions (Figure 6.5-12, top).

Notice in Figure 6.5-12 (top) that the post-processing procedure picked up three gridblocks at 1,300 years with liquid saturations close to 0.9. These gridblocks exhibit a permeability decrease between 2 and 3 orders of magnitude, implying that the elevated liquid saturation in this case is caused by the implementation of the Leverett-scaling formulation (Section 6.4.4.4). Although the post-processing methodology for FLUX waters mostly discards such gridblocks, this represents an example (the only one) where it did not. In this case, water has just rewetted gridblocks containing salts (which contribute to the permeability decrease; see Section 6.5.5.3), exhibiting saline compositions that have not been subject to speciation calculations because of the ionic strength limit of 4 molal imposed on such calculations. As a result, concentration profiles presented below for several dissolved species show three outlying points at 1,300 years, which should not be taken as representative of potential seepage.

Predicted profiles of concentration versus time for CO_2 gas and aqueous species of interest are shown in Figures 6.5-13 through 6.5-24. Except for noticeable exceptions regarding carbonate and calcium concentrations with water W8, the predicted general trends of concentrations are quite similar for all waters. It is useful to first examine the predicted concentration profile of chloride (Figure 6.5-13), a conservative species, because it helps in evaluating the degree of

dilution and evaporative concentration in condensation/reflux (TOP FLUX) areas. Comparing the chloride concentration profiles (Figure 6.5-13) with profiles showing the distance from drift center at which these concentrations are predicted (Figure 6.5-10) helps in distinguishing the following successive stages in the evolution of water compositions in the condensation/reflux zone in fractures:

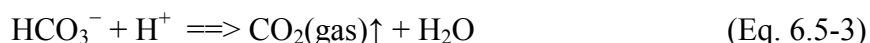
1. A dilution stage occurs when the dryout zone is expanding, roughly from 50 to ~150 years in the repository-center case, and 50 to ~100 years in the repository-edge case. It is caused by steam originating from water boiling in the rock matrix then migrating and condensing into fractures (Section 6.2.1.1).
2. An evaporative concentration stage then takes place, as the water in fractures is concentrated by boiling the percolating water, with no or little additional influx of condensation water derived from boiling matrix water (as explained in Section 6.5.5.2, the collapse of the boiling front in the rock matrix occurs much faster than in fractures; see Figure 6.5-6). In the repository-center case, the boiling front in fractures retracts in two stages, first dropping from ~7 m to ~6 m between 150 and 200 years, then remaining more or less stationary until ~550 years (Figure 6.5-10, top). At ~200 years, the initial retraction appears to temporarily reverse the effect of evaporative concentration at some locations (Figure 6.5-13, top). Evaporative concentration then resumes until the temperature drops below the boiling point, at ~1,280 years in the repository-center case and ~180 years in the repository-edge case (Table 6.5-6).
3. As boiling ends, and the infiltration rate is increased to simulate the different climate transitions (Table 6.5-3), concentrations drop sharply. Dilution by percolating waters overcomes the effect of evaporative concentration and brings concentrations back to their ambient values after ~500 years in the repository-edge case, and ~2,000 years in the repository-center case.

The effects of these three distinct stages are visible on the predicted concentration trends of most constituents. Concentration profiles of other conservative species such as nitrate and sulfate show essentially the same trends as for chloride.

Modeled CO₂ concentrations in the zone of condensation and reflux (Figure 6.5-13) are essentially the same as directly adjacent to the drift wall (Figure 6.5-14), except that the decrease in concentration (below ambient concentrations) at the onset of boiling lasts longer at the drift wall than further into the rock mass. This initial decrease results primarily from CO₂ displacement by steam and, accordingly, occurs for a shorter period of time in the repository-edge case than in the repository-center case. Upon the collapse of the boiling front, CO₂ concentrations rise back to ambient levels but then increase significantly above ambient values from the arrival of percolating water with a significantly higher dissolved CO₂ content than the locally decarbonated water. This temporarily higher dissolved CO₂ content in percolation water results from prior mobilization of CO₂ gas from matrix water into fractures and away from the drift. In all cases, CO₂ concentrations remain above ambient values until ~30,000 years, reaching maximum values of ~100,000 ppm in the repository-center case and ~10,000 ppm for the repository-edge case (Figure 6.5-14 and 6.5-15). In the repository-edge case, the post-boiling rise in CO₂ gas concentrations occurs earlier as boiling ends sooner and less CO₂ is mobilized above and around the drift (Figure 6.1-14, middle). In this case, incoming waters after

the collapse of the boiling front exhibit lower maximum CO₂ gas partial pressure (Figure 6.1-14, middle).

The post-boiling CO₂ concentrations are about 10 times higher than predicted previously (BSC 2005 [DIRS 172862], Figure 6.5-24), even though the CO₂ partial pressure at the upper model boundary has been reduced from 10^{-2.5} to 10⁻³ bar in the current model revision, and the initial bicarbonate content has been reduced by the equilibration of initial waters with calcite (Section 6.2.2.1). This suggests that a larger amount of CO₂ is exsolved from matrix pore waters (decarbonation) than previously predicted, which is also consistent with the more significant pH rise predicted during the boiling period (to values near 9.9; Figure 6.5-16) compared to previous work (maximum pH ~8.4; see BSC 2005 [DIRS 172862], Figure 6.5-25). Whether pH effects related to water–rock interactions affect the CO₂ behavior or vice-versa is not a trivial question. As discussed in Section 6.6.4, pH values above ~9 appear to be the result of carbonate salts dissolution during the early stages of the boiling-front collapse, and thus a potential artifact of the selected dryout mineral assemblage (Section 6.4.5). However, this local effect is not sufficient to affect the CO₂ behavior. This is shown by simulations presented in Section 6.6.4 indicating that the exclusion of carbonate salts from the dryout mineral assemblage has no effect on predicted CO₂ concentrations. The pH rise on a wider scale is likely to be driven by boiling, and to a lesser extent by the decrease in CO₂ solubility with increasing temperature, through the reaction:



However, if enough calcium is present in solution relative to aqueous carbonate, this pH rise is impeded by the precipitation of calcite, i.e.:



These reactions also need to be evaluated in the context of both evaporative concentration effects and condensation effects (i.e., steam transport from the rock matrix and condensation in fractures) in addition to boiling and temperature increase effects. It can be seen in Equation 6.5-3 that if boiling is sufficient to significantly concentrate the pore water, the evaporative concentration of H⁺ could drive pH down if CO₂ cannot quickly dissipate. The extent of steam condensation in fractures (which reverses these reactions) relative to evaporation/boiling will also determine the extent to which the system does become alkaline. Thus, the actual pH trend depends on a delicate balance between the rate of evaporative concentration and the rate of CO₂ volatilization/mobilization, which itself depends on rock properties and fracture–matrix interactions. Changes in matrix properties in this report revision (Table 6-1) cause greater water retention and higher initial liquid saturation in the rock matrix (~0.98; Figure 6.5-6), thus also lower gas relative permeability. Under these conditions, the decrease in steam mobilization from the rock matrix and the diminished effect of condensation in fractures appear to cause a more alkaline pH in fracture pore waters than previously predicted.

The pH trend also depends on the initial relative concentrations of calcium and total aqueous carbonate (expressed as HCO₃⁻ here) in solution. Upon boiling, waters with a ratio of $2m_{\text{Ca}}/m_{\text{HCO}_3} < 1$ become depleted in calcium faster than aqueous carbonate (through Equation 6.5-4), and thus leave more room for the pH to increase by decarbonation (through

Equation 6.5-3). This appears to be the case with water W8, which displays a ratio $2m_{Ca}/m_{HCO_3}$ about 0.4 compared to the other waters exhibiting ratios between 1.2 and 2.2. Indeed, in the repository-edge case, in which the effects of evaporative concentration (and condensation/dilution) are minimized relative to decarbonation, the trends of pH, total aqueous carbonate, and calcium concentrations predicted with water W8 during the evaporative concentration stage in fractures are markedly different than for the other waters (Figures 6.5-16, 6.5-17, and 6.5-18). The stronger depletion of calcium relative to aqueous carbonate for water W8, compared to the other waters, is also evidenced in the profiles of calcium to total aqueous carbonate ratios (expressed here as Ca/CO_3 ; Figure 6.5-19).

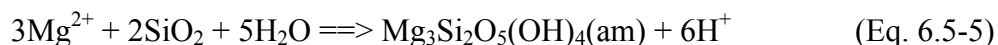
The resulting alkaline character of the boiled/refluxed waters causes significant calcium depletion (Figure 6.5-18, top) through calcite precipitation. In this case, the repository-center simulations with all waters predict a drop in calcium concentrations below ambient values by > 2 orders of magnitude, a trend reversed from that observed previously (see BSC 2005 [DIRS 172862], Figure 6.5-29). Additional simulations presented in Section 6.6.2 are used to rule out effects of other model revisions (initial equilibration with calcite, lower CO_2 boundary concentrations, extraction procedure, and TOUGHREACT upgrades) as the cause of this behavior.

Somewhat lower maximum predicted pH values in the repository-edge case (Figure 6.5-16) appear to be the direct result of reduced boiling in fractures. Reduced boiling, and the shorter length of time during which temperatures remain elevated, result in decreased calcite precipitation (compared to the repository-center case) when percolating waters heat up towards the drift. As a result, the calcium concentrations and Ca/CO_3 ratios at similar temperatures during the post-boiling period show higher values than in the repository-center case (Figures 6.5-18 and 6.5-19).

By dividing aqueous species concentrations by the concentrations of chloride, a conservative species, the relative degree of mineral dissolution and precipitation can be evaluated. However, the variations of these ratios do not necessarily indicate that reactions are taking place in the gridblocks where the ratios are evaluated. Reactions in the rock matrix could also affect these ratios in fracture water if significant diffusion occurs between fractures and matrix. Reactions above areas being investigated could also affect these ratios. In the present simulations, in zones of condensation/reflux above the drift crown, predicted initial increases in Ca/Cl in fractures during the dilution stage (Figure 6.5-20) result from calcite dissolution in fractures. The dissolution is enhanced by the CO_2 content of condensation waters. After this time, when evaporative concentration takes over dilution, Ca/Cl ratios start to decrease significantly, indicating the precipitation of calcite. For the repository-edge case, the trends of Ca/Cl ratios in logarithmic form (Figure 6.5-20) are similar and somewhat parallel for simulations with all waters, suggesting that the degree of reaction involving calcium minerals is similar in these cases. In the repository-edge case, the trend for water W8 illustrates increased calcite precipitation as discussed earlier, because the initial ratio $2m_{Ca}/m_{HCO_3}$ is < 1 in this water.

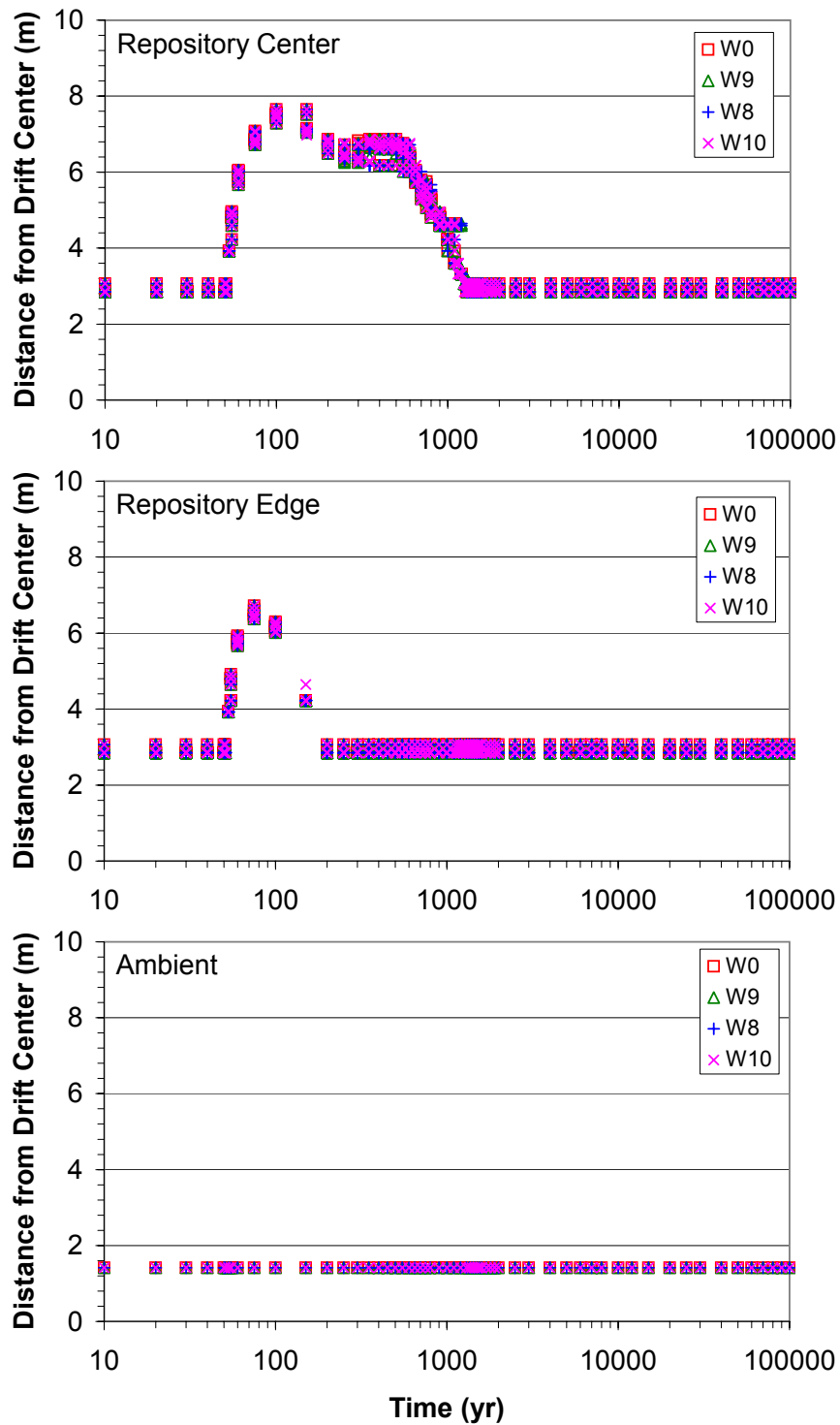
The predicted magnesium concentrations (Figure 6.5-21) reflect the effects of the dilution and evaporative concentration stages discussed earlier, and precipitation of amorphous magnesium silicate (and to a much lesser extent clays). The precipitation of amorphous magnesium silicate

is driven by both the pH increase discussed earlier and higher temperatures (retrograde solubility), in addition to evaporative concentration:



The predicted Mg/Cl ratios show similar trends to the Ca/Cl ratios (Figure 6.5-22), except that the profiles indicate that magnesium silicate starts to precipitate at the onset of boiling, even during the dilution stage. Another significant difference from the calcium behavior is that magnesium concentrations after the collapse of the boiling front rise significantly above ambient values for a few thousand years in the case of simulations with W0, W9, and W10, and for up to ~20,000 years for simulations with water W8 (this water has a very low ambient magnesium concentration). This is caused by the dissolution of magnesium silicate (previously deposited during the boiling period) when the temperature drops below boiling, and is most visible in the repository-center case (Figures 6.5-21 and 6.5-22). Note that younger calcite at Yucca Mountain has been reported to contain up to around 1% (by weight) of magnesium (Wilson et al. 2000 [DIRS 154279]). Therefore, taking this into account in simulations could have an effect on predicted magnesium concentrations, possibly contributing more magnesium in solution when calcite dissolves, but also resulting in magnesium depletion upon calcite precipitation.

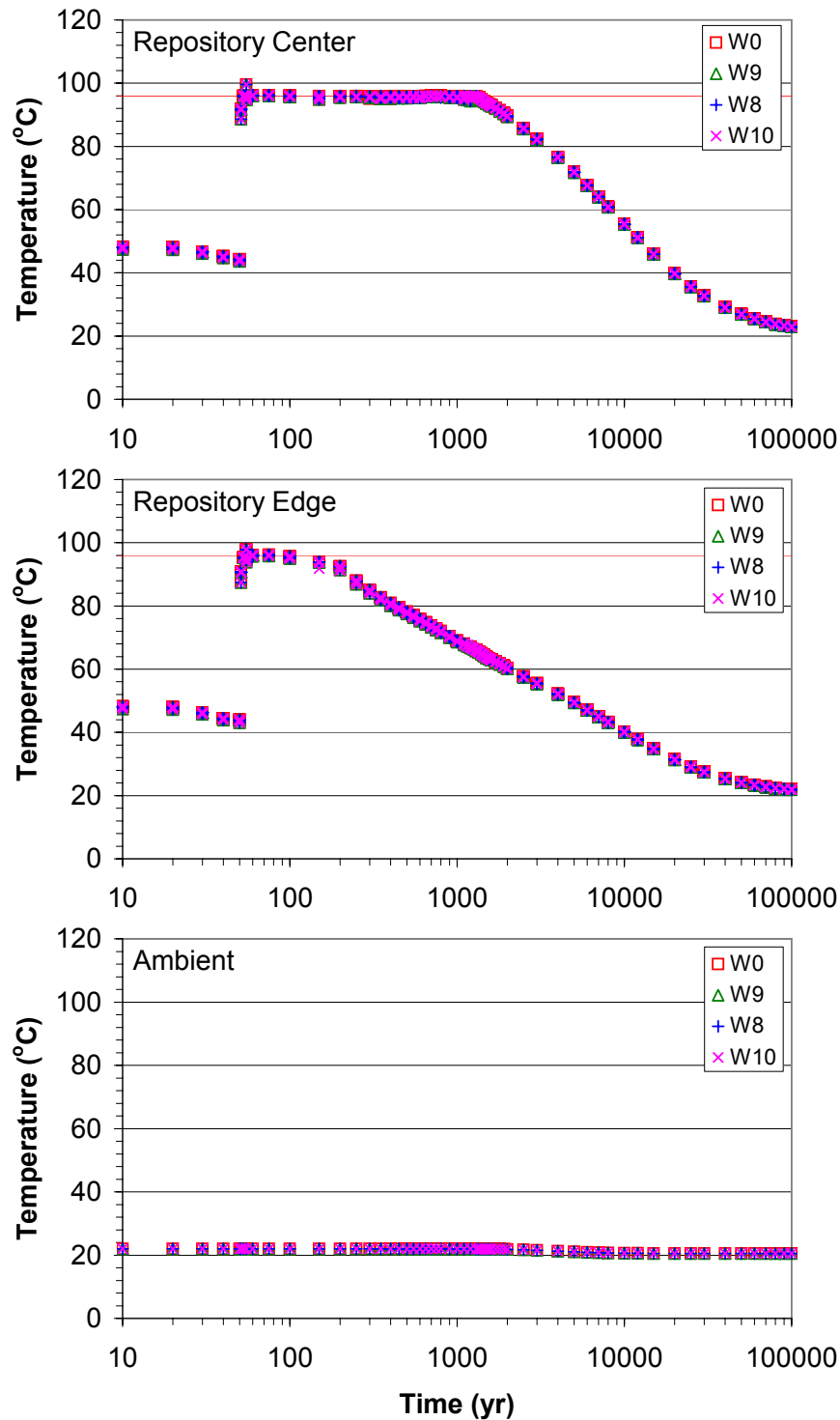
The trends of other aqueous species can be evaluated in terms of the degree of dilution, concentration, and mineral reaction taking place. Sodium concentrations (Figure 6.5-23) show the same effects of dilution and evaporative concentration as discussed earlier for chloride. However, increasing Na/Cl ratios during the boiling periods in the repository-center case (Figure 6.5-24) clearly show the effect of plagioclase dissolution (e.g., Equation 6.5-1). Note that in this model revision, secondary albite is not allowed to form (as was the case in BSC 2005 [DIRS 172862]). Accordingly, the sodium depletion reported in previous model revisions is not observed. Like the Ca/Cl ratios, the similar and parallel trends of Na/Cl ratios (in logarithmic form) would suggest that all waters react to a similar degree with sodium phases. Trends for other species are not shown here, although these data are available in files submitted with this report (Table 6.5-5). Profiles for potassium are similar to the sodium profiles, showing the effect of primarily sanidine dissolution. Ratios of nitrate to chloride remain essentially constant, at least within the variability of initial concentrations. This is expected because redox processes are not considered in these simulations, and solid nitrate and chloride phases are formed only upon complete dryout (Sections 6.4.5 and 6.6.4). The dissolution of nitrate and chloride salts formed during dryout has some effect on the variability of these ratios during and shortly after the boiling period (see Sections 6.6.4 and 6.7.2). Sulfate concentrations show trends quite similar to chloride, except that SO_4/Cl trends show some effects from anhydrite precipitation and dissolution. Predicted dissolved silica concentrations and SiO_2/Cl profiles show significant silica dissolution during the dilution stage, as would be expected. Later, continued reflux and boiling lead to a further increase in silica concentrations. Predicted concentrations essentially do not exceed the solubility of amorphous silica (around 360 ppm at 96°C). The host rock is modeled with a small, ubiquitous amount of primary fluorite (CaF_2). Because the reaction rate of fluorite is fast, waters generally reach saturation with respect to this mineral. The strong calcium depletion in the repository-center case (Figure 6.5-18, top) results in the dissolution of essentially all primary fluorite in the condensation/reflux zone, and fluoride concentrations reaching up to around 150 ppm before returning to ambient values at ~ 5,000 years.



Output DTNs: LB0705DSTHC001.001, LB0705DSTHC002.001, LB0705DSTHC003.001, LB0705DSTHC004.001.

NOTE: Data from gridblocks exhibiting highest liquid mobility in fractures above the modeled drift (TOP FLUX waters as defined in Section 6.4.8). The distance shown is the actual distance from the gridblock node to drift center.

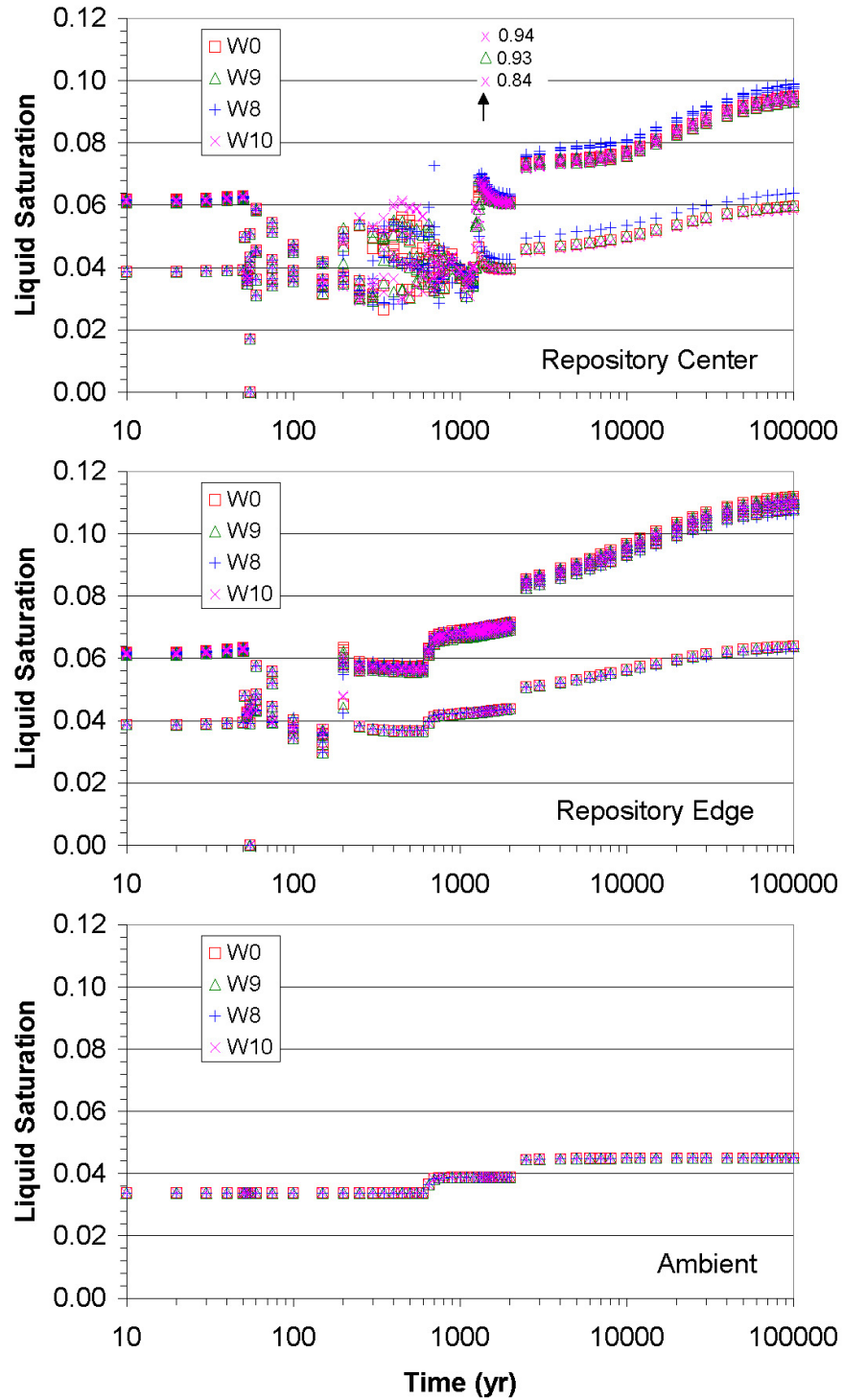
Figure 6.5-10. Location of Model Gridblocks for Data Shown on Figures 6.5-11 through 6.5-22



Output DTNs: LB0705DSTHC001.001, LB0705DSTHC002.001, LB0705DSTHC003.001, LB0705DSTHC004.001.

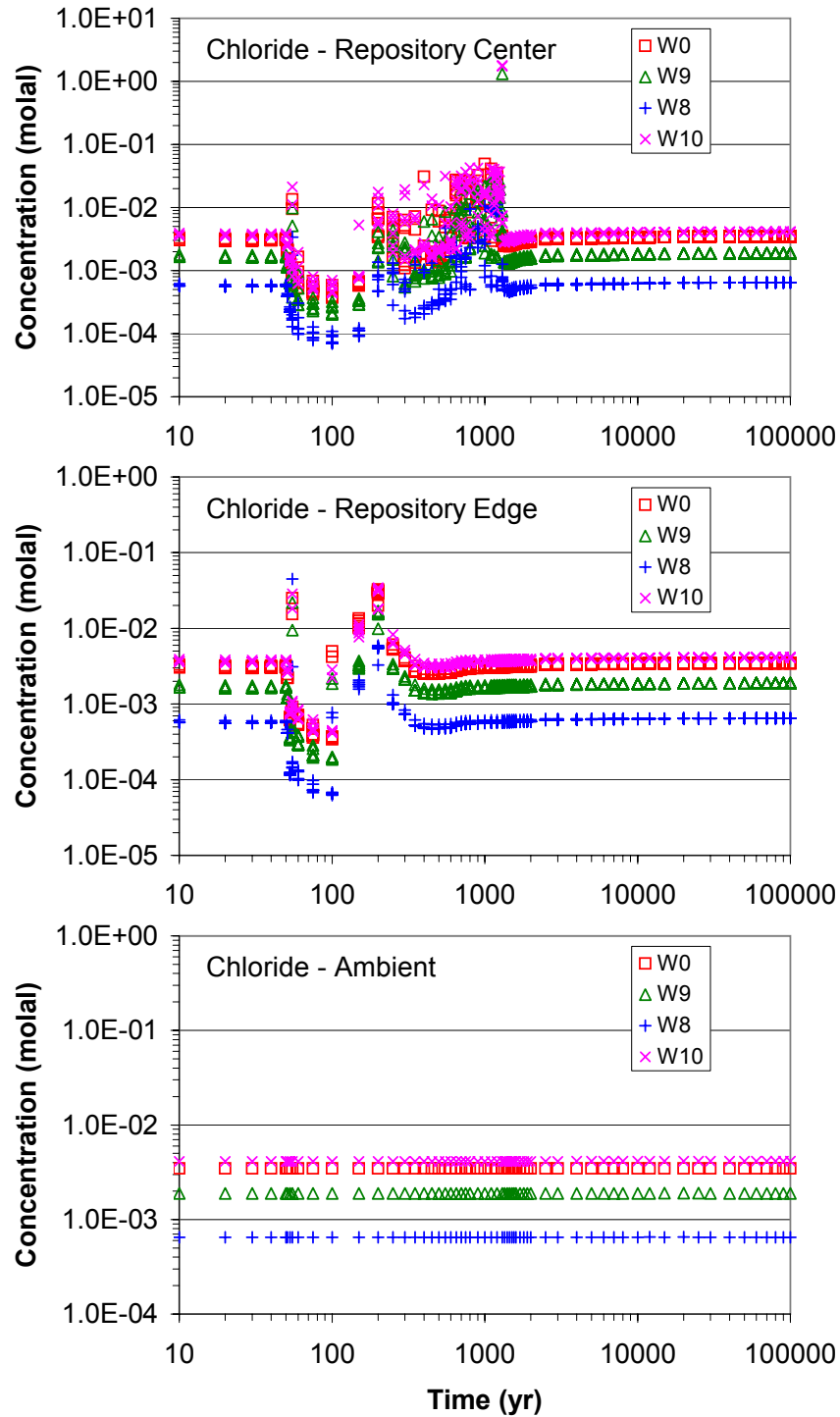
NOTE: Data from gridblocks exhibiting highest liquid mobility in fractures above the modeled drift (TOP FLUX waters as defined in Section 6.4.8).

Figure 6.5-11. Time Profiles of Modeled Temperatures in Fracture Water above the Drift



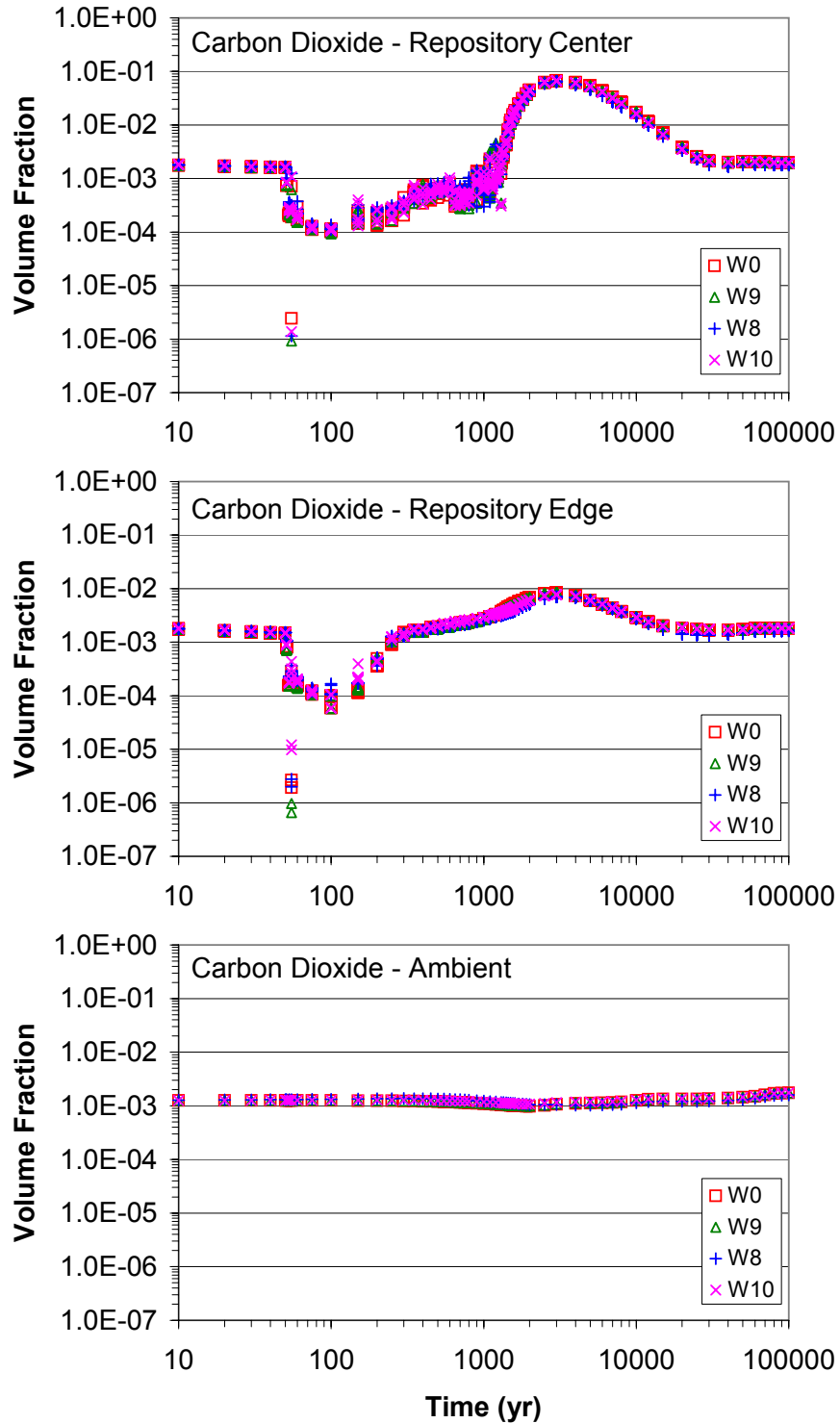
Output DTNs: LB0705DSTHC001.001, LB0705DSTHC002.001, LB0705DSTHC003.001, LB0705DSTHC004.001.
 NOTE: Data from gridblocks exhibiting highest liquid mobility in fractures above the modeled drift (TOP FLUX waters as defined in Section 6.4.8).

Figure 6.5-12. Time Profiles of Modeled Liquid Saturations in Fracture Water above the Drift



Output DTNs: LB0705DSTHC001.001, LB0705DSTHC002.001, LB0705DSTHC003.001, LB0705DSTHC004.001.
 NOTE: Data from gridblocks exhibiting highest liquid mobility in fractures above the modeled drift (TOP FLUX waters as defined in Section 6.4.8).

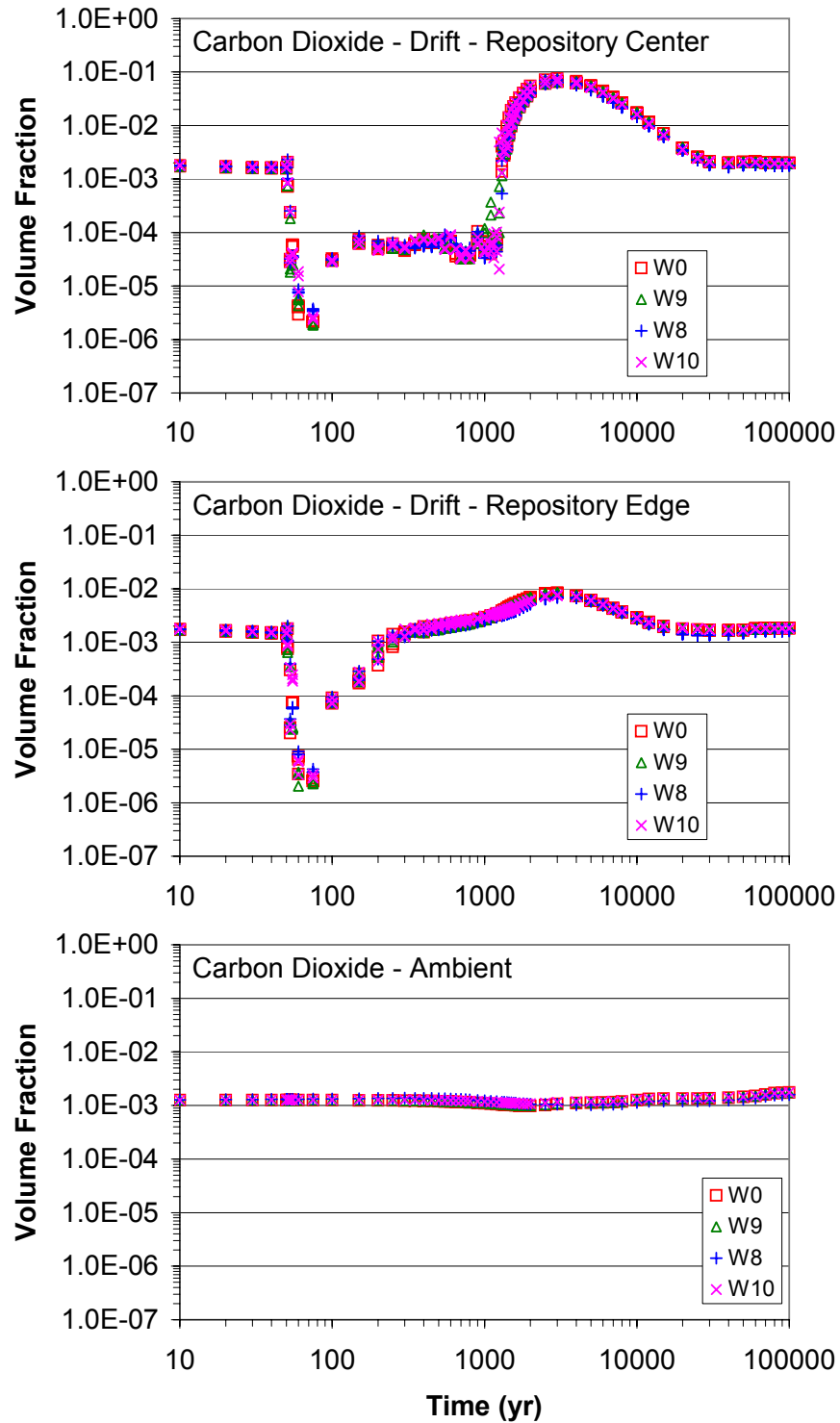
Figure 6.5-13. Time Profiles of Modeled Total Aqueous Chloride Concentrations in Fracture Water above the Drift



Output DTNs: LB0705DSTHC001.001, LB0705DSTHC002.001, LB0705DSTHC003.001, LB0705DSTHC004.001.

NOTE: Data from gridblocks exhibiting highest liquid mobility in fractures above the modeled drift (TOP FLUX waters as defined in Section 6.4.8).

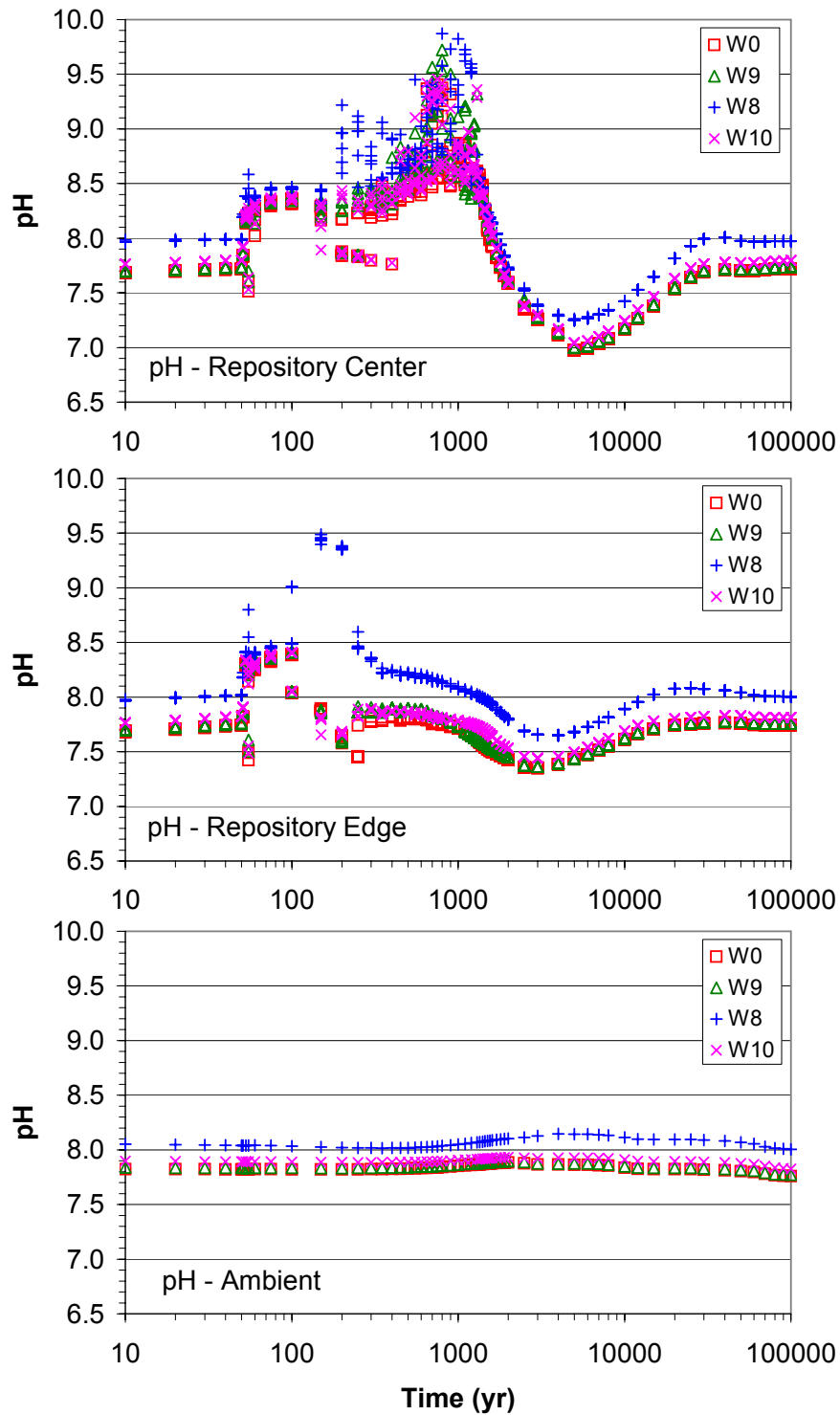
Figure 6.5-14. Time Profiles of Modeled CO₂ Gas Concentrations in Fractures above the Drift



Output DTNs: LB0705DSTHC001.001, LB0705DSTHC002.001, LB0705DSTHC003.001, LB0705DSTHC004.001.

NOTE: Data from gridblocks at the crown, springline, and base of the modeled drift, in rock directly adjacent to the drift wall.

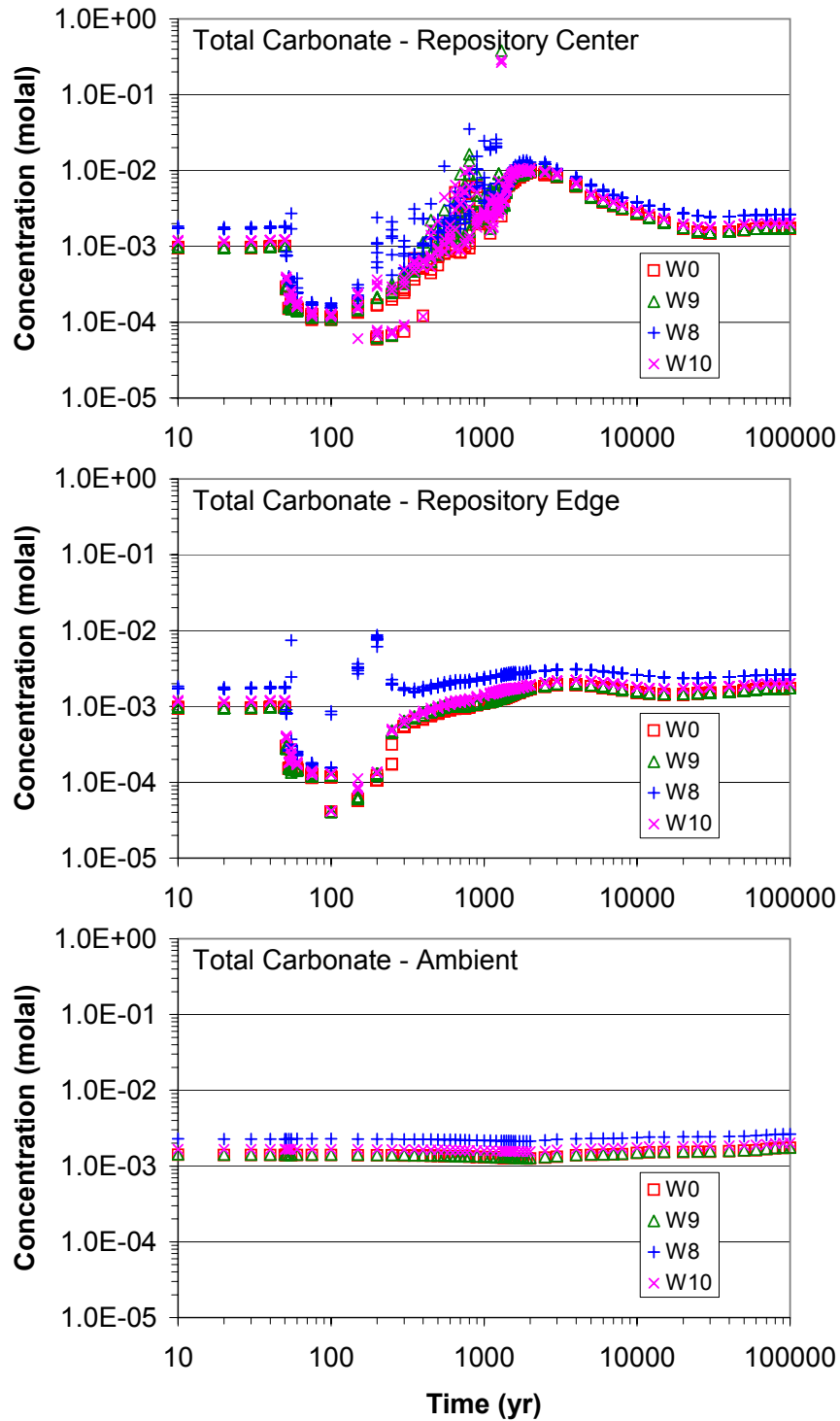
Figure 6.5-15. Time Profiles of Modeled CO₂ Gas Concentrations at the Drift Wall



Output DTNs: LB0705DSTHC001.001, LB0705DSTHC002.001, LB0705DSTHC003.001, LB0705DSTHC004.001.

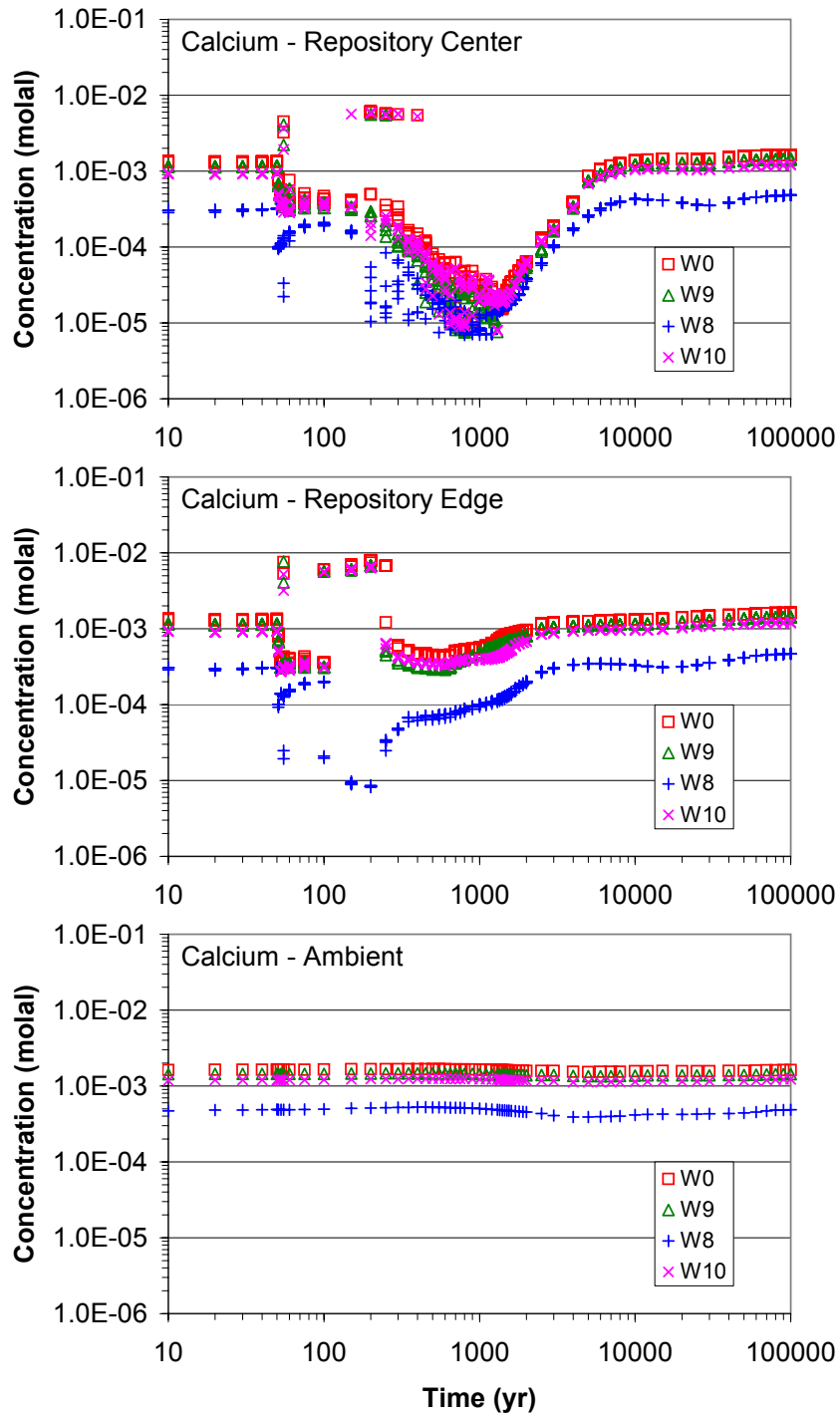
NOTE: Data from gridblocks exhibiting highest liquid mobility in fractures above the modeled drift (TOP FLUX waters as defined in Section 6.4.8).

Figure 6.5-16. Time Profiles of Modeled pH in Fracture Water above the Drift



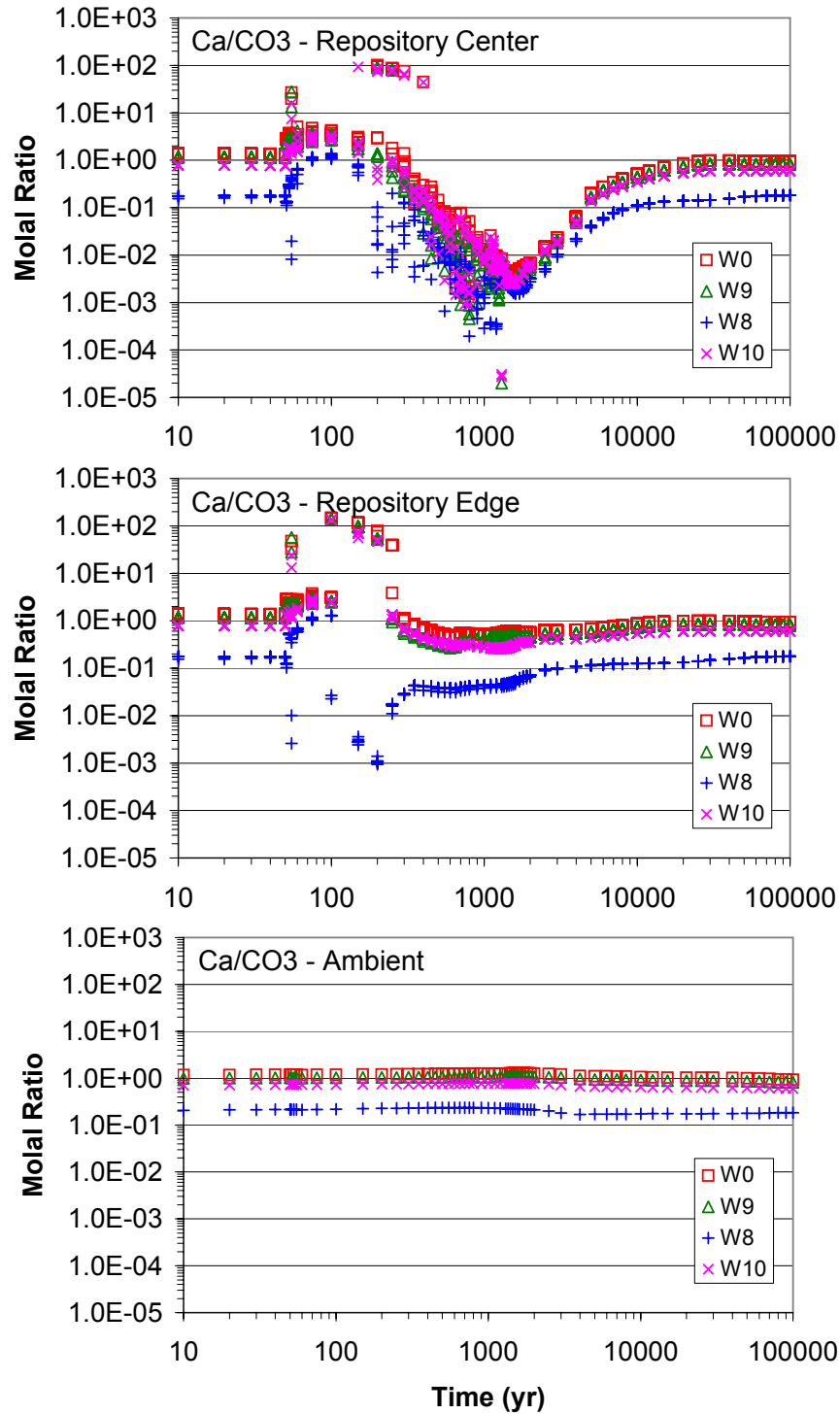
Output DTNs: LB0705DSTHC001.001, LB0705DSTHC002.001, LB0705DSTHC003.001, LB0705DSTHC004.001.
 NOTE: Data from gridblocks exhibiting highest liquid mobility in fractures above the modeled drift (TOP FLUX waters as defined in Section 6.4.8).

Figure 6.5-17. Time Profiles of Modeled Total Aqueous Carbonate Concentrations in Fracture Water above the Drift



Output DTNs: LB0705DSTHC001.001, LB0705DSTHC002.001, LB0705DSTHC003.001, LB0705DSTHC004.001.
 NOTE: Data from gridblocks exhibiting highest liquid mobility in fractures above the modeled drift (TOP FLUX waters as defined in Section 6.4.8).

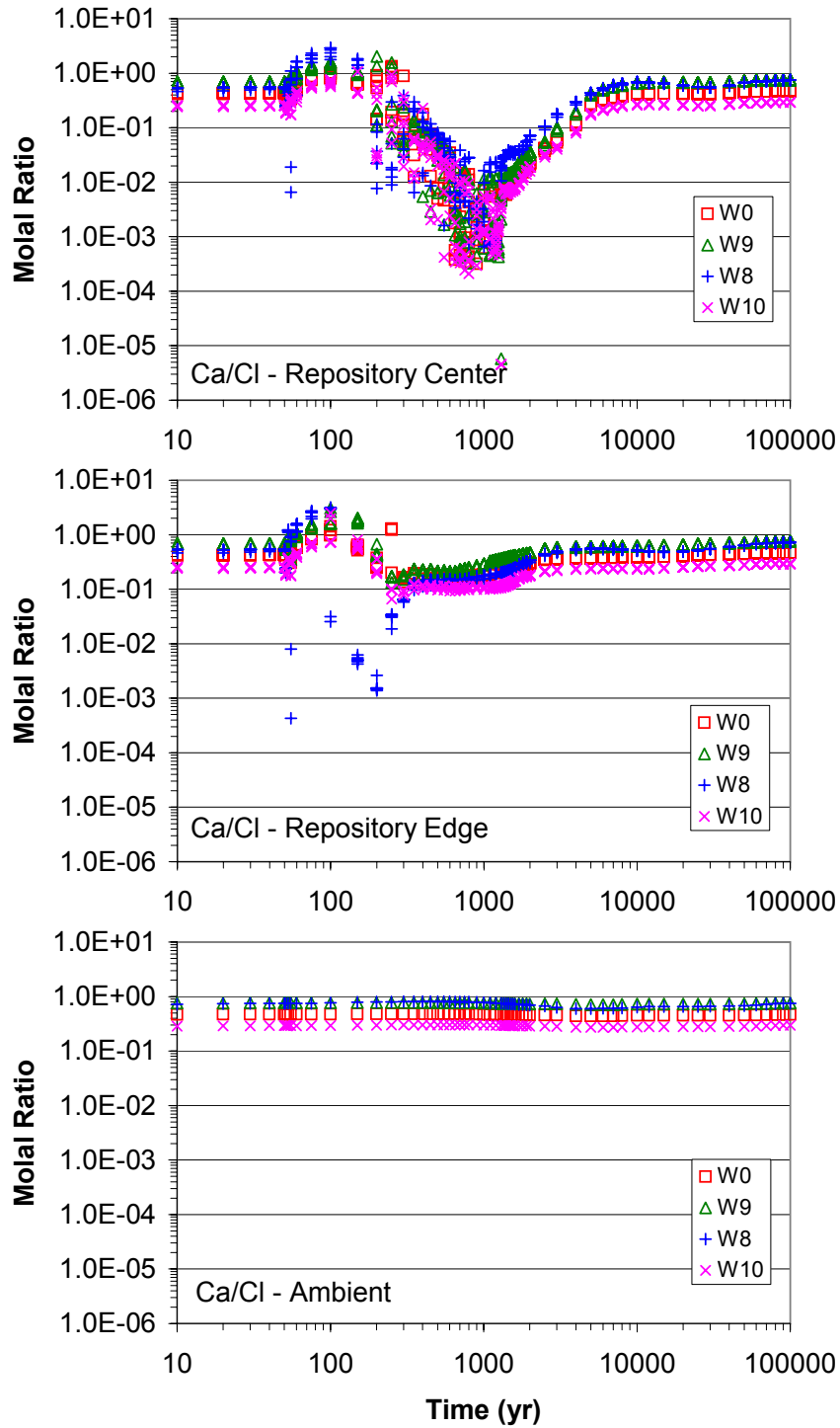
Figure 6.5-18. Time Profiles of Modeled Total Aqueous Calcium Concentrations in Fracture Water above the Drift



Output DTNs: LB0705DSTHC001.001, LB0705DSTHC002.001, LB0705DSTHC003.001, LB0705DSTHC004.001.

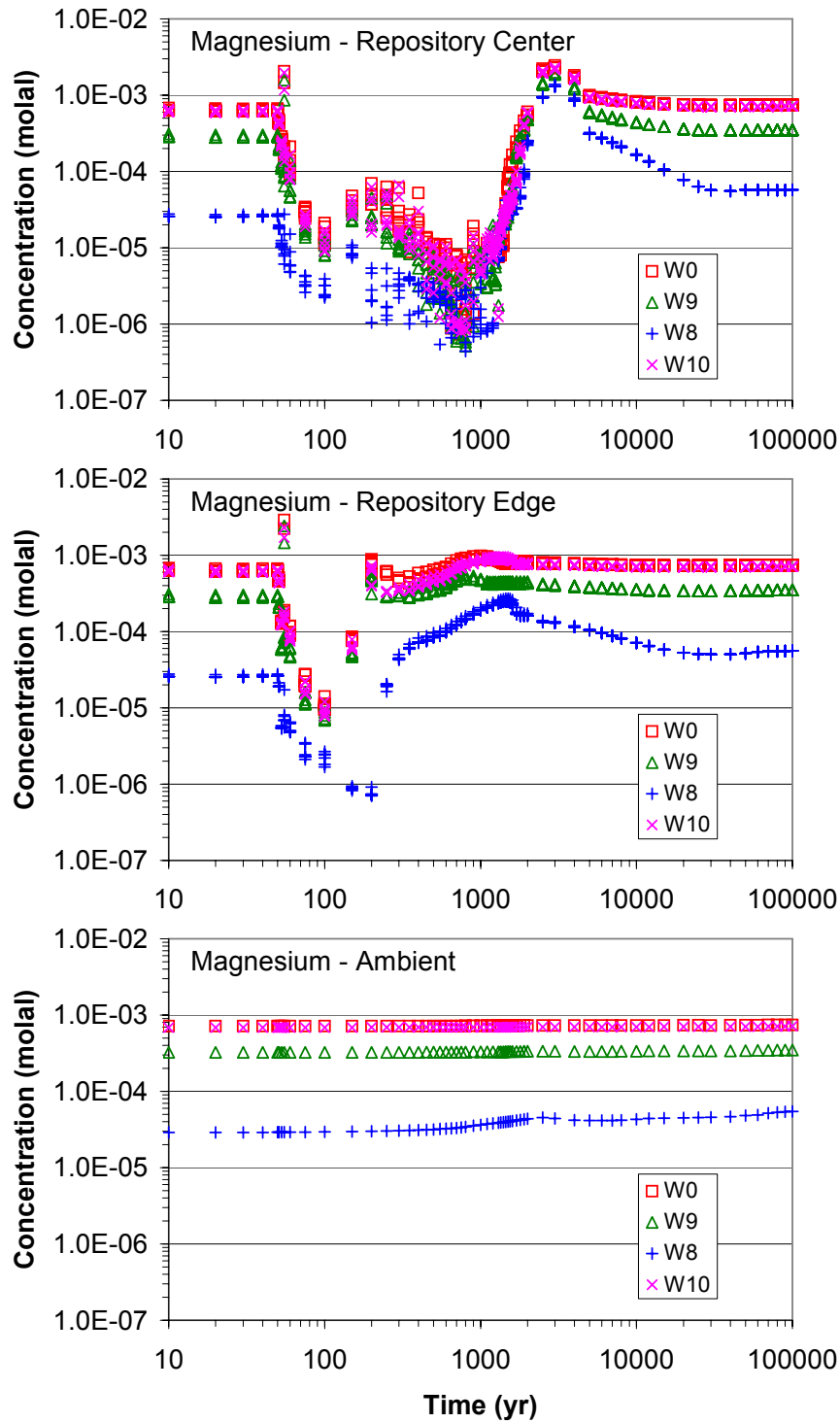
NOTE: Data from gridblocks exhibiting highest liquid mobility in fractures above the modeled drift (TOP FLUX waters as defined in Section 6.4.8).

Figure 6.5-19. Time Profiles of Modeled Total Aqueous Calcium to Total Aqueous Carbonate Ratios in Fracture Water above the Drift



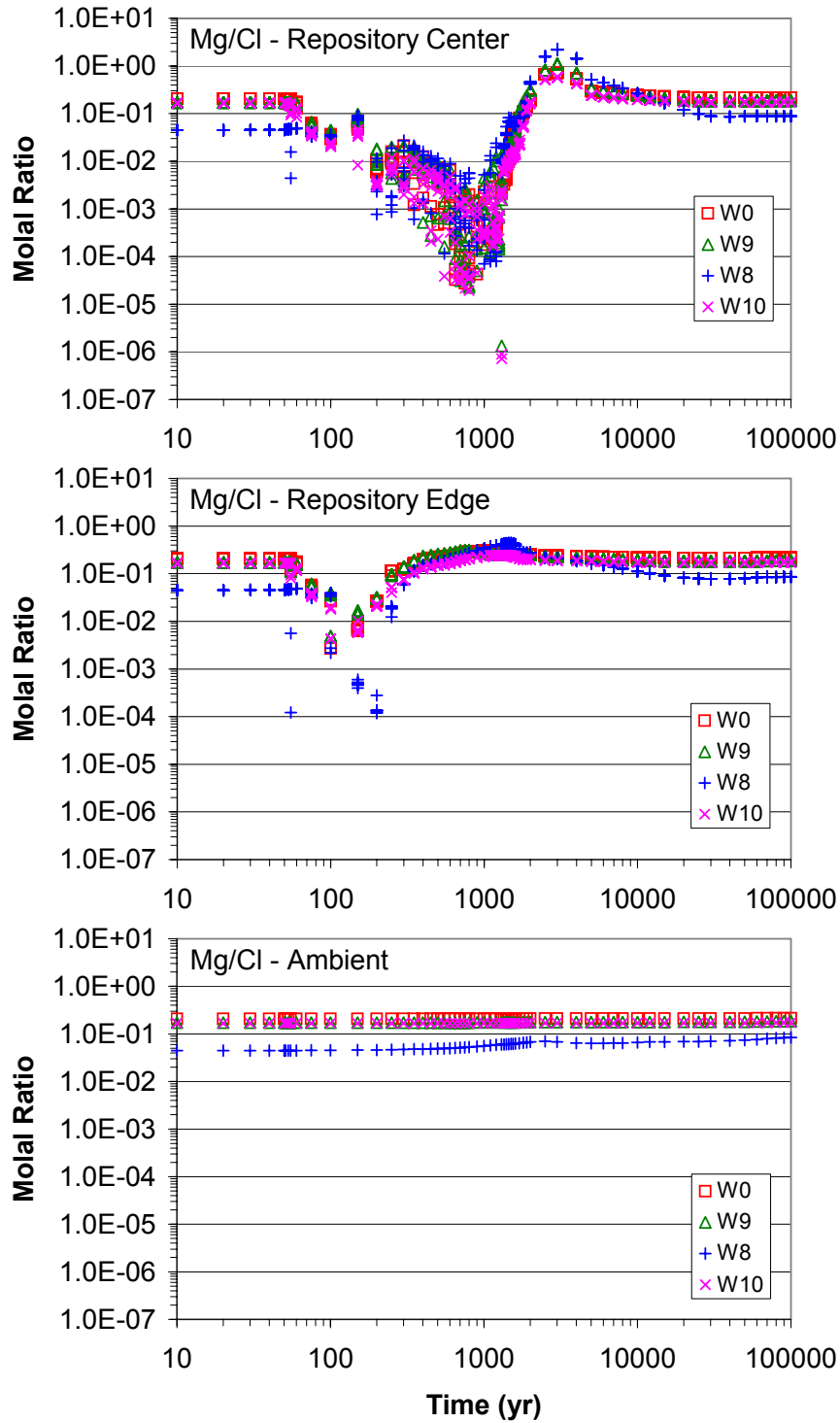
Output DTNs: LB0705DSTHC001.001, LB0705DSTHC002.001, LB0705DSTHC003.001, LB0705DSTHC004.001.
 NOTE: Data from gridblocks exhibiting highest liquid mobility in fractures above the modeled drift (TOP FLUX waters as defined in Section 6.4.8).

Figure 6.5-20. Time Profiles of Modeled Total Aqueous Calcium to Total Aqueous Chloride Ratios in Fracture Water above the Drift



Output DTNs: LB0705DSTHC001.001, LB0705DSTHC002.001, LB0705DSTHC003.001, LB0705DSTHC004.001.
 NOTE: Data from gridblocks exhibiting highest liquid mobility in fractures above the modeled drift (TOP FLUX waters as defined in Section 6.4.8).

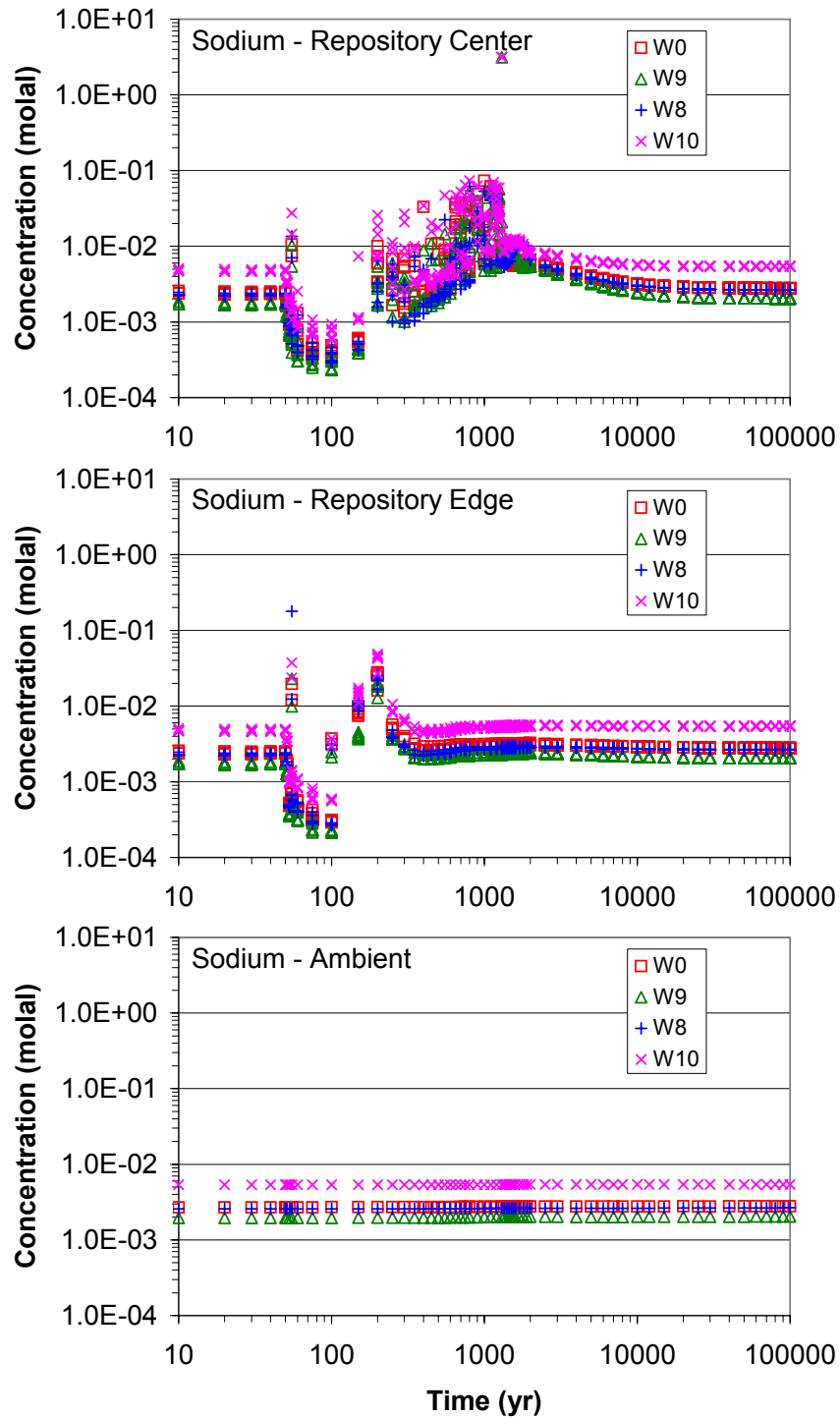
Figure 6.5-21. Time Profiles of Modeled Total Aqueous Magnesium Concentrations in Fracture Water above the Drift



Output DTNs: LB0705DSTHC001.001, LB0705DSTHC002.001, LB0705DSTHC003.001, LB0705DSTHC004.001.

NOTE: Data from gridblocks exhibiting highest liquid mobility in fractures above the modeled drift (TOP FLUX waters as defined in Section 6.4.8).

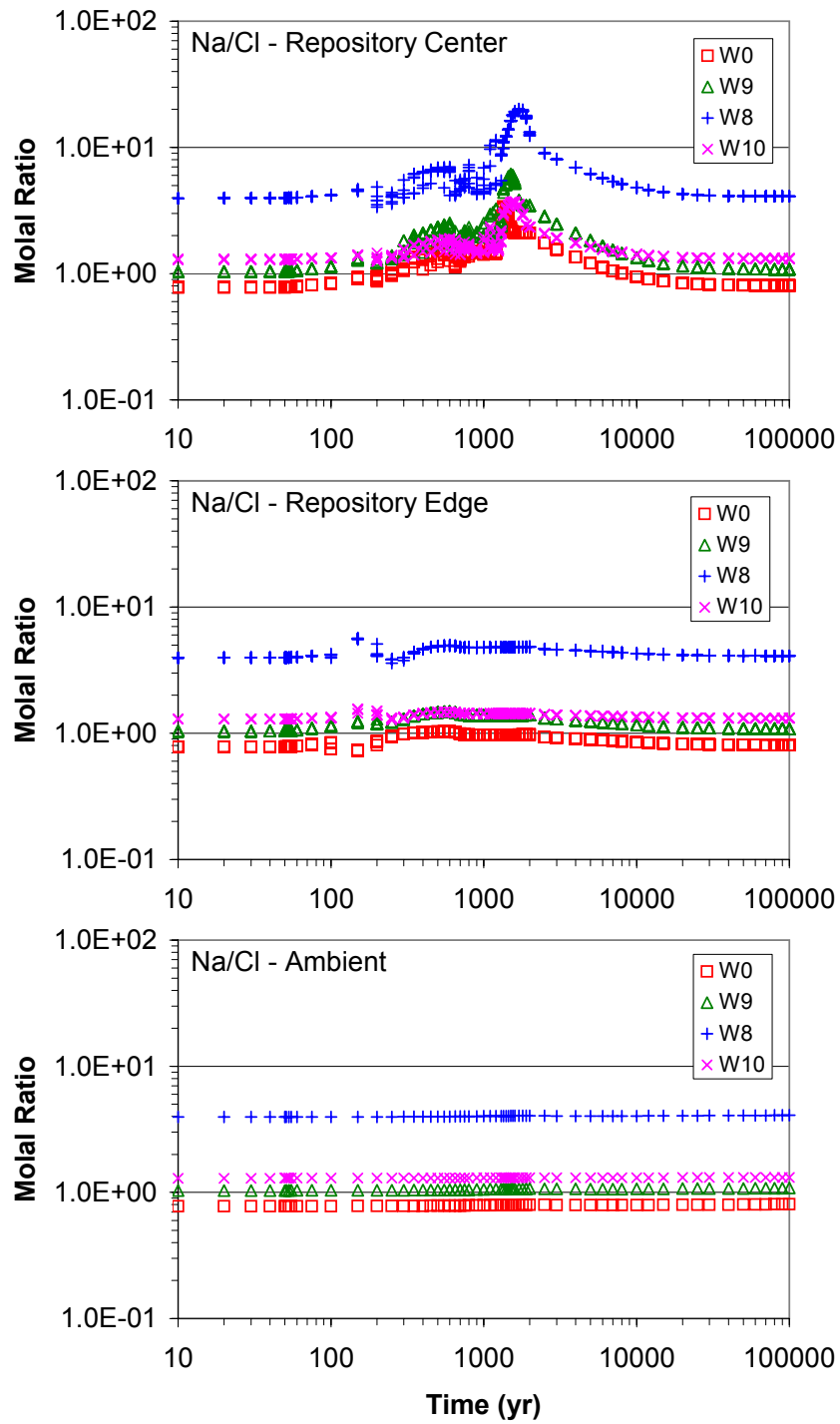
Figure 6.5-22. Time Profiles of Modeled Total Aqueous Magnesium to Total Aqueous Chloride Ratios in Fracture Water above the Drift



Output DTNs: LB0705DSTHC001.001, LB0705DSTHC002.001, LB0705DSTHC003.001, LB0705DSTHC004.001.

NOTE: Data from gridblocks exhibiting highest liquid mobility in fractures above the modeled drift (TOP FLUX waters as defined in Section 6.4.8).

Figure 6.5-23. Time Profiles of Modeled Total Aqueous Sodium Concentrations in Fracture Water above the Drift



Output DTNs: LB0705DSTHC001.001, LB0705DSTHC002.001, LB0705DSTHC003.001, LB0705DSTHC004.001.
 NOTE: Data from gridblocks exhibiting highest liquid mobility in fractures above the modeled drift (TOP FLUX waters as defined in Section 6.4.8).

Figure 6.5-24. Time Profiles of Modeled Total Aqueous Sodium to Total Aqueous Chloride Ratios in Fracture Water above the Drift

6.6 MODEL SENSITIVITY ANALYSES

Results of simulations to evaluate the model sensitivity to various input parameters are presented in this section. Here, the focus is given to analyses addressing comments and/or CRs (Section 4.2) on the previous model revision, and those providing additional insights on the model results presented in Section 6.5.5.4. These sensitivity analyses are by no means comprehensive. Changes in successive model revisions over the last seven years (Table 6-1) provide additional valuable information on the model sensitivity to various model conceptualizations and input data. These developmental model simulations primarily provide a qualitative assessment of the model sensitivity to the geologic host unit (essentially no effect), fracture permeability heterogeneity (essentially no effect), infiltration rates (some effect), CO₂ gas diffusivity (noticeable effect), capillary pressure effect on the water vapor pressure (noticeable effect), and input pore-water compositions (noticeable effect on variability, less effects on trends).

Here, sensitivity analyses are performed using one input water composition (water W0; Table 6.2-1) and a repository-center location (i.e., drift spacing of 81 m, as discussed in Section 6.5.1). The use of additional initial water compositions or repository locations is not expected to change the conclusions reached from these sensitivity analyses. The model sensitivity to time discretization is reported in Section 6.6.1, presenting results that serve as a basis for the time stepping scheme used in the model runs presented in Section 6.5.5. In Section 6.6.2, the effects of some important model revisions (since BSC 2005 [DIRS 172862]) are investigated to provide more insights on the model results presented in Section 6.5.5.4, notably the significantly lower predicted calcium concentrations than reported previously. Parameters affecting CO₂ transport are discussed in Section 6.6.3. The effects of the dryout salt assemblage and sequence (Table 6.4-1) selected for simulations discussed in Section 6.5.5 are evaluated in Section 6.6.4. Finally, Section 6.6.5 presents results from a sensitivity analysis of mineral reaction rates.

All model input and output files have been submitted to the TDMS under DTNs as listed in Table 6.6-1 and Appendix G. For each simulation, Excel tables and plots summarizing the predicted chemistries of fracture (and in one case, matrix) waters around the simulated drift for FLUX waters (Section 6.4.8) have also been generated. These summary tables have been submitted to the TDMS with file names and DTNs as summarized in Table 6.6-1. These files contain many more results and plots than shown in this report.

Table 6.6-1. Summary Output Data Files and DTNs for Sensitivity Analyses

Sensitivity Analysis	Run ID	Specifics	DTN for TOUGHREACT I/O Files	Summary Data File (FLUX waters)	DTN
Time Discretization	thc6_w0_t1	Δt_{max} = Courant limit ^a	LB0705DSTHC020.002	<i>frac_cour_15_30.xls</i> (fractures)	LB0705DSTHC020.001
	thc6_w0_dt15	Δt_{max} = 15 days	LB0705DSTHC020.002	<i>mat_cour_15_30.xls</i> (matrix)	
	thc6_w0_dt30	Δt_{max} = 30–60 days	LB0705DSTHC020.002		
Model Revisions	thc6_w0_dt15	All inputs from Revision 04	LB0705DSTHC020.002	<i>frac_modrev_w0.xls</i> (fractures)	LB0705DSTHC021.001
	thc7_81_w0_gap	Calcite precipitation gap	LB0705DSTHC021.002		
	thc7_81_w0_bnd	pCO ₂ boundary = 10 ^{-2.5} bar	LB0705DSTHC021.002		
Dryout Mineral Assemblage	thc7_81_w0_s0	"Salt0" assemblage	LB0705DSTHC022.002	<i>frac_salts_w0.xls</i> (fractures)	LB0705DSTHC022.001
	thc7_81_w0_s1	"Salt1" assemblage	LB0705DSTHC022.002		
CO ₂ Transport	thc7_81_w0_dif	~10x more CO ₂ diffusion	LB0705DSTHC023.002	<i>frac_CO2_w0.xls</i> (fractures)	LB0705DSTHC023.001
	thc7_81_w0_dif2	~3x more CO ₂ diffusion	LB0705DSTHC023.002		
	thc7_81_w0_grp1	Increased advection (different gas relative permeability function)	LB0705DSTHC023.002		
Reaction Rates	thc7_81_w0_r1	10 ² –10 ³ x increase	LB0705DSTHC024.002	<i>frac_rates_w0.xls</i> (fractures)	LB0705DSTHC024.001
	thc7_81_w0r1_amb	10 ² –10 ³ x increase	LB0705DSTHC024.002		

^a The Courant limit is given by using $N_c = 1$ in Equation 6.6-1, resulting in time steps smaller than ~0.6 days (see Section 6.6.1).

6.6.1 Sensitivity to Time Discretization

For this analysis, four time discretization schemes were considered, as shown in Table 6.6-2. Three of these schemes were implemented with two-dimensional heat-load simulations using the same model setup and numerical mesh as presented in Section 6.5.1 for a drift spacing of 81 m (repository center): a “Courant” case, a “15 days” case and a “30–60 days” case. The “15 days” case was implemented in all new simulations presented in this report (Sections 6.5.5, and other sensitivity analyses in Section 6.6). The fourth “Ambient” scheme was run with one-dimensional simulations without heat load, and a configuration as discussed in Section 6.5.1.

The finer discretization schemes were set using a maximum time step size, Δt_{max} , defined at each model gridblock with the Courant Number, N_c , such that:

$$\Delta t_{max} = N_c \min(\Delta x_i / v_i) \quad (\text{Eq. 6.6-1})$$

where Δx_i and v_i represent the connection length and pore (seepage) velocity, respectively, of liquid or gas for connection i between the given gridblock and adjacent ones, and \min stands for the minimum over all gridblock connections. The “Courant” case was run using $N_c = 1$. The considerable run-time required to implement such fine discretization (~3 months for a simulated period of 2,000 years) and schedule constraints did not allow starting this analysis before the inputs for the current model revisions were finalized. For this reason, all two-dimensional simulations related to the time discretization analysis were run using inputs from the previous model revision (BSC 2005 [DIRS 172862], Section 4.1). The numerical mesh, general model setup, and initial fracture permeability and porosity values did not change between the current and previous model revisions. The modeled heat load essentially did not change, and revisions in infiltration rates were minimal. Because these model inputs have the most effect on fluid flow and have changed little or not at all since the previous revision of this report, the time discretization analysis presented here for two-dimensional simulations is considered applicable to all other two-dimensional simulations in this report.

The “Ambient” case consists of the simulations for which results were presented earlier in Figures 6.5-11 through 6.5-25. Results of the “Ambient” case, which incorporate small time steps with $N_c = 0.5$ in Equation 6.6-1, are used to support the use of coarser time-discretization schemes with two-dimensional simulations for simulated time periods > 2,000 years.

It should be noted that TOUGHREACT always limits the length of time steps if convergence on flow is not reached within a certain number of iterations (four iterations in the present report). Therefore, the steep temperature increase after 50 years, as well as complex multiphase flow behavior, particularly during the collapse of the boiling front, can result in instances when the time step is limited to values less than the Δt_{max} values shown in Table 6.6-2.

All simulations for time-stepping analyses were run using TOUGHREACT V3.1.1. Model results were extracted using CUTCHEM V2.0 for FLUX waters (Section 6.4.8). Predicted concentration time-profiles for CO₂ and several aqueous species in fracture TOP FLUX waters are shown in Figures 6.6-1 through 6.6-3, as well as on plots in summary data files accompanying this report (Table 6.6-1). For comparison, these figures and plots also show results of previous simulations (BSC 2005 [DIRS 172862], Section 6.5.5.2.2), which were run

without Leverett scaling and with an earlier version of TOUGHREACT, using the same time discretization as the “30–60 days” case. These older results, extracted for HISAT waters (Section 6.4.8), are labeled as “Old TSPA” and are provided only for comparison purposes.

Table 6.6-2. Time Discretization Analysis

Simulated Time Period (yr)	Δt_{max} (days)	Run ID
“Courant” Case^a		
0–100	0.06–0.17	thc6_w0_t1
100–300	0.17–0.28	
300–600	0.28–0.36	
600–2,000	0.36–0.55	
“15 days” Case^b		
0–2,000	15	thc6_w0_dt15
2,000–10,000	100	
10,000–30,000	300	
20,000–100,000	1000	
“30–60 days” Case^b		
0–50	15	thc6_w0_dt30
50–600	30	
600–2,400	60	
2,400–20,000	365	
“Ambient” Cases (0.5 × Courant)^c		
0–600	53	thc7_w0_amb, thc7_w8_amb, thc7_w9_amb, thc7_w10_amb
600–2,000	44	
2000–100,000	37	

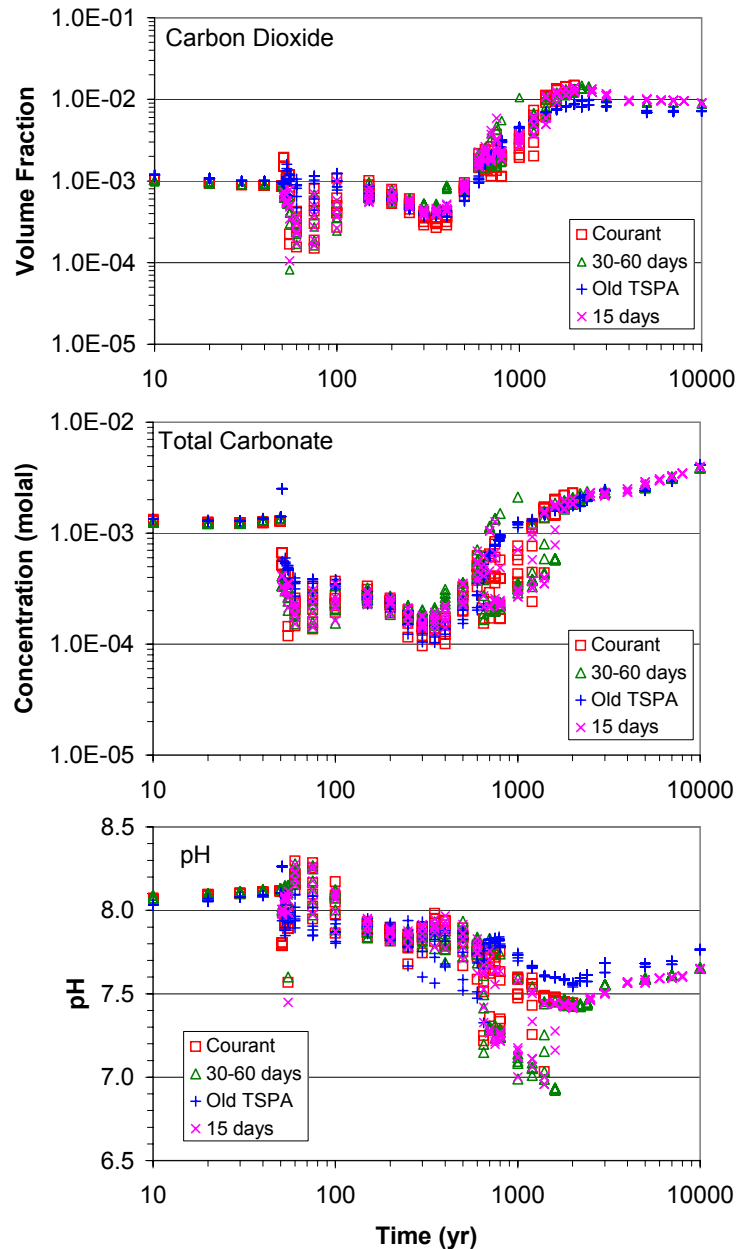
^a Automatic time-step limitation computed using Equation 6.6-1 and $N_c = 1$; values shown are ranges for the simulated time period.

^b Maximum time step values are input for the time period shown.

^c One-dimensional simulations under conditions of ambient temperature and pressure (Section 6.5.5.1), steady flow field between stepped-up infiltration rates, and automatic time-step limitation computed using Equation 6.6-1 and $N_c = 0.5$.

It can be seen from this analysis that the “Courant,” “15 days,” and “30–60 days” cases yield similar results that are well within the spatial variability of modeled concentrations around the drift. The most noticeable differences occur between the “Old TSPA” results and the more recent simulations. These differences are attributed primarily to the fact that the Leverett-scaling formulation (Section 6.4.4.4) was disabled in the old simulations. Comparison of model results for the heat-load and ambient cases presented earlier (Figures 6.5-11 through 6.5-24) also show that starting as early as at ~2,000 years, predicted water compositions using a coarse time discretization begin to return to about the same compositions as those predicted for the ambient case using small time steps equal to half the Courant limit. These analyses, therefore, serve as a justification for adopting the “15 days” case for time discretization in this study. This case was

selected because it provides a reasonable and manageable compromise between computation efficiency and accuracy.

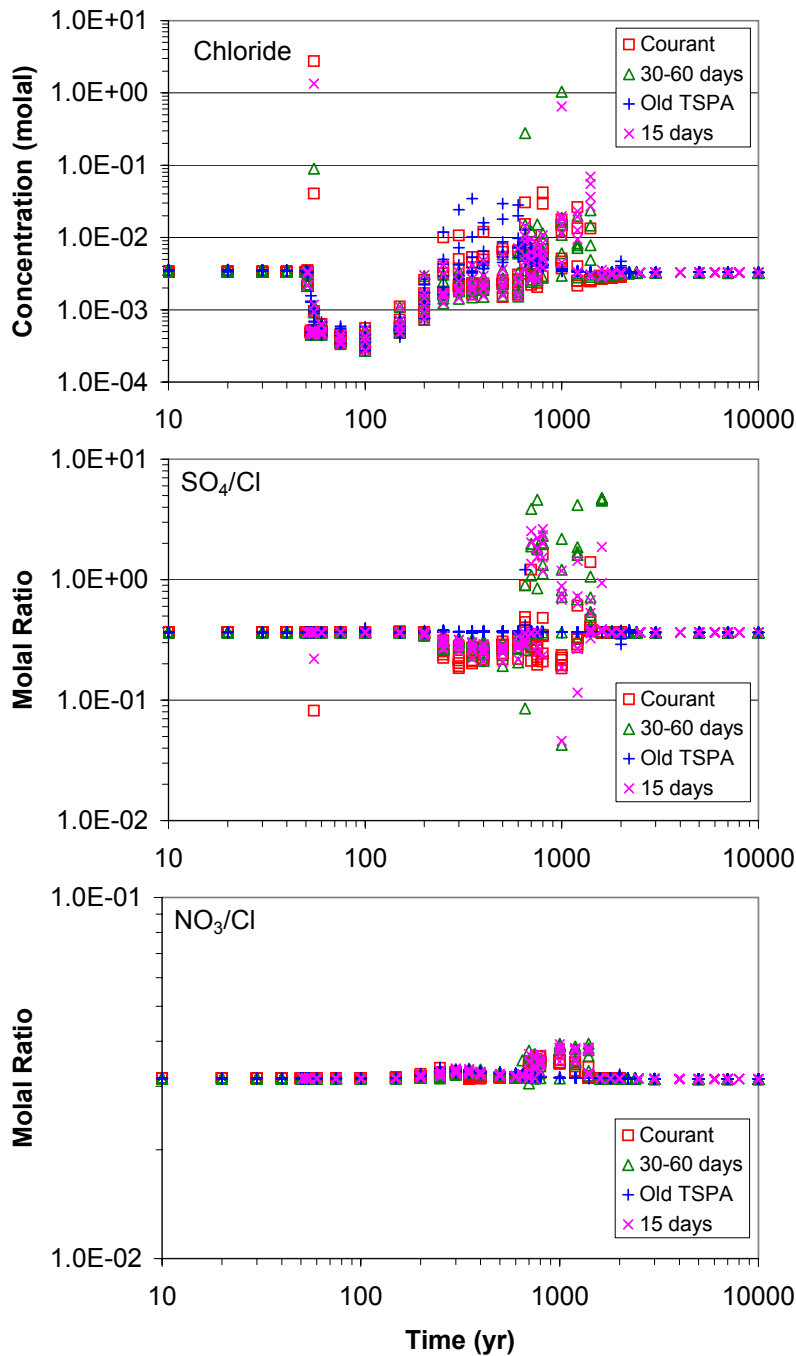


Source DTNs: LB0302DSCPTHCS.001 [DIRS 164744] and LB0302DSCPTHCS.002 [DIRS 161976].

Output DTNs: LB0705DSTHC020.001, LB0705DSTHC001.001.

NOTE: See Table 6.6-2 for the definition of each time discretization scheme. Data are from gridblocks exhibiting the highest liquid mobility in fractures above the modeled drift (TOP FLUX waters), except for the "Old TSPA" case representing zones of highest liquid saturation (HISAT waters) (see Section 6.4.8). These sensitivity analyses were run with inputs from a previous model revision (BSC 2005 [DIRS 172862], Section 4.1).

Figure 6.6-1. Time Discretization Analysis: Time Profiles of Modeled CO₂ Gas Concentrations, Total Aqueous Carbonate Concentrations, and pH

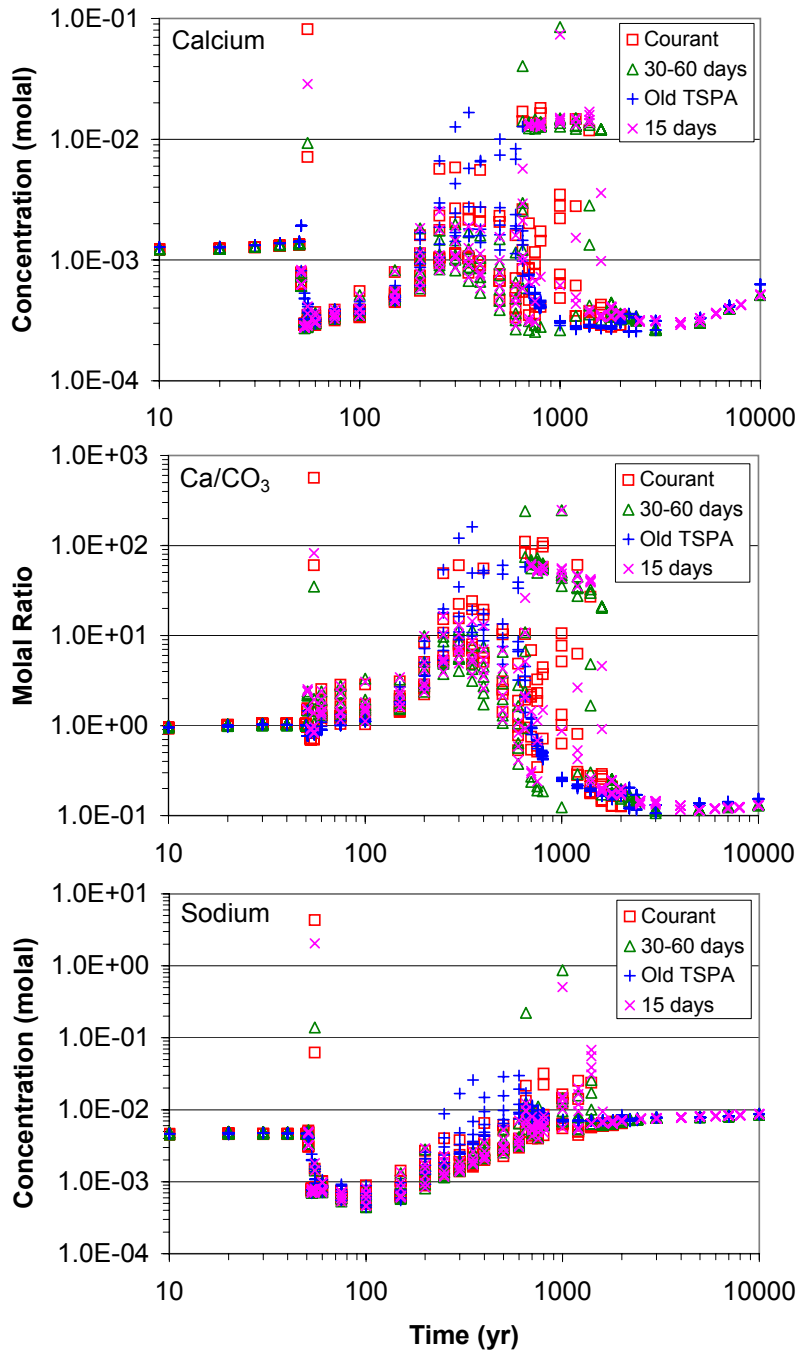


Source DTNs: LB0302DSCPTHCS.001 [DIRS 164744] and LB0302DSCPTHCS.002 [DIRS 161976].

Output DTNs: LB0705DSTHC020.001, LB0705DSTHC001.001.

NOTE: See Table 6.6-2 for the definition of each time discretization scheme. Data are from gridblocks exhibiting the highest liquid mobility in fractures above the modeled drift (TOP FLUX waters), except for the "Old TSPA" case representing zones of highest liquid saturation (HISAT waters) (see Section 6.4.8). These sensitivity analyses were run with inputs from a previous model revision (BSC 2005 [DIRS 172862], Section 4.1).

Figure 6.6-2. Time Discretization Analysis: Time Profiles of Modeled Aqueous Chloride Concentrations, Sulfate to Chloride Ratios, and Nitrate to Chloride Ratios



Source DTNs: LB0302DSCPTHCS.001 [DIRS 164744] and LB0302DSCPTHCS.002 [DIRS 161976].

Output DTNs: LB0705DSTHC020.001, LB0705DSTHC001.001.

NOTE: See Table 6.6-2 for the definition of each time discretization scheme. Data are from gridblocks exhibiting the highest liquid mobility in fractures above the modeled drift (TOP FLUX waters), except for the “Old TSPA” case representing zones of highest liquid saturation (HISAT waters) (see Section 6.4.8). These sensitivity analyses were run with inputs from a previous model revision (BSC 2005 [DIRS 172862], Section 4.1).

Figure 6.6-3. Time Discretization Analysis: Time Profiles of Modeled Aqueous Calcium and Sodium Concentrations, and Calcium to Total Aqueous Carbonate Ratios

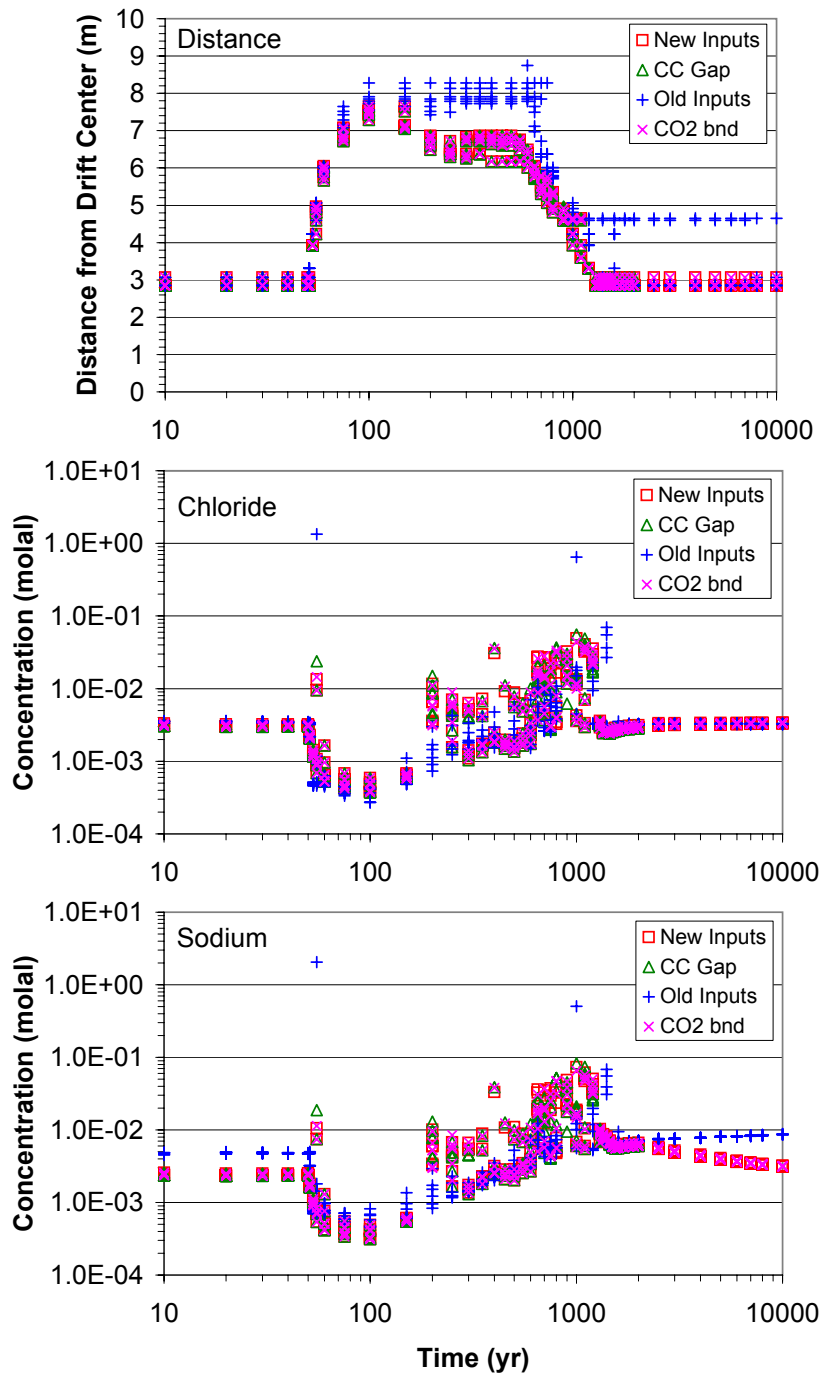
6.6.2 Sensitivity to Model Revisions

Predicted water composition trends discussed in Section 6.5.5.4, for repository-center conditions, are significantly different from the previous model revision (BSC 2005 [DIRS 172862], Section 6.5.5.2.2) for pH, calcium, magnesium, and total aqueous carbonate. Predicted post-boiling CO₂ gas concentrations are also about ~10× higher than predicted previously. The differences in predicted calcium concentrations are particularly large, showing depletion below ambient values by up to 2 orders of magnitude in the present report (Figure 6.5-18) compared to an enrichment by over 1 order of magnitude above ambient values in the previous model revision (BSC 2005 [DIRS 172862], Section 6.5.5.2.2 and Figure 6.5-29). To better understand this difference in behavior, to provide insights on the new model results, and to complement discussions provided in Section 6.5.5.4, simulation results for the following cases were compared:

- “New Inputs” – This is the base case against which other simulations can be compared. This case consists of one of the simulations presented in Section 6.5.5, run with TOUGHREACT V3.1.1, using water W0 and inputs discussed in Section 4.1 (run thc7_81_w0).
- “Old inputs” (same as the “30–60 days” case in Section 6.6.1) – This is a simulation directly comparable to previous model results (BSC 2005 [DIRS 172862], Section 6.5.5.2.2), including the same setup and conceptualization as in the previous model revision, and all previous inputs (BSC 2005 [DIRS 172862], Section 4.1). However, the simulation is rerun here using TOUGHREACT V3.1.1, with Leverett scaling enabled, and results are post-processed using the same extraction procedure (FLUX waters; see Section 6.4.8) as done with the current model revision. For consistency with the previous work, calcite is allowed to remain supersaturated in the initial solution (no initial equilibration with calcite). This simulation is also run using the original water composition W0 from Revision 04 of this report (BSC 2005 [DIRS 172862], Table 6.2-1), which is essentially the same as water W0 in the present revision. The purpose of this run is to separate the effects of TOUGHREACT upgrades, Leverett scaling, and the new extraction procedure (FLUX waters) from other model revisions.
- “CC Gap” – This simulation is run using the same inputs and setup as the “New Inputs” case, with the exception that calcite is allowed to remain supersaturated (instead of initial equilibration of this mineral with the starting solution). The calcite supersaturation gap is set to the value of the calcite saturation index computed for the initial solution (gap of ~0.8 saturation-index units at 20°C). This results in a computed initial pH of ~8.2, a total aqueous carbonate concentration ~182 mg/L at pCO₂ = 10⁻³ bar, and an initial calcium concentration reflecting the measured value of 97 mg/L (Table 6.2-1), close to the initial water chemistry in the “Old Inputs” case.
- “CO₂ bnd” – This simulation is run using the same inputs and setup as the “New Inputs” case, with the exception that the top-boundary CO₂ gas partial pressure is set at 10^{-2.5} bar instead of 10⁻³ bar, as was the case in previous model revisions.

All simulations were run using TOUGHREACT V3.1.1. Model results were extracted using CUTCHEM V2.0 [DIRS 181352] for FLUX waters in fractures (Section 6.4.8). Predicted concentration time-profiles for CO₂ and several aqueous species in fracture TOP FLUX waters are shown in Figures 6.6-4 through 6.6-6, as well as on plots in summary data files accompanying this report (Table 6.6-1).

This sensitivity analysis shows that the “Old Inputs” case reproduces fairly well the results obtained in the previous model revision (BSC 2005 [DIRS 172862], Section 6.5.5.2.2). This can be seen, for example, by comparing the trends of pH, CO₂ gas, calcium, and total aqueous carbonate in Figures 6.6-5 and 6.6-6 with trends for the same species in Figures 6.6-1 and 6.6-3. This indicates that the TOUGHREACT upgrades, Leverett scaling, and the extraction procedure (FLUX waters) can be eliminated as a potential cause for the marked departures between the new and older results. Furthermore, the cases including the calcite saturation gap (“CC Gap”) and increased CO₂ gas partial pressure to 10^{-2.5} bar at the top model boundary (“CO₂ bnd”) show the same departures from older results and almost the same results as the base case (“New Inputs”) (Figures 6.6-4 through 6.6-6), thus ruling out these model changes as the cause for the divergence in results. In the case of magnesium, the use of a more realistic, faster-reacting and more soluble magnesium silicate phase than previously (amorphous antigorite instead of sepiolite) exacerbates the differences in results (Figure 6.6-6), but has been ruled out as a cause of divergence for other species (test simulations not reported here have been run with new inputs, but using sepiolite instead of amorphous antigorite). As discussed in Section 6.5.5.4, the new model results appear to show less pronounced steam condensation/dilution effect in fractures and thus an increase in the effects of CO₂ volatilization (water decarbonation). Decarbonation causes the pH to rise, calcite precipitation, and calcium depletion, whereas condensation of CO₂-enriched steam can reverse these trends. The greater CO₂ volatilization could also explain the higher post-boiling pulse in CO₂ gas concentration (Figure 6.6.-5). This behavior may be caused by revisions in rock properties that tend to favor the retention of water in the rock matrix, and by the smaller CO₂ diffusion coefficient used in the present model revision (see Section 6.6.3).

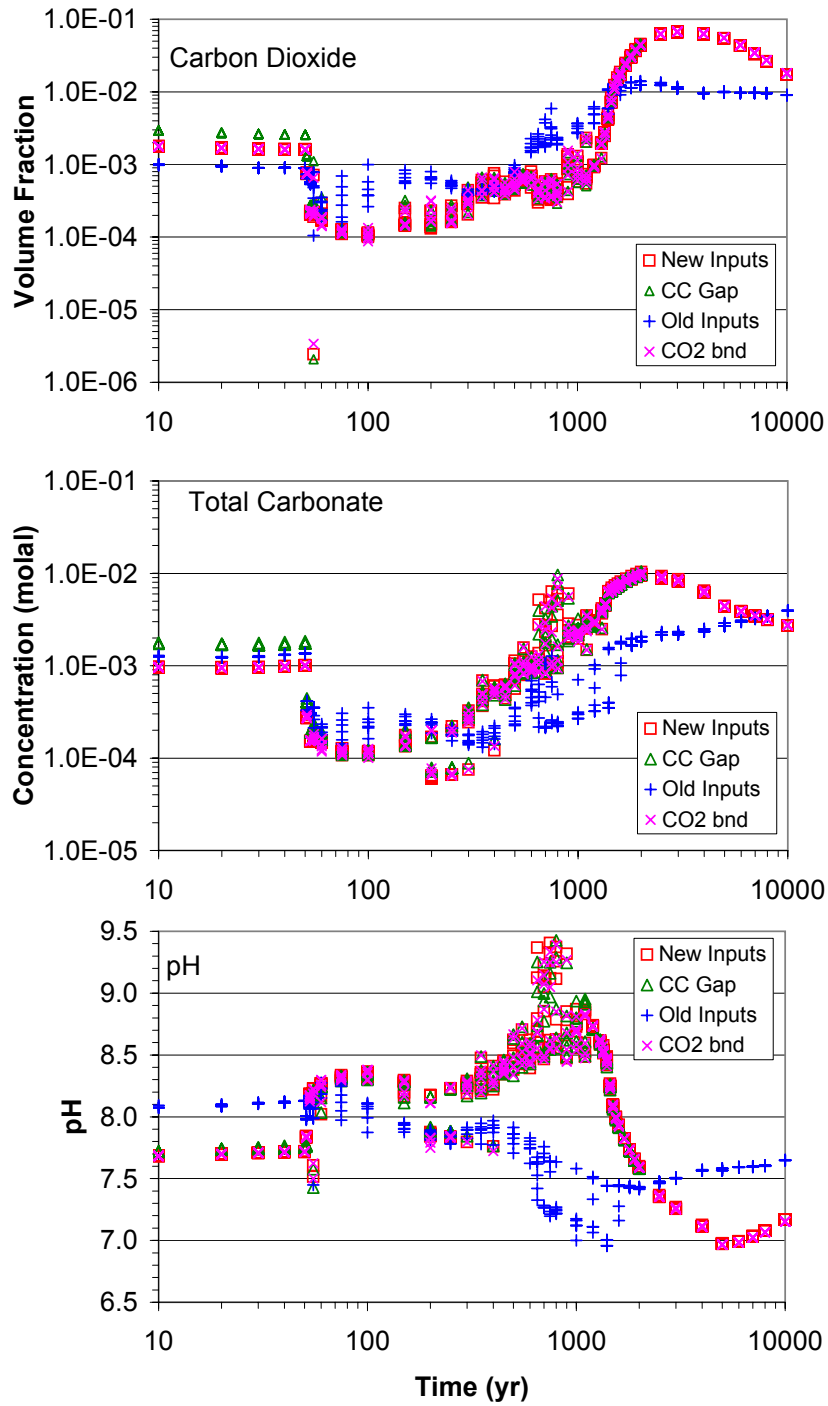


Source DTNs: LB0302DSCPTHCS.002 [DIRS 161976] (“Old Inputs” case).

Output DTNs: LB0705DSTHC001.001, LB0705DSTHC020.001, LB0705DSTHC021.001.

NOTE: Data are from gridblocks exhibiting the highest liquid mobility in fractures above the modeled drift (TOP FLUX waters; see Section 6.4.8). The “CC Gap” simulation was ended at 2,000 years.

Figure 6.6-4. Sensitivity to Model Revisions: Time Profiles of Modeled Distance above Drift Center, and Aqueous Chloride and Sodium Concentrations

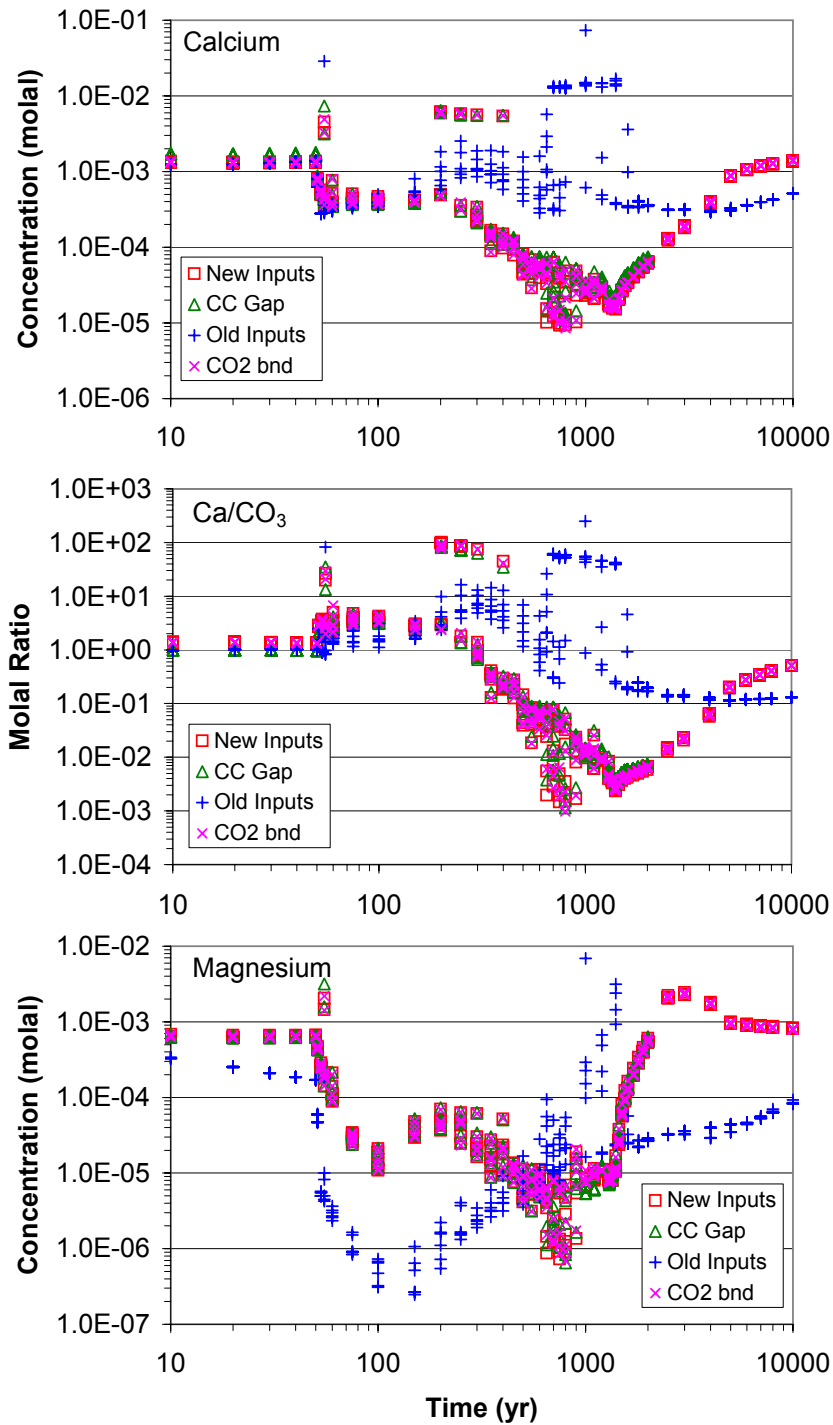


Source DTN: LB0302DSCPTHCS.002 [DIRS 161976] (“Old Inputs” case).

Output DTNs: LB0705DSTHC001.001, LB0705DSTHC020.001, LB0705DSTHC021.001.

NOTE: Data are from gridblocks exhibiting the highest liquid mobility in fractures above the modeled drift (TOP FLUX waters; see Section 6.4.8). The “CC Gap” simulation was ended at 2,000 years.

Figure 6.6-5. Sensitivity to Model Revisions: Time Profiles of Modeled CO₂ Gas Concentrations, Total Aqueous Carbonate Concentrations, and pH



Source DTNs: LB0302DSCPTHCS.002 [DIRS 161976] (“Old Inputs” case).

Output DTNs: LB0705DSTHC001.001, LB0705DSTHC020.001, LB0705DSTHC021.001.

NOTE: Data are from gridblocks exhibiting the highest liquid mobility in fractures above the modeled drift (TOP FLUX waters; see Section 6.4.8). The “CC Gap” simulation was ended at 2,000 years.

Figure 6.6-6. Sensitivity to Model Revisions: Time Profiles of Modeled Calcium and Magnesium Concentrations, and Calcium to Total Aqueous Carbonate Ratios

6.6.3 Sensitivity to CO₂ Transport Properties

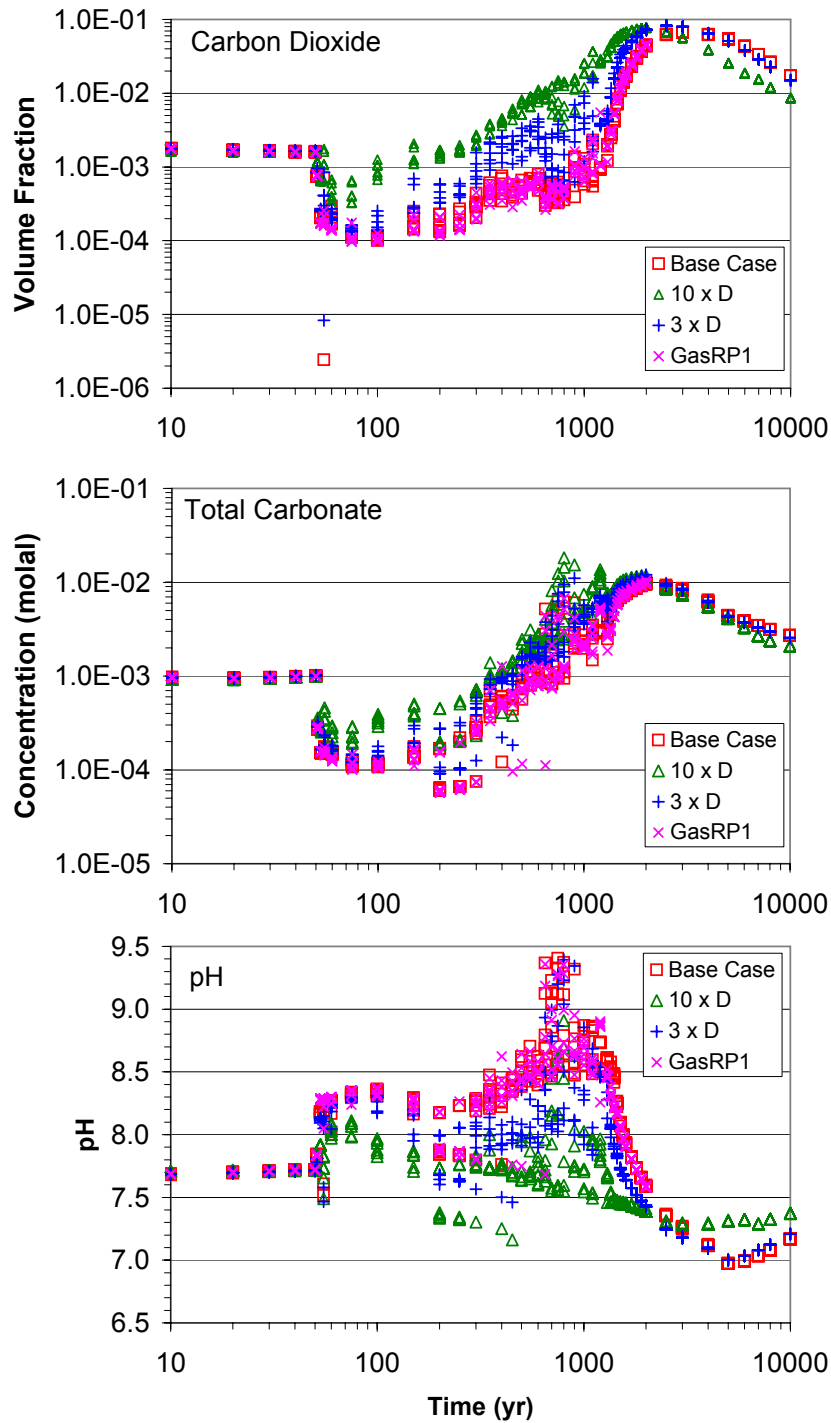
The volatilization and transport of CO₂ is expected to have a strong effect on the chemical evolution of heated and/or boiled waters at Yucca Mountain. Although CO₂ advective transport is likely to dominate diffusive transport in fractures close to boiling areas, diffusion may play a significant role in the transport of CO₂ away from boiling areas. The volatilization of CO₂ gas from matrix pore waters into fractures is also expected to be sensitive to CO₂ diffusion during boiling, because of steep CO₂ gas concentration gradients between fractures and the rock matrix (which contains the bulk of the dissolved CO₂) and the relatively low matrix gas permeability. In addition, the effective diffusivity of CO₂ in repository host units is expected to vary significantly depending on the rock porosity, tortuosity, and degree of heterogeneity around waste emplacement drifts. For example, the presence or absence of lithophysae in the repository host rock could significantly affect the CO₂ diffusive behavior. For these reasons, this sensitivity analysis focuses on CO₂ diffusive transport, considering two cases of increased diffusivity (3× and 10×). Keeping in mind the potential importance of advective transport, one case affecting CO₂ advective transport is also investigated.

To isolate the effects of CO₂ diffusion on water chemistry from other effects that could be introduced by varying the rock porosity or tortuosity, the diffusivity of CO₂ was varied through the CO₂ molecular diameter, which is used in the computation of the CO₂ diffusion coefficient (Equation 6.4-24). The model sensitivity to advective transport was tested through the use of a different gas relative-permeability function. The following four cases were compared:

- “Base Case” – This is the base case against which other simulations can be compared. This case consists of one of the simulations presented in Section 6.5.5, run with TOUGHREACT V3.1.1, using water W0 and inputs discussed in Section 4.1 (run thc7_81_w0). In this simulation, the CO₂ molecular diameter is set to 3.23×10^{-10} m (Lide 1993 [DIRS 123032], p. 14-19), corresponding to a diffusion coefficient of $\sim 1.6 \times 10^{-5}$ m²/s at 96°C. The gas relative-permeability function implemented in this model is a modified Brooks-Corey function as presented by Wu and Mishra (1998 [DIRS 153432] p. 9, Equation 9).
- “3 x D” – This simulation is the same as the base case, but with the CO₂ molecular diameter set to 2×10^{-10} , corresponding to an increase in the CO₂ diffusion coefficient by a factor of ~ 2.6 relative to the base case ($\sim 4.2 \times 10^{-5}$ m²/s at 96°C).
- “10 x D” – This simulation is the same as the base case, but with the CO₂ molecular diameter set to 10^{-10} . This corresponds to an increase in the CO₂ diffusion coefficient by a factor of ~ 10 relative to the base case ($\sim 1.6 \times 10^{-4}$ m²/s at 96°C). Note that the same molecular diameter was used for base-case simulations in the previous model revision (BSC 2005 [DIRS 172862], Section 6.5.3).
- “Gas RP1” – This simulation is the same as the base case, but using a different gas relative permeability function for the TSw rock units. In this simulation, a Corey function is implemented as specified by Pruess et al. (1999 [DIRS 160778], p. 185). The net effect is an increase in the gas relative permeability, by factors of ~ 2 , 10, 100, and 1,000 at liquid saturations of ~ 0.4 , 0.8, 0.95, and 0.98, respectively, in the Tptpl matrix.

All simulations were run using TOUGHREACT V3.1.1. Model results were extracted using CUTCHEM V2.0 for FLUX waters in fractures (Section 6.4.8). Predicted concentration time profiles for CO₂ and several aqueous species in fracture TOP FLUX waters are shown in Figures 6.6-7 and 6.6-8, as well as on plots in summary data files accompanying this report (Table 6.6-1).

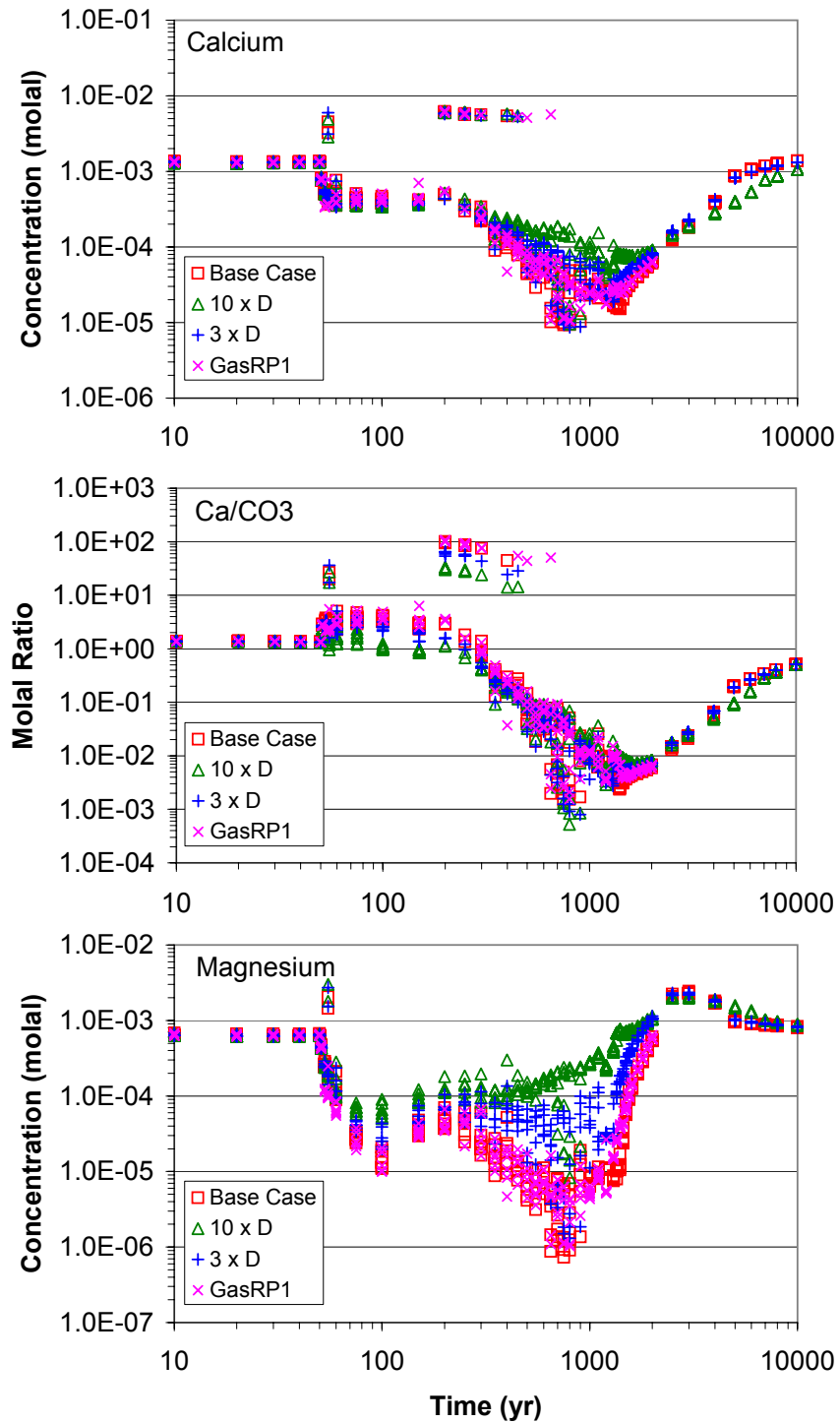
Results of this analysis show that increased CO₂ diffusivity has a significant effect on predicted CO₂ gas concentrations and pH in fractures (Figure 6.6-7). The significantly lower pH values predicted during the boiling period, when the CO₂ diffusivity is increased, impede the precipitation of calcite and magnesium silicate, and result in significantly higher calcium and magnesium concentrations predicted during this period (Figure 6.6-8). The increase in gas relative permeability, however, has no significant effect. These results also indicate that the higher CO₂ diffusion coefficient used in the previous model revision may partly explain the differences in predicted pH, calcium, and magnesium concentrations discussed in Section 6.6.2.



Output DTNs: LB0705DSTHC001.001, LB0705DSTHC023.001.

NOTE: Data are from gridblocks exhibiting the highest liquid mobility in fractures above the modeled drift (TOP FLUX waters; see Section 6.4.8). The "GasRP1" simulation was ended at 2,000 years.

Figure 6.6-7. Sensitivity to CO₂ Transport: Time Profiles of Modeled CO₂ Gas Concentrations, Total Aqueous Carbonate Concentrations, and pH



Output DTNs: LB0705DSTHC001.001, LB0705DSTHC023.001.

NOTE: Data are from gridblocks exhibiting the highest liquid mobility in fractures above the modeled drift (TOP FLUX waters; see Section 6.4.8). The “GasRP1” simulation was ended at 2,000 years.

Figure 6.6-8. Sensitivity to CO₂ Transport: Time Profiles of Modeled Calcium and Magnesium Concentrations, and Calcium to Total Aqueous Carbonate Ratios

6.6.4 Sensitivity to Dryout Mineral Assemblage

In the simulations presented in this report, when water flows into gridblocks that dry out (by boiling or evaporation), solid phases are formed using a normative approach as discussed in Section 6.4.5. The approach is applied once the liquid saturation drops below a certain value, which is set at 10^{-5} in the simulations presented in this report. Once the liquid saturation drops below this value, minerals are formed stoichiometrically in a given, predetermined order that is not necessarily based on thermodynamics. The types of minerals and precipitation sequence is predetermined such that solute mass loss is minimized when a gridblock dries out and most of the solute mass can be accounted for in a solid mineral phase. The mass that is not accounted for in solids, summed over all gridblocks that have dried out at some point in the simulation, is referred to as the *residual* below.

For this sensitivity analysis, the effects of three cases of dryout mineral assemblage on computed residuals and predicted concentration trends were compared, as follows:

- “Selected” – This represents the base case against which the other simulations can be compared. This case consists of one of the simulations presented in Section 6.5.5, run with TOUGHREACT V3.1.1, using water W0 and inputs discussed in Section 4.1 (run the7_81_w0). This simulation makes use of the dryout minerals and sequence shown in the “Selected” column in Table 6.4-1. After the boiling period at ~2,000 years, the largest residuals for this case are ~ 63 moles for total aqueous carbonate and 1.2 moles for calcium, and values less than 1 mole for all other components, as shown in Table 6.6-3.
- “Salt0” – This simulation is identical in setup and input parameters as the “Selected” case, except that it is set to use the dryout minerals and sequence shown in the “Salt0” column in Table 6.4-1. This case intentionally excludes salts other than halite, sylvite, and anhydrite, to maximize the residuals. This results in large residuals for most components (Table 6.6-3) and total loss for non-reactive components such as nitrate.
- “Salt1” – This simulation is identical in setup and input parameters as the “Selected” case, except that it is set to use the dryout minerals and sequence shown in the “Salt1” column in Table 6.4-1. This case is an alternative list that results in somewhat higher residuals than the “Selected” case for chloride, sulfate, and nitrate, and lower residuals for potassium and carbonate (Table 6.6-3).

All simulations were run using TOUGHREACT V3.1.1. Model results were extracted using CUTCHEM V2.0 for FLUX waters in fractures (Section 6.4.8). Predicted concentration time profiles for CO₂ and several aqueous species in fracture TOP FLUX waters are shown in Figures 6.6-9 through 6.6-13, as well as on plots in summary data files accompanying this report (Table 6.6-1).

Computed residuals at ~2,000 years for the three cases described above are shown in Table 6.6-3. The computed mass residuals output from simulations are also expressed in Table 6.6-3 as a percentage of the total mass influx percolating down the system for the same time period, through a 10-m-wide section encompassing the extent of dryout around the drift.

These percentages are shown to provide some point of reference. However, for reactive components, these percentages can significantly overestimate the actual extent of mass “loss.” This is because reaction source terms are not included in the mass influx and typically significantly exceed it (because the infiltrating pore water is fairly dilute; Table 6.2-1). For the non-reactive components chloride, nitrate, and to some extent sulfate (which can precipitate as anhydrite outside of the normative dryout procedure described in Section 6.4.5), these percentages are more representative of the total mass loss.

The time profiles shown on Figures 6.6-9 through 6.6-13 show that differences between the “Selected” and “Salt1” cases are insignificant and within the variability of model results introduced by the different initial water compositions (Section 6.7.2). As would be expected, in the “Salt0” case, the total loss of nitrate and sulfate is visible on the profiles of sulfate-to-chloride and nitrate-to-chloride ratios (Figure 6.6-10), although predicted ratios for this case are still largely within the natural variability (e.g., Table 6.2-1). The differences in the chloride residuals in the three cases considered (from <0.00 to 2.81 moles; Table 6.6-3) also do not affect model results significantly (Figure 6.6-10). The same is true for the large differences in fluoride and potassium residuals observed between the three cases (Figure 6.6-13). Note that relatively large residuals for total aqueous carbonate do not seem to significantly affect model results, because this component is quite reactive with respect to CO₂ gas and calcite.

One noteworthy observation is the difference between the “Salt0” case and the other cases regarding pH, total carbonate (Figure 6.6-9), and potassium (Figure 6.6-13) at times between about 600 and 1,000 years, when the boiling front collapses. The pH is observed to rise above ~9 during this time period, at the same time bicarbonate and potassium rise significantly. This can be explained by the dissolution of K₂CO₃, which forms during boiling in the “Selected” and “Salt1” case, but is excluded from the “Salt0” case. The additional rise in pH then causes the calcium and magnesium concentrations to decrease further during this time period (Figure 6.6-11), through increased precipitation of calcite and magnesium silicate. This process, in itself, is not the cause of the general trends of pH increase and strong calcium and magnesium depletion (compared to model results using older inputs; see, for example, Figures 6.6-5 and 6.6-6), but it appears to exacerbate these trends in the early stages of the boiling-front collapse. This process, however, has no visible impact on the predicted CO₂ concentrations (Figure 6.6-9). Another important observation from this sensitivity analysis is that the predicted water compositions after the time the drift wall rewets (at > ~1,280 years) are not significantly affected by the choice of dryout mineral assemblage.

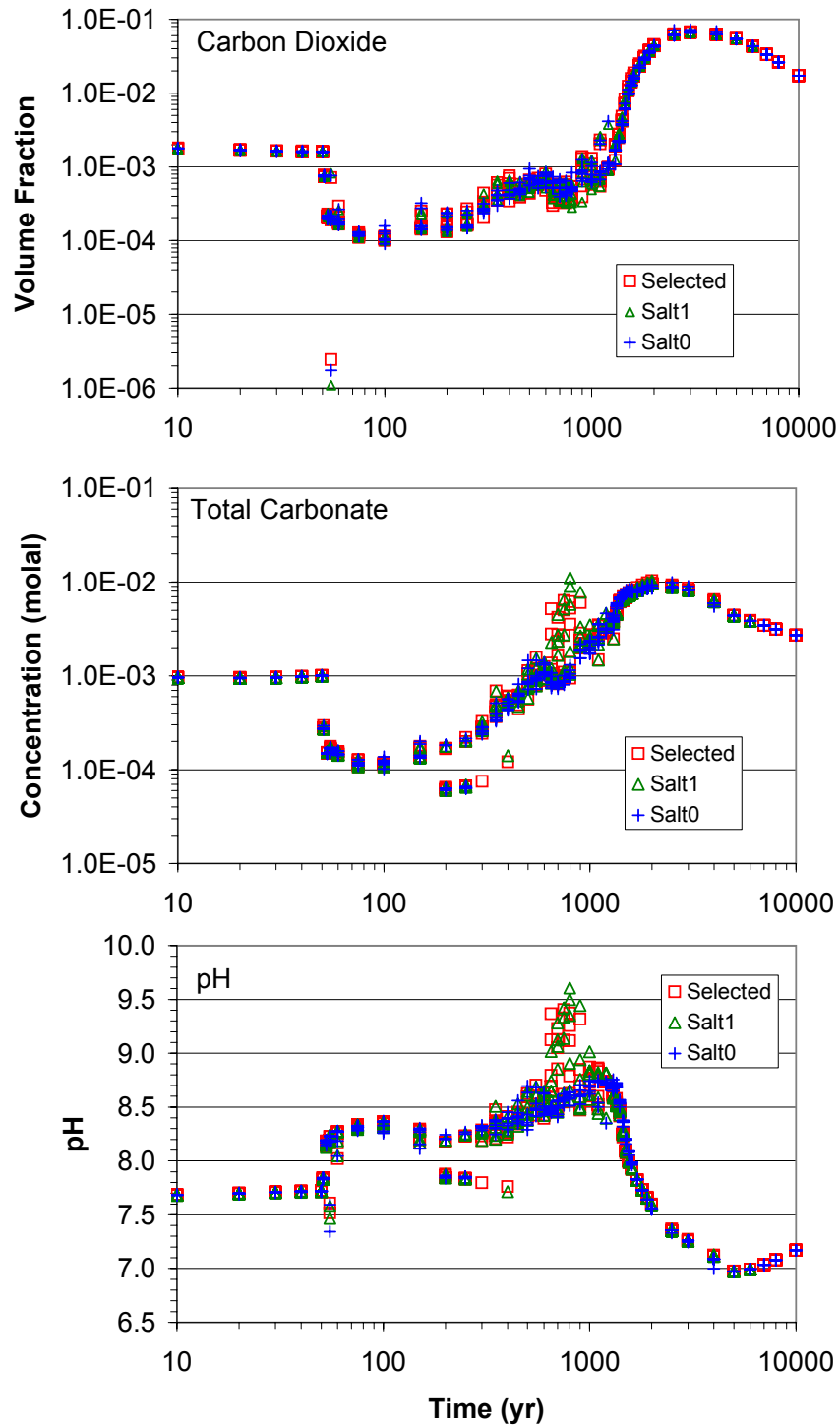
Table 6.6-3. Total Residuals at near 2,000 Years for Three Dryout Mineral Assemblages

Component	"Selected" (moles)	"Salt1" (moles)	"Salt0" (moles)	"Selected" % Influx ^a	"Salt1" % Influx ^a	"Salt0" % Influx ^a
Calcium	1.22	1.39	2.35	0.38	0.44	0.74
Magnesium	0.00	0.00	0.00	0.00	0.00	0.00
Sodium	0.00	0.00	137	0.00	0.00	25.60
Chloride	0.00	1.68	2.81	0.00	0.24	0.41
Silica	0.00	0.00	0.00	0.00	0.00	0.00
Carbonate	61.6	56.4	184	22	20	66
Sulfate	0.41	4.66	106	0.16	1.9	43
Potassium	0.34	0.05	325	0.73	0.11	711
Fluoride	0.00	0.00	26.5	0.00	0.00	334
Nitrate	0.00	0.75	14.4	0.00	2.3	45

Output DTNs: LB0705DSTHC001.002, LB0705DSTHC022.002 (files: *mbalance.out*).

^a Percentage of the cumulative vertical mass influx through a 10-m wide (horizontal) model section, assuming an average infiltration rate of 10 mm/yr, water density of 1,000 kg/s, time period of 1,984 years, and water composition W0 (Table 6.2-1, 20°C, calculated). For reactive components, these percentages can be high and not affect model results because reaction source terms are not included in the influx.

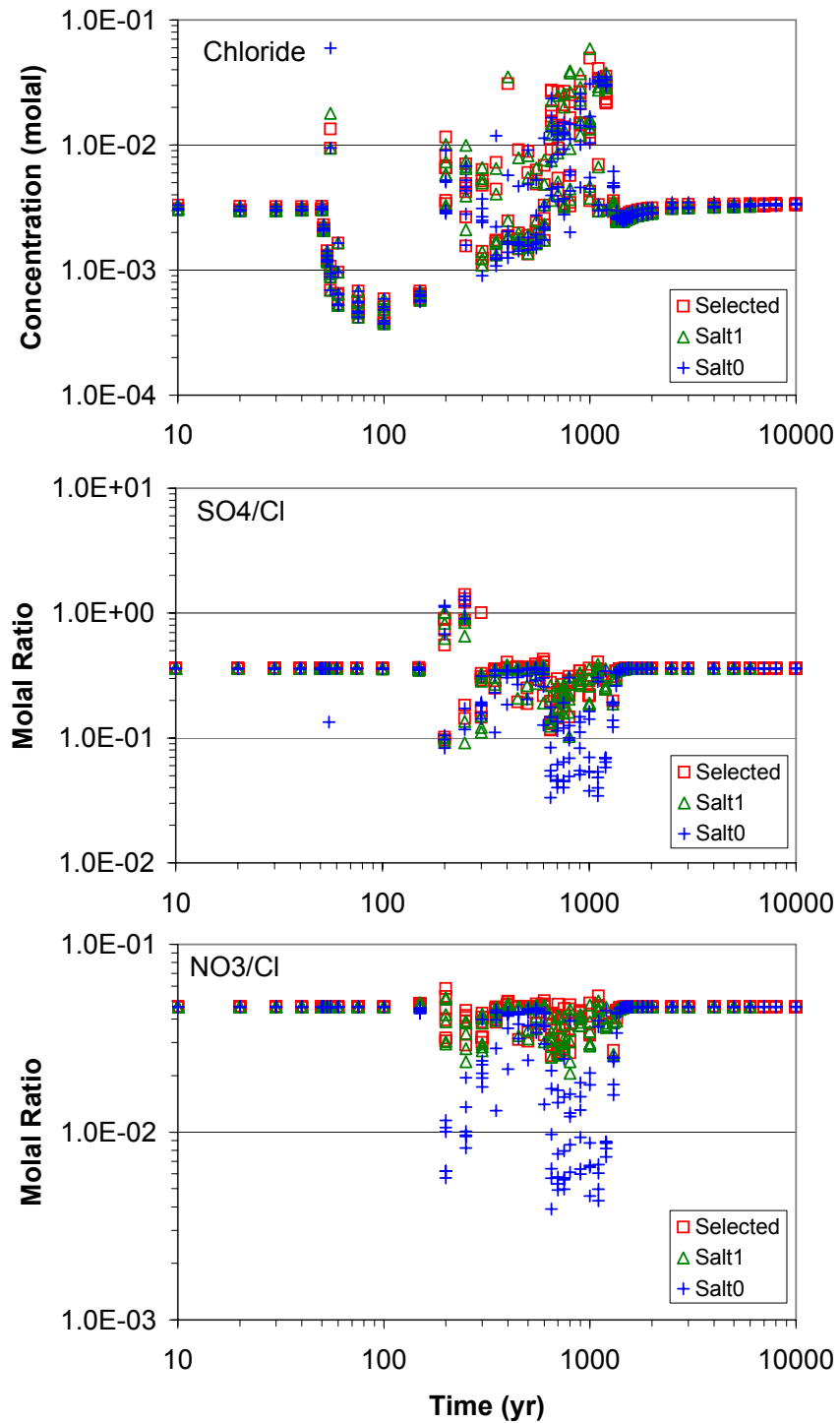
NOTE: See Table 6.4-1 for assemblages and sequences. Residuals are the sum (cumulative over time) over all the model gridblocks for which the dryout procedure (Section 6.4.5) has been applied.



Output DTNs: LB0705DSTHC001.001, LB0705DSTHC022.001.

NOTE: Data are from gridblocks exhibiting the highest liquid mobility in fractures above the modeled drift (TOP FLUX waters; see Section 6.4.8).

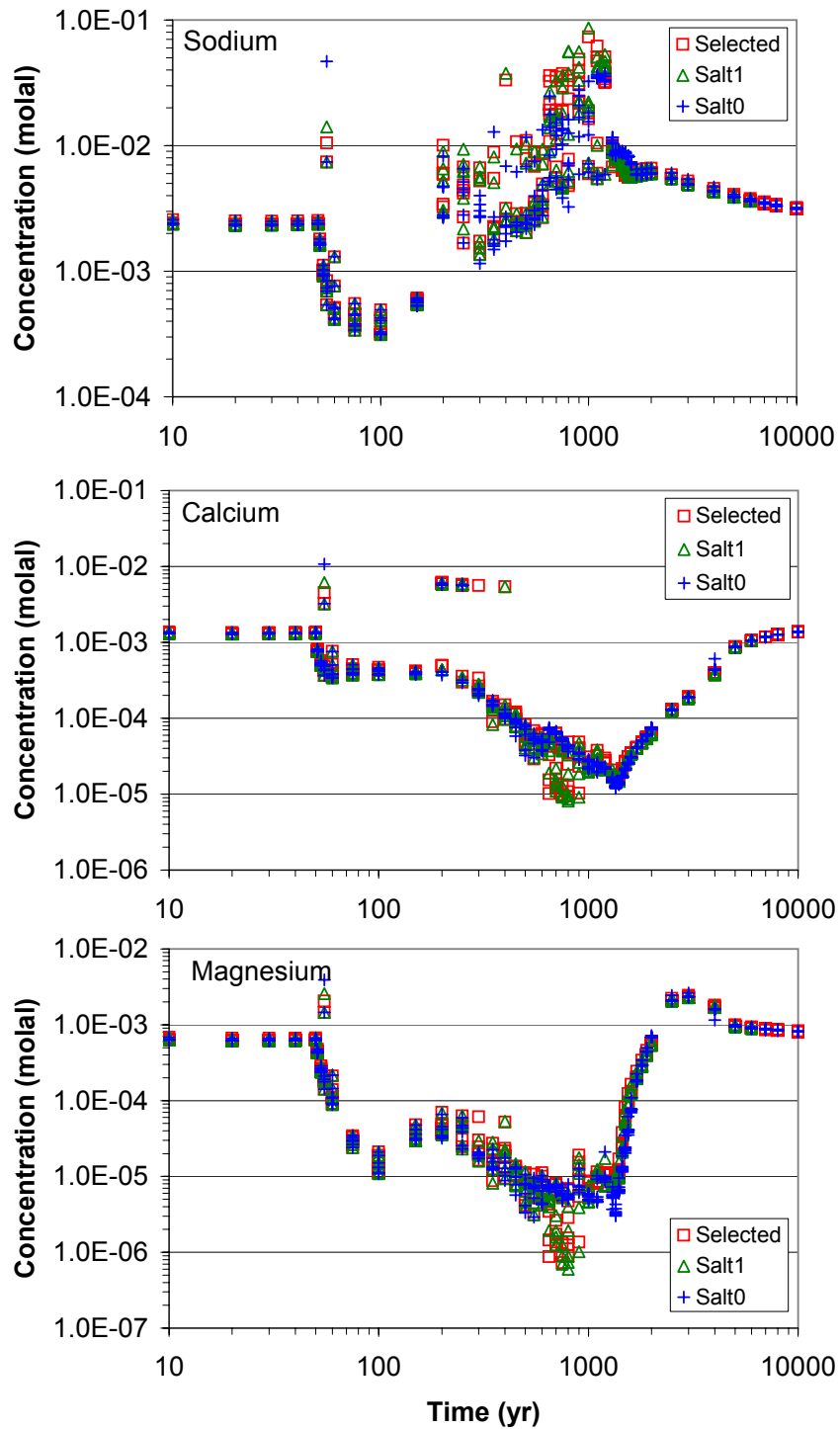
Figure 6.6-9. Sensitivity to Dryout Mineral Assemblage: Time Profiles of Modeled CO₂ Gas Concentrations, Total Aqueous Carbonate Concentrations, and pH



Output DTNs: LB0705DSTHC001.001, LB0705DSTHC022.001.

NOTE: Data are from gridblocks exhibiting the highest liquid mobility in fractures above the modeled drift (TOP FLUX waters; see Section 6.4.8).

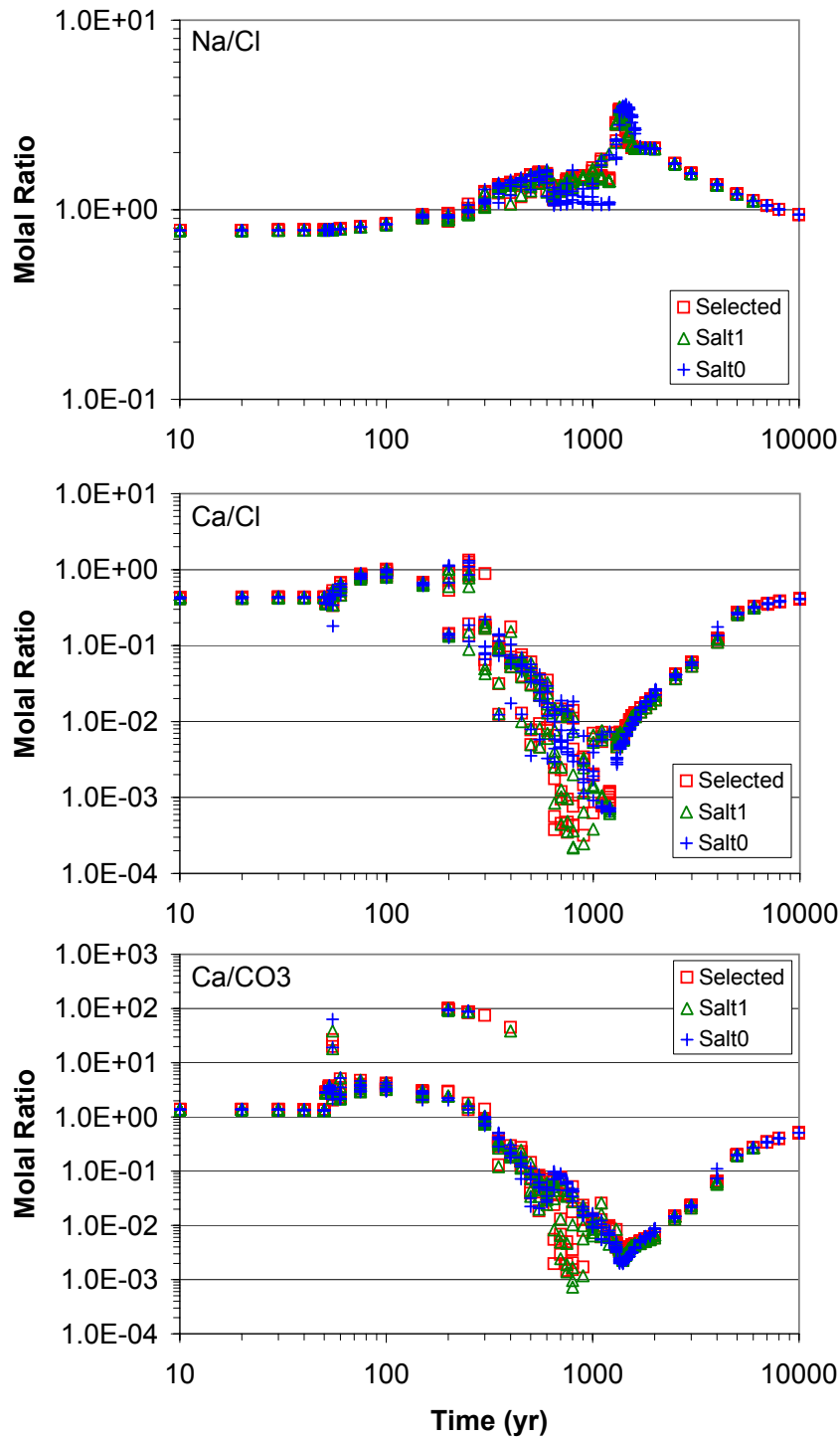
Figure 6.6-10. Sensitivity to Dryout Mineral Assemblage: Time Profiles of Modeled Chloride Concentrations, Sulfate to Chloride Ratios and Nitrate to Chloride Ratios



Output DTNs: LB0705DSTHC001.001, LB0705DSTHC022.001.

NOTE: Data are from gridblocks exhibiting the highest liquid mobility in fractures above the modeled drift (TOP FLUX waters; see Section 6.4.8).

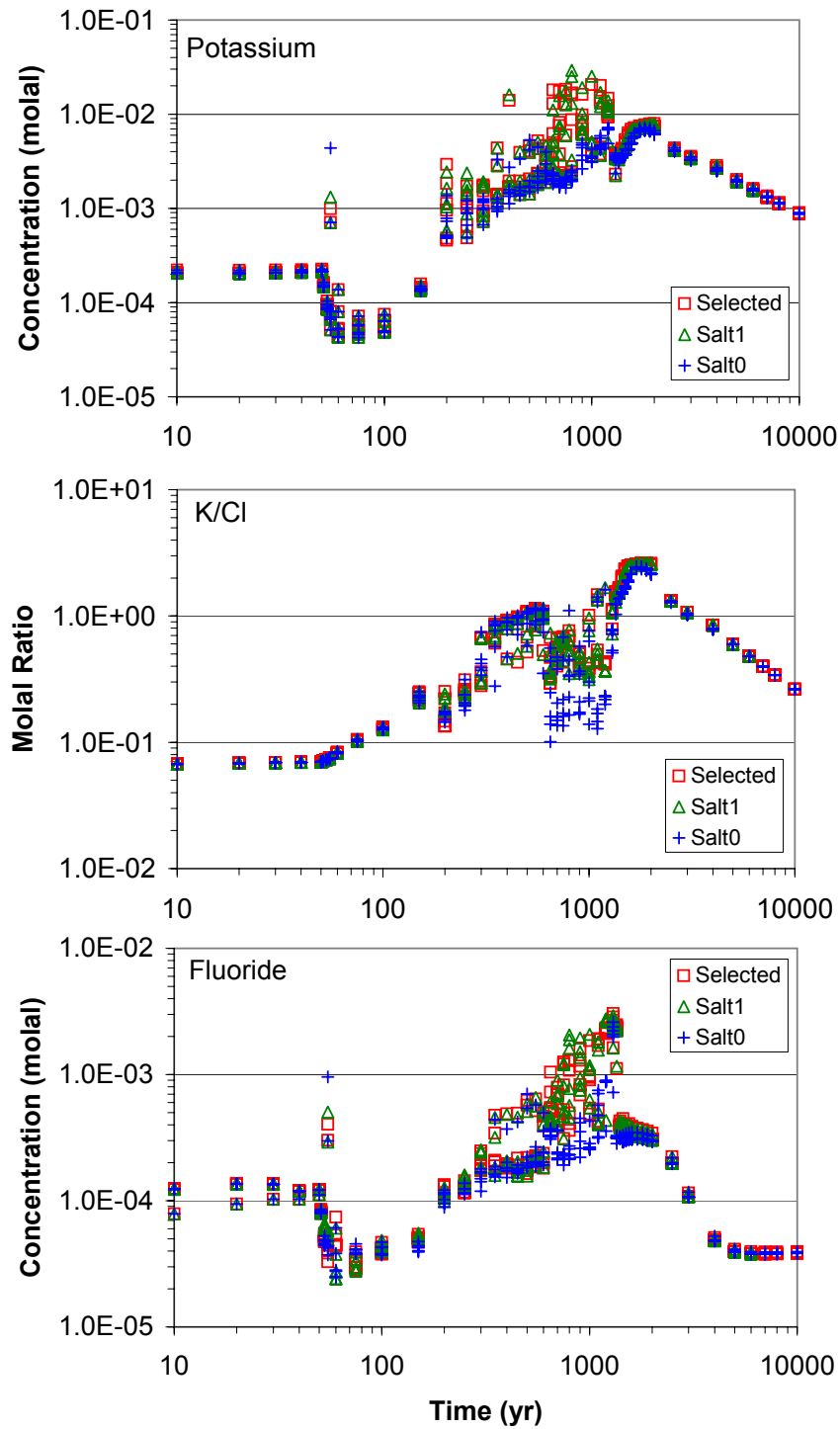
Figure 6.6-11. Sensitivity to Dryout Mineral Assemblage: Time Profiles of Modeled Sodium, Calcium and Magnesium Concentrations



Output DTNs: LB0705DSTHC001.001, LB0705DSTHC022.001.

NOTE: Data are from gridblocks exhibiting the highest liquid mobility in fractures above the modeled drift (TOP FLUX waters; see Section 6.4.8).

Figure 6.6-12. Sensitivity to Dryout Mineral Assemblage: Time Profiles of Modeled Sodium to Chloride, Calcium to Chloride, and Nitrate to Chloride Ratios



Output DTNs: LB0705DSTHC001.001, LB0705DSTHC022.001.

NOTE: Data are from gridblocks exhibiting the highest liquid mobility in fractures above the modeled drift (TOP FLUX waters; see Section 6.4.8).

Figure 6.6-13. Sensitivity to Dryout Mineral Assemblage: Time Profiles of Modeled Potassium and Fluoride Concentrations, and Potassium to Chloride Ratios

6.6.5 Sensitivity to Reaction Rates

Effective mineral reaction rates vary widely because the reactive surface areas of minerals in the subsurface are largely unknown. In addition, data on reaction rate constants are often lacking or have a large uncertainty. It has been well established that reaction rates determined in the laboratory are typically orders of magnitude larger than rates determined from field observations, and for this reason the input rate constants for most primary minerals in this study were significantly reduced from laboratory-determined values, as discussed in Appendix H. As a result, all simulations presented in this report make use of input rate constants that are reduced by 3 orders of magnitude for feldspars, biotite, and rhyolitic glass, and 2 orders of magnitude for clays compared to original data sources. This sensitivity analysis examines the effect of raising these rates back by the same amounts.

The following four cases are compared:

- “Base Case” – This is the base case against which other simulations can be compared. This case consists of one of the simulations (two-dimensional, with heat load) presented in Section 6.5.5, run with TOUGHREACT V3.1.1, using water W0 and inputs discussed in Section 4.1 (run thc7_81_w0). In this simulation, the input rate constants for the minerals of interest were set as shown in Table 6.6-4, column “Base Case” (from Appendix H).
- “BC Ambient” – This is one of the ambient simulation (one-dimensional, no heat load) presented in Section 6.5.5, run with TOUGHREACT V3.1.1, using water W0 and inputs discussed in Section 4.1 (run thc7_w0_amb). In this simulation, the input rate constants for the minerals of interest were set as shown in Table 6.6-4, column “Base Case” (from Appendix H).
- “High” – This case consists of the same simulation as “Base Case,” but with increased rate constants as shown in Table 6.6-4, column “High.”
- “High Ambient” – This case consists of the same simulation as “BC Ambient,” but with increased rate constants as shown in Table 6.6-4, column “High.”

All simulations were run using TOUGHREACT V3.1.1. Model results were extracted using CUTCHEM V2.0. Predicted concentration time-profiles for CO₂ and several aqueous species in fracture TOP FLUX waters (heat-load simulations) and one location in fractures at repository level (ambient conditions) are shown in Figures 6.6-14 through 6.6-16, as well as on plots in summary data files accompanying this report (Table 6.6-1).

The first important observation from this sensitivity analysis is that relatively steady concentration profiles with time, for reactive species, cannot be reproduced in the “High Ambient” case. Wide fluctuations occur in the predicted trends of ambient concentrations for CO₂ gas, pH, and most reactive species (Figures 6.6-14 through 6.6-16). These fluctuations respond in part to changes in infiltration rates at 600 and 2,000 years, as well as occurrences when some minerals completely dissolve (run out), in some cases shifting the reaction network and introducing sharp breaks in the predicted trends. Therefore, this case, by itself, shows that

the high rates used for this sensitivity analysis would not be appropriate for the simulations presented in this report.

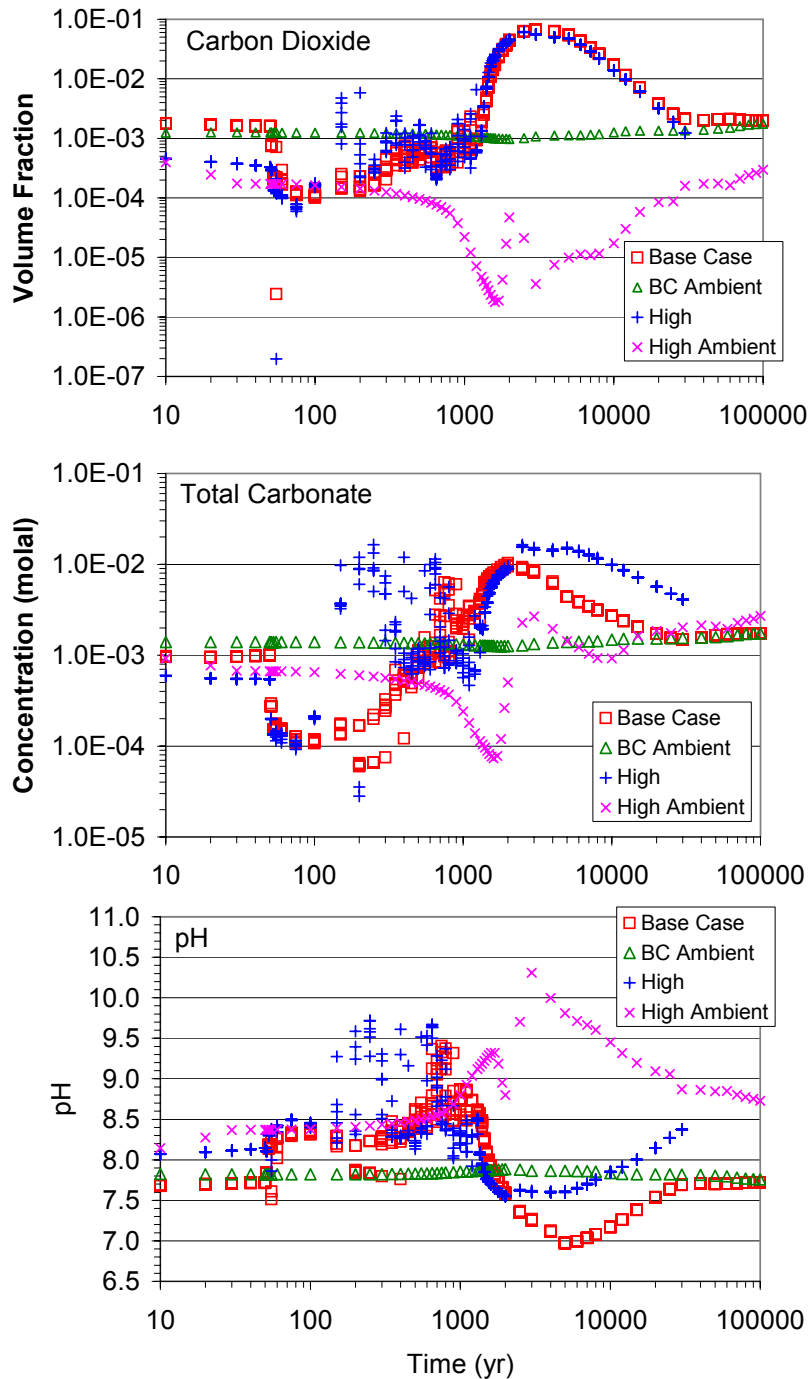
This analysis is also useful to show that despite the wide differences in predicted trends under ambient conditions, predicted trends under heat-load conditions are not affected very much for CO₂ gas (Figure 6.6-14). This is because the behavior of CO₂ gas responds mostly to the volatilization of dissolved carbonate species in matrix pore water (Section 6.5.5.4). As a result, the pH trend under heat-load conditions (which is itself strongly affected by the behavior of CO₂) is not as strongly affected as it is under ambient conditions (Figure 6.6-14). Species that are not strongly reactive, such as sodium and potassium, or those with concentrations dictated by the solubility of one phase, like silica (Figure 6.6-15), are also less affected than more reactive species such as calcium and magnesium (Figure 6.6-16). Conservative species like chloride are not affected (Figure 6.6-16), as would be expected.

These results indicate that in the system being modeled, under heat-load conditions, reactive processes are partly dominated by transport, dilution/concentration, and CO₂ volatilization processes. For this reason, changes in reaction rates have much less effect on predicted concentrations under heat-load conditions than at ambient temperatures. Therefore, constraining reaction rates with simulations of ambient conditions (no heat load) as reported in Section 6.5.5.1 is an important step in building confidence in the model results. Given these results, one could expect that results of heat-load simulations would not be very sensitive to variations in reaction rates that are within the range of values that do not significantly impact the results of ambient simulations.

Table 6.6-4. Sensitivity to Reaction Rates

Mineral	“Base Case”^a Rate Constants (mol/s/m²)	“High” Rate Constants (mol/s/m²)
Plagioclase	2.1×10^{-17}	2.1×10^{-14}
Sanidine	1.3×10^{-17}	1.3×10^{-14}
Rhyolitic glass	7.72×10^{-17}	7.72×10^{-14}
Biotite	9.30×10^{-17}	9.30×10^{-14}
Illite	1.73×10^{-16}	1.73×10^{-14}
Na-beidellite	1.52×10^{-16}	1.52×10^{-14}
Mg-beidellite	1.52×10^{-16}	1.52×10^{-14}
Ca-beidellite	1.52×10^{-16}	1.52×10^{-14}

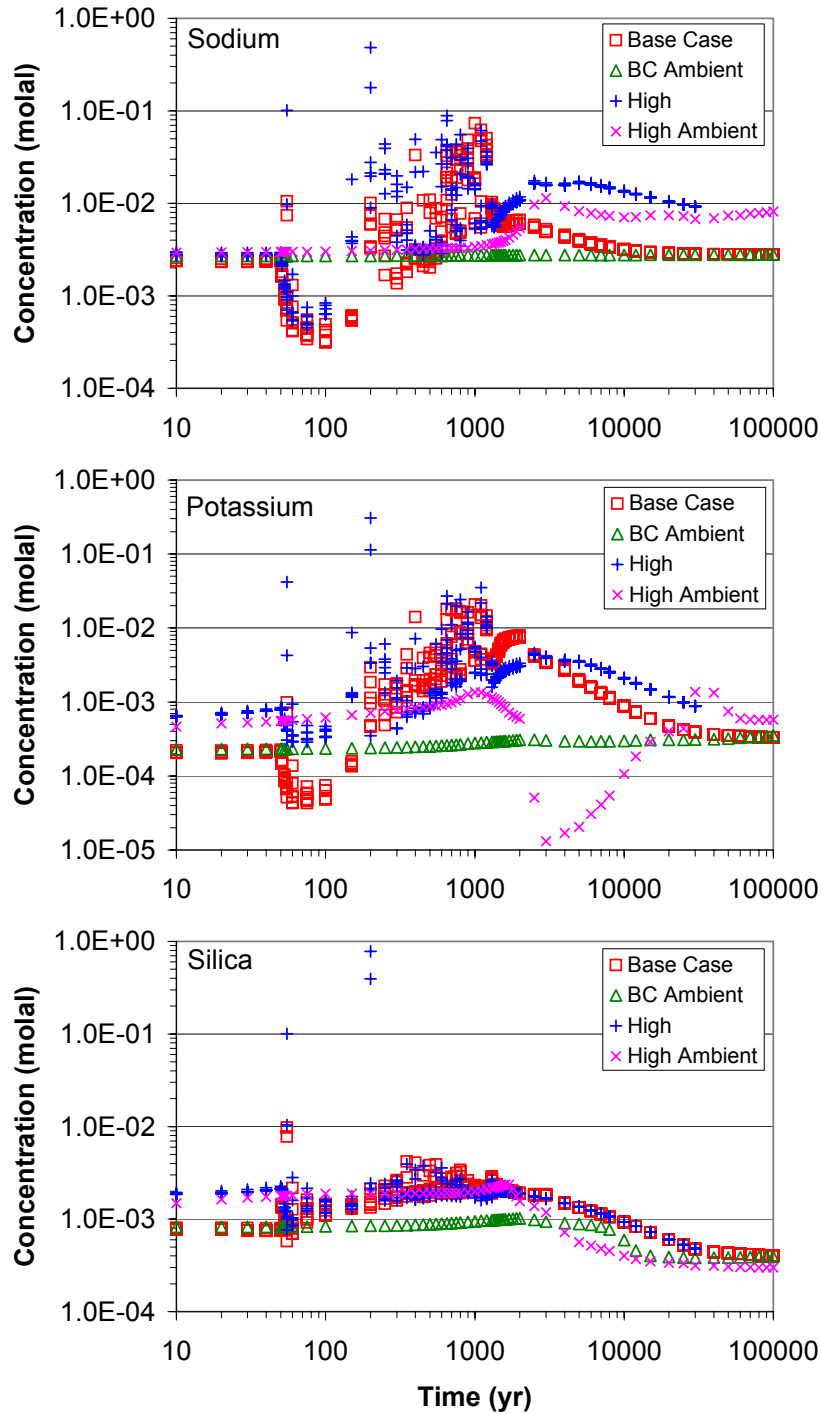
^a See Appendix H for sources of base-case rates.



Output DTNs: LB0705DSTHC001.001, LB0705DSTHC024.001.

NOTE: For heat load conditions (“Base Case” and “High”), data are from gridblocks exhibiting the highest liquid mobility in fractures above the modeled drift (TOP FLUX waters; see Section 6.4.8). For ambient conditions (no heat load; “BC Ambient” and “High Ambient”), data are from one gridblock at repository level. The simulation for the “High” case was ended at 30,000 years.

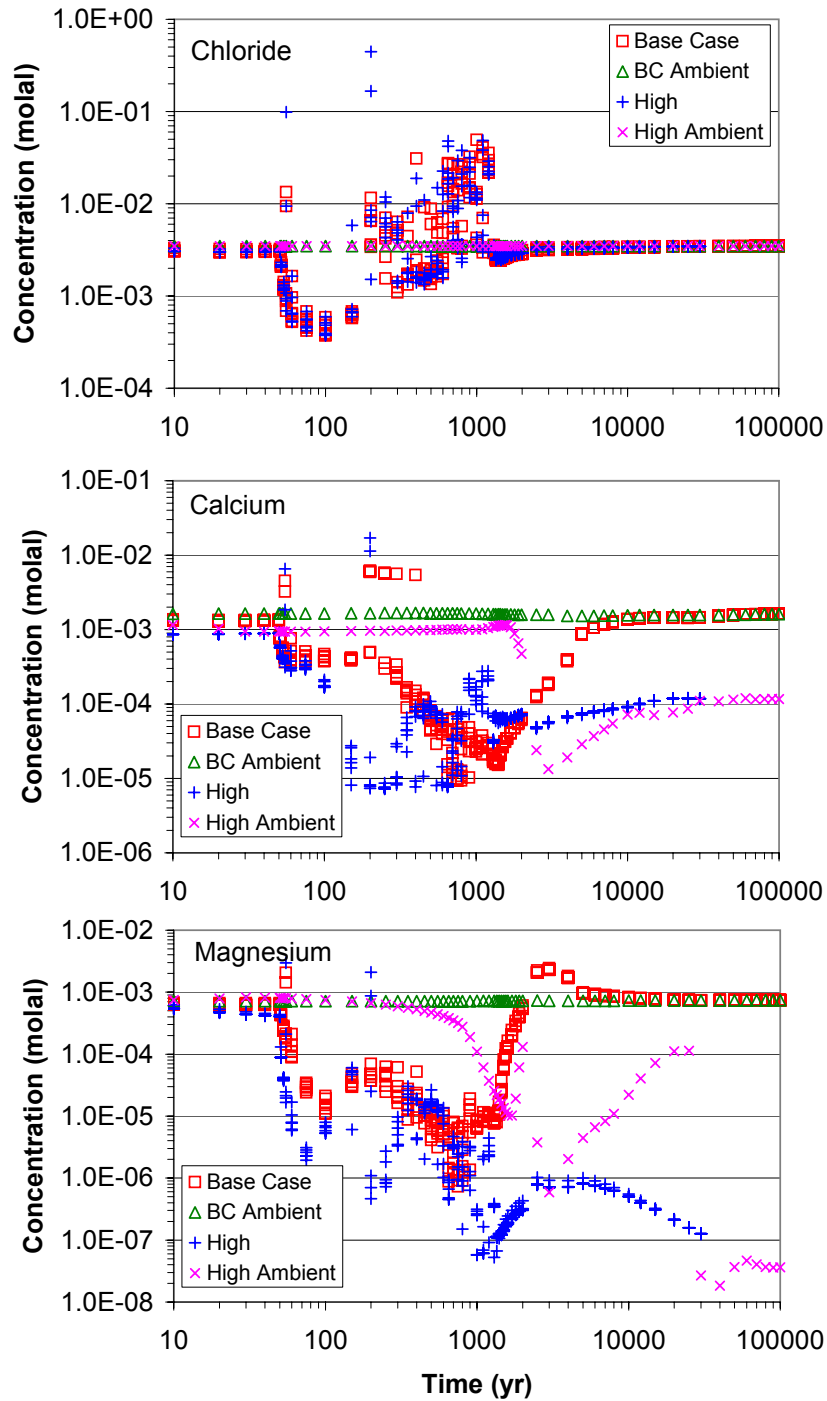
Figure 6.6-14. Sensitivity to Mineral Reaction Rates: Time Profiles of Modeled CO₂ Gas Concentrations, Total Aqueous Carbonate Concentrations, and pH



Output DTNs: LB0705DSTHC001.001, LB0705DSTHC024.001.

NOTE: For heat load conditions (“Base Case” and “High”), data are from gridblocks exhibiting the highest liquid mobility in fractures above the modeled drift (TOP FLUX waters; see Section 6.4.8). For ambient conditions (no heat load; “BC Ambient” and High Ambient”), data are from one gridblock at repository level. The simulation for the “High” case was ended at 30,000 years.

Figure 6.6-15. Sensitivity to Mineral Reaction Rates: Time Profiles of Modeled Sodium, Potassium, and Silica Concentrations



Output DTNs: LB0705DSTHC001.001, LB0705DSTHC024.001.

NOTE: For heat load conditions (“Base Case” and “High”), data are from gridblocks exhibiting the highest liquid mobility in fractures above the modeled drift (TOP FLUX waters; see Section 6.4.8). For ambient conditions (no heat load; “BC Ambient” and High Ambient”), data are from one gridblock at repository level. The simulation for the “High” case was ended at 30,000 years.

Figure 6.6-16. Sensitivity to Mineral Reaction Rates: Time Profiles of Modeled Chloride, Calcium, and Magnesium Concentrations

6.7 MODEL UNCERTAINTY

6.7.1 Potential Sources of Uncertainty

The simulations of THC processes include coupling among heat, water, and vapor flow; aqueous and gaseous species transport; kinetic and equilibrium mineral–water reactions; and feedback of mineral precipitation–dissolution on porosity, permeability, and capillary pressure (hydrologic properties) for a dual-permeability (fracture–matrix) system. As such, the THC seepage model takes into account the effects of mineral dissolution and precipitation, carbon dioxide exsolution and transport in the region surrounding emplacement drifts, and resulting changes to porosity, permeability, seepage, and chemical composition of percolating waters. The large number of input parameters, numerical methods implemented in simulating these complex coupled processes, and simplification and approximations pertaining to the physical setup of the model all contribute to uncertainties in the predictions from these models. Uncertainties in model input data that could affect calculated water and gas compositions include:

- Thermodynamic data (equilibrium constants for mineral–water reactions and aqueous species dissociation)
- Kinetic data (rate constants, reactive surface areas, and activation energies)
- Initial compositions of pore water and pore gas
- Initial composition of infiltrating water and gas
- Infiltration rates
- Transport parameters (diffusion coefficients of aqueous species and gases, tortuosity)
- Initial rock mineralogy (model location and stratigraphy)
- Number of geochemical constituents (including the simulations)
- Number and types of potential secondary mineral phases
- Rock thermal, physical, and hydrologic properties (including input data for both water-saturated and unsaturated rock).

Process-model uncertainties also may affect the calculated water and gas compositions. These include:

- Formulation of models to simulate fluid flow in dual permeability media (e.g., fracture–matrix interactions; and relative permeability and saturation–capillary pressure models)
- Activity coefficient models

- Kinetic mineral precipitation and dissolution models
- Inclusion or exclusion of certain specific thermal, hydrologic, or chemical processes (e.g., active-fracture model, vapor-pressure lowering, mineral solid solutions, redox reactions).

Uncertainties in the setup of the model could also affect the results of the THC seepage model. These include:

- Physical model representation (stratigraphic and geologic extrapolations)
- Representation of the fracture and matrix continua in the model mesh
- Model discretization (in space and time)
- Boundary conditions.

Of these uncertainties, those directly affecting chemical and transport processes would be most likely to have the most effect on predicted water and gas compositions. Such uncertainties, their treatment in the model, and their effect on model results are summarized in Table 6.7-1.

Note that temperature is also a critical parameter affecting modeling results, although it cannot be considered an uncertainty by itself (temperature can generally be predicted to within a few degrees; therefore, it is not included in Table 6.7-1). Temperature directly affects equilibrium constants and reaction rates, the degree of water evaporation and boiling, and the amount of carbon dioxide volatilization from pore water, with direct implications for computed water and gas chemistries. Parameters affecting predicted temperatures could significantly affect computed aqueous and gas species concentrations. However, important changes in design heat load are likely to affect model results more than uncertainties associated with input parameters used to calculate temperatures (e.g., rock thermal conductivity and heat capacity). In this report, only the heat load from the current repository design is considered. This heat load leads to temperatures in the vicinity of emplacement drifts that exceed the boiling point of water for several hundred years at center-repository locations if ventilation is not maintained after the 50-year preclosure period. The increased water–rock–gas interactions resulting from higher temperatures are expected to affect water chemistry and flow to a greater extent than if a lower heat load were considered. However, some of the effects of elevated temperatures, such as dryout and reduced permeabilities caused by mineral precipitation, could have positive aspects with respect to repository performance.

Table 6.7-1. Summary of Uncertainties Affecting Chemical Processes in the THC Seepage Model

Category	Issue	Treatment	Consequences
<p>Conceptual uncertainties</p>	<p>Geochemical system considered (minerals, gases, and aqueous species)</p>	<p>Treated by including major rock-forming minerals, major aqueous species, and major gases of interest (CO₂, air, water vapor) in the system, and also minor minerals such as clays. Effects of secondary mineral phase precipitation is most uncertain at higher temperatures. Uncertainty is limited under ambient conditions if ambient water concentrations can be reproduced. Trace minerals and aqueous species are not considered (not within the current scope for the THC seepage model). However, results of model validation (Section 7) against the Drift Scale Test and other experiments suggest that the geochemical system, as modeled, is constrained enough to reproduce the experimental data within validation criteria. Also, the range of incoming waters considered in the model captures, at least in some part, the range of uncertainties related to the geochemical system.</p>	<p>Precipitation of secondary phases not currently included in simulations could affect the predicted composition of waters around the drift at high temperature. Reactions involving trace minerals (e.g., other clay minerals or Mg, Fe, Mn minerals) could affect pH, which in turn could affect the precipitation/dissolution of other mineral phases and indirectly affect the concentrations of major species. The type of mineral precipitating could also affect the calculated porosity change (i.e., effect of different molar volume), although this effect would be minimal because the bulk of the precipitation consists of amorphous silica. Uncertainties affecting the precipitation of secondary phases would increase at near dryout conditions; however, such conditions (i.e., small liquid saturations) are not conducive to seepage.</p>
	<p>Drift wall boundary conditions</p>	<p>Externally prescribed conditions of relative humidity or CO₂ concentrations at the drift location are not considered. Evaporative concentration effects (due to ventilation) are indirectly taken into account by “downstream” in-drift evaporation models.</p>	<p>Boundary conditions of pressure and relative humidity in the drift could affect evaporative concentration effects at the drift wall, mostly during the preclosure ventilation period. In-drift interactions are not considered (this is not a goal of the THC seepage model).</p>
	<p>Precipitation/nucleation kinetics</p>	<p>Not treated. This affects minerals such as silica and calcite, which have fast reaction rates. Silica precipitation is modeled with a very fast reaction rate.</p>	<p>In areas where rapid boiling occurs, predicted aqueous silica concentrations could be overestimated, and silica precipitation underestimated. However, the liquid saturation in these areas is very small, and therefore the actual amounts of silica are minute.</p>

Table 6.7-1. Summary of Uncertainties Affecting Chemical Processes in the THC Seepage Model (Continued)

Category	Issue	Treatment	Consequences
Conceptual uncertainties (continued)	Water chemistry is not computed below a set water saturation limit (10^{-5}) or above a set ionic strength limit (4) (activity coefficient model limitations)	Salt precipitation in the last remaining water when boiling or evaporating is taken into account using a simple approach (Section 6.4.5). These salts are then available for dissolution upon rewetting, providing a conceptually correct (although simplified) representation of actual processes accompanying dryout and rewetting.	The type and sequence of salts assumed to precipitate upon dryout could affect computed water compositions at early stages of rewetting. Sensitivity analyses in Section 6.6.4 partially address this issue. Also, during the initial rewetting stage, the liquid saturation is low and the associated volume of water is small, immobile, and unlikely to contribute to seepage.
	Vapor pressure lowering due to capillary pressure and salinity	Capillary pressure effect is treated, but salinity effect is not. Also, the maximum capillary pressure in dried rock is uncertain. Here, it is limited to $\sim 1,000$ bar. The previous model revision compared simulations with and without vapor pressure lowering effect from capillary pressure.	A too-high-limit capillary pressure could result in too high water retention in the rock matrix. Underestimating or neglecting vapor-pressure lowering could increase the effect of evaporative concentration around the drift, resulting in higher water salinities.
	Oxidation-reduction processes are neglected	Not treated (considers only oxidized conditions). Oxidizing conditions prevail in the unsaturated zone at Yucca Mountain such that the redox species considered in the THC seepage model (iron and sulfate) occur only in their oxidized state.	Limited anticipated effect because of the prevailing oxidized conditions. Likely no effect for iron and sulfate in the current models. Redox reactions involving microbial processes and species not presently modeled (nitrates, phosphates) could have a limited effect on pH.
	Mineral solid-solutions	Ideal solid-solution treatment for clays; fixed-composition solid-solutions for plagioclase, sanidine, and clinoptilolite. Individual mineral phases with fixed solid-solution compositions (determined by analysis) are included in the simulations and their compositions are used to compute equilibrium constants for these phases.	Limited anticipated effect because solid solutions are partially treated as described in the adjacent table column. This primarily affects the composition of precipitating zeolites.
	Ion-exchange and surface complexation	Not explicitly treated. However, precipitation/dissolution of mineral solid solutions and pure end-member phases (for clays and zeolites, respectively) accounts for this to some degree. Dominant primary rock minerals in the repository host units are not strong ion exchangers (for major ions). THC seepage simulations do not include trace elements that could be strongly affected by surface complexation.	Limited effect for the current application range of the THC seepage model. However, a limited shift in the predicted concentrations of Na, K, Ca, and Mg could still affect significantly the composition of end-brines upon complete evaporation.

Table 6.7-1. Summary of Uncertainties Affecting Chemical Processes in the THC Seepage Model (Continued)

Category	Issue	Treatment	Consequences
Conceptual uncertainties (continued)	Capillary pressure effect on chemical potentials of reacting species	Not treated.	Could potentially shift predicted concentrations of some species and affect the volatilization of CO ₂ . However, these effects would only occur at very small liquid saturations (when the capillary pressure is high), and thus affect very small amounts of water.
Data uncertainties	Infiltration water and initial pore-water composition	Four alternate water analyses are used in the current model revision, covering a range of compositional variability for pore waters in repository host units. Uncertainty can be assessed by comparing predictions of ambient water compositions with measured ambient pore-water compositions and pore-gas CO ₂ concentrations.	Input water compositions affect predicted water compositions around the drift, and likely more so through evaporation/dilution and infiltration/transport than through reaction.
Carbon dioxide partial pressures	Composition of infiltrating water input into the model essentially dictates the boundary CO ₂ pressure; therefore, the uncertainty in infiltrating water composition overcomes this uncertainty. However, various infiltrating waters are assumed to equilibrate at the same boundary CO ₂ pressure (10 ⁻³ bar).	A large effect is not expected within the possible range of observed natural concentrations because the range of thermally induced CO ₂ partial pressures is much larger than (and thus overwhelms) background concentrations. Sensitivity analyses in Section 6.6.3 show no significant effect of raising the top model boundary CO ₂ pressure to 10 ⁻³ bar.	
Thermodynamic and kinetic data	Treated partly through sensitivity studies on long-term behavior of ambient system chemistry (Section 6.5.5.1), assuming a fixed infiltration rate and different thermodynamic data for clays and zeolites (the model is very sensitive to the thermodynamic data for these minerals). When possible within the uncertainty of the original data, treated by revising the data to reproduce observed water compositions and mineralogical data. Other uncertainties treated through model validation (Drift Scale Test and laboratory experiments).	Currently one of the main uncertainties affecting predicted water compositions around the drift. However, it can be constrained by adjustments and model validation against observed data, such that ambient simulations predict concentrations consistent with observed values (see Section 6.6.5).	
Host rock mineralogy	Treated in previous model revisions (Table 6-1) by considering alternative drift locations (Ttpmn versus Ttppl host rock unit), showing no significant effects. Bulk chemical compositions of the repository host units do not differ significantly.	No significant effect on the predicted compositions of major aqueous species. Small amounts of fast-reacting minerals containing elements present in minor quantities in pore water (e.g., fluorite) can have a large effect on the predicted concentrations of these minor species (e.g., F ⁻).	

Table 6.7-1. Summary of Uncertainties Affecting Chemical Processes in the THC Seepage Model (Continued)

Category	Issue	Treatment	Consequences
Data uncertainties (cont.)	Infiltration rates	Alternative infiltration rate scenarios have been used in previous model revisions.	Between 6 and 25 mm/yr, there is a small effect on predicted concentrations at the drift wall. The effect would be greater under lower rates of infiltration (when reaction effects start to dominate transport), but such conditions would be less likely to cause in-drift seepage. At high-infiltration rates, most conducive to in-drift seepage, water compositions are more a function of transport than of reaction with host rock minerals, such that the uncertainty regarding the composition of the infiltration water, rather than the rate of mineral dissolution/precipitation, becomes more important.
Parameter uncertainties	Heterogeneity	The current model assumes homogeneous fracture permeability. Heterogeneous fracture permeability is addressed specifically in another study (SNL 2007 [DIRS 177413]) and was also addressed in an earlier model revision (Table 6-1). Heterogeneity in matrix properties not treated. Local heterogeneity in mineralogy not treated; however, the bulk composition of host rocks is fairly uniform. Heterogeneity in initial water geochemistry not treated directly; treated indirectly through testing with alternate water compositions.	Heterogeneity has no significant effect on predicted water compositions but can have effects on seepage (SNL 2007 [DIRS 177413]).
	Transport parameters (effective diffusivity, gas relative permeability)	Sensitivity analysis to different CO ₂ diffusion coefficient values (increase by factors of ~3 and ~10) and different gas relative permeability functions (Section 6.6.3). Sensitivity to diffusion coefficient for aqueous species was not investigated. However, tortuosity was changed from 0.2 to 0.7 between earlier report revisions without noticeable effect.	CO ₂ diffusivity appears to be an important factor affecting predicted calcium and magnesium concentrations through its effect on Ph, which affects calcite and magnesium silicate precipitation (Section 6.6.3).

6.7.2 Evaluation of Model Result Uncertainty

Model sensitivities to key input parameters are evaluated through the use of several input water compositions (Table 6.2-1, Section 6.5.5) and systematic analyses of the model sensitivity to time discretization (Section 6.6.1), model revisions including TOUGHREACT upgrades (Section 6.6.2), CO₂ transport (Section 6.6.3), dryout mineral assemblage (Section 6.6.4), and mineral reaction rates (Section 6.6.5). Developmental model runs with differing input parameters (Table 6-1) also provide a qualitative assessment of the model uncertainty. Furthermore, confidence in the model is gained by comparing model results against data from the DST (Section 7), and improving the model conceptualization and mathematical formulation (through the developmental history of this model; Table 6-1) to yield a reasonably good agreement between calculated and measured data.

In this study, the spread in predicted concentrations of aqueous species and CO₂ gas concentrations is related to:

- The natural variability of input water compositions (Table 6.2-1, Figure 6.2-4)
- The location (center or edge) within the repository
- Ranges of input parameters other than water composition (Section 6.6).

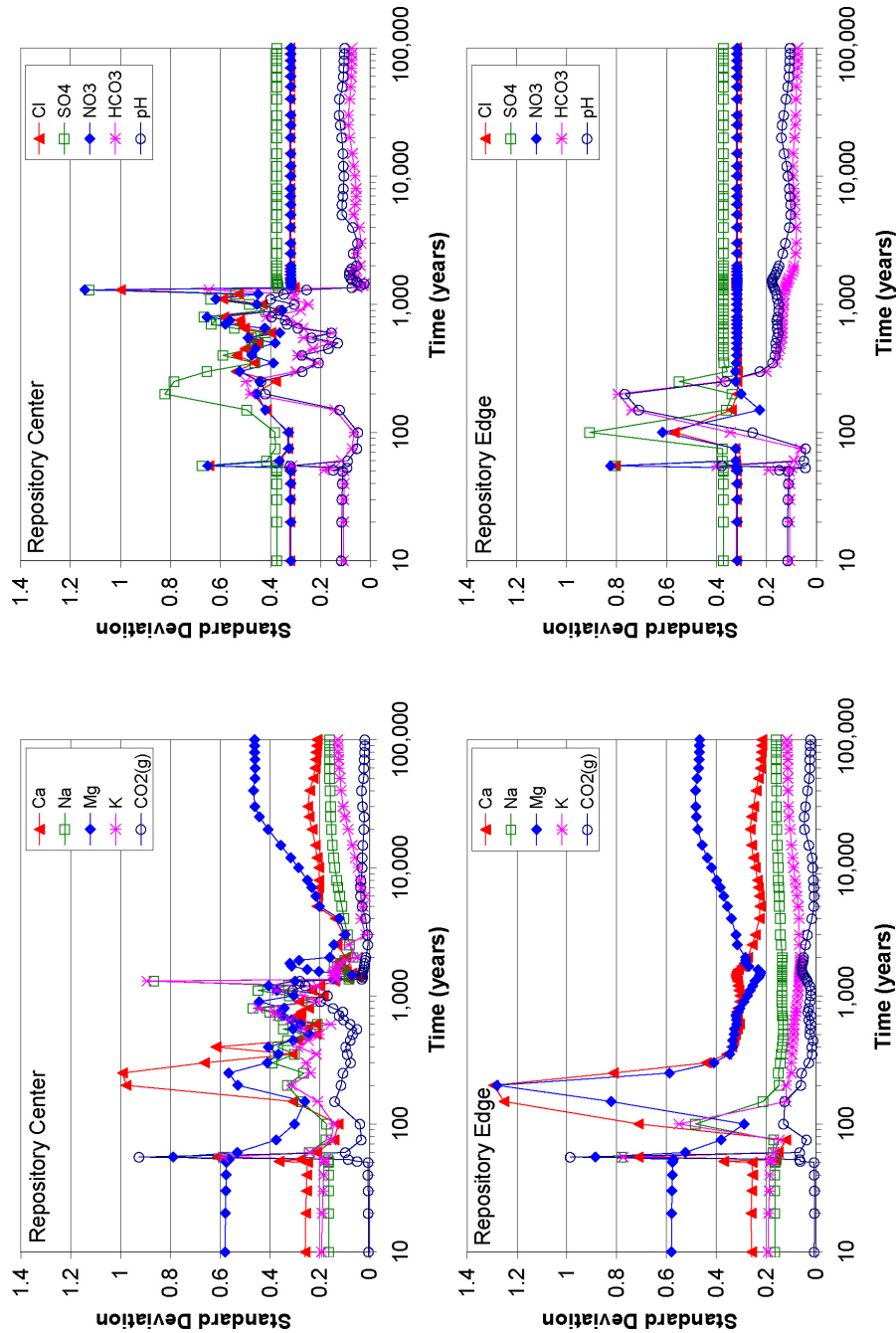
Summary statistical data including minimum, maximum, and standard deviations in differences of model results (i.e., predicted concentrations in fracture TOP FLUX waters) for the four input water compositions considered (i.e., combined W0, W8, W9, and W10 data) are included in Excel spreadsheets accompanying this report, and submitted to the TDMS under Output DTN: LB0705DSTHC008.001. The names of these files are *frac_stat_top-flux81.xls* for repository-center conditions, and *frac_stat_top-flux162.xls* for repository-edge conditions. A subset of these data is shown in Figure 6.7-1, which shows the relative spread in model results expressed as standard deviations of pH values and standard deviations of logarithms of molalities for several important species. This spread is wide during the boiling period, with standard deviations up to ± 1.3 log units for calcium and magnesium (thus, a spread of more than two orders of magnitude). The spread is wider in the repository-edge case, because of the marked differences in calcium and magnesium concentrations predicted using water W8 and the other waters (Figures 6.5-18 and 6.5-20) for repository edge conditions (see discussion in Section 6.5.5.4). Conservative species like chloride and nitrate show essentially the same standard deviations, as would be expected, with values ranging between about ± 0.3 and ± 0.6 log units. The conservative behavior means that the standard deviations for nitrate and chloride should also closely match the values for the initial solutions. Changes in these values occur only during rewetting when previously precipitated salts dissolve, and depend on the model implementation of salt precipitation during dryout (Sections 6.4.5 and 6.6.4). The standard deviations for sulfate vary somewhat more than for nitrate and chloride, because dryout is not required for the precipitation of anhydrite to occur. The parallel behavior of pH and bicarbonate results in almost identical trends in standard deviations (Figure 6.7-1).

The spread for slowly reacting species are mostly constrained by heat- and vapor-transfer processes that are well predicted by the DST THC submodel (Section 7.1). CO₂ diffuses readily and its concentration is mostly a function of the temperature and displacement by water vapor due to boiling, thus resulting in a relatively small spread in predicted concentrations for

simulations using the same rock properties and transport parameters (Figure 6.7-1). However, uncertainties in these parameters could significantly increase this spread, as observed in the simulations presented in Section 6.6.3 for the case of increased CO₂. In this case, the increase in diffusivity affects predicted calcium and magnesium concentrations by orders of magnitude.

Uncertainties in kinetic and thermodynamic data could affect the standard deviations shown in Figure 6.7-1, although the results of model validation against the DST (Section 7) and other laboratory experiments (Dobson et al. 2003 [DIRS 165949]), as well as the results of simulations of ambient conditions (Section 6.5.5.1), suggest these data are constrained to the extent that the model results are generally consistent with measured data. The model validation results (Section 7) also provide confidence that some of the other uncertainties listed in Table 6.7-1 may not significantly affect the spread in model results. This could be because model validation results are either not very sensitive to these uncertainties (at least over the period of time covered by the validation simulations) or that the effects of some of these uncertainties cancel out.

One model validation criterion for use with the DST THC submodel (Section 7) is that gas and aqueous species concentrations are predicted to within an order of magnitude, resulting in an acceptable range for DST comparisons of two orders of magnitude. The relative spread in the concentrations predicted with the THC seepage model (considering all four starting waters) is also about two orders of magnitude during the boiling period (about ± 1 log unit; Figure 6.7-1). However, after the boiling period, the spread is significantly reduced (about ± 0.5 log units; Figure 6.7-1) and mostly reflects the variability in starting water compositions.



Source: Output DTN: LB0705DSTHC008.001.
 NOTE: Standard deviations are computed using data presented in Section 6.5.5.4 for simulations using waters W0, W7, W8, and W9 (spread of combined results for fracture TOP FLUX waters). Standard deviations represent:

- For pH, standard deviation of pH values in (±) pH units.
- For other data, standard deviation of logarithmic molalities: i.e., (±) change in log₁₀ values of concentrations (thus, a value of 0.5 corresponds to a total spread of one order of magnitude).

Figure 6.7-1. Standard Deviations in Predicted Concentrations

7. VALIDATION

This section describes models and data used to validate the THC seepage model and input for the THC seepage model. Validation of the model is accomplished through comparison of simulation results from a submodel of the THC model to data collected from the Drift Scale Test (DST) and to laboratory experiments that explore various specific aspects of the model. The DST THC submodel is derived from the THC seepage model, relying on the same conceptual model, modeling the same coupled processes in the same manner, and using many of the same input data (i.e., intrinsic physical, hydrologic, thermodynamic, and kinetic parameters). Because the DST THC submodel is a special case of the THC seepage model, evaluation of the DST THC submodel serves to validate the THC seepage model.

The DST THC submodel and comparison of model simulation results to measured data are presented in Section 7.1. The validation of the THC models by comparison of DST THC submodel results with chemical data for water and gas samples is subject to a variety of uncertainties. These uncertainties are discussed in detail throughout Section 7, but can be summarized as follows. First, thermal-hydrologic (TH) processes can lead to spatial differences in the chemistry of water and gases by a few orders of magnitude (Section 7.1.10.2) over very small increments in temperature as a result of boiling and mineral–water reactions. In contrast, temperature exhibits much less spatial variation because it is controlled mainly by conduction in the rock matrix. Second, strong differences in aqueous species concentrations that develop in fractures and the adjacent matrix can be maintained, owing to the slow rates of diffusion of aqueous species between them (Section 7.1.11.3). Third, changes that the samples undergo during their extraction from the rock (e.g., cooling, degassing, condensation) have the potential for shifting the aqueous species compositions. Some measured quantities, such as pH, are sensitive to liquid-gas interactions such that shifts in water composition can be orders of magnitude. Therefore, differences between the model results and the measured data are likely, just from the standpoint of the sample collection methods (effect of the extent of volume-averaging of water and gas samples collected from boreholes) and the choice of data from the model results to compare to the measured data (point location, averaged, fracture or matrix). The approach to model validation acknowledges these uncertainties in the evaluation of model–data comparisons, in establishing and applying the validation criteria, and in the description of uncertainty that is provided for downstream use of THC seepage model results. Sources of data used for model validation are shown in Table 7-1.

Methods and criteria for validating the THC seepage model through the DST THC submodel are described in Section 7.1.7; the validation results are described in the rest of Section 7.1. For Level I validation, Section 2.2.1.2 of *Technical Work Plan for: Revision of Model Reports for Near-Field and In-Drift Water Chemistry* (SNL 2007 [DIRS 179287]) specifies the following steps for “Confidence Building During Model Development.” The development of the THC seepage model has been conducted according to these validation requirements in order to establish the scientific basis for the model, as follows:

1. *Selection of appropriate input parameters and/or input data, assumptions, simplifications, and physical principles, consistent with the intended use of the model, and discussion of how the selections build model confidence.*

The inputs to the THC seepage model have been obtained from controlled sources (see Table 4.1-1, Section 4.1), or, if older data, have been evaluated and justified for intended use (Section 4.1) in this report. Selection and development of input and design parameters is described in detail in Sections 4.1, 6.2, 6.4.8, 6.5, and Appendix C. Model assumptions have been described in Section 5. Detailed discussion about model concepts can be found in Section 6.2.

2. *Description of important future state (aleatory), parameter (epistemic), and alternative model uncertainties and how they are represented, commensurate with the intended use of the model.*

Discussion of sensitivity analyses and model uncertainties is provided in Sections 6.6 and 6.7, respectively. A summary discussion on uncertainties and their impact is given in Section 8.4.

3. *Demonstration that model predictions adequately represent the range of possible outcomes, consistent with important uncertainties and modeling assumptions, conceptualizations, and implementation.*

Consistency with physical principles is demonstrated by the conceptual and mathematical formulation in Sections 6.2 and 6.4, and the selection and use of the TOUGHREACT V.3.1.1 code in Section 3.

4. *Documentation of steps taken to ensure that chosen simulation conditions span the range of intended use, and that such conditions avoid inconsistent results, or that any inconsistencies are adequately explained and demonstrated to have little impact on results.*

Detailed discussion of initial and boundary conditions for the THC seepage model can be found in Section 4.1 (initial model inputs); Section 6.2.2.1 (pore-water compositions); Section 6.4.3 (mineral reactive surface areas); and Sections 6.5.2 and 6.5.3 (boundary conditions and initial inputs). Calibration of the model to ambient pore-water compositions is described in Sections 6.4.8 and 6.5.5.4. Section 6.5 provides detailed discussion of various model results (i.e., those of convergence runs). Discussion about issues with non-convergence runs can be found in Section 6.4.8. Additional information regarding convergence issues can be found in the file *chdump.dat* described in Appendix G.

For confidence building after model development, Section 2.2.1.2 of the technical work plan (TWP) (SNL 2007 [DIRS 179287]) imposes the following requirement for model validation to support the scientific basis:

Corroboration of results from a derivative simulation, closely similar to the THC seepage model but adapted to the DST, with data acquired from the DST (SCI-PRO-006, Models, Section 6.3.2, 1st bullet).

Comparison of model results with experimental data is the main method of validation for the THC seepage model. Section 7.1 explains the respective validation and modeling activities in great detail, and discusses explicitly how the criteria for this validation method, as defined in the TWP (SNL 2007 [DIRS 179287]), have been met.

Additional confidence is obtained through technical review by publication in a refereed professional journal, as noted in the TWP (SNL 2007 [DIRS 179287]). Since the following articles on the subject have already been published, additional confidence has been obtained:

- “Fluid Flow and Reactive Transport Around Potential Nuclear Waste Emplacement Tunnels at Yucca Mountain, Nevada.” *Journal of Contaminant Hydrology* (Spycher et al. 2003 [DIRS 162121]).
- “Experimental and Numerical Simulation of Dissolution and Precipitation: Implications for Fracture Sealing at Yucca Mountain, Nevada.” *Journal of Contaminant Hydrology* (Dobson et al. 2003 [DIRS 165949]).

In addition to use of the DST THC submodel, confidence in the THC seepage model is provided by historical work consisting of model–data comparisons from laboratory-scale experiments. Two such experiments have been modeled previously: a plug-flow reactor to evaluate tuff dissolution (Section 7.2) and a fracture sealing experiment (Section 7.3). Comparisons between the experimentally measured and simulated results are used to test conceptual models that were developed for the THC seepage model and the DST THC submodels. These simulations were performed using previous revisions of TOUGHREACT software and using previous versions of the thermodynamic database. Thus, they do not directly validate the current THC model, but provide added confidence in the conceptual model and modeling approach that are implemented. A brief summary of each of these model–data comparison studies is provided here. The simulations are discussed in detail in a previous revision of this report (BSC 2004 [DIRS 168848], Sections 7.2 and 7.3).

Table 7-1. Sources of Data Used for Model Validation or Corroboration

DTNs	Description
Mineralogical Data (DST)	
LA0201SL831225.001 [DIRS 158426]	Sidewall core sample mineralogical analyses
Analytical Water and Gas Chemistry Data	
LB990630123142.003 [DIRS 111476]	4th, 5th, and 6th Qtr. DST CO ₂ data
LB0208ISODSTHP.001 [DIRS 161638]	DST CO ₂ and isotopic data (combined)
LB0303ISODSTCP.001 [DIRS 177538]	DST CO ₂ and isotopic data
LB0309ISODSTCP.001 [DIRS 177539]	DST CO ₂ and isotopic data
LB0403ISODSTCP.001 [DIRS 177540]	DST CO ₂ and isotopic data
LB0410ISODSTCP.001 [DIRS 177541]	DST CO ₂ and isotopic data
LB0509ISODSTCP.001 [DIRS 177542]	DST CO ₂ and isotopic data
MO0005PORWATER.000 [DIRS 150930]	Analyses of pore waters from Alcove 5 core samples in the ESF (HD-PERM-2 and HD-PERM-3 samples)
LL990702804244.100 [DIRS 144922]	Aqueous chemistry of water sampled from the DST (6/4/98 to 3/30/99)
LL001100931031.008 [DIRS 153288]	Aqueous chemistry of water sampled from the DST (collected 10/27/99 to 1/25/00)
MO0207AL5WATER.001 [DIRS 159300]	DST field measurements
SN0203F3903102.001 [DIRS 159133]	DST field measurements
LL020405123142.019 [DIRS 159307]	DST aqueous chemistry
LL020302223142.015 [DIRS 159134]	DST aqueous chemistry
LL001200231031.009 [DIRS 153616]	Aqueous chemistry of water sampled from the DST (8/9/99 and 8/10/99)
MO0101SEPFDDST.000 [DIRS 153711]	Field pH of water sampled from DST on 5/23/00 and 6/29/00

7.1 THE DRIFT SCALE TEST THC SUBMODEL

The DST is the second underground thermal test to be carried out in the Exploratory Studies Facility (ESF) at Yucca Mountain, Nevada. The purpose of the test is to evaluate the coupled thermal, hydrologic, chemical, and mechanical processes that take place in unsaturated fractured tuff over a range of temperatures (approximately 25°C to 200°C). Details regarding the DST layout, borehole orientations, operation of the test, and measurements performed (as well as their uncertainties) are discussed in Section 6.3 of *Thermal Testing Measurements Report* (SNL 2007 [DIRS 177414]) and in *Drift-Scale Test As-Built Report* (CRWMS M&O 1998 [DIRS 111115]). Information on these aspects of the DST is not repeated in this report unless directly related to the geochemical data collected and used for model validation.

In brief, the DST consists of an approximately 50-m-long drift that is 5 m in diameter. Nine electrical floor canister heaters were placed in this drift (the Heated Drift) to simulate nuclear-waste-bearing containers. Electrical heaters were also placed in a series of horizontal boreholes (wing heaters) drilled perpendicular outward from the central axis of the Heated Drift. These heaters were emplaced to simulate the effect of adjacent emplacement drifts. The DST heaters were activated on December 3, 1997, with a planned period of four years of heating, followed by four years of cooling. After just over four years, the heaters were switched off on January 14, 2002, and since that time the test area has been slowly cooling.

This section describes the DST THC submodel, discusses simulations of THC processes during the DST, and presents comparisons to geochemical measurements performed on gas, water, and mineral samples collected from the DST. The DST THC submodel is a forward numerical model used to gain insight into THC processes taking place during heating of the unsaturated devitrified tuffs. The DST THC submodel provides important support for application of the drift-scale THC seepage model to repository simulations. The drift-scale THC conceptual models are described in Sections 6.1 to 6.4. The DST THC submodel is compared with, but not calibrated to, geochemical data collected from the DST. This is important because calibration, if relied upon heavily in model development, could limit the use of the model for representing THC processes over repository time scales. The drift-scale hydrologic and thermal properties used in the DST THC submodel are the same as those used for the THC seepage model (Table 4.1-1); the property values are not calibrated directly to DST results, but are best estimates for the mean properties over the repository footprint. Because the properties are not specific to the Drift Scale Test block, and the tuffs are heterogeneous (especially with respect to fracture density and permeability), differences between model results and data are perhaps greater than if site-specific properties were employed. However, since the THC seepage model uses the same property sets, the DST THC submodel can be used with much better confidence for model validation. Some modifications have been made to the thermodynamic database for the THC seepage model and the DST THC submodel, and to the kinetic-rate constants, to capture aspects of the ambient-system pore-water chemistry (discussed in Section 6.2.2.1). The only other adjustments specific to the DST have been made to include the connectivity of the Heated Drift to the Access Drift, to better represent heat losses through the intervening bulkhead.

7.1.1 Modeling Approach

The modeling approach involves the creation of a numerical grid and the selection or development of thermal, hydrologic, mineralogical, aqueous, and gaseous species geochemical input data. It also involves the selection of appropriate thermal and hydrologic models, as well as chemical, thermodynamic, and kinetic data and models. The development of a comprehensive model that is not calibrated to the test data requires a systematic approach from the evaluation of infiltration rates, hydrological properties and the results of steady-state hydrological simulations, thermal properties and ambient temperature gradients, and long-term ambient chemical evolution using initial geochemical data for water, gas, and minerals. The results of such ambient simulations (described in Sections 6.4.8 and 6.5.5.4) give confidence in the initial conditions, models, and properties used for the coupled THC validation simulations. Because the DST THC submodel uses the same hydrological and geochemical inputs as the ambient simulations, including the same thermodynamic and kinetic data, the initial conditions and data for the DST THC submodel is founded on this systematic approach. The approach and input data are further described in Sections 7.1.2 to 7.1.5 below.

7.1.2 Drift Scale Test Two-Dimensional Numerical Grid

The two-dimensional dual-permeability numerical grid for the DST represents a vertical cross section through the Heated Drift at a distance approximately 30 m from the bulkhead, separating the Heated Drift from the Access Drift (Figure 7.1-1).

The numerical grid used in the simulations in this report (Figures 7.1-2 and 7.1-3) is based on a grid developed for an earlier TH model of the DST (DTN: LB0101DSTTHGRD.001 [DIRS 153687]). It has been modified to account for changes in hydrological properties and to improve the treatment of heat and gas transport. The earlier mesh consisted of 4,485 gridblocks, including fracture and matrix (DTN: LB0101DSTTHGRD.001 [DIRS 153687]). The top boundary is approximately 99 m above the drift center, with the bottom boundary at approximately 157 m below the center. Connections between the interior of the Heated Drift and the Heater Test Alcove included gridblocks designed to act as a bulkhead and as insulating material. Within the drift, heat is applied directly to the drift wall instead of explicitly representing the electric heaters and calculating the heat transfer across the air mass inside the drift. The DST includes a plane of linear wing heaters on each side of the drift that have been given small gridblocks in the model. Small gridblocks are also employed adjacent to the wing heaters and drift wall to capture the strong gradients in temperature and liquid saturation in these regions. Radial mesh blocks in the drift interior are replaced near the drift base by Cartesian gridblocks to represent the concrete invert. Incorporation of the concrete invert is unique to the DST THC submodel; it is not part of the model grid for the THC seepage model. Also, in the DST THC submodel, the concrete is only incorporated with respect to thermal and hydrologic properties—no cement phases are present in the geochemical system used.

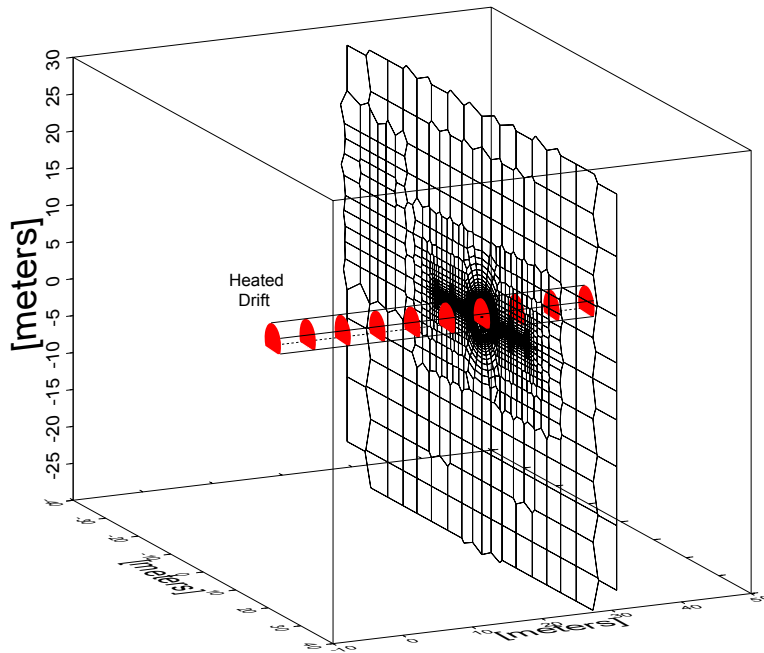
The numerical grid used for the DST THC model (Figures 7.1-2 and 7.1-3) has been modified from DTN: LB0101DSTTHGRD.001 [DIRS 153687] in the following ways:

1. Gridblocks representing the insulation and bulkhead have been removed, and the Heated Drift gridblock is connected directly to the Heater Test Alcove gridblock. The connection area and distance have been adjusted so that heat loss from the drift resulted in roughly similar crown temperatures to the maximum observed values. This is done to simulate heat and mass losses through the bulkhead, instead of reducing power by a set factor, as was done in earlier revisions of this model.
2. The distances from the drift center gridblock and the connecting elements have been modified to represent the true distance, so that heat could be applied to the drift center and not to the elements at the drift walls.
3. In the approximate location of the observation drift, the gridblock volumes are increased to a large value to represent connection to the atmosphere (Figure 7.1-2). These gridblocks connected to adjacent rock gridblocks so that gas flow can take place between the Observation Drift and the surrounding rock.
4. Volumes of fracture and matrix gridblocks were modified to account for a change in the fracture porosity.
5. The current DST THC submodel mesh has 4,490 gridblocks.

7.1.3 Heater Power

The DST THC submodel employs a nine-month initial period at ambient temperature, corresponding approximately to the time that was required to set up the test. The wing heaters are split into inner and outer zones, with more power applied to the outer zone to approximate the presence of an adjacent parallel drift. In the drift, heat is applied solely to the drift-center gridblock, which is connected to all surrounding gridblocks. The positions of gridblocks representing heaters are shown in Figure 7.1-3.

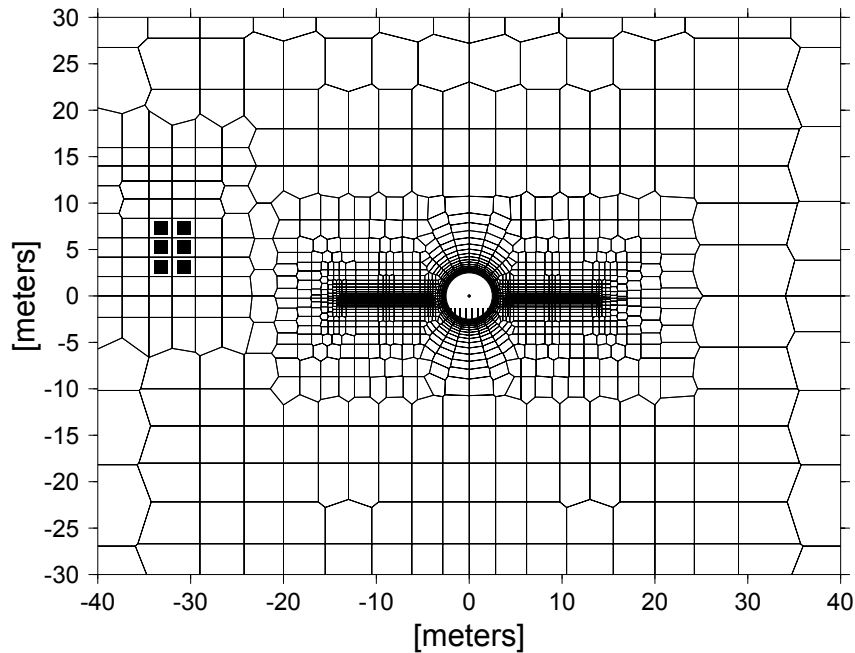
The heating schedule was developed specifically for the DST THC submodel and is based on step-wise averages of the 10-day incremented power data (DTN: MO0208RESTRDST.002 [DIRS 161129]). This detailed power history is especially important for eliminating some of the uncertainty in the validation comparisons, especially for gas-phase CO₂ concentrations, which are affected by changes in vapor fluxes much more than temperature. The sources for this 10-day incremented power data are given in Table 7.1-1. Intentional power reductions are directly accounted for in the power data, using accurate time information gathered from the DTNs listed in Table 7.1-1.



Output DTN: LB0705DSTHC005.002.

NOTE: Mesh extends in all directions from area shown.

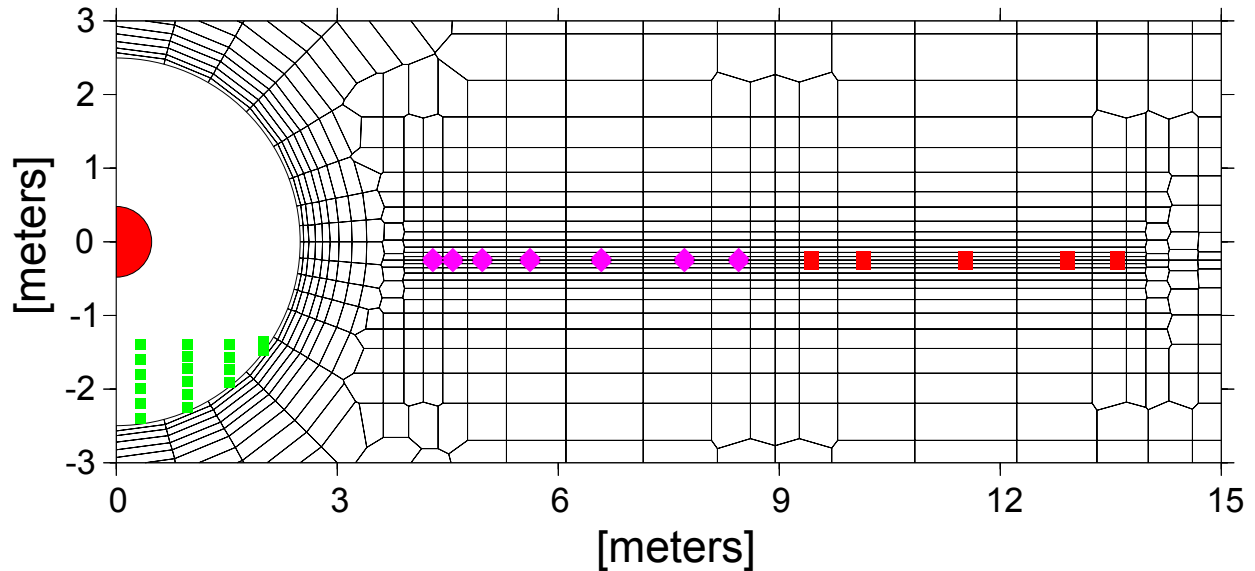
Figure 7.1-1. Three-Dimensional Schematic Diagram of the DST Showing Perspective View of Numerical Mesh for DST THC Submodel Simulations



Output DTN: LB0705DSTHC005.002.

NOTE: The Observation Drift is shown as black squares. Mesh extends outside the area shown (see text). The Heated Drift is a circular region at the center.

Figure 7.1-2. Numerical Mesh for DST THC Submodel Simulations



Output DTN: LB0705DSTHC005.002.

NOTE: Inner (violet diamonds closer to drift) and outer (large red squares) wing heater gridblock coordinates. Heat is applied to gridblock (red filled circle) marked at drift center. Green squares indicate gridblock locations for the concrete invert.

Figure 7.1-3. Enlarged View of the Numerical Grid Showing the Locations of Gridblocks Representing the Heated Drift, Wing Heaters, and Concrete Invert

Table 7.1-1. Input DTNs Used for Estimating Times/Dates of Power Reductions and Outages for DST THC Submodel Simulations

Power Data Sources (DTNs)	Dates
MO0208RESTRDST.002 [DIRS 161129]	Heating Phase (10-day increments)
MO9807DSTSET01.000 [DIRS 113644]	11/7/97 to 5/3/98
MO9810DSTSET02.000 [DIRS 113662]	6/1/98 to 8/31/98
MO9906DSTSET03.000 [DIRS 113673]	9/1/98 to 5/31/99
MO0001SEPDSTPC.000 [DIRS 153836]	6/1/99 to 10/31/99
MO0007SEPDSTPC.001 [DIRS 153707]	11/1/99 to 5/31/00
MO0012SEPDSTPC.002 [DIRS 153708]	6/1/00 to 11/30/00
MO0107SEPDSTPC.003 [DIRS 158321]	12/1/00 to 5/31/01
MO0202SEPDSTTV.001 [DIRS 158320]	6/1/01 to 1/14/02

The DTNs in Table 7.1-1 are also used to estimate the length of the longer (approximately greater than 1/2 day) temporary power outages. Table 7.1-2 gives the step-wise averaged power data implemented in the DST THC submodel simulations. Each time in Table 7.1-2 represents the initiation of a specific period of heating or power loss that continues until the succeeding time. The simulations are run for the full period of heating plus a four-year period of cooling (shown by hypothetical end time at the base of Table 7.1-2).

Table 7.1-2. Step-Wise Averaged Power Data for the DST THC Simulations

Date	Time (s)	Time (days)	Canister Power (watts)	WH (inner) Power (watts)	WH (outer) Power (watts)	Comments
3/5/97	0.00000E+00	0.00	0.0000	0.0000	0.0000	Pre-test
12/3/97	2.35872E+07	273.00	1091.3740	1232.4007	1626.7690	Heaters turned on
3/15/98	3.24000E+07	375.00	1091.3740	0.0000	0.0000	Outage – right rib
3/16/98	3.25080E+07	376.25	1091.3740	1232.4007	1626.7690	
4/12/98	3.48192E+07	403.00	1077.9972	1198.5773	1582.1220	
8/10/98	4.51872E+07	523.00	1119.6842	1201.8035	1586.3807	
1/27/99	5.98752E+07	693.00	0.0000	0.0000	0.0000	Power outage
1/27/99	5.99400E+07	693.75	1123.5789	1204.4465	1589.8693	
2/16/99	6.16032E+07	713.00	1102.5965	1189.0805	1569.5862	
5/27/99	7.02432E+07	813.00	0.0000	0.0000	0.0000	Power outage
5/27/99	7.03080E+07	813.75	1102.5965	1189.0805	1569.5862	
5/29/99	7.04160E+07	815.00	0.0000	0.0000	0.0000	Power outage
5/30/99	7.04808E+07	815.75	1087.8653	1155.5245	1525.2923	
6/18/99	7.21440E+07	835.00	0.0000	0.0000	0.0000	Power outage
6/19/99	7.22088E+07	835.75	1087.8653	1155.5245	1525.2923	
7/9/99	7.39584E+07	856.00	0.0000	0.0000	0.0000	Power outage
7/15/99	7.44768E+07	862.00	1087.8653	1155.5245	1525.2923	
8/27/99	7.81920E+07	905.00	0.0000	0.0000	0.0000	Power outage
8/29/99	7.83216E+07	906.50	1087.8653	1155.5245	1525.2923	
11/22/99	8.57088E+07	992.00	1087.8653	0.0000	0.0000	Outage – right rib
11/24/99	8.58816E+07	994.00	1087.8653	1155.5245	1525.2923	
2/11/00	9.27072E+07	1073.00	0.0000	0.0000	0.0000	Power outage
2/11/00	9.27720E+07	1073.75	1078.8421	1184.6642	1563.7568	
3/2/00	9.44352E+07	1093.00	1029.1930	1115.3660	1472.2831	Power reduction
3/12/00	9.52992E+07	1103.00	0.0000	0.0000	0.0000	Power loss
3/13/00	9.54072E+07	1104.25	1029.1930	1115.3660	1472.2831	
5/2/00	9.97056E+07	1154.00	964.5263	1040.2813	1373.1713	Power reduction
8/15/00	1.08778E+08	1259.00	917.3463	978.7397	1291.9364	Power reduction
1/20/01	1.22429E+08	1417.00	0.0000	0.0000	0.0000	Power outage
1/21/01	1.22515E+08	1418.00	917.3463	978.7397	1291.9364	
5/1/01	1.31155E+08	1518.00	875.5711	925.4672	1221.6168	Power reduction
7/1/01	1.36426E+08	1579.00	0.0000	0.0000	0.0000	Power outage
7/1/01	1.36490E+08	1579.75	875.5711	925.4672	1221.6168	
8/22/01	1.40918E+08	1631.00	826.8171	875.8317	1156.0979	Power reduction
1/14/02	1.53446E+08	1776.00	0.0000	0.0000	0.0000	Heaters turned off
1/14/06	2.79677E+08	3237.00	0.0000	0.0000	0.0000	Cooling period end

NOTE: Input DTNs for power data are listed in Table 7.1-1. Each time represents the initiation of a particular period of heating (or power loss) that continues until the next time in the table. Data are for a two-dimensional vertical slice.

7.1.4 Hydrologic and Geochemical Input Data

Sources of hydrologic and geochemical input data are listed in Table 4.1-1. Other details regarding the use of or modifications to these data are given in Sections 7.1.5 and 7.1.6.

Thermodynamic data are described in Section 4.1.4 and presented in Appendix C. Kinetic data are given in Table 4.1-3. The mineral volume fractions reflect the mineralogical assemblage used in the current Tptpl THC seepage model (Appendix A). Mineral reactive surface areas are given in Appendix B. Calculation of these data is presented in Sections 6.2.2.3, 6.2.2.4, and 6.4.3.

7.1.5 Initial and Boundary Conditions: Hydrologic and Thermal

Hydrologic and thermal initial and boundary conditions are derived from the unsaturated zone (UZ) flow model at the location of borehole SD-9, which is the closest borehole to the location of the DST (DTN: LB0701UZMTHCAL.001 [DIRS 179286]). Hydrologic properties were obtained from DTN: LB0610UZDSCP30.001 [DIRS 179180] for the 30th percentile infiltration rate scenario. Thermal properties are identical to those used for the THC seepage model, and are listed in Section 4.1.1.2.

The infiltration rate at SD-9 from the UZ 3-D flow model using the 30th percentile infiltration rate scenario is about 14.6 mm/yr. This is significantly higher than the value of 0.36 mm/yr used by Birkholzer and Tsang (2000 [DIRS 154608]) that matched temperature data better than simulations using 3.6 mm/yr. Models and data for the ambient geochemistry of the UZ at Yucca Mountain (i.e., Cl, Sr, calcite) support a lower mean infiltration rate (around 5 mm/yr over the UZ flow model domain; Sonnenthal and Bodvarsson 1999 [DIRS 117127], p. 107; Liu et al. 2003 [DIRS 162470]; Xu et al. 2003 [DIRS 162124]) than the 30th percentile infiltration-rate scenario value of about 8 mm/yr. Therefore, the validation to measured data may not be as good as for the case of a model developed specifically from data from the DST site, including the consideration of the local hydrological conditions.

Given these caveats, the nature and extent of this foundation work is substantially the same for the DST THC submodel and the THC seepage model used for repository prediction, and supports confidence that the THC seepage model uses consistent values for hydrologic and thermal properties, initial conditions, and boundary conditions. Further details of the initial and boundary conditions are described below.

The top and bottom boundaries of the DST THC submodel are set to constant temperature, pressure, and liquid saturation, based on steady-state values obtained from simulations of a one-dimensional column extending from the land surface to the water table (borehole SD-9, as discussed above). The top boundary of the two-dimensional model extends 150 m above and below the drift center, but does not reach either the land surface or the water table. The bottom boundary condition is open to gas and to liquid flow. The side boundaries of the domain are located 81.5 m away from the drift center on each side (outside of the test influence area) and are no-flux for mass and heat. The air pressure and temperature in the observation drift are set to constant values, as given in the fracture medium at the approximate depth in the SD-9 steady-state simulation. Therefore, the values do not reflect temporal fluctuations in barometric

pressure or tunnel air temperatures. The heated drift wall is open to advection and conduction of heat and mass (e.g., air, water vapor, and CO₂).

7.1.6 Initial and Boundary Conditions: Geochemical

Initial and boundary geochemical conditions are set using qualified data, based on pore-water and mineralogical analyses and taken from the Technical Data Management System (TDMS). Pore water data have been selected, over successive revisions of the model, from a relatively large set of measured data (Section 6.2.2.1), which provides confidence that the selected compositions represent the range of host rock conditions. Additional discussion of the available pore-water data is provided in Section 4.1.5. Two water samples were selected from this group: HDPERM3 and ESFPERM4. The approach used to set the initial and boundary conditions is described in the following paragraphs.

Initial geochemical data used in the simulations are given in Appendices A through C (sources in Tables 4.1-1). All aqueous and gaseous species concentrations in the rock are initially set to a uniform value (Section 6.2.2.1). The Heater Alcove and Observation Drift CO₂ concentrations are fixed to approximately that of the atmosphere. The Heated Drift CO₂ concentration is initially set to the same value as that in the Observation Drift, but is allowed to exchange CO₂ with the Heater Test Alcove and with the surrounding rock. The simulations are performed with the geochemical system presented in Table 6.2-2.

Both the top and bottom boundary conditions are open to gas and aqueous species transport. The top and bottom boundaries are also set so that no mineral reactions take place (and, therefore, no changes in aqueous species concentrations occur as a result of mineral–water reactions). Their volumes are set to extremely large values so they act, essentially, as constant concentration boundaries. The side boundaries are no-flux for gas and aqueous-species transport.

7.1.7 Model Validation Methods, Criteria, and Limitations

In the following sections, data and predictions are reviewed to demonstrate that the criteria specified in the TWP (SNL 2007 [DIRS 179287]) have been met for the DST THC submodel. Because the THC seepage model uses the same conceptualization and mathematical treatment of THC coupled processes as the DST THC submodel, including the same thermodynamic and kinetic data, DST model validation effectively validates the THC seepage model. Additional validation of the THC modeling approach is presented in Sections 7.2 and 7.3 where results of laboratory plug-flow and fracture-boiling experiments are compared to simulations.

The THC seepage model is validated and the necessary confidence is achieved by the following activities as listed in Section 6.3.2 of SCI-PRO-006: “Corroboration of model results with data” and “Technical review through publication in a refereed professional journal.” These validation methods provide the most confidence in the conceptual and numerical models and their outputs.

7.1.7.1 Corroboration with Experimental Data

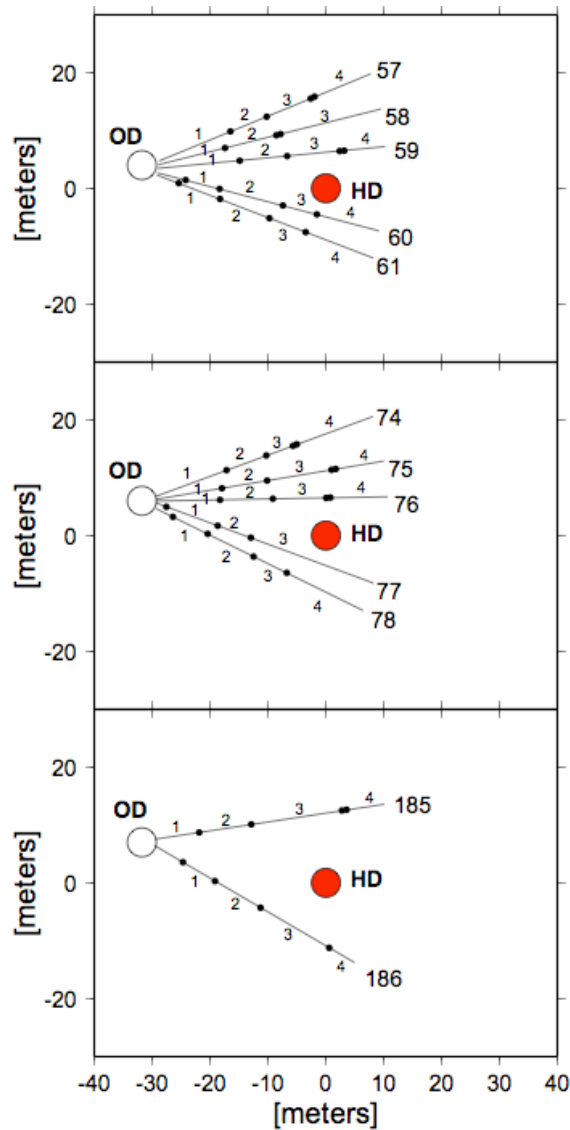
Data from the DST used for comparison consist of analyses of water and gas samples from borehole intervals between packers and observations of mineral precipitation in boreholes. Intervals have been selected for comparison based upon the availability of a long, continuous

sample record and the absence of confounding factors, such as the sampling interval being too long to compare with a particular gridblock or pair of gridblocks, or boreholes being near either end of the DST and affected by three-dimensional transport (see below). The locations of the hydrology boreholes, sampling intervals, and temperature sensors are shown in Figure 7.1-4. The planar radial arrays of hydrology boreholes 57-61, 74-78, and 185-186 are located approximately 10 m, 30 m, and 45 m from the bulkhead along the drift axis, respectively (Figure 6.3-4 and Table 6.3-2 in SNL 2007 [DIRS 177414]). In many figures, the 74-78 array of hydrology boreholes is shown because this is closest to the center of the Heated Drift where temperatures are near a maximum, corresponding best to the 2-D model domain that represents a cross section through the Heated Drift, and where many gas samples were collected. Some figures show the 57-61 array of hydrology boreholes because the majority of water samples were collected from these boreholes.

Differences between the DST THC submodel predictions and DST measurements are important. There are several reasons (listed below) why individual measured data may lie outside the predictions, and yet support use of the DST THC submodel for validation. It is important that these considerations are kept in mind when reviewing the model comparisons to measured data (in the following discussion, the term “model” refers to the DST THC submodel).

1. The continuum model does not simulate individual fractures, which may intersect boreholes near sampling points, their aperture and frequency resulting in different flow rates and temperatures, thus affecting the chemistry of the gas and water samples in that interval.
2. All samples were taken from long borehole intervals (approximately 8 to 10 m long), which cross regions of large gradients in gas species concentrations (up to a few orders of magnitude) and exhibit temperature variations of tens of degrees Celsius. The sampling boreholes may alter composition of the incoming gas and liquid phase compositions from fractures, as a result of reactions with the fresh mineral surface area exposed on the borehole walls.
3. The model does not consider all deviations from planned operation of the DST. These deviations include the exact time periods of power losses, variations in heat loss through the bulkhead, changes in pressure from forced ventilation, the effect of the many DST boreholes, and barometric pressure fluctuation. Changes predicted to occur at a particular time in the model may be shifted relative to the DST measured data by several months or more, resulting in large differences at a particular time even if the trends are followed.
4. Gas and water samples are affected by condensation of water vapor as the sample cools in the collection tubes from the borehole interval to the sample containers. This results in dilution by distillation of water vapor, and changes to CO₂ concentrations. The pH of the water may drop as distillate formed in the sampling apparatus is mixed with water from the sampled borehole. Therefore, collected water samples may be diluted relative to fracture waters, and the modeled concentrations, even if the trends are similar.

The greatest effects from these mechanisms on the magnitude of differences in model–data comparisons may be expressed when the boiling front in the rock is proximal to the measurement location. The magnitude of such differences may be compared to the difference between relatively dilute condensate in fractures, and waters concentrated by evaporation closer to the boiling front.



Coordinates from DTN: MO0002ABBLSLDS.000 [DIRS 147304].

NOTE: OD = Observation Drift; HD = Heated Drift. Borehole intervals are designated as 1, 2, 3, and 4 moving away from the Observation Drift (open circle designated “OD”). Temperature sensors (not labeled) are shown as the small closed circles, and are designated similarly to the intervals (i.e., sensor 60-4 is the 4th sensor from the Observation Drift). Boreholes 57 to 61, 74 to 78, and 185 and 186 are located approximately 10 m, 30 m, and 45 m from the bulkhead along the drift axis, respectively (Figure 6.3-4 and Table 6.3-2 in SNL 2007 [DIRS 177414]).

Figure 7.1-4. Locations of Hydrology Boreholes, Sampling Intervals (numbered), and Temperature Sensors

Given these considerations, the following criteria are adopted for validation using model–data comparisons for the DST:

- Predicted temporal trends in the concentrations of aqueous and gaseous chemical species, and spatial distribution of precipitated mineral phases, should be similar to field measurements. Significant differences are explained qualitatively in terms of the physical and chemical processes. The THC modeling approach uses average properties and simulates average response; local or short-term variability in the measured data is associated with effects that are not included in the model.
- Observed concentrations of gas and aqueous species, once adjusted for sample degassing and water vapor loss, match predicted concentrations to within an order of magnitude (up or down). This range is justified for several reasons. First, natural variability within the repository horizon pore waters is as much as five-fold for any given chemical species. Second, TH (boiling and condensation) and THC processes (mineral–water–gas reactions) can lead to changes in the chemistry of water and gases by one or more orders of magnitude (Section 7.1.10.2) in response to small changes in temperature (e.g., around the boiling temperature of water). Third, differences in aqueous species concentrations in the rock may develop over distances of tens of centimeters or less, because diffusion rates of aqueous species in the rock matrix are limited (Section 7.1.11.3). Fourth, changes that the samples undergo during their extraction from the rock (e.g., cooling, degassing, condensation) have the potential for shifting aqueous species concentrations.

Consistent with these potential contributions to uncertainty, the validation criterion of one order-of-magnitude in concentration (or a pH unit, up or down) is smaller than the potential range, and is appropriate for predicted compositions for fracture and matrix waters over the time period of the DST.

As stated above, the THC seepage model approach uses average properties and simulates averaged responses, and does not predict small-scale or short-term events such as the spike in CO₂ after 48 months in borehole 75 of the DST (Section 7.1.10). Furthermore, experimental measurements of CO₂ and pH are directly impacted by sampling methodology, including changes in temperature and pressure, and sample degassing. Accordingly, validation of a given parameter may be done indirectly through examination of correlated parameters (e.g., pH, which is associated with significant data uncertainty, can be validated by comparing CO₂ gas concentrations as well as the corroborative validation of dissolved carbonate concentrations).

7.1.7.2 Publication in a Refereed Technical Journal

As described in Section 6.3.2 of SCI-PRO-006, technical review through publication in a refereed technical journal provides additional confidence in the THC seepage model. Essentially the same THC seepage model has been published in *Journal of Contaminant Hydrology* (Spycher et al. 2003 [DIRS 162121]). A second article in *Journal of Contaminant Hydrology* (Dobson et al. 2003 [DIRS 165949]) does not directly address the THC seepage model, but evaluates fracture sealing due to mineral precipitation for a Yucca Mountain tuff, and provides added confidence in the conceptual model implemented in simulations.

7.1.8 THC Simulations

In the following sections, DST THC submodel simulations are described. Only the current simulation results are shown. All parameters have been updated to the current property sets and are consistent with the THC seepage model.

Seven THC simulations were performed for this report using TOUGHREACT V3.1.1:

1. 30th percentile properties, 14.46 mm/yr steady-state initial conditions, HDPERM3 initial pore water, maximum time step of 1 hour (simulation dst_thc_r05_1)
2. 30th percentile properties, 1.446 mm/yr steady-state initial conditions, HDPERM3 initial pore water, maximum time step of 20 minutes (simulation dst_thc_r05_2)
3. 30th percentile properties, 1.446 mm/yr steady-state initial conditions, HDPERM3 initial pore water, maximum time step of one day (simulation dst_thc_r05_2dt1day)
4. 30th percentile properties, 1.446 mm/yr steady-state initial conditions, HDPERM3 initial pore water, maximum time step of one hour (simulation dst_thc_r05_3)
5. 30th percentile properties, 1.446 mm/yr steady-state initial conditions, HDPERM3 initial pore water, maximum time step of one hour, amorphous antigorite rate increased (simulation dst_thc_r05_4)
6. 30th percentile properties, 1.446 mm/yr steady-state initial conditions, ESFPERM4 initial pore water, maximum time step of one hour (simulation dst_thc_r05_5)
7. 30th percentile properties, 1.446 mm/yr steady-state initial conditions, HDPERM3 initial pore water, maximum time step of one hour, rates of feldspars increased by a factor of 100 (simulation dst_thc_r05_6).

In most of the DST THC submodel simulations, HDPERM3 water (W0; Table 6.2-1) was used as the starting water, because this water was recovered from borehole core from Alcove 5, near the DST. A similar water from this same area was also used as input: ESFPERM4 (W10; Table 6.2-1). All input and output data files for the DST THC simulations are given in Appendix G, and have been submitted to the TDMS under Output DTN: LB0705DSTHC005.002.

Sections 7.1.9 through 7.1.14 present the model results, representative data from the DST, and the model–data comparisons that support validation of the THC seepage model. Section 7.1.9 describes the prediction of thermal-hydrologic conditions, which is covered in more detail by *Drift-Scale Coupled Processes (DST and TH Seepage) Models* (BSC 2005 [DIRS 172232], Section 7.4). Section 7.1.10 presents the model–data comparisons for gas-phase CO₂, an important variable that controls carbonate chemistry and directly affects the chemical environment in the emplacement drifts. Section 7.1.11 describes model–data comparisons for aqueous species, which were analyzed in samples of fracture water collected in DST boreholes. Section 7.1.12 describes mineralogical changes predicted by the DST THC submodel, with comparison to the available analysis of minerals formed during the test. Section 7.1.13 describes

the predicted changes in fracture and matrix porosity, and the implication for bulk permeability, with discussion of the observed indications of permeability change in the DST. Finally, Section 7.1.14 presents representative ^{14}C isotopic analysis of gas samples, and interprets the evolution of $^{14}\text{CO}_2$ during the heating phase in terms of the operant chemical processes in the DST THC submodel.

7.1.9 Simulation Results: Thermal and Hydrologic Evolution

The main driving force for changes in the hydrologic and chemical behavior of the system is the thermal load applied to the system. The resulting changes in temperature, liquid saturation, and gas-phase composition lead to changes in the chemistry of water and gas, as well as mineral dissolution and precipitation. A more complete discussion of thermal-hydrologic processes is presented in *Drift-Scale Coupled Processes (DST and TH Seepage) Models* (BSC 2005 [DIRS 172232]). Key aspects of the thermal-hydrologic behavior of the DST that drive the chemical evolution of the system are discussed briefly in this section.

The simulation results for the TH evolution of the DST, as well as all other simulation results shown in this section, are based on simulations 1 and 4 above, performed using the EOS4 module in TOUGHREACT V3.1.1. These simulations were chosen for comparison because they start with different initial matrix liquid saturations, owing to the order-of-magnitude difference in infiltration rate used for the steady-state simulations. The higher initial liquid saturations in the first simulation (14.46 mm/yr infiltration rate steady-state) led to an initial matrix liquid saturation of about 0.99, compared to about 0.92 for the simulation at the 1.446 mm/yr infiltration rate.

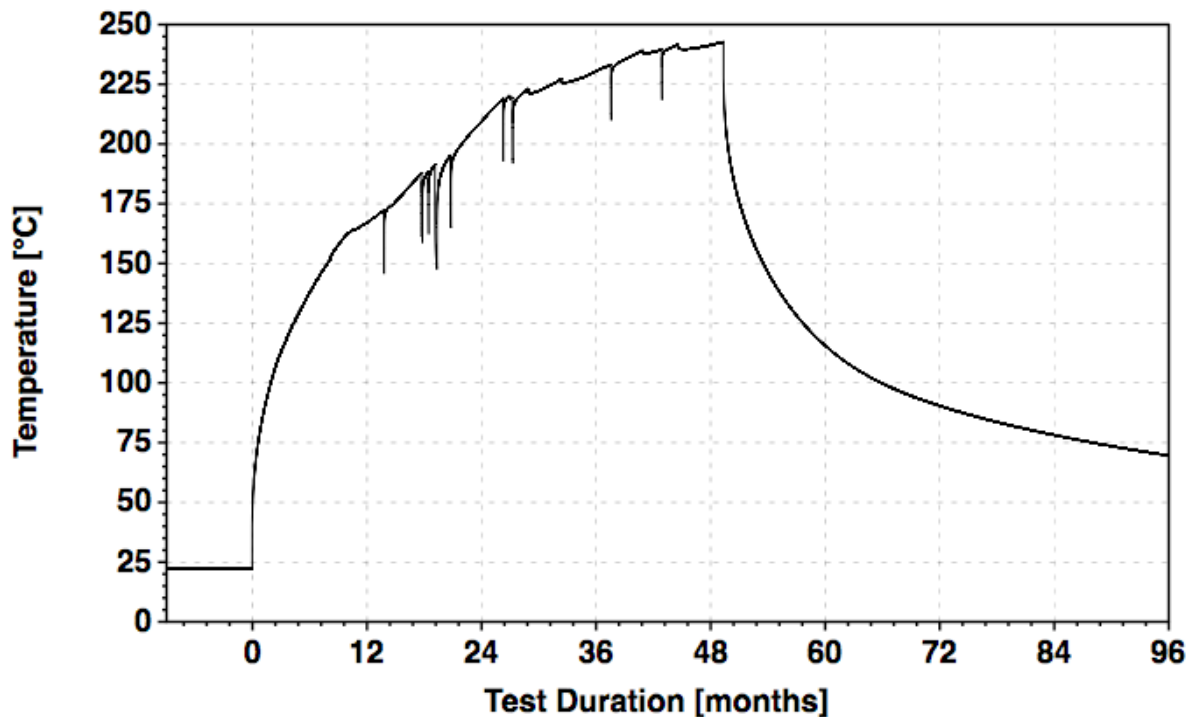
Combined with the high initial liquid saturation, low matrix permeabilities in the model parameter set and a small gas relative permeability led to higher matrix pore pressure, thus delaying boiling more substantially than the capillary-pressure-lowering effect. In addition, coupled effects of mineral precipitation/dissolution on flow did not significantly affect the TH evolution of the DST.

The modeled temperatures in the drift reflect the heat input at the drift center (at the approximate location of the electrical canister heater) and subsequent heat transfer to the drift wall (Figure 7.1-5). Differences in temperature between the drift center (Figure 7.1-5) and drift wall near the top (drift crown) are approximately 20°C , similar to the differences observed between electrical canister temperatures and drift-crown temperature measurements (DTN: MO0007SEPDSTPC.001 [DIRS 153707]). Sharp temperature drops are the result of power losses, heater failures, and/or intentional power reductions.

Drift-wall temperatures predicted by the two-dimensional model eventually exceed the maximum measured values by about 20°C (not shown – they parallel the drift temperature). However, predicted temperatures in the rock are typically closer to measured values (Figure 7.1-6). There are several reasons for the elevated temperature in the drift. First, the two-dimensional cross section can only approximate the exchange of heat through the rock along the axis of the DST. Second, heat lost through the bulkhead by a combination of advection and diffusion is uncertain and is approximated using a bulkhead correction that is essentially one-dimensional. Therefore, this model is most applicable to areas near the center of the test:

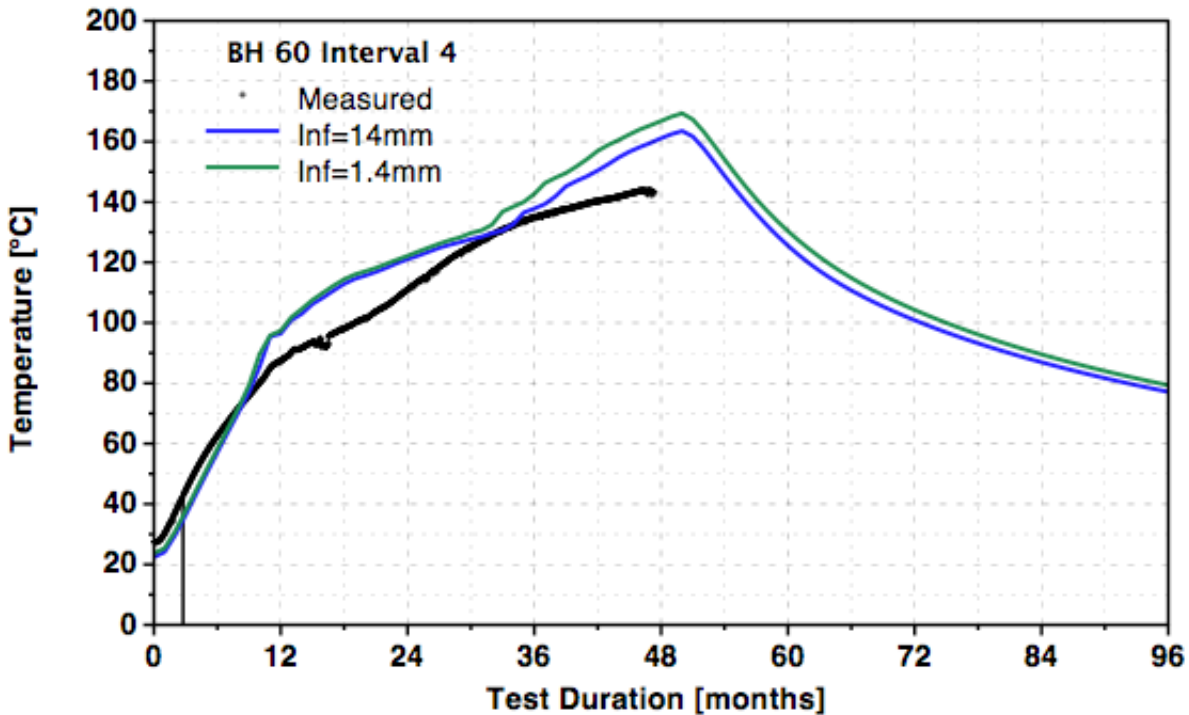
away from both the bulkhead and the distal end of the Heated Drift. For application to repository simulation, the THC seepage model is used similarly, to predict the composition of waters in the host rock that could potentially seep into drifts.

Other factors that control the temperature response of the drift wall include thermal properties (conductivity, heat capacity) of the rock and the representation of heat-transfer processes in the drift (i.e., the approximate treatment of thermal radiation and convection). However, comparison of temperatures measured in the rock with simulated temperatures provides an effective test of validity for treatment of heat transfer to the rock. Confidence in the approach used is supported by the close agreement with measured temperatures (Figure 7.1-6).



Output DTN: LB0705DSTHC005.002.

Figure 7.1-5. Drift Center Modeled Temperatures over the Preheating, Heating, and Cooling Periods of the DST

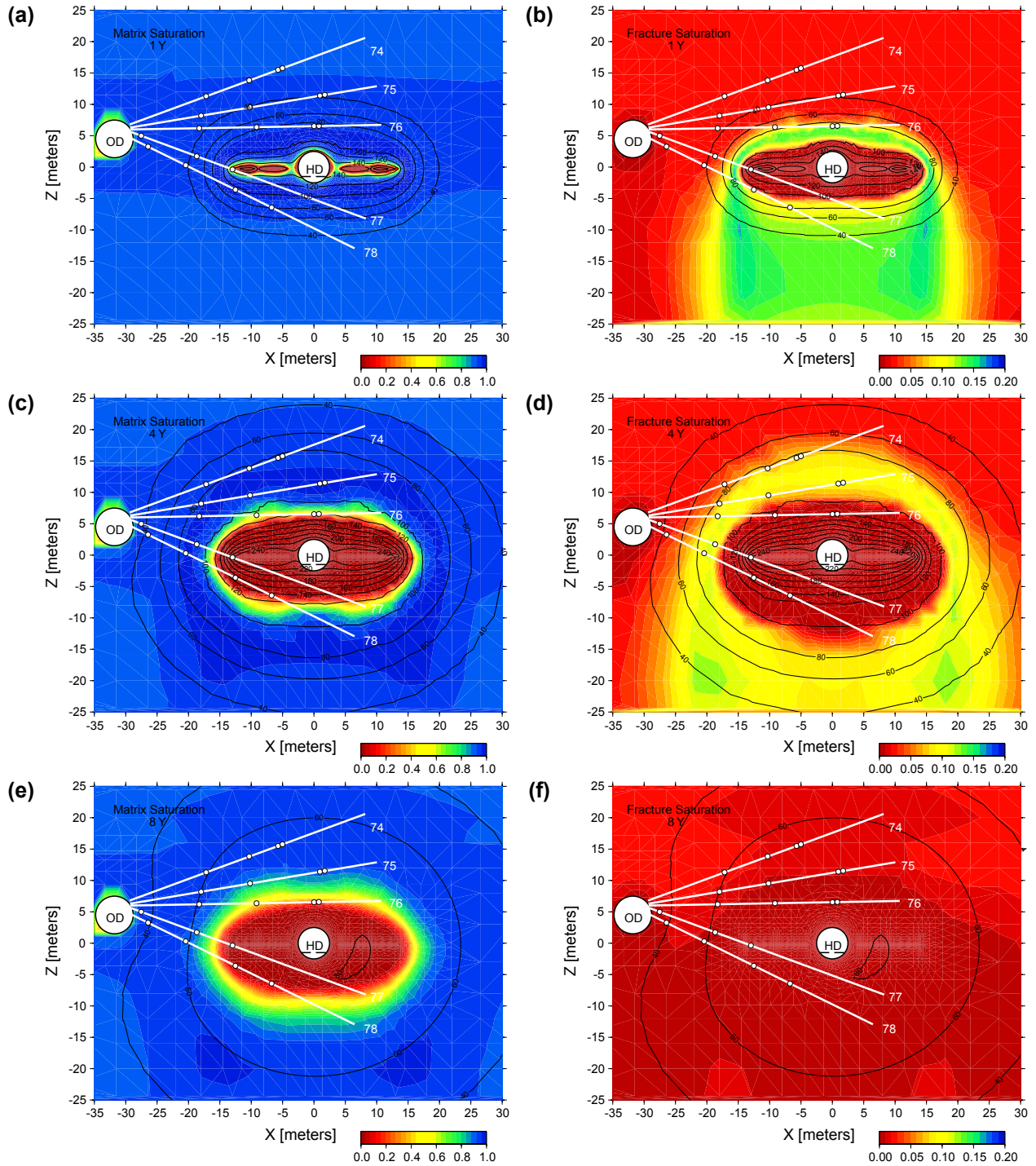


Output DTN: LB0705DSTHC005.002 (modeled values).

NOTE: Modeled temperatures are for a nearby grid node. Location of temperature sensor is indicated on Figure 7.1-4. See Table 7.1-1 for DTNs for measured temperatures.

Figure 7.1-6. Comparison of Modeled and Measured Temperatures over Time (infiltration rates of about 14 and 1.4 mm/yr) for the Sensor Located at Hydrology Borehole Packer 60-4

The modeled distributions of fracture and matrix liquid saturation (with temperature contours overlain) are shown in Figure 7.1-7. The plots correspond to one and four years from the initiation of the heating phase, and at eight years (planned end of cooling phase). The extent of the dryout zone increases over the heating period and is larger in the fractures than in the matrix. A wider spatial interval between the 90°C and 100°C isotherms indicates the presence of an isothermal boiling/condensation (heat pipe) zone, which is especially well developed above the wing heaters. An extensive drainage zone extending several tens of meters in the fractures below the heaters contrasts with a very narrow high-saturation zone above the heaters, where water is continuously diverted around the heated zone. The narrow band of increased fracture saturation above the heaters is characterized by temperatures of about 90°C to 95°C. Typically, water was collected from hydrology boreholes when this heat-pipe zone intersected the borehole intervals (Figure 7.1-4) (BSC 2005 [DIRS 172232], Section 7.4.3). During the DST, saturation changes in the rock were monitored using ground-penetrating radar and electrical resistance tomography (BSC 2005 [DIRS 172232], Section 7.4.1). The spatial distribution of the observed changes in matrix saturation are similar to model results, as discussed further in *Drift-Scale Coupled Processes (DST and TH Seepage) Models* (BSC 2005 [DIRS 172232], Section 7.4.3.2).



Output DTN: LB0705DSTHC005.002.

NOTE: Borehole intervals where water and/or gas samples were collected are shown in Figure 7.1-4.

Figure 7.1-7. Modeled Liquid Saturation (colors) and Temperature (contour lines) in the DST at One, Four, and Eight Years (matrix: a, c, and e; fracture: b, d, and f).

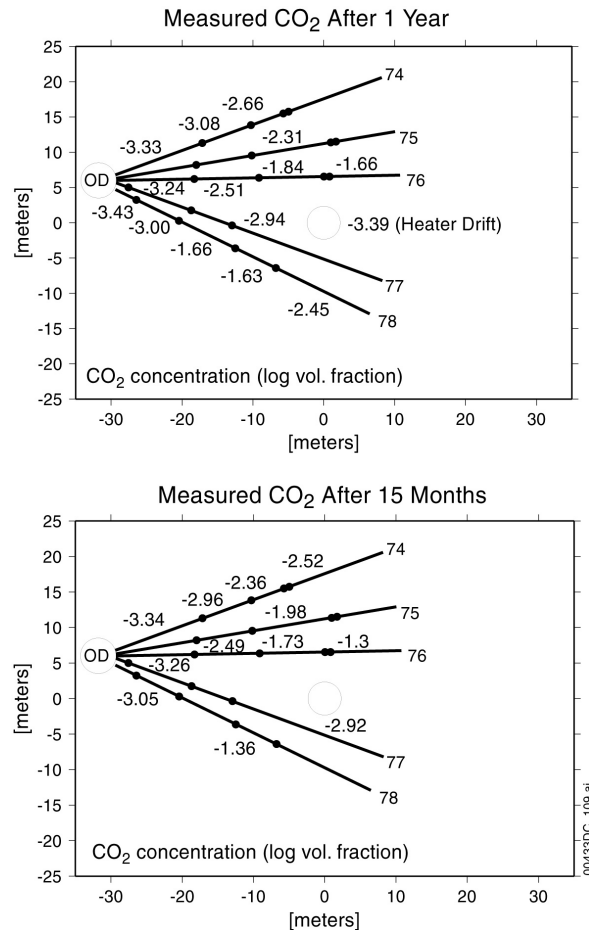
7.1.10 Gas-Phase CO₂ Evolution: Measured Compositions and Simulation Results

The evolution of CO₂ concentrations in the gas phase is discussed in this section. Simulation results are compared to concentrations measured in gas samples taken from boreholes during the entire heating phase of the DST. The concentration of CO₂ in the gas phase is a function of temperature, pressure, aqueous-phase chemistry, mineral–water reactions, and advective and diffusive transport. From a model validation standpoint, the strong effect of CO₂ partial pressure on water pH and the final brine composition formed upon evaporation make the analysis of CO₂ distributions in the DST important. Numerous measurements of CO₂ concentrations in gas collected from the DST have been made as a function of space and time, and therefore a more complete comparison of the model results to CO₂ data can be made than to the relatively fewer number of water-chemistry measurements. CO₂ concentrations in gases collected from the DST also provide a qualitative measure of the influence of atmospheric gas on the system, because of the relatively low and constant value in the atmosphere (≈ 400 ppmv). Isotopic compositions of CO₂ (discussed in Section 7.1.14) yield insight into the sources of CO₂.

7.1.10.1 Gas Sampling and CO₂ Measurements

Gas sampling, analytical methods, and compositional data are discussed in *Thermal Testing Measurements Report* (SNL 2007 [DIRS 177414], Section 6.3.4.2). Gas samples were taken from several meter-long borehole intervals that spanned a wide range of temperatures as a result of their orientation relative to the heaters. As part of the sampling procedure, the gas samples had much of their water vapor removed before analyses were performed, and therefore measured CO₂ concentrations are for the noncondensable gas fraction. The noncondensable gas fraction is very high (>95%) at the ambient temperature of about 25°C, but may drop to extremely low values (<1%) under boiling conditions. Hence, reported CO₂ concentrations at temperatures close to boiling are much higher than if the measurements were made on a “complete” gas composition (air + CO₂ + H₂O). This effect must be considered when comparing model results to measured values.

An example of the distributions of measured CO₂ concentrations (DTNs are listed in Table 7-1) after one year and after 15 months of heating is shown in Figure 7.1-8. Comparison of the 15-month to the one-year data shows that in nearly all of the boreholes, the CO₂ concentrations are higher at 15 months, owing to heating of pore water and exsolution of CO₂ into the gas phase. Areas that have maintained CO₂ concentrations close to the ambient value in the “rock” of around 1,000 ppmv (log volume fraction = -3) can be seen near the observation drift. However, very close to the Observation Drift, some of the values are lower, suggesting that mixing with atmospheric gas may have taken place.



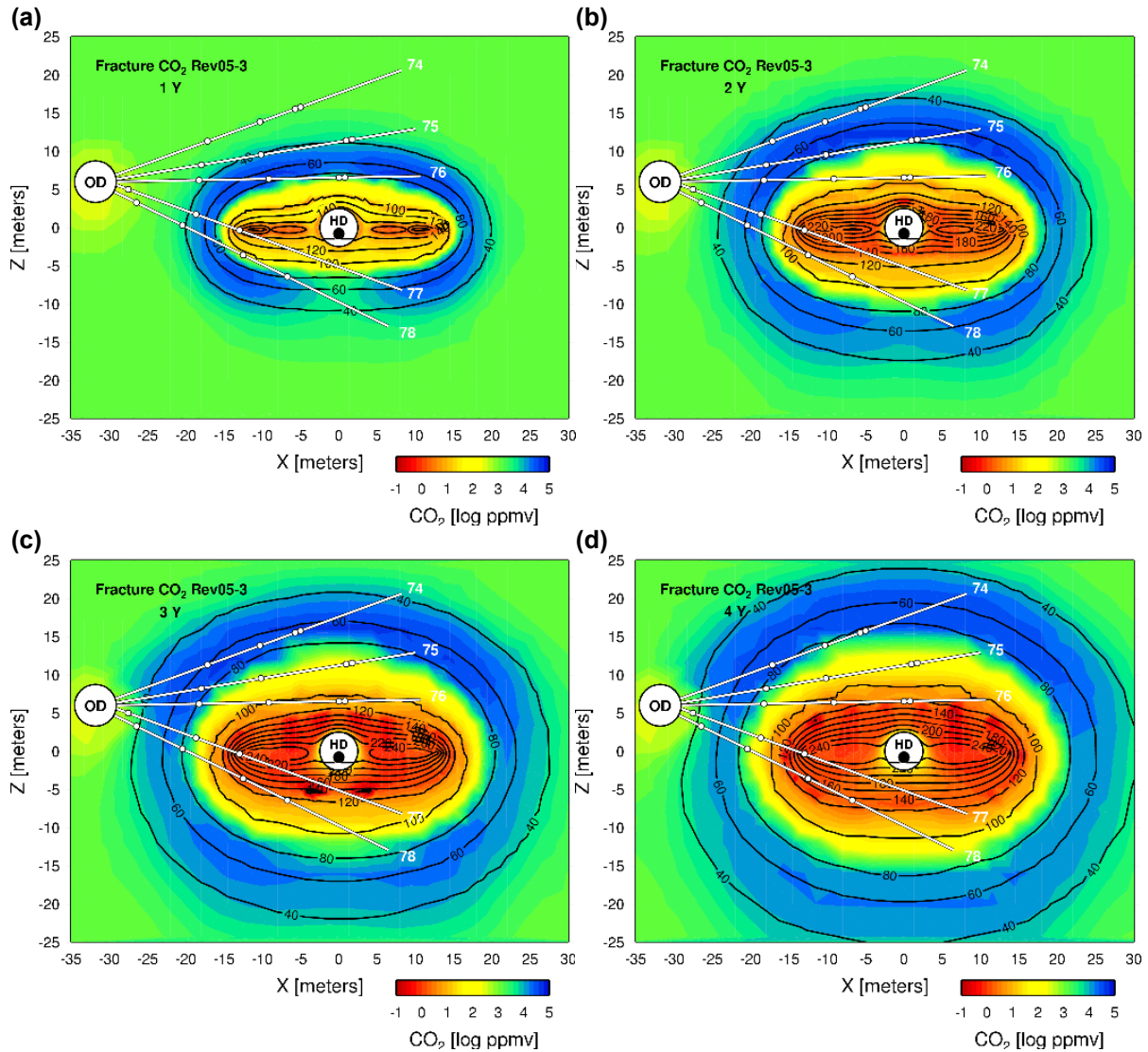
Source: DTN: LB990630123142.003 [DIRS 111476].

NOTE: Concentrations refer to intervals between pairs of points.

Figure 7.1-8. Measured Concentrations of CO₂ (log vol. fraction) in Gas Phase around the DST at 1 Year and at 15 Months

7.1.10.2 Modeled Spatial Distribution of CO₂

Model results are presented for Simulation 4 (1.446 mm/yr infiltration rate case), because the overall initial conditions (matrix liquid saturation) are closest to that observed at the DST, as described previously. Modeled distributions of CO₂ concentrations (log ppmv) in fractures are shown at yearly intervals during the heating phase (Figure 7.1-9) and during the cooling phase (Figure 7.1-10). Temperature contours for the rock matrix are overlain. Over the heating phase of four years, a region of highly elevated CO₂ concentrations, centered approximately at the 60°C isotherm, is seen to move gradually outward from the heaters. Outside this region, CO₂ concentrations gradually decrease to the ambient value in equilibrium with pore water (approximately 1,000 ppmv). Maximum CO₂ concentrations of around 50,000 ppmv are located above and below the wing heaters and Heated Drift. Toward the heaters, CO₂ concentrations drop off more sharply with increasing temperature, decreasing to values below 10 ppmv. This sharp decline takes place as a result of the CO₂ degassed during heating of the pore water, its transport outward, and displacement of air and CO₂ by steam generated during boiling.



Output DTN: LB0705DSTHC005.002.

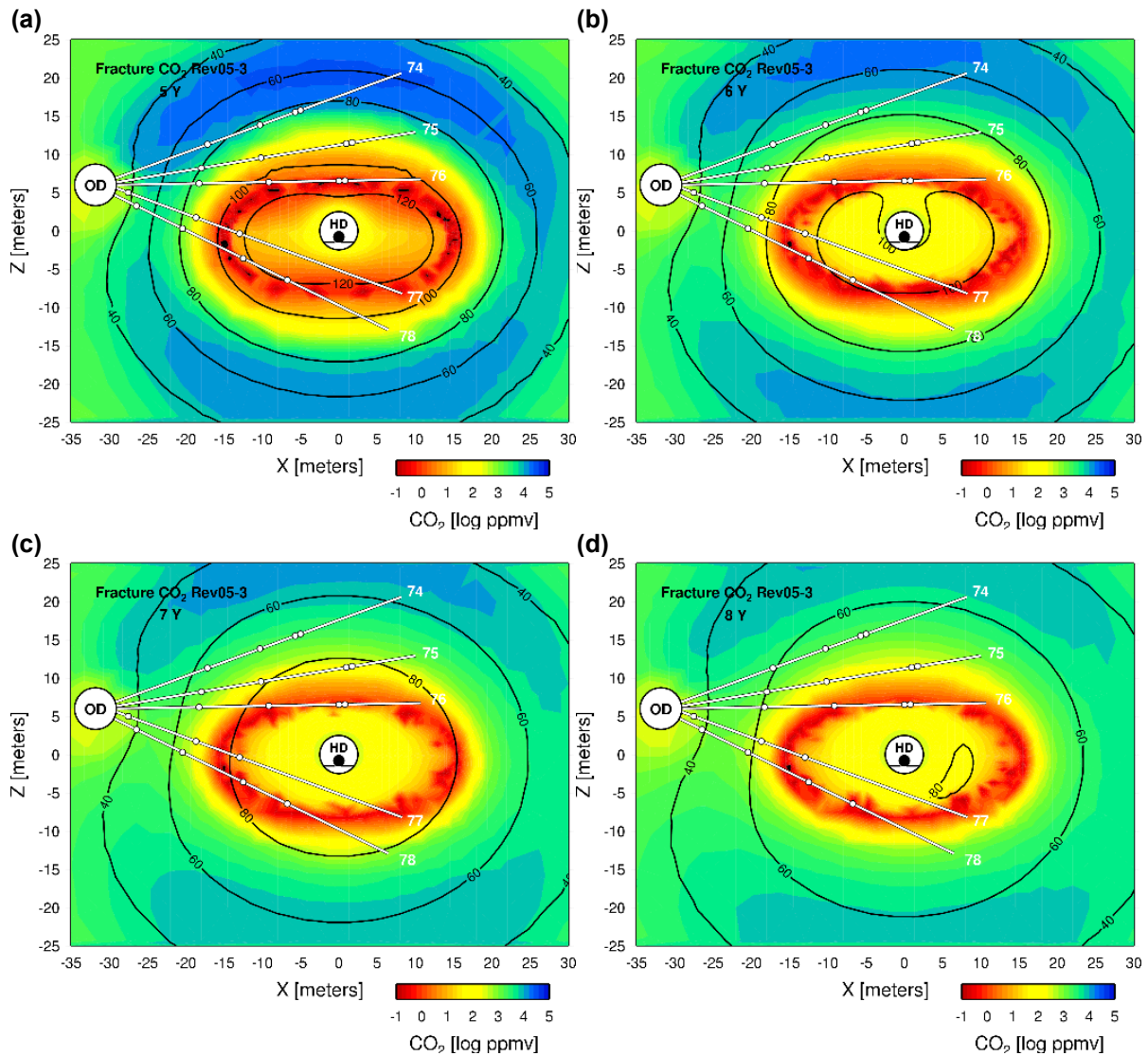
NOTE: Compare to measured concentrations in Figures 7.1-8, 7.1-12, and 7.1-13.

Figure 7.1-9. Modeled Gas Phase CO₂ Concentrations (log ppmv) in Fractures, and Matrix Temperatures (contour lines) during the Heating Phase of the DST at 1, 2, 3, and 4 Years

The zone of maximum CO₂ concentrations also transects the hydrology borehole intervals as it migrates outwards, with some intervals registering a two order-of-magnitude variation between them.

The effect of the atmospheric CO₂ concentration of the gas in the Observation Drift on its surroundings is evident up to about 10 m from the drift wall. However, effects on the fracture gas composition are relatively minor beyond about 5 m from the drift wall. Carbon dioxide concentrations in the Heated Drift stay close to the atmospheric value, owing to transport (advection and diffusion) between the Heater Test Alcove (set to atmospheric CO₂) and the Heated Drift.

The modeled cooling phase of the DST (Figure 7.1-10) is characterized by a gradual re-equilibration of CO₂ concentrations throughout the DST area, via cooling, gas-phase diffusion, and flow of gas and water. The zone of peak CO₂ concentrations continues to migrate outward, though the temperature at the peak concentration decreases to about 50°C at six years to 40°C after eight years. Exchange of atmospheric gas among the Heated Drift, Heater Test Alcove, and rock around the Heated Drift is clearly evident.

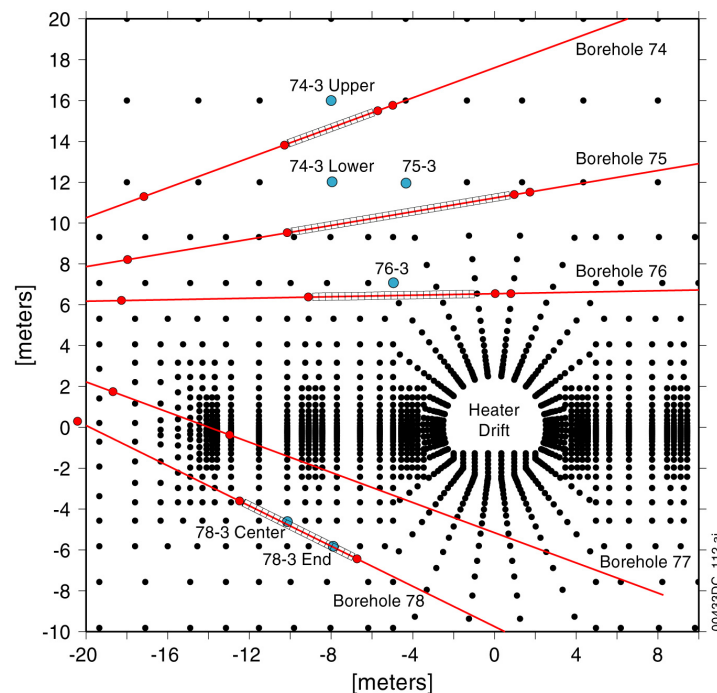


Output DTN: LB0705DSTHC005.002.

Figure 7.1-10. Modeled Gas Phase CO₂ Concentrations (log ppmv) in Fractures, and Matrix Temperatures (contour lines) during the Cooling Phase of the DST at 5, 6, 7, and 8 Years

7.1.10.3 Modeled and Measured CO₂ Concentrations over Time

Validation of the DST THC submodel for the prediction of the temporal evolution of CO₂ concentrations is performed by comparison of measured values from intervals repeatedly sampled from February 1998 through January 2002 (DTNs listed in Table 7-1) to model results. The locations of the gridblock central coordinates relative to the gas collected in borehole intervals from which the gas samples were taken are illustrated in Figure 7.1-11. Because the measured concentrations come from borehole intervals that are several meters long, and not from a specific location, model data are chosen from the gridblock closest to the center of the interval. If a gridblock is not centered on the borehole, a gridblock closest to the center is chosen on the outer (cooler) side of the borehole. Gridblocks on the cooler side should compare more closely to the measured data because the two-dimensional model, having no heat loss in the rock perpendicular to the drift, produces temperatures that are somewhat higher than the measured temperatures after approximately the first year of heating. However, measured temperatures may be higher prior to that time (refer back to the temperature comparison in Figure 7.1-6).



Output: DTN: LB0705DSTHC005.002.

NOTE: Borehole intervals from which gas samples were taken are shown in the hachured regions.

Figure 7.1-11. Close-Up of DST Grid, Showing Nodes Used to Extract Model Data for Comparison to Concentrations Measured in Gas Samples

The modeled values in Figure 7.1-12 have been modified to reflect the proportion of CO₂ in the noncondensable gas (NCG) proportion for comparison to measured data. Modeled CO₂ concentrations have been corrected for the approximate amount of water removed during chilling of the gas sample from the temperature of the sampling interval to 4°C, 25°C, and assuming all water was removed. The actual temperature of the chiller was 4°C; however, the efficiency of the unit was such that not all water was taken out when the gas was at boiling temperatures

(SNL 2007 [DIRS 177414], Section 6.3.4.2.5). For gases with temperatures below approximately 60°C, the correction is relatively small; however, at temperatures near boiling, the correction may be several orders of magnitude (Section 7.1.10.1). Figure 7.1-12 shows an example of the effect of the correction on the CO₂ concentrations for borehole interval 75-3.

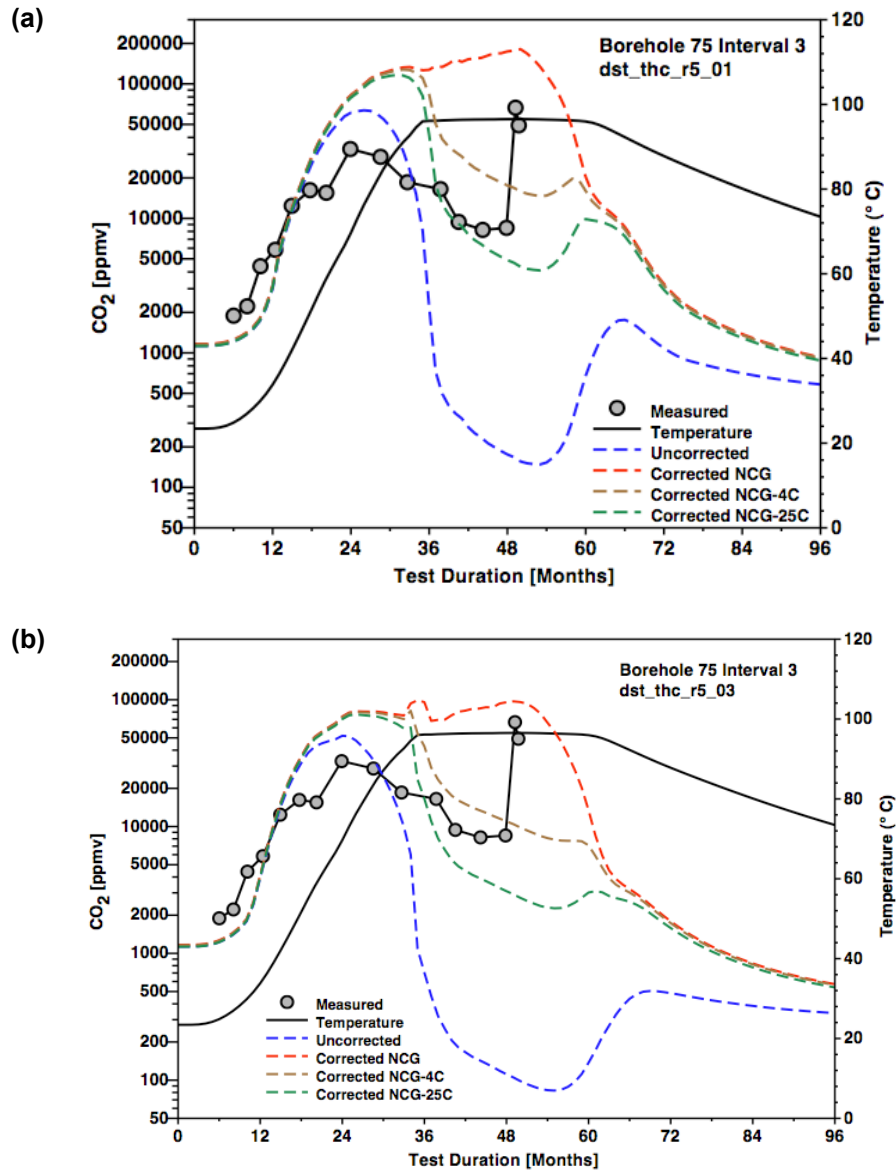
Figure 7.1-13 shows measured CO₂ concentrations compared to modeled values corrected to varying levels of moisture removal, as discussed in the previous paragraph. The model results are fairly similar from the initial time up to the peak concentration, but then are very different as the proportion of air in the gas phase declines. The correction for calculating the proportion of CO₂ becomes very large as the NCG content of the gas declines to well below 1%. For the measurements, some contamination with air takes place if the water condenses and the pressure drops strongly. Therefore, the most representative correction is probably somewhere between the value at 4°C and that at 25°C.

Model results are presented up to the end of the cooling phase of the DST, with measurements primarily during the heating phase and early in the cooling phase (up to nearly 2 years into the cooling phase). In many locations, as a result of prolonged elevated temperatures, the packers were deflated and the data no longer reflected a single interval. At this point, the data were not plotted because they reflected mixing over too large a volume.

In the hottest interval above the Heated Drift (76-3), the measured concentrations remained low from 2 years after heating was initiated until after the cooling phase had begun. Except for one sample that may have been predominantly water vapor, similar but delayed behavior took place in 75-3. Modeled compositions shown for 74-3 are given as an average of the values from the “upper” and “lower” gridblocks shown in Figure 7.1-11. For interval 78-3, only the concentrations from the center are plotted.

Trends in modeled CO₂ concentrations are clearly followed for all borehole intervals evaluated. Deviations in concentrations for certain samples can be attributed to the factors discussed in Section 7.1.7.1. The comparisons of simulated and measured (corrected) CO₂ concentrations are generally within an order of magnitude, except for low-concentration, high-temperature samples, where the correction due to condensation of water vapor is large. It was clear that higher initial liquid saturations lead to higher maximum CO₂ concentrations, further from the measured concentrations. The effect of a different maximum time step was significant for the CO₂ concentrations, where a smaller maximum time step led to higher maximum concentrations and lower minimum values. However, the difference between the twenty-minute and one-hour maximum time step was relatively minor, so the hour time step was chosen for the majority of the simulations.

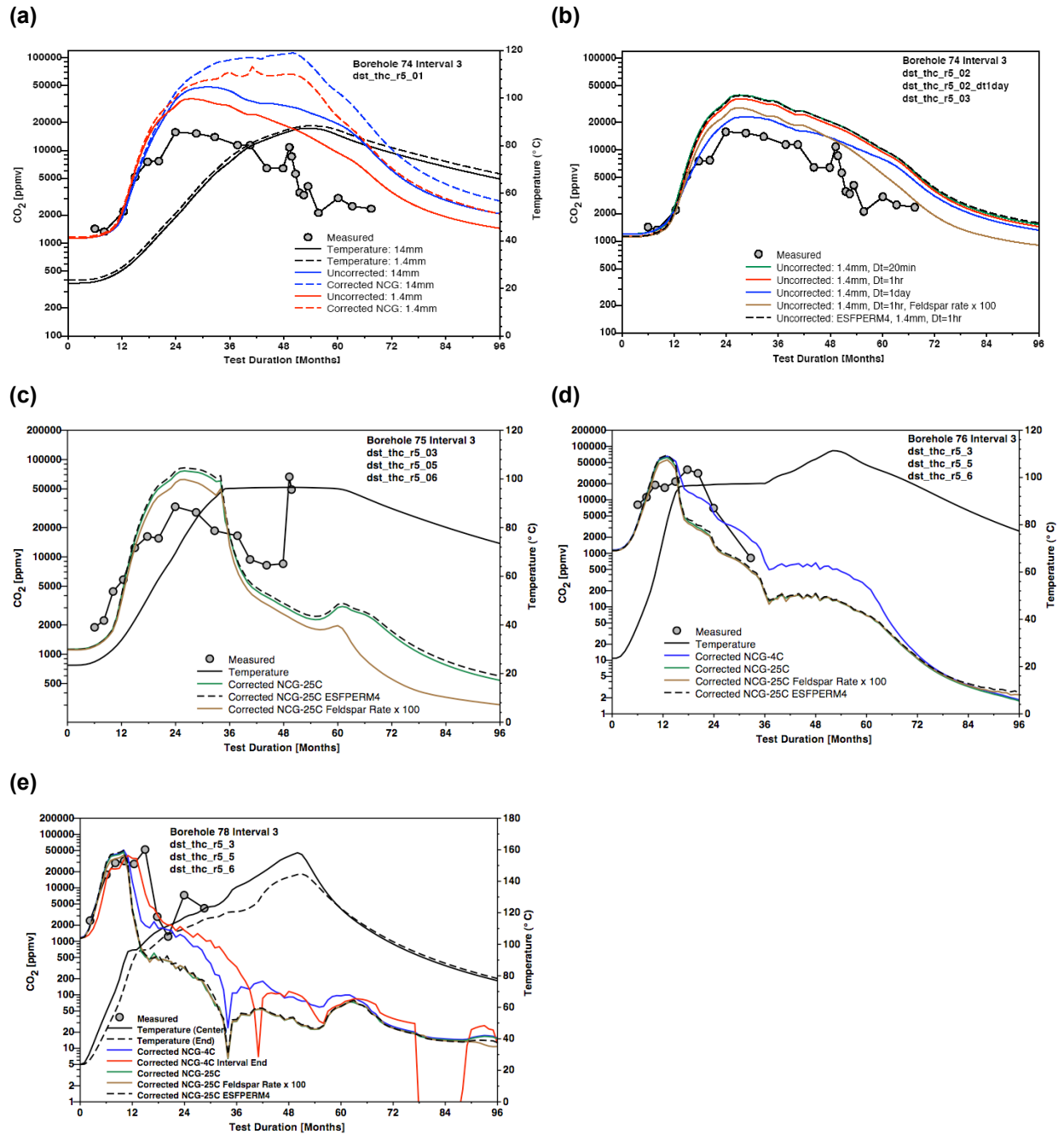
The high initial saturations led to a near-fully saturated matrix and a slower loss of vapor into fractures. The “second” peak in the data at 48 months is not consistent with any process predicted to occur in the rock and is associated with near-boiling sampling conditions, when only a tiny fraction of the gas is noncondensable and the potential error in the correction for water-vapor extraction is relatively large. Accordingly, the validation criteria discussed in Section 7.1.7 are met.



Source: Appendix M (measured CO₂); Output DTN: LB0705DSTHC005.002 (modeled).

NOTE: Temperatures are shown with values corresponding to right axis. See text for discussion of the outliers at 48 months.

Figure 7.1-12. Comparison of Measured and Corrected Model CO₂ Concentrations for Borehole Interval 75-3 for Simulations dst_thc_r5_01 (high infiltration rate) and dst_thc_r5_03 (low infiltration rate)



Source: Appendix M (measured CO₂); Output DTN: LB0705DSTHC005.002 (modeled).

NOTE: Temperatures are shown with values corresponding to right axis.

Figure 7.1-13. Comparison of Modeled CO₂ Concentrations (corrected to different NCG fractions) in Fractures to Measured Concentrations in Boreholes: (a) Borehole Interval 74-3 (average of bounding gridblocks); (b) Borehole Interval 74-3 (average of bounding gridblocks); (c) Borehole Interval 75-3; (d) Borehole Interval 76-3; (e) Borehole Interval 78-3 (interval center)

7.1.11 Aqueous Species Evolution

7.1.11.1 Chemistry of Waters Sampled during the Drift Scale Test

Water samples were collected from several hydrology boreholes during the heating phase of the DST. Collection dates, volumes, and field measurements (e.g., pH) for all water samples are presented in *Thermal Testing Measurements Report* (SNL 2007 [DIRS 177414], Table 6.3-24). Cation and anion analyses of the water samples are given in Table 6.3-25 (DTN: LL020709923142.023 [DIRS 161677]) of the same report. The latter table lists all samples that were analyzed, regardless of their origin. In particular, many samples were collected from borehole intervals above boiling temperatures and were clearly derived from water vapor that condensed in the tubing leading out of the interval. In most cases, such samples are clearly recognizable from the water samples pumped directly out of boreholes (and in contact with rock), based on (1) their significantly lower pH (most below pH 5) relative to water samples that accumulated inside the boreholes (nearly all above pH 6), (2) their extremely low anion and cation content (total dissolved solids around 10 ppm or less), and (3) very low total Si concentrations (most much less than 10 mg/L) compared to water samples having total Si concentrations mostly greater than 40 mg/L.

Specific exceptions to these criteria are those samples collected from intervals at high temperatures (>140°C) that have relatively low pH values (< pH 4), elevated F⁻ concentrations (>10 mg/L), and relatively high total Si values, but contain few other measurable constituents. Experimental studies confirmed the hypothesis that the breakdown of fluoroelastomer packer materials at elevated temperatures was responsible for the unusual water compositions that formed as high-temperature vapor condensed in tubing and was collected as water (SNL 2007 [DIRS 177414], Table 6.3.4.1-1). In addition, some waters may have been affected by degradation of neoprene packers in sub-boiling zones, such as the high-Cl water collected from borehole 59, interval 4 (Williams 2003 [DIRS 163765]).

Chemical analyses of water samples that, based upon the compositional criteria discussed above, were wholly or mostly derived from water that had resided in a borehole (rather than formed during condensation of water vapor in the collection tube) are given in Table 7.1-3. The intervals where these waters were collected are shown as the blue shaded zones in Figure 7.1-14. The water samples collected during the test were obtained from zones that were hotter than the temperatures given for the samples, because the samples cooled substantially as they were pumped out of the rock through the sample collection tubing and into the sample containers. Also listed in Table 7.1-3 are the compositions of pore waters that had been ultracentrifuged out of the rock matrix from a dry-drilled borehole near the DST (HD-PERM designations). Although the samples that were considered as forming from condensed vapor in the extraction lines are not listed in this table, they are plotted when available.

Table 7.1-3. Measured Concentrations in Tipmm Pore Water from Alcove 5 and Chemistry of Water Samples from Hydrology Boreholes

SMF No. (SPCO...)	1002488	1002586	1002525	05279699	05279689	0527915 ^a	0527977 ^a	0527916 ^a	0541804 ^a	1541804 ^{ab}	05043968	0529637-#1 ^b	0529637-#2 ^a
Collection Date			Pre-Heating	06/04/98	06/04/98	08/12/98	06/04/98	08/12/98	11/12/98	11/12/98	01/26/99	03/30/99	03/30/99
Collection Time			Pre-Heating									9:50 AM	9:55 AM
Sample ID	PERM-1 ^c	PERM-2 ^c	PERM-3 ^c	BH 60-2	BH 60-2	BH 60-2	BH 60-3	BH 60-3	BH 60-3	BH 60-3	BH 60-3	BH 60-3	BH 60-3
Field pH ^d	7.79	8.32	8.31	7.5	na	6.9	7.7	6.8	6.92	6.92	7.4	8.0	na
Metals / Cations													
Na (mg/L)	60.5	61.0	61.5	20.0	na	20.4	24.0	17.2	10.1	20.3	19.1	11.2	11.0
Si (mg/L)	37	31	35	56	na	51.8	41	43.5	60.0	53.8	65.0	62.8	59.8
Ca (mg/L)	98.17	106.17	96.67	20	na	19.9	25	18.7	15.3	13.9	5.93	2.06	2.27
K (mg/L)	6.0	7.0	9.0	6.0	na	5.4	4.5	4.5	8.7	7.8	4.1	2.4	2.4
Mg (mg/L)	25.65	16.55	17.35	2.9	na	1.21	5.7	4.0	3.35	3.00	1.17	0.27	0.26
Al (mg/L)	< 0.06	< 0.06	< 0.06	0.12	na	< 0.06	0.017 ^e	0.003 ^e	0.033 ^e	0.033 ^e	< 0.06	0.36, 0.27 ^e	0.36, 0.27 ^e
B (mg/L)	3.05	2.75	2.75	1.2	na	1.84	0.92	1.14	1.58	1.41	1.75	2.10	2.11
S (mg/L)	42.25	38.6	38.65	5.5	na	4.5	9.2	5.2	11.6	10.5	6.4	1.83	1.82
Fe (mg/L)	< 0.02	< 0.02	< 0.02	0.04	na	0.02	< 0.02	0.12	0.02	< 0.02	< 0.02	< 0.02	< 0.02
Li (mg/L)	0.1	0.45	0.05	0.07	na	0.03	0.07	0.040	0.040	0.040	0.02	0.02	< 0.01
Sr (mg/L)	1.4	1	1.05	0.18	na	0.11	0.34	2.21	0.22	0.20	0.09	0.02	0.02
Anions													
HCO ₃ (mg/L) ^f				na	na	na	na	na	na	na	41	25.0	na
F (mg/L)	0.36	0.96	0.76	na	1.00	0.71	0.82	0.43	0.49	0.50	1.27	1.02	0.97
Cl (mg/L)	122.73	109.93	123.13	na	10	6.14	16	5.52	19.5	19.6	10.3	4.15	3.92
Br (mg/L)	0.6	0.76	1.2	na	0.84	0.05	0.73	0.21	0.6	0.51	0.15	< 0.04	< 0.04
SO ₄ (mg/L)	124.18	111.38	119.78	na	17	4.88	30	8.81	30.6	30.8	13.5	3.83	3.75
PO ₄ (mg/L)	< 0.07	< 0.07	< 0.07	na	< 0.07	0.25	< 0.07	0.16	< 0.2	< 0.2	< 0.05	< 0.05	< 0.05
NO ₂ (mg/L)	< 0.04	< 0.04	< 0.04	na	< 0.01	< 0.04	< 0.01	< 0.04	< .10	< .10	< .03	< 0.03	< 0.03
NO ₃ (mg/L)	21.72	2.52	10.40	na	3.00	0.46	3.6	0.60	3.38	3.17	2.56	0.92	0.84

INTENTIONALLY LEFT BLANK

Table 7.1-3. Measured Concentrations in Tppmm Pore Water from Alcove 5 and Chemistry of Water Samples from Hydrology Boreholes (Continued)

SMF No. (SPCO...)	0551159 ^a	0551160 ^a	0557029 ^a	0557032	0557033 ^a	0557080	0557081	0557083	0557022	0550671	0550673	0550681	0550682
Collection Date	08/09/99	08/09/99	10/27/99	10/27/99	10/27/99	11/30/99	11/30/99	11/30/99	01/25/00	01/25/00	01/25/00	05/23/00	05/23/00
Collection Time													
Sample ID	BH 59-2(AC)	BH 59-2(BC)	BH 59-2	BH 59-2	BH 59-2	BH 59-2	BH 59-2	BH 59-2	BH 59-2	BH 59-2	BH 59-2	BH 59-2	BH 59-2
Field pH ^d	na	na	na	5.93	6.08	6.86	7.24	na	7.07	6.68	na	6.96	6.96
Metals / Cations													
Na (mg/L)	30	24	na	9.2	9.2	6.6	7.7	na	8.1	6.6	na	17	18
Si (mg/L)	78	81	na	44.5	44.9	38.0	39.9	na	42.8	41.7	na	59.4	59.2
Ca (mg/L)	47	39	na	7.53	7.47	4.33	5.63	na	7.54	2.89	na	4.7	4.4
K (mg/L)	8	6	na	3.4	3.6	2.6	3.0	na	3.6	2.8	na	4.3	4.4
Mg (mg/L)	13	11	na	1.81	1.72	1.02	1.38	na	1.78	0.72	na	1.1	1.1
Al (mg/L)	<0.2	<0.2	na	0.033 ^b	0.033 ^b	0.030	0.030	na	<0.05	0.043	na	<0.053	<0.053
B (mg/L)	0.8	0.6	na	0.27	0.21	0.14	0.17	na	0.29	0.21	na	na	na
S (mg/L)	22	17	na	2.52	2.50	0.76	1.33	na	6.44	0.65	na	na	na
Fe (mg/L)	0.41	0.32	na	0.20	0.19	0.09	0.14	na	0.07	<0.02	na	<0.038	<0.038
Li (mg/L)	<4	<4	na	0.16	0.01	0.01	0.01	na	<0.01	<0.01	na	0.021	0.022
Sr (mg/L)	0.54	0.45	na	0.11	0.08	0.06	0.08	na	0.091	0.036	na	<0.013	<0.013
Anions													
HCO ₃ (mg/L) ^f	na	na	23.5	na	23.5	na	na	22.3	na	na	22.8	31.4	31.4
F (mg/L)	0.725	0.575	0.27	na	0.27	na	na	0.35	na	na	0.73	0.58	0.55
Cl (mg/L)	88.3	71.0	9.5	na	9.1	na	na	5.0	na	na	3.8	10.15	10.6
Br (mg/L)	0.515	0.46	0.61	na	0.58	na	na	<0.03	na	na	<0.1	<0.1	0.38
SO ₄ (mg/L)	64.2	53.5	6.2	na	6.3	na	na	2.8	na	na	1.8	2.9	3.18
PO ₄ (mg/L)	<0.02	<0.02	<0.02	na	<0.02	na	na	<0.02	na	na	0.62	<0.2	<0.2
NO ₂ (mg/L)	<0.007	<0.007	<0.007	na	<0.007	na	na	<0.007	na	na	<0.05	<0.06	<0.06
NO ₃ (mg/L)	3.79	2.83	1.32	na	1.40	na	na	<0.02	na	na	0.77	0.56	0.54

INTENTIONALLY LEFT BLANK

Table 7.1-3. Measured Concentrations in Tppmm Pore Water from Alcove 5 and Chemistry of Water Samples from Hydrology Boreholes (Continued)

SMF No. (SPCO...)	0550684	0550693	0550694	0550691	0550689	0550690	0530398	0557036 ^a	0557038 ^a	0552575	0557043	0541803 ^a	0541803 ^{a,b}
Collection Date	05/23/00	06/29/00	06/29/00	06/29/00	06/29/00	06/29/00	01/23/01	10/27/99	10/27/99	11/30/99	11/30/99	11/12/98	11/12/98
Collection Time													
Sample ID	BH 59-2	BH 59-2	BH 59-2	BH 59-2	BH 59-2	BH 59-2	BH 59-2	BH 59-3	BH 59-3	BH 59-3	BH 59-3	BH 59-4	BH 59-4
Field pH ^d	6.95	6.99 to 7.08	6.99 to 7.08	7.00	na	na	na	na	6.64	7.47	na	6.63	6.63
Metals / Cations													
Na (mg/L)	17	16	15	< 4.8	na	na	29	na	19.3	15.6	na	22.6	135
Si (mg/L)	59.3	62.7	57.5	36.3	na	na	84.5	na	84.2	92.5	na	33.5	44.2
Ca (mg/L)	4.5	4.3	3.8	2.0	na	na	7.8	na	13.2	2.86	na	476	450
K (mg/L)	4.4	4.7	4.2	2.5	na	na	5.8	na	5.6	3.9	na	29.5	37.8
Mg (mg/L)	1.1	1.1	1.0	0.54	na	na	1.8	na	1.49	0.29	na	64.1	83.9
Al (mg/L)	< 0.053	< 0.053	< 0.053	< 0.11	na	na	< 0.053	na	0.040	0.071	na	0.01 ^e	< 0.06
B (mg/L)	na	na	na	na	na	na	na	na	0.86	1.06	na	4.47	4.13
S (mg/L)	na	na	na	na	na	na	na	na	14.48	3.25	na	50.7	64.8
Fe (mg/L)	< 0.038	< 0.038	< 0.038	< 0.076	na	na	< 0.038	na	< 0.02	< 0.02	na	< 0.02	< 0.02
Li (mg/L)	0.021	0.019	0.018	0.010	na	na	0.033	na	0.02	0.02	na	0.21	0.20
Sr (mg/L)	< 0.013	< 0.013	< 0.013	< 0.026	na	na	< 0.013	na	0.13	0.03	na	4.02	3.71
Anions													
HCO ₃ (mg/L) ^f	31.4	na	na	na	29.4	29.4	na	12.4	12.4	na	20.7	na	na
F (mg/L)	0.49	na	na	na	0.18	0.15	0.78	0.64	0.73	na	1.3	0.8	4.3
Cl (mg/L)	10.15	na	na	na	0.90	0.32	25.20	12.9	12.9	na	8.8	1,130	1,250
Br (mg/L)	< 0.1	na	na	na	0.62	0.48	< 0.1	0.89	0.51	na	< 0.03	1.13	< 0.07
SO ₄ (mg/L)	3.1	na	na	na	0.5	0.42	9.5	40.7	40.3	na	8.2	226	213
PO ₄ (mg/L)	< 0.2	na	na	na	< 0.2	< 0.2	< 0.2	< 0.04	< 0.04	na	< 0.02	< 5	< 0.2
NO ₂ (mg/L)	< 0.06	na	na	na	< 0.06	< 0.06	< 0.06	< 0.01	< 0.01	na	< 0.007	< 3	< 10
NO ₃ (mg/L)	0.71	na	na	na	0.65	0.48	0.99	3.06	3.05	na	2.4	3.12	7.81

INTENTIONALLY LEFT BLANK

Table 7.1-3. Measured Concentrations in Tppm Pore Water from Alcove 5 and Chemistry of Water Samples from Hydrology Boreholes (Continued)

SMF No. (SPCO...)	0504397 ^a	0551169 ^a	0559464	0559458	0559456	1016082	0557040 ^a	0552578	0552579	0550697	0541805 ^a	0541805 ^{ab}	0527961 ^a
Collection Date	01/26/99	08/10/99	04/17/01	04/17/01	04/17/01	01/07/02	10/27/99	11/30/99	11/30/99	05/23/00	11/12/98	11/12/98	01/26/99
Collection Time	BH 59-4	BH 61-3	BH 76-2	BH 76-2	BH 76-2	BH 76-2	BH 76-3	BH 76-3	BH 76-3	BH 76-3	BH 186-3	BH 186-3	BH 186-3
Sample ID	na	na	BH 76-2	BH 76-2	BH 76-2	BH 76-2	BH 76-3	BH 76-3	BH 76-3	BH 76-3	BH 186-3	BH 186-3	BH 186-3
Field pH ^d	na	na	7.68	8.22	8.29	7.8	6.14 to 6.46	6.94	na	6.92 to 6.96	6.83	6.83	7.2
Metals / Cations													
Na (mg/L)	219	19	9	9	9	na	64.5	28.2	na	29	105	17.0	25.9
Si (mg/L)	12.0	67	42.6	44.1	45.6	na	133.4	92.8	na	96.0	16.0	27.2	49.3
Ca (mg/L)	429	14	1.3	1.1	1.3	na	59.5	22.3	na	7.1	11.5	20.2	2.92
K (mg/L)	29.7	5	1.6	1.6	1.9	na	13.4	7.4	na	6.5	3.5	3.9	5.9
Mg (mg/L)	164	3.2	0.27	0.22	0.23	na	13.8	4.71	na	1.4	5.1	5.68	6.32
Al (mg/L)	0.086 ^e	< 0.2	0.42	0.43	0.45	na	0.010	0.031	na	< 0.053	< 0.003 ^e	< 0.003 ^e	< 0.06
B (mg/L)	6.68	1.5	na	na	na	na	2.38	0.81	na	na	0.51	0.58	0.84
S (mg/L)	109	3.1	na	na	na	na	34.55	9.46	na	na	8.47	9.42	7.9
Fe (mg/L)	< 0.02	1.2	0.40	0.40	0.39	na	< 0.02	0.10	na	< 0.038	0.02	< 0.02	0.09
Li (mg/L)	0.33	< 4	0.0098	0.010	0.0076	na	0.13	0.04	na	0.045	0.05	0.05	0.05
Sr (mg/L)	5.84	0.14	< 0.013	< 0.013	< 0.013	na	0.78	0.26	na	< 0.013	0.30	0.34	0.37
Anions													
HCO ₃ (mg/L) ^f	na	na	na	na	na	< 5	na	na	82.3	na	na	na	116
F (mg/L)	0.51	0.835	na	0.38	0.47	0.4	1.11	na	1.3	0.76	0.56	0.62	1.20
Cl (mg/L)	1,160	24.1	na	1.9	1.71	2.75	81.9	na	19	14.5	18.7	18.6	23.3
Br (mg/L)	1.51	0.35	na	< 0.1	< 0.1	< 0.2	0.97	na	< 0.03	< 0.1	0.67	0.60	0.32
SO ₄ (mg/L)	240	9.13	na	0.89	0.65	1.02	94.6	na	26.0	4.98	26.3	26.2	21
PO ₄ (mg/L)	< 0.5	< 0.02	na	< 0.2	< 0.2	< 0.3	< 0.02	na	< 0.02	< 0.2	< 0.2	< 0.2	< 0.1
NO ₂ (mg/L)	< .3	< 0.007	na	< 0.06	< 0.06	< 0.2	< 0.007	na	< 0.007	< 0.06	< .1	< .1	< 0.05
NO ₃ (mg/L)	11.6	0.825	na	< 0.09	< 0.09	< 0.2	6.42	na	2.5	1.47	7.47	7.27	6.73

^a Analytical results are corroborating data (as defined in SCI-PRO-006) and non-qualified. See Table 7-1 for source DTNs.

^b Sample filtered in the field and laboratory (Lawrence Livermore National Laboratory) prior to analyses.

^c Pore water samples (baseline): sample ultracentrifuged from borehole core.

^d See entry in SNL 2007 [DIRS 177414], Table 6.3.4.1-1, for temperature of pH measurements.

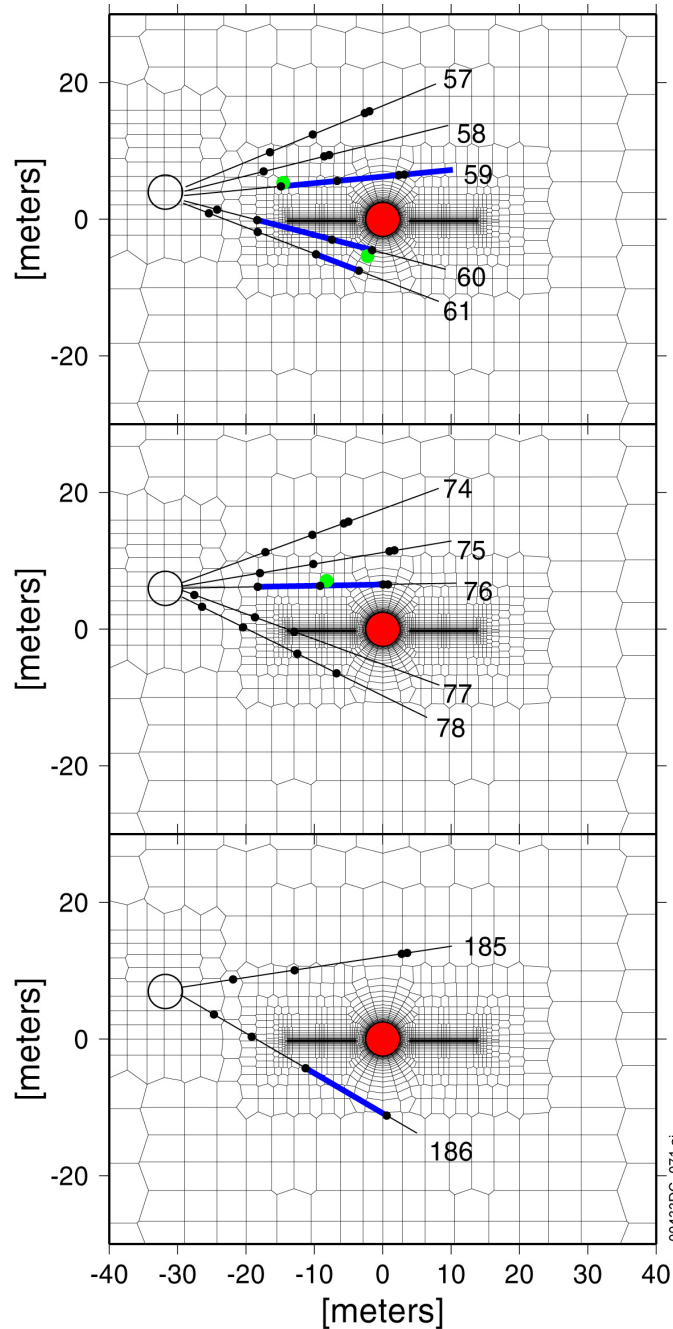
^e Low detection limit analysis – sample filtered to 0.10 mm and acidified.

^f HCO₃ – field measurement.

^g Sample ID SPC0057028 submitted for low detection for Al analysis.

NOTE: na = not available; < = not detected (less than "practical reporting limit"). Field chemistry of samples for high fluoride study (11/8/01 to 12/5/01) are reported in SNL 2007 [DIRS 177414], Table 6.3.4.5-1.

INTENTIONALLY LEFT BLANK



Source: SNL 2007 [DIRS 177414], Table 6.3.4.1-1 (water collection locations); DTN: MO0002ABBLSLDS.000 [DIRS 147304] (sensors and boreholes).

Output DTN: LB0705DSTHC005.002 (mesh).

NOTE: Only those waters having the distinct criteria discussed in this section are considered to have been liquid in the borehole. Locations where comparisons are made to measured compositions are shown as green circles. The Heater Drift is shown in red. Boreholes 57 to 61, 74 to 78, and 185 and 186 are located approximately 10 m, 30 m, and 45 m from the bulkhead along the drift axis, respectively (Figure 6.3-4 and Table 6.3-2 in SNL 2007 [DIRS 177414]).

Figure 7.1-14. Zones Where Water Was Collected from Hydrology Boreholes Superimposed (thick shading in blue) on the Model Grid

Some of the processes that could explain the water chemistry of samples collected in the hydrology boreholes include mixing of pure condensate water with fracture pore waters, equilibration of condensate waters with matrix pore waters via molecular diffusion, reaction of condensate waters with fracture-lining minerals, and mineral precipitation. Waters that were collected from the hydrology boreholes at elevated temperatures are generally more dilute (lower Cl^- and SO_4^{2-}) and lower in pH than the initial pore water. Aqueous silica concentrations are similar to or much higher than in the pore water, indicating that these waters are not simple mixtures of pore water and pure condensate water. Some clear trends in water chemistry of the condensate waters over time are increases in pH and $\text{SiO}_2(\text{aq})$ concentration and a drop in Ca^{2+} . The higher silica concentration in the waters collected at later times in several boreholes (and at higher temperatures), relative to chloride and the initial pore-water silica concentration, is consistent with dissolution of a silicate phase, rather than with increased concentration via boiling. Concentrations of K^+ , Mg^{2+} , and Na^+ are also higher than what would be expected by dilution of original pore water (as evidenced by the low chloride concentrations). Therefore, the silicate phases that dissolved must have been some combination of silica polymorphs (i.e., opal, cristobalite, tridymite, and quartz) and feldspar, clays, or zeolites, rather than just a pure silica phase. Many of the waters show a drop in Ca^{2+} over time, consistent with calcite precipitation as the water was heated further and underwent CO_2 degassing.

These water samples are considered to be representative of fracture waters produced by THC processes in the region around the DST. However, the borehole intervals from which the waters were collected are approximately 8 to 10 m in length and at times have temperatures several tens of degrees different at each end (Section 7.1.7). Therefore, vapor flow from the hot end to the cool end of an interval, accompanied by condensation and reaction with the rock lining the borehole, could account for some of the water found in the boreholes. Because the borehole surface mineralogy is not identical to the fracture surface mineralogy, the water chemistry in the borehole may have some differences from the chemistry of water in the fractures. Yet, because the rock surface in the borehole was freshly drilled, it may be more reactive with respect to silicate mineral reactions, hence potentially producing higher concentrations of species comprising the silicate mineral phases. The fresh mineral surfaces in the borehole could, therefore, result in dissolution rates greater than those in the fractures, even though the surface area of the smooth borehole is likely to be less than that of the irregular fracture surface.

Further discussion of water chemistry in the DST and comparisons to simulation results is given in Section 7.1.11.2. Model results are compared to a more complete data set from these intervals and also to borehole interval 76-3, which is above the heaters in an array closer to the area where the maximum drift crown temperature is reached (30 m from the bulkhead). Waters were collected from other borehole intervals, but on only one or two occasions, and are therefore of limited value for validation. However, they do provide additional information on the range of potential water compositions.

7.1.11.2 Evolution in the pH of Waters from the DST

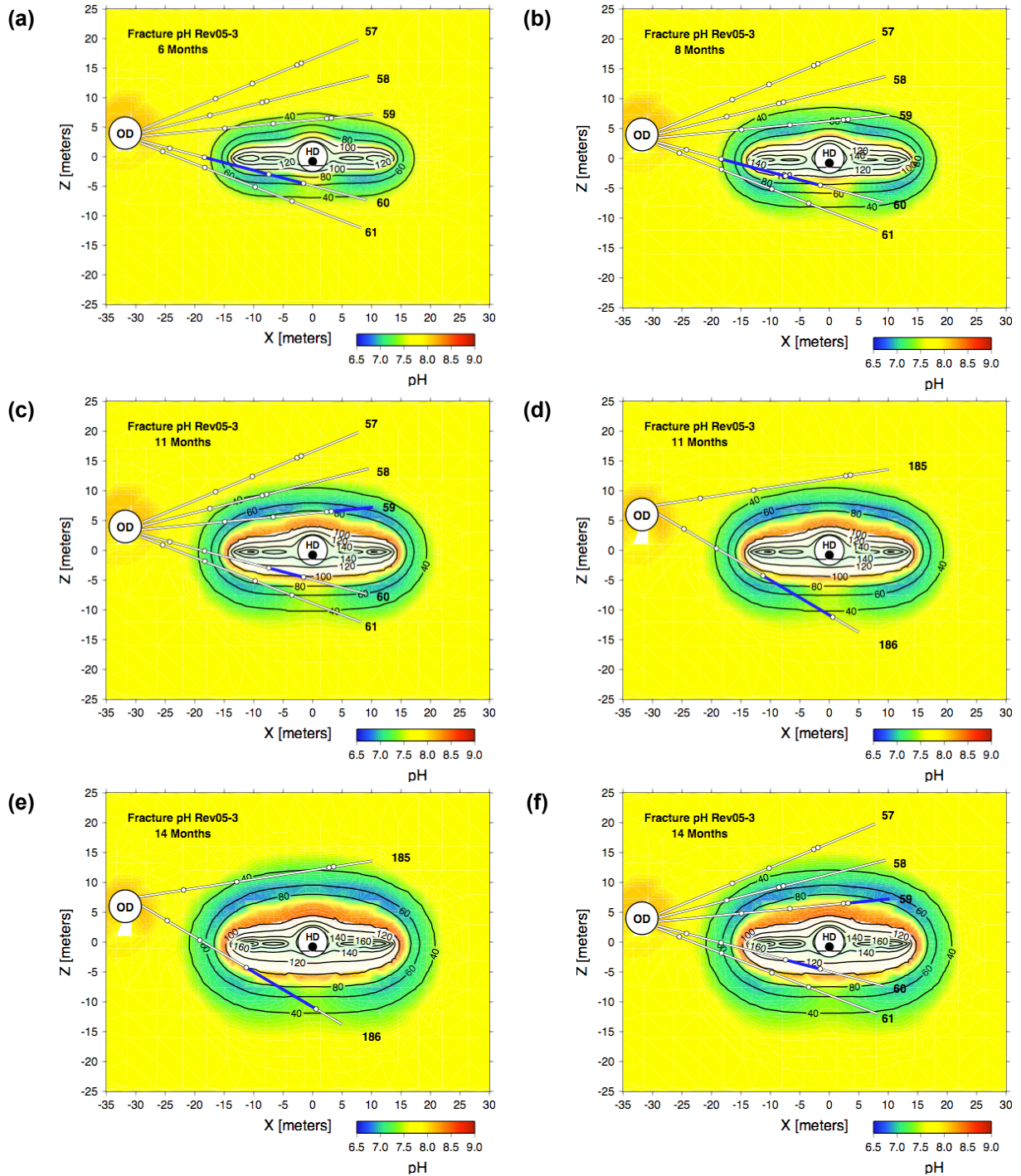
In this section, simulations of the evolution of pH in space and time are shown, followed by comparisons of pH measurements of waters collected from boreholes and model results at specific locations. The pH of waters in the rock is a function of the coupled thermal, chemical, and transport processes taking place in the fractures and matrix as the system undergoes heating.

The water chemistry can also be affected near rock interfaces, such as at the drift wall. Here, exchange of atmospheric air with gas in the rock takes place via advective transport and diffusion, or by simple degassing of water owing to barometric pressure changes.

The modeled spatial distribution of pH in fracture water at various times during the heating phase is shown in Figure 7.1-15. The times correspond approximately to the dates when water was sampled from hydrology borehole intervals, which are also highlighted. Based on the compositions of ambient pore water ultracentrifuged from the rock in the DST block, the pH of waters in the region of the DST likely started out between approximately 7.8 and 8.3 (Table 7.1-3). The initial pH of the water used in the DST THC submodel simulation is approximately 8.3. The most obvious effect of heating is a reduction in pH to about 6.8 in the condensate region, corresponding approximately to the increases in CO₂ concentrations shown in Figure 7.1-12. As with the CO₂ concentrations, the low pH zone increases in size and moves outward with time. Close to the dryout zone, the pH of the water increases, owing to boiling, degassing, and outward transport of the CO₂. Another important factor affecting the pH is the reaction rates of certain minerals, such as feldspars, that upon dissolution consume H⁺, resulting in a rise in pH.

There is greater uncertainty in measured pH values than in other compositional parameters. The pH is temperature-sensitive, and the measured values are for partially cooled samples. For example, over the temperature range from 60°C to ambient (25°C), the dissociation constant for water changes by approximately one order of magnitude (lowering the pH at higher temperature) (Garrels and Christ 1965 [DIRS 144877], Table 2.8). In addition, some CO₂ degassing and exchange with the ambient drift atmosphere occurred during sampling. Finally, as discussed in Section 7.1.11.1, some samples were contaminated by acid vapor released from degradation of the fluoroelastomer and chloroelastomer packer materials. Because of these factors, model–data comparisons for pH are presented here, but as supporting information only and not as part of the planned validation strategy. Confidence in the predicted pH values is based on superior fits between the predicted and measured HCO₃⁻, temperature, and pCO₂ data, as these parameters are among the dominant controls on pH.

Model–data comparisons for fracture water pH are shown for borehole intervals 60-3, 59-2, and 76-3 in Figure 7.1-16. The measured and simulated pH values generally fall within circumneutral pH range of approximately 6 to 8. All of the simulations showed nearly identical pH values, suggesting that this parameter was strongly governed by temperature and by reactions with the rock, and to a lesser extent the rate of degassing of CO₂. At all three sampling locations, an initial decrease in pH was followed by an increase, and the model results show similar trends at comparable times. Modeled pH values are not quite as low as those measured, possibly because of the delayed transport of steam out of the matrix (due to its high capillarity and low permeability). Also, the modeled fracture domain tended to dry out much earlier than in the boreholes, so the trends for the model are shifted to earlier times. Samples that were indicated to have been derived from vapor that condensed in the sampling lines or in the collection bags are shown as the red squares. At the early stages (just above the boiling temperature) they typically have pH values between 4 and 5, typical of condensed water from such temperatures and partial pressures of CO₂. At highly elevated temperatures, the samples show very low pH values down to almost 3.0, as a result of packer degradation and highly increased HF in the gas phase and in the condensate (see Figure 7.1-27a).

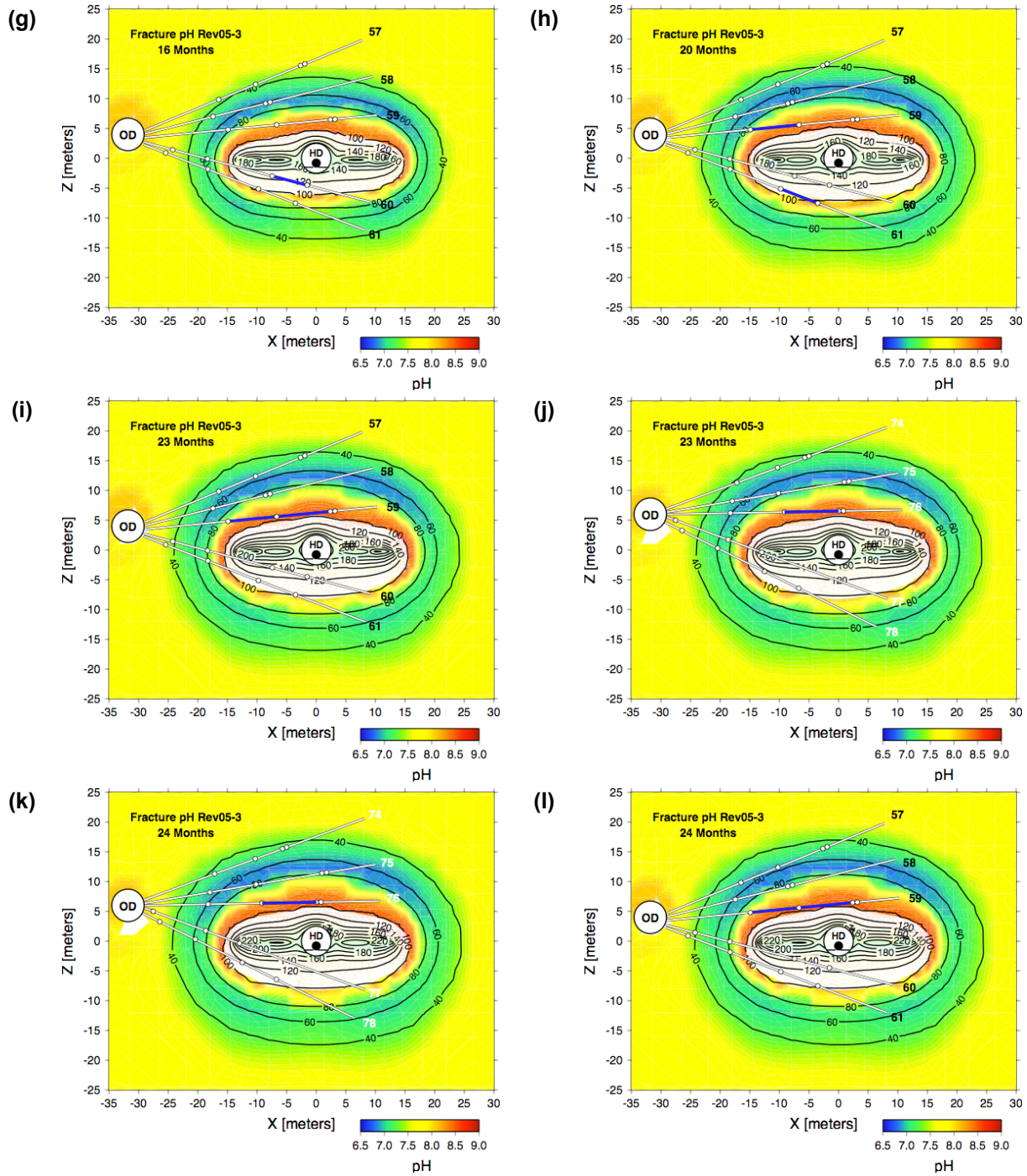


Output DTN: LB0705DSTHC005.002 (modeled).

Source: SNL 2007 [DIRS 177414], Table 6.3.4.1-1 (water collection locations).

NOTE: The intervals where water was sampled are more thickly shaded (in blue). Areas of zero liquid saturation are blanked out in white.

Figure 7.1-15. Modeled Distribution of pH in Fractures at Various Times When Water Was Sampled from Hydrology Borehole Intervals (months): (a) 6, (b) 8, (c) 11, (d) 11, (e) 14, (f) 14, (g) 16, (h) 20, (i) 23, (j) 23, (k) 24, (l) 24, (m) 26, (n) 30, (o) 30, (p) 31, (q) 38, (r) 40

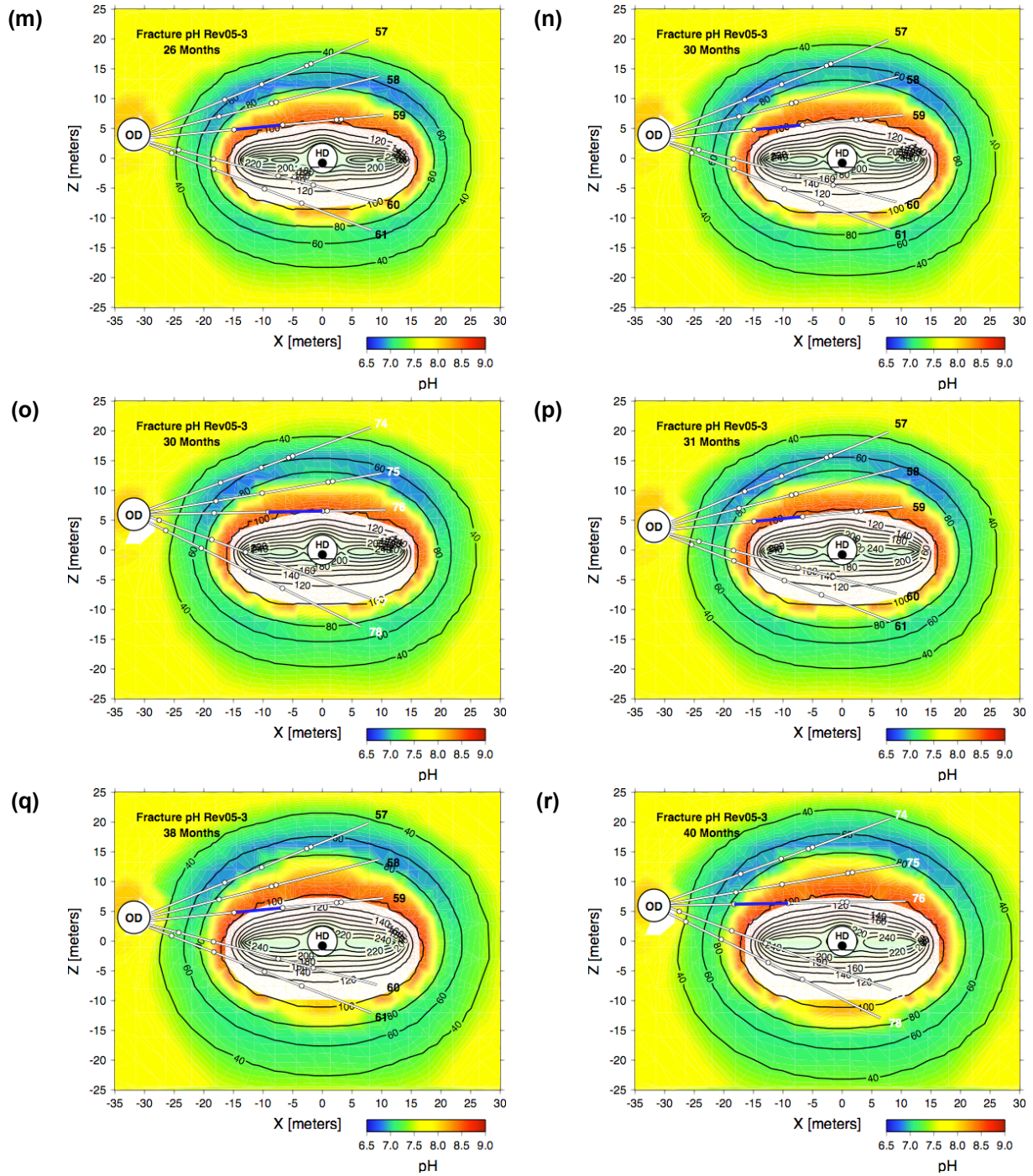


Output DTN: LB0705DSTHC005.002 (modeled).

Source: SNL 2007 [DIRS 177414], Table 6.3.4.1-1 (water collection locations).

NOTE: The intervals where water was sampled are more thickly shaded (in blue). Areas of zero liquid saturation are blanked out in white.

Figure 7.1-15. Modeled Distribution of pH in Fractures at Various Times When Water Was Sampled from Hydrology Borehole Intervals (months): (a) 6, (b) 8, (c) 11, (d) 11, (e) 14, (f) 14, (g) 16, (h) 20, (i) 23, (j) 23, (k) 24, (l) 24, (m) 26, (n) 30, (o) 30, (p) 31, (q) 38, (r) 40 (Continued)

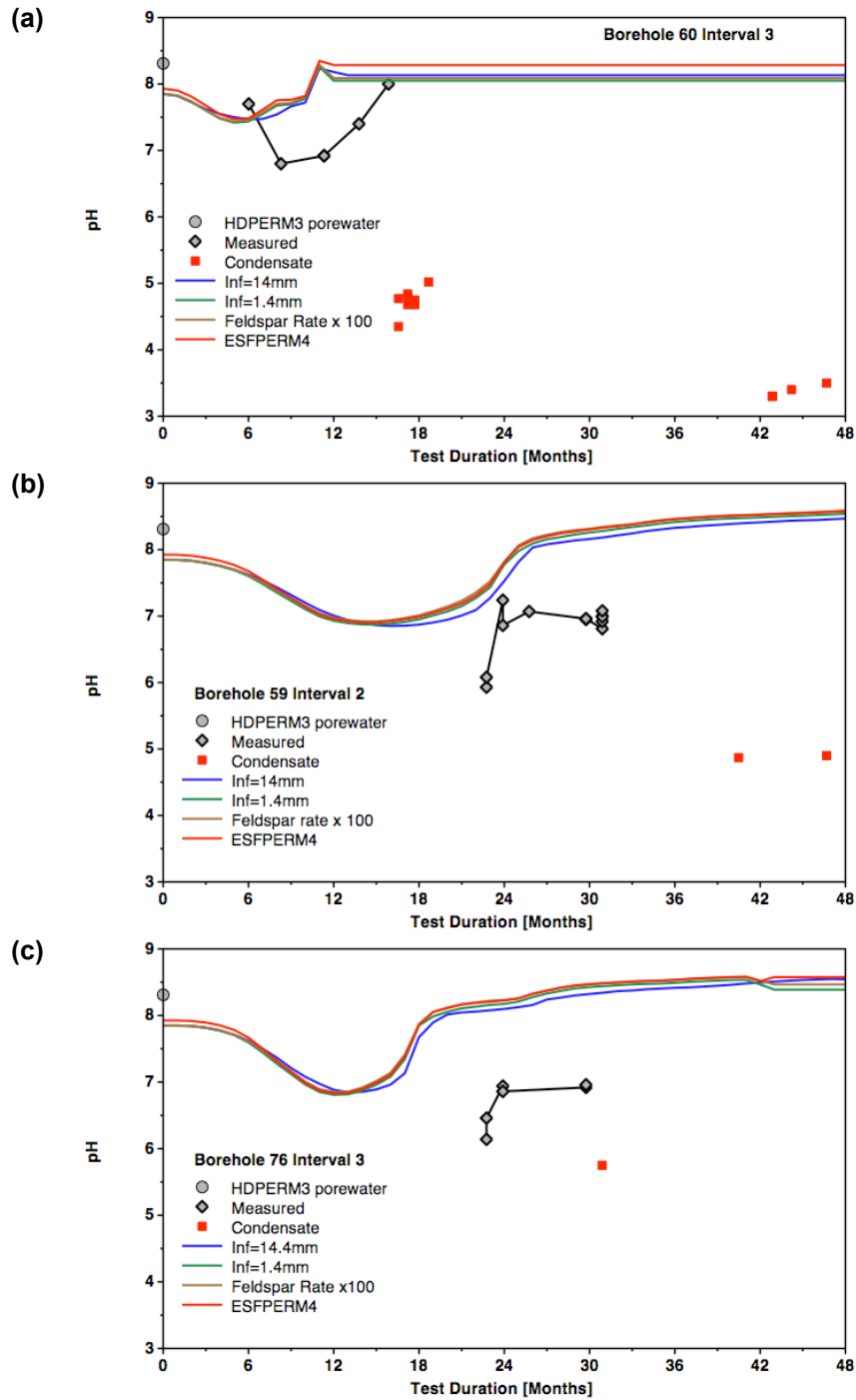


Output DTN: LB0705DSTHC005.002 (modeled).

Source: SNL 2007 [DIRS 177414], Table 6.3.4.1-1 (water collection locations).

NOTE: The intervals where water was sampled are more thickly shaded (in blue). Areas of zero liquid saturation are blanked out in white.

Figure 7.1-15. Modeled Distribution of pH in Fractures at Various Times When Water Was Sampled from Hydrology Borehole Intervals (months): (a) 6, (b) 8, (c) 11, (d) 11, (e) 14, (f) 14, (g) 16, (h) 20, (i) 23, (j) 23, (k) 24, (l) 24, (m) 26, (n) 30, (o) 30, (p) 31, (q) 38, (r) 40 (Continued)



Source DTN: LL020709923142.023 [DIRS 161677] (measured).

Output DTN: LB0705DSTHC005.002 (modeled).

NOTE: The ambient pore-water pH is approximately 8.3. The measured pH values are selected from Table 7.1-3, as representative for model-data comparison.

Figure 7.1-16. Comparison of Measured pH in Water Samples Collected from Borehole Intervals (a) 60-3, (b) 59-2, and (c) 76-3 to the Modeled Fracture Water pH at Representative Model Gridblocks

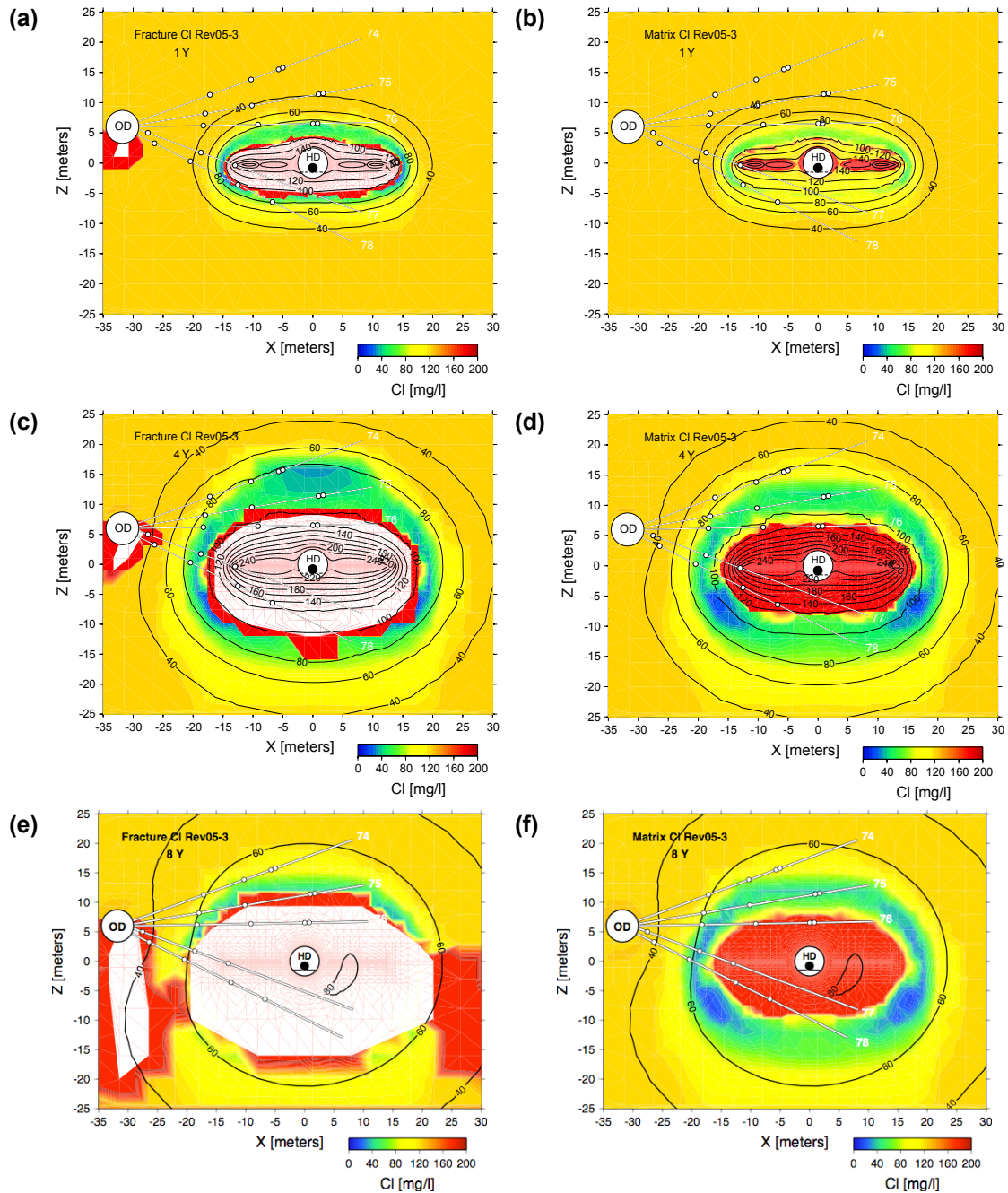
7.1.11.3 Evolution of Anion and Cation Concentrations

The effects of dilution through condensation of pure water vapor, increases in concentration caused by boiling, and fracture-matrix interaction can be assessed by examining the variation in conservative species such as chloride (Cl^-) and sulfate (SO_4^{2-}). These species are conservative because chloride and sulfate-bearing minerals, such as halite and gypsum (or anhydrite), are not present in the rock initially and precipitate under more saline conditions, expected only at the final drying stages of the dilute waters observed in the rock at Yucca Mountain.

The modeled spatial variations in Cl^- concentrations in fracture and matrix are plotted in Figure 7.1-17, at times of 1 year and 4 years during the heating phase, and at eight years at the end of the cooling phase. The main effect is a marked decrease in Cl^- concentrations within fractures in the condensation and drainage zones. In the matrix, there is significant dilution in the condensation zones and significant increases in concentration near the edge of the dryout zone.

The predicted trends in fracture-water Cl^- and SO_4^{2-} concentrations from the simulation (Figures 7.1-18 and 7.1-19) are generally corroborated by the measurements from borehole intervals 60-3, 59-2, and 76-3, in particular the strong dilution trend from the initial pore-water concentration. In Figure 7.1-18, the modeled fracture liquid saturations are shown (for the high and low infiltration cases), indicating a fairly good correspondence between the time periods when increases in fracture liquid saturation are predicted and the timing of the collection of water samples. All of the simulations show nearly identical results during the early stages, with the high infiltration case (blue curve) showing a delayed increase in concentration at later times owing to a strongly delayed onset of dryout. The delayed onset of dryout for the high infiltration case resulted from the higher initial liquid saturation in the rock matrix, which led to a longer time period for the rock matrix to dry out and a longer period of time over which the fractures were receiving vapor from the matrix through boiling/evaporation. Dilution of Cl in the fractures is directly related to the addition of vapor from the rock matrix, and increases in Cl concentration result from the drying rock matrix and associated drying fractures. The very low concentrations in the measured chloride and sulfate concentrations compared to the model results (outside the order-of-magnitude validation criterion) likely also results from a large proportion of water that condensed in the borehole, rather than directly in fractures, and having a smaller component of admixed pore water. Some species (e.g., Na, K, and SiO_2 , as discussed below) are not as strongly diluted or are enriched relative to the initial pore water and likely became more concentrated due to reaction with fresh silicate mineral surfaces exposed on the borehole wall. Therefore, dilution by water condensing in the collection tubes (concentrations shown as red squares) was likely not an important process for those samples. Despite the differences between the measured and modeled concentrations, the modeled trends are to more dilute compositions compared to the pore water, and most measured concentrations are within an order of magnitude of the modeled values. Model-data agreement could have been improved by changes in hydrologic properties to enhance water-vapor transport out of the matrix and formation of dilute condensate in the fractures. The reduction in vapor transport out of the matrix led to lower liquid saturations in the fractures and a weaker dilution effect on the ambient fracture pore water. However, site-average properties are judged to be more representative for application of the THC seepage model for the reasons discussed in Section 7.1.7.1. Also, given that the waters are collected from boreholes and not individual fractures, it is not necessarily an issue with the

behavior of the model. Therefore, the DST THC submodel meets the model validation requirements for the trends and for some of the chloride and sulfate concentrations.



Output DTN: LB0705DSTHC005.002.

NOTE: Temperature contours are overlain. Areas of zero liquid saturation are blanked out in white (only for fractures).

Figure 7.1-17. Modeled Distribution of Cl⁻ in Fractures and Matrix at One and Four Years during the Heating Phase of the DST, and at the End of the Cooling Phase (eight years): (a) Fracture (1Y), (b) Matrix (1Y), (c) Fracture (4Y), (d) Matrix (4Y), (e) Fracture (8Y), and (f) Matrix (8Y)

Na⁺ concentrations in the simulation (Figure 7.1-20) are elevated with respect to the measured concentrations in the 60-3 and 59-2 boreholes, but are closer to the measured values in borehole interval 76-3. They do not show quite the same degree of dilution as Cl and SO₄, likely as a result of feldspar dissolution. All the simulations using the HDPERM3 initial pore-water composition show very similar results, whereas the ESFPERM4 water exhibits values about twice as high, and not as close to the measured high-temperature water samples. The similarity in all of the HDPERM3 simulations indicates that the water saturation and pCO₂ (within variability in these simulations) have a limited effect on the pH, Na, Cl, and SO₄ concentrations, except nearing the final dryout stages. Probably the reactivity of plagioclase buffers the system, leading to increases in pH and a reduction in the partial pressure of CO₂, as long as the conservative species are behaving similarly. The trends in Na concentrations in boreholes 59-2 and 76-3 are very similar to the measured values and concentrations converge to similar values. Therefore, the validation criteria for Na have been met.

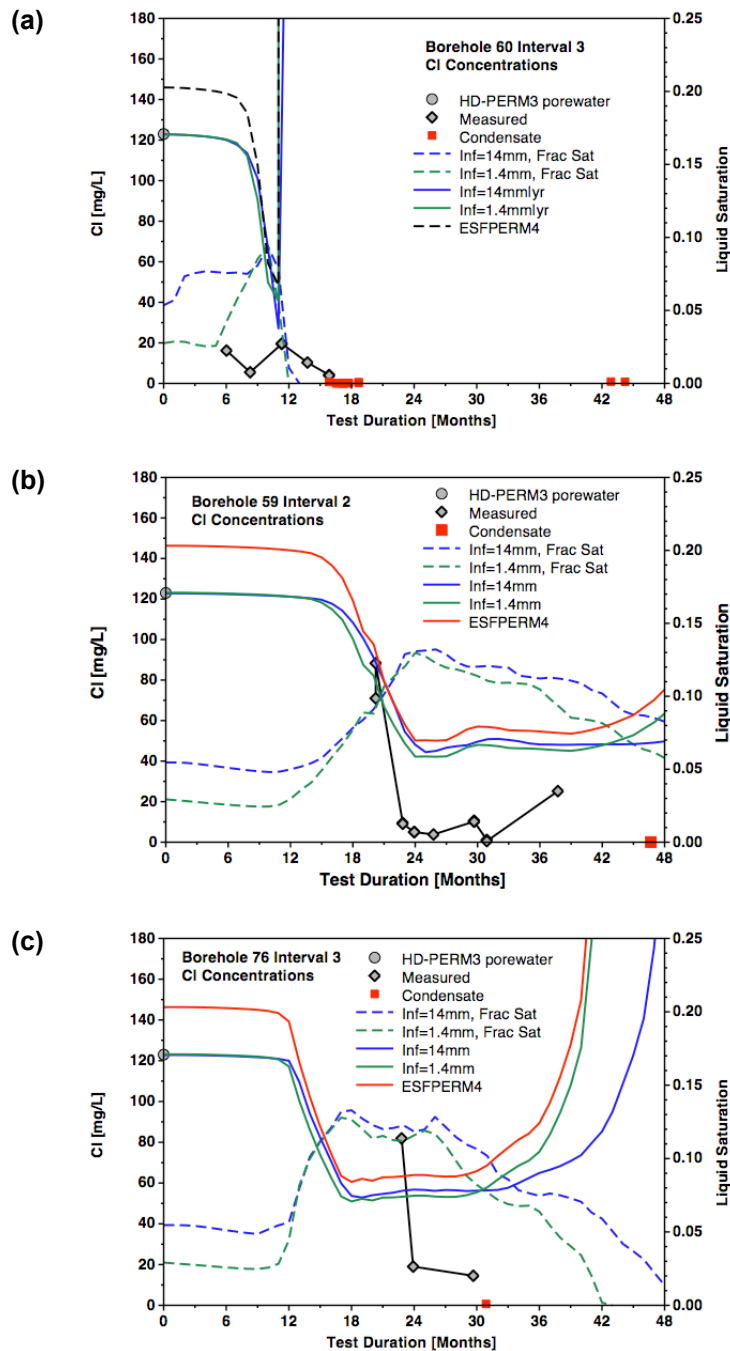
Calcium is more sensitive to water–rock interaction than most other species because of the fast reaction rate of calcite, its much lower solubility with increasing temperature, and the common occurrence of calcite in fractures. Other potential sources of Ca²⁺ in the rock include Ca-rich zeolites such as stellerite and Ca-rich smectite, which are abundant in fractures.

Ca²⁺ concentrations in the simulation (Figure 7.1-21) are similar to measured concentrations in the 60-3, 59-2, and 76-3 borehole intervals at the early times, but are noticeably elevated over the measured values at later times. The shape of the simulated Ca²⁺ history curve for 60-3 does not exhibit as early an initial dilution-induced drop in concentration. Instead, the reduction occurs later, when the strong condensation pulse is encountered and increasing temperature results in calcite precipitation. The Ca²⁺ concentration increases as boiling proceeds and the remaining water is evaporated. The rate of dryout is much faster in the model simulation than in the actual borehole, where waters were collected for nearly a year. This extended time period may be due in part to the length of the actual interval that could sample fracture waters, or allow waters to condense in different regions at different times. The Ca²⁺ dilution is similar to that observed for Cl⁻ and SO₄²⁻ concentrations, indicating little rock–water interaction and significant dilution, most likely in the borehole rather than solely in fractures or in the collection tubes. Because calcite is much more abundant in fractures, rather than in the rock matrix, the borehole wall is likely to have little calcite to dissolve. In addition, at higher temperatures calcite is much less soluble, and therefore even if present, calcite dissolution would not lead to significant increases in Ca concentrations.

The effect of a different maximum time step on aqueous species concentrations would more likely effect Ca because of its reaction relationship with bicarbonate and CO₂, so the results for three different maximum time steps (20 minutes, 1 hour, and 1 day) were plotted for borehole intervals 60-3 and 59-2. The differences are clearly much smaller than for CO₂, as would be expected by the much smaller diffusivity of aqueous species. Also, the effect of differing time-stepping (within this range) does not affect either the kinetic or equilibrium mineral–water reactions in this system to the extent that the results are noticeably different.

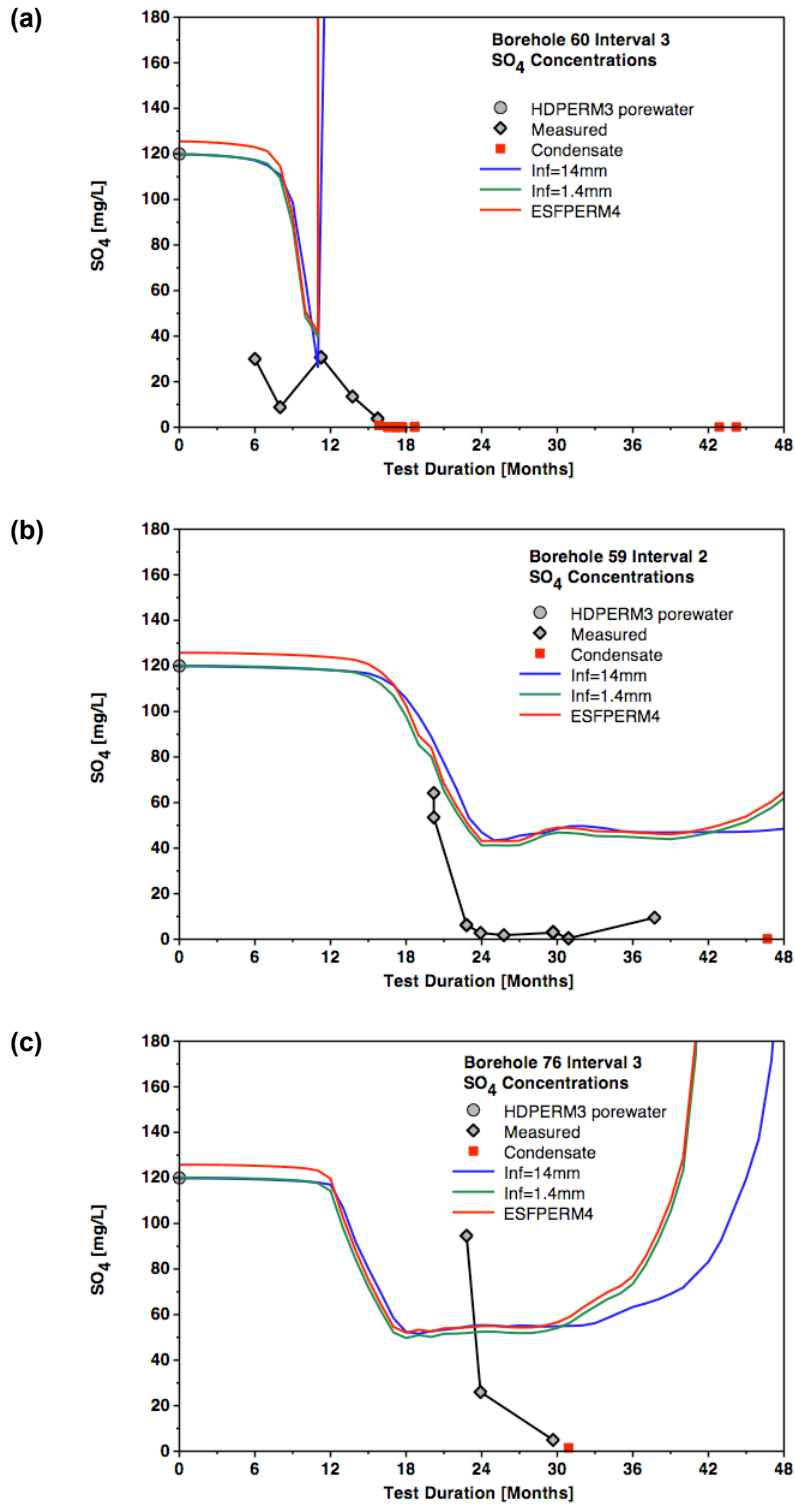
The model results capture the trend in the Ca²⁺ concentrations and are, in most cases, within one order of magnitude of the measured values. The deviations can be attributed to differences in the location of water condensation and collection (in boreholes rather than solely in fractures) and

possibly also a slower vapor release from the rock matrix in the simulation, as discussed above. Therefore, the validation criteria for Ca^{2+} in the DST THC submodel have been met for many of the samples.



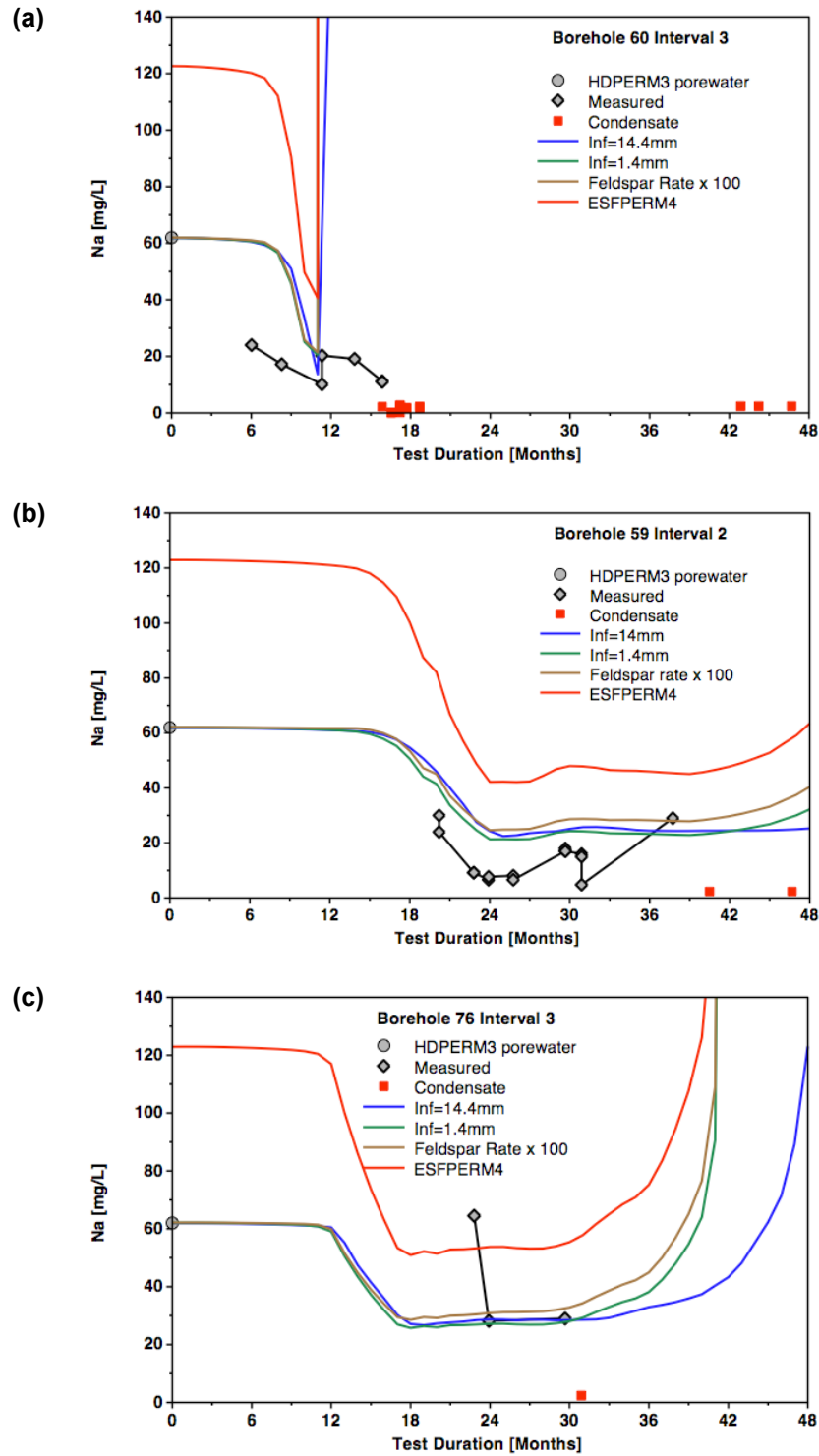
Source DTN: LL020709923142.023 [DIRS 161677] (measured).
 Output DTN: LB0705DSTHC005.002 (modeled).

Figure 7.1-18. Cl^- Concentrations (mg/L) in Water Samples and Condensates Collected from Borehole Intervals (a) 60-3, (b) 59-2, and (c) 76-3 Compared to the Modeled Fracture Water Cl^- and Fracture Liquid Saturations



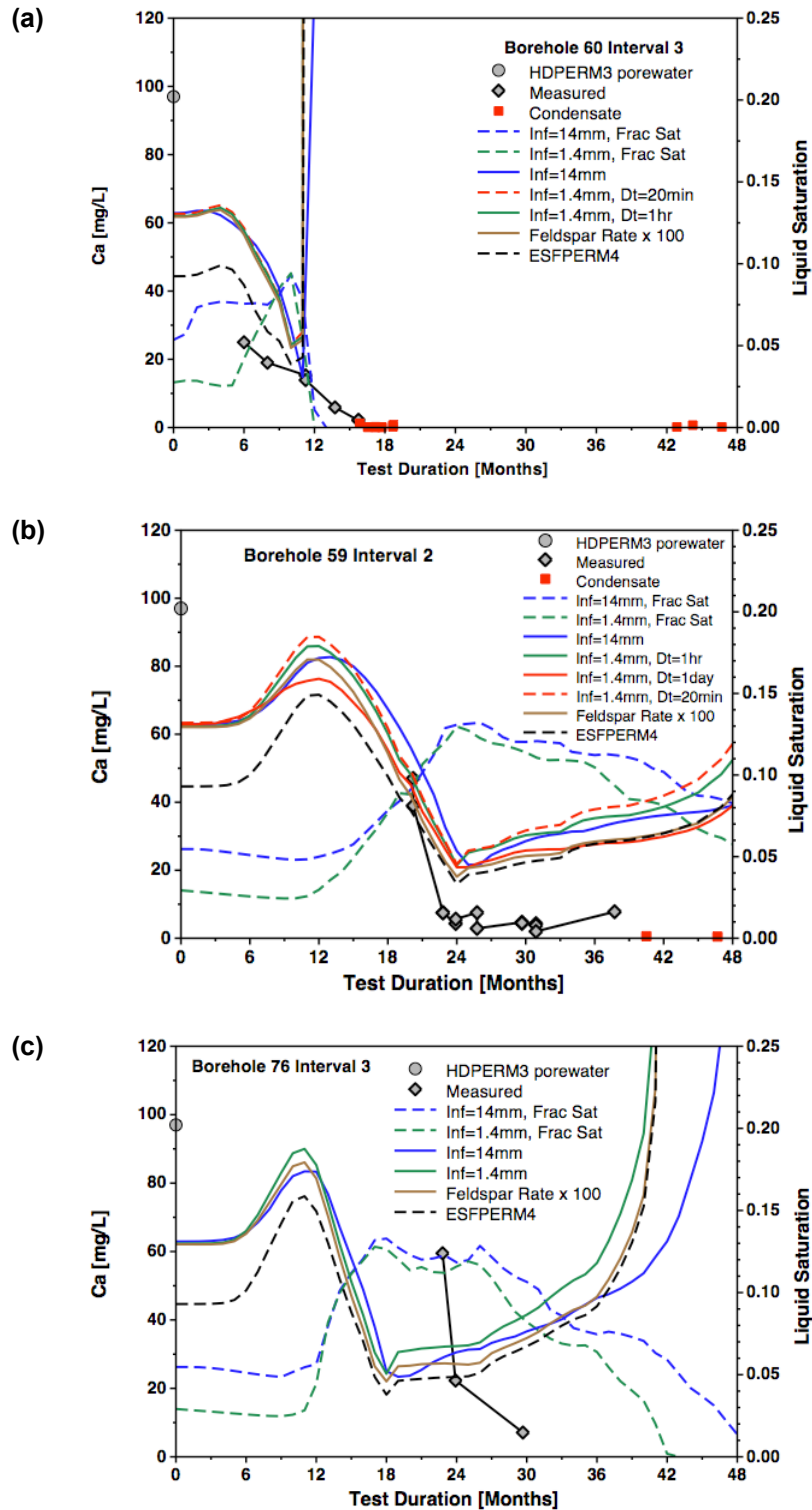
Source DTN: LL020709923142.023 [DIRS 161677] (measured).
 Output DTN: LB0705DSTHC005.002 (modeled).

Figure 7.1-19. SO₄²⁻ Concentrations (mg/L) in Water Samples and Condensates Collected from Borehole Intervals (a) 60-3, (b) 59-2, and (c) 76-3 Compared to the Modeled Fracture Water SO₄²⁻



Source DTN: LL020709923142.023 [DIRS 161677] (measured).
 Output DTN: LB0705DSTHC005.002 (modeled).

Figure 7.1-20. Na⁺ Concentrations (mg/L) in Water Samples and Condensates Collected from Borehole Intervals (a) 60-3, (b) 59-2, and (c) 76-3 Compared to Modeled Na⁺ Concentrations in Fractures



Source DTN: LL020709923142.023 [DIRS 161677] (measured).
 Output DTN: LB0705DSTHC005.002 (modeled).

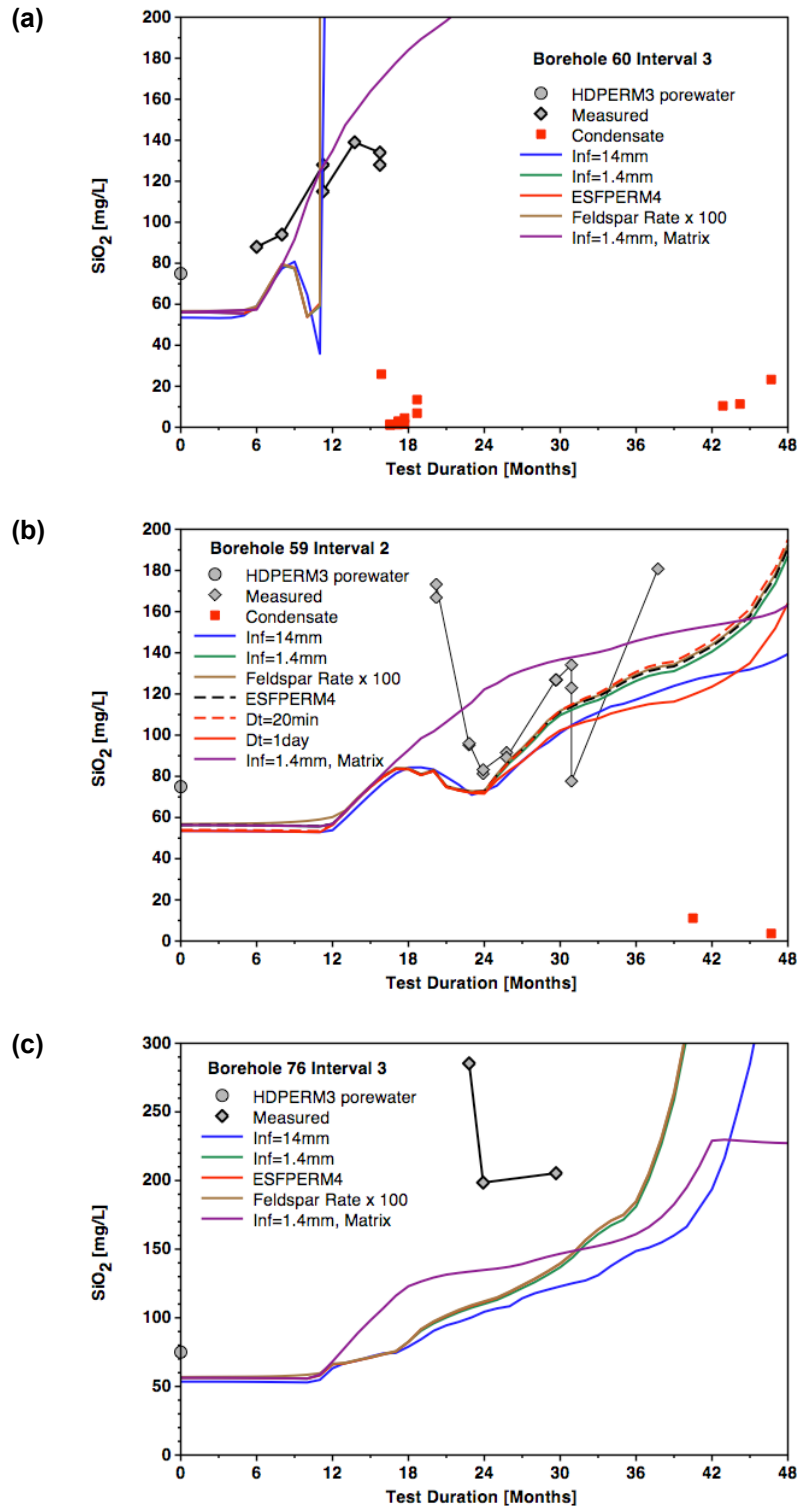
Figure 7.1-21. Ca^{2+} Concentrations (mg/L) in Water Samples and Condensates Collected from Borehole Intervals (a) 60-3, (b) 59-2, and (c) 76-3 Compared to Modeled Ca^{2+} in Fracture Water and Fracture Liquid Saturations

The modeled aqueous silica ($\text{SiO}_2(\text{aq})$) concentrations in fracture waters (Figure 7.1-22) capture the strong increases observed in the measured compositions, especially those seen in the borehole intervals overlying the heaters (59-2 and 76-3). Initial equilibration with opal-CT results in a slightly lower initial concentration than that measured in the HDPERM3 pore water, which tends to shift the curves downward. Simulated $\text{SiO}_2(\text{aq})$ values are therefore somewhat lower than the measured values, but within an order of magnitude of the observed ones and trend to higher concentrations than the initial pore water (after an intermediate time dip owing to high rates of condensation). A plot of matrix $\text{SiO}_2(\text{aq})$ concentrations trends to higher values (until the fractures dryout) and shows a smoother overall increase, but only compares more favorably with measured data from borehole interval 60-3 and for some samples in 59-2. Overall, the model results meet the validation requirements.

The modeled concentrations of K^+ (Figure 7.1-23), are very close the measured concentrations. The increase in the feldspar reaction rate did not improve the match to the measured concentrations.

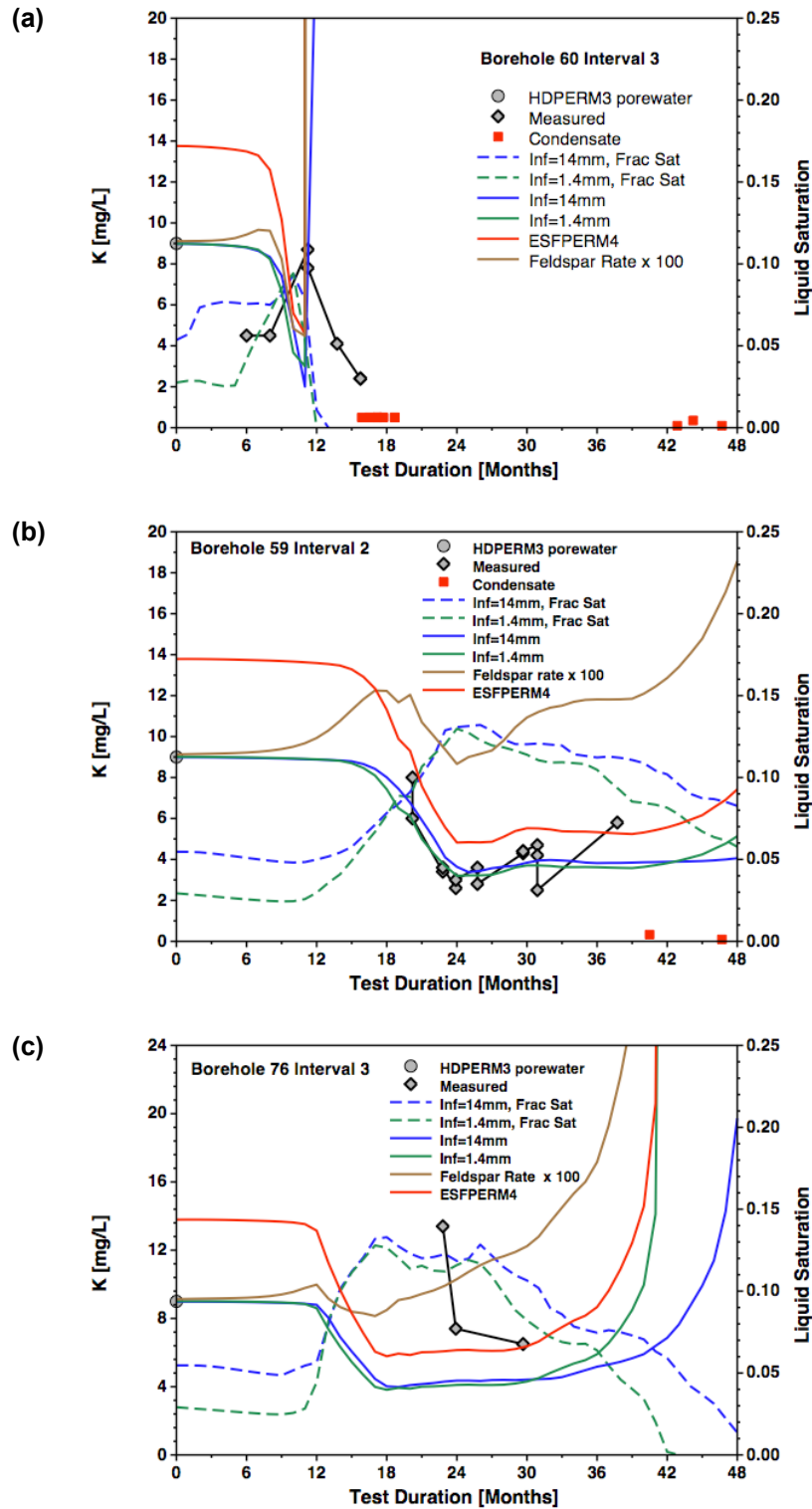
The fact that Na^+ and K^+ show similar trends over time is consistent with their predominance in either an alkali feldspar solid-solution phase, such as sanidine, and/or as closely intergrown exsolved phases from a precursor solid-solution alkali feldspar mineral. All model results meet the validation requirements (trend to higher concentrations than in the initial pore water and within an order of magnitude).

Fewer bicarbonate (HCO_3^-) concentrations were measured in the borehole waters because of difficulties making the measurements in the field. Available data are plotted in Figure 7.1-24, along with the modeled concentrations. Although the few measured values do not allow complete trends to be defined, for several samples modeled HCO_3^- concentrations compare well to the measured concentrations. The deviations seemed to be related to a much faster rise in temperature in the model simulation relative to that in borehole intervals 60-3 and 76-3, because the measured values for HCO_3^- are shifted forward in time by about 8 to 10 months in each sample, and roughly the same time shift is evident for most of the other measured concentrations of other species. Thus, the model appears to capture the correct THC behavior, but since it is just an idealized 2-D cross section of a 3-D test block, the temperature increases in the simulation take place more rapidly. Given that many samples meet the validation criterion, and the model deviations can be explained by relatively straightforward shifts in time, the model results for HCO_3^- meet the model validation criteria.



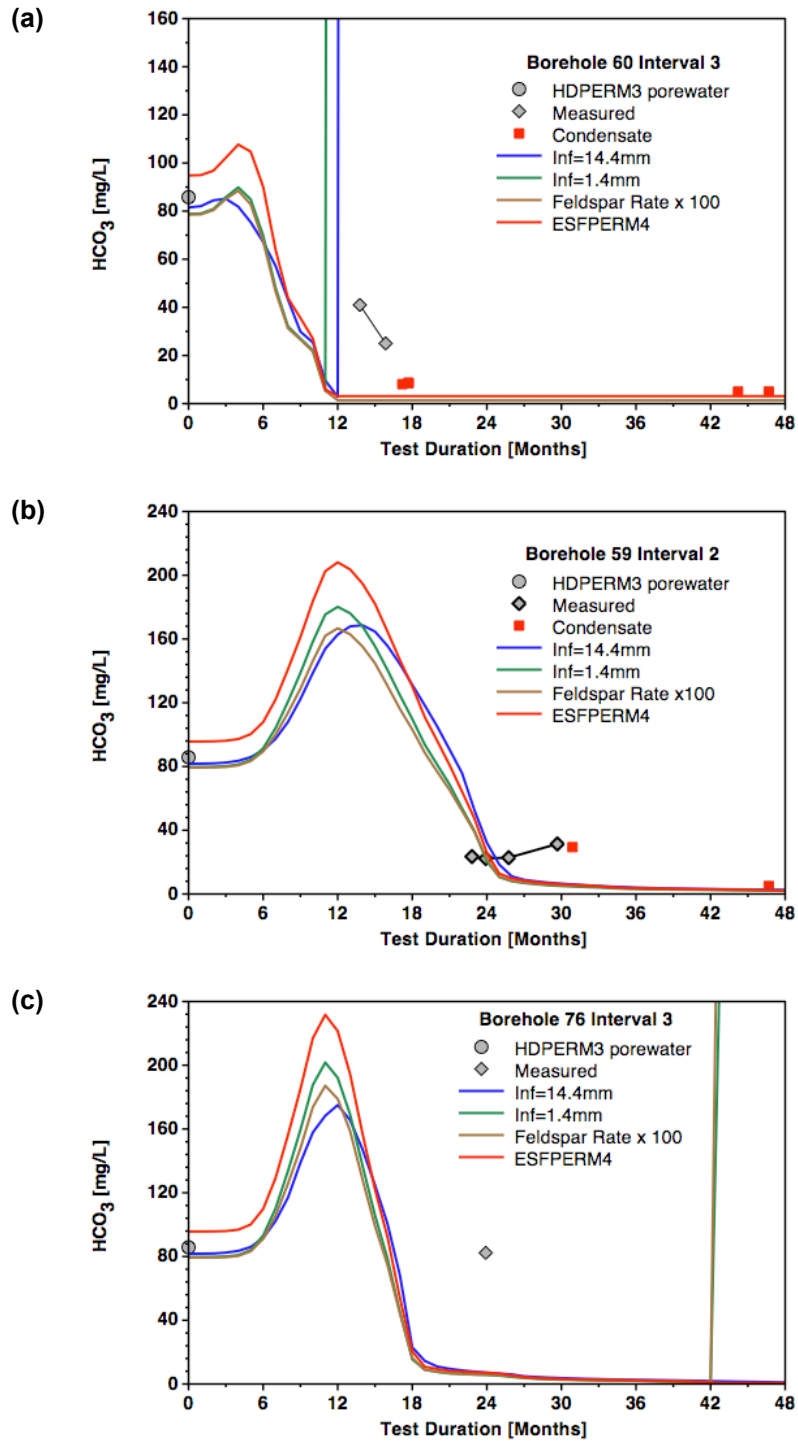
Source DTN: LL020709923142.023 [DIRS 161677] (measured).
 Output DTN: LB0705DSTHC005.002 (modeled).

Figure 7.1-22. $\text{SiO}_2(\text{aq})$ Concentrations (mg/L) in Water Samples and Condensates Collected from Borehole Intervals (a) 60-3, (b) 59-2, and (c) 76-3 Compared to Modeled Fracture Water $\text{SiO}_2(\text{aq})$ Concentrations



Source DTN: LL020709923142.023 [DIRS 161677] (measured).
 Output DTN: LB0705DSTHC005.002 (modeled).

Figure 7.1-23. K⁺ Concentrations (mg/L) in Water Samples and Condensates Collected from Borehole Intervals (a) 60-3, (b) 59-2, and (c) 76-3 Compared to Modeled Fracture Water K⁺ Concentrations and Fracture Liquid Saturations



Source DTN: LL020709923142.023 [DIRS 161677] (measured).
 Output DTN: LB0705DSTHC005.002 (modeled).

Figure 7.1-24. HCO_3^- Concentrations (mg/L) in Water Samples and Condensates Collected from Borehole Intervals (a) 60-3, (b) 59-2, and (c) 76-3 Compared to Modeled Fracture Water HCO_3^- Concentrations

Modeled concentrations of some additional aqueous species (Mg^{2+} , NO_3^- , and F^-) in the simulation are compared to measured compositions from 59-2, 60-3, and 76-3 in Figures 7.1-25 through 7.1-27. Measured Mg^{2+} concentrations (Figure 7.1-25) show initial concentrations closer to the pore-water value of about 17 mg/L, and then a considerable drop in all the borehole intervals. Modeled Mg^{2+} concentrations show a similar pattern and are close to the measured concentrations. The sharp drop in the modeled concentrations is related to a combination of dilution from condensate and the precipitation of amorphous antigorite (an Mg-rich sheet silicate). The increase in the rate for this phase causes the minimum concentration to be slightly lower, but otherwise the results are similar to the other simulations. It is not clear whether precipitation of a Mg-rich phase takes place in the boiling zone in the rock, because the extent of dilution of Mg^{2+} is roughly similar to that observed for the conservative species, such as Cl^- . Some Mg^{2+} is likely incorporated into calcite that is precipitated as the condensate water above the heaters drains down and boils, or as fracture-lining calcite is dissolved, although this may have a minimal effect on Mg^{2+} concentrations. The thermodynamic model for calcite does not include Mg^{2+} , and therefore another Mg-bearing phase (i.e., amorphous antigorite or Mg-beidellite) must take up some of the Mg^{2+} . Previous model revisions used the lower solubility Mg-silicate sepiolite; however, precipitation of this mineral resulted in near-complete depletion of Mg in the waters. Owing to this depletion effect, and the likely formation of an amorphous phase under the rapid precipitation rates induced by boiling, the higher solubility Mg-silicate mineral, amorphous antigorite, was chosen. Overall, most samples fall within an order of magnitude of the model results, thus meeting the validation requirements for Mg^{2+} .

Nitrate (NO_3^-) is included in the list of modeled species for the simulations, owing to its importance for the evolution of final salt compositions in potential seepage waters. Nitrate is highly soluble, and there are no nitrate minerals initially present in the tuff. The pore water has somewhat more variable nitrate concentrations compared to Cl^- and SO_4^{2-} . The greater variability in pore-water concentrations may be a result of biologically mediated nitrogen reduction, possibly after sample collection. Measured and modeled nitrate concentrations are shown in Figure 7.1-26. Concentrations measured in waters collected from the hydrology boreholes are almost all lower than those from the pore water, showing a similar pattern as Cl^- and SO_4^{2-} . This finding suggests that over the time scale of the experiment, nitrate acts as a conservative species and may not have been affected significantly by biological activity in the rock. The modeled concentrations using the HDPERM3 pore water capture the measured pattern of nitrate concentrations quite well, although the dilution effect is not as strong. This effect is similar to that seen for most other weakly reactive or nonreactive species. The simulation using the ESFPERM4 water composition starts with an NO_3^- concentration close to 60 mg/L, which results in values nearly an order of magnitude greater than those observed in the hydrology boreholes. The good agreement for the HDPERM3 simulations indicates that the model validation requirements for NO_3^- have been met, both in terms of the trend and range of values.

Fluorite has been added to the initial mineral assemblage for the simulations. Fluorite is observed sporadically in the Yucca Mountain tuffs, and observed fluoride concentrations in some pore-water samples reflect the presence of this mineral. Many pore waters from the repository level are near saturation with respect to fluorite (around 4 to 5 mg/L; see Table 6.2-1). Therefore, in the THC seepage model, fluorite is assumed to be present in the rock mass, and fluoride concentrations are limited by fluoride precipitation/dissolution. Fluoride is included in

the THC seepage model because it may contribute to uniform corrosion of the titanium drip shield (SNL 2007 [DIRS 180778], Section 6.5.7).

However, F^- concentrations were lower in the water samples recovered from the DST. Concentrations in the initial pore waters from the DST block (HD-PERM3; Table 7.1-3) were found to be less than 1 mg/L, much lower than the equilibrium solubility of fluorite (around 4 to 5 mg/L at ambient temperatures). In addition, almost all waters from the hydrology boreholes in the DST have measured F^- concentrations of around 1 mg/L or less, with only one sample at about 4 mg/L. The measured values are shown in Figure 7.1-27 for borehole intervals 60-3, 59-2, and 76-3, compared to the model results. The modeled F^- concentrations stay level and then drop from their initial concentrations of around 1 mg/L to about half that value, eventually attaining much higher values as increasing temperatures result in evaporative concentration. The model results generally capture the trend and values of the F^- concentrations, especially in borehole interval 59-2, where numerous water samples were collected over a prolonged period of about 18 months. The low F^- concentrations in the waters indicate that contamination from introduced materials was negligible. At later times, though, some of the condensates show highly elevated F^- concentrations (Figure 7.1-27a, and other borehole samples to several tens of ppm) and very low pH values, even though other anions and cations are close to or below detection limits. The good agreement for the simulations indicate that the model validation requirements for F^- have been met, both in terms of the trend and range of values.

Model results for aqueous Fe and Al concentrations are not compared to DST measured values in this report. There are several reasons for this. First, measured concentrations for these elements are sparse. Data for Fe and Al were either not measured or below the detection limit for more than half of the water samples listed in Table 7.1-3. Also, the water samples were only filtered through 0.45 micron filters. These are not sufficient to exclude colloidal particles, which could significantly contribute to the reported concentrations of a few tens of nanograms per milliliter. For these reasons, the potential errors in the measured Fe and Al values are large.

For iron, most of the reported values exceed by several orders of magnitude the calculated solubility of crystalline Fe(III) mineral phases, and even amorphous $Fe(OH)_3$, at the measured pH values (Langmuir 1997 [DIRS 100051], Figures 7.10 and 7.11). Because iron oxides precipitate rapidly and readily, this also suggests that the iron analyses are not reliable.

DST THC submodel predictions for Fe are also several orders of magnitude lower than the measured values. Since Fe values from this report are not used by downstream models, and measured concentrations from the DST are sparse and probably unreliable, Fe concentrations have not been validated and are presented for information only.

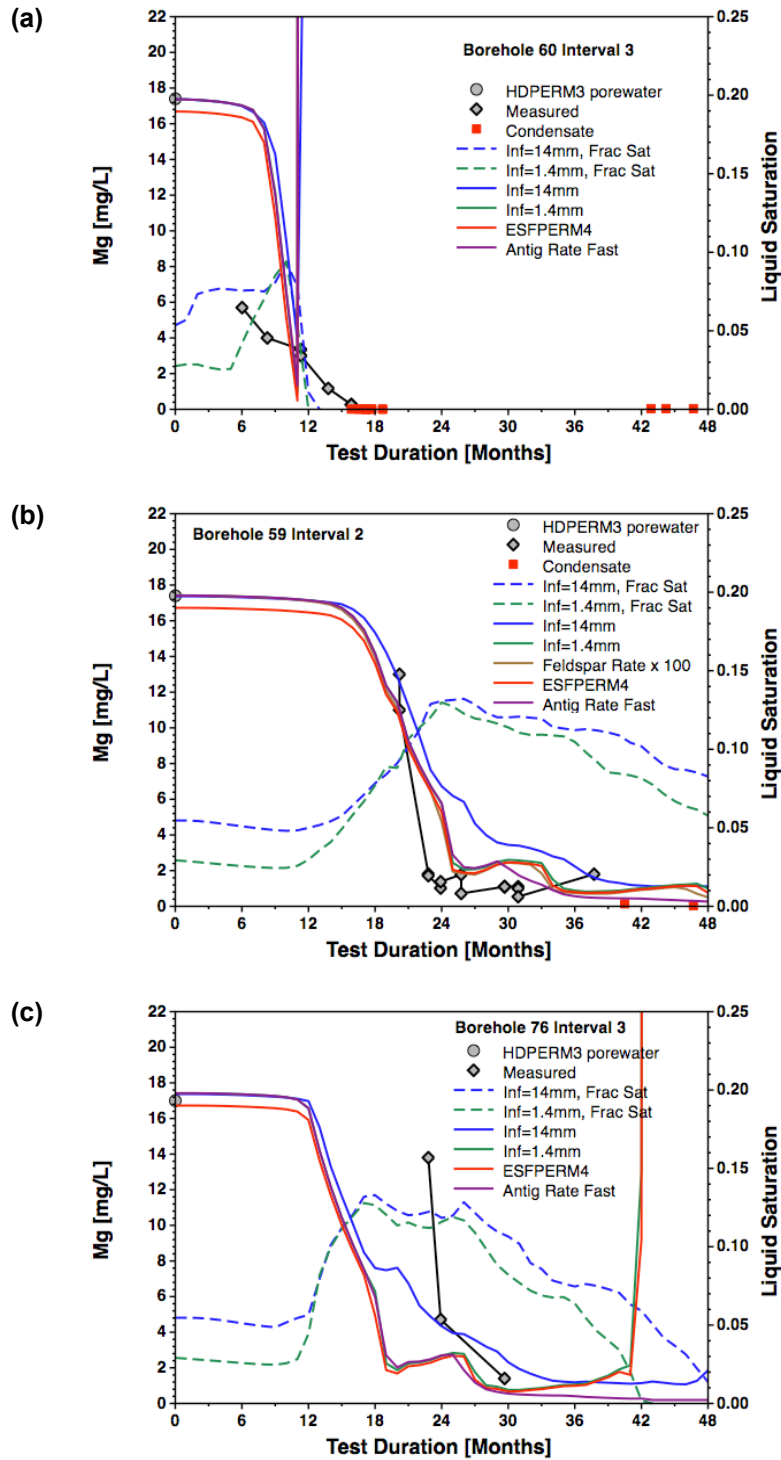
The values for dissolved Al that were measured in DST waters are much higher than expected from the model. As stated earlier, this is probably an artifact of not filtering the solutions appropriately to remove colloidal Al and thus miscounting colloidal aluminum mass as “dissolved.” Large overestimates in Al concentrations due of inclusion of colloidal material are extensively documented throughout the literature. Although the Al concentrations reported in THC seepage model output files have little direct effect on downstream models, as concentrations are very low and do not affect the predicted major element concentrations of evolving brines presented in *Engineered Barrier System: Physical and Chemical Environment*

(SNL 2007 [DIRS 177412]), the predicted Al values have a significant impact within the THC model, which may propagate indirectly to downstream models. Although Al concentrations are very small, they contribute to the predicted ion activity product (Q) for aluminosilicate minerals, which affects mineral dissolution/precipitation rates through the Q/K relationship described in Section 6.4.2. If modeled Al concentrations were too low, this would lead to lower Q values for aluminosilicate mineral dissolution reactions (corresponding to farther-from-equilibrium conditions), which would translate into higher mineral dissolution rates (and lower aluminosilicate precipitation rates in the converse). This would affect other dissolved components released from the aluminosilicates such as Ca^{+2} , K^+ , Na^+ , and silica, and could lead to higher than expected dissolved concentrations of these components. This effect would in fact be magnified for the cation components because the Al has a larger stoichiometric coefficient that multiplies its effect on the rates. For this reason, it is important to validate the Al concentrations predicted by the THC seepage model.

Because Al concentrations measured in the DST are likely to be in error, it is not possible to directly validate the Al concentrations predicted by the THC model. Predicted major element concentrations (Na, K, Ca, SiO_2) are corroborated by DST results, providing supporting evidence that aluminosilicate mineral dissolution and precipitation, and hence aluminum concentrations, are being accurately modeled. However, pH is already assessed as a dependent variable, and because it is involved in all mineral dissolution/precipitation reactions, it is not possible to argue that Al concentrations must be accurate simply because the cation concentrations are matched adequately.

The DST THC submodel results do not capture the measured aluminum concentrations because the measured values are very small and have large uncertainties. However, matches in major element concentrations for the DST and plug-flow reactor provide support that mineral dissolution and precipitation are being handled in a reasonable manner, and, as stated in the TWP (SNL 2007 [DIRS 179287]), because the deviation in measured and predicted Al concentrations can be readily explained in terms of simple physical and chemical processes, these data do not invalidate the DST THC submodel.

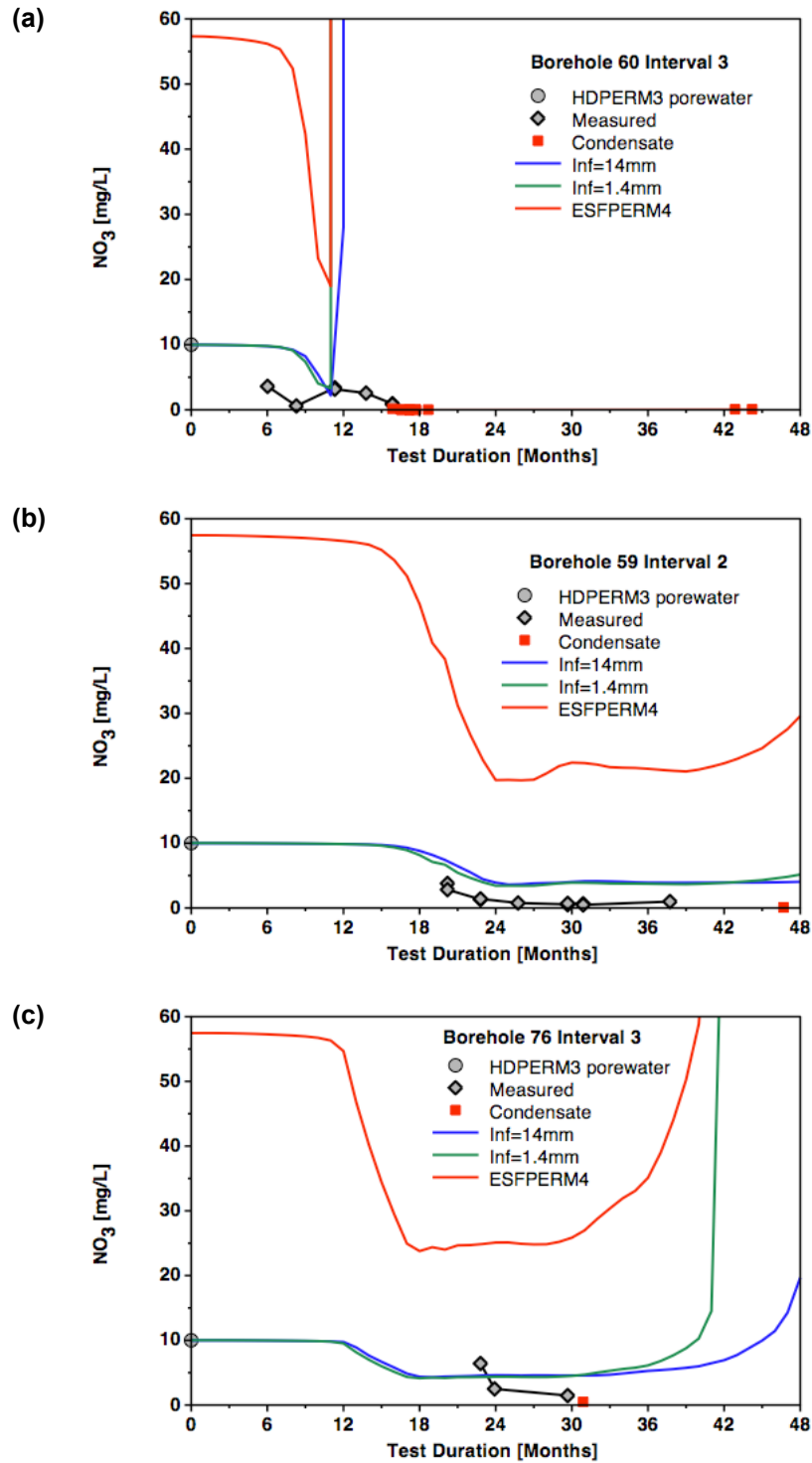
Overall, the trends for aqueous species indicate that the high initial saturations and low matrix permeability led to a near fully saturated matrix and a slower loss of vapor into fractures, with a slower rate of condensed water being formed. For conservative aqueous species, the agreement with the measured values was not as close as the simulations using the lower initial saturation. For most aqueous species, all the simulations showed nearly the same results. Simulation 4 (dst_the_r5_03) with the HDPERM3 water was closest to the measured data for CO_2 , and equally as good for all aqueous species. Mg and K concentrations were especially close to those measured, whereas silica was somewhat low, and calcium was higher than the generally dilute samples. Simulations using the ESFPERM4 pore water were very similar to those using the HDPERM3 pore water, except for Cl, NO_3 , and Na, which were all highly elevated with respect to the measured values. The simulation using the increased sanidine and plagioclase reactions rates (by a factor of 100) gave similar results to the other simulations using the HDPERM3 water, except for elevated K concentrations at higher temperatures. In this case, the simulations with the lower reaction rates were closer to the measured K concentrations. The higher antigorite rate did not result in significantly different Mg concentrations, and some effect may be from a difference in time stepping related to the poorer convergence behavior when using the faster rate.



Source DTN: LL020709923142.023 [DIRS 161677] (measured).
 Output DTN: LB0705DSTHC005.002 (modeled).

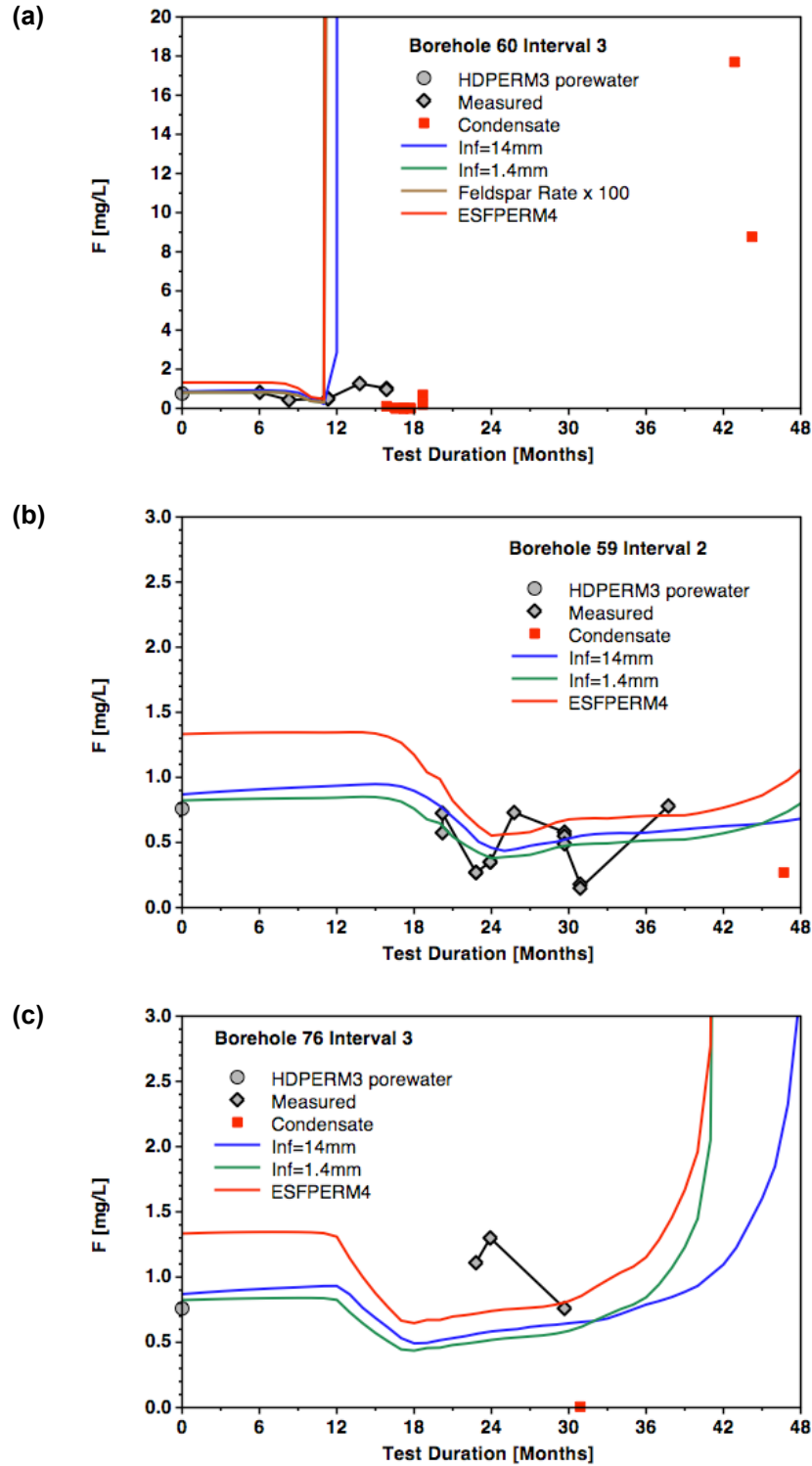
NOTE: Modeled fracture liquid saturations are also shown.

Figure 7.1-25. Mg²⁺ Concentrations (mg/L) in Water Samples and Condensates Collected from Borehole Intervals (a) 60-3, (b) 59-2, and (c) 76-3 Compared to Modeled Fracture Water Mg²⁺ Concentrations



Source DTN: LL020709923142.023 [DIRS 161677] (measured).
 Output DTN: LB0705DSTHC005.002 (modeled).

Figure 7.1-26. NO_3^- Concentrations (mg/L) in Water Samples Collected from Borehole Intervals (a) 60-3, (b) 59-2, and (c) 76-3 Compared to Modeled Fracture Water NO_3^- Concentrations



Source DTN: LL020709923142.023 [DIRS 161677] (measured).
 Output DTN: LB0705DSTHC005.002 (modeled).

Figure 7.1-27. F⁻ Concentrations (mg/L) in Water Samples Collected from Borehole Intervals (a) 60-3, (b) 59-2, and (c) 76-3 Compared to Modeled Fracture Water F⁻ Concentrations

7.1.12 Mineralogical Changes

As the last few sections have documented, marked changes have taken place in the water and gas chemistry in the DST, owing to thermal-hydrologic processes as well as mineral–water–gas reactions. The total amount of minerals precipitated or dissolved, though, may be exceedingly small, even though the effect on the water composition is quite strong. The strong effect on the water composition is related to the water–rock ratio, which is very low in the unsaturated low-porosity fractured tuff. The system is also characterized by an exceedingly low percolation flux of only a few millimeters per year or less, and therefore the ambient water has a long residence time. This section documents the predicted changes in mineralogy over the heating phase of the DST and compares the results to a few measurements made from in situ sidewall core samples obtained from above-boiling zones. Since the last revision of this report, a series of small core samples was analyzed for evidence of mineral alteration during the heating phase of the DST. The first set of samples was obtained in November 2000 by sidewall coring of fractures in “chemistry” boreholes 53 and 54, which were originally designed for water sampling. However, the SEAMIST pad system employed in those boreholes failed to provide uncontaminated water samples owing to the engineering materials in the boreholes and the unknown compositions of the pads. The collection and analyses of the rock samples are documented in *Thermal Testing Measurements Report* (SNL 2007 [DIRS 177414], Section 6.3.4.3). Chemical analyses, identification, and description of mineral alteration products for a few of the samples are given in DTN: LA0201SL831225.001 [DIRS 158426]. These data represent observations and analyses from two locations taken about 1 m apart in an above-boiling region above the heaters.

Calcite, amorphous silica, and a calcium sulfate phase (tentatively identified as gypsum) are the only phases in these samples identified so far as products of the processes taking place during the DST (DTN: LA0201SL831225.001 [DIRS 158426]). Amorphous silica was common in both samples, whereas calcite and gypsum were only described from the sample further into the above-boiling zone (the other sample was from the outer edge). Although anhydrite is thermodynamically more stable than gypsum under the conditions of the DST, gypsum was observed in analyses of borehole surfaces from the Single Heater Test (DTN: LA0009SL831151.001 [DIRS 153485]). On the basis of this identification, the calcium sulfate phase observed in the DST sidewall core samples was considered to be gypsum (SNL 2007 [DIRS 177414], Section 6.3.4.3). This phase may have been precipitated as anhydrite and then during the cooling period converted to gypsum. Therefore, the model simulations consider anhydrite to be the precipitating calcium sulfate mineral.

From the descriptions of mineral alteration given in Section 6.3.4.3 of the *Thermal Testing Measurements Report* (SNL 2007 [DIRS 177414]), amorphous silica was the dominant phase precipitated during boiling, with much lesser amounts of calcite and gypsum. Amorphous silica appears as glassy coatings covering larger areas of the surface, commonly in the form of thin curled sheets and fine tubules. Calcite typically is found as scattered, small late-stage mounds, with gypsum as very late-formed scattered crystals on top of other phases. Although calcite is not a major phase in the tuffs at Yucca Mountain, its rapid reaction rate, strong effect on pH, and ubiquitous presence in fracture coatings make it an important mineral phase. The actual percentage of mineral precipitates in the fracture system could not be determined from this type of localized analysis. Some of the silica coatings were approximately 10 to 20 μm thick, with

discrete gypsum crystals up to 80 μm long. Given a uniform 10- μm -thick layer of mineral precipitates on one side of all fractures, with a hypothetical range in fracture aperture of 100 to 1,000 μm , the proportion of fracture volume filled would range from 1% to 10%. Because many of the coatings are much less than 10 μm thick and do not cover all areas of every fracture, the volume filled is likely to be less than 1%.

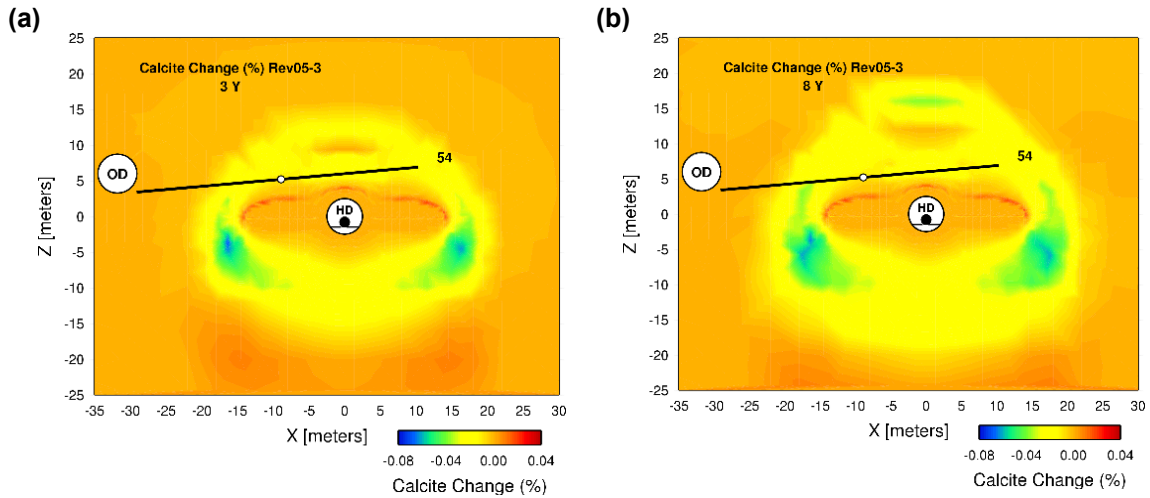
Figures 7.1-28 through 7.1-30 show the modeled distributions of calcite, amorphous silica, and anhydrite in the DST at the time the samples were collected and at the end of the eight-year cooling period. The location of borehole 54 is plotted, as well as the sites where the mineral was observed in a sidewall core sample. The modeled distributions of other, much more minor phases are not shown, because it is not possible yet to validate their abundances, and they contribute very little to potential changes in hydrological properties. Also, minerals such as sanidine or cristobalite are so abundant that little dissolution is required to affect water compositions, and definitive dissolution of these minerals has not been observed.

The modeled distribution of calcite in the simulation (Figure 7.1-28) shows a precipitation zone above the heaters, as is expected in the boiling zone, and strong dissolution in the drainage zones below the wing heaters. A broad region of very slight dissolution is observed in the large condensation area, where pH values are slightly lower as well. The maximum amount of precipitation is less than 0.04% of the fracture volume and dissolution less than 0.08%. The observed calcite is just at the edge of the modeled precipitation zone, and therefore the model results are validated for calcite. Further evidence from carbon-14 discussed in the following section supports the model results showing strong dissolution in the drainage zones. One additional note is the presence of enhanced precipitation below the zones of dissolution, probably formed earlier in the heating phase as Ca-rich water drained into zones of higher pH pore water.

Like calcite, the modeled distribution of amorphous silica in the current DST simulation (Figure 7.1-29) shows the presence of a precipitation zone above the heaters. The maximum amount of amorphous silica precipitated is less than about 1% for the entire duration of the DST. There is also an excellent correspondence in the region of modeled amorphous silica precipitation and the observed amorphous silica in the sidewall core samples from borehole 54. Although the observations of mineral coatings on a few samples cannot be used to judge the total amount of mineral precipitated, the small volumes precipitated in the model are consistent with the generally thin coatings observed.

Precipitation of anhydrite is localized to the zones where modeled sulfate concentrations become very high as a result of boiling (Figure 7.1-30). The observed location of gypsum in the sidewall core sample is consistent with the model results that show this sample to be just within the edge of the modeled zone of anhydrite precipitation.

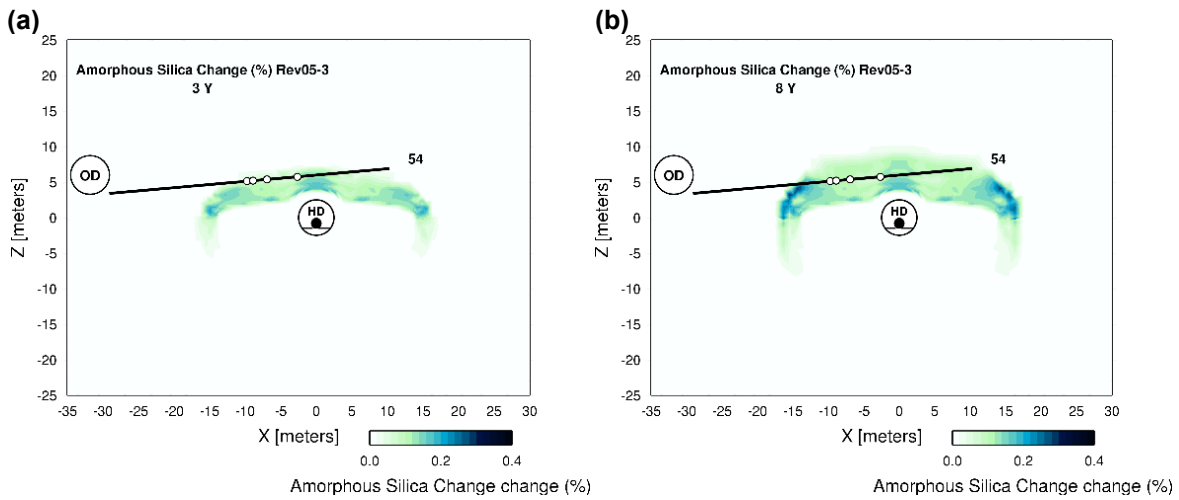
The sidewall core sample observations of significantly greater amorphous silica precipitation compared to calcite and gypsum, with the latter phases occurring in roughly equivalent amounts, are also consistent with the DST THC submodel results. Although the maximum amount of amorphous silica precipitated is about an order of magnitude greater than calcite, there are not enough samples to determine the spatial distribution of these phases and whether areas exist where the relative proportions differ. Given that the three observed mineral phases are in the locations predicted by the model simulations, the validation criteria have been met.



Source DTN: LA0201SL831225.001 [DIRS 158426] (measured).
 Output DTN: LB0705DSTHC005.002 (modeled).

NOTE: Chemistry borehole 54 is shown with location of observed calcite (open circle) formed during DST.

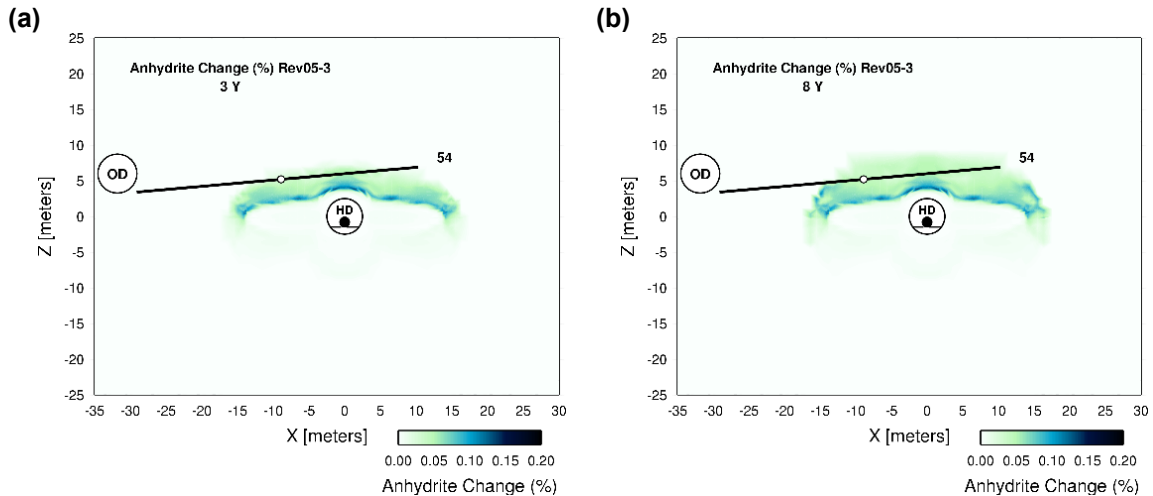
Figure 7.1-28. Modeled Volume Percent Change in Calcite in Fractures Compared to Observed Calcite Location in Borehole 54: (a) November 2000 (35 months of heating) and (b) 8 Years



Source DTN: LA0201SL831225.001 [DIRS 158426] (measured).
 Output DTN: LB0705DSTHC005.002 (modeled).

NOTE: Chemistry borehole 54 is shown with location of observed amorphous silica (open circles) formed during the DST.

Figure 7.1-29. Modeled Volume Percent Amorphous Silica in Fractures Compared to Observed Amorphous Silica Locations in Borehole 54: (a) November 2000 (35 months of heating) and (b) 8 Years



Source DTN: LA0201SL831225.001 [DIRS 158426] (measured).

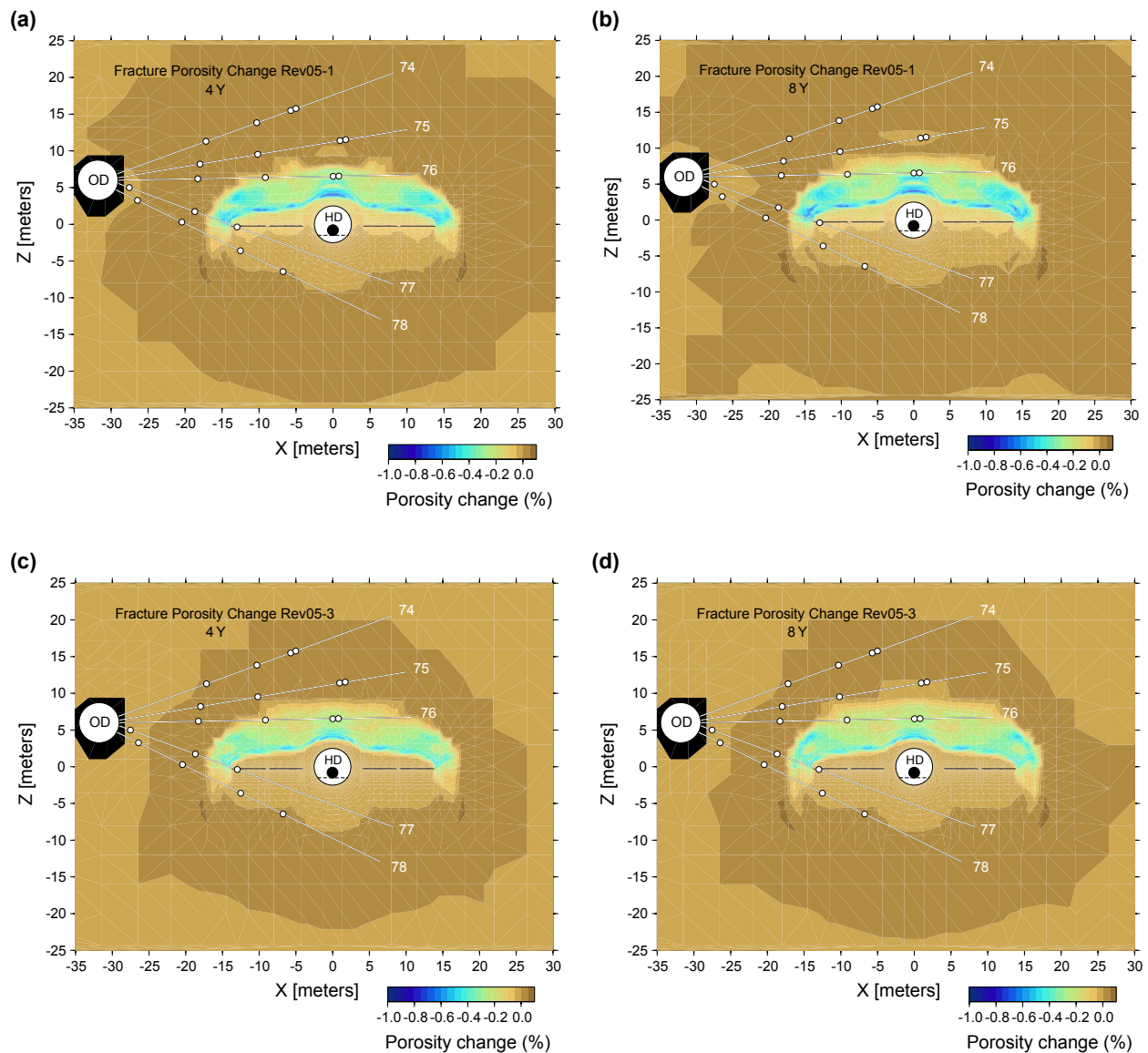
Output DTN: LB0705DSTHC005.002 (modeled).

NOTE: Chemistry borehole 54 is shown with location of observed gypsum (open circle) formed during the DST.

Figure 7.1-30. Modeled Volume Percent Anhydrite in Fractures Compared to Observed Gypsum Locations in Borehole 54: (a) November 2000 (35 months of heating) and (b) 8 Years

7.1.13 Porosity and Permeability Changes

Figure 7.1-31 shows the change in fracture porosity after four years of heating in the DST for simulations using the initial conditions at the 14.4 mm/yr infiltration rate (a, b) and for the 1.446 mm/yr rate (c, d). The areas above the Heated Drift and near the edges of the wing heaters show the greatest reduction in fracture porosity, reaching somewhat less than 1.0%. Nearly all of the change in fracture porosity has taken place during the initial four-year heating period, with little change after eight years. The lack of a significant increase in porosity (redissolution of precipitated phases) during the cooling period is due to the very slow rate of rewetting, and the much slower rate of dissolution compared to precipitation during boiling. Areas of slight fracture porosity increases in the model results can be found in the outer condensation zones, but are much less than the maximum reduction in porosity seen in the boiling regions above the heaters. The simulation with the higher initial liquid saturation (a, b) shows a slightly greater reduction in fracture porosity above the heaters.



Output DTN: LB0705DSTHC005.002.

NOTE: Negative values indicate a net porosity reduction resulting from mineral precipitation, and positive values indicate a net porosity increase resulting from mineral dissolution.

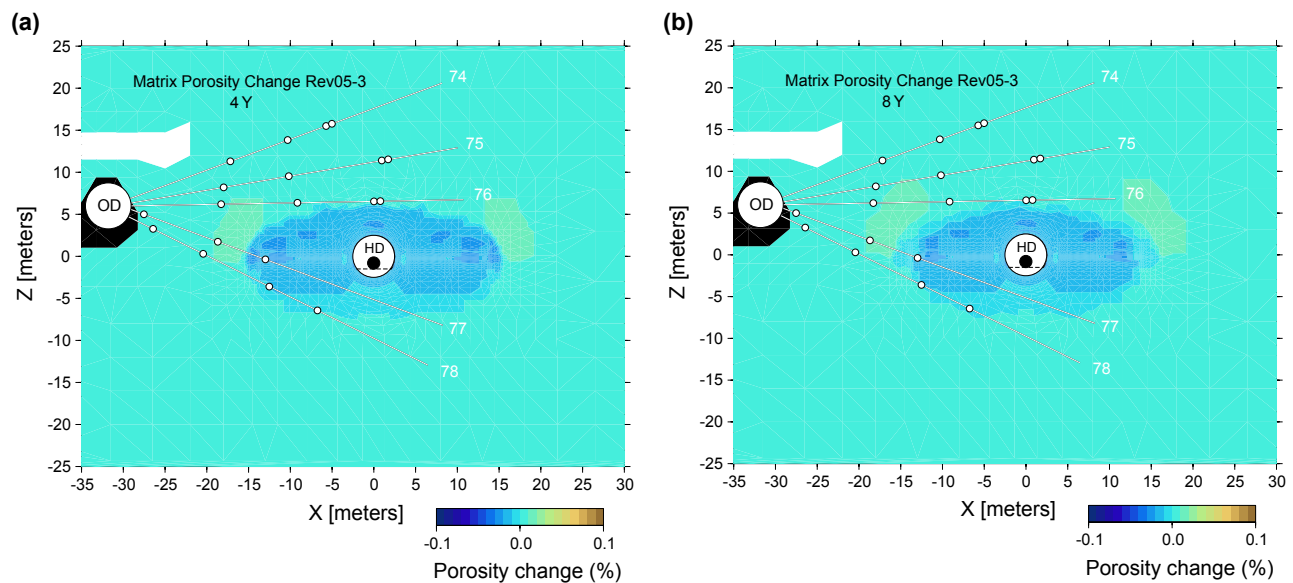
Figure 7.1-31. Change in Fracture Porosity after Four Years of Heating and at the End of the Cooling Period (8 years) for Simulations Using the Initial Conditions at the 14.4 mm/yr Infiltration Rate (a, b) and for the 1.446 mm/yr Rate (c, d)

Changes in matrix porosity after four years of heating and at the end of the eight-year cooling period are shown in Figure 7.1-32. Reductions in matrix porosity are limited solely to the dryout zone where mineral precipitation accompanied boiling of the in situ pore water. Increases in matrix porosity are actually greater than the reductions and are evident throughout the condensation zones, where imbibition of dilute water led to mineral dissolution. Areas of strong fracture drainage around the outer edges of the heated zone apparently led to the highest level of

matrix imbibition and mineral dissolution in the matrix. The porosity increase in the matrix is, however, approximately two orders of magnitude less than the porosity decrease in the fractures.

Fracture permeability changes resulting from mineral precipitation and dissolution are tied to changes in porosity and more directly to fracture aperture changes. Changes in fracture porosity of less than 1% of the original value would have a correspondingly small effect on fracture permeability. These results are consistent with the observations of minor changes in air permeability during the DST, which have been attributed predominantly to water saturation changes (mostly in the condensation zones, where mineral precipitation is negligible) and in some cases due to changes in the rock mass owing to thermal-mechanical effects (SNL 2007 [DIRS 177414]), p. 6-191).

Thermal-hydrologic-mechanical (THM) coupled processes have also been evaluated using data from the DST and are also predicted to cause changes in the repository host rock permeability (BSC 2004 [DIRS 169864], Section 6.9). Thermal stress tends to close fractures oriented radially to the opening, and open fractures oriented tangentially. For the same simulation conditions (equivalent thermal-hydrology), the effects from the THM simulations are centered closer to the drift openings than the THC effects.



Output DTN: LB0705DSTHC005.002.

NOTE: Negative values indicate a net porosity reduction resulting from mineral precipitation, and positive values indicate a net porosity increase resulting from mineral dissolution.

Figure 7.1-32. Change in Matrix Porosity after (a) Four Years of Heating and (b) End of the Cooling Phase (eight years)

7.1.14 Isotopic Compositions of Gases and Water: Model Corroboration Using ^{14}C in CO_2

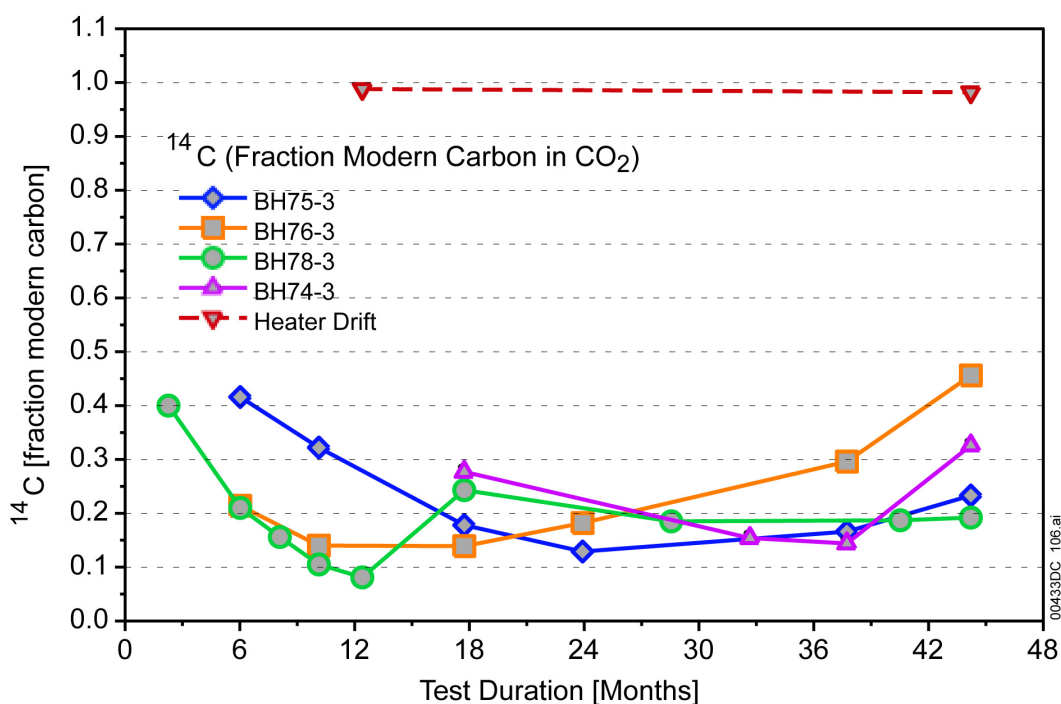
Gas-phase CO_2 concentrations and stable isotopic ratios ($\delta^{13}\text{C}$, $\delta^{18}\text{O}$, δD , and ^{14}C) were measured from gases pumped from hydrology boreholes (SNL 2007 [DIRS 177414], Table 6.3.4.2-1). For the gas-phase compositions, direct comparisons of model results have been made only to CO_2 concentrations. Isotopic ratios of carbon ($\delta^{13}\text{C}$), oxygen ($\delta^{18}\text{O}$), and hydrogen (δD) are sensitive to fractionation effects between the liquid and gas phases, as well as to diffusive fractionation, owing to the differing masses of the isotopes. Thus, they are useful in interrogating thermal-hydrologic transport processes. These fractionation effects are pronounced at lower temperatures, such that the relatively minor extent of water–rock interaction is strongly masked; thus, they are less useful for directly investigating mineral alteration during the DST.

Relative to the stable carbon isotopes (^{12}C and ^{13}C), carbon-14 (^{14}C) abundances are minimally affected by fractionation because their activities vary over a large range, owing to the geologically short time for the radioactive decay of this species ($t_{1/2} \approx 5,000$ years). The virtual lack of ^{14}C in carbonate minerals at Yucca Mountain (because these materials are predominantly tens of thousands to millions of years old) allows for a sensitive indicator of the dissolution of calcite. Fortuitously, ^{14}C activities in the gas phase in the rock, at approximately the level of the Tptpmn unit, are around 0.5 (fraction modern carbon) for several measurements done in different areas (Yang et al. 1996 [DIRS 100194], p. 46). The convention “fraction modern carbon” refers to the activity of ^{14}C prior to atmospheric testing of nuclear weapons. Thus, the present-day activity of atmospheric ^{14}C is somewhat greater than one, because of the addition of ^{14}C through weapons testing. In the subsurface at Yucca Mountain, therefore, any addition of atmospheric CO_2 to the rock gas will drive its ^{14}C activity from about 0.5 towards 1.0, whereas dissolution of calcite will drive the activity to close to zero.

Measured ^{14}C activities in CO_2 from several hydrology borehole intervals (BH74-3, BH75-3, BH76-3, and BH78-3) are shown in Figure 7.1-33 over much of the heating phase of the DST. Unfortunately, an initial, unperturbed gas sample was not analyzed; however, the earliest samples collected had ratios around 0.4. All of the zones show a significant drop-off over time to values below 0.2 and several to around 0.1 or less. By projecting the trajectories of these early slopes back to time zero, the zones appear to converge to an initial activity close to 0.5. Note that all of the samples analyzed from rock gas (over 40 measurements) had activities below 0.5. Two measurements of gas from the Heated Drift (taken after about 12 and 44 months) were also analyzed and show nearly identical values of about 0.98, which is almost entirely atmospheric in composition. Thus, it is clear that the gas in the Heated Drift is exchanging freely with the atmosphere, even though the pore water in the rock is generating abundant CO_2 with low ^{14}C activities.

It can be concluded from these data that little atmospheric CO_2 has affected the CO_2 in the rock gas. Although atmospheric gas has undoubtedly been introduced into the system through gas-permeability testing and drilling, the relatively low CO_2 concentration in atmospheric air (≈ 400 ppmv) compared to the ambient rock gas ($\approx 1,000$ ppmv) and to the large concentrations generated during heating ($> 10,000$ ppmv) make contamination by atmospheric CO_2 difficult.

The strong drop-off of ^{14}C in the gas over time is caused primarily by the dissolution of calcite having little or no ^{14}C . The pore water could also be heterogeneous with respect to ^{14}C , the interior of the matrix blocks having “older” water than the exterior. The latter explanation, though, is implausible, owing to the rapid diffusivity of CO_2 in the gas phase in the unsaturated matrix and the rapid equilibration of CO_2 with bicarbonate in the aqueous phase. Furthermore, this possibility is not supported by the gradual return in all of the measured borehole intervals to higher ^{14}C activities. Finally, ^{14}C activities as low as 0.08 have not been observed in the gas phase in the UZ at Yucca Mountain and would imply isolated water with ages over 15,000 years.

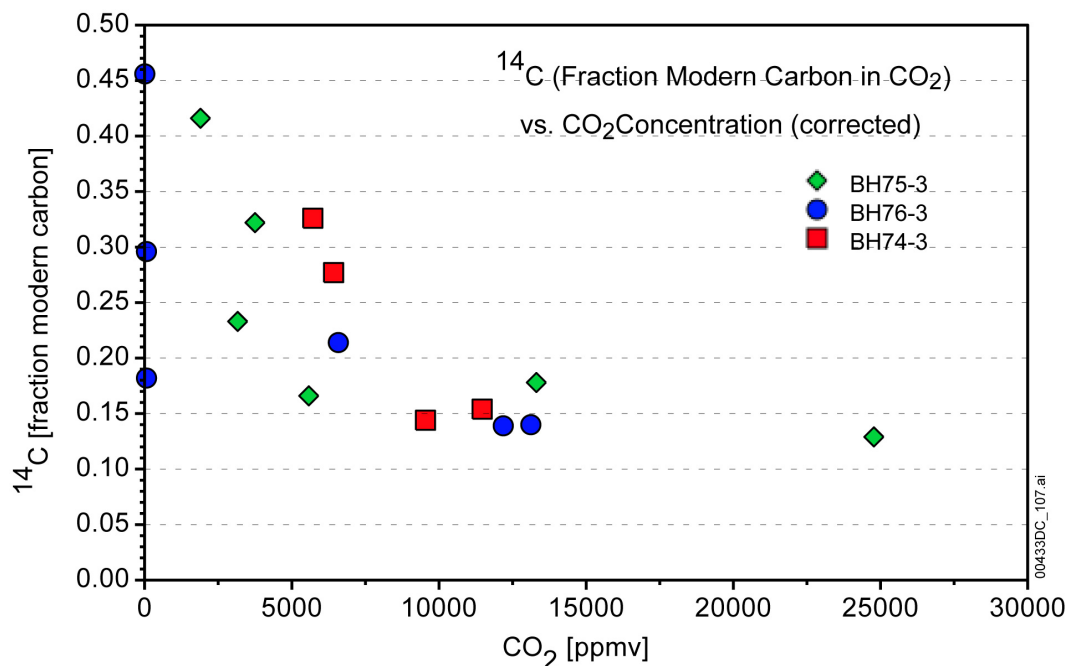


Source: SNL 2007 [DIRS 177414], Table 6.3.4.2-1.

NOTE: Two samples collected from the Heater Drift were also analyzed.

Figure 7.1-33. Measured Activities of ^{14}C (expressed as a fraction of modern carbon) in CO_2 from Gas Collected in Several Hydrology Boreholes over Most of the Heating Phase of the DST

Another aspect to the trend in ^{14}C activities can be found by examining their relation to the CO_2 in the gas phase. The abundance of ^{14}C in the gas is governed by the equilibrium between HCO_3^- in the water and CO_2 in the gas phase. Under closed conditions, the gas should be in equilibrium with the water. This is assumed in modeling the CO_2 concentrations in the DST, where there is good correspondence between modeled and measured values. The overall trend in ^{14}C activities seen in Figure 7.1-33 is inversely related to the changes in CO_2 concentrations observed in these intervals. The timing of the peak in CO_2 concentration and the low in ^{14}C activity is also very close (Figure 7.1-12). A comparison of measured CO_2 (corrected for water-vapor removal) and ^{14}C is shown for three borehole intervals in Figure 7.1-34. It is apparent that at the highest CO_2 concentrations reached in each zone, the ^{14}C activities are also among the lowest.



Source: SNL 2007 [DIRS 177414], Table 6.3.4.2-1.

Figure 7.1-34. Measured Activities of ¹⁴C (expressed as a fraction of modern carbon) Compared to Measured CO₂ (corrected for water vapor removal) from Gas Collected in Some Hydrology Boreholes over Most of the Heating Phase of the DST

The peak in CO₂ concentrations observed in the model results, and in the measured values, takes place at temperatures of close to 60°C, well below boiling and prior to the dilution of the gas phase by significant quantities of water vapor. This temperature region is characterized by some vapor condensation (Figure 7.1-7), a lowering of pH (Figure 7.1-15), and calcite dissolution (Figure 7.1-28) in the model simulations. Therefore, the trend to low ¹⁴C activities in the areas where calcite is predicted to dissolve is consistent with the model results and with the aqueous- and gas-phase chemical data that have been used to validate the model.

7.1.15 Summary of Model–Data Comparisons Using the Drift Scale Test

The foregoing discussion in Sections 7.1.9 through 7.1.14 has described the corroboration of the THC seepage model, through the DST THC submodel, using experimental data. The validation approach described in Section 7.1.7.1 is completed through comparison with thermal-hydrologic data (Section 7.1.9), gas-phase CO₂ concentration data (Section 7.1.10), measured aqueous composition of sampled fracture waters (Section 7.1.11), and sampled mineralogical data (Section 7.1.12). Consideration is also given to fracture and matrix porosity changes, changes in bulk permeability, and the corroborative indications from the DST (Section 7.1.13). Also, data for the ¹⁴C isotopic composition of the gas phase are interpreted to corroborate the simulation of reactions involving CO₂. The DST is the largest, most comprehensive test of its kind ever performed, and the results provide extensive corroboration of the THC seepage model approach and predictive capability. Where model–data comparisons exhibit differences, the magnitude is incorporated into a general assessment of uncertainty that is propagated to the LA.

7.2 SIMULATION OF THE PLUG-FLOW REACTOR EXPERIMENT

These simulations were performed as part of historical work, using older versions of TOUGHREACT and older thermodynamic databases, and not repeated for the present report. As part of this historical work, comparisons between a laboratory-scale tuff dissolution experiment and simulated results using TOUGHREACT were used to test geochemical models that were developed for the THC seepage model and the DST THC submodel. Because these simulations were performed with previous versions of TOUGHREACT and older thermodynamic databases, they cannot directly address validation of the current THC model. However, a brief summary is provided here because these simulations do provide added confidence in the conceptual model that is the basis of the THC seepage model. The simulations are discussed in detail in a previous revision of this report (BSC 2004 [DIRS 168848], Section 7.2).

The experiment was a plug-flow reactor experiment using crushed tuff from the Tptpmn lithostratigraphic unit, and was performed under isothermal elevated temperature conditions (94°C) with well-constrained initial water and rock compositions. Measured water compositions of samples obtained during the duration of the experiment allowed the evaluation of kinetically controlled reactions (e.g., mineral dissolution and precipitation) with time. A series of isothermal one-dimensional simulations were performed to model this dissolution using TOUGHREACT Versions 2.2 (TOUGHREACT V. 2.2 [DIRS 153219], STN: 10154-2.2-00) and 2.3 (TOUGHREACT V. 2.3 [DIRS 153101], STN: 10396-2.3-00). Measured and predicted effluent concentrations were compared to evaluate the conceptual models developed for the THC seepage model.

Although some simulations exhibited closer matches than others, depending on the estimated mineral surface areas and the thermodynamic database used, predicted concentrations for the major aqueous species in the effluent generally matched the measured values well, usually within a factor of 3, and always within an order of magnitude. Measured pH values were not modeled well. The discrepancy in pH can be attributed to the exposure of the plug-flow effluent to air and the subsequent cooling and degassing of the outflow solution before analysis. The outflow pH values matched the simulated results closely after they had been corrected for these processes.

Two important conclusions can be derived from the tuff dissolution experiment and simulations, even though they do not serve to directly validate the current THC seepage model:

- A good match was obtained between the water compositions for the observed and simulated plug-flow experiment, providing additional confidence in the THC seepage model conceptualization.
- Differences between the modeled and measured values in pH result from cooling and degassing of the experimental samples after exiting the tuff dissolution column. This illustrates the potential for fluid-chemistry changes during sample collection for the DST experiment, and supports the conclusion (Section 7.1.11.2) that the poor fits between the measured DST pH values and those predicted by the DST THC submodel are due to cooling, condensation, and degassing during sample collection.

7.3 SIMULATION OF THE FRACTURE SEALING EXPERIMENT

As with the plug-reactor experiment, these simulations were performed as part of historical work, using older versions of TOUGHREACT and older thermodynamic databases, and not repeated for the present report. As part of this historical work, a laboratory-scale fracture-sealing experiment has also been simulated using TOUGHREACT. Because these simulations were performed with previous versions of TOUGHREACT and older thermodynamic databases, they do not directly address validation of the current THC model, but provide added confidence in the conceptual model basis and parameterization. The simulations are discussed in detail in the previous revision of this report (BSC 2004 [DIRS 168848], Section 7.3) and in the report by Dobson et al. (2003 [DIRS 165949]) and are summarized here.

The fracture sealing experiment was designed to emulate and evaluate the effects of condensate reflux through a fracture network and into a boiling environment. Two saw-cut blocks of welded rhyolitic ash-flow tuff (from unit Tptpmn in Alcove 6 of the ESF), were separated by gold shims to create a vertical planar fracture. The outer surfaces of the blocks were sealed and the temperature gradient of 80°C at the top and 130°C at the bottom was established with heaters. Effluent from the plug-flow reactor (Section 7.2) was directed into the top of the fracture (at a constant rate of about 10.8 mL/hr) and vapor was removed from the bottom. Fracture sealing occurred after five days. After cooling, the fracture was opened and examined to determine the location and nature of secondary mineral formation. The precipitate (identified as mainly amorphous silica from scanning electron microscopy x-ray analyses and visual and petrographic examination) was deposited almost exclusively in zones where the temperature had exceeded 100°C.

Simulations with TOUGHREACT Version 2.4 (TOUGHREACT V. 2.4 [DIRS 160880], STN: 10396-2.4-00) were performed to model fracture sealing, using a mesh configuration with dimensions (in one dimension) identical to those of the tuff fracture experiment. The initial rock mineralogy was considered to be the same as that used in the plug-flow experiment. Different simulations were run for a period of 5.8 days, with amorphous silica controlled by either equilibrium or kinetic conditions.

The simulation results indicated the formation of a nearly isothermal two-phase region with an overlying water column above and a vapor zone below. The precipitation of amorphous silica at the base of the two-phase zone accounted for all of the porosity and permeability reduction in the fracture system. The base of the boiling zone (and region of silica precipitation) shifted downward over time due to a gradual pressure buildup, caused by the reduction of the fracture aperture at the top of the fracture system. The thickness and location of the silica precipitation zone were different in the kinetic and equilibrium simulations. Simulations conducted using equilibrium precipitation and dissolution for amorphous silica showed the effects of both precipitation and dissolution, as the trailing (upper) edge of the silica front underwent dissolution with time. In the kinetic simulations, almost no dissolution of precipitated amorphous silica occurred, resulting in a thicker band of silica that occluded less of the fracture aperture. Significant permeability reductions occurred within five days after initiation of fluid flow for both the experiment and simulations. The presence of silica precipitate throughout the boiling zone in the experimental fracture system suggests that the kinetic simulation, which retains early-formed precipitate, is a more appropriate match to the experimental results.

These simulations provide confidence in the geochemical model developed for the THC seepage model and the DST THC submodel presented in this report. Both of the simulations accurately predicted the distribution and type of secondary mineral precipitation. Amorphous silica was the dominant secondary mineral phase, and simulated amorphous silica precipitation was restricted to the lower portion of the two-phase zone at temperatures of around 105°C to 109°C, consistent with the observed pattern of mineralization along the fracture surface in the experiment. The predicted total fracture-porosity-reduction values resulting from silica precipitation in the equilibrium and kinetic simulations were 2.2% and 3.9%, respectively, comparable to the estimated values of 0.9% to 3.6% for the experiment. The experimentally determined distribution of silica precipitation was predicted more accurately by the simulation assuming kinetic control of silica precipitation, providing support for the use of this approach in the THC seepage model and the DST THC submodel.

7.4 VALIDATION SUMMARY

The THC seepage model has been validated by applying acceptance criteria based on an evaluation of the model's relative importance to the potential performance of the repository system. All validation requirements defined in the TWP (SNL 2007 [DIRS 179287], Section 2.2.2) have been fulfilled, including corroboration of model results with experimental data and additional confidence building by publication in a refereed professional journal (Section 7). Activity requirements for confidence building during model development have also been satisfied. The model development activities and post-development validation activities described establish the scientific bases for the drift-scale THC seepage model. Based on this, the drift-scale THC seepage model is considered to be sufficiently accurate and adequate for the intended purpose and to the level of confidence required by the model's relative importance to the potential performance of the repository system. No future validation activities are required for the drift-scale THC seepage model.

8. CONCLUSIONS

This report documents the thermal-hydrologic-chemical (THC) seepage model (Sections 4 and 6), the Drift Scale Test (DST) THC submodel (Section 7), and results of model simulations. The models describe coupled THC processes at the drift scale to assess (1) the chemistry of water and gas potentially entering drifts and (2) changes in permeability and flow around drifts. The THC seepage model is used primarily to predict the composition of waters and gases around and potentially seeping into waste emplacement drifts and the effect of water–rock interaction on flow. Key findings of this model are summarized in Figure 8-1. The DST THC submodel is used primarily to validate the THC seepage model, with a brief description and conclusions given in Section 8.3. The THC seepage model results are intended to provide confidence in the results of simpler models discussed in *Engineered Barrier System: Physical and Chemical Environment* (SNL 2007 [DIRS 177412]). Specifically, simulation results from the THC seepage model are used for validation of the near-field chemistry model component of the physical and chemical environment model (SNL 2007 [DIRS 177412], Section 7.1.3).

The underlying conceptual and mathematical models (Sections 6.1 to 6.4) provide the basis for modeling the thermal and hydrologic effects of the relevant mineral–water–gas reactions and transport processes in the host rock for 100,000 years, a time period sufficient to capture the entire duration of the thermal pulse and the return to ambient conditions. Confirmatory actions include evaluating the sensitivity of the models to different input parameters. Validation (Section 7) is accomplished through comparison of simulation results to data collected from the DST. Additional confidence building is also accomplished through publication in refereed journals (Spycher et al. 2003 [DIRS 162121]; Dobson et al. 2003 [DIRS 165949]; Sonnenthal et al. 2005 [DIRS 176005]; Mukhopadhyay et al. 2007 [DIRS 180822]). Model results have been submitted to the Technical Data Management System (TDMS) as output under DTNs listed in Appendix G of this report. Applicable acceptance criteria from the YMRP addressed by this report are discussed in Section 4.2, with pointers referring to sections of this report where these criteria are addressed. The barrier capabilities of the natural system, including host rocks and the capillary barrier effects of drift openings, are considered throughout this report (Sections 6.5.2). Potential barrier effects from mineral precipitation during the thermal period are also considered (Section 6.5.5.3).

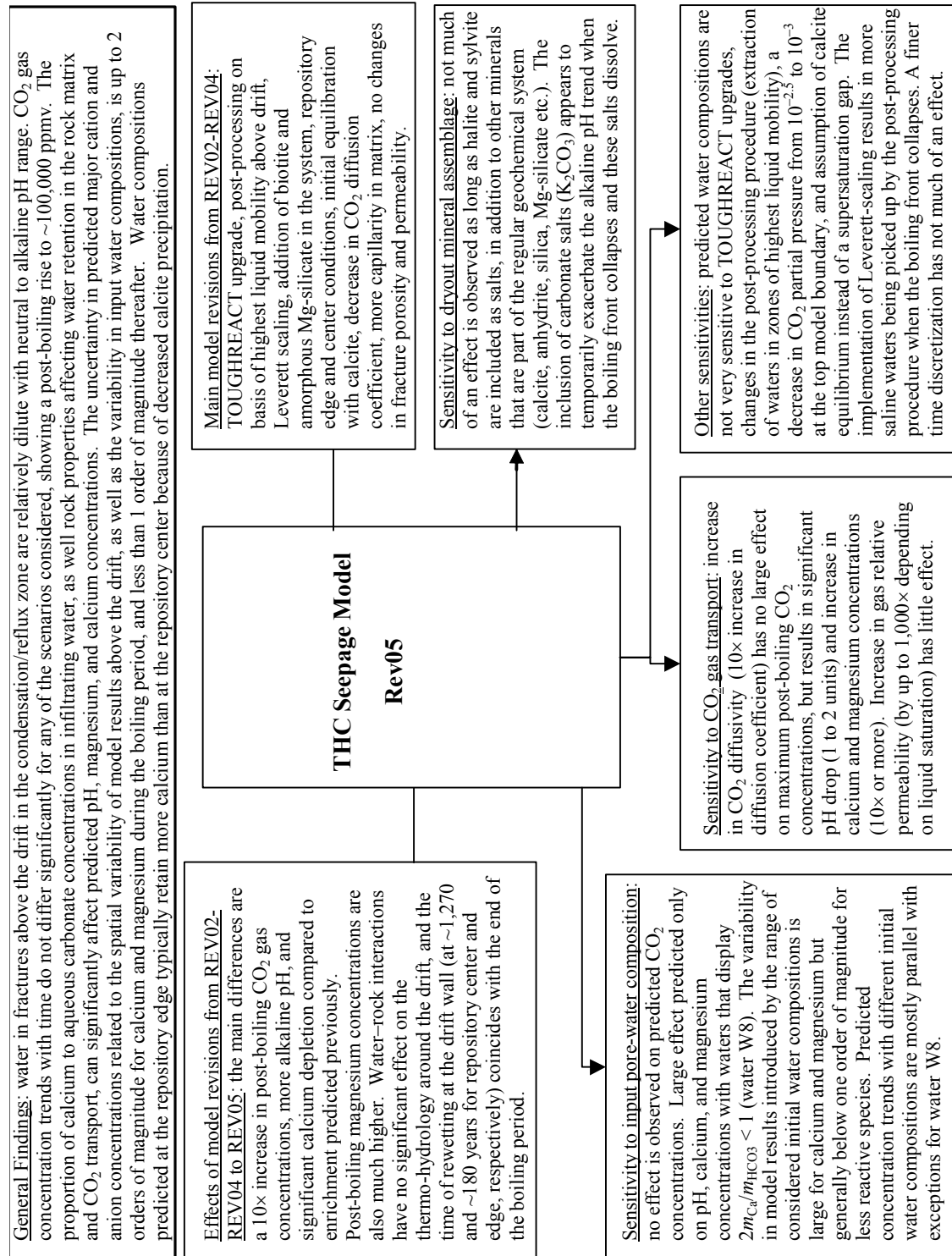


Figure 8-1. Key Findings of the THC Seepage Model

8.1 MODELED COUPLED PROCESSES AND UNCERTAINTY

Simulations of THC processes include coupling among heat, water, and vapor flow; aqueous and gaseous species transport; kinetic and/or equilibrium mineral–water reactions; equilibrium between aqueous species; and feedback of mineral precipitation/dissolution on porosity, permeability, and capillary pressure for a dual-permeability (fracture–matrix) system. Treatment of CO₂ include gas–water equilibration, gas species diffusion, and advection. Data are incorporated from the calibrated thermal-hydrologic property sets, the three-dimensional mineralogical model, the unsaturated zone flow and transport model, thermal test geochemical data (fracture and matrix mineralogy, aqueous geochemistry, and gas chemistry), thermodynamic data (minerals, gases, and aqueous species), kinetic data for mineral–water reactions, and transport (diffusion coefficient) data (Section 4.1). The THC seepage model and the DST THC submodel include a wide range of major and minor aqueous species and minerals (primary and potential secondary phases). The following primary aqueous species are considered: H⁺, Ca²⁺, Mg²⁺, Na⁺, K⁺, SiO₂(aq), AlO₂⁻, HFeO₂(aq), SO₄²⁻, HCO₃⁻, Cl⁻, NO₃⁻, and F⁻. Minerals include several silica phases (α-cristobalite, quartz, tridymite, amorphous silica, and opal-CT), calcite, feldspars, clays, biotite, an amorphous magnesium silicate, zeolites, fluorite, hematite, goethite, anhydrite, and volcanic (rhyolitic) glass. In addition to the calibration of the hydrologic properties, some thermodynamic and kinetic data have been revised (within their ranges of uncertainty) to yield model results for the ambient system that are consistent with measured pore-water compositions over long simulated time periods.

Many sources of uncertainty exist in modeling coupled THC processes (Section 6.7), because of the large number of parameters needed to describe the natural system, as described in Sections 4, 6, and 7. Model validation provides a test of whether the system can be described sufficiently well for the intended purposes of the model. Validation is accomplished through analyses of the DST under temperatures, pressures, and chemical compositions corresponding to the range expected for the repository thermal loading conditions and drift design. As summarized further in this section, results of DST THC simulations captured the important changes in pH, aqueous species concentrations, gas-phase CO₂ concentrations, and mineral deposition at specific locations over time. This provides confidence in the modeling capability to predict trends of spatial and temporal variations in water and gas chemistry around emplacement drifts. Although the duration of the DST heating phase is approximately four years, the DST results exhibit the same processes known to control water chemistry, gas compositions, and permeability over longer time periods.

Simulations presented in this report (Sections 6.5.5 and 6.6) address the model sensitivity to:

1. Input water compositions
2. Repository-center versus repository-edge location
3. Time discretization

4. Model revisions including: TOUGHREACT upgrades; the use (or not) of a supersaturation gap for calcite; change in post-processing procedure (from zones of highest liquid saturation to highest liquid mobility); and changes in CO₂ partial pressure at the top model boundary
5. Parameters affecting CO₂ gas transport
6. Types and sequence of minerals assumed to form upon complete dryout
7. Reaction rates of primary minerals.

The developmental history of the THC seepage model provides additional qualitative information on the model sensitivity to a range of conceptualizations and input parameters, including (Table 6-1):

1. Different repository host-rock geologic units (Ttptmn and Ttptll)
2. Alternative geochemical systems (base case and extended case, additional minerals and chemical components)
3. Alternative thermodynamic data sets (different equilibrium constants for key minerals)
4. Different treatments of mineral–water reactions (different kinetic rate constants and reactive surface areas; equilibrium vs. kinetic reactions)
5. Spatial heterogeneity in fracture permeability
6. Different infiltration rates and effects of climate change
7. Alternative water vapor pressure models
8. Alternative initial water compositions
9. Different effective CO₂ diffusivities
10. Alternative drift wall conceptualizations (open vs. closed to liquid flow).

These THC seepage model simulations cover a wide range of important uncertainties. From this work, it appears that one of the principal sources of uncertainty is the natural variability in input water compositions. From this variability alone, the uncertainty in predicted concentrations of reactive aqueous species like calcium and magnesium reaches up to about two orders of magnitude during the boiling period (Section 6.7.2). After the boiling period, the spread in model results introduced by the different input water compositions, at any given time, is typically half to one order of magnitude.

8.2 THC SEEPAGE MODEL RESULTS

The THC seepage model is designed to represent waste package heating over time, changes in heat load caused by ventilation, the effective heat transfer within the drift, and THC processes in the unsaturated zone around waste emplacement drifts. Simulations considered an initial heat load of 1.45 kW/m, including a preclosure period of 50 years using a ventilation efficiency of 88%. Model results predict the chemistry of matrix and fracture water at various locations around a drift, the times of rewetting around the drifts, and the net fluxes of water and gas near and across the drift wall for a period of 100,000 years.

The scope of this report includes one design heat load for two cases of lateral location within the repository: center and edge. At the repository center, temperatures near emplacement drifts exceed the boiling point of water for approximately 1,270 years after repository closure. At the edge, temperature drops below boiling at about 180 years after closure. Temperature is an important parameter because it affects the extent of water–rock interaction taking place around proposed emplacement drifts.

The predicted extent of the dryout zone (6 to 7 m above the drift center) is similar under both repository-center and repository-edge conditions. The time of rewetting at the drift wall essentially coincides with the time at which temperatures drop below boiling at the drift wall. The extent of dryout, as well as the rewetting time and rewetting fluxes at the crown of the drift, are essentially not affected by water–rock interaction, and thus are not sensitive to the water compositions input into the model. This is in contrast to previous model results that showed a significant delay in rewetting times induced by mineral precipitation above the modeled drift. The difference here is attributed to the consideration of capillary pressure increase when porosity decreases because of mineral precipitation (Leverett scaling; this option was enabled but not operative in the previous model revision).

The predicted magnitude of fracture porosity change caused by water–rock interaction around waste emplacement drifts depends on the initial fracture porosity (with the largest relative change for the smallest porosity), and results in large part from the precipitation of amorphous silica at the boiling front above the drift opening. Because the silica solubility decreases with declining temperature, the amorphous silica precipitated in fractures does not dissolve significantly into percolating water over 100,000 years. The long-term effect is a decrease of up to 7% of the fracture porosity, resulting in a long-term fracture permeability decrease less than half an order of magnitude. Shorter-term effects from the precipitation of evaporite minerals at the boiling front (anhydrite, halite, and other salts) result in a permeability decrease up to 3.5 orders of magnitude. However, these minerals readily dissolve as the boiling front collapses around the modeled drift.

Predicted water compositions in the zone of condensation and reflux in fractures above the modeled drift were examined. Waters from this zone, in model gridblocks showing high liquid mobility, were taken as most representative of potential seepage. In all the modeled cases, including four simulations using different input water compositions, relatively dilute and neutral to alkaline water compositions are predicted. General trends of CO₂ gas concentrations above the modeled drift do not differ significantly for any of the cases considered, with elevated post-boiling concentrations up to ~100,000 ppmV at the repository center, and about 10 times

less at the repository edge. In all cases considered, upon boiling, these waters evolve to alkaline conditions. This effect is less pronounced at the repository edge, compared to the repository center, because the boiling period is significantly shorter. Upon the collapse of the boiling front, and accentuated by the elevated post-boiling CO₂ concentrations, predicted pH values drop below ambient values for thousands of years before returning to initial values.

In fractures above the modeled drift, similar trends of aqueous species concentrations are predicted using waters W0, W9, or W10 as input compositions (Table 6.2-4). However, the pH and calcium concentrations predicted using water W8 at the repository edge differ significantly from trends predicted with the other waters. At rewetting times, these differences are up to 2 pH units and 3 orders of magnitude in calcium concentration. This is attributed to the lower initial calcium-to-aqueous-carbonate ratio in water W8 compared to the other waters, which accentuates the evolution of this water towards alkaline conditions upon boiling.

Predicted trends of pH, calcium, and magnesium concentrations are quite different from the trends predicted in earlier model revisions. Predicted post-boiling CO₂ gas concentrations are also about 10 times higher than predicted previously. The differences in predicted calcium concentrations are particularly large, showing depletion below ambient values by up to 2 orders of magnitude in the present report, compared to an increase of over 1 order of magnitude above ambient values in the previous model revision. These differences appear to be related, at least in part, to revisions in rock properties that tend to increase water retention in the rock matrix (less condensation and calcite dissolution in fractures) as well as a significant decrease in the value used for the CO₂ diffusion coefficient in this model revision. The change in the mineral controlling the solubility of magnesium (from sepiolite to an amorphous magnesium silicate), plus the inclusion of biotite as a primary mineral in the geochemical system, reverse the general trend of magnesium depletion predicted in earlier model revisions. Furthermore, magnesium concentrations in waters percolating above the drift after the boiling period are predicted to rise above ambient values, because of the dissolution of magnesium silicate deposited above the modeled drift during the boiling period.

A noticeable effect of the shorter boiling length at the repository edge is the generally more elevated calcium concentrations (by up to several orders of magnitude) in fracture waters during the collapse of the boiling front. The higher calcium concentrations predicted at the repository edge are attributed to the decrease in CO₂ degassing (from the reduced boiling and calcite precipitation) and the higher calcite solubility at lower temperatures. The decreased dissolution of host rock minerals when the boiling period is shorter results in lower predicted concentrations of other less reactive species like sodium and potassium.

Sensitivity analyses indicate that model results, and most notably pH, carbonate, calcium, and magnesium concentrations, are sensitive to the diffusivity of CO₂ in the modeled system. The types of minerals, including salts, assumed to form upon complete dryout do not significantly affect predicted concentrations above the drift in fractures after rewetting of the drift wall. Simulations that do not model a thermal pulse (ambient conditions) appear to be much more sensitive to changes in reaction rates of primary minerals than heat-load simulations. Therefore, the uncertainty in model results caused by uncertain reaction rates is anticipated to be smaller if reaction rates are constrained such that relatively steady and reasonable concentration trends are obtained under ambient conditions, as done here.

During the boiling period, the spread in predicted concentrations in fractures above the modeled drift, at a given time, can be quite large (standard deviations up to ± 1 log unit for calcium and magnesium). This spread represents the model-result spatial variability above the drift in the condensation/reflux zone, combined with the variability introduced by the four different input water compositions. This range in predicted concentrations is likely too wide to constrain with confidence the type of brines that could form upon evaporative concentration of these waters. This is because the chemical evolution of these brines can be quite sensitive to their initial composition, and particularly their starting calcium and magnesium concentrations. For these reasons, it would appear that additional confidence in the predicted composition of potential seepage could only be achieved by integrating model results with additional experiments in the repository host units, carefully designed to measure the compositions of induced thermal seepage under a range of thermal histories and infiltration compositions.

8.3 DST THC SUBMODEL RESULTS (VALIDATION)

Validation of the modeling approach and parameters used in the THC seepage model is accomplished using a submodel developed for direct comparison to observations of gas composition, water chemistry, and mineral deposition in the DST. The DST THC submodel is used for sensitivity studies in addition to direct comparisons of model output to measured data.

Several sensitivity tests were performed to assess the response of the system to differing inputs and simulation parameters. Some of these sensitivity tests were determined to be important prior to the modeling study, in particular the sensitivity to the maximum time step and the sensitivity to the initial water composition. The other simulations were deemed necessary after the results of the initial simulations were reviewed. The initial setup of the model was performed to be consistent with inputs of the THC seepage model, while also maintaining consistency with the local conditions at the location of the DST. Specifically, the 30th percentile hydrological properties were used as inputs to the DST THC model, and to the steady-state simulation used to set the initial hydrological conditions for the DST. Because the location of the DST is closest to the surface-based borehole SD-9, the steady-state field was obtained for this column using the infiltration rate derived from the corresponding infiltration map. The infiltration rate at this location for the modern-day climate is 14.46 mm/yr, which results in a matrix liquid saturation of approximately 99%. This liquid saturation is much higher than the values typically found in the Tptpmn unit of about 85% to 90%. Therefore, another steady-state simulation was performed using one-tenth of this value, 1.446 mm/yr, which yielded a steady-state matrix liquid saturation of about 92%. Since the hydrological response of the system was more closely reflected by the 1.446 mm/yr results, this was deemed to be the base case for the initial conditions. These findings were also consistent with earlier published results (Birkholzer and Tsang 2000 [DIRS 154608]), which indicated that using a value of 0.36 mm/yr resulted in a better match to temperatures than using 3.6 mm/yr. The high chloride concentrations in the pore waters also indicate an infiltration that is less than about 1 mm/yr (Sonnenthal and Bodvarsson 1999 [DIRS 117127]), as well as other data as discussed in Section 7.1.5. The simulations performed are as follows:

1. 30th percentile properties, 14.46 mm/yr steady-state initial conditions, HDPERM3 initial pore water, maximum time step of 1 hour

2. 30th percentile properties, 1.446 mm/yr steady-state initial conditions, HDPERM3 initial pore water, maximum time step of 20 minutes
3. 30th percentile properties, 1.446 mm/yr steady-state initial conditions, HDPERM3 initial pore water, maximum time step of one day
4. 30th percentile properties, 1.446 mm/yr steady-state initial conditions, HDPERM3 initial pore water, maximum time step of one hour
5. 30th percentile properties, 1.446 mm/yr steady-state initial conditions, HDPERM3 initial pore water, maximum time step of one hour, amorphous antigorite rate increased
6. 30th percentile properties, 1.446 mm/yr steady-state initial conditions, ESFPERM4 initial pore water, maximum time step of one hour
7. 30th percentile properties, 1.446 mm/yr steady-state initial conditions, HDPERM3 initial pore water, maximum time step of one hour, rates of feldspars increased by 100.

Simulation results compared to measured gas-phase CO₂ concentrations and the chemistry of waters collected from hydrology boreholes indicate that the model captures the general trend in concentrations in the borehole intervals where comparisons have been made. It was clear that higher initial liquid saturations lead to higher maximum CO₂ concentrations, further from the measured concentrations. The high initial saturations led to a near fully saturated matrix and a slower loss of vapor into fractures. For conservative aqueous species, the agreement with the measured values was not as close as the simulations using the lower initial saturation. For most aqueous species, simulation number “3” above with the HDPERM3 water was closest to the measured data. Mg, K, NO₃, and F concentrations were especially close to those measured, whereas silica was somewhat low, and calcium higher than the dilute samples collected at later times in the borehole intervals. The ESFPERM4 water was less consistent with measured data, although for several species it was very close to the HDPERM3 water. The higher feldspar rates did not affect most aqueous species, although, as expected, K concentrations were elevated and generally much higher than the measured values. The higher antigorite rate did not result in significantly different Mg concentrations, and some effect may be from a difference in time stepping related to the poorer convergence behavior when using the faster rate.

The effect of a different maximum time step was significant for the CO₂ concentrations, where a smaller maximum time step led to higher maximum concentrations and lower minimum values. However, the difference between the twenty-minute and one-hour maximum time step was relatively minor, so the hour time step was chosen for the majority of the simulations. The effects on the aqueous species were much smaller than for CO₂, as would be expected by the much smaller diffusivity of aqueous species.

Predicted locations and relative abundances of secondary minerals are consistent with in situ sidewall core samples retrieved from zones that have undergone boiling. The most important mineral phase is amorphous silica, followed by significantly lesser amounts of calcite and anhydrite (potentially converting to gypsum at lower temperatures). The higher initial saturation simulation showed slightly greater mineral precipitation in fractures, but the pattern was the

same as for the lower initial saturation. Analyses of ^{14}C concentrations in CO_2 also corroborate the model results, because of their sensitivity to calcite dissolution and drift air contamination.

The evidence based on field and laboratory measurements demonstrates that model validation criteria have been met for CO_2 concentrations in gas, for several aqueous species concentrations, and for mineral precipitation in fractures. Although some disagreements between modeled and measured values exist, they could be attributed to sampling issues (discussed in Section 7) or to the selection of an initial pore-water concentration (possibly chloride, sodium, and nitrate in pore water ESFPERM4) that is higher than that in the rock. These differences serve to quantify the sensitivity of the model to the associated input parameters. Some heterogeneity in the measured data could not be matched by the model results, which is not unexpected for simulation of such an extensive field test. Ideally, hydrological properties would have to be used from the DST site, and the infiltration rate reduced to values probably less than 1 mm/yr, to obtain the best matches to data. However, the main purpose of the DST THC model is to use properties and conditions consistent with those for the THC seepage model and evaluate sensitivities rather than to use wholly site-specific data. The results achieved provide confidence in the modeling approach and the use of average properties for the purpose of the THC seepage model, which is to represent the chemical composition of water that could potentially seep into emplacement drifts, and the composition of the gas phase in the drifts.

Although not required for the planned validation strategy, the THC responses of the Yucca Mountain Drift Scale Test have been independently analyzed by the participants of the DECOVALEX III project, an international research project to develop coupled models and their validation against experiments. The outcome of the analyses by the DECOVALEX participants, generally corroborative of the contents of this report, has been presented in the GeoProc2003 conference held in Stockholm, Sweden, and has been published in a special issue of the *International Journal of Rock Mechanics* (Sonnenthal et al. 2005 [DIRS 176005]).

Based on the results presented in Section 7 and summarized here, the drift-scale THC seepage model is considered to be sufficiently accurate and adequate for the intended purpose and to the level of confidence required by the model's relative importance to the performance of the repository system.

8.4 UNCERTAINTIES AND RESTRICTIONS FOR DOWNSTREAM USE

Section 1.3 states the general model limitations. Potential uncertainties affecting model results are discussed in a qualitative manner in Section 6.7.1, and addressed more quantitatively in Sections 6.6 and 6.7.2. Various alternative conceptualizations and ranges of input data are considered (summarized in Section 8.1; see also Table 6-1). In addition, confidence in the model results is obtained by comparing model results to experimental data from the DST (Section 7). A large spread in the output compositions from the THC seepage model simulations is caused by the natural variability of input water compositions. This spread is up to approximately two orders of magnitude, and in many cases less (Section 6.7.2).

8.5 CRITERIA

The acceptance criteria identified in Section 2.2.1.3.3.3 of the YMRP (NRC 2003 [DIRS 163274]) are given below, with applicable subcriteria, followed by a short description of how these criteria have been addressed in this report:

- Acceptance Criterion 1, *System Description and Model Integration Are Adequate*
 - (1) *Total system performance assessment adequately incorporates important design features, physical phenomena, and couplings, and uses consistent and appropriate assumptions throughout the quantity and chemistry of water contacting engineered barriers and waste forms abstraction process.*

This subcriterion is addressed in Sections 6.2, 6.3, and 6.4.

- (2) *The abstraction of the quantity and chemistry of water contacting engineered barriers and waste forms uses assumptions, technical bases, data, and models, that are appropriate and consistent with other related U.S. Department of Energy abstractions.*

Sections 5, 6, and 7 address this subcriterion regarding water chemistry.

- (3) *Important design features, such as waste package design and material selection, backfill, drip shield, ground support, thermal loading strategy, and degradation processes, are adequate to determine the initial and boundary conditions for calculations of the quantity and chemistry of water contacting engineered barriers and waste forms.*

Design criteria used as model inputs are addressed in Section 4.1.10.

- (5) *Sufficient technical bases and justification are provided for total system performance assessment assumptions and approximations for modeling coupled thermal-hydrologic-mechanical-chemical effects on seepage and flow, the waste package chemical environment, and the chemical environment for radionuclide release. The effects of distribution of flow on the amount of water contacting the engineered barriers and waste forms are consistently addressed, in all relevant abstractions.*

This report addresses coupled THC effects on water chemistry and flow in the UZ up to the drift wall (Section 6). It therefore addresses parts of this subcriterion.

- (8) *Adequate technical bases are provided, including activities such as independent modeling, laboratory or field data, or sensitivity studies, for inclusion of any thermal-hydrologic-mechanical-chemical couplings and features, events, and processes.*

Features, events, and processes (FEPs) are addressed in Section 6.1, technical bases in Sections 6.2 to 6.4, modeling and sensitivity studies in Sections 6.5 and 6.6, and modeling of field experiments in Section 7, thus addressing this subcriterion.

- (9) *Performance-affecting processes that have been observed in thermal-hydrologic tests and experiments are included into the performance assessment.*

Simulations presented in this report reproduce coupled THC effects observed in thermal test (Section 7.1) and laboratory experiments (Dobson et al., 2003 [DIRS 165949]) and, therefore, address this subcriterion.

- (10) *Likely modes for container corrosion (Section 2.2.1.3.1 of the Yucca Mountain Review Plan) are identified and considered in determining the quantity and chemistry of water entering the engineered barriers and contacting waste forms. For example, the model abstractions consistently address the role of parameters, such as pH, carbonate concentration, and the effect of corrosion on the quantity and chemistry of water contacting engineered barriers and waste forms.*

The geochemical system used in the THC seepage model includes chemical components needed as inputs for modeling the corrosion environment. This subcriterion is addressed in Section 6.2.2.2, where the geochemical system is described.

- (12) *Guidance in NUREG-1297 (Altman et al. 1988 [DIRS 103597]) and NUREG-1298 (Altman et al. 1988 [DIRS 103750]), or other acceptable approaches, is followed.*

This report follows this guidance such that this subcriterion is addressed.

- Acceptance Criterion 2, *Data Are Sufficient for Model Justification*

- (1) *Geological, hydrological, and geochemical values used in the license application are adequately justified. Adequate description of how the data were used, interpreted, and appropriately synthesized into the parameters is provided.*

This subcriterion is addressed in Sections 4.1, 6.2 (and in particular 6.2.2), 6.3, and 6.4.

- (2) *Sufficient data were collected on the characteristics of the natural system and engineered materials to establish initial and boundary conditions for conceptual models of thermal-hydrological-mechanical-chemical coupled processes, that affect seepage and flow and the engineered barrier chemical environment.*

This report addresses parts of this subcriterion by considering variations in pore-water compositions (Sections 6.2.2.1 and 6.5.5.4) and rock properties (Section 6.4.7) representative of the natural system.

- (3) *Thermo-hydrologic tests were designed and conducted with the explicit objectives of observing thermal-hydrologic processes for the temperature ranges expected for repository conditions and making measurements for mathematical models. Data are sufficient to verify that thermal-hydrologic conceptual models address important thermal-hydrologic phenomena.*

Section 7.1, which presents details on results of the Drift Scale Test and simulations reproducing results of this test, addresses this subcriterion.

- (4) *Sufficient information to formulate the conceptual approach(es) for analyzing water contact with the drip shield, engineered barriers, and waste forms is provided.*

Because this report determines water compositions in the host rock surrounding the drifts (Sections 6.4.7 and 6.5.5), this subcriterion is addressed.

- Acceptance Criterion 3, *Data Uncertainty Is Characterized and Propagated Through the Model Abstraction*

- (1) *Models use parameter values, assumed ranges, probability distributions, and bounding assumptions that are technically defensible, reasonably account for uncertainties and variabilities, and do not result in an under-representation of the risk estimate.*

This subcriterion is addressed by using ranges of input data (Section 6.2.2.1, pore-water composition) and alternative conceptualizations of the modeled systems (Section 6.3) to evaluate model sensitivities and uncertainty (Sections 6.6 and 6.7).

- (2) *Parameter values, assumed ranges, probability distributions, and bounding assumptions used in the total system performance assessment calculations of quantity and chemistry of water contacting engineered barriers and waste forms are technically defensible and reasonable, based on data from the Yucca Mountain region (e.g., results from large block and drift-scale heater and niche tests), and a combination of techniques that may include laboratory experiments, field measurements, natural analog research, and process-level modeling studies.*

This report addresses the parts of this subcriterion that relate to the uncertainty of the chemistry of water that could potentially enter drifts, with inputs and results discussed in Sections 6.2.2.1, 6.4.7, 6.5.5, and 6.6 and validation, including the results of the DST presented in Section 7.

- (3) *Input values used in the total system performance assessment calculations of quantity and chemistry of water contacting engineered barriers (e.g., drip shield and waste package) are consistent with the initial and boundary conditions and the assumptions of the conceptual models and design concepts for the Yucca Mountain site. Correlations between input values are appropriately established in the U.S. Department of Energy total system performance assessment. Parameters used to define initial conditions, boundary conditions, and computational domain in sensitivity analyses involving coupled thermal-hydrologic-mechanical-chemical effects on seepage and flow, the waste package chemical environment, and the chemical environment for radionuclide release, are consistent with available data. Reasonable or conservative ranges of parameters or functional relations are established.*

This subcriterion is addressed with respect to the chemistry of water that could potentially enter drifts, with the conceptual models described in Sections 6.3 to 6.4, initial and boundary conditions discussed in Sections 6.5.2, and ranges of input parameters discussed in Section 6.4 and summarized in Sections 6.5.3.

- (4) *Adequate representation of uncertainties in the characteristics of the natural system and engineered materials is provided in parameter development for conceptual models, process-level models, and alternative conceptual models. The U.S. Department of Energy may constrain these uncertainties using sensitivity analyses or conservative limits. For example, the U.S. Department of Energy demonstrates how parameters used to describe flow through the engineered barrier system bound the effects of backfill and excavation-induced changes.*

This subcriterion is addressed by considering ranges of input parameters and alternative conceptualizations (Table 6-1 and Sections 6.2.2 and 6.3), as well as evaluations of the spread of model results (Section 6.7.2).

- Acceptance Criterion 4, *Model Uncertainty Is Characterized and Propagated Through the Model Abstraction*
 - (1) *Alternative modeling approaches of features, events, and processes are considered and are consistent with available data and current scientific understanding, and the results and limitations are appropriately considered in the abstraction.*

This subcriterion is addressed by reviewing FEPs (Section 6.1), by using alternative conceptual models (Section 6.3), and evaluating model limitation and uncertainty (Sections 1.3, 6.7, and 8.4).

- (2) *Alternative modeling approaches are considered and the selected modeling approach is consistent with available data and current scientific understanding. A description that includes a discussion of alternative modeling approaches not considered in the final analysis and the limitations and uncertainties of the chosen model is provided.*

This subcriterion is addressed by considering various model conceptualizations (Section 6.3), evaluating spread in model results (Sections 6.5.5.4, 6.6, and 6.7.2), and reporting on limitations and uncertainties (Section 1.3, 6.7, and 8.4).

- (3) *Consideration of conceptual-model uncertainty is consistent with available site characterization data, laboratory experiments, field measurements, natural analog information and process-level modeling studies; and the treatment of conceptual-model uncertainty does not result in an under-representation of the risk estimate.*

This subcriterion is addressed by using site-specific data (Section 4.1), as well as data from field (Section 7) and laboratory experiments (Dobson et al. 2003 [DIRS 165949]), and considering ranges of key input parameters (e.g., Section 6.2.2), alternative conceptualizations (Section 6.3), and spread in model results (Sections 6.5.5.4, 6.6, and 6.7.2).

- (4) *Adequate consideration is given to effects of thermal-hydrologic-mechanical-chemical coupled processes in the assessment of alternative conceptual models.*

This report addresses this subcriterion through conceptual and mathematical models described in Sections 6.2 and 6.4, and model results presented in Sections 6.5.5 and 6.6.

- (5) *If the U.S. Department of Energy uses an equivalent continuum model for the total system performance assessment abstraction, the models produce conservative estimates of the effects of coupled thermal-hydrologic-mechanical-chemical processes on calculated compliance with the postclosure public health and environmental standards.*

This subcriterion is not applicable for this model because it does not contain a model for the total system performance assessment, nor does it make estimates that assess calculated compliance.

- Acceptance Criterion 5, *Model Abstraction Output is Supported by Objective Comparisons*

- (3) *Accepted and well-documented procedures are used to construct and test the numerical models that simulate coupled thermal-hydrologic-mechanical-chemical effects on seepage and flow, engineered barrier chemical environment, and the chemical environment for radionuclide release. Analytical and numerical models are appropriately supported. Abstracted model results are compared with different mathematical models, to judge robustness of results.*

This report addresses this subcriterion through conceptual and mathematical models described in Sections 6.2 and 6.4, and through evaluation of alternative conceptual models in Section 6.3.

9. INPUTS AND REFERENCES

9.1 DOCUMENTS CITED

- 160446 Advocat, T.; Chouchan, J.L.; Crovisier, J.L.; Guy, C.; Daux, V.; Jegou, C.; Gin, S.; and Vernaz, E. 1998. "Borosilicate Nuclear Waste Glass Alteration Kinetics: Chemical Inhibition and Affinity Control." *Scientific Basis for Nuclear Waste Management XXI, Symposium held September 28-October 3, 1997, Davos, Switzerland*. McKinley, I.G. and McCombie, C., eds. 506, 63-70. Warrendale, Pennsylvania: Materials Research Society. TIC: 240702.
- 103750 Altman, W.D.; Donnelly, J.P.; and Kennedy, J.E. 1988. *Qualification of Existing Data for High-Level Nuclear Waste Repositories: Generic Technical Position*. NUREG-1298. Washington, D.C.: U.S. Nuclear Regulatory Commission. TIC: 200652.
- 103597 Altman, W.D.; Donnelly, J.P.; and Kennedy, J.E. 1988. *Peer Review for High-Level Nuclear Waste Repositories: Generic Technical Position*. NUREG-1297. Washington, D.C.: U.S. Nuclear Regulatory Commission. TIC: 200651.
- 153329 Arnorsson, S. and Stefansson, A. 1999. "Assessment of Feldspar Solubility Constants in Water in the Range 0° to 350°C at Vapor Saturation Pressures." *American Journal of Science*, 299, (3), 173-209. New Haven, Connecticut: Yale University, Kline Geology Laboratory. TIC: 249258.
- 157865 Barin, I. and Platzki, G. 1995. *Thermochemical Data of Pure Substances*. 3rd Edition. Two volumes. New York, New York: VCH Publishers. TIC: 251934.
- 160181 Barnes, H.L. 1971. "Investigations in Hydrothermal Sulfide Systems." Chapter 12 of *Research Techniques for High Pressure and High Temperature*. Ulmer, G.C., ed. New York, New York: Springer-Verlag. TIC: 235147.
- 101379 Bear, J. 1988. *Dynamics of Fluids in Porous Media*. New York, New York: Dover Publications. TIC: 217568.
- 181221 Berger, G.; Beaufort, D.; and Lachapagne, J-C. 2002. "Experimental Dissolution of Sanidine Under Hydrothermal Conditions: Mechanism and Rate." *American Journal of Science*, 302, 663-685. New Haven, Connecticut: Yale University, Kline Geology Laboratory. TIC: 259467.
- 103524 Bird, R.B.; Stewart, W.E.; and Lightfoot, E.N. 1960. *Transport Phenomena*. New York, New York: John Wiley & Sons. TIC: 208957.
- 154608 Birkholzer, J.T. and Tsang, Y.W. 2000. "Modeling the Thermal-Hydrologic Processes in a Large-Scale Underground Heater Test in Partially Saturated Fractured Tuff." *Water Resources Research*, 36, (6), 1431-1447. Washington, D.C.: American Geophysical Union. TIC: 248278.

- 101430 Bish, D.L.; Carey, J.W.; Levy, S.S.; and Chipera, S.J. 1996. *Mineralogy-Petrology Contribution to the Near-Field Environment Report*. Milestone LA3668. Los Alamos, New Mexico: Los Alamos National Laboratory. ACC: MOL.19971111.0588.
- 169638 Bish, D.L.; Vaniman, D.T.; Chipera, S.J.; and Carey, J.W. 2003. "The Distribution of Zeolites and their Effects on the Performance of a Nuclear Waste Repository at Yucca Mountain, Nevada, U.S.A.." *American Mineralogist*, 88, (11-12, Part 2), 1889–1902. Washington, D.C.: Mineralogical Society of America. TIC: 255986.
- 126590 Blum, A.E. and Stillings, L.L. 1995. "Feldspar Dissolution Kinetics." Chapter 7 of *Chemical Weathering Rates of Silicate Minerals*. White, A.F. and Brantley, S.L., eds. Reviews in Mineralogy Volume 31. Washington, D.C.: Mineralogical Society of America. TIC: 222496.
- 176638 Booth, T.C. 2006. "Independent Validation Review Team (IVRT) Issues, Bechtel-SAIC Responses, and IVRT Assessment of Responses Related to Review of the TSPA Model and Supporting Analyses and Model Reports (AMRs)." Interoffice memorandum from T.C. Booth (BSC) to File, March 16, 2006, 0315068011, with enclosures. ACC: MOL.20060320.0115.
- 101562 Bourcier, W.L.; Weed, H.C.; Nguyen, S.N.; Nielsen, J.K.; Morgan, L.; Newton, L.; and Knauss, K.G. 1992. "Solution Compositional Effects on Dissolution Kinetics of Borosilicate Glass." *Proceedings of the 7th International Symposium on Water-Rock Interaction, Park City, Utah, July 13-18, 1992*. Kharaka, Y.K. and Maest, A.S., eds. 1, 81-84. Rotterdam, The Netherlands: A.A. Balkema. TIC: 208527.
- 110748 Brady, P.V. and Walther, J.V. 1989. "Controls on Silicate Dissolution Rates in Neutral and Basic pH Solutions at 25°C." *Geochimica et Cosmochimica Acta*, 53, 2823-2830. New York, New York: Pergamon Press. TIC: 235216.
- 160189 Bruno, J.; Stumm, W.; Wersin, P.; and Brandberg, F. 1992. "On the Influence of Carbonate in Mineral Dissolution: I. The Thermodynamics and Kinetics of Hematite Dissolution in Bicarbonate Solutions at T = 25°C." *Geochimica et Cosmochimica Acta*, 56, (3), 1139-1147. New York, New York: Pergamon Press. TIC: 253396.
- 156276 BSC (Bechtel SAIC Company) 2001. *Repository Multiple Waste Package Thermal Calculation*. CAL-WIS-TH-000010 REV 00. Las Vegas, Nevada: Bechtel SAIC Company. ACC: MOL.20010814.0330.
- 170268 BSC 2004. *Data Qualification for Thermodynamic Data Used to Support THC Calculations*. ANL-NBS-HS-000043 REV 00. Las Vegas, Nevada: Bechtel SAIC Company. ACC: DOC.20041118.0004.
- 169855 BSC 2004. *Development of Numerical Grids for UZ Flow and Transport Modeling*. ANL-NBS-HS-000015 REV 02. Las Vegas, Nevada: Bechtel SAIC Company. ACC: DOC.20040901.0001.

- 169864 BSC 2004. *Drift Scale THM Model*. MDL-NBS-HS-000017 REV 01. Las Vegas, Nevada: Bechtel SAIC Company. ACC: DOC.20041012.0001; DOC.20060103.0002.
- 168848 BSC 2004. *Drift-Scale Coupled Processes (DST and THC Seepage) Models*. MDL-NBS-HS-000001 REV 02 Errata 002. Las Vegas, Nevada: Bechtel SAIC Company. ACC: DOC.20030804.0004; DOC.20040219.0002; DOC.20040405.0005.
- 170029 BSC 2004. *Geologic Framework Model (GFM2000)*. MDL-NBS-GS-000002 REV 02. Las Vegas, Nevada: Bechtel SAIC Company. ACC: DOC.20040827.0008.
- 169858 BSC 2004. *Post-Processing Analysis for THC Seepage*. ANL-NBS-HS-000045 REV 00. Las Vegas, Nevada: Bechtel SAIC Company. ACC: DOC.20040929.0002; DOC.20050606.0006.
- 172232 BSC 2005. *Drift-Scale Coupled Processes (DST and TH Seepage) Models*. MDL-NBS-HS-000015 REV 02. Las Vegas, Nevada: Bechtel SAIC Company. ACC: DOC.20050114.0004; DOC.20051115.0002.
- 172862 BSC 2005. *Drift-Scale THC Seepage Model*. MDL-NBS-HS-000001 REV 04. Las Vegas, Nevada: Bechtel SAIC Company. ACC: DOC.20050218.0001; DOC.20050801.0012.
- 174101 BSC 2005. *Mountain-Scale Coupled Processes (TH/THC/THM) Models*. MDL-NBS-HS-000007 REV 03. Las Vegas, Nevada: Bechtel SAIC Company. ACC: DOC.20050825.0007.
- 174104 BSC 2006. *THC Sensitivity Study of Repository Edge and Heterogeneous Permeability Effects*. ANL-NBS-HS-000047 REV 00. Las Vegas, Nevada: Bechtel SAIC Company. ACC: DOC.20060112.0001.
- 100617 Buscheck, T.A. and Nitao, J.J. 1993. "Repository-Heat-Driven Hydrothermal Flow at Yucca Mountain, Part I: Modeling and Analysis." *Nuclear Technology*, 104, (3), 418-448. La Grange Park, Illinois: American Nuclear Society. TIC: 224039.
- 109051 Carey, J.W.; Chipera, S.J.; Vaniman, D.T.; and Bish, D.L. 1998. *Three-Dimensional Mineralogic Model of Yucca Mountain, Nevada: Rev 2.0*. Deliverable SP32BSM4. Los Alamos, New Mexico: Los Alamos National Laboratory, Earth and Environmental Sciences Division. ACC: MOL.20000110.0159.
- 105210 Carlos, B.A.; Chipera, S.J.; Bish, D.L.; and Craven, S.J. 1993. "Fracture-Lining Manganese Oxide Minerals in Silicic Tuff, Yucca Mountain, Nevada, U.S.A." *Chemical Geology*, 107, 47-69. Amsterdam, The Netherlands: Elsevier. TIC: 208629.

- 105213 Carlos, B.A.; Chipera, S.J.; Bish, D.L.; and Raymond, R. 1995. "Distribution and Chemistry of Fracture-Lining Zeolites at Yucca Mountain, Nevada." *Natural Zeolites '93: Occurrence, Properties, Use, Proceedings of the 4th International Conference on the Occurrence, Properties, and Utilization of Natural Zeolites, June 20-28, 1993, Boise, Idaho*. Ming, D.W. and Mumpton, F.A., eds. Pages 547-563. Brockport, New York: International Committee on Natural Zeolites. TIC: 243086.
- 124275 Carroll, S.; Mroczek, E.; Alai, M.; and Ebert, M. 1998. "Amorphous Silica Precipitation (60 to 120°C): Comparison of Laboratory and Field Rates." *Geochimica et Cosmochimica Acta*, 62, (8), 1379-1396. New York, New York: Elsevier. TIC: 243029.
- 160681 Carroll, S.A. and Walther, J.V. 1990. "Kaolinite Dissolution at 25°, 60°, and 80°C." *American Journal of Science*, 290, (7), 797-810. New Haven, Connecticut: Yale University, Kline Geology Laboratory. TIC: 253554.
- 105073 Chermak, J.A. and Rimstidt, J.D. 1989. "Estimating the Thermodynamic Properties (Delta G and Delta H) of Silicate Minerals at 298 K from the Sum of Polyhedral Contributions." *American Mineralogist*, 74, 1023-1031. Washington, D.C.: Mineralogical Society of America. TIC: 237564.
- 171017 Chipera S.J. and Apps, J.A. 2001. "Geochemical Stability of Natural Zeolites." In *Natural Zeolites: Occurrence, Properties, Applications*. Bish, D.L. and Ming, D.W., eds. Chapter 13 of *Reviews in Mineralogy and Geochemistry*. Volume 45. Washington, D.C.: Mineralogical Society of America. TIC: 256369.
- 111115 CRWMS (Civilian Radioactive Waste Management System) M&O (Management and Operating Contractor) 1998. *Drift Scale Test As-Built Report*. BAB000000-01717-5700-00003 REV 01. Las Vegas, Nevada: CRWMS M&O. ACC: MOL.19990107.0223.
- 154426 CRWMS M&O 2001. *Drift-Scale Coupled Processes (DST and THC Seepage) Models*. MDL-NBS-HS-000001 REV 01. Las Vegas, Nevada: CRWMS M&O. ACC: MOL.20010314.0003.
- 100439 de Marsily, G. 1986. *Quantitative Hydrogeology: Groundwater Hydrology for Engineers*. San Diego, California: Academic Press. TIC: 208450.
- 171183 Deer, W.A.; Howie, R.A.; and Zussman, J. 1978. *Rock-Forming Minerals, Single-Chain Silicates*. Volume 2A. 2nd Edition. New York, New York: John Wiley & Sons. TIC: 209334.
- 181454 Dewers, T. and Ortoleva, P. 1990. "A Coupled Reaction/Transport/Mechanical Model for Intergranular Pressure Solution, Stylolites, and Differential Compaction and Cementation in Clean Sandstones." *Geochimica et Cosmochimica Acta*, 54, 1609-1625. New York, New York: Pergamon Press. TIC: 259549.

- 165949 Dobson, P.F.; Kneafsey, T.J.; Sonnenthal, E.L.; Spycher, N.; and Apps, J.A. 2003. "Experimental and Numerical Simulation of Dissolution and Precipitation: Implications for Fracture Sealing at Yucca Mountain, Nevada." *Journal of Contaminant Hydrology*, 62-63, 459-476. New York, New York: Elsevier. TIC: 254205.
- 182183 DOE (U.S. Department of Energy) 2007. *User Information Document for: TOUGHREACT Version 3.1.1*. Document ID: 10396-UID-3.1.1-00. Las Vegas, Nevada: U.S. Department of Energy, Office of Repository Development. ACC: MOL.20070626.0172.
- 135997 Doughty, C. 1999. "Investigation of Conceptual and Numerical Approaches for Evaluating Moisture, Gas, Chemical, and Heat Transport in Fractured Unsaturated Rock." *Journal of Contaminant Hydrology*, 38, (1-3), 69-106. New York, New York: Elsevier. TIC: 244160.
- 157903 Drummond, S.E., Jr. 1981. *Boiling and Mixing of Hydrothermal Fluids: Chemical Effects on Mineral Precipitation*. Ph.D. dissertation. University Park, Pennsylvania: Pennsylvania State University, Department of Geosciences. TIC: 246545.
- 117799 Ehrlich, R.; Etris, E.L.; Brumfield, D.; Yuan, L.P.; and Crabtree, S.J. 1991. "Petrography and Reservoir Physics III: Physical Models for Permeability and Formation Factor." *AAPG Bulletin*, 75, (10), 1579-1592. Tulsa, Oklahoma: American Association of Petroleum Geologists. TIC: 246294.
- 182723 Flood, T.P.; Schuraytz, B.C.; and Vogel, T.A. 1989. "Magma Mixing Due to Disruption of a Layered Magma Body." *Journal of Volcanology and Geothermal Research*, 36, 241-255. Amsterdam, The Netherlands: Elsevier. TIC: 259698.
- 153464 Fournier, R.O. 1973. "Silica in Thermal Waters: Laboratory and Field Investigations." *Proceedings of Symposium on Hydrogeochemistry and Biogeochemistry, Tokyo, Japan, September 7-9, 1970. Volume I - Hydrogeochemistry*, 122-139. Washington, D.C.: The Clarke Company. TIC: 235117.
- 124282 Fournier, R.O. and Rowe, J.J. 1962. "The Solubility of Cristobalite Along the Three-Phase Curve, Gas Plus Liquid Plus Cristobalite." *The American Mineralogist*, 47, 897-902. Washington, D.C.: Mineralogical Society of America. TIC: 235380.
- 160460 Fridriksson, T.; Neuhoff, P.S.; Arnórsson, S.; and Bird, D.K. 2001. "Geological Constraints on the Thermodynamic Properties of the Stilbite—Stellerite Solid Solution in Low-Grade Metabasalts." *Geochimica et Cosmochimica Acta*, 65, (21), 3993-4008. New York, New York: Elsevier. TIC: 253460.
- 144877 Garrels, R.M. and Christ, C.L. 1990. *Solutions, Minerals, and Equilibria*. Boston, Massachusetts: Jones and Bartlett Publishers. TIC: 223483.

- 160465 Gunnarsson, I. and Arnórsson, S. 2000. "Amorphous Silica Solubility and the Thermodynamic Properties of H_4SiO_4 in the Range of 0° to $350^\circ C$ at P_{sat} ." *Geochimica et Cosmochimica Acta*, 64, (13), 2295-2307. New York, New York: Elsevier. TIC: 250506.
- 176844 Gunnarsson, I.; Arnórsson, S.; and Jakobsson, S. 2005. "Precipitation of Poorly Crystalline Antigorite Under Hydrothermal Conditions." *Geochimica et Cosmochimica Acta*, 69, (11), 2813-2828. New York, New York: Elsevier. TIC: 258287.
- 101596 Helgeson, H.C.; Delany, J.M.; Nesbitt, H.W.; and Bird, D.K. 1978. "Summary and Critique of the Thermodynamic Properties of Rock Forming Minerals." *American Journal of Science*, 278-A. New Haven, Connecticut: Yale University, Kline Geology Laboratory. TIC: 220013.
- 106024 Helgeson, H.C.; Kirkham, D.H.; and Flowers, G.C. 1981. "Theoretical Prediction of the Thermodynamic Behavior of Aqueous Electrolytes at High Pressures and Temperatures: IV. Calculation of Activity Coefficients, Osmotic Coefficients, and Apparent Molal and Standard and Relative Partial Molal Properties to $600^\circ C$ and 5 kb." *American Journal of Science*, 281, (10), 1249-1516. New Haven, Connecticut: Yale University, Kline Geology Laboratory. TIC: 238264.
- 160183 Hellmann, R. 1994. "The Albite-Water System: Part I. The Kinetics of Dissolution as Function of pH at 100, 200 and $300^\circ C$." *Geochimica et Cosmochimica Acta*, 58, (2), 595-611. New York, New York: Elsevier. TIC: 235348.
- 160190 Hersman, L.; Lloyd, T.; and Sposito, G. 1995. "Siderophore-Promoted Dissolution of Hematite." *Geochimica et Cosmochimica Acta*, 59, (16), 3327-3330. Tarrytown, New York: Elsevier. TIC: 234034.
- 128129 Inskeep, W.P. and Bloom, P.R. 1985. "An Evaluation of Rate Equations for Calcite Precipitation Kinetics at pCO_2 Less than 0.01 atm and pH Greater than 8." *Geochimica et Cosmochimica Acta*, 49, 2165-2180. New York, New York: Pergamon Press. TIC: 241125.
- 161694 Jeschke, A.A.; Vosbeck, K.; and Dreybrodt, W. 2001. "Surface Controlled Dissolution Rates of Gypsum in Aqueous Solutions Exhibit Nonlinear Dissolution Kinetics." *Geochimica et Cosmochimica Acta*, 65, (1), 27-34. New York, New York: Elsevier. TIC: 253857.
- 101630 Johnson, J.W.; Knauss, K.G.; Glassley, W.E.; DeLoach, L.D.; and Tompson, A.F.B. 1998. "Reactive Transport Modeling of Plug-Flow Reactor Experiments: Quartz and Tuff Dissolution at $240^\circ C$." *Journal of Hydrology*, 209, 81-111. Amsterdam, The Netherlands: Elsevier. TIC: 240986.

- 180314 Kerrick, D.M. and Darken, L.S. 1975. "Statistical Thermodynamic Models for Ideal Oxide and Silicate Solid Solutions, with Application to Plagioclase." *Geochimica et Cosmochimica Acta*, 39, 1431-1442. Oxford, Great Britain: Pergamon Press. TIC: 259293.
- 160184 Knauss, K.G. and Wolery, T.J. 1986. "Dependence of Albite Dissolution Kinetics on pH and Time at 25°C and 70°C." *Geochimica et Cosmochimica Acta*, 50, (11), 2481-2497. Elmsford, New York: Pergamon Journals. TIC: 221756.
- 124300 Knauss, K.G. and Wolery, T.J. 1989. "Muscovite Dissolution Kinetics as a Function of pH and Time at 70°C." *Geochimica et Cosmochimica Acta*, 53, 1493-1501. Elmsford, New York: Pergamon Press. TIC: 236215.
- 145636 Kneafsey, T.J. and Pruess, K. 1998. "Laboratory Experiments on Heat-Driven Two-Phase Flows in Natural and Artificial Rock Fractures." *Water Resources Research*, 34, (12), 3349-3367. Washington, D.C.: American Geophysical Union. TIC: 247468.
- 124306 Knowles-Van Cappellan, V.; Van Cappellan, P.; and Tiller, C. 1997. "Probing the Charge of Reactive Sites at the Mineral-Water Interface: Effect of Ionic Strength on Crystal Growth Kinetics of Fluorite." *Geochimica et Cosmochimica Acta*, 61, (9), 1871-1877. New York, New York: Pergamon Press. TIC: 246450.
- 181363 Konzuk, J.S. and Kueper, B.H. 2004. "Evaluation of Cubic Law Based Models Describing Single-Phase Flow through a Rough-Walled Fracture." *Water Resources Research*, 40, (W02402), 1-17. Washington, D.C.: American Geophysical Union. TIC: 259512.
- 100051 Langmuir, D. 1997. *Aqueous Environmental Geochemistry*. Upper Saddle River, New Jersey: Prentice Hall. TIC: 237107.
- 117091 Lasaga, A.C. 1998. *Kinetic Theory in the Earth Sciences*. Princeton, New Jersey: Princeton University Press. TIC: 246279.
- 182921 Lassin A., Azaroual M., Mercury L., 2005. "Geochemistry of unsaturated soil systems: Aqueous speciation and solubility of minerals and gases in capillary solutions." *Geochimica et Cosmochimica Acta*, 69, (22), 5187-5201. Amsterdam, Netherlands: Elsevier.
- 160480 Leturcq, G.; Berger, G.; Advocat, T.; and Vernaz, E. 1999. "Initial and Long-Term Dissolution Rates of Aluminosilicate Glasses Enriched with Ti, Zr, and Nd." *Chemical Geology*, 160, (1-2), 39-62. Amsterdam, The Netherlands: Elsevier. TIC: 253428.

- 126599 Levy, S.S.; Fabryka-Martin, J.T.; Dixon, P.R.; Liu, B.; Turin, H.J.; and Wolfsberg, A.V. 1997. "Chlorine-36 Investigations of Groundwater Infiltration in the Exploratory Studies Facility at Yucca Mountain, Nevada." *Scientific Basis for Nuclear Waste Management XX, Symposium held December 2-6, 1996, Boston, Massachusetts*. Gray, W.J. and Triay, I.R., eds. 465, 901-908. Pittsburgh, Pennsylvania: Materials Research Society. TIC: 238884.
- 151989 Lichtner, P.C. and Seth, M.S. 1996. *User's Manual for MULTIFLO: Part II—MULTIFLO 1.0 and GEM 1.0 Multicomponent-Multiphase Reactive Transport Model*. CNWRA 96-010. San Antonio, Texas: Center for Nuclear Waste Regulatory Analyses. TIC: 248807.
- 123032 Lide, D.R., ed. 1993. *CRC Handbook of Chemistry and Physics*. 74th Edition. Boca Raton, Florida: CRC Press. TIC: 209252.
- 162470 Liu, H-H.; Haukwa, C.B.; Ahlers, C.F.; Bodvarsson, G.S.; Flint, A.L.; and Guertal, W.B. 2003. "Modeling Flow and Transport in Unsaturated Fractured Rock: An Evaluation of the Continuum Approach." *Journal of Contaminant Hydrology*, 62-63, 173-188. New York, New York: Elsevier. TIC: 254205.
- 105729 Liu, H.H.; Doughty, C.; and Bodvarsson, G.S. 1998. "An Active Fracture Model for Unsaturated Flow and Transport in Fractured Rocks." *Water Resources Research*, 34, (10), 2633-2646. Washington, D.C.: American Geophysical Union. TIC: 243012.
- 157900 Lowry, W.E. 2001. *Engineered Barrier Systems Thermal-Hydraulic-Chemical Column Test Report*. TDR-EBS-MD-000018 REV 00. Las Vegas, Nevada: Bechtel SAIC Company. ACC: MOL.20020102.0206.
- 181209 Malmström, M.; Banwart, S.; Lewenhagen, J.; Duro, L.; and Bruno, J. 1996. "The Dissolution of Biotite and Chlorite at 25°C in the Near-Neutral pH Region." *Journal of Contaminant Hydrology*, 21, 201-213. New York, New York: Elsevier. TIC: 259465.
- 124354 Mazer, J.J.; Bates, J.K.; Bradley, J.P.; Bradley, C.R.; and Stevenson, C.M. 1992. "Alteration of Tektite to Form Weathering Products." *Nature*, 357, 573-576. London, England: Macmillan Magazines. TIC: 246479.
- 180822 Mukhopadhyay, S.; Sonnenthal, E.L.; and Spycher, N. 2006. "Modeling Coupled Thermal-Hydrological-Chemical Processes in the Unsaturated Fractured Rock of Yucca Mountain, Nevada: Heterogeneity and Seepage." *Physics and Chemistry of the Earth*, 31, 626-633. New York, New York: Elsevier. TIC: 259367.
- 142167 Murphy, W.M.; Pabalan, R.T.; Prikryl, J.D.; and Goulet, C.J. 1996. "Reaction Kinetics and Thermodynamics of Aqueous Dissolution and Growth of Analcime and Na-Clinoptilolite at 25°C." *American Journal of Science*, 296, 128-186. New Haven, Connecticut: Yale University, Kline Geology Laboratory. TIC: 235949.

- 163274 NRC (U.S. Nuclear Regulatory Commission) 2003. *Yucca Mountain Review Plan, Final Report*. NUREG-1804, Rev. 2. Washington, D.C.: U.S. Nuclear Regulatory Commission, Office of Nuclear Material Safety and Safeguards. TIC: 254568.
- 111051 Oelkers, E.H.; Schott, J.; and Devidal, J.L. 1994. "The Effect of Aluminum, pH, and Chemical Affinity on the Rates of Aluminosilicate Dissolution Reactions." *Geochimica et Cosmochimica Acta*, 58, (9), 2011-2024. Oxford, England: Pergamon. TIC: 236030.
- 160485 Paul, A. 1977. "Chemical Durability of Glasses; a Thermodynamic Approach." *Journal of Materials Science*, 12, (11), 2246-2268. London, England: Chapman and Hall. TIC: 219989.
- 109941 Penman, H.L. 1940. "Gas and Vapor Movement in Soils I. The Diffusion of Vapours Through Porous Solids." *Journal of Agricultural Science*, 30, 437-462. Cambridge, England: The University Press. TIC: 236561.
- 162576 Peterman, Z.E. and Cloke, P.L. 2002. "Geochemistry of Rock Units at the Potential Repository Level, Yucca Mountain, Nevada (includes Erratum)." *Applied Geochemistry*, 17, (6, 7), 683-698, 955-958. New York, New York: Pergamon. TIC: 252516; 252517; 254046.
- 144794 Pruess, K. 1997. "On Vaporizing Water Flow in Hot Sub-Vertical Rock Fractures." *Transport in Porous Media*, 28, (3), 335-372. Boston, Massachusetts: Kluwer Academic Publishers. TIC: 238922.
- 160778 Pruess, K.; Oldenburg, C.; and Moridis, G. 1999. *TOUGH2 User's Guide, Version 2.0*. LBNL-43134. Berkeley, California: Lawrence Berkeley National Laboratory. TIC: 253038.
- 144801 Pruess, K.; Tsang, Y.W.; and Wang, J.S.Y. 1984. *Numerical Studies of Fluid and Heat Flow Near High-Level Nuclear Waste Packages Emplaced in Partially Saturated Fractured Tuff*. LBL-18552. Berkeley, California: Lawrence Berkeley Laboratory. TIC: 211033.
- 100818 Pruess, K.; Wang, J.S.Y.; and Tsang, Y.W. 1990. "On Thermohydrologic Conditions Near High-Level Nuclear Wastes Emplaced in Partially Saturated Fractured Tuff, 1. Simulation Studies with Explicit Consideration of Fracture Effects." *Water Resources Research*, 26, (6), 1235-1248. Washington, D.C.: American Geophysical Union. TIC: 221923.
- 126601 Ragnarsdottir, K.V. 1993. "Dissolution Kinetics of Heulandite at pH 2-12 and 25°C." *Geochimica et Cosmochimica Acta*, 57, (11), 2439-2449. New York, New York: Pergamon Press. TIC: 243920.

- 117901 Reed, M.H. 1982. "Calculation of Multicomponent Chemical Equilibria and Reaction Processes in Systems Involving Minerals, Gases and an Aqueous Phase." *Geochimica et Cosmochimica Acta*, 46, (4), 513-528. New York, New York: Pergamon Press. TIC: 224159.
- 107088 Renders, P.J.N.; Gammons, C.H.; and Barnes, H.L. 1995. "Precipitation and Dissolution Rate Constants for Cristobalite from 150 to 300°C." *Geochimica et Cosmochimica Acta*, 59, 77-85. New York, New York: Elsevier. TIC: 226987.
- 160486 Richet, P. and Bottinga, Y. 1984. "Glass Transitions and Thermodynamic Properties of Amorphous SiO₂, NaAlSi_nO_{2n+2} and KAlSi₃O₈." *Geochimica et Cosmochimica Acta*, 48, (3), 453-470. New York, New York: Pergamon Press. TIC: 250714.
- 101708 Rimstidt, J.D. and Barnes, H.L. 1980. "The Kinetics of Silica–Water Reactions." *Geochimica et Cosmochimica Acta*, 44, 1683-1699. New York, New York: Pergamon Press. TIC: 219975.
- 160198 Savage, D.; Cave, M.R.; Haigh, D.; Milodowski, A.E.; and Young, M.E. 1993. "The Reaction Kinetics of Laumontite Under Hydrothermal Conditions." *European Journal of Mineralogy*, 5, (3), 523-535. Stuttgart, Germany: E. Schweizerbart'sche Verlagsbuchhandlung. TIC: 253021.
- 100075 Sawyer, D.A.; Fleck, R.J.; Lanphere, M.A.; Warren, R.G.; Broxton, D.E.; and Hudson, M.R. 1994. "Episodic Caldera Volcanism in the Miocene Southwestern Nevada Volcanic Field: Revised Stratigraphic Framework, ⁴⁰Ar/³⁹Ar Geochronology, and Implications for Magmatism and Extension." *Geological Society of America Bulletin*, 106, (10), 1304-1318. Boulder, Colorado: Geological Society of America. TIC: 222523.
- 128146 Slider, H.C. 1976. *Practical Petroleum Reservoir Engineering Methods, An Energy Conservation Science*. Tulsa, Oklahoma: Petroleum Publishing Company. TIC: 247798.
- 177412 SNL (Sandia National Laboratories) 2007. *Engineered Barrier System: Physical and Chemical Environment*. ANL-EBS-MD-000033 REV 06. Las Vegas, Nevada: Sandia National Laboratories. ACC: DOC.20070907.0003.
- 180778 SNL 2007. *General Corrosion and Localized Corrosion of the Drip Shield*. ANL-EBS-MD-000004 REV 02 ADD 01. Las Vegas, Nevada: Sandia National Laboratories. ACC: DOC.20060427.0002; DOC.20070807.0004.
- 181648 SNL 2007. *In-Drift Natural Convection and Condensation*. MDL-EBS-MD-000001 REV 00 AD 01. Las Vegas, Nevada: Sandia National Laboratories. ACC: DOC.20041025.0006; DOC.20050330.0001; DOC.20051122.0005; DOC.20070907.0004.

- 177411 SNL 2007. *In-Drift Precipitates/Salts Model*. ANL-EBS-MD-000045 REV 03. Las Vegas, Nevada: Sandia National Laboratories. ACC: DOC.20070306.0037.
- 181383 SNL 2007. *Multiscale Thermohydrologic Model*. ANL-EBS-MD-000049 REV 03 ADD 01. Las Vegas, Nevada: Sandia National Laboratories. ACC: DOC.20070831.0003.
- 174294 SNL 2007. *Simulation of Net Infiltration for Present-Day and Potential Future Climates*. MDL-NBS-HS-000023 REV 01. Las Vegas, Nevada: Sandia National Laboratories. ACC: DOC.20070530.0014.
- 179287 SNL 2007. *Technical Work Plan for: Revision of Model Reports for Near-Field and In-Drift Water Chemistry*. TWP-MGR-PA-000038 REV 02. Las Vegas, Nevada: Sandia National Laboratories. ACC: DOC.20070110.0004.
- 177413 SNL 2007. *THC Sensitivity Study of Heterogeneous Permeability and Capillarity Effects*. ANL-NBS-HS-000047 REV 01. Las Vegas, Nevada: Sandia National Laboratories. ACC: DOC.20070807.0006.
- 177414 SNL 2007. *Thermal Testing Measurements Report*. TDR-MGR-HS-000002 REV 01. Las Vegas, Nevada: Sandia National Laboratories. ACC: DOC.20070307.0010.
- 179567 SNL 2007. *Total System Performance Assessment Data Input Package for Requirements Analysis for DOE SNF/HLW and Naval SNF Waste Package Physical Attributes Basis for Performance Assessment*. TDR-TDIP-ES-000009 REV 00. Las Vegas, Nevada: Sandia National Laboratories. ACC: DOC.20070921.0009.
- 179354 SNL 2007. *Total System Performance Assessment Data Input Package for Requirements Analysis for Engineered Barrier System In-Drift Configuration*. TDR-TDIP-ES-000010 REV 00. Las Vegas, Nevada: Sandia National Laboratories. ACC: DOC.20070921.0008.
- 179466 SNL 2007. *Total System Performance Assessment Data Input Package for Requirements Analysis for Subsurface Facilities*. TDR-TDIP-PA-000001 REV 00. Las Vegas, Nevada: Sandia National Laboratories. ACC: DOC.20070921.0007.
- 179394 SNL 2007. *Total System Performance Assessment Data Input Package for Requirements Analysis for Transportation Aging and Disposal Canister and Related Waste Package Physical Attributes Basis for Performance Assessment*. TDR-TDIP-ES-000006 REV 00. Las Vegas, Nevada: Sandia National Laboratories. ACC: DOC.20070918.0005.
- 175177 SNL 2007. *UZ Flow Models and Submodels*. MDL-NBS-HS-000006 REV 03. Las Vegas, Nevada: Sandia National Laboratories. ACC: DOC.20070907.0001.

- 176005 Sonnenthal E.; Ito, A.; Spycher, N.; Yui, M.; Apps, J.; Sugita, Y.; Conrad, M.; and Kawakami, S. 2005. "Approaches to Modeling Coupled Thermal, Hydrological, and Chemical Processes in the Drift Scale Heater Test at Yucca Mountain." *International Journal of Rock Mechanics and Mining Sciences*, 42, 698-719. New York, New York: Elsevier. TIC: 258018.
- 117127 Sonnenthal, E.L. and Bodvarsson, G.S. 1999. "Constraints on the Hydrology of the Unsaturated Zone at Yucca Mountain, NV from Three-Dimensional Models of Chloride and Strontium Geochemistry." *Journal of Contaminant Hydrology*, 38, (1-3), 107-156. New York, New York: Elsevier. TIC: 244160.
- 162121 Spycher, N.F.; Sonnenthal, E.L.; and Apps, J.A. 2003. "Fluid Flow and Reactive Transport Around Potential Nuclear Waste Emplacement Tunnels at Yucca Mountain, Nevada." *Journal of Contaminant Hydrology*, 62-63, 653-673. New York, New York: Elsevier. TIC: 254205.
- 101480 Steefel, C.I. and Lasaga, A.C. 1994. "A Coupled Model for Transport of Multiple Chemical Species and Kinetic Precipitation/Dissolution Reactions with Application to Reactive Flow in Single Phase Hydrothermal Systems." *American Journal of Science*, 294, (5), 529-592. New Haven, Connecticut: Yale University, Kline Geology Laboratory. TIC: 235372.
- 144878 Steefel, C.I. and Lichtner, P.C. 1998. "Multicomponent Reactive Transport in Discrete Fractures: I. Controls on Reaction Front Geometry." *Journal of Hydrology*, 209, 186-199. New York, New York: Elsevier. TIC: 247524.
- 100827 Steefel, C.I. and Yabusaki, S.B. 1996. *OS3D/GIMRT Software for Modeling Multicomponent-Multidimensional Reactive Transport User Manual & Programmer's Guide*. PNL-11166. Richland, Washington: Pacific Northwest Laboratory. TIC: 240572.
- 127978 Svensson, U. and Dreybrodt, W. 1992. "Dissolution Kinetics of Natural Calcite Minerals in CO₂-Water Systems Approaching Calcite Equilibrium." *Chemical Geology*, 100, 129-145. Amsterdam, The Netherlands: Elsevier. TIC: 246497.
- 160501 Techer, I.; Advocat, T.; Lancelot, J.; and Liotard, J-M. 2001. "Dissolution Kinetics of Basaltic Glasses: Control by Solution Chemistry and Protective Effect of the Alteration Film." *Chemical Geology*, 176, (1-4), 235-263. New York, New York: Elsevier. TIC: 253429.
- 101732 Tester, J.W.; Worley, G.W.; Robison, B.A.; Grigsby, C.O.; and Feerer, J.L. 1994. "Correlating Quartz Dissolution Kinetics in Pure Water from 25° to 625°C." *Geochimica et Cosmochimica Acta*, 58, (11), 2407-2420. New York, New York: Elsevier. TIC: 236776.

- 137577 Tsang, Y.W. and Birkholzer, J.T. 1999. "Predictions and Observations of the Thermal-Hydrological Conditions in the Single Heater Test." *Journal of Contaminant Hydrology*, 38, (1-3), 385-425. New York, New York: Elsevier. TIC: 244160.
- 157427 Vaniman, D.T.; Chipera, S.J.; Bish, D.L.; Carey, J.W.; and Levy, S.S. 2001. "Quantification of Unsaturated-Zone Alteration and Cation Exchange in Zeolitized Tuffs at Yucca Mountain, Nevada, USA." *Geochimica et Cosmochimica Acta*, 65, (20), 3409-3433. New York, New York: Elsevier. TIC: 251574.
- 159216 Wagman, D.D.; Evans, W.H.; Parker, V.B.; Schumm, R.H.; Halow, I.; Bailey, S.M.; Churney, K.L.; and Nuttall, R.L. 1982. "The NBS Tables of Chemical Thermodynamic Properties, Selected Values for Inorganic and C₁ and C₂ Organic Substances in SI Units." *Journal of Physical and Chemical Reference Data*, 11, (Supplement No. 2), 2-276 - 2-282. Washington, D.C.: American Chemical Society. TIC: 239715.
- 133240 Walther, J.V. and Helgeson, H.C. 1977. "Calculation of the Thermodynamic Properties of Aqueous Silica and the Solubility of Quartz and Its Polymorphs at High Pressures and Temperatures." *American Journal of Science*, 277, 1315-1351. New Haven, Connecticut: Yale University, Kline Geology Laboratory. TIC: 223171.
- 160442 Whelan, J.F.; Paces, J.B.; and Peterman, Z.E. 2002. "Physical and Stable-Isotope Evidence for Formation of Secondary Calcite and Silica in the Unsaturated Zone, Yucca Mountain, Nevada." *Applied Geochemistry*, 17, (6), 735-750. New York, New York: Elsevier. TIC: 253462.
- 168088 White, A.F. and Brantley, S.L. 2003. "The Effect of Time on the Weathering of Silicate Minerals: Why Do Weathering Rates Differ in the Laboratory and Field?" *Chemical Geology*, 202, (3-4), 479-506. New York, New York: Elsevier. TIC: 255730.
- 163765 Williams, N.H. 2003. "Contract No. DE-AC28-01RW1210 – Transmittal of White Paper, Effects of Neoprene on Water in the Drift Scale Test." Letter from N.H. Williams (BSC) to J.D. Ziegler (DOE/ORD), February 4, 2003, 0129035843, with enclosure. ACC: MOL.20030206.0211.
- 154279 Wilson, N.S.F.; Cline, J.S.; and Lundberg, S.A.W. 2000. "Paragenesis and Chemical Composition of Secondary Mineralization at Yucca Mountain, Nevada." *Abstracts with Programs - Geological Society of America*, 32, (7), A-260. Boulder, Colorado: Geological Society of America. TIC: 249113.
- 153432 Wu, Y.S. and Mishra, A.K. 1998. *Modifications and Additions to Selected TOUGH2 Modules*. Berkeley, California: Lawrence Berkeley National Laboratory. ACC: MOL.19980615.0221.

- 117167 Wu, Y.S.; Ritcey, A.C.; and Bodvarsson, G.S. 1999. "A Modeling Study of Perched Water Phenomena in the Unsaturated Zone at Yucca Mountain." *Journal of Contaminant Hydrology*, 38, (1-3), 157-184. New York, New York: Elsevier. TIC: 244160.
- 117170 Xu, T. and Pruess, K. 1998. *Coupled Modeling of Non-Isothermal Multi-Phase Flow, Solute Transport and Reactive Chemistry in Porous and Fractured Media: 1. Model Development and Validation*. LBNL-42050. Berkeley, California: Lawrence Berkeley National Laboratory. TIC: 243735.
- 156280 Xu, T. and Pruess, K. 2001. "Modeling Multiphase Non-Isothermal Fluid Flow and Reactive Geochemical Transport in Variably Saturated Fractured Rocks: 1. Methodology." *American Journal of Science*, 301, 16-33. New Haven, Connecticut: Yale University, Kline Geology Laboratory. TIC: 251482.
- 101751 Xu, T.; Pruess, K.; and Brimhall, G. 1998. *An Improved Equilibrium-Kinetics Speciation Algorithm for Redox Reactions in Variably Saturated Subsurface Flow Systems*. LBNL-41789. Berkeley, California: Lawrence Berkeley National Laboratory. TIC: 240019.
- 162124 Xu, T.; Sonnenthal, E.; and Bodvarsson, G. 2003. "A Reaction-Transport Model for Calcite Precipitation and Evaluation of Infiltration Fluxes in Unsaturated Fractured Rock." *Journal of Contaminant Hydrology*, 64, (1-2), 113-127. New York, New York: Elsevier. TIC: 254008.
- 161864 Xu, T.; Sonnenthal, E.; Spycher, N.; Pruess, K.; Brimhall, G.; and Apps, J. 2001. "Modeling Multiphase Non-Isothermal Fluid Flow and Reactive Geochemical Transport in Variably Saturated Fractured Rocks: 2. Applications to Supergene Copper Enrichment and Hydrothermal Flows." *American Journal of Science*, 301, (1), 34-59. New Haven, Connecticut: Yale University, Kline Geology Laboratory. TIC: 253949.
- 100194 Yang, I.C.; Rattray, G.W.; and Yu, P. 1996. *Interpretation of Chemical and Isotopic Data from Boreholes in the Unsaturated Zone at Yucca Mountain, Nevada*. Water-Resources Investigations Report 96-4058. Denver, Colorado: U.S. Geological Survey. ACC: MOL.19980528.0216.
- 171364 Yokoyama, T. and Banfield, J.F. 2002. "Direct Determination of the Rates of Rhyolite Dissolution and Clay Formation Over 52,000 Years and Comparison with Laboratory Measurements." *Geochimica et Cosmochimica Acta*, 66, (15), 2665-2681. New York, New York: Pergamon. TIC: 256435.

9.2 CODES, STANDARDS, REGULATIONS, AND PROCEDURES

180319 10 CFR 63. 2007. Energy: Disposal of High-Level Radioactive Wastes in a Geologic Repository at Yucca Mountain, Nevada. Internet Accessible.

IM-PRO-001, Rev. 2, ICN 0. *Control of the Electronic Management of Information*. Washington, D.C.: U.S. Department of Energy, Office of Civilian Radioactive Waste Management. ACC: DOC.20070920.0004.

IM-PRO-003, Rev. 3, ICN 0. *Software Management*. Washington, D.C.: U.S. Department of Energy, Office of Civilian Radioactive Waste Management. ACC: DOC.20070918.0001.

LS-PRO-0203, Rev. 3, ICN 0. *Preparation and Maintenance of the Q-List*. Washington, D.C.: U.S. Department of Energy, Office of Civilian Radioactive Waste Management. ACC: ENG.20070809.0002.

SCI-PRO-001, Rev. 4, ICN 0. *Qualification of Unqualified Data*. Washington, D.C.: U.S. Department of Energy, Office of Civilian Radioactive Waste Management. ACC: DOC.20070725.0002.

SCI-PRO-006, Rev. 5, ICN 0. *Models*. Washington, D.C.: U.S. Department of Energy, Office of Civilian Radioactive Waste Management. ACC: DOC.20070810.0004.

9.3 SOURCE DATA, LISTED BY DATA TRACKING NUMBER

162015 GS000308313211.001. Geochemistry of Repository Block. Submittal date: 03/27/2000.

160899 GS020408312272.003. Collection and Analysis of Pore Water Samples for the Period from April 2001 to February 2002. Submittal date: 04/24/2002.

166569 GS020808312272.004. Analysis of Water-Quality Samples for the Period from July 1999 to July 2002. Submittal date: 09/18/2002.

165226 GS030408312272.002. Analysis of Water-Quality Samples for the Period from July 2002 to November 2002. Submittal date: 05/07/2003.

166570 GS031008312272.008. Analysis of Pore Water and Miscellaneous Water Samples for the Period from December 2002 to July 2003. Submittal date: 11/13/2003.

178057 GS041108312272.005. Analysis of Pore Water and Miscellaneous Water Samples for the Period from July 2003 to September 2004. Submittal date: 02/25/2005.

- 179065 GS060908312272.004. Chemical Analysis of Pore Water Samples Extracted from HD-PERM, USW SD-9, and ESF-SAD-GTB#1 Core for the Period from April 29, 2006 to July 21, 2006. Submittal date: 09/14/2006.
- 165858 GS951208312272.004. Analysis for Chemical Composition of Perched-Water from Boreholes USW UZ-14, USW NRG-7A, USW SD-9, USW SD-7 and Groundwater from Boreholes UE-25 ONC#1 and USW G-2 from 8/18/89 to 3/21/95. Submittal date: 09/12/2001.
- 153485 LA0009SL831151.001. Fracture Mineralogy of the ESF Single Heater Test Block, Alcove 5. Submittal date: 09/28/2000.
- 158426 LA0201SL831225.001. Chemical, Textural, and Mineralogical Characteristics of Sidewall Samples from the Drift Scale Test. Submittal date: 01/10/2002.
- 113495 LA9908JC831321.001. Mineralogic Model “MM3.0” Version 3.0. Submittal date: 08/16/1999.
- 146447 LA9912SL831151.001. Fracture Mineralogy of Drill Core ESF-HD-TEMP-2. Submittal date: 01/04/2000.
- 146449 LA9912SL831151.002. Percent Coverage by Fracture-Coating Minerals in Core ESF-HD-TEMP-2. Submittal date: 01/05/2000.
- 171957 LASL831322AN96.002. Petrology of Samples from Drill Holes USW H-3, H-4, and H-5. Submittal date: 08/28/1996.
- 153687 LB0101DSTTHGRD.001. 2D Finite Element Mesh Used for DST THC Model Simulations (Input to AMR N0120/U0110 REV. 01). Submittal date: 01/05/2001.
- 159525 LB0205REVUZPRP.001. Fracture Properties for UZ Model Layers Developed from Field Data. Submittal date: 05/14/2002.
- 160108 LB02081DKMGRID.001. 2002 UZ 1-D and 2-D Calibration Grids. Submittal date: 08/26/2002.
- 161638 LB0208ISODSTHP.001. Isotope Data and CO2 Analysis for the Heating Phase of the DST. Submittal date: 08/09/2002.
- 161243 LB0208UZDSCPMI.002. Drift-Scale Calibrated Property Sets: Mean Infiltration Data Summary. Submittal date: 08/26/2002.
- 164744 LB0302DSCPTHCS.001. Drift-Scale Coupled Processes (THC Seepage) Model: Simulations. Submittal date: 02/11/2003.
- 161976 LB0302DSCPTHCS.002. Drift-Scale Coupled Processes (THC Seepage) Model: Data Summary. Submittal date: 02/11/2003.

- 177538 LB0303ISODSTCP.001. Isotope Data and CO2 Analysis for the Cooling Phase of the DST. Submittal date: 03/28/2003.
- 177539 LB0309ISODSTCP.001. Isotope Data and CO2 Analysis for the Cooling Phase of the DST. Submittal date: 09/24/2003.
- 177540 LB0403ISODSTCP.001. H2O and CO2 Isotope Analysis for the Cooling Phase of the DST. Submittal date: 03/16/2004.
- 177541 LB0410ISODSTCP.001. H2O and CO2 Isotope Analysis for the Cooling Phase of the DST. Submittal date: 11/24/2004.
- 177542 LB0509ISODSTCP.001. H2O and CO2 Isotope Analysis for the Cooling Phase of the DST. Submittal date: 09/29/2005.
- 179180 LB0610UZDSCP30.001. Drift-Scale Calibrated Property Set for the 30-Percentile Infiltration Map. Submittal date: 11/02/2006.
- 178587 LB06123DPDUZFF.001. 3-D UZ Flow Fields for Present-Day Climate of 10th-, 30th-, 50th- and 90th -Percentile Infiltration Maps. Submittal date: 12/19/2006.
- 179066 LB07013DGTUZFF.001. 3-D UZ Flow Fields for Glacial Transition Climate of 10th-, 30th-, 50th-, and 90th-Percentile Infiltration Maps. Submittal date: 01/03/2007.
- 179064 LB07013DMOUZFF.001. 3-D UZ Flow Fields for Monsoon Climate of 10th-, 30th-, 50th-, and 90th-Percentile Infiltration Maps. Submittal date: 01/03/2007.
- 179286 LB0701UZMTHCAL.001. Input and Output of 3-D UZ Ambient Thermal Model for Present-Day Climate of 10th-, 30th-, 50th- and 90th-Percentile Infiltration Maps. Submittal date: 01/22/2007.
- 181318 LB0704THRMLPRP.001. Thermal Properties of UZ Model Layers: Data Summary. Submittal date: 04/10/2007.
- 111475 LB990501233129.004. 3-D UZ Model Calibration Grids for AMR U0000, "Development of Numerical Grids of UZ Flow and Transport Modeling." Submittal date: 09/24/1999.
- 111476 LB990630123142.003. Fourth, Fifth, and Sixth Quarters TDIF Submission for the Drift Scale Test, September 1998 to May 1999. Submittal date: 06/30/1999.
- 153288 LL001100931031.008. Aqueous Chemistry of Water Sampled from Boreholes of the Drift Scale Test (DST). Submittal date: 11/10/2000.
- 153616 LL001200231031.009. Aqueous Chemistry of Water Sampled from Boreholes of the Drift Scale Test (DST). Submittal date: 12/04/2000.

- 159134 LL020302223142.015. Aqueous Geochemistry of DST Samples Collected from HYD Boreholes. Submittal date: 03/07/2002.
- 159307 LL020405123142.019. Aqueous Geochemistry of Condensed Fluids Collected During Studies of Introduced Materials. Submittal date: 05/22/2002.
- 161677 LL020709923142.023. Aqueous Geochemistry of Borehole Waters Collected in the Heating Phase of the DST. Submittal date: 07/26/2002.
- 144922 LL990702804244.100. Borehole and Pore Water Data. Submittal date: 07/13/1999.
- 153836 MO0001SEPDSTPC.000. Drift Scale Test (DST) Temperature, Power, Current, and Voltage Data for June 1, 1999 through October 31, 1999. Submittal date: 01/12/2000.
- 147304 MO0002ABBLSLDS.000. As-Built Borehole Locations and Sensor Locations for the Drift Scale Test Given in Local (DST) Coordinates. Submittal date: 02/01/2000.
- 148850 MO0003RIB00071.000. Physical and Chemical Characteristics of Alloy 22. Submittal date: 03/13/2000.
- 150930 MO0005PORWATER.000. Perm-Sample Pore Water Data. Submittal date: 05/04/2000.
- 151029 MO0006J13WTRCM.000. Recommended Mean Values of Major Constituents in J-13 Well Water. Submittal date: 06/07/2000.
- 153707 MO0007SEPDSTPC.001. Drift Scale Test (DST) Temperature, Power, Current, and Voltage Data for November 1, 1999 through May 31, 2000. Submittal date: 07/13/2000.
- 152576 MO0009THRMODYN.001. Input Transmittal for Thermodynamic Data Input Files for Geochemical Calculations. Submittal date: 09/20/2000.
- 153708 MO0012SEPDSTPC.002. Drift Scale Test (DST) Temperature, Power, Current, and Voltage Data for June 1, 2000 through November 30, 2000. Submittal date: 12/19/2000.
- 153711 MO0101SEPFDDST.000. Field Measured Data of Water Samples from the Drift Scale Test. Submittal date: 01/03/2001.
- 158321 MO0107SEPDSTPC.003. Drift Scale Test (DST) Temperature, Power, Current, and Voltage Data for December 1, 2000 through May 31, 2001. Submittal date: 07/06/2001.

- 158320 MO0202SEPDSTTV.001. Drift Scale Test (DST) Temperature, Power, Current, and Voltage Data for June 1, 2001 through January 14, 2002. Submittal date: 02/28/2002.
- 159300 MO0207AL5WATER.001. Water Sampling in Alcove 5 (Results from 2/4/1997 through 4/20/1999). Submittal date: 07/11/2002.
- 161129 MO0208RESTRDST.002. Restructured Drift Scale Test (DST) Heating Phase Power and Temperature Data. Submittal date: 08/06/2002.
- 179085 MO0701VENTCALC.000. Analytical Ventilation Calculation for the Base Case Analysis with a 1.45 KW/M Initial Line Load. Submittal date: 01/23/2007.
- 179925 MO0702PASTREAM.001. Waste Stream Composition and Thermal Decay Histories for LA. Submittal date: 02/15/2007.
- 182093 MO0703PAHYTHRM.000. Hydrological and Thermal Properties of the Invert. Submittal date: 07/19/2007.
- 181613 MO0706SPAFEPLA.001. FY 2007 LA FEP List and Screening. Submittal date: 06/20/2007.
- 113644 MO9807DSTSET01.000. Drift Scale Test (DST) Temperature, Power, Current, Voltage Data for November 7, 1997 through May 31, 1998. Submittal date: 07/09/1998.
- 104850 MO9808RIB00041.000. Reference Information Base Data Item: Rock Geomechanical Properties. Submittal date: 08/05/1998.
- 113662 MO9810DSTSET02.000. Drift Scale Test (DST) Temperature, Power, Current, Voltage Data for June 1 through August 31, 1998. Submittal date: 10/09/1998.
- 113673 MO9906DSTSET03.000. Drift Scale Test (DST) Temperature, Power, Current, Voltage Data for September 1, 1998 through May 31, 1999. Submittal date: 06/08/1999.
- 153364 SN0002T0872799.009. Effective Thermal Conductivity Parameter for the No Backfill Case Implemented in the Drift-Scale Models used in TSPA-SR. Submittal date: 02/10/2000.
- 159133 SN0203F3903102.001. Drift Scale Test Water Sampling (with Results from 4/17/2001 through 1/14/2002). Submittal date: 03/29/2002.
- 164196 SN0307T0510902.003. Updated Heat Capacity of Yucca Mountain Stratigraphic Units. Submittal date: 07/15/2003.

- 170939 SN0407T0507803.026. Fluent 6.0.12 Files for 2-D Natural Convection Simulations for Equivalent Thermal Conductivity Determination. Submittal date: 07/15/2004.
- 179067 SN0609T0502404.012. Pitzer Thermodynamic Database (DATA0.YP2). Submittal date: 09/28/2006.
- 178113 SN0610T0502404.013. Thermodynamic Database Input File for EQ3/6 - DATA0.YMP.R5. Submittal date: 10/13/2006.
- 178850 SN0612T0502404.014. Thermodynamic Database Input File for EQ3/6 - DATA0.YMP.R5. Submittal date: 12/15/2006.
- 108437 SN9908T0872799.004. Tabulated In-Drift Geometric and Thermal Properties Used in Drift-Scale Models for TSPA-SR (Total System Performance Assessment-Site Recommendation). Submittal date: 08/30/1999.

9.4 SOFTWARE CODES

- 153067 2kgridv1a.for V. 1.0. 2000. DOS Emulation. STN: 10382-1.0-00.
- 147561 AMESH V. 1.0. 1999. Sun O.S. 5.5.1, OS V4.0. STN: 10045-1.0-00.
- 153090 assign.f V. 1.0. 2000. SUN O.S. 5.5.1. STN: 10315-1.0-00.
- 181352 CUTCHEM V. 2.0. 2007. PC, Windows XP/32bit. STN: 10898-2.0-00.
- 161263 DBCONV V. 1.0. 2002. PC/Windows 98/NT; DEC-Alpha/OSF1 V5.1; SunOS 5.5.1. STN: 10893-1.0-00.
- 126891 EQ3/6 V. 7.2b. 1999. PC. LLNL: UCRL-MA-110662.
- 162228 EQ3/6 V. 8.0. 2003. WINDOWS 2000, WIN NT 4.0, WIN 98, WIN 95. STN: 10813-8.0-00.
- 176889 EQ3/6 V. 8.1. 2005. WINDOWS 2000. STN: 10813-8.1-00.
- 153089 exclude.f V. 1.0. 2000. SUN O.S. 5.5.1. STN: 10316-1.0-00.
- 161258 KREG V. 1.1. 2002. SUN UltraSparc with Unix SunOS 5.5.1, WINDOWS 2000/NT/98, Dec Alpha with OSF1 V5.1. STN: 10318-1.1-00.
- 161259 KSWITCH V. 1.1. 2002. PC with WINDOWS 2000/NT/98, Dec Alpha with OSF1 V5.1, SUN OS 5.5.1. STN: 10319-1.1-00.
- 153091 merggrid2.f V. 1.0. 2000. SUN w/Unix OS. STN: 10314-1.0-00.
- 153092 mk_circ2 V. 1.0. 2000. SUN w/Unix OS. STN: 10312-1.0-00.

153068 mk_grav2.f V. 1.0. 2000. DOS Emulation, SUN O.S. 5.5.1. STN: 10379-1.0-00.

153093 mk_rect2 V. 1.0. 2000. SUN w/Unix OS. STN: 10313-1.0-00.

153082 mrgdrift.f V. 1.0. 2000. DOS Emulation, SUN O.S. 5.5.1. STN: 10380-1.0-00.

153083 sav1d_dst2d.f V. 1.0. 2000. SUN w/Unix OS. STN: 10381-1.0-00.

153218 SUPCRT92 V. 1.0. 1999. PC w/Windows OS and MAC w/MAC OS.
STN: 10058-1.0-00.

112017 SUPCRT92 V1.0 V. STN: 10058-1.0-00.

161262 THERMOCHK V. 1.1. 2002. WINDOWS 98/NT 4.0, OSFI V5.1, SUNOS 5.5.1.
STN: 10895-1.1-00.

161491 TOUGH2 V. 1.6. 2003. DOS Emulation (win95/98), SUN OS 5.5.1., OSF1 V4.0.
STN: 10007-1.6-01.

153219 TOUGHREACT V. 2.2. 1999. DEC and SUN w/Unix OS. STN: 10154-2.2-00.

153101 TOUGHREACT V. 2.3. 2001. SUN and DEC w/Unix OS. STN: 10396-2.3-00.

160880 TOUGHREACT V. 2.4. 2001. SunOS 5.5.1, Dec Alpha TRU64 Unix & OS1 V4.0.
STN: 10396-2.4-00.

180937 TOUGHREACT V. 3.1.1. 2007. OSF1 V5.1/Linux/WINDOWS XP.
STN: 10396-3.1.1-00.

INTENTIONALLY LEFT BLANK

APPENDIX A
MINERAL INITIAL VOLUME FRACTIONS

INTENTIONALLY LEFT BLANK

Table A-1. Mineral Initial Volume Fractions (1)

Zone	Type	Hydro Unit	calcite	beidel-ca	beidel-mg	beidel-na	illite	tridymite	crystoba-a	opal_CT	quartz
1	matrix	Tcw11	0.00371	0.00538	0.00269	0.00090	0.00104	0.05168	0.15587	0.12772	0.00797
2	matrix	Tcw12	0.00371	0.00538	0.00269	0.00090	0.00104	0.05168	0.15587	0.12772	0.00797
3	matrix	Tcw13	0.01952	0.05881	0.02940	0.00987	0.01140	0.00000	0.07258	0.05947	0.00060
4	matrix	Ptn21	0.00000	0.10560	0.05280	0.01773	0.02048	0.00000	0.00000	0.00000	0.00088
5	matrix	Ptn22	0.00000	0.09311	0.04656	0.01563	0.01806	0.00000	0.00000	0.03753	0.01497
6	matrix	Ptn23	0.00000	0.02629	0.01315	0.00441	0.00510	0.00000	0.00000	0.10775	0.00084
7	matrix	Ptn24	0.00000	0.02232	0.01116	0.00375	0.00433	0.00000	0.00000	0.05489	0.00887
8	matrix	Ptn25	0.00000	0.01469	0.00734	0.00247	0.00285	0.00000	0.00296	0.01944	0.00891
9	matrix	Ptn26	0.00652	0.05319	0.02660	0.00893	0.01031	0.00000	0.00782	0.00000	0.01335
10	matrix	Tsw31	0.01414	0.00221	0.00110	0.00037	0.00043	0.00084	0.02009	0.00000	0.00096
11	matrix	Tsw32	0.00488	0.00587	0.00294	0.00099	0.00114	0.12772	0.14060	0.00000	0.01490
12	matrix	Tsw33	0.00378	0.01243	0.00621	0.00209	0.00241	0.06769	0.23385	0.00000	0.06632
13	matrix	Tsw34	0.00051	0.01023	0.00511	0.00172	0.00198	0.02696	0.20270	0.00000	0.13087
14	matrix	Tsw35	0.00065	0.01258	0.00629	0.00211	0.00244	0.02388	0.16081	0.00000	0.19437
15	matrix	Tsw36	0.00007	0.00574	0.00287	0.00096	0.00111	0.01014	0.14254	0.00000	0.20908
16	matrix	Tsw37	0.00007	0.00575	0.00288	0.00097	0.00112	0.01016	0.14275	0.00000	0.20939
17	matrix	Tsw38	0.00021	0.05740	0.02870	0.00964	0.01113	0.00000	0.04283	0.10686	0.01935
18	matrix	Tsw39	0.00020	0.01414	0.00707	0.00237	0.00274	0.00000	0.11014	0.00000	0.02817
19	matrix	Ch1	0.00128	0.00245	0.00122	0.00041	0.00047	0.00181	0.05152	0.00000	0.03267
20	matrix	Ch2	0.00000	0.00343	0.00172	0.00058	0.00067	0.00054	0.00000	0.06365	0.06786
21	matrix	Ch3	0.00000	0.00727	0.00363	0.00122	0.00141	0.00000	0.00000	0.05985	0.04264
22	matrix	Ch4	0.00003	0.00584	0.00292	0.00098	0.00113	0.00000	0.00000	0.17597	0.04445
23	matrix	Ch5	0.00004	0.00388	0.00194	0.00065	0.00075	0.00000	0.00000	0.14398	0.07022
24	matrix	Ch6	0.00099	0.02538	0.01269	0.00426	0.00492	0.00002	0.00000	0.05779	0.17606
25	matrix	Pp4	0.00058	0.01755	0.00878	0.00295	0.00340	0.00206	0.00000	0.14039	0.07557
26	matrix	Pp3	0.00054	0.01087	0.00543	0.00182	0.00211	0.01202	0.08415	0.00000	0.24972
27	matrix	pp2	0.00054	0.01092	0.00546	0.00183	0.00212	0.01208	0.08456	0.00000	0.25094
28	matrix	pp1	0.00000	0.02243	0.01122	0.00377	0.00435	0.00064	0.09595	0.00000	0.07826
29	matrix	bf3	0.00160	0.01036	0.00518	0.00174	0.00201	0.00230	0.05318	0.00000	0.27980
30	matrix	bf2	0.00272	0.04253	0.02127	0.00714	0.00825	0.00000	0.02100	0.00000	0.18273
31	fracture	Tcw11	0.02341	0.03180	0.01590	0.00534	0.00617	0.04754	0.14340	0.12750	0.00733

Table A-1. Mineral Initial Volume Fractions (1) (Continued)

Zone	Type	Hydro Unit	calcite	beidel-ca	beidel-mg	beidel-na	illite	tridymite	crystoba-a	opal_CT	quartz
32	fracture	Tcw12	0.02341	0.03180	0.01590	0.00534	0.00617	0.04754	0.14340	0.12750	0.00733
33	fracture	Tcw13	0.03796	0.08096	0.04048	0.01359	0.01570	0.00000	0.06677	0.06471	0.00055
34	fracture	Ptn21	0.02000	0.12401	0.06201	0.02082	0.02405	0.00000	0.00000	0.01000	0.00081
35	fracture	Ptn22	0.02000	0.11252	0.05626	0.01889	0.02182	0.00000	0.00000	0.04453	0.01378
36	fracture	Ptn23	0.02000	0.05105	0.02552	0.00857	0.00990	0.00000	0.00000	0.10913	0.00078
37	fracture	Ptn24	0.02000	0.04739	0.02370	0.00796	0.00919	0.00000	0.00000	0.06049	0.00816
38	fracture	Ptn25	0.02000	0.04037	0.02018	0.00678	0.00783	0.00000	0.00272	0.02789	0.00820
39	fracture	Ptn26	0.02600	0.07579	0.03790	0.01272	0.01470	0.00000	0.00720	0.01000	0.01228
40	fracture	Tsw31	0.03300	0.02889	0.01444	0.00485	0.00560	0.00077	0.01849	0.01000	0.00089
41	fracture	Tsw32	0.02290	0.03035	0.01517	0.00509	0.00589	0.07598	0.08364	0.01000	0.00887
42	fracture	Tsw33	0.02225	0.03425	0.01712	0.00575	0.00664	0.04027	0.13911	0.01000	0.03945
43	fracture	Tsw34	0.02030	0.03294	0.01647	0.00553	0.00639	0.01604	0.12059	0.01000	0.07786
44	fracture	Tsw35	0.02038	0.03434	0.01717	0.00576	0.00666	0.01421	0.09566	0.01000	0.11563
45	fracture	Tsw36	0.02004	0.03027	0.01514	0.00508	0.00587	0.00604	0.08480	0.01000	0.12438
46	fracture	Tsw37	0.02004	0.03028	0.01514	0.00508	0.00587	0.00604	0.08492	0.01000	0.12457
47	fracture	Tsw38	0.02019	0.07967	0.03983	0.01337	0.01545	0.00000	0.03941	0.10831	0.01781
48	fracture	Tsw39	0.02019	0.03986	0.01993	0.00669	0.00773	0.00000	0.10133	0.01000	0.02591
49	fracture	Ch1	0.02117	0.02911	0.01455	0.00489	0.00564	0.00166	0.04739	0.01000	0.03005
50	fracture	Ch2	0.02000	0.03001	0.01501	0.00504	0.00582	0.00050	0.00000	0.06855	0.06243
51	fracture	Ch3	0.02000	0.03354	0.01677	0.00563	0.00650	0.00000	0.00000	0.06506	0.03922
52	fracture	Ch4	0.02002	0.03223	0.01612	0.00541	0.00625	0.00000	0.00000	0.17189	0.04089
53	fracture	Ch5	0.02004	0.03043	0.01521	0.00511	0.00590	0.00000	0.00000	0.14246	0.06460
54	fracture	Ch6	0.02091	0.05020	0.02510	0.00843	0.00974	0.00002	0.00000	0.06317	0.16197
55	fracture	Pp4	0.02053	0.04300	0.02150	0.00722	0.00834	0.00190	0.00000	0.13916	0.06952
56	fracture	Pp3	0.02049	0.03685	0.01843	0.00619	0.00715	0.01106	0.07742	0.01000	0.22974
57	fracture	pp2	0.02050	0.03690	0.01845	0.00619	0.00716	0.01111	0.07779	0.01000	0.23087
58	fracture	pp1	0.02000	0.04749	0.02375	0.00797	0.00921	0.00059	0.08828	0.01000	0.07200
59	fracture	bf3	0.02147	0.03639	0.01819	0.00611	0.00706	0.00212	0.04893	0.01000	0.25742
60	fracture	bf2	0.02250	0.06599	0.03299	0.01108	0.01280	0.00000	0.01932	0.01000	0.16811

Output DTN: LB0707DSTHC006.003.

Table A-2. Mineral Initial Volume Fractions (2)

Zone	Type	Hydro Unit	sanidi-ym	plagio-ym	glass-rhyol	biotite-ox	hematite	fluorite	stell-ym/10	clinpt-ym/10	mordenit/10
1	matrix	Tcw11	0.53981	0.00863	0.08959	0.00345	0.00000	0.00000	0.00000	0.00156	0.00000
2	matrix	Tcw12	0.53981	0.00863	0.08959	0.00345	0.00000	0.00000	0.00000	0.00156	0.00000
3	matrix	Tcw13	0.25509	0.00896	0.47428	0.00000	0.00000	0.00000	0.00000	0.00000	0.00000
4	matrix	Ptn21	0.05411	0.00886	0.73953	0.00000	0.00000	0.00000	0.00000	0.00000	0.00000
5	matrix	Ptn22	0.06596	0.00884	0.69894	0.00025	0.00015	0.00000	0.00000	0.00000	0.00000
6	matrix	Ptn23	0.01722	0.00846	0.81678	0.00000	0.00000	0.00000	0.00000	0.00000	0.00000
7	matrix	Ptn24	0.08769	0.00862	0.79102	0.00735	0.00000	0.00000	0.00000	0.00000	0.00000
8	matrix	Ptn25	0.15088	0.00872	0.77201	0.00744	0.00229	0.00000	0.00000	0.00000	0.00000
9	matrix	Ptn26	0.13173	0.00893	0.71306	0.01733	0.00223	0.00000	0.00000	0.00000	0.00000
10	matrix	Tsw31	0.18146	0.00884	0.75584	0.00898	0.00464	0.00000	0.00000	0.00009	0.00000
11	matrix	Tsw32	0.67410	0.00977	0.00080	0.01037	0.00445	0.00000	0.00000	0.00149	0.00000
12	matrix	Tsw33	0.58883	0.00958	0.00000	0.00253	0.00362	0.00000	0.00000	0.00067	0.00000
13	matrix	Tsw34	0.60634	0.00971	0.00000	0.00340	0.00036	0.00000	0.00000	0.00010	0.00000
14	matrix	Tsw35	0.58087	0.00978	0.00000	0.00172	0.00166	0.00000	0.00000	0.00283	0.00000
15	matrix	Tsw36	0.60549	0.00978	0.00000	0.00311	0.00196	0.00000	0.00000	0.00714	0.00000
16	matrix	Tsw37	0.60638	0.00979	0.00000	0.00311	0.00049	0.00000	0.00000	0.00715	0.00000
17	matrix	Tsw38	0.13709	0.00869	0.48318	0.00191	0.00000	0.00000	0.00000	0.09299	0.00000
18	matrix	Tsw39	0.17370	0.00872	0.61443	0.00172	0.00000	0.00000	0.00000	0.03660	0.00000
19	matrix	Ch1	0.16401	0.00858	0.70290	0.00071	0.00000	0.00000	0.00000	0.03156	0.00041
20	matrix	Ch2	0.23018	0.00869	0.58625	0.00407	0.00000	0.00000	0.00000	0.03134	0.00102
21	matrix	Ch3	0.22672	0.00864	0.59459	0.00754	0.00000	0.00000	0.00000	0.04224	0.00425
22	matrix	Ch4	0.16857	0.00826	0.06443	0.00545	0.00000	0.00000	0.00000	0.42008	0.10187
23	matrix	Ch5	0.17300	0.00838	0.06770	0.01117	0.00000	0.00000	0.00000	0.39875	0.11953
24	matrix	Ch6	0.30422	0.00926	0.07328	0.01619	0.00000	0.00000	0.00000	0.26566	0.04927
25	matrix	Pp4	0.27854	0.00860	0.12717	0.00177	0.00000	0.00000	0.00000	0.22966	0.10299
26	matrix	Pp3	0.60464	0.00973	0.00281	0.00572	0.00487	0.00000	0.00000	0.00557	0.00000
27	matrix	pp2	0.60760	0.00978	0.00283	0.00575	0.00000	0.00000	0.00000	0.00560	0.00000
28	matrix	pp1	0.22047	0.00889	0.02835	0.00317	0.00000	0.00000	0.00000	0.52249	0.00000
29	matrix	bf3	0.60321	0.00997	0.00205	0.02584	0.00000	0.00000	0.00000	0.00277	0.00000
30	matrix	bf2	0.33208	0.00963	0.00000	0.02511	0.00000	0.00000	0.00000	0.34755	0.00000
31	fracture	Tcw11	0.49663	0.00794	0.08242	0.00318	0.00000	0.00000	0.00000	0.00144	0.00000

Table A-2. Mineral Initial Volume Fractions (2) (Continued)

Zone	Type	Hydro Unit	sanidi-ym	plagio-ym	glass-rhyol	biotite-ox	hematite	fluorite	stell-ym/10	clinpt-ym/10	mordenit/10
32	fracture	Tcw12	0.49663	0.00794	0.08242	0.00318	0.00000	0.00000	0.00000	0.00144	0.00000
33	fracture	Tcw13	0.23468	0.00825	0.43634	0.00000	0.00000	0.00000	0.00000	0.00000	0.00000
34	fracture	Ptn21	0.04978	0.00815	0.68037	0.00000	0.00000	0.00000	0.00000	0.00000	0.00000
35	fracture	Ptn22	0.06068	0.00813	0.64302	0.00023	0.00014	0.00000	0.00000	0.00000	0.00000
36	fracture	Ptn23	0.01584	0.00778	0.75144	0.00000	0.00000	0.00000	0.00000	0.00000	0.00000
37	fracture	Ptn24	0.08068	0.00793	0.72774	0.00676	0.00000	0.00000	0.00000	0.00000	0.00000
38	fracture	Ptn25	0.13881	0.00802	0.71025	0.00685	0.00211	0.00000	0.00000	0.00000	0.00000
39	fracture	Ptn26	0.12119	0.00821	0.65602	0.01594	0.00205	0.00000	0.00000	0.00000	0.00000
40	fracture	Tsw31	0.16694	0.00813	0.69537	0.00826	0.00427	0.00000	0.00000	0.00008	0.00000
41	fracture	Tsw32	0.40102	0.00581	0.00047	0.00617	0.00265	0.00010	0.32500	0.00088	0.00000
42	fracture	Tsw33	0.35030	0.00570	0.00000	0.00150	0.00215	0.00010	0.32500	0.00040	0.00000
43	fracture	Tsw34	0.36071	0.00578	0.00000	0.00202	0.00022	0.00010	0.32500	0.00006	0.00000
44	fracture	Tsw35	0.34556	0.00582	0.00000	0.00102	0.00099	0.00010	0.32500	0.00169	0.00000
45	fracture	Tsw36	0.36020	0.00582	0.00000	0.00185	0.00116	0.00010	0.32500	0.00424	0.00000
46	fracture	Tsw37	0.36073	0.00582	0.00000	0.00185	0.00029	0.00010	0.32500	0.00425	0.00000
47	fracture	Tsw38	0.12613	0.00800	0.44453	0.00176	0.00000	0.00000	0.00000	0.08556	0.00000
48	fracture	Tsw39	0.15981	0.00803	0.56527	0.00158	0.00000	0.00000	0.00000	0.03368	0.00000
49	fracture	Ch1	0.15089	0.00789	0.64667	0.00066	0.00000	0.00000	0.00000	0.02904	0.00038
50	fracture	Ch2	0.21176	0.00800	0.53935	0.00375	0.00000	0.00000	0.00000	0.02884	0.00094
51	fracture	Ch3	0.20859	0.00795	0.54702	0.00693	0.00000	0.00000	0.00000	0.03886	0.00391
52	fracture	Ch4	0.15509	0.00760	0.05928	0.00501	0.00000	0.00000	0.00000	0.38648	0.09372
53	fracture	Ch5	0.15916	0.00771	0.06228	0.01028	0.00000	0.00000	0.00000	0.36685	0.10997
54	fracture	Ch6	0.27989	0.00852	0.06741	0.01489	0.00000	0.00000	0.00000	0.24441	0.04533
55	fracture	Pp4	0.25625	0.00791	0.11700	0.00162	0.00000	0.00000	0.00000	0.21128	0.09475
56	fracture	Pp3	0.55627	0.00895	0.00259	0.00526	0.00448	0.00000	0.00000	0.00512	0.00000
57	fracture	pp2	0.55899	0.00899	0.00260	0.00529	0.00000	0.00000	0.00000	0.00515	0.00000
58	fracture	pp1	0.20284	0.00818	0.02608	0.00292	0.00000	0.00000	0.00000	0.48069	0.00000
59	fracture	bf3	0.55495	0.00917	0.00189	0.02377	0.00000	0.00000	0.00000	0.00255	0.00000
60	fracture	bf2	0.30551	0.00886	0.00000	0.02310	0.00000	0.00000	0.00000	0.31974	0.00000

Output DTN: LB0707DSTHC006.003.

APPENDIX B
MINERAL REACTIVE SURFACE AREAS

INTENTIONALLY LEFT BLANK

Table B-1. Primary Mineral Initial Reactive Surface Areas (1)

Zone	Type	Hydro Unit	calcite	beidel-ca	beidel-mg	beidel-na	illite	tridymite	crisoba-a	opal_CT	quartz
1	matrix	Tcw11	2,753	2,712	2,712	2,724	2,708	283	274	3,600	241
2	matrix	Tcw12	934	920	920	924	919	96	93	1,221	82
3	matrix	Tcw13	1,922	1,893	1,893	1,902	1,890	187	181	2,513	160
4	matrix	Ptn21	4,313	4,249	4,249	4,268	4,243	415	402	5,641	355
5	matrix	Ptn22	1,523	1,500	1,500	1,507	1,498	144	139	1,992	123
6	matrix	Ptn23	1,908	1,880	1,880	1,888	1,877	193	187	2,495	165
7	matrix	Ptn24	2,072	2,041	2,041	2,050	2,038	224	217	2,710	192
8	matrix	Ptn25	7,450	7,339	7,339	7,372	7,328	849	822	9,744	725
9	matrix	Ptn26	2,030	1,999	1,999	2,009	1,996	217	210	2,655	185
10	matrix	Tsw31	919	905	905	910	904	108	104	1,202	92
11	matrix	Tsw32	6,984	6,880	6,880	6,912	6,870	819	793	9,135	699
12	matrix	Tsw33	6,465	6,369	6,369	6,398	6,359	751	727	8,456	641
13	matrix	Tsw34	5,883	5,796	5,796	5,822	5,787	691	669	7,695	590
14	matrix	Tsw35	5,476	5,395	5,395	5,419	5,386	638	618	7,162	544
15	matrix	Tsw36	5,223	5,145	5,145	5,169	5,137	614	594	6,831	524
16	matrix	Tsw37	5,586	5,503	5,503	5,528	5,495	658	637	7,307	561
17	matrix	Tsw38	317	312	312	313	311	26	25	414	22
18	matrix	Tsw39	2,126	2,094	2,094	2,104	2,091	239	231	2,780	204
19	matrix	Ch1	2,339	2,304	2,304	2,315	2,301	270	261	3,059	230
20	matrix	Ch2	591	583	583	585	582	64	62	774	54
21	matrix	Ch3	580	571	571	574	570	61	59	759	52
22	matrix	Ch4	1,484	1,462	1,462	1,469	1,460	52	50	1,941	44
23	matrix	Ch5	1,555	1,532	1,532	1,539	1,529	62	60	2,034	53
24	matrix	Ch6	1,765	1,739	1,739	1,746	1,736	123	119	2,308	105
25	matrix	Pp4	1,895	1,867	1,867	1,875	1,864	112	109	2,478	96
26	matrix	Pp3	6,669	6,569	6,569	6,599	6,559	775	750	8,722	661
27	matrix	pp2	8,726	8,596	8,596	8,635	8,583	1,019	986	11,413	869

Table B-1. Primary Mineral Initial Reactive Surface Areas (1) (Continued)

Zone	Type	Hydro Unit	calcite	beidel-ca	beidel-mg	beidel-na	illite	tridymite	crystoba-a	opal_CT	quartz
28	matrix	pp1	1,551	1,528	1,528	1,534	1,525	81	78	2,028	69
29	matrix	bf3	2,645	2,605	2,605	2,617	2,601	310	300	3,459	264
30	matrix	bf2	1,347	1,327	1,327	1,333	1,325	92	89	1,762	79
31	fracture	Tcw11	130	130	130	130	130	130	130	130	130
32	fracture	Tcw12	1,575	1,575	1,575	1,575	1,575	1,575	1,575	1,575	1,575
33	fracture	Tcw13	580	580	580	580	580	580	580	580	580
34	fracture	Ptn21	217	217	217	217	217	217	217	217	217
35	fracture	Ptn22	282	282	282	282	282	282	282	282	282
36	fracture	Ptn23	1,667	1,667	1,667	1,667	1,667	1,667	1,667	1,667	1,667
37	fracture	Ptn24	68	68	68	68	68	68	68	68	68
38	fracture	Ptn25	396	396	396	396	396	396	396	396	396
39	fracture	Ptn26	2,297	2,297	2,297	2,297	2,297	2,297	2,297	2,297	2,297
40	fracture	Tsw31	1,544	1,544	1,544	1,544	1,544	1,544	1,544	1,544	1,544
41	fracture	Tsw32	773	773	773	773	773	773	773	773	773
42	fracture	Tsw33	1,531	1,531	1,531	1,531	1,531	1,531	1,531	1,531	1,531
43	fracture	Tsw34	3,186	3,186	3,186	3,186	3,186	3,186	3,186	3,186	3,186
44	fracture	Tsw35	2,017	2,017	2,017	2,017	2,017	2,017	2,017	2,017	2,017
45	fracture	Tsw36	1,894	1,894	1,894	1,894	1,894	1,894	1,894	1,894	1,894
46	fracture	Tsw37	1,894	1,894	1,894	1,894	1,894	1,894	1,894	1,894	1,894
47	fracture	Tsw38	2,425	2,425	2,425	2,425	2,425	2,425	2,425	2,425	2,425
48	fracture	Tsw39	1,372	1,372	1,372	1,372	1,372	1,372	1,372	1,372	1,372
49	fracture	Ch1	984	984	984	984	984	984	984	984	984
50	fracture	Ch2	1,117	1,117	1,117	1,117	1,117	1,117	1,117	1,117	1,117
51	fracture	Ch3	1,117	1,117	1,117	1,117	1,117	1,117	1,117	1,117	1,117
52	fracture	Ch4	2,324	2,324	2,324	2,324	2,324	2,324	2,324	2,324	2,324
53	fracture	Ch5	2,324	2,324	2,324	2,324	2,324	2,324	2,324	2,324	2,324
54	fracture	Ch6	1,375	1,375	1,375	1,375	1,375	1,375	1,375	1,375	1,375

Table B-1. Primary Mineral Initial Reactive Surface Areas (1) (Continued)

Zone	Type	Hydro Unit	calcite	beidel-ca	beidel-mg	beidel-na	illite	tridymite	cristoba-a	opal_CT	quartz
55	fracture	Pp4	2,324	2,324	2,324	2,324	2,324	2,324	2,324	2,324	2,324
56	fracture	Pp3	1,258	1,258	1,258	1,258	1,258	1,258	1,258	1,258	1,258
57	fracture	pp2	1,258	1,258	1,258	1,258	1,258	1,258	1,258	1,258	1,258
58	fracture	pp1	2,324	2,324	2,324	2,324	2,324	2,324	2,324	2,324	2,324
59	fracture	bf3	1,258	1,258	1,258	1,258	1,258	1,258	1,258	1,258	1,258
60	fracture	bf2	2,324	2,324	2,324	2,324	2,324	2,324	2,324	2,324	2,324

Output DTN: LB0707DSTHC006.003.

NOTE: Matrix mineral reactive surface areas are in units of cm²/g (mineral). Fracture mineral surface areas are in units of m²/m³ fracture medium solids.

Table B-2. Primary Mineral Initial Reactive Surface Areas (2)

Zone	Type	Hydro Unit	sanidi-ym	plagio-ym	glass-rhyol	biotite-ox	hematite	fluorite	stell-ym/10	clinpt-ym/10	mordenit/10
1	matrix	Tcw11	246	242	289	207	1,414	3,600	3,600	3,487	3,583
2	matrix	Tcw12	84	82	98	70	480	1,221	1,221	1,183	1,216
3	matrix	Tcw13	163	160	191	137	987	2,513	2,513	2,434	2,502
4	matrix	Ptn21	362	356	424	304	2,216	5,641	5,641	5,463	5,615
5	matrix	Ptn22	126	123	147	105	782	1,992	1,992	1,929	1,982
6	matrix	Ptn23	168	165	197	141	980	2,495	2,495	2,417	2,484
7	matrix	Ptn24	196	192	229	164	1,064	2,710	2,710	2,624	2,697
8	matrix	Ptn25	740	727	867	621	3,827	9,744	9,744	9,435	9,698
9	matrix	Ptn26	189	186	222	159	1,043	2,655	2,655	2,571	2,642
10	matrix	Tsw31	94	92	110	79	472	1,202	1,202	1,164	1,196
11	matrix	Tsw32	714	702	836	599	3,588	9,135	9,135	8,846	9,092
12	matrix	Tsw33	654	643	767	549	3,321	8,456	8,456	8,188	8,416
13	matrix	Tsw34	602	592	706	505	3,022	7,695	7,695	7,451	7,658
14	matrix	Tsw35	556	546	651	466	2,813	7,162	7,162	6,936	7,128
15	matrix	Tsw36	535	526	627	448	2,683	6,831	6,831	6,615	6,799

Table B-2. Primary Mineral Initial Reactive Surface Areas (2) (Continued)

Zone	Type	Hydro Unit	sanidi-ym	plagio-ym	glass-rhyol	biotite-ox	hematite	fluorite	stell-ym/10	clinpt-ym/10	mordent/10
16	matrix	Tsw37	573	563	671	480	2,870	7,307	7,307	7,076	7,272
17	matrix	Tsw38	23	23	27	19	163	414	414	401	412
18	matrix	Tsw39	208	204	244	174	1,092	2,780	2,780	2,692	2,767
19	matrix	Ch1	235	231	275	197	1,202	3,059	3,059	2,962	3,045
20	matrix	Ch2	55	55	65	47	304	774	774	749	770
21	matrix	Ch3	53	52	62	45	298	759	759	735	755
22	matrix	Ch4	45	44	53	38	762	1,941	1,941	1,880	1,932
23	matrix	Ch5	54	53	63	45	799	2,034	2,034	1,969	2,024
24	matrix	Ch6	107	105	125	90	907	2,308	2,308	2,235	2,297
25	matrix	Pp4	98	96	114	82	973	2,478	2,478	2,400	2,466
26	matrix	Pp3	675	663	791	566	3,426	8,722	8,722	8,446	8,681
27	matrix	pp2	888	872	1,040	744	4,483	11,413	11,413	11,052	11,359
28	matrix	pp1	71	69	83	59	797	2,028	2,028	1,964	2,018
29	matrix	bf3	270	265	316	226	1,359	3,459	3,459	3,350	3,443
30	matrix	bf2	80	79	94	67	692	1,762	1,762	1,706	1,754
31	fracture	Tcw11	130	130	130	130	130	130	130	130	130
32	fracture	Tcw12	1,575	1,575	1,575	1,575	1,575	1,575	1,575	1,575	1,575
33	fracture	Tcw13	580	580	580	580	580	580	580	580	580
34	fracture	Ptn21	217	217	217	217	217	217	217	217	217
35	fracture	Ptn22	282	282	282	282	282	282	282	282	282
36	fracture	Ptn23	1,667	1,667	1,667	1,667	1,667	1,667	1,667	1,667	1,667
37	fracture	Ptn24	68	68	68	68	68	68	68	68	68
38	fracture	Ptn25	396	396	396	396	396	396	396	396	396
39	fracture	Ptn26	2,297	2,297	2,297	2,297	2,297	2,297	2,297	2,297	2,297
40	fracture	Tsw31	1,544	1,544	1,544	1,544	1,544	1,544	1,544	1,544	1,544
41	fracture	Tsw32	773	773	773	773	773	773	773	773	773
42	fracture	Tsw33	1,531	1,531	1,531	1,531	1,531	1,531	1,531	1,531	1,531

Table B-2. Primary Mineral Initial Reactive Surface Areas (2) (Continued)

Zone	Type	Hydro Unit	sanidi-ym	plagio-ym	glass-rhyol	biotite-ox	hematite	fluorite	stell-ym/10	clinpt-ym/10	mordenit/10
43	fracture	Tsw34	3,186	3,186	3,186	3,186	3,186	3,186	3,186	3,186	3,186
44	fracture	Tsw35	2,017	2,017	2,017	2,017	2,017	2,017	2,017	2,017	2,017
45	fracture	Tsw36	1,894	1,894	1,894	1,894	1,894	1,894	1,894	1,894	1,894
46	fracture	Tsw37	1,894	1,894	1,894	1,894	1,894	1,894	1,894	1,894	1,894
47	fracture	Tsw38	2,425	2,425	2,425	2,425	2,425	2,425	2,425	2,425	2,425
48	fracture	Tsw39	1,372	1,372	1,372	1,372	1,372	1,372	1,372	1,372	1,372
49	fracture	Ch1	984	984	984	984	984	984	984	984	984
50	fracture	Ch2	1,117	1,117	1,117	1,117	1,117	1,117	1,117	1,117	1,117
51	fracture	Ch3	1,117	1,117	1,117	1,117	1,117	1,117	1,117	1,117	1,117
52	fracture	Ch4	2,324	2,324	2,324	2,324	2,324	2,324	2,324	2,324	2,324
53	fracture	Ch5	2,324	2,324	2,324	2,324	2,324	2,324	2,324	2,324	2,324
54	fracture	Ch6	1,375	1,375	1,375	1,375	1,375	1,375	1,375	1,375	1,375
55	fracture	Pp4	2,324	2,324	2,324	2,324	2,324	2,324	2,324	2,324	2,324
56	fracture	Pp3	1,258	1,258	1,258	1,258	1,258	1,258	1,258	1,258	1,258
57	fracture	pp2	1,258	1,258	1,258	1,258	1,258	1,258	1,258	1,258	1,258
58	fracture	pp1	2,324	2,324	2,324	2,324	2,324	2,324	2,324	2,324	2,324
59	fracture	bf3	1,258	1,258	1,258	1,258	1,258	1,258	1,258	1,258	1,258
60	fracture	bf2	2,324	2,324	2,324	2,324	2,324	2,324	2,324	2,324	2,324

Output DTN: LB0707DSTHC006.003.

NOTE: Matrix mineral reactive surface areas are in units of cm²/g (mineral). Fracture mineral surface areas are in units of m²/m³ fracture medium solids.

INTENTIONALLY LEFT BLANK

APPENDIX C
THERMODYNAMIC DATA

INTENTIONALLY LEFT BLANK

C.1 INTRODUCTION

This appendix documents the thermodynamic data used in the THC seepage model and also the qualification for intended use of any external outside data sources used as a source or in the derivation of these data. The thermodynamic data used in this report and the sources of these data are shown in Tables C.1-1 and C.1-2. Except for a few minerals, the source of the $\log(K)$ (equilibrium constants), molecular weight, and molar volume data was the qualified Yucca Mountain Project-controlled databases *data0.ymp.R5*, which was originally submitted to the Technical Data Management System (TDMS) under DTN: SN0610T0502404.013 [DIRS 178113], and *data0.ymp.R2*, which is from DTN: SN0609T0502404.012 [DIRS 179067]. The original *data0.ymp.R5* database, however, was later finalized and superseded with a new DTN: SN0612T0502404.014 [DIRS 178850]. Changes from DTN: SN0610T0502404.013 [DIRS 178113] to DTN: SN0612T0502404.014 [DIRS 178850] were evaluated and determined to be inconsequential (Section C.9). Because the original database filed under DTN: SN0610T0502404.013 [DIRS 178113] was superseded and is no longer available, this appendix refers to the superseding database (DTN: SN0612T0502404.014 [DIRS 178850]) as the source of all data that have not changed when the original database was superseded.

Regression of $\log(K)$ data as a function of temperature, and transformation of stoichiometries using alternate primary species, as necessary for input into simulations, were performed using utilities kreg V1.1 and kswitch V1.1 (see Table 3-1), respectively.

Thermodynamic data differing from those reported in DTN: SN0612T0502404.014 [DIRS 178850] and their sources or derivations are reported below. External data sources used to either obtain or calculate these thermodynamic data are qualified here for their intended use following the qualification plan, *Qualification Plan for the Intended Use of Thermodynamic Data from the Literature*, documented in Appendix N (Section N.2).

External data sources such as mineral compositions and abundances that were required in some of the thermodynamic data derivations are qualified separately in Appendix O (Section O.3), following the qualification plan, *Qualification Plan for the Intended Use of Mineralogical Data from the Literature*, documented in Appendix N (Section N.5).

Table C.1-1. Thermodynamic Data: Minerals and Gases

Mineral/Gas	Molecular Weight (g/mol) ^a	Molar Volume ^{a,b} (cm ³ /mol)	Reaction Stoichiometry ^c	log(K)							Source ^d	
				0 (°C)	25 (°C)	60 (°C)	100 (°C)	150 (°C)	200 (°C)	250 (°C)		300 (°C)
'anhydrite'	136.142	45.94	(1)'ca+2', (1)'so4-2'	-4.1043	-4.3064	-4.7587	-5.3851	-6.2741	-7.2829	-8.4644	-9.9598	1
'antigo_am'	277.112	102.89	(-6)'h+', (3)'mg+2', (2)'sio2(aq)', (5)'h2o'	37.3589	34.5025	31.2224	28.2271	25.2793	22.9545	21.0741	19.5218	1
'beidel-ca'	366.562	129.766	(2)'h+', (0.165)'ca+2', (3.67)'sio2(aq)', (2.33)'alo2-'	-50.6061	-46.7997	-42.9473	-39.7348	-36.8347	-34.8161	-33.5417	-33.1069	1
'beidel-mg'	363.96	128.725	(2)'h+', (0.165)'mg+2', (3.67)'sio2(aq)', (2.33)'alo2-'	-50.5939	-46.8378	-43.0418	-39.8781	-37.0222	-35.0357	-33.7855	-33.3695	1
'beidel-na'	367.536	130.727	(2)'h+', (0.33)'na+', (3.67)'sio2(aq)', (2.33)'alo2-'	-50.6536	-46.7438	-42.7665	-39.4308	-36.3966	-34.2595	-32.8772	-32.3417	1
'beidel-k'	372.852	134.152	(2)'h+', (0.33)'k+', (3.67)'sio2(aq)', (2.33)'alo2-'	-51.0733	-47.0827	-43.0176	-39.6086	-36.5108	-34.3307	-32.9186	-32.3612	1
'biotite-ox'	471.193	152.316	(-2.58)'h+', (1)'k+', (1.29)'mg+2', (1.71)'hfeo2(aq)', (3)'sio2(aq)', (1.44)'h2o', (1)'alo2-'	3.691	2.914	1.379	-0.4434	-2.623	-4.708	-6.797	-9.076	2
'calcite'	100.087	36.934	(-1)'h+', (1)'ca+2', (1)'hco3-'	2.2257	1.8487	1.333	0.7743	0.0999	-0.5838	-1.3262	-2.2154	1
'clinpt-ca/10'	134.3928	63.205	(0.17335)'ca+2', (1.4533)'sio2(aq)', (1.0922)'h2o', (0.3467)'alo2-'	-8.984	-8.251	-7.581	-7.079	-6.701	-6.536	-6.568	-6.83	2
'clinpt-k/10'	141.0006	63.205	(0.3467)'k+', (1.4533)'sio2(aq)', (1.0922)'h2o', (0.3467)'alo2-'	-9.606	-8.645	-7.712	-6.969	-6.35	-5.99	-5.857	-5.975	2
'clinpt-na/10'	135.4158	63.205	(0.3467)'na+', (1.4533)'sio2(aq)', (1.0922)'h2o', (0.3467)'alo2-'	-9.118	-8.263	-7.447	-6.8	-6.266	-5.963	-5.871	-6.018	2
'clinpt-ym/10'	135.2304	63.205	(0.1428)'ca+2', (0.0203)'na+', (0.0408)'k+', (1.4533)'sio2(aq)', (1.0922)'h2o', (0.3467)'alo2-'	-9.091	-8.323	-7.614	-7.075	-6.659	-6.463	-6.469	-6.607	2

Table C.1-1. Thermodynamic Data: Minerals (Continued)

Mineral/Gas	Molecular Weight (g/mol) ^a	Molar Volume ^{a,b} (cm ³ /mol)	Reaction Stoichiometry ^c	log(K)								Source ^d
				0 (°C)	25 (°C)	60 (°C)	100 (°C)	150 (°C)	200 (°C)	250 (°C)	300 (°C)	
'cristoba-a'	60.084	25.74	(1)'sio2(aq)	-4.0213	-3.4488	-2.9921	-2.6605	-2.3644	-2.1326	-1.9402	-1.7832	2
'fluorite'	78.075	24.542	(1)'ca+2, (2)'f-	-10.3098	-10.0371	-9.9067	-9.967	-10.2653	-10.7841	-11.555	-12.7028	1
'goethite'	88.852	20.82	(1)'hfeo2(aq)	-12.7796	-11.4833	-10.2087	-9.2435	-8.5081	-8.1147	-7.948	-7.9359	1
'glass-rhyol'	64.96	29.342	(4)'h+, (1)'alo2-, (-2)'h2o'	1.524	1.365	1.175	0.992	0.793	0.61	0.425	0.223	2
'gypsum'	172.172	74.69	(1)'ca+2, (1)'so4-2, (2)'h2o'	-4.5331	-4.4823	-4.6094	-4.9035	500	500	500	500	1
'hematite'	159.688	30.274	(-1)'h2o, (2)'hfeo2(aq)	-26.4379	-23.9274	-21.4857	-19.6613	-18.2926	-17.5725	-17.2716	-17.2479	1
'illite'	383.901	139.346	(1.2)'h+, (0.25)'mg+2, (0.6)'k+, (3.5)'sio2(aq), (0.4)'h2o, (2.3)'alo2-	-46.2836	-42.6981	-39.0801	-36.0675	-33.3525	-31.4734	-30.3096	-29.9646	1
'kaolinite'	258.16	99.52	(2)'h+, (2)'sio2(aq), (1)'h2o, (2)'alo2-	-41.6188	-38.4537	-35.07	-32.1217	-29.3603	-27.3587	-26.0006	-25.3392	1
'mordenit/10'	132.5541	63.675	(0.08685)'ca+2, (0.1083)'na+, (1.518)'sio2(aq), (1.0404)'h2o, (0.282)'alo2-	-8.344	-7.624	-6.92	-6.311	-5.712	-5.243	-4.899	-4.722	1
'opal_CT'	60.084	29	(1)'sio2(aq)	-3.5013	-3.0053	-2.6268	-2.3583	-2.1179	-1.9264	-1.7646	-1.6319	2
'plagio-ym'	266.069	100.818	(1.17)'alo2-, (0.76)'na+, (0.07)'k+, (0.17)'ca+2, (2.83)'sio2(aq)	-21.662	-20.323	-18.731	-17.275	-15.933	-15.052	-14.573	-14.45	2
'quartz'	60.084	22.688	(1)'sio2(aq)	-4.1605	-3.7501	-3.3553	-3.0132	-2.6679	-2.3823	-2.149	-1.9822	1
'sanidi-ym'	270.755	104.396	(1.05)'alo2-, (0.47)'na+, (0.48)'k+, (0.05)'ca+2, (2.95)'sio2(aq)	-21.697	-20.239	-18.508	-16.921	-15.44	-14.437	-13.843	-13.609	2
'sio2(am)'	60.084	29	(1)'sio2(aq)	-2.947	-2.714	-2.445	-2.202	-1.971	-1.802	-1.684	-1.605	2

Table C.1-1. Thermodynamic Data: Minerals (Continued)

Mineral/Gas	Molecular Weight (g/mol) ^a	Molar Volume ^{a,b} (cm ³ /mol)	Reaction Stoichiometry ^c	log(K)								Source ^d
				0 (°C)	25 (°C)	60 (°C)	100 (°C)	150 (°C)	200 (°C)	250 (°C)	300 (°C)	
'stell-ym/10'	140.865	66.55	(1,4)'h2o', (0.395)'alO2-', (0.195)'ca+2', (0.005)'na+', (1.405)'sio2(aq)	-8.946	-8.29	-7.514	-6.794	-6.104	-5.615	-5.301	-5.147	2
'tridymite'	60.084	26.586	(1)'sio2(aq)	-4.4254	-3.8278	-3.3175	-2.9063	-2.4712	-2.0568	500	500	2
'ca(no3)2'	164.088	50	(1)'ca+2', (2)'no3-'	5.7482	5.5269	5.0984	4.5333	3.7473	2.8627	1.8277	0.5123	3
'arcanite'	174.252	65.5	(2)'k+', (1)'so4-2'	-2.1629	-1.7916	-1.4973	-1.397	-1.5208	-1.8398	-2.2979	500	3
'bischofite'	203.301	129.57	(1)'mg+2', (2)'cl-', (6)'h2o'	4.5811	4.357	4.0253	3.6643	3.2042	2.6742	1.9838	0.9732	3
'halite'	58.442	27.015	(1)'cl-', (1)'na+'	1.492	1.5855	1.6176	1.578	1.4499	1.2422	0.9364	0.4683	1
'hydrophilite'	110.983	51.03	(1)'ca+2', (2)'cl-'	13.177	11.942	10.325	8.649	6.738	4.935	3.124	1.126	3
'k2co3'	138.205	50	(2)'k+', (1)'hco3-', (-1)'h+'	15.9754	15.3005	14.4517	13.606	12.6772	11.8278	10.99	10.0667	3
'kieserite'	138.384	56.6	(1)'h2o', (1)'mg+2', (1)'so4-2'	0.72	-0.024	-1.0716	-2.2058	-3.5575	-4.9071	-6.3552	-8.0716	3
'mg(no3)2'	148.315	50	(1)'mg+2', (2)'no3-'	16.5292	15.1741	13.4524	11.7254	9.8189	8.0672	6.3389	4.4551	3
'natrite'	105.989	41.86	(2)'na+', (1)'hco3-', (-1)'h+'	11.6028	10.984	10.2336	9.5237	8.7835	8.1278	7.477	6.7236	3
'niter'	101.103	48.14	(1)'k+', (1)'no3-'	-0.8418	-0.2344	0.3772	0.8541	1.2188	1.3891	1.3856	1.1754	3
'sellaite'	62.301	19.61	(1)'mg+2', (2)'f-'	-9.2699	-9.3939	-9.7091	-10.1577	-10.817	-11.6053	-12.5872	-13.9059	3
'soda_niter'	84.995	37.61	(1)'na+', (1)'no3-'	0.7192	1.0915	1.4321	1.6649	1.8721	500	500	500	3
'sylvite'	74.551	37.524	(1)'cl-', (1)'k+'	0.5252	0.8459	1.1224	1.2845	1.3297	1.2382	1.0128	0.6044	1

Table C.1-1. Thermodynamic Data: Minerals (Continued)

Mineral/Gas	Molecular Weight (g/mol) ^a	Molar Volume ^{a,b} (cm ³ /mol)	Reaction Stoichiometry ^c	log(K)							Source ^d	
				0 (°C)	25 (°C)	60 (°C)	100 (°C)	150 (°C)	200 (°C)	250 (°C)		300 (°C)
'thenardite'	142.043	53.33	(2)'na+', (1)'so4-2'	-0.1329	-0.255	-0.4272	-0.6877	-1.1778	-1.8153	-2.6255	500	3
'villiaumite'	41.988	15.05	(1)'na+', (1)'f-'	-0.2797	-0.2538	-0.2923	-0.3848	-0.5531	-0.7861	-1.1129	-1.6039	3
'co2(g)'	44.01	3.23E-10	(-1)'h2o', (1)'h+', (1)'hco3-'	-7.6765	-7.8136	-8.0527	-8.3574	-8.7692	-9.2165	-9.7202	-10.3394	1

^a Molecular weights and molar volumes from qualified database *data0.ymp.R5* (DTN: SN0612T0502404.014 [DIRS 178850]) unless listed differently in Section C.3.

^b For CO₂, this column contains the molecular diameter (in meters) from Lide (1993 [DIRS 123032], pp. 14 to 19).

^c Negative numbers in parentheses indicate the species is on the left side of equation.

^d Sources for log(K) and stoichiometry, as follows:

1. Data from qualified database *data0.ymp.R5* (DTN: SN0612T0502404.014 [DIRS 178850]).
2. Sources and calculations, if any, as described in this appendix.
3. Data from qualified database *data0.ymp.R2* (DTN: SN0609T0502404.012 [DIRS 179067]).

NOTE: Mineral names or abbreviations above are those used in the input file and may not exactly match names used in the text of the report. Names ending in /10 indicate the stoichiometry, molecular weight, molar volume, and log(K) values for those minerals were divided by 10 compared to the original data.

Table C.1-2. Thermodynamic Data: Aqueous Species

Secondary Aqueous Species	Molecular Weight (g/mol) ^a	r _{ej} ^b	Charge ^a	Reaction Stoichiometry ^c	log(K) ^a							
					0 (°C)	25 (°C)	60 (°C)	100 (°C)	150 (°C)	200 (°C)	250 (°C)	300 (°C)
'al+3'	26.982	3.33	3	(4)'h+', (1)'alo2-', (-2)'h2o'	-24.9891	-22.2038	-19.0435	-16.2051	-13.4626	-11.3393	-9.6575	-8.343
'alo+'	42.981	2.31	1	(2)'h+', (-1)'h2o', (1)'alo2-'	-13.0063	-11.862	-10.5479	-9.3616	-8.2252	-7.3761	-6.7618	-6.3922
'aloh++'	43.989	2.8	2	(3)'h+', (-1)'h2o', (1)'alo2-'	-19.2227	-17.2034	-14.9834	-13.0552	-11.2674	-9.958	-8.9969	-8.3416
'halo2(aq)'	59.988	0	0	(1)'h+', (1)'alo2-'	-6.9244	-6.6022	-6.1452	-5.6577	-5.1267	-4.6987	-4.3982	-4.2853
'co2(aq)'	44.01	0	0	(-1)'h2o', (1)'h+', (1)'hco3-'	-6.5804	-6.3447	-6.2684	-6.3882	-6.7235	-7.1969	-7.7868	-8.528
'co3--'	60.009	2.81	-2	(-1)'h+', (1)'hco3-'	10.6241	10.3288	10.1304	10.0836	10.2003	10.4648	10.8707	11.4638
'caco3(aq)'	100.087	0	0	(-1)'h+', (1)'ca+2', (1)'hco3-'	7.5046	7.0017	6.4546	5.9746	5.4924	5.057	4.5885	3.9784
'cahco3+'	101.095	2.31	1	(1)'ca+2', (1)'hco3-'	-1.094	-1.0467	-1.1579	-1.4134	-1.8483	-2.383	-3.0268	-3.8398
'caf+'	59.076	2.31	1	(1)'ca+2', (1)'f-'	-0.6546	-0.6817	-0.8624	-1.1708	-1.6504	-2.2173	-2.8881	-3.7282
'caoh+'	57.085	2.31	1	(-1)'h+', (1)'ca+2', (1)'h2o'	14.0851	12.8333	11.4163	10.1423	8.9034	7.9283	7.1264	6.4342
'caso4(aq)'	136.142	0	0	(1)'ca+2', (1)'so4-2'	-2.0713	-2.1111	-2.2647	-2.5111	-2.9102	-3.4333	-4.1436	-5.1877
'feo+'	71.844	2.31	1	(1)'h+', (-1)'h2o', (1)'hfeo2(aq)'	-7.324	-6.3682	-5.3723	-4.5614	-3.8649	-3.3929	-3.0599	-2.8073
'feo2-'	87.844	1.81	-1	(-1)'h+', (1)'hfeo2(aq)'	10.2309	9.6023	8.8391	8.1111	7.3806	6.8216	6.4302	6.2494
'feoh++'	72.852	2.8	2	(2)'h+', (-1)'h2o', (1)'hfeo2(aq)'	-11.4093	-9.8133	-8.1736	-6.8533	-5.7273	-4.9638	-4.4151	-3.9794
'fef++'	74.843	2.8	2	(1)'f-', (3)'h+', (-2)'h2o', (1)'hfeo2(aq)'	-20.032	-18.0177	-16.0383	-14.5457	-13.4176	-12.8268	-12.6081	-12.6965
'fef2+'	93.842	2.31	1	(2)'f-', (3)'h+', (-2)'h2o', (1)'hfeo2(aq)'	-22.3228	-20.3679	-18.4587	-17.0371	-16.0107	-15.5689	-15.5896	-16.0864
'feso4+'	151.909	2.31	1	(1)'so4-2', (3)'h+', (-2)'h2o', (1)'hfeo2(aq)'	-15.8455	-13.9456	-12.0892	-10.7002	-9.6806	-9.2129	-9.1791	-9.6018
'fe+++'	55.845	3.46	3	(3)'h+', (1)'hfeo2(aq)', (-2)'h2o'	-14.3047	-12.018	-9.6021	-7.5941	-5.8067	-4.5205	-3.5296	-2.6957
'fecl++'	91.298	2.8	2	(1)'cl-', (3)'h+', (-2)'h2o', (1)'hfeo2(aq)'	-15.7702	-13.4979	-11.2173	-9.4491	-8.0466	-7.2301	-6.8133	-6.7213

Table C.1-2. Thermodynamic Data: Aqueous Species (Continued)

Secondary Aqueous Species	Molecular Weight (g/mol) ^a	r_{ej} ^b	Charge ^a	Reaction Stoichiometry ^c	log(K) ^a							
					0 (°C)	25 (°C)	60 (°C)	100 (°C)	150 (°C)	200 (°C)	250 (°C)	300 (°C)
'hf(aq)'	20.006	0	0	(1)'f-', (1)'h+'	-2.9654	-3.1791	-3.4948	-3.8477	-4.3264	-4.9345	-5.7479	-6.8164
'hf2-'	39.005	1.81	-1	(2)'f-', (1)'h+'	-3.4639	-3.7101	-4.1266	-4.5367	-5.0532	-5.8324	500	500
'hno3(aq)'	63.013	0	0	(1)'h+', (1)'no3-'	1.5397	1.3026	0.9516	0.5563	0.0741	-0.4117	-0.9362	-1.5794
'hso4-'	97.072	2.37	-1	(1)'h+', (1)'so4-2'	-1.7193	-1.9791	-2.4371	-3.0002	-3.7234	-4.4683	-5.2633	-6.1799
'hsio3-'	77.092	1.81	-1	(-1)'h+', (1)'h2o', (1)'sio2(aq)'	10.2895 ^d (9.8105)	9.8419 ^d (9.5853)	9.3658 ^d (9.2406)	9.0315 ^d (8.9596)	8.8598 ^d (8.8018)	8.8949 ^d (8.8329)	9.0985 ^d (9.0353)	9.4741 ^d (9.4329)
'khsa4(aq)'	136.17	0	0	(1)'h+', (1)'k+', (1)'so4-2'	2.0393	1.4953	0.5948	-0.4756	-1.8165	-3.172	-4.6006	-6.2423
'kso4-'	135.162	1.81	-1	(1)'k+', (1)'so4-2'	-0.8855	-0.8796	-0.9908	-1.195	-1.5212	-1.9206	-2.4186	-3.0896
'mgco3(aq)'	84.314	0	0	(-1)'h+', (1)'hco3-', (1)'mg+2'	7.7424	7.3499	6.9292	6.5742	6.2284	5.9109	5.5428	5.0192
'mgf+'	43.303	2.31	1	(1)'f-', (1)'mg+2'	-1.3869	-1.3524	-1.4781	-1.7394	-2.1692	-2.6911	-3.321	-4.1254
'mghco3+'	85.322	2.31	1	(1)'hco3-', (1)'mg+2'	-1.077	-1.0357	-1.1604	-1.4229	-1.8523	-2.3688	-2.9844	-3.7577
'mgoh+'	41.312	2.31	1	(-1)'h+', (1)'h2o', (1)'mg+2'	12.6741	11.6825	10.5017	9.3988	8.2907	7.3921	6.6344	5.9667
'mgso4(aq)'	120.369	0	0	(1)'mg+2', (1)'so4-2'	-2.1842	-2.2298	-2.3929	-2.6408	-3.0307	-3.5393	-4.2363	-5.2714
'naf(aq)'	41.988	0	0	(1)'f-', (1)'na+'	1.0818	0.9976	0.8328	0.6233	0.3376	0.0096	-0.3965	-0.9574
'nahco3(aq)'	84.007	0	0	(1)'hco3-', (1)'na+'	-0.3983	-0.1541	0.075	0.2444	0.3582	0.374	0.2765	0.0043
'naso4-'	119.053	1.81	-1	(1)'na+', (1)'so4-2'	-0.6765	-0.7	-0.8416	-1.0629	-1.3893	-1.7724	-2.2416	-2.873
'oh-'	17.007	1.4	-1	(-1)'h+', (1)'h2o'	14.9398	13.9951	13.0272	12.2551	11.6308	11.2836	11.1675	11.3002

Table C.1-2. Thermodynamic Data: Aqueous Species (Continued)

Primary Aqueous Species	Molecular Weight (g/mol) ^a	r_{ej} ^b	Charge ^a
'h2o'	18.015	0	0
'h+'	1.008	3.08	1
'alo2-'	58.98	1.81	-1
'ca+2'	40.078	2.87	2
'cl-'	35.453	1.81	-1
'f-'	18.998	1.33	-1
'hco3-'	61.017	2.1	-1
'k+'	39.098	2.27	1
'mg+2'	24.305	2.54	2
'na+'	22.99	1.91	1
'so4-2'	96.064	3.15	-2
'sio2(aq)'	60.084	0	0
'hfeo2(aq)'	88.852	0	0
'no3-'	62.005	2.81	-1

^a Data from qualified database *data0_ypm.R5* (DTN: SN0612T0502404.014 [DIRS 178850]) unless indicated differently.

^b Effective ionic radius for calculation of activity coefficients. See Section C.2 of this appendix.

^c Negative numbers in parentheses indicate that the species is on the left side of equation.

^d Data from a superseded version of *data0_ypm.R5* (DTN: SN0610T0502404.013 [DIRS 178113]) were used as input. Actual revised data from DTN: SN0612T0502404.014 [DIRS 178850] are shown in parentheses. The model results are not significantly impacted by this revision (see Section C.9).

C.2 DATA FOR THE CALCULATION OF ACTIVITY COEFFICIENTS

C.2.1 Source of Data

Effective ionic radii r_{ej} are used for the calculation of activity coefficients for charged aqueous species, and are from Helgeson et al. (1981 [DIRS 106024], Table 3). These data are an integral part of the activity coefficient formulation implemented into TOUGHREACT V3.1.1 (see Section 3.1), which is also from Helgeson et al. (1981 [DIRS 106024]). Approximations for r_{ej} values were made for species not listed by these authors, as shown in Table C.2-1. For neutral species, the r_{ej} values are set to zero and activity coefficients set to 1.

Table C.2-1. Values of Effective Ionic Radii ($r_{e,j}$)

Ion Charge	r_{ej}	Source ^a
-1	1.81	Cl ⁻ value
-2	3.00	Rounded average of CO ₃ ²⁻ and SO ₄ ²⁻ values
-3	4.2	Estimated from straight line fit with charge
+1	2.31	NH ₄ ⁺ value
+2	2.8	Rounded average for +2 species
+3	3.6	Rounded average for +3 species

^a Values are either directly from Helgeson et al. (1981 [106024], Table 3) or, if not available, calculated from the data of these authors as indicated in this column.

Further information on the calculation and verification of activity coefficients can be found in the User Information Document for TOUGHREACT V3.1.1 (DOE 2007 [DIRS 182183], Attachment A, Section H).

C.2.2 Qualification of the Effective Ionic Radii r_{ej} from Helgeson et al. (1981 [DIRS 106024], Table 3)

The effective ionic radii data from Helgeson et al. (1981 [DIRS 106024], Table 3) are qualified for intended use with Method 5 of SCI-PRO-001 (Technical Assessment). The data shown in Table C.2-1 are considered qualified for intended use based on the following attributes:

- Attribute 1: The first author of this data, Harold C. Helgeson, was a world-renowned professor of geochemistry (Ph.D. in Geochemistry) in the Department of Geology and Geophysics at the University of California, Berkeley. Co-author George C. Flowers is a professor of geochemistry (Ph.D. in Geochemistry) at the Department of Earth and Environmental Sciences at Tulane University. The qualifications of these authors are comparable to, or exceed, the qualification requirements of personnel generating thermodynamic data under Yucca Mountain Project procedures that support the YMP license application process or postclosure science.
- Attribute 7: These data were developed specifically for, and are an integral part of, the implemented activity coefficient model (an extended Debye-Hückel equation, referred to as the “HKF” model). These data, as well as the HKF formulation, are an integral part of TOUGHREACT V3.1.1 (see Section 3.1), used in the simulations for this model report. These data and the HKF model have been extensively verified and validated with

experimental data in the User Information Document for TOUGHREACT V3.1.1 (DOE 2007 [DIRS 182183], Attachment A, Section H).

- Attribute 8: The paper by Helgeson et al. (1981 [DIRS 106024]) was published in the *American Journal of Science*. This journal is considered one of the top peer-reviewed journals in its field. Papers published in this journal are carefully reviewed by typically at least three independent experts, such that the quality of the paper is assured.

C.3 MOLECULAR WEIGHTS AND MOLAR VOLUMES

C.3.1 Source of Data

When available, molecular weights and molar volumes were taken from qualified DTN: SN0612T0502404.014 [DIRS 178850] (also see Section C.9). Data sources for a few minerals for which these data were not available are discussed below.

For mordenite, the molar volume was taken from Chipera and Apps (2001 [DIRS 171017], Table 3), for the phase listed as diagenetic alteration of volcanic tuff. This data source is qualified for intended use in Section C.3.2. The value given by Chipera and Apps for a mineral formula on the basis of 72 oxygen atoms was divided by 2, then by 10, for the formula used here on the basis of 36/10 oxygen atoms.

For amorphous antigorite, the molar volume of antigorite given in qualified DTN: SN0612T0502404.014 [DIRS 178850] was taken. The value on the basis of 34 oxygen atoms was divided by 17 for the given amorphous antigorite formula, which is on the basis of 2 oxygen atoms.

For tridymite, the molar volume was obtained by dividing the molecular weight of 60.084 g/mol from qualified DTN: SN0612T0502404.014 [DIRS 178850] by the density of 2.26 g/cm³ given by Deer et al. (1978 [DIRS 171183], p. 340). The latter source is a widely used reference book, from which the density of tridymite is considered established fact data.

Molar volumes of hydrophilite, niter, soda-niter, and villiaumite were obtained by dividing the densities of these salts (from Lide 1993 [DIRS 123032], established fact data) by their molecular weights (from qualified DTN: SN0612T0502404.014 [DIRS 178850]). Molar volume values for Ca(NO₃)₂, Mg(NO₃)₂, and K₂CO₃ were not readily available and were set to 50 cm³/mol, within the range of values of other salts such as natrite (Na₂CO₃, 41.86 cm³/mol), niter (KNO₃, 48.14 cm³/mol), hydrophilite (CaCl₂, 51.03 cm³/mol), arcanite (K₂SO₄, 65.5 cm³/mol), and thenardite (Na₂SO₄, 53.33 cm³/mol).

C.3.2 Qualification of Mordenite Molar Volume from Chipera and Apps (2001 [DIRS 171017], Table 3)

Chipera and Apps (2001 [DIRS 171017], Table 3) published thermodynamic data for zeolite minerals from boreholes at Yucca Mountain and molar volumes for various zeolites, including mordenite. The mordenite molar volume from this source is qualified for the intended use in this report using Method 5, Technical Assessment. These data are considered qualified for intended use based on the following attributes:

- Attribute 2: The zeolite compositions and estimated molar volumes from Chipera and Apps (2001 [DIRS 171017], Table 3) represent zeolites from Yucca Mountain borehole cores. The use of site-specific data is highly desirable. The molar volume of mordenite from this data source is adequate for intended use because it was derived from data collected and developed using standard scientific practices. It is relevant to Yucca Mountain because it is based on mineral compositions specific to Yucca Mountain. The zeolite formulas reported by Chipera and Apps (2001 [DIRS 171017], Table 3) were derived from electron microprobe analyses of the vitric Topopah Springs Tuff, and the molar volume of mordenite was then based on these formulae.

One way to check the adequacy for intended use of the mordenite molar volume value given by Chipera and Apps (2001 [DIRS 171017], Table 3) is to use the partial molar volumes of raw oxides in qualified database *data0.ymp.R5* (DTN: SN0612T0502404.014 [DIRS 178850]), multiply these volumes by the mole fraction of each oxide in the mineral (using the implemented mineral formula), then sum the corresponding volume to get the total volume. This is an approximate method, ignoring mixing effects and differences in thermodynamic properties of zeolitic versus pure water. Nevertheless, the method is useful to estimate an approximate molar volume. The table below shows that by applying this method using the mordenite formula from the qualified *data0.ymp.R5* database (adopted in this study), a value close to that given by Chipera and Apps is obtained (within ~ 6%), well within the uncertainty of the THC seepage model results (Section 6.7.2).

Table C.3-1. Verification of Suitability for Intended Use of the Mordenite Molar Volume from Chipera and Apps (2001 [DIRS 171017], Table 3)

Mordenite formula: $\text{Ca}_{0.2895}\text{Na}_{0.361}\text{Al}_{0.94}\text{Si}_{5.06}\text{O}_{12} \cdot 3.468\text{H}_2\text{O}^{(a)}$			
Mordenite molar volume (cm^3/mol): 212.25 ^(b)			
Mole Fraction in Formula	Oxide	V (cm^3/mol) ^(a,c)	V × Mole Fraction (cm^3/mol)
0.2895	CaO	16.764	4.85
0.47	Al ₂ O ₃	25.575	12.02
3.468	H ₂ O	18.02	62.48
0.1805	Na ₂ O	25	4.51
5.06	SiO ₂	22.688	114.80
			sum = 198.66
			% difference = -6.4

^a From qualified DTN SN0612T0502404.014 [DIRS 178850] (adopted in this study).

^b Value of 1273.5 cm^3/mol from Chipera and Apps (2001 [DIRS 171017], Table 3), divided by 6 to reflect a formula on the basis of 12 oxygen atoms instead of 72 (adopted in this study).

^c For H₂O, the molar volume is estimated from the molecular weight in DTN: SN0612T0502404.014 [DIRS 178850] divided by the density of 1 cm^3/g approximated from Lide (1993 [DIRS 123032], established fact data).

- Attribute 8: An assessment of the methods of data collection and development used by Chipera and Apps (2001 [DIRS 171017]) also provides confidence in the zeolite formulae and molar volumes presented in their paper. The paper is published in the well-known *Reviews in Mineralogy and Geochemistry* and presents a scholarly

investigation into the stability of zeolite minerals in Yucca Mountain pore waters. This provides confidence in the data from this source.

C.4 SILICA PHASES

C.4.1 Amorphous Silica Log(K) Values from Gunnarsson and Arnórsson 2000 [DIRS 160465]

C.4.1.1 Source of Data

Log(K) values for this study were taken from Gunnarsson and Arnórsson (2000 [DIRS 160465]). Gunnarsson and Arnórsson (2000 [DIRS 160465], Figure 2) show that their data closely fit experimental amorphous silica solubilities from about 8°C to 300°C. These data are close to log(K) values for amorphous silica in the qualified database *data0.ymp.R5* (DTN: SN0612T0502404.014 [DIRS 178850]) (Table C.4-1). However, no values are given in *data0.ymp.R5* above 100°C, and the solubility in *data0.ymp.R5* below 25°C appears to be underestimated. The data of Gunnarsson and Arnórsson (2000 [DIRS 160465]) are qualified for intended use in Section C.4.1.2.

Calculations of the log(K) values from regression coefficients provided by Gunnarsson and Arnórsson (2000 [DIRS 160465], p. 2295) and conversions to solubilities shown in Table C.4-1 were implemented in spreadsheet *amorphous_sio2.xls* and submitted to the TDMS under Output DTN: LB0706DSTHC006.001.

Table C.4-1. Amorphous Silica Equilibrium Constants and Solubility

Temperature in (°C) >	0	25	60	100	150	200	250	300
Source	Log(K) for reaction $\text{SiO}_{2(s)} \rightleftharpoons \text{SiO}_{2(aq)}$							
Gunnarsson and Arnórsson 2000 [DIRS 160465]	-2.947	-2.714	-2.445	-2.202	-1.971	-1.802	-1.684	-1.605
<i>data0.ymp.R5</i>	-3.124	-2.7136	-2.4067	-2.1843	No data	No data	No data	No data
Source	Solubility in ppm SiO_2							
Gunnarsson and Arnórsson 2000 [DIRS 160465]	68	116	216	378	643	947	1,245	1,491
<i>data0.ymp.R5</i>	45	116	236	393	No data	No data	No data	No data

Output DTN: LB0706DSTHC006.001.

C.4.1.2 Qualification of Amorphous Silica Log(K) Values from Gunnarsson and Arnórsson (2000 [DIRS 160465])

The log(K) data obtained from Gunnarsson and Arnórsson (2000 [DIRS 160465]) are qualified for intended use with Method 5 of SCI-PRO-001 (Technical Assessment). These data are considered qualified for intended use based on the following attributes:

- Attribute 1: The first author of the data, Ingvi Gunnarsson, is a research associate in geology and his research area is chemistry of groundwater. The second author of this

data, Stefán Arnórsson, is a professor in geochemistry. Both authors are from the Science Institute, University of Iceland. The qualifications of these authors are comparable to, or exceed, the qualification requirements of personnel generating thermodynamic data under Yucca Mountain Project procedures that support the YMP license application process or postclosure science.

- Attribute 2: The solubility of amorphous silica was experimentally determined by Gunnarsson and Arnórsson (2000 [DIRS 160465]). In their experiments, the equilibrium of the amorphous silica solution was approached from (1) undersaturation, (2) supersaturation without silica gel present, and (3) supersaturation with silica gel present, respectively. The $\log(K)$ values for amorphous silica were then calculated using the measured solubilities. The $\log(K)$ values have been corroborated by the authors by comparisons to other data from 11 other sources (see Figure 2 in Gunnarsson and Arnórsson 2000 [DIRS 160465]). The comparison indicates that significant deviations are observed only for a few old data points (published in 1935) and for temperatures higher than 300°C. Otherwise, all data from the different sources reviewed by Gunnarsson and Arnórsson agree well. This comparison supports the technical adequacy of the procedures used by Gunnarsson and Arnórsson to derive their $\log(K)$ values.
- Attribute 3: The amorphous silica solubility measurements of Gunnarsson and Arnórsson (2000 [DIRS 160465]) were conducted from 8°C to 310°C at 1 bar below 100°C and at water saturation pressures at higher temperatures, and therefore their $\log(K)$ values derived from these measurements are valid for the same temperature and pressure range. These temperature and pressure ranges encompass the ranges used in the present report.
- Attribute 8: The paper by Gunnarsson and Arnórsson (2000 [DIRS 160465]) was published in *Geochimica et Cosmochimica Acta*. This journal is considered one of the top peer-reviewed journals in its field. Papers published in this journal are carefully reviewed by typically at least three independent experts, such that the quality of the paper is assured.

C.4.2 α -Cristobalite $\log(K)$ Values Derived from Fournier and Rowe (1962 [DIRS 124282])

C.4.2.1 Source of Data

$\log(K)$ values for α -cristobalite were derived from solubility measurements by Fournier and Rowe (1962 [DIRS 124282]), which were used by Helgeson et al. (1978 [DIRS 101596]) to derive reference thermodynamic properties for this phase. These reference properties were then used by others to derive $\log(K)$ values in the EQ3/6 database *data0.ymp.R0* (DTN: MO0009THERMODYN.001 [DIRS 152576]), which is qualified. The same values as in this qualified database are used here. The differences between these selected data and those in *data0.ymp.R5* are small (Table C.4-2). However, the data selected in the present study reproduce more accurately the original solubility measurements reported by Fournier and Rowe (1962 [DIRS 124282]) (Figure C.4-1). The qualification of the data from Fournier and Rowe is presented in Section C.4.2.2.

Conversions of log(K) data to solubilities for Table C.4-2 were implemented in spreadsheet *crystalite-a.xls* and submitted to the TDMS under Output DTN: LB0706DSTHC006.001.

C.4.2.2 Qualification of the Data from Fournier and Rowe (1962 [DIRS 124282])

The solubility measurements of Fournier and Rowe (1962 [DIRS 124282]) are qualified for intended use with Method 5 of SCI-PRO-001 (Technical Assessment). These data are considered qualified based on the following attributes:

- Attribute 1: The author of the data, Robert O. Fournier, is a geochemist at the U.S. Geological Survey in Menlo Park, California. The qualifications of this author are comparable to, or exceed, the qualification requirements of personnel generating thermodynamic data under the Yucca Mountain Project procedures that support the YMP license application process or postclosure science.
- Attribute 8: Data from Fournier and Rowe (1962 [DIRS 124282]) were published in *American Mineralogist* by the Mineralogical Society of America. The Mineralogical Society of America (MSA) was founded in 1919 for the advancement of mineralogy, crystallography, geochemistry, and petrology, and promotion of their uses in other sciences, industry, and the arts. The MSA is one of the top organizations in its field. Papers published by the MSA are carefully reviewed by typically at least three independent experts such that the quality of the paper is assured.
- Attribute 2: The solubility data from Fournier and Rowe (1962 [DIRS 124282]) can be independently verified with data from Rimstidt and Barnes (1980 [DIRS 101708], Table 1). These authors present a regression equation for the temperature-dependent log(K) values of α -cristobalite (at 1 bar and along the water saturation pressure curve above 100°C):

$$\log(K)_{\alpha\text{-cristobalite}} = -0.0321 - 998.2/T \quad (\text{Eq. C.4-1})$$

where T is absolute temperature in K. Log(K) values obtained with Equation C.4-1 were converted to solubility (S in ppm) at different temperatures using the following relationship (assuming ideal solutions):

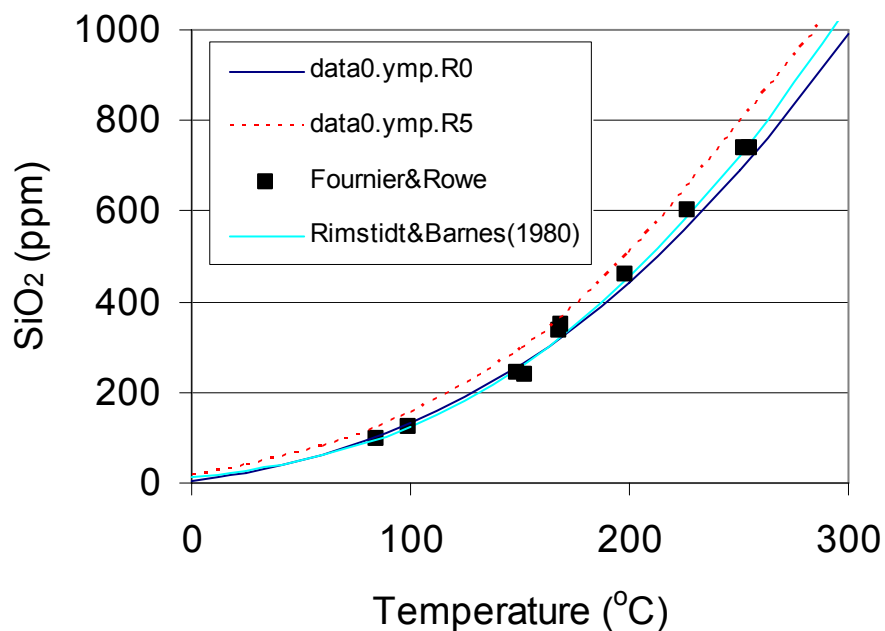
$$S = 10^{\log(K)} 1000 MW_{\text{SiO}_2} \quad (\text{Eq. C.4-2})$$

where MW_{SiO_2} is the molecular weight of SiO_2 (60.084, from the qualified *data0.ymp.R5* database; DTN: SN0612T0502404.014 [DIRS 178850]). The solubility values obtained in this way are compared in Table 4.7-1 and Figure C.4-1 with the data of Fournier and Rowe (1962 [DIRS 124282]). These data are also compared with solubilities calculated in the same manner using log(K) values from qualified databases *data0.ymp.R0* and *data0.ymp.R5*. The data from Rimstidt and Barnes (1980 [DIRS 101708], Table 1) fall very close to the data from Fournier and Rowe (1962 [DIRS 124282]) and from *data0.ymp.R0* (DTN: MO0009THRMODYN.001 [DIRS 152576]), thus supporting the adequacy of procedures used to derive the log(K) values selected for this study, as well as the adequacy of the α -cristobalite log(K) values selected for this study.

Table C.4-2. α -Cristobalite Equilibrium Constants and Solubility

Temperature in (°C) >	0	25	60	100	150	200	250	300
Source	Log(K) for reaction $\text{SiO}_{2(s)} \rightleftharpoons \text{SiO}_{2(aq)}$							
<i>data0.ymp.R0</i> (DTN: MO0009THERMODYN.001 [DIRS 152576])	-4.0213	-3.4488	-2.9921	-2.6605	-2.3644	-2.1326	-1.9402	-1.7832
Data from Rimstidt and Barnes 1980 [DIRS 101708], Table 1	-3.6486	-3.3454	-2.9974	-2.6797	-2.3669	-2.1202	-1.9207	-1.7560
<i>data0.ymp.R5</i> (DTN: SN0612T0502404.014 [DIRS 178850])	-3.5423	-3.1922	-2.867	-2.5887	-2.3064	-2.0706	-1.877	-1.742
Source	Solubility in ppm SiO2							
<i>data0.ymp.R0</i> (DTN: MO0009THERMODYN.001 [DIRS 152576])	6	21	61	131	260	443	690	990
Data from Rimstidt and Barnes 1980 [DIRS 101708], Table 1	13	27	60	126	258	456	721	1,054
<i>data0.ymp.R5</i> (DTN: SN0612T0502404.014 [DIRS 178850])	17	39	82	155	297	511	798	1,088

Output DTN: LB0706DSTHC006.001.



Output DTN: LB0706DSTHC006.001.

Figure C.4-1. α -Cristobalite Solubility

C.4.3 Opal-CT Log(K) Values Derived from Fournier (1973 [DIRS 153464])

C.4.3.1 Source of Data

Fournier (1973 [DIRS 153464]) reported on the aqueous solubility of a phase described as “natural sinter with a β -cristobalite x-ray pattern,” derived from a hot spring in Yellowstone National Park. This was inferred by Walther and Helgeson (1977 [DIRS 133240]) to be a “cryptocrystalline” form of β -cristobalite. Using the solubility data given graphically by Fournier and their own thermodynamic properties of $\text{SiO}_2(\text{aq})$, Walther and Helgeson derived thermodynamic properties for this phase, which were subsequently incorporated in a thermodynamic database by Helgeson et al. (1978 [DIRS 101596]). These data were subsequently used in the development of qualified database *data0.ymp.R0* (DTN: MO0009THERMODYN.001 [DIRS 152576]), all under the name of β -cristobalite. There can be no doubt that this phase is not β -cristobalite. Apart from the fact that β -cristobalite is highly unlikely to persist metastably below the α - β -cristobalite transition at 210°C (Richet and Bottinga 1982 [DIRS 160486]), the solubility curve does not even become close to intersecting the α -cristobalite solubility curve at the transition temperature, whether “cryptocrystalline” or not, which it would if it were a true β -cristobalite.

Because the log(K) values for β -cristobalite in *data0.ymp.R0* correspond to the solubility measurements by Fournier (1973 [DIRS 153464]) (Figure C.4-2), and thus presumably to measured opal-CT solubilities, these values were adopted in this study for opal-CT. The choice of these data is also supported by the fact that these log(K) values represent quite well the measured silica solubility at ambient temperatures (typically in the 50 to 60 mg/L range) in most analyses of pore waters in repository host units (e.g., samples from the ECRB (DTN: GS020408312272.003 [DIRS 160899]); from SD-9 (DTN: GS041108312272.005 [DIRS 178057]); and from the ESF (DTN: GS031008312272.008 [DIRS 166570])). Indeed, opal-CT is one of the most common fracture- and cavity-lining minerals in Yucca Mountain besides calcite (e.g., Whelan et al. 2002 [DIRS 160442]). Note that the β -cristobalite log(K) values in *data0.ymp.R5* yield solubilities that are too high to be representative of opal-CT (Table C.4-3). The qualification for intended use of Fournier’s solubility data is presented in Section C.4.3.2.

Conversions of log(K) data to solubilities were implemented in spreadsheet *opal-CT.xls* and submitted to the TDMS under Output DTN: LB0706DSTHC006.001.

C.4.3.2 Qualification of Data from Fournier (1973 [DIRS 153464])

The solubility measurements of Fournier (1973 [DIRS 153464]) are qualified using Method 5 of SCI-PRO-001 (Technical Assessment). These data are considered qualified based on the following attributes:

- Attribute 1: The author of the data, Robert O. Fournier, is a geochemist at the U.S. Geological Survey in Menlo Park, California. The qualifications of this author are comparable to, or exceed, qualification requirements of personnel generating thermodynamic data under Yucca Mountain Project procedures that support the YMP license application process or postclosure science.

- Attribute 8: This paper by Fournier (1973 [DIRS 153464]) was published in *Proceedings of Symposium on Hydrogeochemistry and Biogeochemistry*. Papers published in these proceedings were carefully reviewed by at least one independent expert such that the quality of the paper is assured.
- Attribute 2: The data from Fournier (1973 [DIRS 153464]) can be verified using data from Rimstidt and Barnes (1980 [DIRS 101708], Table 1). These authors present a regression equation for the temperature-dependent log(K) values of β -cristobalite (at 1 bar and along the water saturation pressure curve above 100°C):

$$\log(K)_{\beta\text{-cristobalite}} = -0.2560 - 793.6/T \quad (\text{Eq. C.4-3})$$

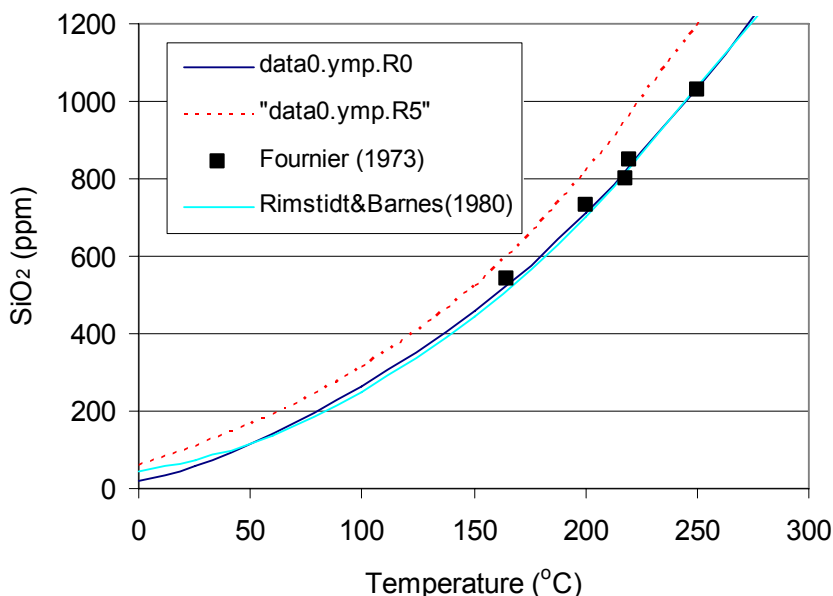
where T is absolute temperature in K. Using log(K) values calculated with this equation, then converting these values to solubility using Equation C.4-2, yields solubility values in close agreement with the data of Fournier (1973 [DIRS 153464]). For temperatures of 25°C and higher, the data are also very close to the data from *data0.ymp.R0* (DTN: MO0009THERMODYN.001 [DIRS 152576]), thus supporting the adequacy of procedures used to derive the log(K) values selected for this study.

Table C.4-3. Equilibrium Constants and Solubility for “ β -cristobalite”

Temperature in (°C) >	0	25	60	100	150	200	250	300
Source	Log(K) for reaction $\text{SiO}_{2(s)} \rightleftharpoons \text{SiO}_{2(aq)}$							
<i>data0.ymp.R0</i> (DTN: MO0009THERMODYN.001 [DIRS 152576])	-3.501	-3.005	-2.627	-2.358	-2.118	-1.926	-1.765	-1.632
Data from Rimstidt and Barnes 1980 [DIRS 101708], Table 1	-3.1603	-2.9168	-2.6374	-2.3822	-2.1310	-1.9329	-1.7727	-1.6404
<i>data0.ymp.R5</i> (DTN: SN0612T0502404.014 [DIRS 178850])	-3.0224	-2.7488	-2.5016	-2.2865	-2.0599	-1.8643	-1.7014	-1.5907
	Solubility in ppm SiO₂							
<i>data0.ymp.R0</i> (DTN: MO0009THERMODYN.001 [DIRS 152576])	19	59	142	263	458	712	1,032	1,402
Data from Rimstidt and Barnes 1980 [DIRS 101708], Table 1	42	72	138	249	444	701	1,041	1,375
<i>data0.ymp.R5</i> (DTN: SN0612T0502404.014 [DIRS 178850])	57	107	189	311	523	821	1,195	1,542

Output DTN: LB0706DSTHC006.001.

NOTE: Bold log(K) values represent the values adopted for opal-CT in this study (see text of Section C.4.3).



Output DTN: LB0706DSTHC006.001.

Figure C.4-2. β -Cristobalite solubility

C.4.4 Tridymite Log(K) Values from the EQ3/6 Database *data0.com*

C.4.4.1 Source of Data

The tridymite log(K) value at 25°C was taken from the qualified *data0.ymp.R5* database (DTN: SN0612T0502404.014 [DIRS 178850]), reflecting reference data reported by Wagman et al. (1982 [DIRS 159216]). There are no log(K) values for tridymite listed at temperatures other than 25°C in the *data0.ymp.R5* database. However, the 25°C value in this database is the same as that in the EQ3/6 database *data0.com* (dated 02-aug-1995) (database distributed with EQ3/6 V. 7.2b [DIRS 126891], LLNL: UCRL-MA-110662), which also lists log(K) values from 0°C to 200°C estimated (from the 25°C data) using a constant enthalpy of reaction with temperature. The data from *data0.com* at temperatures other than 25°C were not included in the qualified *data0.ymp.R5* database because of uncertainties regarding the constant-enthalpy extrapolation method. However, as discussed below, the log(K) values for tridymite in this study do not need to be known with great accuracy, such that their uncertainty at elevated temperature is acceptable, at least for the intended use of these data in the present report. For this reason, the tridymite log(K) values at temperatures different than 25°C were taken directly from the *data0.com* database. These log(K) values are qualified for intended use in Section C.4.4.2.

C.4.4.2 Qualification of the Tridymite Log(K) Values in EQ3/6 Database *data0.com*

The log(K) values for tridymite in the EQ3/6 database *data0.com* are qualified using Method 5 of SCI-PRO-001 (Technical Assessment). These data are considered qualified for intended use based on the following attributes:

- Attribute 1: The author of the database, Thomas Wolery, is a geochemist at Lawrence Livermore National Laboratory in Livermore, California. The qualifications of this

author are comparable to, or exceed, qualification requirements of personnel generating thermodynamic data under Yucca Mountain Project procedures that support the YMP license application process or postclosure science.

- Attribute 2: The range of tridymite log(K) values in *data0.com* is verified using log(K) values for quartz from the qualified project database *data0.ymp.R5*. There is little difference in the thermodynamic properties of quartz and tridymite (see DTN: SN0612T0502404.014 [DIRS 178850]), and thus one would expect the log(K) values of these two phases to be of similar magnitude, and to behave similarly with temperature. The data in Table C.4-4 show that between 25°C and 100°C (which is about the temperature range for aqueous reactions in this study), the log(K) values for these minerals differ by ~0.1 log(K) units or less. This difference is considered small, given that the uncertainty in concentrations predicted by the model is up to two orders of magnitude (Section 6.7.2). As noted earlier, the value at 25°C from *data0.com* also matches exactly the value in the qualified database *data0.ymp.R5*, which is consistent with the use of log(K) values from *data0.com* at temperatures other than 25°C. These comparisons provide confidence in the adequacy of procedures used to derive the log(K) values selected for this study. It should also be noted that pore waters generally remain supersaturated with respect to tridymite and this mineral is not allowed to precipitate in the simulations presented in this report. Also, when tridymite dissolves, which occurs only in zones of high condensation and dilution, its dissolution rate is very small (Appendix H). Because this mineral is not reacting at equilibrium, the accuracy of the tridymite log(K) values is not critical. Therefore, justifying the use of these values on the basis that they do not differ much from quartz is reasonable.

The comparison of quartz and tridymite thermodynamic data was summarized in spreadsheet *tridymite.xls* and submitted to the TDMS under Output DTN: LB0706DSTHC006.001.

Table C.4-4. Equilibrium Constants of Tridymite and Quartz

Temperature in (°C) >	0	25	60	100	150	200	250	300
Source	Log(K) for reaction $\text{SiO}_2(\text{s}) \rightleftharpoons \text{SiO}_2(\text{aq})$							
Tridymite from <i>data0.com</i> (database distributed with EQ3/6 V. 7.2b)	-4.4254	-3.8278 ^(a)	-3.3175	-2.9063	-2.4712	-2.0568	No data	No data
Quartz from <i>data0.ymp.R5</i> (DTN: SN0612T0502404.014 [DIRS 178850])	-4.1605	-3.7501	-3.3553	-3.0132	-2.6679	-2.3823	-2.149	-1.9822
Difference in log(K) values	-0.26	-0.08	0.04	0.11	0.20	0.33	—	—

Output DTN: LB0706DSTHC006.001.

^(a) Same value as in qualified database *data0.ymp.R5* (DTN: SN0612T0502404.014 [DIRS 178850]).

C.5 FELDSPARS

The feldspars considered in this study consist of plagioclase and sanidine. There are no data for mixed feldspars in the project database *data0.ymp.R5*. Log(K) values for these phases were derived from regression coefficients of log(K) as a function of temperature presented by Arnórsson and Stefansson (1999 [DIRS 153329]). The study by these authors can be considered

the best recent comprehensive assessment of thermodynamic data for feldspars. The data from this paper are qualified for intended use in Section C.5.3.

Calculations of feldspar log(K) values were implemented in spreadsheet *ymp-feldspar.xls*. This spreadsheet was submitted to the TDMS under Output DTN: LB0706DSTHC006.001.

C.5.1. Plagioclase Log(K) Calculations

The plagioclase composition (Ab76, An17, San7) was taken from Johnson et al. (1998 [DIRS 101630], Table 6) (qualified for intended use in Appendix O, Section O.3). It is representative of analyses of Yucca Mountain tuffs and corresponds to the formula $\text{Na}_{0.76}\text{K}_{0.07}\text{Ca}_{0.17}\text{Al}_{1.17}\text{Si}_{2.83}\text{O}_8$.

First, log(K) values were calculated for a solid-solution of low-albite and anorthite, in normalized proportions excluding sanidine (Ab81.72, An18.28). This was done by linear interpolation of log(K) values obtained from Arnórsson and Stefansson (1999 [DIRS 153329], Table 6, “low” series) for Ab90-An10 and Ab80-An20 compositions. Log(K) values were thus obtained in this way for a phase without sanidine.

The log(K) values for pure sanidine were then calculated using the data of Arnórsson and Stefansson (1999 [DIRS 153329], p. 173). Final log(K) values for the phase Ab76-An17-San7 were then calculated assuming an ideal solution of the Ab-An phase with pure sanidine, using the formula:

$$\log(K) = \sum_i x_i \log K_i + \sum_i x_i \log x_i \quad (\text{Eq. C.5-1})$$

where x_i and $\log K_i$ are the molar fractions and log(K) values, respectively, of the Ab-An and pure sanidine phases. This formula can be easily derived from standard thermodynamic relationships.

Details of this calculation can be found in spreadsheet *ymp-feldspar.xls*, worksheet “plagioclase.”

C.5.2. Sanidine Log(K) Calculations

The sanidine composition (San48, Ab47, An5) was calculated by least squares regression using bulk rock composition from DTN: GS000308313211.001 [DIRS 162015], after subtracting 1% plagioclase and calcite equivalent to CO₂ in the rock, as documented in spreadsheet *tsw_plag_bulk_rev05.xls*. This composition is representative of Yucca Mountain tuff, and corresponds to the formula $\text{Na}_{0.47}\text{K}_{0.48}\text{Ca}_{0.05}\text{Al}_{1.05}\text{Si}_{2.95}\text{O}_8$.

First, log(K) values were calculated for a solid-solution of sanidine and albite, in normalized proportions excluding anorthite (San50.53, Ab49.47). This was done by linear interpolation of log(K) values obtained with the data of Arnórsson and Stefansson (1999 [DIRS 153329], Table 4, sanidine series) for San40-Ab60 and San50-Ab50 compositions. Log(K) values were thus obtained in this way for a phase without anorthite.

The log(K) values for pure anorthite were then calculated using the data of Arnórsson and Stefansson (1999 [DIRS 153329], p. 173). Final log(K) values for the phase San48-Ab47-An7

were then calculated assuming an ideal solution of the San-Ab and pure anorthite phases, using Equation C.5-1 as done above for plagioclase.

Details of this calculation can be found in spreadsheet *ymp-feldspar.xls*, worksheet “sanidine.”

C.5.3. Qualification of Log(K) Data for Low-albite, Anorthite, and Sanidine from Arnórsson and Stefansson (1999 [DIRS 153329])

Log(K) data for low-albite, anorthite, and sanidine from Arnórsson and Stefansson (1999 [DIRS 153329]) are qualified using Method 5 of SCI-PRO-001 (Technical Assessment). These data are considered qualified for intended use based on the following attributes:

- Attribute 1: The first author of these data, Stefán Arnórsson, is a professor of geochemistry from the Science Institute, University of Iceland. He holds a Ph.D. in geochemistry. The coauthor of the data, Andri Stefánsson, is from the same university and has a Ph.D. in geology. His research area is chemistry of groundwater. Qualifications of these authors are comparable to, or exceed, the qualification requirements of personnel generating thermodynamic data under Yucca Mountain Project procedures that support the YMP license application process or postclosure science.
- Attribute 2: The regression coefficients to obtain log(K) values as a function of temperature for low-albite, anorthite, sanidine, and their solid solutions were determined from a comprehensive literature review of multiple and reliable measurements on the Gibbs free energy, enthalpy, entropy, heat capacity, and molar volume for the feldspar phases, as shown in Table 1 of the authors’ paper. These data, listed in their Table 1, mostly corroborate each other and were critically reviewed by the authors. The best of these data were used by the authors to derive log(K) values as a function of temperature for feldspar phases and solid solutions. Their detailed analyses provide confidence in the adequacy of procedures used by these authors to derive their log(K) values.
- Attribute 3: The regression coefficients and the equation provided by Arnórsson and Stefansson (1999 [DIRS 153329]) are valid from 0°C to 350°C (at 1 bar and water saturation pressures above 100°C). These temperature and pressure ranges cover the ranges for simulations in the present report.
- Attribute 8: The paper by Arnórsson and Stefansson (1999 [DIRS 153329]) was published in the *American Journal of Science*. This journal is considered one of the top peer-reviewed journals in its field. Papers published in this journal are carefully reviewed by typically at least three independent experts, such that the quality of the paper is assured.

C.6 ZEOLITES

Zeolites considered in this study include mordenite, stellerite, and clinoptilolite. Log(K) values for mordenite were taken directly from the qualified database *data0.ymp.R5* (DTN: SN0612T0502404.014 [DIRS 178850]) and are not discussed further. Log(K) values for clinoptilolite were also taken from this database, although these values were somewhat modified

to account for different compositions, as discussed later in this section. Data for stellerite were modified after the study by Fridriksson et al. (2001 [DIRS 160460]). The data from this paper are qualified for intended use in Section C.6.3.

Log(K) calculations for these zeolites were implemented in the spreadsheets discussed below and submitted to the TDMS under Output DTN: LB0706DSTHC006.001.

C.6.1 Clinoptilolite Log(K) Derivation and Sources of Data

Four clinoptilolite phases were considered in this study. One primary phase, named clinpt-ym/10, was allowed only to dissolve. Three separate Na, K, and Ca secondary phases were allowed to precipitate (and possibly redissolve), named clinpt-na/10, clinpt-k/10, and clinpt-ca/10, respectively. As further explained below, the primary phase is a solid-solution of the other phases reflecting a composition representative of Yucca Mountain tuffs. This treatment provided the best results for reactive-transport simulation of infiltration at Yucca Mountain under ambient conditions of temperature and pressure, as discussed in Section 6.5.1.

Log(K) values for Na-, K-, and Ca-clinoptilolite were derived from the values given for these phases in the qualified database *data0.ymp.R5* (DTN: SN0612T0502404.014 [DIRS 178850]). The data in database *data0.ymp.R5* are for phases including iron. To avoid linking the behavior of clinoptilolite to iron geochemistry, which is only approximately modeled in this study using hematite and goethite, it was judged desirable to consider iron-free clinoptilolite phases. To do so, the log(K) values given in the database *data0.ymp.R5* for iron-bearing clinoptilolite were corrected to represent iron-free phases. This was done in two stages. First, the Gibbs free-energy of formation of iron-bearing clinoptilolite at 25°C and 1 bar was calculated from the log(K) data and Gibbs free-energy values of reaction components given in *data0.ymp.R5*. The Gibbs free-energy of formation of each iron-bearing clinoptilolite obtained in this way was then corrected for removal of iron by subtracting a free energy value corresponding to the silicated amount of Fe₂O₃, then by adding the value corresponding to the same amount of silicated Al₂O₃. These silicated values were taken as the free energies of polyhedral oxides reported in the study by Chermak and Rimstidt (1989 [DIRS 105073], Table 2). Data from this paper are qualified for intended use in Section 6.3. The corrected free-energy values for iron-free phases 25°C and 1 bar were then converted back to log(K) values using the appropriate reactions excluding iron. In doing so, the original log(K) data from *data0.ymp.R5* for the formulae Na_{3.467}Al_{3.45}Fe_{0.017}Si_{14.533}O₃₆:10.922 H₂O, K_{3.467}Al_{3.45}Fe_{0.017}Si_{14.533}O₃₆:10.922 H₂O, and Ca_{1.7335}Al_{3.45}Fe_{0.017}Si_{14.533}O₃₆:10.922 H₂O were adjusted for respective iron-free formulae Na_{3.467}Al_{3.467}Si_{14.533}O₃₆:10.922 H₂O, K_{3.467}Al_{3.467}Si_{14.533}O₃₆:10.922 H₂O, and Ca_{1.7335}Al_{3.467}Si_{14.533}O₃₆:10.922 H₂O. Because the amount of iron removed was very small, the corrections were small, and the log(K) values at temperatures other than 25°C could be mapped after the log(K) variation with temperature for the iron-bearing phases without significant error.

These calculations were implemented in spreadsheets *Ca-clinoptil.xls*, *Na-clinoptil.xls*, and *K-clinoptil.xls*.

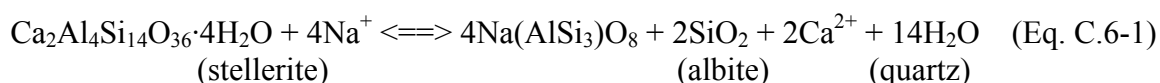
Log(K) values for the primary clinoptilolite phase were obtained assuming an ideal solid-solution of the iron-free Na, K, and Ca phases described above, using Equation C.5-1 and Na, K, and Ca proportions as close as possible to the formula given by Chipera and Apps (2001

[DIRS 171017], Table 3, Diagenetic Alteration of Volcanic Tuff), which is representative of Yucca Mountain tuffs. The formula obtained in this way is: $K_{0.408}Na_{0.203}Ca_{1.428}Al_{3.467}Si_{14.533}O_{36} \cdot 10.922H_2O$. These calculations were implemented in spreadsheet *ymp_clinoptil.xls*.

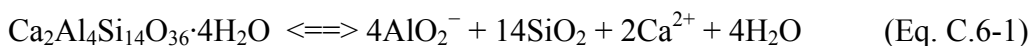
C.6.2 Stellerite Log(K) Derivation and Sources of Data

Log(K) values for stellerite are given in the *data0.ymp.R5* (DTN: SN0612T0502404.014 [DIRS 178850]). However, these data were estimated using methods described by Chipera and Apps (2001 [DIRS 171017]) involving summing free-energy contributions from polyhedral oxides (Chermak and Rimstidt 1989 [DIRS 105073], Table 2) and zeolitic water. The log(K) values estimated in this way appear to overestimate the stability of stellerite relative to albite at equilibrium with Yucca Mountain pore waters, as will be further discussed below. For these reasons, these data were revised after the study of Fridriksson et al. (2001 [DIRS 160460]) and measured pore-water compositions at Yucca Mountain. The data from Fridriksson et al. (2001 [DIRS 160460]) are used in Section 6.3.

Fridriksson et al. (2001 [DIRS 160460], Table 4) provide reference thermodynamic data that can be used to compute log(K) values for stellerite as a function of temperature and pressure using SUPCRT92 (SUPCRT92 V1.0 V [DIRS 112017], STN: 10058-1.0-00). These authors derived their data from experimental studies and field measurements of the solubility of stibnite-stellerite solid-solutions in geothermal waters. Their reference data for stellerite were calculated using different Gibbs free energies (Helgeson et al. 1978 [DIRS 101596]) for reactants and products than used in this study. For consistency with their study, SUPCRT92 was used to compute log(K) values for the following reaction, using the same reference data as these authors for all reactants and products:



The log(K) values for Equation C.6-1 obtained with SUPCRT92 were then converted for a reaction expressing the full dissolution of stellerite. This was done by adding the reactions and log(K) values for albite and quartz dissolution used in the present study to Equation C.6-1, thus obtaining log(K) values for the reaction:

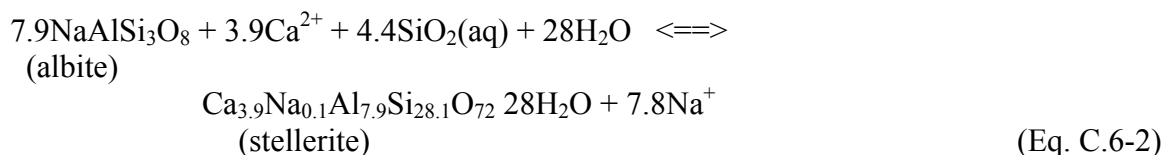


This first calculation was implemented in spreadsheet *stellerite.xls* (worksheet: “pure_stell_logK”). The SUPCRT92 input and output data for this calculation step were cut-and-pasted in worksheet “SUPCRT” of this spreadsheet (for reference), and the actual SUPCRT92 data files were included in the output DTN containing the spreadsheet (Output DTN: LB0706DSTHC006.001).

Chipera and Apps (2001 [DIRS 171017], Table 3, Diagenetic Alteration of Volcanic Tuff) give a composition of stellerite representative of Yucca Mountain tuff containing a small amount of sodium: $(Ca_{3.9}Na_{0.1})Al_{7.9}Si_{28.1}O_{72} \cdot 28(H_2O)$ (qualified for intended use in Appendix O). This composition was used in the present study, and therefore the log(K) values for Equation C.6-1 had to be revised to incorporate a small amount of sodium in the stellerite formula. This was accomplished by revising the Gibbs free energy of sodium-free stellerite at 25°C, 1 bar, by

adding and subtracting free energy contributions of polyhedral oxides from Chermak and Rimstidt (1989 [DIRS 105073], Table 2), in a similar fashion as described previously for the case of clinoptilolite. These calculations are implemented in spreadsheet *stellerite.xls* (worksheet: “YMP_stell_logK”). The small amount of sodium added resulted in a small correction. Because the correction at 25°C is quite small and largely within the data uncertainty, it was applied at all temperatures without considering potential additional temperature effects.

Log(K) values calculated in this manner still appear to make stellerite too stable relative to albite, although to a much lesser degree than the log(K) values in *data0.ymp.R5*. This is shown using the equilibrium boundary defined by albite and stellerite, according to the reaction:



Because stellerite is the most common fracture-lining zeolite in repository host units (e.g., Carlos et al. 1995 [DIRS 105213]) it would be expected that the compositions of pore waters at Yucca Mountain fall mostly near the boundary defined by this reaction. If the equilibrium constant for this reaction is given as $\log(K_{\text{eq}})$, and the water and mineral activities are taken as unity, then:

$$\log(K_{\text{eq}}) = -3.9 \log(a\text{Ca}^{2+}) + 7.8 \log(a\text{Na}^+) - 4.4 \log(a\text{SiO}_2) \quad (\text{Eq. C.6-3})$$

which, after some rearrangement and approximating activities (a) by molalities (m), yields:

$$\log[(m\text{Na}^+)^2 / m\text{Ca}^{2+}] \cong 0.256 \log(K_{\text{eq}}) + 1.128 \log(m\text{SiO}_2) \quad (\text{Eq. C.6-4})$$

This relationship yields a straight line of the form $Y = A + B X$ where:

$$X = \log(m\text{SiO}_2) \quad (\text{Eq. C.6-5})$$

$$Y = \log[(m\text{Na}^+)^2 / m\text{Ca}^{2+}] \quad (\text{Eq. C.6-6})$$

$$A = 0.256 \log(K_{\text{eq}}) \quad (\text{Eq. C.6-7})$$

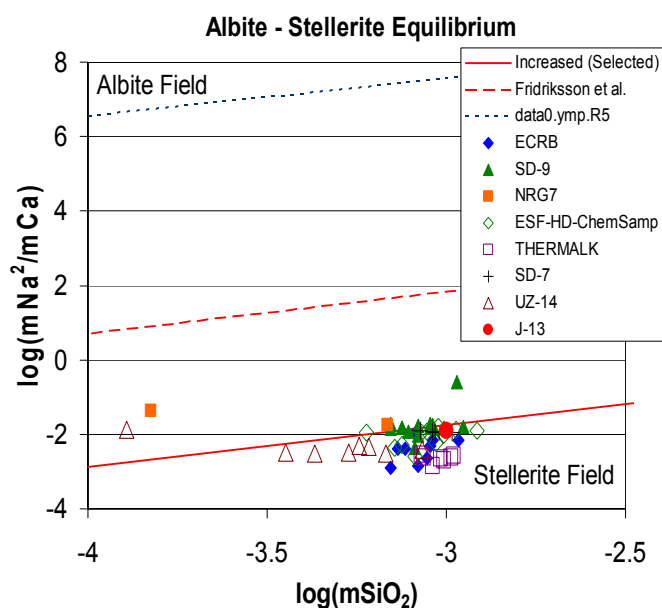
$$B = 1.128 \quad (\text{Eq. C.6-8})$$

Figure C.6-1 shows a plot of this equilibrium boundary using values of $\log(K_{\text{eq}})$ at 25°C from three sources:

- (1) Database *data0.ymp.R5* (DTN: SN0612T0502404.014 [DIRS 178850])
- (2) The value derived after Fridriksson et al. (2001 [DIRS 160460]) as described above
- (3) The value from (2) increased by an amount of 0.7 log(K) units (on the basis of a stellerite formula with 3.6 oxygen atoms). This log(K) increase was estimated and corresponds to decreasing the Gibbs free energy of stellerite by ~0.2%, a small amount largely within the uncertainty of these data.

Figure C.6-1 shows that Yucca Mountain pore waters plot much closer to the albite-stellerite equilibrium boundary when the $\log(K)$ value from (3) is used than with either (1) or (2). Furthermore, test THC simulations of infiltration under ambient conditions of temperature and pressure using $\log(K)$ values from (1) or (2) yielded unrealistically high amounts of stellerite precipitation, calcite dissolution in fractures (e.g., see Equation 6.5-2 in Section 6.5.1 of the main report), as well as unrealistically elevated CO_2 gas partial pressures not supported by field measurements. For these reasons, selected $\log(K)$ values for this study were derived by taking the values determined after Fridriksson et al. (2001 [DIRS 160460]) as described above and increasing these values by the same amount as in (3) at all temperatures.

These calculations were implemented in spreadsheet *stelleritel.xls* (worksheet “Adjustment of $\log K$ for THC”). Calculations for Figure C.6-1 were implemented in spreadsheet *albite-stellerite.xls*.



NOTE: Boundary drawn using three different $\log(K)$ values for stellerite at 25°C (see text of Section C.6.2). Symbols represent various pore water analyses (data with <10% charge imbalance) taken from DTNs: GS020408312272.003 [DIRS 160899], GS020808312272.004 [DIRS 166569], GS041108312272.005 [DIRS 178057], GS951208312272.004 [DIRS 165858], GS030408312272.002 [DIRS 165226], GS031008312272.008 [DIRS 166570], and MO0006J13WTRCM.000 [DIRS 151029].

Figure C.6-1. Plot of YMP Pore-Water Analyses Relative to the Albite-Stellerite Equilibrium Boundary

C.6.3 Qualification of External Data Used in the Derivation of Zeolite $\log(K)$ Values

C.6.3.1 Silicated Oxides (Silicated Fe_2O_3 and Al_2O_3) from Chermak and Rimstidt (1989 [DIRS 105073])

Free energies of silicated oxides from Chermak and Rimstidt (1989 [DIRS 105073]) are qualified for intended use with Method 5 of SCI-PRO-001 (Technical Assessment). These data are considered qualified for intended use based on the following attributes:

- Attribute 1: The first author of the data, John A. Chermak, is a Ph.D. in Geology (geochemistry emphasis). The coauthor of the data, Donald J. Rimstidt, is a professor of geochemistry. Both are from the Department of Geological Sciences, Virginia Polytechnic Institute and the State University. The qualifications of these authors and their organizations are comparable to, or exceed, the qualification requirements of personnel generating thermodynamic data under Yucca Mountain Project procedures that support the YMP license application process or postclosure science.
- Attribute 2: The Gibbs free energies (ΔG_f^0) of polyhedral Fe_2O_3 and Al_2O_3 were determined using a multiple regression method based on measured Gibbs free energies (using calorimetric measurements) of 34 relevant minerals. The measurement method of Gibbs free energies, calorimetric measurement, is adequate. The multiple regression method used to analyze the data is also adequate. The authors show that the predicted ΔG_f^0 using their determined values of ΔG_f^0 of silicated oxides are very close to the measured data (the average residual of their regression is only 0.26%; see Table 3 the authors' paper).
- Attribute 8: The paper by Chermak and Rimstidt (1989 [DIRS 105073]) was published in *American Mineralogist*. This journal is considered one of the top peer-reviewed journals in its field. Papers published in this journal are carefully reviewed by typically at least three independent experts, such that the quality of the paper is assured.

C.6.3.2 Stellerite Thermodynamic Data from Fridriksson et al. (2001 [DIRS 160460], Table 4)

Reference thermodynamic data from Fridriksson et al. (2001 [DIRS 160460], Table 4), used in the derivation of $\log(K)$ values for stellerite, are qualified for intended use with Method 5 of SCI-PRO-001 (Technical Assessment). These data are considered qualified for intended use based on the following attributes:

- Attribute 1: The first author of the data, Thráinn Fridriksson, is a geochemist at the National Energy Authority, Iceland. He earned his Ph.D. from Stanford University in 2003. Another author of these data, Stefán Arnórsson, is a professor of geochemistry at the Science Institute, University of Iceland. Qualifications of these authors are comparable to, or exceed, qualification requirements of personnel generating thermodynamic data under Yucca Mountain Project procedures that support the YMP license application process or postclosure science.
- Attribute 2: Fridriksson et al. (2001 [DIRS 160460], Table 4) provide reference thermodynamic data that can be used to compute $\log(K)$ values for stellerite as a function of temperature and pressure using SUPCRT92. These authors derived their data from experimental studies and field measurements of the solubility of stibnite-stellerite phases in geothermal waters. The fact that these authors can reproduce solubilities measured in the field by calculations based on reference thermodynamic properties derived from these data provides confidence in the adequacy of the procedures applied to derive these data. Additional confidence is gained by the analyses presented in Section 6.2, showing that the stellerite Gibbs free energy value obtained from pore-water compositions in the

Yucca Mountain repository host units is within about 0.2% of the value reported by Fridriksson et al. (2001 [DIRS 160460], Table 4) (when corrected for consistency in the Gibbs free energy values of reactants and products used by these authors).

- Attribute 8: The paper by Fridriksson et al. (2001 [DIRS 160460]) was published in *Geochimica et Cosmochimica Acta*. This journal is considered one of the top peer-reviewed journals in its field. Papers published in this journal are carefully reviewed by typically at least three independent experts, such that the quality of the paper is assured.

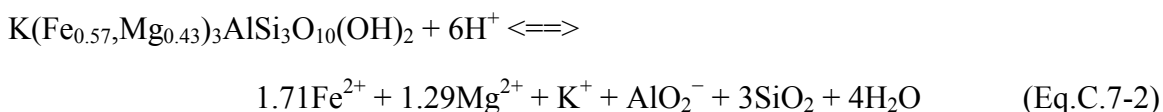
C.7 BIOTITE

Log(K) values for biotite were derived from the values given in the qualified database *data0.ymp.R5* (DTN: SN0612T0502404.014 [DIRS 178850]) for annite and phlogopite, and the solid-solution model described by Kerrick and Darken (1975 [DIRS 180314]). Using this model, the activities of the annite ($\text{KFe}_3\text{AlSi}_3\text{O}_{10}(\text{OH})_2$) and phlogopite ($\text{KAlMg}_3\text{Si}_3\text{O}_{10}(\text{OH})_2$) endmembers are calculated as $a_{\text{annite}} = x_{\text{Fe}}^3$ and $a_{\text{phlogopite}} = x_{\text{Mg}}^3$, respectively, where x denotes mole fraction in the solid solution. Log(K) values for the mixed phase are then computed using the formula:

$$\log(K) = \sum_i x_i \log K_i + \sum_i x_i \log a_i \quad (\text{Eq. C.7-1})$$

where x_i , $\log K_i$, and a_i are the mole fractions, log(K) values, and activities, respectively, of the solid-solution endmembers.

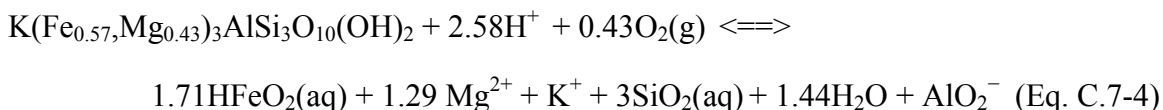
This approach was applied using a biotite composition from Johnson et al. (1998 [DIRS 101630], Table 6), $\text{K}(\text{Fe}_{0.57}, \text{Mg}_{0.43})_3\text{AlSi}_3\text{O}_{10}(\text{OH})_2$, representative of Yucca Mountain tuff (qualified for intended use in Appendix O, Section O.3). Switching the aluminum primary species from Al^{3+} to AlO_2^- , the biotite dissolution reaction becomes:



By combining Equation C.7-2 with the following oxidation reaction:



and switching primary Fe(III) species from Fe^{3+} to $\text{HFeO}_2(\text{aq})$, one obtains:



Conditions in the vadose zone at Yucca Mountain are oxidizing. Under such conditions, the oxygen fugacity is expected to remain near the atmospheric value of $10^{-0.7}$ bar. To avoid explicitly modeling redox, the reaction expressed by Equation C.7-4 is assumed to always

remain buffered at an O₂ fugacity of 10^{-0.7} bar. This is done by defining an effective reaction for an “oxidized biotite”, *biotite-ox*, which takes the same form as Equation C.7-3 but with the O₂ term ignored, and with oxygen imbedded as an implicit reactant by adding the value of (-0.43)×(-0.7) to the log(K) values of Equation C.7-4.

The calculations are implemented in spreadsheet *biotite.xls* submitted with files accompanying this report under Output DTN: LB0706DSTHC006.001. Worksheet “biotite-Fe(II)” documents the calculation of log(K) values for Equation C.7-2. Worksheet “biotite-ox” documents the calculation of log(K) values for “oxidized biotite” as described above. Log(K) values for Equation C.7-4 were obtained by combining the values for Equation C.7-2 (from worksheet “biotite-Fe(II)”) with log(K) data from the qualified database *data0.ymp.R5* (DTN: SN0612T0502404.014 [DIRS 178850]) for Equation C7-3 and the conversion from Fe³⁺ to HFeO₂(aq).

The log(K) values for biotite and “oxidized biotite” calculated as described above are considered justified for use in this study on the basis of reliability of the data sources.

C.8 RHYOLITIC GLASS

All calculations supporting the composition and log(K) values for the rhyolitic glass used in this study were implemented in spreadsheets accompanying this report and submitted to the TDMS under Output DTN: LB0706DSTHC006.001. Input and output files of supporting calculations using SUPCRT92 were also submitted to the TDMS under the same DTN.

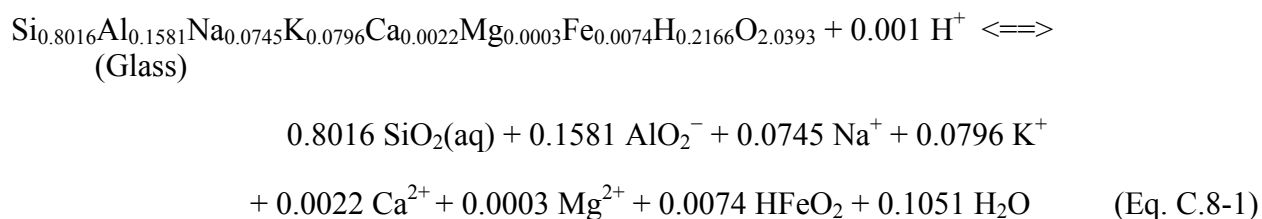
C.8.1 Glass Composition

The glass composition was taken from electron microprobe analyses of a Yucca Mountain vitrophyre reported by Bish et al. (1996 [DIRS 101430], Table 1) (sample GU-3 1195C) (qualified for intended use in Appendix O, Section O.3). Oxides TiO₂ and BaO, which make up only 0.15 wt % of the total glass composition, were ignored because titanium and barium are not included in the geochemical system being modeled. From these analyses, the composition of the glass in terms of oxide mole fractions and the glass stoichiometric formula were determined as follows:

- (1) In absence of analyses for ferric iron and to account for fully oxidized conditions, ferrous iron (FeO) was stoichiometrically replaced with ferric iron (Fe₂O₃).
- (2) The weight-percent analysis was normalized to 100% and then converted to a mole basis by dividing the weight percent by molecular weights (from DTN: SN0612T0502404.014 [DIRS 178850]).
- (3) Water molecules were associated with Al₂O₃ to form amorphous aluminum hydroxide in stoichiometric amounts consistent with the reaction Al₂O₃ + 3H₂O = 2 Al(OH)₃(am).

- (4) Oxide and hydroxide mole fractions were then computed by normalizing the molar amounts to unity.
- (5) Stoichiometric amounts of components (e.g., Al, Ca, H, O, etc.) in the glass were then obtained by multiplying the oxide/hydroxide mole fractions by the stoichiometric amount of each component in the corresponding oxide and summing identical components.

These calculations were implemented in spreadsheet *glass_logKrev.xls* (worksheet: “composition”). The resulting glass composition yields the following glass formula and dissolution reaction:



C.8.2 Determination of Glass Log(K) Values

Calculations of log(K) values for Equation C.8-1 are based on a theoretical approach originally proposed by Paul (1977 [DIRS 160485]) that considered the glass as an oxide mixture. Thus, the solubility of the material can be estimated from the ideal solid solution relation:

$$\log(K)_{\text{glass}} = \sum_i x_i \log K_i + \sum_i x_i \log x_i \quad (\text{Eq. C.8-2})$$

where x_i and K_i are the molar fractions and solubility products, respectively, of the glass-constituting oxides and hydroxides (Table C.8-1). This method of estimating solubility products of borosilicate and aluminosilicate glasses has already been successfully applied by Bourcier (1992 [DIRS 101562]) and Advocat et al. (1998 [DIRS 160446]), as well as by Leturcq et al. (1999 [DIRS 160480]). Techer et al. (2001 [DIRS 160501]) also obtained a good result using the same approach to model the dissolution of synthetic basaltic glass at 90°C.

Values of log(K_i) for use with Equation C.8-1 were taken from qualified sources shown in Table C.8-1. Maier-Kelley heat capacity regression coefficients a , b , and c for amorphous Al(OH)₃, for use in SUPCRT92 calculations, were obtained by regressing heat capacities reported in *Thermochemical Data of Pure Substances* (Barin and Platzki 1995 [DIRS 157865], p. 55). This two-volume compilation was published by ACH Publishers, New York, in 1995 as the third edition, and is considered a handbook of thermochemical data. Therefore, the heat capacities of amorphous Al(OH)₃ are considered established fact data and not subject to further qualification.

The regression of heat-capacity data for amorphous Al(OH)₃ was accomplished in spreadsheet *Al(OH)3regression.xls* using the *tools/data_analysis/regression* Excel function.

The log(K) values for the glass were then calculated at each temperature using Equation C.8-1 with the oxide mole fractions (x_i) and log(K_i) values determined above. Values obtained in this way are considered justified for use in this study on the basis of reliability of the data sources and prior uses of similar methods.

Table C.8-5. Oxide and Hydroxide Dissociation Reactions Used for Glass Log(K) Calculation

Solid	Reaction	Log(K) Source
SiO ₂ (am)	SiO ₂ (am) <=> SiO ₂ (aq)	Gunnarsson and Arnórsson (2000 [DIRS 160465])
Al ₂ O ₃ (corundum)	Al ₂ O ₃ + H ₂ O <=> 2AlO ₂ ⁻ + 2H ⁺	<i>data0.ymp.R5</i> ^a
Al(OH) ₃ (am)	Al(OH) ₃ (am) <=> AlO ₂ ⁻ + H ₂ O + H ⁺	Calculated ^b
Na ₂ O	Na ₂ O + 2H ⁺ <=> 2Na ⁺ + H ₂ O	<i>data0.ymp.R5</i> ^a
K ₂ O	K ₂ O + 2H ⁺ <=> 2K ⁺ + H ₂ O	<i>data0.ymp.R5</i> ^a
CaO (lime)	CaO + 2H ⁺ <=> Ca ²⁺ + H ₂ O	<i>data0.ymp.R5</i> ^a
MgO (periclase)	MgO + 2H ⁺ <=> Mg ²⁺ + H ₂ O	<i>data0.ymp.R5</i> ^a
Fe ₂ O ₃ (hematite)	Fe ₂ O ₃ + H ₂ O <=> 2HFeO ₂	<i>data0.ymp.R5</i> ^a

^a Project database *data0.ymp.R5* (DTN: SN0612T0502404.014 [DIRS 178850]).

^b Calculated using SUPCRT92 and reference data from Barin and Platzki (1995 [DIRS 157865]) for Al(OH)₃(am), and from *data0.ymp.R5* (DTN: SN0612T0502404.014 [DIRS 178850]) for reaction products.

C.9 CHANGES BETWEEN PRELIMINARY AND FINAL VERSIONS OF DATABASE *DATA0.YMP.R5* AFFECTING THIS REPORT

The version of database *data0.ymp.R5* (DTN: SN0610T0502404.013 [DIRS 178113]) used in this study was preliminary and has been superseded with the version archived in DTN: SN0612T0502404.014 [DIRS 178850]. For the geochemical species, minerals, and gases used in this study, changes from DTN: SN0610T0502404.013 [DIRS 178113] to DTN: SN0612T0502404.014 [DIRS 178850] only affected the log(K) values for HSiO₃⁻, as shown in Table C-2. The differences in log(K) values shown in Table C-2 for this species are quite small and decrease with temperature. The net effect is a slightly higher pK for the dissociation of SiO₂(aq) in this study, by about 0.3 pH units at 25°C to less than 0.1 pH units at 100°C compared to the more recent data. These differences do not affect significantly speciation results at pH values below the pK for SiO₂(aq) dissociation, which is around 10 at 25°C and around 9 at 100°C. In addition, these differences are small compared to the spread in model results discussed in Section 6.7.2 of the main report, which shows standard deviations in pH around ±0.3 to 0.8 units at times when pH is in the range of the pK for SiO₂(aq) dissociation (during the boiling period). At other times, pH values remain significantly below 9, thus significantly below the pK for SiO₂(aq) dissociation. Given these considerations, the revisions from DTN: SN0610T0502404.013 [DIRS 178113] to DTN: SN0612T0502404.014 [DIRS 178850] are deemed inconsequential for this study.

Another difference to point out between the preliminary and final version of database *data0.ymp.R5* is that molecular weights for derived species and minerals were not included in the final database. However, the molecular weights for derived species and minerals can be easily checked from the molecular weights of component species given in the final database.

Finally, using the four starting water chemistries input into the THC seepage model (listed in Table 6.2-1 of the main report), equilibrium speciation computations using EQ3/6 Version 8.1 (EQ3/6 V8.1 [DIRS 176889], STN: 10813-8.1-00) were carried out at 100°C and 25°C, and CO₂ partial pressure of 10⁻³ bar. The purpose of the analysis was to compare equilibrium speciation between the preliminary and final versions of *data0.ymp.R5* (DTNs: SN0610T0502404.013 and SN0612T0502404.014 [DIRS 178850]). The results were submitted to the TDMS under Output DTN: MO0706SPECOMPA.000 and confirm that differences in results from the changes between these database versions are quite small and well below the uncertainty of the model results discussed in Section 6.7.2.

INTENTIONALLY LEFT BLANK

APPENDIX D
WASTE PACKAGE AVERAGE HEAT TRANSFER

INTENTIONALLY LEFT BLANK

Table D-1. Waste Package Average Heat Transfer

Time (years)	Total Heat (no ventilation) (W/m)	Model Heat Load (W/m)
0	1450.000	174.000
1	1400.000	168.000
2	1360.000	163.200
3	1320.000	158.400
4	1290.000	154.800
5	1260.000	151.200
6	1230.000	147.600
7	1210.000	145.200
8	1180.000	141.600
9	1160.000	139.200
10	1130.000	135.600
11	1110.000	133.200
12	1090.000	130.800
13	1070.000	128.400
14	1050.000	126.000
15	1030.000	123.600
16	1010.000	121.200
17	993.000	119.160
18	976.000	117.120
19	960.000	115.200
20	944.000	113.280
21	927.000	111.240
22	910.000	109.200
23	895.000	107.400
24	881.000	105.720
25	867.000	104.040
26	853.000	102.360
27	838.000	100.560
28	824.000	98.880
29	811.000	97.320
30	799.000	95.880
31	786.000	94.320
32	773.000	92.760
33	761.000	91.320
34	749.000	89.880
35	738.000	88.560
36	726.000	87.120
37	715.000	85.800
38	704.000	84.480
39	694.000	83.280
40	684.000	82.080
41	673.000	80.760
42	663.000	79.560
43	653.000	78.360
44	644.000	77.280

Table D-1. Waste Package Average Heat Transfer (Continued)

Time (years)	Total Heat (no ventilation) (W/m)	Model Heat Load (W/m)
45	635.000	76.200
46	626.000	75.120
47	617.000	74.040
48	608.000	72.960
49	600.000	72.000
50	592.000	71.040
50.001	592.000	592.000
51	584.000	584.000
52	576.000	576.000
53	568.000	568.000
54	560.000	560.000
55	553.000	553.000
56	546.000	546.000
57	538.000	538.000
58	531.000	531.000
59	525.000	525.000
60	518.000	518.000
61	511.000	511.000
62	505.000	505.000
63	499.000	499.000
64	493.000	493.000
65	487.000	487.000
66	481.000	481.000
67	475.000	475.000
68	469.000	469.000
69	464.000	464.000
70	459.000	459.000
71	453.000	453.000
72	448.000	448.000
73	443.000	443.000
74	438.000	438.000
75	433.000	433.000
76	429.000	429.000
77	424.000	424.000
78	419.000	419.000
79	415.000	415.000
80	410.000	410.000
81	406.000	406.000
82	402.000	402.000
83	398.000	398.000
84	394.000	394.000
85	390.000	390.000
86	386.000	386.000
87	382.000	382.000
88	378.000	378.000

Table D-1. Waste Package Average Heat Transfer (Continued)

Time (years)	Total Heat (no ventilation) (W/m)	Model Heat Load (W/m)
89	375.000	375.000
90	371.000	371.000
91	368.000	368.000
92	364.000	364.000
93	361.000	361.000
94	358.000	358.000
95	355.000	355.000
96	351.000	351.000
97	348.000	348.000
98	345.000	345.000
99	343.000	343.000
100	340.000	340.000
110	314.000	314.000
120	293.000	293.000
130	274.000	274.000
140	258.000	258.000
150	244.000	244.000
160	234.000	234.000
170	224.000	224.000
180	215.000	215.000
190	207.000	207.000
200	200.000	200.000
250	175.000	175.000
300	158.000	158.000
350	144.000	144.000
400	133.000	133.000
450	124.000	124.000
500	116.000	116.000
550	109.000	109.000
600	102.000	102.000
650	96.500	96.500
700	91.200	91.200
750	86.400	86.400
800	82.000	82.000
850	78.000	78.000
900	74.300	74.300
950	70.900	70.900
1,000	67.700	67.700
1,500	46.700	46.700
2,000	36.600	36.600
2,500	31.500	31.500
3,000	28.700	28.700
3,500	27.000	27.000
4,000	25.700	25.700
4,500	24.700	24.700

Table D-1. Waste Package Average Heat Transfer (Continued)

Time (years)	Total Heat (no ventilation) (W/m)	Model Heat Load (W/m)
5,000	23.800	23.800
5,500	22.900	22.900
6,000	22.100	22.100
6,500	21.400	21.400
7,000	20.700	20.700
7,500	20.000	20.000
8,000	19.400	19.400
8,500	18.800	18.800
9,000	18.200	18.200
9,500	17.600	17.600
10,000	17.100	17.100
15,000	12.800	12.800
20,000	9.950	9.950
25,000	7.980	7.980
30,000	6.580	6.580
35,000	5.520	5.520
40,000	4.720	4.720
45,000	4.080	4.080
50,000	3.580	3.580
55,000	3.170	3.170
60,000	2.810	2.810
65,000	2.530	2.530
70,000	2.280	2.280
75,000	2.070	2.070
80,000	1.880	1.880
85,000	1.730	1.730
90,000	1.620	1.620
95,000	1.500	1.500
100,000	1.390	1.390

Source DTN: MO0702PASTREAM.001 [DIRS 179925], worksheet:
"decay curves."

Output DTN: LB0706DSTHC006.002.

NOTE: Point at 50.001 years was interpolated between original data points at 50 and 55 years. From 0 to 50 years: Model Heat Load = Total Heat × (1 to 0.88) (88% heat removal; rounded value after values in DTN: MO0701VENTCALC.000 [DIRS 179085] for a 600-m drift).

APPENDIX E

EFFECTIVE THERMAL CONDUCTIVITY FOR IN-DRIFT OPEN SPACES

INTENTIONALLY LEFT BLANK

Table E-1. Effective Thermal Conductivity for In-Drift Open Spaces during Preclosure

Time		Factor
(sec)	(year)	
3.15360E+03	0.0	0.395
3.15360E+07	1.0	0.777
4.73040E+07	1.5	0.825
6.30720E+07	2	0.856
9.46080E+07	3	0.898
1.26144E+08	4	0.921
1.57680E+08	5	0.939
1.89216E+08	6	0.955
2.20752E+08	7	0.966
2.52288E+08	8	0.975
2.83824E+08	9	0.982
3.15360E+08	10	0.988
3.46896E+08	11	0.993
3.78432E+08	12	0.997
4.73040E+08	15	1
6.30720E+08	20	0.993
7.88400E+08	25	0.977
8.19936E+08	26	0.974
8.51472E+08	27	0.97
9.46080E+08	30	0.958
1.10376E+09	35	0.936
1.26144E+09	40	0.915
1.57680E+09	50	0.879

Source: DTN: SN0002T0872799.009 [DIRS 153364], file: *tough2-input_noBF.txt* in zip file *effKth_noBF.zip*.

NOTES: Kthermal is calculated as Max. Kthermal × Factor.
Maximum Kthermal (W/m-K) = 10.568.

Table E-2. Effective Thermal Conductivity for In-Drift Open Spaces during Postclosure (no backfill)

Time		Factor	
(sec)	(years)	Inner	Outer
1.57680E+09	50	0.879	0.879
1.608336E+09	51	0.844	0.829
1.639872E+09	52	0.892	0.878
1.734480E+09	55	0.951	0.944
1.892160E+09	60	0.988	0.986
2.049840E+09	65	1	1
2.207520E+09	70	0.995	0.998
2.365200E+09	75	0.985	0.99
2.396736E+09	76	0.983	0.988
2.428272E+09	77	0.981	0.986
2.522880E+09	80	0.973	0.98
2.838240E+09	90	0.954	0.963
3.153600E+09	100	0.932	0.943
3.185136E+09	101	0.929	0.941
3.311280E+09	105	0.918	0.929
3.468960E+09	110	0.905	0.917
3.784320E+09	120	0.882	0.896
4.099680E+09	130	0.872	0.886
4.415040E+09	140	0.864	0.879
5.045760E+09	160	0.852	0.869
5.676480E+09	180	0.839	0.857
6.307200E+09	200	0.83	0.849
6.937920E+09	220	0.818	0.838
7.884000E+09	250	0.798	0.818
9.460800E+09	300	0.763	0.784
1.103760E+10	350	0.736	0.758
1.261440E+10	400	0.707	0.729
1.419120E+10	450	0.689	0.711
1.576800E+10	500	0.677	0.7
1.734480E+10	550	0.672	0.694
1.892160E+10	600	0.667	0.69
2.207520E+10	700	0.656	0.68
2.522880E+10	800	0.646	0.67
2.838240E+10	900	0.637	0.661
3.153600E+10	1,000	0.627	0.651
3.468960E+10	1,100	0.619	0.643
3.784320E+10	1,200	0.611	0.635

Table E-2. Effective Thermal Conductivity for In-Drift Open Spaces during Postclosure (No Backfill)
(Continued)

Time		Factor	
(sec)	(years)	Inner	Outer
4.099680E+10	1,300	0.602	0.626
4.415040E+10	1,400	0.592	0.616
4.730400E+10	1,500	0.582	0.605
5.045760E+10	1,600	0.574	0.597
5.676480E+10	1,800	0.559	0.583
6.307200E+10	2,000	0.543	0.566
6.937920E+10	2,200	0.533	0.555
7.884000E+10	2,500	0.519	0.541
9.460800E+10	3,000	0.503	0.523
1.103760E+11	3,500	0.491	0.51
1.261440E+11	4,000	0.48	0.499
1.419120E+11	4,500	0.472	0.491
1.576800E+11	5,000	0.465	0.484
1.892160E+11	6,000	0.453	0.471
2.207520E+11	7,000	0.444	0.461
2.522880E+11	8,000	0.436	0.452
3.153600E+11	10,000	0.422	0.438
4.730400E+11	15,000	0.395	0.411
6.307200E+11	20,000	0.378	0.393
9.460800E+11	30,000	0.354	0.367
1.261440E+12	40,000	0.341	0.354
1.576800E+12	50,000	0.333	0.346
1.892160E+12	60,000	0.326	0.339
2.522880E+12	80,000	0.318	0.33
3.153600E+12	100,000	0.314	0.325

Source: DTN: SN0002T0872799.009 [DIRS 153364], file: *tough2-input_noBF.txt* in zip file *effKth_noBF.zip*.

NOTES: Kthermal is calculated as Max. Kthermal × Factor.
Maximum Kthermal (W/m-K) Inner = 2.298, Outer = 14.407.

INTENTIONALLY LEFT BLANK

APPENDIX F
PARAMETERS FOR FRACTURE PERMEABILITY MODIFICATION

INTENTIONALLY LEFT BLANK

Table F-1. Parameters for Fracture Permeability Modification

Rock Unit	b_g (m) ^a	s (m ⁻¹) ^a
tcw11	1.5385E-02	0.1087E+01
tcw12	1.2696E-03	0.5240E+00
tcw13	3.4483E-03	0.3580E+00
ptn21	9.2000E-03	0.1493E+01
ptn22	7.0922E-03	0.2174E+01
ptn23	1.2000E-03	0.1754E+01
ptn24	2.9412E-02	0.2174E+01
ptn25	5.0459E-03	0.1923E+01
ptn26	8.7079E-04	0.1031E+01
tsw31	1.2953E-03	0.4610E+00
tsw32	2.5857E-03	0.8930E+00
tsw33	1.3063E-03	0.1235E+01
tsw34	6.2777E-04	0.2310E+00
tsw35	9.9174E-04	0.3160E+00
tsw3[67]	1.0561E-03	0.2490E+00
tsw38	8.2459E-04	0.2290E+00
tsw39	1.4576E-03	0.1042E+01
ch1VI	2.0333E-03	0.1000E+02
ch[23456]VI	1.7907E-03	0.7143E+01
ch[2345]Ze	8.6047E-04	0.7143E+01
ch6	1.7907E-03 ^b	0.2500E+02
pp4	8.6047E-04	0.7143E+01
pp3	1.5902E-03	0.5000E+01
pp2	1.5902E-03	0.5000E+01
pp1	8.6047E-04	0.7143E+01
bf3	1.5902E-03	0.5000E+01
bf2	8.6047E-04	0.7143E+01

^a Some values may show very small, inconsequential differences from the source values as a result of round-off error when transcribing these data from original sources. The effect on model results would be orders of magnitude smaller than the spread in model results discussed in Section 6.7.2.

^b This value was inadvertently taken for the vitric instead of the zeolitic unit (1.4545E-03 m). This difference is inconsequential and does not affect the model results presented in this report for areas in the near field because it applies to a hydrogeologic unit ~190 m below the modeled drift. In addition, the local effect on model results ~190 m below the drift would be orders of magnitude smaller than the spread in model results discussed in Section 6.7.2.

NOTE: The calculation and use of the b_g and s parameters are presented in Section 6.4.4.2. Parameter b_g is the geometric fracture aperture calculated using Equation 6.4-35, as reported in spreadsheet *minabund_areas_rev05_final_c1.xls* (parameter a in sheet 3), submitted to the TDMS under Output DTN LB0707DSTHC006.003. Parameter s is equal to the fracture spacing in Equation 6.4-34, the inverse of the fracture frequency (derived from DTN: LB0205REVUZPRP.001 [DIRS 159525]).

INTENTIONALLY LEFT BLANK

APPENDIX G
LIST OF MODEL OUTPUT DTNS

INTENTIONALLY LEFT BLANK

Table G-1. List of Model Output DTNs

DTN	Description	Report Sections
Summary of model results		
LB0704DSTHONLY.001	TH simulations, summary spreadsheets of simulation results	6.5.5.2
LB0705DSTHC001.001	THC simulations using water W0: summary spreadsheets of predicted concentrations, initial water composition and speciation	6.5.5, 6.6
LB0705DSTHC002.001	THC simulations using water W8: summary spreadsheets of predicted concentrations, initial water composition and speciation	6.5.5
LB0705DSTHC003.001	THC simulations using water W9: summary spreadsheets of predicted concentrations, initial water composition and speciation	6.5.5
LB0705DSTHC004.001	THC simulations using water W10: summary spreadsheets of predicted concentrations, initial water composition and speciation	6.5.5
LB0705DSTHC020.001	THC simulations using water W0 for model sensitivity analyses (to time discretization): summary spreadsheets of predicted concentrations and gas partial pressure around drift	6.6.1
LB0705DSTHC021.001	THC simulations using water W0 for model sensitivity analyses (to model revisions): summary spreadsheets of predicted concentrations and gas partial pressure around drift	6.6.2
LB0705DSTHC022.001	THC simulations using water W0 for model sensitivity analyses (to dryout mineral assemblage): summary spreadsheets of predicted concentrations and gas partial pressure around drift	6.6.4
LB0705DSTHC023.001	THC simulations using water W0 for model sensitivity analyses (to CO ₂ transport): summary spreadsheets of predicted concentrations and gas partial pressure around drift	6.6.3
LB0705DSTHC024.001	THC simulations using water W0, for model sensitivity analyses (to mineral reaction rates): summary spreadsheets of predicted concentrations and gas partial pressure around drift	6.6.5
Steady-state flow field simulations, TOUGHREACT V3.1.1 input and output files		
LB0704DSSSTFLW.002	Steady-state flow field simulations	6.5.5
TH simulations, TOUGHREACT V3.1.1 input and output files		
LB0704DSTHONLY.002	TH simulations for repository center (design drift spacing 81 m) and repository edge (effective drift spacing 162 m)	6.5.5.2
THC simulations, TOUGHREACT V3.1.1 input and output files		
LB0705DSTHC001.002	THC simulation using water W0: three simulations, i.e., (1) repository center (design drift spacing 81m), (2) repository edge (effective drift spacing 162 m), and (3) ambient (without drift, without heat load)	6.5.5
LB0705DSTHC002.002	THC simulation using water W8: three simulations, i.e., (1) repository center (design drift spacing 81m), (2) repository edge (effective drift spacing 162 m), and (3) ambient (without drift, without heat load)	6.5.5
LB0705DSTHC003.002	THC simulation using water W9: three simulations, i.e., (1) repository center (design drift spacing 81m), (2) repository edge (effective drift spacing 162 m), and (3) ambient (without drift, without heat load)	6.5.5
LB0705DSTHC004.002	THC simulation using water W10: three simulations, i.e., (1) repository center (design drift spacing 81m), (2) repository edge (effective drift spacing 162 m), and (3) ambient (without drift, without heat load)	6.5.5

Table G-1. List of Model Output DTNs (Continued)

DTN	Description	Report Sections
LB0705DSTHC005.002	THC simulations of Drift Scale Test for model validation: seven simulations with waters W0 and W10, including steady-state SD-9 one-dimensional simulation	Chapter 7
LB0705DSTHC020.002	THC simulations using water W0 for sensitivity analyses (to time discretization): three simulations are included, i.e., (1) time-step size is constrained by Courant limitation; (2) maximum time-step size is 15 days for 0 to 50 years, 30 days for 50 to 600 years and 60 days for 600 to 2,000 years; and (3) maximum time step is 15 days for 0 to 2,000 years.	6.6.1; 6.6.2
LB0705DSTHC021.002	THC simulations using water W0 for sensitivity analyses (to model revisions): two simulations are included, i.e., (1) with consideration of calcite supersaturation gap; (2) with higher boundary CO ₂ partial pressure (10 ^{-2.5} bar)	6.6.2
LB0705DSTHC022.002	THC simulations using water W0 for sensitivity analyses (to dryout mineral assemblage): two simulations with different dryout mineral assemblages are included	6.6.4
LB0705DSTHC023.002	THC simulations using water W0 for sensitivity analyses (to CO ₂ transport): three simulations are included, i.e., (1) CO ₂ diffusion coefficient increased by a factor of ~2.6; (2) CO ₂ diffusion coefficient increased by a factor of ~10; and (3) gas phase relative permeability for TSw units is calculated using Corey function	6.6.3
LB0705DSTHC024.002	THC simulations using water W0 for sensitivity analyses (to mineral reaction rates): two simulations are included, i.e., (1) kinetic rate constants of some minerals are 2 to 3 orders of magnitudes higher than the base case; (2) kinetic rate constants of some minerals are 2 to 3 orders of magnitudes higher than the base case and run under ambient condition.	6.6.5
Development calculations for inputs		
LB0706DSTHC006.001	Thermodynamic data calculation spreadsheets	Appendix C
LB0706DSTHC006.002	Heat load calculation spreadsheets	Appendix D
LB0707DSTHC006.003	Mineralogy, volume fractions, and surface areas calculation spreadsheets	Appendices A and B
MO0706SPECOMPA.000	EQ3/6 calculations for verification of database upgrade effect	Appendix C (see C.9)
Statistical analyses of variability in predicted concentrations		
LB0705DSTHC008.001	Calculation of standard deviations, minimum, maximum, and average values for predicted water/gas compositions	Section 6.7.2
THC seepage model grid development		
LB0706DSTHC009.001	Numerical grid-construction related files	Appendices J and K
CO₂ concentrations during the DST		
LB0708DSTCO207.001	Standardization of CO ₂ concentrations	Appendix M

APPENDIX H
MINERAL KINETIC DATA

INTENTIONALLY LEFT BLANK

H.1 INTRODUCTION

This appendix documents the kinetic data used in the THC seepage model. This appendix also serves as the qualification of these data for intended use in the report, following the qualification plan presented in Appendix N (Section N.4), and discussed in detail in Section H.3.

The experimental mineral dissolution-rate constants and activation energies in this report are taken from papers published in peer-reviewed journals, and therefore they have already undergone a peer review by several experts in this field of study. Four of the referenced studies were done with YMP support, and one was done with support from the U.S. Nuclear Regulatory Commission; these studies are those reported by Carroll et al. (1998 [DIRS 124275]), Murphy et al. (1996 [DIRS 142167]), Ragnarsdóttir (1993 [DIRS 126601]), and Renders et al. (1995 [DIRS 107088]).

H.2 SUMMARY OF EXPERIMENTAL MINERAL DISSOLUTION-RATE CONSTANTS AND ACTIVATION ENERGIES

The dissolution rate constants ($k_{+/-}$) and activation energies (E_a) used in the THC seepage model are listed in Table H.2-1. The listed values of the mineral dissolution rate constants are for the temperature 298.15 K (25°C) and neutral to near-neutral pH values. The qualification method(s) are listed in the far right column of Table H.2-1, corresponding to those listed in Section H.1 above. Detailed discussion of the attributes used to qualify the data are presented in Section H.3.

The tabulated experimental rate constants at 298.15 K are given to the same number of significant figures as reported in the source documents (i.e., generally to two or three significant figures). However, because of the uncertainties introduced by the surface-area determinations, and because of the natural variation in chemical composition of most minerals, the listed values of the experimental rate constants at 298.15 K should be considered uncertain by approximately a factor of 10 when applied to mineral samples from different locations having significantly different chemical compositions. As discussed in the uncertainty section below, the effects of alteration resulting in transport-limited reactions, and the unknown reactive surface area, can result in uncertainties of potentially 3 to 4 orders of magnitude in the overall rate. Therefore, the behavior of the ambient system over long time periods must be used to constrain the rates of reaction in the field, as discussed in Section 6.5.5.1.

The corresponding data for muscovite have also been added to this table, because they are the source for estimated values of the dissolution-rate constants and activation energies for several clay minerals.

Table H.2-1. Mineral Dissolution/Precipitation Reaction Rate Constants ($k_{+/-}$) and Activation Energies (E_a) to Be Qualified

Mineral	$k_{+/-}$ ($\text{mol m}^{-2} \text{s}^{-1}$) ^(a) at 298.15 K	E_a (kJ/mol) ^(b)	m ^(c)	n ^(d)	Formula Used to Calculate Rate Constant ^(e)	Comment ^(e)	Reference	Qualification Method(s) ^(f)
α -Cristobalite (cristoba-a) SiO_2	3.45×10^{-13}	68.9	1	1	$\ln k_{+/-} = (-0.9) - E_a / (R \cdot T(K))$	Dissolution, no precipitation	Renders et al. 1995 [DIRS 107088], pp. 77, 81	2, 5
Quartz SiO_2	4.52×10^{-14}	90.1	1	1	$k_{f, \text{geom.}} = (276 \pm 193) \exp[-E_a / R \cdot T(K)]$ ^(g)	Dissolution, no precipitation	Tester et al. 1994 [DIRS 101732], p. 2415	2, 5
Tridymite SiO_2	3.45×10^{-13}	68.9	1	1		Dissolution rate constant set to α -cristobalite, no precipitation	N/A	5, E
Amorphous silica (sio2(am)) SiO_2	7.32×10^{-13}	60.9	1	1	$\log k_{+/-} = -0.369 + (-7.890 \cdot 10^{-4} \cdot T(K)) + (-3438 / T(K))$	Dissolution	Rimstidt and Barnes 1980 [DIRS 101708], pp. 1683, 1690	2, 5
Opal-CT SiO_2	1.0×10^{-10}	50	4.4	1		Precipitation	Carroll et al. 1998 [DIRS 124275], pp. 1379, 1389	2, 5
Opal-CT SiO_2	7.32×10^{-13}	60.9	1	1		Dissolution rate constant and E_a set to that for dissolution of amorphous silica; precipitation rate law same as for dissolution	N/A	5, E
Oligoclase (plagio-ym) $\text{Na}_{0.76}\text{K}_{0.07}\text{Ca}_{0.17}\text{Al}_{1.17}\text{Si}_{2.83}\text{O}_8$	2.1×10^{-17} (2.1×10^{-15})	67.7	0.353	1		Dissolution only Rate constant reduced by a factor of 10^{-2} for weathering, based on White and Brantley 2003 [DIRS 168088], p. 479, p. 485, Table 4, and p. 494, Figure 6	$k_{+/-}$: White and Brantley 2003 [DIRS 168088] E_a : Blum and Stillings 1995 [DIRS 126590], p. 313, Table 2	2, 5

Table H.2-1. Mineral Dissolution/Precipitation Reaction Rate Constants ($k_{+/-}$) and Activation Energies (E_a) to Be Qualified (Continued)

Mineral	$k_{+/-}$ ($\text{mol m}^{-2} \text{s}^{-1}$) ^(a) at 298.15 K	E_a (kJ/mol) ^(b)	m ^(h)	(c)	Formula Used to Calculate Rate Constant ^(d)	Comment ^(e)	Reference	Qualification Method(s) ^(f)
Sanidine (sanidi-ym) $\text{Na}_{0.47}\text{K}_{0.48}\text{Ca}_{0.05}\text{Al}_{1.05}\text{Si}_{2.95}\text{O}_8$	1.3×10^{-17} (1.3×10^{-15})	63.0	0.353	1		Dissolution only Rate constant based on weathered Shap granite, then reduced by a factor of 10^{-2} for weathering, estimated from White and Brantley 2003 [DIRS 168088], p. 488, Table 5, and p.495, Figure 7	$k_{+/-}$: White and Brantley 2003 [DIRS 168088] E_a : Berger et al. 2002 [DIRS 181221], p. 669	2, 5
Biotite (biotite-ox) $\text{K}(\text{Fe}_{0.57}\text{Mg}_{0.43})\text{AlSi}_3\text{O}_{10}(\text{OH})_2$	9.30×10^{-17} (9.30×10^{-13})	58.6	0.333	1	Scaled by Si	Dissolution only Rate constant reduced by a factor of 10^{-4} for weathering, White and Brantley 2003 [DIRS 168088], p. 497, Figure 9	$k_{+/-}$: Malmstrom et al. 1996 [DIRS 181209], p. 208, Table 2, for pH 8.1 and 1.0% CO_2 gas E_a : from muscovite	2, 5
Muscovite formula $\text{K}_{1.64}\text{Na}_{0.16}(\text{Al}_{3.75}\text{Fe}_{0.22}\text{Mg}_{0.12}\text{Ti}_{1.02})[\text{Si}_{16.06}\text{Al}_{1.92}\text{O}_{20}](\text{OH})_4$	1.0×10^{-14}							2, 5
Illite $\text{K}_{0.6}\text{Mg}_{0.25}\text{Al}_{1.6}\text{Al}_{0.5}\text{Si}_{3.5}\text{O}_{10}(\text{OH})_2$	1.73×10^{-16}	58.6	0.286	1	Scaled by Si	Reversible, rate constant set to muscovite, and corrected for stoichiometry	N/A	5, E
Ca-Beidellite (beidel-ca) $\text{Ca}_{0.165}\text{Al}_{2.33}\text{Si}_{3.67}\text{O}_{10}(\text{OH})_2$	1.52×10^{-16}	58.6	1	1	Scaled by Si	Reversible, rate constant set to illite	N/A	5, E
Mg-Beidellite (beidel-mg) $\text{Mg}_{0.165}\text{Al}_{2.33}\text{Si}_{3.67}\text{O}_{10}(\text{OH})_2$	1.52×10^{-16}	58.6	1	1	Scaled by Si	Reversible, rate constant set to illite	N/A	5, E
Na-Beidellite (beidel-na) $\text{Na}_{0.33}\text{Al}_{2.33}\text{Si}_{3.67}\text{O}_{10}(\text{OH})_2$	1.52×10^{-16}	58.6	1	1	Scaled by Si	Reversible, rate constant set to illite	N/A	5, E
K-Beidellite (beidel-k) $\text{K}_{0.33}\text{Al}_{2.33}\text{Si}_{3.67}\text{O}_{10}(\text{OH})_2$	1.52×10^{-16}	58.6	1	1	Scaled by Si	Reversible, rate constant set to illite	N/A	5, E
Amorphous Antigorite (antigo_am) $\text{Mg}_3\text{Si}_2\text{O}_5(\text{OH})_4$	3.66×10^{-13}	60.9	0.5	1	Scaled by Si	Dissolution rate constant based on amorphous silica	N/A	5, E
	5.0×10^{-11}	60.9	0.5	1	Scaled by Si	Precipitation, using rate constant for amorphous silica		5, E
	1.0×10^{-10}	50	2.2	1		Sensitivity runs		5

Table H.2-1. Mineral Dissolution/Precipitation Reaction Rate Constants ($k_{+/-}$) and Activation Energies (E_a) to Be Qualified (Continued)

Mineral	$k_{+/-}$ ($\text{mol m}^{-2} \text{s}^{-1}$) ^(a) at 298.15 K	E_a (kJ/mol) ^(b)	m ^(c)	Formula Used to Calculate Rate Constant ^(d)	Comment ^(e)	Reference	Qualification Method(s) ^(f)
Kaolinite $\text{Al}_2\text{Si}_2\text{O}_5(\text{OH})_4$	1.0×10^{-13}	7.1	1		Reversible	$k_{+/-}$: Brady and Walther 1989 [DIRS 110748], p. 2826, Figure 6 E_a : Carroll and Walther 1990 [DIRS 160681], p. 806, Table 2	2, 5
Clinoptilolite (climpt-ym/10) $(\text{Ca}_{0.0408}\text{Na}_{0.0203})\text{Ca}_{0.1428}$ $\text{Al}_{0.3467}\text{Si}_{1.4533}\text{O}_{3.6} \cdot 1.0922\text{H}_2\text{O}$	4.89×10^{-13}	58.0	1	Scaled by Si	Dissolution only E_a : laumontite	$k_{+/-}$: Murphy et al. 1996 [DIRS 142167], p. 160 E_a : based on Savage et al. 1993 [DIRS 160198], p. 533, for laumontite	2, 5
Clinoptilolite-Na (climpt-na/10) $\text{Na}_{0.3467}\text{Al}_{0.3467}\text{Si}_{1.4533}\text{O}_{3.6}$ $\cdot 1.0922\text{H}_2\text{O}$	4.89×10^{-13}	58.0	1	Scaled by Si	Reversible E_a : laumontite	$k_{+/-}$: Murphy et al. 1996 [DIRS 142167], p. 160 E_a : based on Savage et al. 1993 [DIRS 160198], p. 533, for laumontite	2, 5
Clinoptilolite-K (climpt-k/10) $\text{K}_{0.3467}\text{Al}_{0.3467}\text{Si}_{1.4533}\text{O}_{3.6}$ $\cdot 1.0922\text{H}_2\text{O}$	4.89×10^{-13}	58.0	1	Scaled by Si	Reversible E_a : laumontite	$k_{+/-}$: Murphy et al. 1996 [DIRS 142167], p. 160 E_a : based on Savage et al. 1993 [DIRS 160198], p. 533, for laumontite	2, 5
Clinoptilolite-Ca (climpt-ca/10) $\text{Ca}_{0.17335}\text{Al}_{0.3467}\text{Si}_{1.4533}\text{O}_{3.6}$ $\cdot 1.0922\text{H}_2\text{O}$	4.89×10^{-13}	58.0	1	Scaled by Si	Reversible E_a : laumontite	$k_{+/-}$: Murphy et al. 1996 [DIRS 142167], p. 160 E_a : based on Savage et al. 1993 [DIRS 160198], p. 533, for laumontite	2, 5

Table H.2-1. Mineral Dissolution/Precipitation Reaction Rate Constants ($k_{+/-}$) and Activation Energies (E_a) to Be Qualified (Continued)

Mineral	$k_{+/-}$ ($\text{mol m}^{-2} \text{s}^{-1}$) ^(a) at 298.15 K	E_a (kJ/mol) ^(b)	m ^(h)	(c)	Formula Used to Calculate Rate Constant ^(d)	Comment ^(e)	Reference	Qualification Method(s) ^(f)
Stellerite (stell-ym/10) $\text{Ca}_{0.195}\text{Na}_{0.005}(\text{Al}_{0.395}\text{Si}_{1.405}\text{O}_{3.6})$ $1.4\text{H}_2\text{O}$	1.13×10^{-12}	58.0	0.712	1	Scaled by Si	Reversible, rate constant set to heulandite E _a : laumontite	$k_{+/-}$: based on Ragnarsdóttir 1993 [DIRS 126601], pp. 2442 to 2447, for heulandite E _a : based on Savage et al. 1993 [DIRS 160198], p. 533, for laumontite	5, E
Mordenite (mordenit/10) $\text{Ca}_{0.00685}\text{Na}_{0.1083}(\text{Al}_{0.282}\text{Si}_{1.518}\text{O}_{3.6})$ $1.0404\text{H}_2\text{O}$	1.04×10^{-12}	58.0	0.659	1	Scaled by Si	Reversible, rate constant set to heulandite	$k_{+/-}$: based on Ragnarsdóttir 1993 [DIRS 126601], pp. 2442 to 2447, for heulandite E _a : based on Savage et al. 1993 [DIRS 160198], p. 533, for laumontite	5, E
Calcite ^e CaCO_3	1.60×10^{-6}	48.1	1	1		Reversible (synthetic calcite)	$k_{+/-}$: Svensson and Dreybrodt 1992 [DIRS 127978], p. 129 E _a : Inskeep and Bloom 1985 [DIRS 128129], p. 2165	2, 5
Anhydrite CaSO_4	equilibrium	N/A	N/A	N/A		Equilibrium used for all simulations		2, 5
Fluorite CaF_2	equilibrium	N/A	N/A	N/A		Equilibrium used for all simulations		5, E
	1.22×10^{-7}	0.0	1	2	See text	Reversible	$k_{+/-}$: Knowles-Van Cappellan et al. 1997 [DIRS 124306], p. 1873	5
Hematite Fe_2O_3	8.59×10^{-12}	N/A	1	1	$R = k1 [\text{HCO}_3^-]^{0.23}$ $k1 = 1.42 \times 10^{-7} \text{ h}^{-1}$ $[\text{HCO}_3^-] = 1.317 \times 10^{-3} \text{ M}$	Dissolution only	Bruno et al. 1992 [DIRS 160189], p. 1139 [HCO_3^-] approximated; see text	2, 5

Table H.2-1. Mineral Dissolution/Precipitation Reaction Rate Constants ($k_{+/-}$) and Activation Energies (E_a) to Be Qualified (Continued)

Mineral	$k_{+/-}$ (mol m ⁻² s ⁻¹) ^(a) at 298.15 K	E_a (kJ/mol) ^(b)	m ^(c)	n ^(d)	Formula Used to Calculate Rate Constant ^(d)	Comment ^(e)	Reference	Qualification Method(s) ^(f)
Goethite FeOOH	equilibrium	N/A	N/A	N/A		Equilibrium used for all simulations		5
Glass (glass-rhyol) Si _{0.8016} Al _{0.1581} Na _{0.0745} K _{0.0796} Ca _{0.0022} Mg _{0.0003} Fe _{0.0074} H _{0.21} 66O _{2.0393}	7.72 × 10 ⁻¹⁷ (7.72 × 10 ⁻¹⁵)	91.0	1	1	See text	Dissolution only Rate constant reduced by a factor of 10 ⁻² owing to weathering, to be consistent with other silicates, based on White and Brantley 2003 [DIRS 168088]	k+/-: Mazer et al. 1992 [DIRS 124354], p. 574	2, 5

^(a) $k_{+/-}$: dissolution/precipitation rate constants at 298.15 K; some values may slightly differ from source values due to unit conversions.

^(b) E_a : activation energy; some values may differ slightly from source values due to unit conversions.

^(c) Exponents m and n in Equation 6.4-5, also scaled by the number of Si atoms in the stoichiometry (Section 6.4.2).

^(d) Formulas are given only for instances where rates were calculated from data in cited references. No formulas are given if the rate was taken directly from the cited references.

^(e) "No precipitation" means precipitation of this mineral is not allowed; "reversible" indicates that the absolute values of the precipitation rate constant are equal to the dissolution rate constant.

^(f) For the qualification methods, "2" denotes data qualified by Method 2 (Corroborating Data), "5" denotes data qualified by Method 5 of SCI-PRO-001 (Technical Assessment), "E" denotes an estimated value that is usually based on using qualified data for a chemically related mineral. "N/A" denotes "not applicable," and is usually used for minerals that are assumed to be equilibrium minerals, or are assigned values based on a similar mineral. If different methods are used to qualify and $k_{+/-}$ and E_a , then the first entry refers to $k_{+/-}$ and the second to E_a .

^(g) The \pm error limits represent fits to a 95% confidence level; the overall log(K) error using a geometric area basis was estimated by the authors to be ± 0.63 .

^(h) The rate law proposed by Carroll et al. (1998 [DIRS 124275]) corresponds to: Rate_{ppt} ([Si] m⁻² s⁻¹) = 1.0 × 10^{-10 ± 0.06} (exp ΔGr / R × T(K))^{4.4 ± 0.3}, temperature dependence is accounted for in the rate law.

⁽ⁱ⁾ $R_{EMP} = \alpha (1 - C / C_s)$; α denotes the rate constant, C the Ca²⁺ concentration in solution, and C_s the equilibrium concentration of Ca²⁺ with respect to calcite.

^(j) ϕ_0 calculated from linear growth rate of Knowles-Van Cappellen et al. (1997 [DIRS 124306], p. 1873); for details of calculations, see text.

^(k) Recalculated rate constant based on diffusion-limited model of Mazer et al. (1992 [DIRS 124354], p. 574); for details of calculations, see text.

H.3 QUALIFICATION OF KINETIC DATA

Following the qualification plan in Section N.4, data are qualified using Method 2 (Corroborating Data) and/or Method 5 (Technical Assessment) of SCI-PRO-001, as noted in Table H.2-1.

A few to several of the qualification process attributes listed in the qualification plan (Section 4) are examined as part of the qualification process, as noted in each subsection below.

H.3.1 Silica Phases: Quartz, Amorphous Silica, α -Cristobalite, Tridymite, and Opal-CT

The discussion below documents the qualification of the kinetic data for the silica minerals using the following methods and attributes:

- Quartz: Methods 2 and 5; Attributes 1, 2, 3, 4, 8, 9, and 10
- Amorphous Silica: Methods 2 and 5; Attributes 1, 2, 3, 4, 8, 9, and 10
- α -Cristobalite: Methods 2 and 5; Attributes 1, 2, 3, 4, 8, 9, and 10
- Tridymite: Method 5; Attributes 3, 9, and 10
- Opal-CT: Method 5; Attributes 3, 9, and 10.

All of the measured data were reported in peer-reviewed publications by well-known researchers at universities or national laboratories, with qualifications comparable to that of YMP personnel/institutions. Most of the data were collected under temperatures and environmental conditions similar to those expected in the near-field environment (approximately 20°C to 200°C).

Data on quartz dissolution kinetics have been provided by Tester et al. (1994 [DIRS 101732], p. 2410). The dissolution experiments of these authors spanned temperatures from 23°C to 255°C, and were conducted using five different apparatuses. The paper was published in the leading peer-reviewed journal in geochemistry, *Geochimica et Cosmochimica Acta*. The results of these experiments, combined with data from 10 previous investigations ranging up to 625°C, including those of Rimstidt and Barnes (1980 [DIRS 101708], pp. 1687 to 1689); see discussion below), revealed a dissolution-rate variation of eleven orders of magnitude over the studied temperature range (e.g., from 4×10^{-14} to 1×10^{-3} mol m⁻² s⁻¹). The selected values in Table H.2-1 for the dissolution-rate constant of quartz at 25°C on a geometric surface area basis ($k_+ = 4.52 \times 10^{-14}$ mol m⁻² s⁻¹ and $E_a = 90.1 \pm 2.5$ kJ mol⁻¹) were calculated from Equation 17a of Tester et al. (1994 [DIRS 101732], p. 2415) and are based on an analysis of a combined set of consistent data from numerous independent studies.

As noted above, the value of $k_+ = 4.52 \times 10^{-14}$ mol m⁻² s⁻¹ for quartz was based on use of the surface area determined by the “geometric area basis” by Tester et al. (1994 [DIRS 101732], p. 2415). The “geometric area basis” calculation is based on the approximation that the mineral particles have the same surface area as perfectly smooth spheres of similar size. Because mineral

grains have irregular surfaces, the “geometric area basis” calculation may underestimate the reactive surface area. The authors also reported the surface area for one sample determined by measurements based on the Brunauer, Emmet, Teller (BET) static volume method, and the value is about a factor of seven larger than the “geometric area basis” value. The values based on the BET surface area measurements are:

$$k_+ = 1.04 \times 10^{-14} \text{ mol m}^{-2} \text{ s}^{-1}$$

and

$$E_a = 87.7 \pm 4.7 \text{ kJ mol}^{-1}$$

calculated using Equation 17b from Tester et al. (1994 [DIRS 101732], p. 2415). The two values of E_a agree to well within their experimental uncertainties, but the values of k_+ differ by a factor of 4. The selected values in Table H.2-1 for the dissolution rate constant of quartz at 25°C are $k_+ = 4.52 \times 10^{-14} \text{ mol m}^{-2} \text{ s}^{-1}$ and $E_a = 90.1 \pm 2.5 \text{ kJ mol}^{-1}$, which were calculated from Tester et al.’s Equation 17a (1994 [DIRS 101732], p. 2415) and are based on consistent data from numerous studies. These values are based on use of the surface area determined by the “geometric area basis” by Tester et al. (1994 [DIRS 101732], p. 2415), which may underestimate the reactive surface area of mineral grains (depending on the roughness of the grains). The values based on the BET surface area measurements are $k_+ = 1.04 \times 10^{-14} \text{ mol m}^{-2} \text{ s}^{-1}$ and $E_a = 87.7 \pm 4.7 \text{ kJ mol}^{-1}$, and were calculated from Equation 17b of Tester et al. (1994 [DIRS 101732], p. 2415). The two values of E_a agree to well within their experimental uncertainties, with some of the difference being due to using dissolution rate constants for a wider temperature range for evaluation of the “geometric area basis” value. Given the uncertainties of these two E_a values, the differences are not experimentally meaningful. Although the values of k_+ differ by about a factor of 4 at 25°C, both values agree within the scatter of the literature values used by Tester et al. (1994 [DIRS 101732]) in their evaluation, as indicated by Figures 8 and 9 of their study.

To derive reaction rates for quartz and amorphous silica, Rimstidt and Barnes (1980 [DIRS 101708]) performed closed-system dissolution and precipitation experiments at temperatures between 18°C and 305°C, using distilled water and Barnes-type rocking autoclaves (Barnes 1971 [DIRS 160181]), as well as a system for circulating hydrothermal fluids, and they compiled their results along with data reported by other investigators. Measurements by Rimstidt and Barnes, and the other studies cited by them, were made with a variety of different silica samples: quartz sand, fused silica powder, silica gel, porous leached glass, and quartz powder with disturbed surfaces, covering a range of temperatures greater than that expected under the thermally perturbed conditions in the near-field environment. The paper was published in *Geochimica et Cosmochimica Acta*. According to the assessed results of Rimstidt and Barnes (1980 [DIRS 101708], Table 4), which include not only their data, but also data from numerous other studies, the activation energies for dissolution of the silica polymorphs are: for quartz, $E_a = 67.4$ to 76.6 kJ mol^{-1} ; for α -cristobalite, $E_a = 68.7 \text{ kJ mol}^{-1}$; for b -cristobalite, $E_a = 65.0 \text{ kJ mol}^{-1}$; and for amorphous silica, $E_a = 60.9$ to 64.9 kJ mol^{-1} . These values are nearly the same, indicating that the rate-limiting step for these reactions is the breaking of strong Si-O bonds. Figure 4 of Rimstidt and Barnes (1980 [DIRS 101708]) is an Arrhenius plot for precipitation of silica polymorphs ($\log k_-$ as a function of the inverse of the temperature). This

plot indicates that values of k_{-} for precipitation of the various silica polymorphs coincide within experimental error (corroborating their use), which is expected because the same activated complex in solution should control the precipitation rates, with the least-squares value being $E_a = 49.8 \text{ kJ mol}^{-1}$. The dissolution rate constant of amorphous silica, $7.32 \times 10^{-13} \text{ mol m}^{-2} \text{ s}^{-1}$, was taken from these authors. More recently, Carroll et al. (1998 [DIRS 124275], p. 1386 and Table 3) report $E_a = 61 \pm 1 \text{ kJ mol}^{-1}$ for precipitation from slightly acidic solutions (pH = 3 to 7), and $E_a = 50 \text{ kJ mol}^{-1}$ for precipitation from near-neutral solutions (pH = 7 to 8), corroborating the activation energy chosen.

Experimentally based dissolution and precipitation rates for α -cristobalite were determined by Renders et al. (1995 [DIRS 107088]), whose paper was also published in *Geochimica et Cosmochimica Acta*. These closed-system experiments were conducted at high temperatures (145°C to 301°C), and at water-saturation pressures. The determined activation energy for the precipitation of cristobalite, $E_a = 52.9 \pm 10 \text{ kJ mol}^{-1}$, was found to be, within the uncertainties, equal to those for quartz and amorphous silica determined by Rimstidt and Barnes (1980 [DIRS 101708], Table 4), $E_a = 49.8 \text{ kJ mol}^{-1}$. They also determined $E_a = 68.9 \pm 11 \text{ kJ mol}^{-1}$ for dissolution of synthetic α -cristobalite. The dissolution rate constant of α -cristobalite at 25°C, $k_{+} = 3.45 \times 10^{-13} \text{ mol m}^{-2} \text{ s}^{-1}$, was calculated from Renders et al. (1995 [DIRS 107088], p. 77), using an equation given in their abstract (assuming the value $R = 8.314 \text{ J K}^{-1} \text{ mol}^{-1}$), and it is an extrapolated value obtained from higher-temperature data.

To investigate the effect of pH, temperature, and aqueous silica concentration on the precipitation rates of amorphous silica, Carroll et al. (1998 [DIRS 124275], p. 1380 and Figure 3) performed laboratory and field experiments in the temperature range between 80°C and 150°C, and with pH values between 3.0 and 8.7, the results of which were published in *Geochimica et Cosmochimica Acta*. Fluidized bed reactors and quartz sand were used in the field experiments, whereas laboratory rates were derived from experiments on silica gel. The starting materials were either dissolved in buffer solutions or geothermal waters until amorphous silica saturation was achieved. Results of the experiments reveal that, in the absence of impurities and in solutions supersaturated with respect to amorphous silica by a factor < 1.3 , precipitation rates have a first-order dependence, whereas in chemically complex field solutions, the precipitation mechanism changes from elementary reaction control to surface defect/surface nucleation control reflected by a nonlinear rate law. The overall activation energy was determined to be $E_a = 50 \pm 3 \text{ kJ mol}^{-1}$ (Carroll et al. 1998 [DIRS 124275], p. 1389). Carroll et al. (1998 [DIRS 124275], p. 1387 and Table 3) also reported $E_a = 50 \text{ kJ mol}^{-1}$ for precipitation from near-neutral solutions (pH = 7 to 8), which is in good agreement with the value of $E_a = 49.8 \text{ kJ mol}^{-1}$ reported by Rimstidt and Barnes (1980 [DIRS 101708], Table 4).

There are several determinations of the activation energy for precipitation of various silica polymorphs at near-neutral pHs that are in very good agreement:

$E_a = 49.8 \text{ kJ mol}^{-1}$ from Rimstidt and Barnes (1980 [DIRS 101708], Table 4)

$E_a = 52.9 \pm 10 \text{ kJ mol}^{-1}$ from Renders et al. (1995 [DIRS 107088], pp. 77, 81)

$E_a = 50 \text{ kJ mol}^{-1}$ from Carroll et al. (1998 [DIRS 124275], Table 3).

Because of the three independent studies yielding results that corroborate each other, the selected value of $E_a = 50 \text{ kJ mol}^{-1}$ can be accepted with confidence. The selected values of E_a for dissolution of the various polymorphs of silica (excluding quartz), in Table H.2-1, fall in a narrow range of $E_a = 60.9$ to 68.7 kJ mol^{-1} , and are based mainly on the measurements of Rimstidt and Barnes (1980 [DIRS 101708], Table 4), along with assessed results from numerous literature studies, and are supplemented for α -cristobalite by results from the more recent study of Renders et al. (1995 [DIRS 107088], pp. 77, 81). Assessed values of k_+ and k_- for the phases are taken from the same studies of Rimstidt and Barnes (1980 [DIRS 101708], Tables 4 and 3) and Renders et al. (1995 [DIRS 107088], pp. 77 and 81). These values are based on many independent studies yielding results that corroborate each other, and the assessed results give confidence in the data and are therefore qualified for use.

No specific data for the tridymite dissolution rate were found. Tridymite has the same composition as quartz and cristobalite, and is a high-temperature form of silica formed during devitrification of tuffs during cooling. Therefore, the dissolution rate constant at 25°C was set to that of the other high-temperature silica phase α -cristobalite, as well as its activation energy. Because tridymite is also much less abundant than quartz or α -cristobalite, and the reactive surface area is not known precisely, any differences in the rate are within the uncertainties in the data (technical assessment). The wealth of experimental data discussed above shows that the silica polymorphs have similar activation energies, and therefore the value for tridymite should also be similar to these other minerals.

Because opal-CT is a high-solubility, poorly ordered form of silica, the dissolution rate constant at 25°C and activation energy were set to the same values as that for the very similar phase amorphous silica (Technical Assessment). The abundance of opal-CT is generally a few percent or less in the repository units and therefore uncertainties in its surface area are likely to be greater than uncertainties in its reaction rate.

H.3.2 Plagioclase (Ca-Na Feldspars)

The discussion below documents the qualification of the kinetic data for plagioclase using the following methods and attributes:

- Methods 2 and 5; Attributes 1, 2, 3, 4, 8, 9, and 10.

Various experimental determinations of the dissolution rate constant for low-albite $\text{NaAlSi}_3\text{O}_8$ (Na endmember of plagioclase) have been compiled and summarized by Blum and Stillings (1995 [DIRS 126590], Table 3), and these studies cover the pH range from around 1 to over 12 and a temperature range of 5°C to 300°C . Figure 4 of the report by Blum and Stillings (1995 [DIRS 126590]) shows the variation of $\log k_+$ with pH at 25°C . Experimental data from nine separate studies are plotted, and the data from eight of these studies are consistent within about ± 0.5 log unit of a smooth curve through these data. The values of $\log k_+$ are essentially independent of pH for the range $\text{pH} = 5$ to 8 , yielding $k_+ \approx 10^{-16.15} \text{ mol cm}^{-2} \text{ s}^{-1} = 7.08 \times 10^{-13} \text{ mol m}^{-2} \text{ s}^{-1}$ for this region. Recent studies of plagioclase artificially weathered in the laboratory and in the field show rates that are several orders of magnitude smaller than those measured on fresh samples in the laboratory (White and Brantley 2003 [DIRS 168088]). In particular, an oligoclase (Na-rich plagioclase feldspar) that was artificially weathered in the laboratory over a

period of six years by White and Brantley (2003 [DIRS 168088], p. 479) showed a decline in the dissolution rate from $7.0 \times 10^{-14} \text{ mol m}^{-2} \text{ s}^{-1}$ to $2.1 \times 10^{-15} \text{ mol m}^{-2} \text{ s}^{-1}$. Other rates for oligoclase (White and Brantley 2003 [DIRS 168088], p. 485 Table 4; p. 494, Figure 6) from samples weathered in the field showed rates as low as $5 \times 10^{-17} \text{ mol m}^{-2} \text{ s}^{-1}$. In order to start with a measured value, and to scale the rate to the effective rate in the field, the measured rate constant was further reduced to $2.1 \times 10^{-17} \text{ mol m}^{-2} \text{ s}^{-1}$.

The activation energies for albite dissolution under neutral pH conditions have been determined by various authors (e.g., Knauss and Wolery (1986 [DIRS 160184], pp. 2481 to 2497; Hellmann 1994 [DIRS 160183], Table 6). Based on these compiled data, Blum and Stillings (1995 [DIRS 126590], Table 2) calculated an apparent activation energy of 67.7 kJ mol^{-1} , which was accepted and used in the THC simulations. It should be noted that the activation energy, $E_a = 68.8 \pm 4.5 \text{ kJ mol}^{-1}$, determined by Hellmann (1994 [DIRS 160183], Table 6) is very close to this value, whereas those values determined by two of the other authors are lower, ranging between 51 and 54 kJ mol^{-1} . Because of the numerous independent studies yielding results that corroborate each other, the assessed results in Table H.2-1 give confidence in the data and are therefore qualified for use.

H.3.3 Sanidine (Na-K Feldspars)

The discussion below documents the qualification of the kinetic data for sanidine using the following methods and attributes:

- Methods 2 and 5; Attributes 1, 2, 3, 4, 8, 9, and 10.

Various experimental determinations of the dissolution rate constant for various Na-K feldspars have been compiled and summarized by Blum and Stillings (1995 [DIRS 126590], Table 4), and these studies cover the pH range from around 1 to over 12 and temperature range of 5°C to 200°C . This work was published in Volume 31 of the book series *Reviews in Mineralogy*, which is a standard reference series for mineralogical data. Figure 5 of the report by Blum and Stillings (1995 [DIRS 126590]) shows the variation of $\log k_+$ with pH at 25°C . Experimental data from six separate studies are plotted, involving data measured for feldspars from different locations, and they are consistent within about ± 0.5 log unit of a smooth curve through these data. The values of $\log k_+$ are essentially independent of pH for the range $\text{pH} = 5$ to 11, yielding $k_+ \approx 10^{-16.75} \text{ mol cm}^{-2} \text{ s}^{-1}$, which is equivalent to $k_+ = 1.78 \times 10^{-13} \text{ mol m}^{-2} \text{ s}^{-1}$ for this pH region. As for plagioclase, recent studies of Na-K feldspars weathered in the field show rates that several orders of magnitude smaller than those measured on fresh samples in the laboratory, as was the case in the study by White and Brantley (2003 [DIRS 168088]). This study was published in the peer-reviewed journal *Chemical Geology*, which is one of the most important sources in this field. In particular, a K-feldspar from the Shap granite has a rate of $1.3 \times 10^{-13} \text{ mol m}^{-2} \text{ s}^{-1}$ (White and Brantley 2003 [DIRS 168088], p. 488, Table 5, sample 13), but rates for samples weathered in the field (White and Brantley 2003 [DIRS 168088], p. 488, Table 5, samples 1 and 2) were as low as $1.6 \times 10^{-17} \text{ mol m}^{-2} \text{ s}^{-1}$. In order to start with a measured value, and to scale the rate to the effective rate in the field, the measured rate constant was further reduced to $1.3 \times 10^{-17} \text{ mol m}^{-2} \text{ s}^{-1}$.

The activation energy for K-feldspar dissolution in neutral pH environments is given by Blum and Stillings (1995 [DIRS 126590], Table 2) as ranging between 35 and 38 kJ mol⁻¹ for neutral pH. More recent data indicated that the activation energy for sanidine should be close to that of the other silicates and feldspars, as for example in the study by Berger et al. (2002 [DIRS 181221], p. 669), who give an activation energy of 63 kJ mol⁻¹, with a range of 61-65 kJ mol⁻¹. This latter study was published in peer-reviewed journal the *American Journal of Science*, which publishes many important papers in the geosciences. The value of 63 kJ mol⁻¹ was used for sanidine in the THC seepage model simulations. The recent determination of this value for sanidine under hydrothermal conditions, and the corroboration to other feldspar activation energies (corroborating data), gives confidence in the data and is therefore qualified for use.

H.3.4 Micas and Clay Minerals: Muscovite, Illite, Smectite (Beidellites), Amorphous Antigorite, and Biotite

The discussion below documents the qualification of the kinetic data for micas and clay minerals using the following methods and attributes:

- Muscovite: Methods 2 and 5; Attributes 1, 2, 3, 4, 8, 9, and 10
- Illite: Method 5; Attributes 3, 9, and 10
- Beidellites: Method 5, Attributes 3, 9, and 10
- Amorphous Antigorite: Method 5; Attributes 3, 9, and 10
- Biotite: Method 5; Attributes 1, 2, 3, 4, 8, 9, and 10.

The dissolution-rate constant for illite was assumed to be the same as the dissolution-rate constant given by Knauss and Wolery (1989 [DIRS 124300], pp. 1493 to 1501) for the very similar mineral muscovite. Knauss and Wolery measured the dissolution rates of electronic-grade ruby mica muscovite as a function of pH and at 70°C. They performed 11 experiments spanning the pH range of 1.4 to 11.8 at roughly equal intervals of pH. The 50-day dissolution experiments were conducted in a single-pass, flow-through apparatus (open-system) using muscovite grains of 100-µm size and dilute buffer solutions. The mica grains were ultrasonically cleaned to remove finer particles. The composition of their mica, as determined from 20 analyses using an electron microprobe, was K_{1.84}Na_{0.16}(Al_{3.75}Fe_{0.22}Mg_{0.12}Ti_{0.02})(Si_{6.06}Al_{1.92}O₂₀)(OH)₄. To determine dissolution rates under far from equilibrium conditions, the ionic strengths of the reacting solutions were very low (3.0×10^{-4} to 0.13 mol kg⁻¹), and solutions were undersaturated with respect to muscovite or any other possible secondary phase. The concentrations of silicon and aluminum released during dissolution were determined using inductively coupled plasma emission spectroscopy, and those of potassium by atomic absorption spectroscopy. The specific surface area of the muscovite was determined by BET surface area analysis using argon gas and was found to be 1.10 m² g⁻¹.

Based on their experimental results, Knauss and Wolery (1989 [DIRS 124300], p. 1500) derived a generalized rate expression describing the dissolution behavior of muscovite under far from equilibrium conditions and at any pH:

$$r = 10^{-14.7} \left[a_{H^+} \right]^{-0.37} + 10^{-16.6} + 10^{-18.1} \left[a_{H^+} \right]^{+0.22} \quad (\text{Eq. H-1})$$

The rate constant for near-neutral pH conditions at 25°C was calculated by assuming surface-controlled dissolution with an activation energy of $E_a = (14 \text{ kcal mol}^{-1})(4.184 \text{ kJ kcal}^{-1}) = 58.6 \text{ kJ mol}^{-1}$, which yields $k_+ = 1.0 \times 10^{-14} \text{ mol m}^{-2} \text{ s}^{-1}$ (Knauss and Wolery 1989 [DIRS 124300], p. 1500).

The assessed value of $k_{+/-}$ for ruby muscovite determined by Knauss and Wolery (1989 [DIRS 124300], p. 1500) at 70°C was published in *Geochimica et Cosmochimica Acta* and can be accepted with confidence. This technical assessment is based on the authors' detailed description of their use of a variety of experimental techniques to characterize the chemical and mineralogical composition of their muscovite sample and analyses of solution concentrations, along with the very detailed presentation of their experimental results. However, the value of k_+ at 25°C is also based on an assumed value of the activation energy. The assessed dissolution rate constants in this report (Table H.2-1) for dissolution of most silicate minerals fall in the range of $k_+ = 1 \times 10^{-14} \text{ mol m}^{-2} \text{ s}^{-1}$ to $3 \times 10^{-12} \text{ mol m}^{-2} \text{ s}^{-1}$. The estimated values of $k_{+/-}$ for clay minerals in Table H.2-1 fall in this range and are likely to be correct within an order of magnitude.

The rate constant for muscovite was recalculated with respect to the number of oxygens per formula unit (k_+ multiplied by 2) to account for differences in chemical formula between the muscovite and the illite stoichiometry, $\text{K}_{0.5}(\text{Mg}_{0.22}\text{Al}_{1.78})(\text{Si}_{3.72}\text{Al}_{0.28}\text{O}_{10})(\text{OH})_2$, assumed here.

The rate constants of the Ca-, Mg-, K-, and Na-beidellites were assumed to be the same as that for illite (determined from muscovite), with a correction for the difference in the number of the oxygens per formula unit between muscovite and smectite (in this case, the original muscovite rate was multiplied by a factor of 2). The assumed beidellite compositions are given in Table H.2-1. The beidellite clay minerals were further reduced by a factor of 10^{-2} , to make their dissolution and precipitation rates closer to those of the primary minerals. These clays must be quite stable in the sense that only a few percent have formed over 10 million years, and the abundances in the repository units are relatively constant.

No measurements were located for the rates of precipitation and dissolution of amorphous antigorite in the aqueous phase. Because amorphous antigorite is noncrystalline, it should form much faster than crystalline sheet silicates of similar composition, and since it is amorphous, it is assumed to precipitate at a rate (adjusted for the Si stoichiometry) similar to amorphous silica (Technical Assessment). Simulations showed that the rate of depletion of Mg caused by using such a fast rate resulted in convergence problems. Therefore, most simulations used the dissolution rate law for amorphous silica for precipitation as well, instead of the amorphous silica precipitation rate law. This still resulted in a relatively fast rate of precipitation, without the associated convergence problems.

The dissolution rate constant for biotite was obtained from Malmstrom et al. (1996 [DIRS 181209], p. 208, Table 2) for a solution pH of 8.1 at equilibrium with 1% CO₂ gas. Biotite is a mica mineral, similar to muscovite, and the rate of $9.30 \times 10^{-13} \text{ mol m}^{-2} \text{ s}^{-1}$ is very close to the rate for muscovite of $1 \times 10^{-14} \text{ mol m}^{-2} \text{ s}^{-1}$ reported by Knauss and Wolery (1989 [DIRS 124300], pp. 1493 to 1501). To be consistent with the observations of the rates of dissolution of naturally weathered biotites by White and Brantley (2003 [DIRS 168088], p. 497, Figure 9) the rate was further reduced to $9.30 \times 10^{-17} \text{ mol m}^{-2} \text{ s}^{-1}$. The effect of this modification is that the rate of dissolution for biotite is also similar to the rates for the other primary aluminosilicate minerals, which was shown in the latter paper to be characteristic of naturally weathered samples. Also, the much slower rate is consistent with the presence of biotite in rocks for over ten million years. Thus, the data from White and Brantley (2003 [DIRS 168088]), combined with these specific observations from the site (Technical Assessment), justify the qualification for use in the THC seepage model report.

H.3.5 Kaolinite

The discussion below documents the qualification of the kinetic data for kaolinite using the following methods and attributes:

- Kaolinite: Methods 2 and 5; Attributes 1, 2, 3, 4, 8, 9, and 10.

The dissolution-rate constant of kaolinite, $\text{Al}_2\text{Si}_2\text{O}_5(\text{OH})_4$, was estimated from a graph in the study by Brady and Walther (1989 [DIRS 110748], Figure 6), based on measurements from their laboratory. According to this figure, the dissolution-rate constant in the pH region between 5 and 8 is equal to $10^{-17.3} \text{ mol cm}^{-2} \text{ s}^{-1}$, which is equivalent to $k_+ = 5 \times 10^{-14} \text{ mol m}^{-2} \text{ s}^{-1}$. This value is corroborated by subsequent measurements of Carroll and Walther (1990 [DIRS 160681], Figure 2), which yield a value of $k_+ \approx 10^{-12.9} \text{ mol m}^{-2} \text{ s}^{-1} = 1.3 \times 10^{-13} \text{ mol m}^{-2} \text{ s}^{-1}$ at pH = 7. Carroll and Walther reported careful dissolution measurements for kaolinite at 25°C, 60°C, and 80°C in buffered solutions with a wide range of solution pHs (pH ~ 1 to 12). The average value from these two studies is $(0.9 \pm 0.4) \times 10^{-13} \text{ mol m}^{-2} \text{ s}^{-1}$, which was rounded off to $k_+ = 1 \times 10^{-13} \text{ mol m}^{-2} \text{ s}^{-1}$ for the accepted value. The values derived by Carroll and Walther (1990 [DIRS 160681], p. 797) for the activation energy vary strongly with pH, and at pH = 7 the value is $E_a = (1.7 \text{ kcal mol}^{-1})(4.184 \text{ kJ kcal}^{-1}) = 7.1 \text{ kJ mol}^{-1}$. Because the results of the two studies yield values that corroborate each other, and because the measurements were made in Walther's laboratory (Walther is one of the leading researchers in mineral dissolution studies), the assessed results in Table H.2-1 are qualified for use.

H.3.6 Zeolites: Clinoptilolite, Mordenite, and Stellerite

The discussion below documents the qualification of the kinetic data for the zeolites using the following methods and attributes:

- Clinoptilolite: Methods 2 and 5; Attributes 1, 2, 3, 4, 8, 9, and 10
- Mordenite: Method 5; Attributes 3, 9, and 10
- Stellerite: Method 5; Attributes 3, 9, and 10.

Murphy et al. (1996 [DIRS 142167], pp. 128 to 186) conducted long-term batch-type experiments to study the dissolution and growth kinetics of an Na-clinoptilolite (work supported by the U.S. Nuclear Regulatory Commission) that is isostructural with Ragnarsdóttir's (1993 [DIRS 126601]) heulandite, discussed below. The measurements of Murphy et al. (1996 [DIRS 142167]) were made at 25°C and pH \approx 9 and was published in the *American Journal of Science*. The authors chose the 100 to 200 mesh-size fraction (75 to 150 μ m) for their experiments, and the surface area of the Na-clinoptilolite was determined by N₂ gas BET analysis to be $10.1 \pm 0.3 \text{ m}^2 \text{ g}^{-1}$. The experimental system was open to atmospheric CO₂, and the initial solutions (NaCl-NaHCO₃ mixtures) were pre-equilibrated for several days before the solid was added. The authors reported very detailed analysis results for the solution concentrations of sodium, silica, and aluminum as a function of time. The Na concentrations were determined using an Na-ion selective electrode, and the SiO₂ and Al were determined with their colored complexes using UV-visible spectrophotometry. The dissolution-rate constant of Na-clinoptilolite given by these authors corresponds to $7.1 \times 10^{-14} \text{ mol m}^{-2} \text{ s}^{-1}$ and was determined for a chemical formula based on 24 structural oxygens per formula unit, Na₂Al₂Si₁₀O₂₄·8H₂O. Because the clinoptilolite formula used here is based on 7.2 oxygens per formula unit, Ca_{0.28}K_{0.08}Na_{0.04}Al_{0.68}Si_{2.92}O_{7.2}·2.6H₂O, the rate constant was multiplied by a factor of (24/7.2) = 3.33 to account for the difference between these chemical formulas.

An activation energy of $E_a = 58 \text{ kJ mol}^{-1}$ for the dissolution of Na-clinoptilolite is based on the value obtained by Savage et al. (1993 [DIRS 160198], p. 533) for laumontite, which is another zeolite mineral. As noted for the silica polymorphs, most of these silicates have similar activation energies.

Heulandite is isostructural with Na-clinoptilolite, has a similar chemical composition, and thus can be used to corroborate the values used for clinoptilolite. Ragnarsdóttir (1993 [DIRS 126601], pp. 2442 to 2447) (published in *Geochimica et Cosmochimica Acta*) determined the dissolution rates for heulandite in the pH range 2.0 to 12.2 and at (25 \pm 2)°C, at conditions maintained far from equilibrium, by measuring the concentrations of silica, aluminum, calcium, sodium, and potassium that were released into solution upon dissolution. The dissolution experiments were performed in fluidized-bed reactors using various solutions and buffers. The sieved grain size fraction used in the experiments ranged between 75 and 125 μ m with a surface area determined by krypton BET analysis being $1715 \pm 11 \text{ cm}^2 \text{ g}^{-1}$. The structural formula of heulandite, Na_{2.2}K_{1.4}Ca_{2.2}Al_{14.2}Si_{23.3}O₇₂·24H₂O, was determined by electron microprobe analysis. The stability of various zeolites was described in terms of their dependence on pH and sodium concentration. Alumina and silica release at intermediate and high pH were approximately stoichiometric, whereas at low pH Al was released preferentially compared to Si, resulting in the formation of a residual Si-rich surface layer. Steady-state dissolution rates plotted as function of pH (see Ragnarsdóttir 1993 [DIRS 126601], Figure 9) show a characteristic U-shaped pattern, typical of most silicates, with decreasing rates from pH 2 to about 5.5, a pH-independent dissolution rate in the near-neutral and neutral pH region, and increasing rates in the high pH region (pH = 7 to 12). The dissolution rate constant at pH = 7.2 is $k_+ = 10^{-11.8} \text{ mol m}^{-2} \text{ s}^{-1}$, or $1.585 \times 10^{-12} \text{ mol m}^{-2} \text{ s}^{-1}$. Because the steady-state dissolution rates for heulandite given by Ragnarsdóttir (1993 [DIRS 126601], pp. 2442 to 2447) were based on the rate of silica release into solution, the value of the rate constant was divided by a factor of 2.8 to give

$k_+ = 5.66 \times 10^{-13} \text{ mol m}^{-2} \text{ s}^{-1}$, corresponding to the number of silica formula units contained in the heulandite formula used here, $\text{Ca}_{0.33}\text{K}_{0.04}\text{Na}_{0.1}\text{Al}_{0.8}\text{Si}_{2.8}\text{O}_{7.2} \cdot 2.6\text{H}_2\text{O}$.

The rate constants of stellerite and mordenite were taken as having the same value. Ragnarsdóttir assumed an activation energy of $E_a = 58 \text{ kJ mol}^{-1}$ for the dissolution of heulandite based on the value obtained by Savage et al. (1993 [DIRS 160198], p. 533) for laumontite, and this value was accepted for stellerite and mordenite.

The assessed results given in Table H.2-1 for $k_{+/-}$ of heulandite and Na-clinoptilolite at 25°C can be accepted with confidence. This technical assessment is based on the authors' detailed description of their use of a variety of experimental techniques to characterize the chemical and mineralogical composition of their mineral, and the determination of the solution concentrations as a function of time. However, the values of E_a are estimated from an experimental value for a chemically related mineral, as are $k_{+/-}$ values for other zeolites.

H.3.7 Calcite

In the THC seepage model, calcite is assumed to be an equilibrium mineral based on its fast dissolution rate. The discussion below documents the qualification of the kinetic data for calcite, which are used to justify its use as an equilibrium mineral, using the following methods and attributes:

- Calcite: Methods 2 and 5; Attributes 2, 3, 4, 8, 9, and 10.

Svensson and Dreybrodt (1992 [DIRS 127978], pp. 129 to 145) (published in *Chemical Geology*) investigated the dissolution kinetics of various natural carbonate samples (e.g., marbles, limestones, calcareous marine pelagic sediments) and National Bureau of Standards synthetic calcite. The batch experiments (free drift technique) were conducted on the 100- μm sieved fractions, at 20°C in aqueous CO_2 solutions (CO_2 pressure of $5 \times 10^{-3} \text{ atm}$) under close to equilibrium conditions with respect to calcite. Calcium and magnesium solution concentrations were analyzed using inductively coupled plasma mass spectrometry. The dissolution rates of the natural carbonate samples were fitted by the authors to an empirical rate law of the form:

$$R_{\text{EMP}} = \alpha_1 (1 - C/C_s)^n \quad (\text{Eq. H-2})$$

with values for n being different when $C \leq (0.6-0.8)C_s$ and when $C > 0.8C_s$, where C denotes the Ca^{2+} concentration in the solution and C_s the equilibrium concentration of Ca^{2+} with respect to a saturated solution of calcite. The α denotes a rate constant. Literature data at 5°C, 15°C, and 25°C were analyzed with the same rate law. In contrast, National Bureau of Standards synthetic calcite was found to exhibit a linear-rate law of the form:

$$R = \alpha (1 - C/C_s) \quad (\text{Eq. H-3})$$

Furthermore, the results revealed lower rates for the natural samples than those of pure calcite. The different dissolution behavior of the natural samples and pure calcite is attributed to adsorbed impurities on the surface of the natural samples, as well as other unknown dissolution inhibitors that may have been present during the formation of these natural phases.

Svensson and Dreybrodt did not determine any activation energies for the dissolution reactions. Thus, an activation energy value of $E_a = 48.1 \text{ kJ mol}^{-1}$ determined by Inskeep and Bloom (1985 [DIRS 128129], p. 2165), from seeded calcite growth measurements, is used in those simulations where kinetics dissolution/precipitation are considered. The paper by Inskeep and Bloom was published in *Geochimica et Cosmochimica Acta*.

The assessed results given in Table H.2-1 for E_a can be accepted with confidence. In the course of reviewing this document, however, it was discovered that the accepted value of $k_{+/-} = 1.60 \times 10^{-6} \text{ mol m}^{-2} \text{ s}^{-1}$ was appropriate for the experimental temperature of 20°C rather than the assumed 25°C. Svensson and Dreybrodt (1992 [DIRS 127978], Table 2) also analyzed literature data and their results imply that $k_{+/-} = 1.9 \times 10^{-6} \text{ mol m}^{-2} \text{ s}^{-1}$ is a more appropriate choice for 25°C, which is 19% larger. This value was taken from Svensson and Dreybrodt (1992 [DIRS 127978], Table 2) for measurements made with a CO_2 pressure of $3 \times 10^{-3} \text{ atm}$. Given the experimental uncertainty in the dissolution-rate constant of Svensson and Dreybrodt and other studies cited by them, the 19% difference between the two values is negligible compared to the experimental error. Calcite is assumed to be an equilibrium mineral in the THC seepage model simulations because the rate on the order of $10^{-6} \text{ mol m}^{-2} \text{ s}^{-1}$ is at least 6 orders of magnitude faster than the silicate minerals (Technical Assessment). Given the time scale of THC processes of years to thousands of years, the assumption is justified and corroborated by multiple studies giving values having the same order of magnitude.

H.3.8 Anhydrite

In the THC seepage model, anhydrite is assumed to be an equilibrium mineral based on its fast dissolution rate. The discussion below documents the qualification of the kinetic data for anhydrite, which justify its use as an equilibrium mineral, using the following methods and attributes:

- Anhydrite: Method 5; Attributes 3, 4, 8, 9, and 10.

Anhydrite (CaSO_4) is a more stable form of calcium sulfate above temperatures around 70°C than the common low-temperature mineral gypsum ($\text{CaSO}_4 \cdot 2\text{H}_2\text{O}$). Anhydrite is similar to gypsum, and the dissolution/precipitation rate constant for gypsum, $\text{CaSO}_4 \cdot 2\text{H}_2\text{O}$, is quite high: $k_{+/-} \sim 10^{-3} \text{ mol m}^{-2} \text{ s}^{-1}$ (see Jeschke et al. 2001 [DIRS 161694], p. 27, and references therein). (The latter paper was published in *Geochimica et Cosmochimica Acta*.) This rate constant is many orders of magnitude larger than the rate constants for other minerals in this report, and implies reaction rates much faster than the time scale considered in this study. For this reason, anhydrite is assumed to react at equilibrium in this study. Therefore, no values of $k_{+/-}$ and E_a need to be assigned for anhydrite.

H.3.9 Fluorite

The discussion below documents the qualification of the kinetic data for fluorite, using the following methods and attributes:

- Fluorite: Method 5; Attributes 2, 3, 4, 8, 9, and 10.

Knowles-Van Cappellen et al. (1997 [DIRS 124306], pp. 1871 to 1877) conducted seeded fluorite (CaF_2) growth experiments at $T = 25 \pm 0.1^\circ\text{C}$ and pH values ranging between 5.1 and 5.6, the results of which were published in *Geochimica et Cosmochimica Acta*. (Experiments at lower pH values are not desirable because the dissolution rate and solubility are increased by formation of neutral HF in solution.) After pre-equilibration of the seeded solutions and initial saturation of solutions with respect to fluorite, the titrants 0.200 mol L^{-1} NaF and 0.100 mol L^{-1} $\text{Ca}(\text{NO}_3)_2$ were added at a constant rate and samples periodically taken for grain-size analysis. The experiments were performed at three different initial ionic strengths of 0.01, 0.085, and 0.1 mol L^{-1} , with NaNO_3 being added to control the ionic strength. Two different seed crystal concentrations were used in order to study both aggregating and non-aggregating conditions. Dynamic light scattering was used to determine the size and size distribution of the crystals in solution, and the initial surface area of the particles was determined to be $11.3 \text{ m}^2 \text{ g}^{-1}$ by BET N_2 gas absorption measurements. The experimental results indicate that at low relative degrees of supersaturation, the precipitation of fluorite is a surface-controlled process that can be described by a second-order rate law of the form:

$$v = k_l (S - 1)^2 \quad (\text{Eq. H-4})$$

where v is the linear growth rate (of cubic grains), k_l is the linear-growth rate constant, which was determined to range between $k_l = 1.4 \times 10^{-3}$ and $3.8 \times 10^{-3} \text{ nm s}^{-1}$, and $(S - 1)$ corresponds to the relative degree of supersaturation (Knowles-Van Cappellen et al. 1997 [DIRS 124306], Equation 2, p. 1873).

The rate constant for fluorite dissolution/precipitation was recalculated as follows from the linear growth rate constants:

$$\text{rate constant} = (\text{linear growth constant}) / \text{molar volume} \quad (\text{Eq. H-5})$$

Assuming an intermediate linear growth rate of $3.0 \times 10^{-3} \text{ nm s}^{-1}$ (Knowles-Van Cappellen et al. 1997 [DIRS 124306], p. 1873) and a molar fluorite volume of $24.542 \text{ cm}^3 \text{ mol}^{-1}$, the rate constant was calculated as follows:

$$k_0 = \left(\frac{3 \cdot 10^{-3} \text{ nm}}{\text{s}} \right) \cdot \left(\frac{10^{-9} \text{ m}}{\text{nm}} \right) / \left[\left(\frac{24.542 \text{ cm}^3}{\text{mol}} \right) \cdot \left(\frac{10^{-6} \text{ m}^3}{\text{cm}^3} \right) \right] = 1.2224 \cdot 10^{-7} \text{ mol m}^{-2} \text{ s}^{-1} \quad (\text{Eq. H-6})$$

The same rate constant was assumed to apply to dissolution of fluorite. Because the study by Knowles-Van Cappellen et al. (1997 [DIRS 124306], pp. 1871 to 1877) was restricted to 25°C , the value of E_a was set equal to zero. However, the dissolution/precipitation rate constants for most minerals have a strong dependence on temperature, and the use of $E_a = 0$ is likely to significantly underestimate the value of $k_{+/-}$ at high temperatures.

The experiments of Knowles-Van Cappellen et al. (1997 [DIRS 124306], pp. 1871 to 1877) were described in detail and appear to have been performed with care. Unfortunately, their experimental rate constants were not reported (i.e., the information was only presented graphically and as values of k_i). Yucca Mountain pore waters are generally saturated with respect to fluorite, and it is present in trace amounts in the rock. Therefore, fluoride concentrations are controlled by fluorite solubility (Section 6.2.2.2), and the assumption that $E_a = 0$ is expected to have negligible effect on predicted fluoride concentrations. The reaction rate at 25°C is several orders of magnitude faster than the silicate minerals and nearly as fast as calcite, and therefore the temperature effect on the rate is also likely to be small.

H.3.10 Hematite and Goethite

The discussion below documents the qualification of the kinetic data for hematite, and the assumption of equilibrium for goethite, using the following methods and attributes:

- Hematite: Methods 2 and 5; Attributes 2, 3, 4, 8, 9, and 10
- Goethite: Method 5; Attributes 3 and 10.

The thermodynamics and kinetics of hematite dissolution in bicarbonate solutions under constant CO₂ pressure (0.3 atm and 0.97 atm) were studied at 25°C by Bruno et al. (1992 [DIRS 160189]) and published in *Geochimica et Cosmochimica Acta*. Results of their investigation reveal that the dissolution of hematite under the above-mentioned conditions and total bicarbonate concentrations higher than $3.2 \times 10^{-3} \text{ mol L}^{-1}$ is surface-controlled and enhanced by the presence of bicarbonate ions. The rate expression given in their paper for the dissolution of hematite in the presence of bicarbonate is:

$$\text{Rate} = k_+ [\text{HCO}_3^-]^{0.23} \quad (\text{Eq. H-7})$$

with $k_+ = 3.9 \times 10^{-11} \text{ mol m}^{-2} \text{ s}^{-1}$ (Bruno et al. 1992 [DIRS 160189], p. 1139). The authors also stated that in the absence of CO₂, they were unable to detect dissolution of hematite below the iron detection limit of $\approx 10^{-8} \text{ mol L}^{-1}$. In neither the study by Hersman et al. (1995 [DIRS 160190], pp. 3327 to 3330) nor the study by Bruno et al. (1992 [DIRS 160189]) were measurements made at higher temperatures.

In this study, the bicarbonate concentration was taken as approximately that of the initial pore water (HDPERM3) equilibrated with calcite at 22.82°C and $p\text{CO}_2 = 1.0 \times 10^{-3} \text{ bars}$. This yields a rate of $8.59 \times 10^{-12} \text{ mol m}^{-2} \text{ s}^{-1}$, which is in the range of the dissolution rates given above, and is corroborated by another study discussed below. Since each model simulation is slightly different and temperatures vary through the model domain, it is only necessary to have an approximate value of the temperature and bicarbonate concentration for calculation of the rate constant. For comparison, the equilibrated bicarbonate concentration for the initial water HDPERM3 at 23.59°C in the *chdump.out* file (simulation *dst_thc_r5_01*; Output DTN: LB0705DSTHC005.001) is 0.12355E-02, which is within 10% of the estimated value used to calculate the reaction rate.

Very little dissolution of minerals containing Fe(III), such as hematite (Fe_2O_3) and goethite (FeOOH), occur under oxic conditions at near-neutral pH values because of the extremely low solubility of Fe(III). However, in the presence of high acidity and certain bidentate ligands, the dissolution of Fe(III) becomes much larger (e.g., Hersman et al. 1995 [DIRS 160190], pp. 3327 to 3330). The dissolution mechanisms and the solubility of iron oxide minerals have been extensively studied in the last decades. A consensus seems to exist that proton- and ligand-promoted dissolution of iron oxide minerals can be described by surface complexation models. Very few data, however, exist on the dissolution and precipitation kinetics of these minerals, especially for hematite. Hersman et al. (1995 [DIRS 160190], pp. 3327 to 3330) studied the effect of siderophores (highly specific, bidentate, iron chelating ligands produced by microorganisms), $3 \times 10^{-3} \text{ mol L}^{-1}$ oxalate, and $2 \times 10^{-3} \text{ mol L}^{-1}$ ascorbate ligands on dissolution of hematite at $\text{pH} = 3$ and temperature $21 \pm 0.5^\circ\text{C}$ (published in *Geochimica et Cosmochimica Acta*). They determined a dissolution rate constant of $k_+ = 1.4 \times 10^{-11} \text{ mol m}^{-2} \text{ s}^{-1}$ in the presence of oxalate and ascorbate, and $k_+ = 3 \times 10^{-12} \text{ mol m}^{-2} \text{ s}^{-1}$ in the presence of siderophores at concentrations comparable to those in natural systems. These values bracket the rate calculated above of $8.59 \times 10^{-12} \text{ mol m}^{-2} \text{ s}^{-1}$, even though the conditions are not identical.

Because hematite and goethite are minor minerals in the tuffs, and Fe solubility is very low under the chemical conditions of the pore waters (e.g., near-neutral pH), the assumption that aqueous concentrations are controlled by local equilibrium with one of these phases is appropriate. Thus, the secondary mineral, goethite, was assumed to be the controlling equilibrium phase, with hematite, a primary mineral in the tuffs, as a dissolving kinetic mineral (Technical Assessment).

H.3.11 Rhyolitic Glass (Vitric Units and Vitrophyres)

The discussion below documents the qualification (following methods and attributes as shown) of the kinetic data for rhyolitic glass, which is a major phase in the vitric units and in the vitrophyres.

- Rhyolitic glass: Methods 2 and 5; Attributes 2, 3, 4, 8, 9, and 10.

To get insight into the alteration mechanisms of clay-based, silica-rich glass, Mazer et al. (1992 [DIRS 124354], pp. 573 to 576) examined naturally occurring tektites (Indochinite) by optical microscopy, transmission electron microscopy, selected-area electron microdiffraction, and energy-dispersive x-ray spectroscopy to determine mineral phases present. The overall chemical composition of the tektites was determined by dissolving a sample in acid solution followed by chemical analysis using an inductively coupled plasma analysis. They performed dissolution experiments with polished monoliths of tektite under selected laboratory conditions. The alteration experiments were performed in the temperature range between 150°C and 225°C at 25°C intervals and for periods between 3 and 400 days. Results of these experiments reveal that the degree of corrosion of the tektites strongly depends on the glass surface-to-water volume ratio (S/V). Under high-dilution conditions (low S/V ratio), etching of the outer glass surface is the dominant reaction process. Under conditions of restricted water contact (high S/V ratios), such as would be expected to occur at Yucca Mountain, the alteration process is initiated by water diffusion into the glass, followed by in situ hydrolysis of the silica network and formation of a poorly crystalline surface layer, which restructures with time to form a complete clay layer.

The rate at which the thickness of the altered layer grows was measured using optical microscopy and with dark-field imaging using transmission electron microscopy. In this case, the dissolution rate of silica-rich glass follows the dependence of water diffusion through a reaction-product layer.

The volcanic glass in the rocks at Yucca Mountain is 12.5 to 13 million years old (Sawyer et al. 1994 [DIRS 100075], p. 1305), and has undergone varying degrees of alteration based on the moderate abundances of clays and zeolites in these units. Therefore, the dissolution rate of the glass is likely to be much slower because of the alteration layer, as was documented for the tectite glass. As an approximation, a constant-thickness product layer on the glass surface was assumed for recalculation of the dissolution-rate constant at 25°C. To estimate the thickness of the coating, some considerations can be applied. First, the layer cannot be thicker than a typical grain diameter (100 μm). At the lower limit, if the coating is too thin, a typical grain would have been completely dissolved in less than 10 million years, using the above relationship derived for the tectite glass. Using the relationships derived below, a thickness of 10 μm results in an inferred grain thickness dissolved of about 30 μm, thus satisfying both the above requirements.

The water diffusion rate (hydration rate) at 25°C was extrapolated from the data obtained for the studied temperature region, yielding $1.6 \times 10^{-7} \mu\text{m}^2 \text{d}^{-1}$ or $1.85 \times 10^{-24} \text{m}^2 \text{s}^{-1}$ (Mazer et al. 1992 [DIRS 124354], pp. 574). The selected dissolution rate constant for the glass, $k_+ = 7.72 \times 10^{-15} \text{mol m}^{-2} \text{s}^{-1}$, was calculated by applying Fick's law, assuming a uniform alteration layer of 10-μm thickness and spherical grain geometry, as follows:

$$J = -D\nabla C$$

$$J = -D \left(\frac{C - C_0}{\Delta X} \right)$$

If $C_0 = 0$, then:

$$J = -D \left(\frac{C}{\Delta X} \right)$$

Dividing by concentration units yields an approximate rate of transport through the alteration layer, as follows:

$$r = - \left(\frac{D}{\Delta X} \right)$$

Plugging in the diffusion coefficient, and a thickness (ΔX) of 10 μm, yields a transport rate of $-1.8519 \times 10^{-19} \text{m/s}$. The rate of dissolution, R , in $\text{mol m}^{-2} \text{s}^{-1}$ for a spherical grain is obtained as follows:

$$R = \frac{V_g}{V_m A t}$$

where V_g is the grain volume, V_m is the glass molar volume, A is the grain area, and t is time. Expanding the volume and area equations yields the following:

$$R = \frac{\frac{4}{3}\pi r^3}{V_m 4\pi r^2 t}$$

$$R = \frac{r}{V_m t}$$

$$R = \frac{\Delta r}{V_m \Delta t}$$

A value of about 24 cm³/mol was estimated for the molar volume of the glass (e.g., the molar volume of quartz is 22.688 cm³/mol), and $\Delta r/\Delta t$ was approximated as the rate of transport calculated above. This yields a transport-limited dissolution rate of 7.72×10^{-15} mol m⁻² s⁻¹, the value used in the THC seepage model. For comparison, the molar volume in the thermodynamic database used in the current THC seepage model is actually higher (29.342 cm³/mol). This difference is relatively small for the calculation of the rate, given the many uncertainties, but if employed would result in a rate of about 6.3×10^{-15} mol m⁻² s⁻¹.

These dissolution rate values are corroborated by data from Yokoyama and Banfield (2002 [DIRS 171364], Section 5), who measured rhyolite glass dissolution rates in field studies and laboratory experiments. Their field value ($\sim 6 \times 10^{-19}$ mol cm⁻² s⁻¹, or $\sim 6 \times 10^{-15}$ mol m⁻² s⁻¹) corresponds closely to the dissolution rate used here. Their experimentally determined rates were one-to-two orders of magnitude higher, which they attribute to changes in the surface properties of the rhyolite glass during crushing, and to differences between the natural and laboratory weathering conditions. Based upon the laboratory experiments, Yokoyama and Banfield (2002 [DIRS 171364], Section 4.6.1) determined an activation energy of 63 kJ mol⁻¹. This value is lower than the value used here, but the differences in the field and laboratory dissolution rates suggest that it may not be applicable to dissolution under natural conditions.

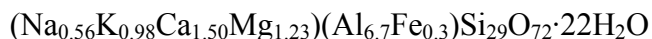
The selected value $E_a = 91$ kJ mol⁻¹ was the experimental activation energy for water diffusion determined by Mazer et al. (1992 [DIRS 124354], p. 574). A technical assessment of the methods used by Mazer et al. (1992 [DIRS 124354], pp. 573 to 576) also suggests that these data are high quality, based on the authors' detailed description of their use of a variety of experimental techniques to characterize the chemical and mineralogical composition of their tektite sample, and the rate at which the surface was altered by water.

Based upon corroborative data and technical assessment, the results given in Table H.2-1 can be accepted with confidence. However, because of the natural chemical variability of tektites and volcanic glasses, the listed value of the experimental rate constant $k_+ = 7.72 \times 10^{-15}$ mol m⁻² s⁻¹ at 25°C is strongly dependent on the thickness of the alteration layer. Since the other silicate minerals started with very similar dissolution rates, and then were typically adjusted by a factor of 10^{-2} to 10^{-4} to bring the rates to the range of 10^{-16} to 10^{-17} , the glass rate was also reduced by a factor of 10^{-2} , to yield a dissolution rate of 7.72×10^{-17} mol m⁻² s⁻¹ at 25°C.

H.4 UNCERTAINTY AND QUALIFICATION OF RATE ADJUSTMENTS

The selected experimental mineral dissolution-rate constants and activation energies are based on measurements using well-characterized mineral samples with adequately described experimental methods. However, the tabulated dissolution-rate constants depend inversely on the estimated surface area of the mineral grains used for the experiments. The usual method of determining mineral surface areas is by using gas absorption measured with the BET static volume method. This type of surface-area measurement is made using a non-reacting gas, generally nitrogen, krypton, or argon. BET measurements using different gases do not yield the same estimated surface areas. For example, Ragnarsdóttir (1993 [DIRS 126601], p. 2441) determined the surface area of a crushed sample of heulandite as being $1,715 \pm 11 \text{ cm}^2 \text{ g}^{-1}$ using krypton BET measurements, and $4,176 \pm 2,435 \text{ cm}^2 \text{ g}^{-1}$ using nitrogen BET measurements. Surface-area measurements using the inert gases are generally considered to be more reliable than those using nitrogen gas. However, because three different gases were used among the various mineral dissolution studies cited above, any comparison of numerical mineral dissolution- and precipitation-rate constants needs to consider the uncertainties resulting from the surface-area measurements.

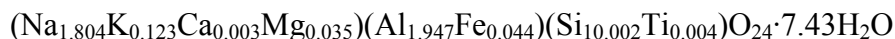
With the exception of a few simple minerals such as quartz and hematite, most natural minerals show significant variations in the composition of samples collected at different locations and even of different samples taken from the same deposit. For example, Murphy et al. (1996 [DIRS 142167], pp. 133, 139, and 129) cited the chemical composition of a clinoptilolite from Lake Tecopa, Inyo County, California, as being:



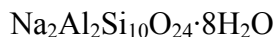
and another one from Malheur County, Oregon, as being:



They also reported analysis results for a Na-clinoptilolite from Death Valley Junction, California, yielding a composition of:



They gave the formula of the idealized (pure) Na-clinoptilolite as being:



These different formulae are based on use of different-sized structural formula units and can be compared on an equivalent basis by normalizing them to the same number of (nonwater) oxygens. However, even without this normalization, it is apparent from these few sample compositions that clinoptilolite and most other natural minerals show significant variations in chemical composition for samples collected at different locations.

In addition, it must also be recognized that weathered minerals exhibit much lower dissolution rates (several orders of magnitude) than experimental values, as shown in the study by White and Brantley (2003 [DIRS 168088]) (published in *Chemical Geology*). This work also showed that

different silicate minerals trend to similar dissolution rates as the rock is weathered, even if their unweathered initial dissolution rates are very different, thus suggesting transport-controlled rates (White and Brantley 2003 [DIRS 168088], p. 479). Since this work has documented dissolution rates for minerals similar to those making up the Yucca Mountain tuffs, over time periods of thousands to millions of years, the rates used in this study have been reduced and scaled to a similar order of magnitude. These modifications reflect the long history of the tuffs (over 10 million years) in the unsaturated zone, after undergoing some early post-depositional elevated temperature alteration. The rates are not unique, though, because the reactive surface area can only be estimated within a few orders of magnitude, since the wetted surface area in the pore space and in fractures that is active for flow and reaction in an unsaturated rock can only be estimated. Furthermore, the effective rate is also dependent on the deviation from equilibrium, which is dependent on the thermodynamic data, the rates of flow in the matrix and fractures, and the percolating pore-water compositions. Therefore, further adjustment of the rates is performed so that reasonable rates of reaction for the ambient system are obtained over long time periods (tens to hundreds of thousands of years). These results are described in Section 6.5.5.1 and throughout Section 6.6, and show very steady chemical profiles over 100,000 years, which do not deviate significantly from the initial conditions. Therefore the final rates are judged to be qualified for the model use by this technical assessment. These rates are then independently validated through the modeling of the Drift Scale Test under thermally perturbed conditions, similar to that expected for the repository.

APPENDIX I
DESIGN INFORMATION FOR ASSUMPTIONS 7, 8, AND 9

INTENTIONALLY LEFT BLANK

INTENTIONALLY LEFT BLANK

APPENDIX J
ORIGINAL NUMERICAL GRID DEVELOPMENT

INTENTIONALLY LEFT BLANK

J.1 INTRODUCTION

This appendix documents the numerical grid development for the THC seepage model one-dimensional and two-dimensional simulations. In addition, this appendix includes the qualification for intended use of elevations of stratigraphic contacts used in the grid development (data from Table 6.5-1, from historical DTN: LB990501233129.004 [DIRS 111475]), because these data have been superseded with similar but not identical data.

The two-dimensional grid is developed for a drift spacing of 81 m by design, representing repository-center conditions (see Section 6.5.1). Enlargement of the model grid to represent a drift spacing of 162 m, representing repository-edge conditions, is documented in Appendix K.

Calculation spreadsheets and input/output data files for the various utilities used in the development of these numerical grids were submitted to the TDMS under Output DTN: LB0706DSTHC009.001. Except for 2kgridv1a running on a PC, all other utilities were run on a Sun workstation.

The model grid was developed in three stages. First, a mesh of the geologic column was constructed, without drift opening, as described in Section J.2 (this mesh is shown on Figure 6.5-1, left-hand side). In a second stage, the drift and its engineered components were discretized as a separate mesh, as described in Section J.3 (this mesh is shown on Figure 6.5-2). In a third stage, the geologic mesh and drift mesh were merged in one final mesh, as described in Section J.4.

The qualification, for intended use, of stratigraphic elevations used in the grid development is presented in Section J.5.

J.2 GEOLOGIC COLUMN MESH DEVELOPMENT (NO DRIFT)

This section describes the steps taken for developing the two-dimensional and one-dimensional grids of the geologic column described in Section 6.5.1, without a drift opening.

J.2.1 Development of the Two-Dimensional Grid

This stage of grid development consisted of the following steps:

1. Generate initial subgrids of points (x,y coordinates):
 - 1a. Run `mk_rect2 V1.0` and `mk_circ2 V1.0` to generate individual fields of points (subgrids) as shown in Table J.2-1 (note: actual file names to run these utilities are fixed as `inp_circ` and `inp_rect` for input, and `crea.circ` and `crea.rect` for output).
 - 1b. Using the output from 1a as input, run `exclude V1.0` to exclude points from the subgrids within areas of sizes shown in Table J.2-1.

Table J.2-1. Two-Dimensional Subgrid Development: Input and Output files

Input File	Utility	Output File of Step 1a (input file for Step 1b)	Subgrid Dimensions (m)	Subgrid spacing (m)	Size of excluded area (m) (exclude V1.0 input parameters)	Final Output File
<i>inp_circ1</i>	<i>mk_circ2</i>	<i>crea.c1</i>	Circular, radius=4.5	Variable	None	<i>crea.c1</i> (unchanged)
<i>inp_rect1</i>	<i>mk_rect2</i>	<i>crea.r1</i>	7×7	0.5	Circular, inside, from <0;0> radius=4.35	<i>crea.r1x</i>
<i>inp_rect2</i>	<i>mk_rect2</i>	<i>crea.r2</i>	14×14	1	Rectangle, inside, x=0 to 7, y= -7 to 7	<i>crea.r2x</i>
<i>inp_rect3</i>	<i>mk_rect2</i>	<i>crea.r3</i>	14×24	2	Rectangle, inside, x=0 to 14, y= -14 to 14	<i>crea.r3x</i>
<i>inp_rect4</i>	<i>mk_rect2</i>	<i>crea.r4</i>	To top of model	Variable	Rectangle, inside, x=0 to 14, y= -24 to 24	<i>crea.r4x</i>
<i>inp_rect5</i>	<i>mk_rect2</i>	<i>crea.r5</i>	To bottom of model	Variable	Rectangle, inside, x=0 to 14, y= -24 to 24	<i>crea.r5x</i>

2. Run *merggrid2* V1.0 (with 6 non-overlapping meshes, 0 overlapping meshes) to merge all the subgrids from Step 1b. Input files are those shown in the last column of Table J.2-1 (from top down, in the same order!) The output file is: *in.merge*.
3. From the output of Step 2, generate a TOUGH2-formatted mesh running *amesh* V1.0:
 - 3a. Copy file *in.merge* to new file *in*.
 - 3b. Run *amesh* V1.0. The input file is: *in*. The output files are: *eleme*, *conne*, and *segmt* (the latter file is used only to plot the mesh if needed; it is not part of the grid development).
 - 3c. Edit the file *eleme* to insert one more blank character between the X and Y columns.
4. Run *mk_grav2* V1.0 to generate TOUGH2-formatted files including gravity vectors:
 - 4a. Run *mk_grav2* V1.0. The input files are: *eleme* and *conne*. The output files are: *ELEME.new* and *CONNE.new*.
 - 4b. Edit output files from Step 4a to remove gridblocks and connections starting with *dr*, and manually insert correct top and bottom connections, including elevations from Table 6.5-1 (Section 6.5.1 of main report).
5. Run *assign* V1.0 to assign hydrogeologic unit names to model layers:
 - 5a. Run *assign* V1.0. The input files are: *ELEME.new* and *contact.dat*. The output file is: *elem_new.dat*. The file *contact.dat* contains the elevations of contacts between hydrogeologic units as shown in Table 6.5-1 of the main report.
 - 5b. Edit *elem_new.dat* to insert the correct rock type, at the bottom of the file, for the top boundary and remove the gridblock starting with *dr*.

6. Run dummy TOUGHREACT V3.1.1 simulation for one second or less to generate a *MESH* file. This is done by creating a *flow.inp* file, with a dummy ROCKS input block, and inserting the contents of files *ELEME.new* and *CONNE.new* in the place for the ELEME and CONNE input blocks. The input file is: *flow.inp*. The output file is: *MESH*. Note: this dummy run may abort on errors on some machines.
7. Create input files for dual-permeability mesh generator 2kgridv1a V1.0:
 - 7a. Create/open a new file named *2kgrid.dat*. In this file, insert the element data from file *eleme_new.dat*, then insert the connection data from file *MESH*, without the CONNE header, and down to the “+++” record, excluded. Then insert at the top of the file the number of element records, the number of connection records, and a zero separated by one or more spaces.
 - 7b. Edit file *2kgrid.dat* to replace “tt” in top-boundary element names by “tb.”
 - 7c. Create/open a new file named *connec.dat*. In this file, insert the bottom part of the *MESH* file that is below the “+++” record.
 - 7d. Create or obtain file *framtr.dat*, which contains the fracture properties necessary for the generation of a dual-permeability grid: porosity, 1/spacing, and active-fracture parameter. The data in this file are from sources listed in Section 4.1 of the main report.
8. Generate the dual-continuum mesh:
 - 8a. Run 2kgridv1a V1.0. Input files: *2kgrid.dat*, *connec.dat*, and *framtr.dat*. Output files: *eleme.dat* and *conne.dat*.
 - 8b. Copy files *elem.dat* and *conne.dat* into a new file called *mesh_2D.dat*.
9. Manually edit *mesh_2D.dat* to remove unused flags and to modify the conceptualization of flow at the interface between the PTn and TSw, and TSw and CH hydrogeologic units (to avoid perching of water at these contacts where adjacent units have sharply different rock properties, consistent with SNL 2007 [DIRS 175177]). Also, in Step 8, the fracture and matrix gridblocks were automatically offset on the x coordinate by 0.5 m. This is for older plotting options that are no longer used; thus, the x coordinates of fracture and matrix gridblocks need to be reset to the same values. Save the edited file as *mesh_2Dfinal.dat*.
 - 9a. Edit the x coordinates in this file such that fractures and matrix blocks have the same x coordinate (this is done with Excel; see spreadsheet *xcoord.xls*; this is done only to facilitate plotting of output; coordinates are not read by TOUGHREACT).
 - 9b. Remove the indices “1” or “2” in the last column of connection data (from the *conne.dat* file; these indices are no longer used).
 - 9c. Add connections between gridblocks of: tcwF3 and ptnM1; ptnM6 and tswF1; and tswF8 and tswM9.

- 9d. Make sure no downstream weighting is specified for any contacts.
- 9e. Remove all fracture connections involving ch1Fv through ch6Fv and tswF9 (here taken as vitric tswF9) gridblocks. Leave the gridblocks in the ELEME list as place holders (to keep the gridblock order uniform for plotting).
- 9f. Add connections between ch3Mv and ch4Fz to avoid water perching on ch4Mz. This is because all the fractures were removed from the vitric units in step 9e and the ch4Mz matrix permeability is very low. This is done by copying the ch3Mv-to- ch4Mz connections and changing their designation to specify ch3Mv-to-ch4Fz connections.

The mesh of the geological column without a drift opening is now complete. The two-dimensional steady-state flow fields were developed using this mesh. The steady-state flow fields are also used to verify that the pressure, temperature, and liquid saturation gradients are uniform and strictly vertical (horizontal contours) in both fracture and matrix gridblocks, thus verifying that the dual-permeability mesh was developed properly.

J.2.2 Development of the One-Dimensional Grid

The procedure is the same as described in Section J.2.1, but starting with one-dimensional subgrids.

1. Run *mk_rect2* V1.0. The input files are (two separate runs): *inp_rect6* and *inp_rect7*. The output files are (two separate runs): *crea.r6* and *crea.r7*. (Note: the actual file names to run this utility are fixed as *inp_rect* for input, and *crea.rect* for output).
2. Run *merggrid2* V1.0. The input files are: *crea.r6* and *crea.r7*. The output file is *in.merge*.
3. Same as Steps 3 to 9 in Section J.2.1, except that the mesh files created in Step 8 are named *mesh_1D.dat* and *mesh_1Dgeol.dat*.

The one-dimensional mesh of the geologic column is now complete. The one-dimensional steady-state flow fields and THC simulations of ambient conditions were developed using this mesh. The steady state flow fields are also used to verify that the pressure, temperature, and liquid saturation gradients are uniform and strictly vertical (horizontal contours) in both fracture and matrix gridblocks, thus verifying that the dual-permeability mesh was developed properly.

J.3 DRIFT MESH DEVELOPMENT

This section documents the steps taken to develop the two-dimensional numerical grid representing the drift and its components. The discretization of the drift is based on dimensions shown on Figure 4.1.1 of the main report. Justification of these dimensions is presented in Appendix I.

1. Run *mk_circ2* V1.0. Input files are (two separate runs): *inp_circ1* and *inp_circ2*. The first file defines points centered on the drift center (radial grid from drift center), defining the drift wall and “dummy” wall rock around the drift. The second file defines points centered on the waste package (radial grid from the center of the waste package) defining the waste package

and other in-drift components. Corresponding output files are *crea.circ1* and *crea.circ2*. (Note: the actual file names to run this utility are fixed as *inp_circ* for input, and *crea.circ* for output.)

2. Run *exclude* V1.0 to weed out points at radius > 2.48 m (determined by trial and error) from *crea.circ2* to avoid overlap with points in *crea.circ1*. Input file is *crea.circ2*. Specify “circle,” “outside,” radius = 2.48 from <0;0>. Output file is *crea.circ2a*.
3. Edit *crea.circ2a* to change the boundaries (points at the bottom of the file) to:

0.0	3.0	(x_{\min} , x_{\max})
-3.0	3.0	(y_{\min} , y_{\max})

4. Run *merggrid* V1.0 (with non-overlapping option). The input files are: *creac.circ2a* and *crea.circ1* (in this order!). The output file is: *in.merge*.
5. Copy file *in.merge* to file *in*.
6. Run *amesh2* (provided in with the input/output files; this is an earlier version of *amesh* V1.0 yielding identical results except that the coordinates of points are output with more significant digits). Input file is: *in*. The output files are: *eleme*, *conne*, and *segmt* (the latter file is used only to plot the mesh if needed; it is not part of the grid development).
7. Run *mk_grav2* V1.0. Input files are *eleme* and *conne*. Output files are *ELEME.new* and *CONNE.new*.
8. Combine files *ELEME.new* and *CONNE.new* into new file *mesh_dr_ini.dat*.
9. Edit file *mesh_ini_dr.dat* and save as *mesh_dr.dat* as follow:

9a. Remove the last three gridblocks at the bottom of the ELEME list (tt001, bb001 and dr001) and remove all connections with dr001 at the bottom of the CONNE list.

9b. The *mk_grav2* utility is “hard-wired” to name gridblocks according to their location within the drift, based on earlier drift designs. For consistency with a more recent design (see Figure 4.1-1 in main report), some of these automatic assignments need to be changed manually as follows:

innr: gridblock within the “inner” zone (the zone between the waste package surface and a radius of 1.251 m from the waste package center).

outr: gridblock within the “outer” zone (the zone from the drip shield surface to the drift wall); however, gridblocks at the drift wall are excluded.

wall: gridblocks in the “outer” zone at the drift wall.

invu: gridblocks in the upper invert excluding those at the drift wall.

wallu: gridblocks in the upper invert at the drift wall.

- invl: gridblocks in the lower invert excluding those at the drift wall.
- walll: gridblocks in the lower invert at the drift wall.
- wpck: gridblock representing the waste package (one gridblock).

The resulting file with the above assignments is named *mesh_dr.dat*. The single-continuum mesh of the drift is now complete, and ready for merging with the dual-continuum mesh of the geologic column developed in Section J.2.1.

J.4 MERGING THE DRIFT AND GEOLOGIC COLUMN MESHES

This section describes the merging of two-dimensional geologic column mesh developed following the steps described in Section J.2.1, with the drift mesh developed following the steps described in Section J.3. The resulting two-dimensional mesh is that used for all heat-load simulations in this report. The merging is done using the utility *mrgdrift V1.0*. This utility labels the drift gridblocks with names starting with *dr*.

1. Copy *mesh_2Dfinal* to new file *mesh_geo.dat*
2. Edit *mesh_geo.dat* to reset the x coordinates of gridblocks as they were originally (offset by 0.5 m; this is needed for *mrgdrift V1.0*). This is done by copying the column with the x coordinates from file *mesh_2D.dat* over the column of x coordinates in file *mesh_geo.dat*.
3. Run *mrgdrift V1.0*. Input files are *mesh_geol.dat* and *mesh_dr.dat*. The output mesh file is *mesh.out*. Accept the defaults for all prompts, and ignore warnings, if any.
4. Edit file *mesh.out* as follows and save it as *mesh_final*:
 - 4a. Reset the x coordinates of matrix and fractures to the same values (this is done with Excel; see spreadsheet *xcoord2.xls*; this is done only to facilitate plotting of output; coordinates are not read by TOUGHREACT)
 - 4b. Change the “D” format exponent in the gridblock volume values (within the ELEM records) to “E.” The “D” can cause errors on reading with some compilers.
 - 4c. In the connections between the drift gridblocks and surrounding rock (i.e., first connections starting with *dr* within the CONNE records), change the first connection distance from 0.1 to 0.0.
 - 4d. Insert a blank line at the bottom of the file.

The mesh of the geological column including the drift opening and drift components is now complete. This mesh is used for simulations of heat load, with the source of heat specified in the gridblock representing the waste package.

J.5 QUALIFICATION OF STRATIGRAPHIC CONTACT ELEVATIONS

DTN: LB990501233129.004 [DIRS 111475] is an historical DTN representing the unsaturated zone (UZ) model grid that was current at the time the THC seepage modeling first began. This DTN is qualified for intended use here, using data from the most current UZ model grid (DTN: LB0701UZMTHCAL.001 [DIRS 179286]). This qualification effort is conducted in accordance with SCI-PRO-001 and the Data Qualification Plan presented in Appendix N (Section N.6). The data are qualified using the Corroborating Data and Technical Assessment approaches (SCI-PRO-001, Attachment 3).

The corroborating method was chosen because: (a) Corroborating data are available for comparison: DTN: LB0701UZMTHCAL.001 [DIRS 179286] includes stratigraphic data for the most current UZ model grid; this data set provides an opportunity to compare model layer elevation as well as model layer thicknesses between the two data sets; (b) Inferences drawn to corroborate the unqualified data can be clearly identified, justified, and documented: the model grids in both data sets were derived using similar methods and represent the same properties of interest (model layer elevation and thickness) at similar model locations.

The Technical Assessment method is also used because: (a) The confidence in the data is in question because data collection procedures are unavailable for review: the DTN in question is output from a superseded document; (b) Documentation or proof of proper data acquisition is unavailable for review: the DTN in question is output from a superseded document.

The data from DTN: LB990501233129.004 [DIRS 111475] are qualified below for intended use using the attributes shown (from the qualification plan).

- Attribute 1: The personnel and organizations that generated the data in DTN: LB990501233129.004 [DIRS 111475] are the same as those generating the updated, and corroborative, data set in DTN: LB0701UZMTHCAL.001 [DIRS 179286]. The personnel and organizations have the level of qualification required for generating data supporting the YMP license application.
- Attributes 2, 3, and 10. The stratigraphy of the THC model is extracted at a location near the center of the repository, located at column 'j34' of the old UZ model grid from DTN: LB990501233129.004 [DIRS 111475] (at Nevada State Plane coordinates E 170572.39 m, N 233194.54 m). The elevations of the contacts between various hydrostratigraphic units as implemented in the THC model are shown in Table J.5-1. This table also gives the thickness of each unit in column 'j34'. A model column very close to the location of column 'j34' exists in the revised UZ numerical grid in DTN: LB0701UZMTHCAL.001 [DIRS 179286] (Column 'c82' in file *MESH_THN.V1*, at coordinate E 170521.151 and N 233141.264 m). The elevation and thickness of each hydrostratigraphic unit in Column 'c82' in DTN: LB0701UZMTHCAL.001 [DIRS 179286] are shown in Table J.5-1 for comparison with the older data. The top elevations and thicknesses of the units in Column 'c82' are quite similar to those of Column 'j34', particularly for the repository units 'tsw33', 'tsw34', 'tsw35', and 'tsw36'. In the THC seepage model, the waste emplacement drift (and the source of heat) is located in the 'tsw35' unit. For this unit, the difference in adopted and revised thickness

is only 2.1 m (a difference of about 2%). The thickness of the 'tsw34' layer differs by about 2.7 m (a difference of about 6%). These differences are largely within the natural variability of stratigraphy as well as uncertainty in locating geologic contacts from boreholes. In addition, the 'tsw34' layer is situated more than 50 m away from the source of heat in the THC model and the impact of heating in the THC model is not realizable that far away. Thus, the difference in thickness in the tsw34 layer between the adopted and updated values is unlikely to have any impact on the thermal seepage simulations in the THC seepage model. The differences in thickness between adopted and updated values far away (both top and bottom) from the source of heat in the THC model are similarly not expected to have any significant impact on the THC simulations.

On these bases, the stratigraphic data from the historic DTN: LB990501233129.004 [DIRS 111475] are considered qualified for intended use in this report.

Table J.5-1. Comparison of Adopted and Revised Values of Elevation and Thickness of Hydrostratigraphic Units for the THC Seepage Model

Model Layer	Adopted Data		Revised Data	
	Elevation, Column 'j34' in LB990501233129.004 [DIRS 111475] (m)	Thickness, Column 'j34' in LB990501233129.004 [DIRS 111475] (m)	Elevation, Column 'c82' in LB0701UZMTHCAL.001 [DIRS 179286] (m)	Thickness, Column 'c82' in LB0701UZMTHCAL.001 [DIRS 179286] (m)
Top	1446.6	—	1452.7	—
tcw11	1446.6	27.4	1452.7	22.9
tcw12	1419.2	77.1	1429.8	97.5
tcw13	1342.1	15.6	1332.3	5.5
ptn21	1326.5	3.4	1326.8	2.1
ptn22	1323.1	2.1	1324.7	5.4
ptn23	1321.0	2.8	—	—
ptn24	1318.2	5.5	1319.3	4.6
ptn25	1312.7	9.1	1314.7	7.2
ptn26	1303.6	9.5	1307.5	13.4
tsw31	1294.1	14.4	1294.1	2.0
tsw32	1279.7	30.4	1292.1	38.2
tsw33	1249.3	80.1	1253.9	79.8
tsw34	1169.2	37.2	1174.1	35.0
tsw35	1132.0	101.4	1139.1	103.5
tsw36	1030.6	33.2	1035.6	32.0
tsw37	997.4	16.6	1003.6	15.9
tsw38	980.8	13.8	987.7	17.2
tsw39	967.0	10.1	970.5	3.4
ch1v	956.9	21.7	967.1	13.7
ch2v	945.2	13.3	953.4	12.2
ch3v	931.9	12.7	941.2	12.2
ch4z	919.2	12.8	929.0	12.2

Table J.5-1. Comparison of Adopted and Revised Values of Elevation and Thickness of Hydrostratigraphic Units for the THC Seepage Model (Continued)

Model Layer	Adopted Data		Revised Data	
	Elevation, Column 'j34' in LB990501233129.004 [DIRS 111475] (m)	Thickness, Column 'j34' in LB990501233129.004 [DIRS 111475] (m)	Elevation, Column 'c82' in LB0701UZMTHCAL.001 [DIRS 179286] (m)	Thickness, Column 'c82' in LB0701UZMTHCAL.001 [DIRS 179286] (m)
ch5z	906.4	14.0	916.8	12.3
ch6	892.4	13.9	904.5	17.9
pp4	878.5	12.6	886.6	7.9
pp3	865.9	32.7	878.7	37.5
pp2	833.2	15.0	841.2	12.6
pp1	818.2	61.5	828.6	61.9
bf3	756.7	33.7	766.7	12.4
Bottom	730.0	—	754.3	—

Source: DTNs: LB990501233129.004 [DIRS 111475; LB0701UZMTHCAL.001 [DIRS 179286], file: *MESH_THN.V1*.

NOTE: Note that in Column 'c82' of DTN: LB0701UZMTHCAL.001 [DIRS 179286] there is no ptn23 geologic layer.

INTENTIONALLY LEFT BLANK

APPENDIX K
MESH MODIFICATIONS CALCULATIONS

INTENTIONALLY LEFT BLANK

K.1 MESH MODIFICATIONS CALCULATIONS

Modifications were made to existing model *MESH*, *GENER*, and *INCON* files to increase the effective drift spacing from 81 m to 93 m and 162 m. These modifications were made using standard Excel97 functions as summarized below. These calculations refer to materials discussed in Section 6.5.1 of this report.

K.1.1 Outputs

The calculations were implemented and output in the following spreadsheets, submitted to the TDMS under Output DTN: LB0706DSTHC009.001:

meshdat_162m.xls Generation of three added model columns for the 162-m case, as shown on Figure 6.1-1

infiltra_162m.xls Calculations of infiltration rate for the added model column for the 162-m case.

K.1.2 Inputs

Inputs to the above spreadsheets consisted of TOUGHREACT V3.1.1 model input files for the 81-m drift spacing case (Section 6.5.1):

MESH Original model mesh input file (same for all simulations) generated as described in Appendix J

INCON Original model initial thermal and hydrological conditions (same for all simulations) from steady state runs as submitted in this report under Output DTN: LB0705DSSSTFLW.002.

Other inputs included the following fracture properties from DTN: LB0205REVUZPRP.001 [DIRS 159525], file: *FRACTURE_PROPERTY.xls*:

Active fracture/matrix interface area for each modeled hydrogeologic unit
Fracture spacing for each modeled hydrogeologic unit

and infiltration flux rates computed as described below from sources listed in Section 4.1.

K.1.3 Functions and Equations

Standard Excel arithmetic functions (addition, division, multiplication etc.) were used. In addition, the function VLOOKUP was used to look up fracture properties for each gridblock (from a fracture property table). Mesh data were calculated from the following relationships (for a 2-D, one-meter-thick, vertical mesh, with added 1-D columns ordered with gridblocks in descending elevation):

Width of added model column:	Δx [m] (given as input)
Model layer i center elevation:	Z_i [m] (input, unchanged from original)
Active fracture/matrix area:	afm [m^2/m^3] (input, unchanged from original)
Fracture spacing:	F_{sp} [m] (input, unchanged from original)
Model layer i top:	$Z_{i\ top} = (Z_i + Z_{i-1}) / 2$
Model layer i bottom:	$Z_{i\ bot} = (Z_i + Z_{i+1}) / 2$
X coordinate:	X_{coord_0} = coordinate of original (existing) right-most block $X_{coord_1} = 40.5 + \Delta x / 2$ for first added column $X_{coord} = X_{coord_1} + \Delta x / 2$ for subsequent added columns
Matrix volume:	$V_m = \Delta x (Z_{top} - Z_{bot})$
Fracture volume:	V_{f_orig} = volume of original (existing) fracture block V_{m_orig} = volume of original (existing) matrix block $V_f = V_m \Phi_f / (1 - \Phi_f)$ with $\Phi_f = V_{f_orig} / (V_{f_orig} + V_{m_orig})$ $= V_m (V_{f_orig} / V_{m_orig})$
Horizontal connections:	Distance $D_1 = 40.5 - X_{coord_0}$ for first added column Distance $D_1 = \Delta x / 2$ for subsequent added columns Distance $D_2 = \Delta x / 2$ Area = $(Z_{i\ top} - Z_{i\ bot})$ (Note: cross-section thickness = 1 m)
Vertical connections:	Distance $D_1 = Z_i - Z_{i\ bot}$ Distance $D_2 = Z_{i\ bot} - Z_{i+1}$ Area = Δx (Note: cross-section thickness = 1 m)
Fracture-matrix connections:	Distance $D_1 = 0$ Distance $D_2 = F_{sp} / 6$ Area = $afm * (0.5 V_f + V_m)$.

Infiltration data were calculated from the following relationship:

$$Q = I\ dens\ A\ 10^{-3} / (60 \times 60 \times 24 \times 365.25)$$

where Q is the injection rate (kg/sec) input into simulations, I is the infiltration rate (mm/yr), $dens$ is water density (taken as $1,000\ kg/m^3$), and A is the connection area through which recharge occurs (m^2).

APPENDIX L
STATISTICAL CALCULATIONS

INTENTIONALLY LEFT BLANK

L.1 STATISTICAL CALCULATIONS

Minimum, maximum, average, and standard deviations for abstracted concentrations of aqueous species and CO₂ gas were calculated using standard Excel functions as summarized below. These calculations refer to materials discussed in Section 6.7.2 of this report.

L.1.1 Outputs

The calculations were implemented and output in the following spreadsheets, submitted to the TDMS under Output DTN: LB0705DSTHC008.001:

frac_stat_top-flux81_f.xls Repository center (81-m drift spacing): calculations for fracture gridblocks with attributes FLUX, TOP, INDX = 1 through 6, water W0, as a function of time and temperature

frac_stat_top-flux162_f.xls Repository edge (162-m drift spacing): calculations for fracture gridblocks with attributes FLUX, TOP, INDX = 1 through 6, water W0, as a function of time and temperature.

L.1.2 Inputs

Inputs to the above spreadsheets consisted of records from other spreadsheets submitted with this report under separate DTNs as shown below:

frac_81_162_w0.xls Predicted concentrations using water W0
(Output DTN: LB0705DSTHC001.001)

frac_81_162_w8.xls Predicted concentrations using water W8
(Output DTN: LB0705DSTHC001.001)

frac_81_162_w9.xls Predicted concentrations using water W9
(Output DTN: LB0705DSTHC001.001)

frac_81_162_w10.xls Predicted concentrations using water W10
(Output DTN: LB0705DSTHC001.001).

Records from these files were filtered for the desired specific attributes (FLUX, HISAT, TOP, and INDX values) using the Excel97 menu "Data/Auto Filter," then cut and pasted into the calculation (and output) spreadsheets listed earlier.

L.1.3 Functions

The function LOG10() was used to log the input data.

The following array functions were used to calculate summary statistics:

Mean:	{ =AVERAGE (IF (<i>time_range</i> = <i>time</i> , <i>data_range</i>)) }
Maximum:	{ =MAX (IF (<i>time_range</i> = <i>time</i> , <i>data_range</i>)) }
Minimum:	{ =MIN (IF (<i>time_range</i> = <i>time</i> , <i>data_range</i>)) }
Std. Deviation:	{ =STDEV (IF (<i>time_range</i> = <i>time</i> , <i>data_range</i>)) }
Count (for info only):	{ =COUNT (IF (<i>time_range</i> = <i>time</i> , <i>data_range</i>)) }

with arguments defined as:

<i>time_range</i>	Array of input data containing the time values for all points
<i>time</i>	The specific desired time value for which to apply the function
<i>data_range</i>	Array of input data on which to apply the function (e.g., pH, CO ₂ concentrations).

Calculations for multiple time periods were implemented by cutting and pasting the above array functions next to a column containing the desired specific *time* values.

APPENDIX M
STANDARDIZATION OF CO₂ CONCENTRATIONS

INTENTIONALLY LEFT BLANK

Table M-1. Standardization of CO₂ Concentrations

Sample Interval (Borehole-Zone)	YMP Tracking Number	Date Sampled	CO ₂ ^(a) (v/v-percent)	Measurement Technique	High Conc Correction ^(b)
57-3	SPC 0052 7911	2/10/98	0.102	Li-Cor low std	
59-3	SPC 0052 7900	2/9/98	0.084	Li-Cor low std	
60-3 ^e	SPC 0052 7906	2/9/98	0.100	Li-Cor low std	
61-3	SPC 0052 7914	2/10/98	0.112	Li-Cor low std	
74-4	SPC 0052 7903	2/9/98	0.062	Li-Cor low std	
77-3	SPC 0052 7901	2/9/98	0.644	Li-Cor low std	0.76
78-3	SPC 0052 7913	2/10/98	0.244	Li-Cor low std	
Heated Drift	SPC 0052 7909	2/10/98	0.040	Li-Cor low std	
Observation Drift	SPC 0052 7907	2/10/98	0.043	Li-Cor low std	
57-3	SPC 0052 7978	6/4/98	0.170	Li-Cor low std	
58-3	SPC 0052 7979	6/4/98	0.189	Li-Cor low std	
59-3	SPC 0052 7980	6/4/98	0.222	Li-Cor low std	
59-4	SPC 0052 7988	6/4/98	0.538	Li-Cor low std	0.63
74-3	SPC 0052 7981	6/4/98	0.143	Li-Cor low std	
75-3	SPC 0052 7982	6/4/98	0.189	Li-Cor low std	
76-3	SPC 0052 7983	6/4/98	0.687	Li-Cor low std	0.81
77-3	SPC 0052 7984	6/4/98	0.621	Li-Cor low std	0.73
78-3	SPC 0052 7986	6/4/98	1.494	Li-Cor low std	1.76
185-3	SPC 0052 7987	6/4/98	0.160	Li-Cor low std	
Observation Drift	SPC 0052 7989	6/4/98	0.046	Li-Cor low std	
57-3	SPC 0052 7278	8/6/98	0.152	Li-Cor low std	
58-3	SPC 0052 7279	8/6/98	0.234	Li-Cor low std	
59-3	SPC 0052 7281	8/6/98	0.342	Li-Cor low std	0.40
60-3	SPC 0052 7283	8/6/98	14.160	Li-Cor low std	16.70
61-3	SPC 0052 7285	8/6/98	2.986	Li-Cor low std	3.52
74-3	SPC 0052 7267	8/5/98	0.133	Li-Cor low std	
75-3	SPC 0052 7268	8/5/98	0.222	Li-Cor low std	
76-3	SPC 0052 7269	8/5/98	0.949	Li-Cor low std	1.12
77-3	SPC 0052 7271	8/5/98	3.330	Li-Cor low std	3.93
78-3	SPC 0052 7273	8/5/98	2.474	Li-Cor low std	2.92
185-3	SPC 0052 7275	8/6/98	0.186	Li-Cor low std	
186-2	SPC 0052 7277	8/6/98	1.497	Li-Cor low std	1.77
182 (56')	SPC 0052 7276	8/6/98	0.092	Li-Cor low std	
182 (64')	SPC 0052 7266	8/5/98	0.054	Li-Cor low std	
Observation Drift	SPC 0052 7287	8/6/98	0.038	Li-Cor low std	
57-3	SPC 0052 7288	10/7/98	0.189	Li-Cor low std	
58-3	SPC 0052 7289	10/7/98	0.414	Li-Cor low std	0.49
59-3	SPC 0052 7290	10/7/98	0.633	Li-Cor low std	0.75
61-3	SPC 0052 7293	10/7/98	5.335	Li-Cor low std	6.29
75-3	SPC 0052 7994	10/7/98	0.374	Li-Cor low std	0.44
76-3	SPC 0052 7296	10/7/98	1.611	Li-Cor low std	1.90
77-3	SPC 0052 7990	10/8/98	0.216	Li-Cor low std	
78-3	SPC 0052 7992	10/8/98	2.702	Li-Cor low std	3.19

Table M-1. Standardization of CO₂ Concentrations (Continued)

Sample Interval (Borehole-Zone)	YMP Tracking Number	Date Sampled	CO ₂ ^(a) (v/v-percent)	Measurement Technique	High Conc Correction ^(b)
185-3	SPC 0052 7995	10/8/98	0.264	Li-Cor low std	
186-2	SPC 0052 7996	10/8/98	2.239	Li-Cor low std	2.64
Observation Drift	SPC 0052 7998	10/8/98	0.046	Li-Cor low std	
Heated Drift	SPC 0052 7999	10/8/98	0.044	Li-Cor low std	
57-1	SPC 0054 1258	12/16/98	0.068	Li-Cor low std	
57-2	SPC 0054 1259	12/16/98	0.191	Li-Cor low std	
57-3	SPC 0054 1260	12/16/98	0.220	Li-Cor low std	
57-4	SPC 0054 1261	12/16/98	0.130	Li-Cor low std	
58-3	SPC 0054 1262	12/16/98	0.392	Li-Cor low std	0.46
59-1	SPC 0054 1263	12/16/98	0.087	Li-Cor low std	
59-3	SPC 0054 1264	12/16/98	0.501	Li-Cor low std	0.59
59-4	SPC 0054 1267	12/16/98	1.562	Li-Cor low std	1.84
60-2	SPC 0054 1269	12/16/98	0.099	Li-Cor low std	
61-1	SPC 0054 1271	12/16/98	0.051	Li-Cor low std	
61-2	SPC 0054 1272	12/16/98	0.083	Li-Cor low std	
61-4	SPC 0054 1274	12/16/98	0.331	Li-Cor low std	0.39
74-1	SPC 0054 1236	12/14/98	0.047	Li-Cor low std	
74-2	SPC 0054 1235	12/14/98	0.084	Li-Cor low std	
74-3	SPC 0054 1234	12/14/98	0.220	Li-Cor low std	
75-3	SPC 0054 1232	12/14/98	0.495	Li-Cor low std	0.58
76-1	SPC 0054 1231	12/14/98	0.058	Li-Cor low std	
76-2	SPC 0054 1237	12/15/98	0.308	Li-Cor low std	0.36
76-3	SPC 0054 1239	12/15/98	1.430	Li-Cor low std	1.69
76-4	SPC 0054 1241	12/15/98	2.164	Li-Cor low std	2.55
77-3	SPC 0054 1243	12/15/98	0.115	Li-Cor low std	
78-1	SPC 0054 1245	12/15/98	0.100	Li-Cor low std	
78-2	SPC 0054 1246	12/15/98	2.188	Li-Cor low std	2.58
78-3	SPC 0054 1248	12/15/98	2.370	Li-Cor low std	2.80
78-4	SPC 0054 1250	12/15/98	0.358	Li-Cor low std	0.42
185-1	SPC 0054 1252	12/15/98	0.159	Li-Cor low std	
185-2	SPC 0054 1253	12/15/98	1.387	Li-Cor low std	1.64
185-3	SPC 0054 1254	12/15/98	0.293	Li-Cor low std	
185-4	SPC 0054 1255	12/15/98	0.136	Li-Cor low std	
186-2	SPC 0054 1256	12/15/98	2.043	Li-Cor low std	2.41
Observation Drift	SPC 0054 1266	12/16/98	0.038	Li-Cor low std	
Heated Drift	SPC 0054 1276	12/16/98	0.040	Li-Cor low std	
57-3	SPC 0055 0611	3/2/99	0.277	Li-Cor low std	
58-3	SPC 0055 0612	3/2/99	0.552	Li-Cor low std	0.65
59-3	SPC 0055 0613	3/2/99	0.746	Li-Cor low std	0.88
60-2	SPC 0055 0616	3/2/99	0.087	Li-Cor low std	
61-2	SPC 0055 0618	3/2/99	0.097	Li-Cor low std	
74-1	SPC 0054 1278	3/1/99	0.046	Li-Cor low std	
74-2	SPC 0054 1279	3/1/99	0.110	Li-Cor low std	
74-3	SPC 0054 1280	3/1/99	0.437	Li-Cor low std	0.52

Table M-1. Standardization of CO₂ Concentrations (Continued)

Sample Interval (Borehole-Zone)	YMP Tracking Number	Date Sampled	CO ₂ ^(a) (v/v-percent)	Measurement Technique	High Conc Correction ^(b)
74-4	SPC 0054 1281	3/1/99	0.302	Li-Cor low std	0.36
75-3	SPC 0054 1282	3/1/99	1.051	Li-Cor low std	1.24
76-1	SPC 0054 1283	3/1/99	0.055	Li-Cor low std	
76-2	SPC 0054 1285	3/1/99	0.324	Li-Cor low std	0.38
76-3	SPC 0054 1287	3/1/99	1.860	Li-Cor low std	2.19
76-4	SPC 0055 0600	3/1/99	4.987	Li-Cor low std	5.88
77-3	SPC 0055 0603	3/2/99	0.119	Li-Cor low std	
78-1	SPC 0054 1284	3/2/99	0.090	Li-Cor low std	
78-3	SPC 0055 0605	3/2/99	4.409	Li-Cor low std	5.20
185-2	SPC 0055 0607	3/2/99	2.020	Li-Cor low std	2.38
185-3	SPC 0055 0608	3/2/99	0.331	Li-Cor low std	0.39
186-2	SPC 0055 0609	3/2/99	2.455	Li-Cor low std	2.90
Observation Drift	SPC 0055 0602	3/1/99	0.039	Li-Cor low std	
57-3	SPC 0055 1123	5/25/99	0.333	Li-Cor low std	0.39
58-3	SPC 0055 1121	5/25/99	0.681	Li-Cor low std	0.80
59-3	SPC 0055 1119	5/25/99	1.101	Li-Cor low std	1.30
60-2	SPC 0055 1115	5/25/99	0.074	Li-Cor low std	
60-3	SPC 0055 1113	5/25/99	0.072	Li-Cor low std	
61-2	SPC 0055 1117	5/25/99	0.073	Li-Cor low std	
74-1	SPC 0055 1124	5/25/99	0.047	Li-Cor low std	
74-2	SPC 0055 1125	5/25/99	0.129	Li-Cor low std	
74-3	SPC 0055 1126	5/25/99	0.639	Li-Cor low std	0.75
74-4	SPC 0055 1127	5/25/99	0.406	Li-Cor low std	0.48
75-3	SPC 0055 1128	5/25/99	1.374	Li-Cor low std	1.62
76-1	SPC 0055 1130	5/26/99	0.058	Li-Cor low std	
76-2	SPC 0055 1131	5/26/99	0.535	Li-Cor low std	0.63
76-3	SPC 0055 1133	5/26/99	3.112	Li-Cor low std	3.67
76-4	SPC 0055 1135	5/26/99	13.077	Li-Cor low std	15.43
77-3	SPC 0055 1137	5/26/99	0.187	Li-Cor low std	
78-3	SPC 0055 1139	5/26/99	0.288	Li-Cor low std	
185-2	SPC 0055 1142	5/26/99	2.311	Li-Cor low std	2.73
186-3	SPC 0055 1143	5/26/99	0.426	Li-Cor low std	0.50
186-2	SPC 0055 1141	5/26/99	0.041	Li-Cor low std	
Observation Drift	SPC 0055 1144	5/26/99	0.042	Li-Cor low std	
57-2	SPC 0055 1145	8/9/99	0.362	Li-Cor low std	0.43
57-3	SPC 0055 1146	8/9/99	0.330	Li-Cor low std	0.39
57-4	SPC 0055 1147	8/9/99	0.173	Li-Cor low std	
58-3	SPC 0055 1148	8/9/99	1.209	Li-Cor low std	1.43
59-2	SPC 0055 1161	8/9/99	1.016	Li-Cor low std	
59-3	SPC 0055 1163	8/9/99	1.273	Li-Cor low std	1.50
59-4	SPC 0055 1165	8/9/99	6.573	Li-Cor low std	7.75
60-3	SPC 0055 1167	8/10/99	0.332	Li-Cor low std	0.39
74-2	SPC 0055 1170	8/10/99	0.158	Li-Cor low std	
74-3	SPC 0055 1171	8/10/99	0.649	Li-Cor low std	0.77

Table M-1. Standardization of CO₂ Concentrations (Continued)

Sample Interval (Borehole-Zone)	YMP Tracking Number	Date Sampled	CO ₂ ^(a) (v/v-percent)	Measurement Technique	High Conc Correction ^(b)
74-4	SPC 0055 1172	8/10/99	0.328	Li-Cor low std	0.39
75-3	SPC 0055 1173	8/10/99	1.315	Li-Cor low std	1.55
76-3	SPC 0055 1175	8/10/99	2.658	Li-Cor low std	3.14
77-3	SPC 0055 1177	8/10/99	0.152	Li-Cor low std	
78-3	SPC 0055 1179	8/10/99	0.123	Li-Cor low std	
185-2	SPC 0055 1182	8/10/99	3.214	Li-Cor low std	3.79
185-3	SPC 0055 1183	8/10/99	0.496	Li-Cor low std	0.59
186-3	SPC 0055 1184	8/10/99	0.613	Li-Cor low std	0.72
Observation Drift	SPC 0055 1181	8/10/99	0.038	Li-Cor low std	
57-3	SPC 0055 1186	11/29/99	0.431	Li-Cor low std	0.51
57-4	SPC 0055 1187	11/29/99	0.275	Li-Cor low std	
58-3	SPC 0055 1188	11/29/99	1.210	Li-Cor low std	1.43
59-4	SPC 0055 1191	11/29/99	9.016	Li-Cor low std	10.64
61-4	SPC 0055 1194	11/29/99	3.551	Li-Cor low std	4.19
74-3	SPC 0055 1197	11/29/99	1.330	Li-Cor low std	1.57
74-4	SPC 0055 1198	11/29/99	0.698	Li-Cor low std	0.82
75-3	SPC 0055 1199	11/29/99	2.779	Li-Cor low std	3.28
76-3	SPC 0055 7071	11/30/99	0.594	Li-Cor low std	0.70
76-4	SPC 0055 7058	11/30/99	6.861	Li-Cor low std	8.09
77-3	SPC 0055 7060	11/30/99	0.220	Li-Cor low std	
78-3	SPC 0055 7062	11/30/99	0.619	Li-Cor low std	0.73
78-4	SPC 0055 7064	11/30/99	1.059	Li-Cor low std	1.25
185-2	SPC 0055 7067	11/30/99	5.208	Li-Cor low std	6.14
185-3	SPC 0055 7068	11/30/99	0.895	Li-Cor low std	1.06
186-3	SPC 0055 7069	11/30/99	1.796	Li-Cor low std	2.12
Heated Drift	SPC 0055 1196	11/30/99	0.043	Li-Cor low std	
Observation Drift	SPC 0055 7066	11/30/99	0.040	Li-Cor low std	
57-3	SPC 0055 9314	4/19/00	0.383	Li-Cor low std	0.45
58-3	SPC 0055 9315	4/19/00	1.672	Li-Cor low std	1.97
59-3	SPC 0055 9317	4/19/00	0.210	Li-Cor low std	
60-4	SPC 0055 9319	4/19/00	0.132	Li-Cor low std	
61-3	SPC 0055 9321	4/19/00	0.075	Li-Cor low std	
61-4	SPC 0055 9323	4/19/00	6.308	Li-Cor low std	7.44
74-3	SPC 0055 9304	4/18/00	1.291	Li-Cor low std	1.52
74-4	SPC 0055 9305	4/18/00	0.724	Li-Cor low std	0.85
75-3	SPC 0055 9306	4/18/00	2.430	Li-Cor low std	2.87
77-3	SPC 0055 9308	4/18/00	0.156	Li-Cor low std	
78-3	SPC 0055 9310	4/18/00	0.353	Li-Cor low std	0.42
78-4	SPC 0055 9312	4/18/00	1.657	Li-Cor low std	1.95
185-2	SPC 0055 9300	4/18/00	3.877	Li-Cor low std	4.57
185-3	SPC 0055 9301	4/18/00	0.823	Li-Cor low std	0.97
186-3	SPC 0055 9302	4/18/00	1.418	Li-Cor low std	1.67
Heated Drift	SPC 0055 9326	4/19/00	0.042	Li-Cor low std	
Observation Drift	SPC 0055 9325	4/19/00	0.042	Li-Cor low std	

Table M-1. Standardization of CO₂ Concentrations (Continued)

Sample Interval (Borehole-Zone)	YMP Tracking Number	Date Sampled	CO ₂ ^(a) (v/v-percent)	Measurement Technique	High Conc Correction ^(b)
57-3/4	SPC 0055 9328	8/21/00	0.605	Li-Cor low std	0.71
58-3	SPC 0055 9329	8/21/00	3.262	Li-Cor low std	3.85
59-3	SPC 0055 9331	8/21/00	0.108	Li-Cor low std	
60-2/3/4	SPC 0055 9333	8/21/00	0.077	Li-Cor low std	
61-3/4	SPC 0055 9335	8/21/00	0.056	Li-Cor low std	
74-3	SPC 0055 9337	8/22/00	1.179	Li-Cor low std	1.39
74-4	SPC 0055 9338	8/22/00	0.978	Li-Cor low std	1.15
75-3	SPC 0055 9339	8/22/00	1.573	Li-Cor low std	1.86
76-3	SPC 0055 9341	8/22/00	0.082	Li-Cor low std	
77-2/3	SPC 0055 9343	8/22/00	0.095	Li-Cor low std	
78-2/3	SPC 0055 9346	8/22/00	0.355	Li-Cor low std	0.42
185-2	SPC 0055 9348	8/22/00	5.115	Li-Cor low std	6.03
185-3	SPC 0055 9350	8/22/00	1.405	Li-Cor low std	1.66
186-3	SPC 0055 9352	8/22/00	4.408	Li-Cor low std	5.20
Heated Drift	SPC 0055 9354	8/22/00	0.046	Li-Cor low std	
Observation Drift	SPC 0055 9345	8/22/00	0.040	Li-Cor low std	
57-3/4	SPC 0055 9395	1/22/01	0.670	Columbus Inst	
58-3	SPC 0055 9397	1/22/01	2.840	Columbus Inst	
59-3	SPC 0055 9399	1/22/01	0.110	Columbus Inst	
60-3/2/4	SPC 0055 9401	1/22/01	0.110	Columbus Inst	
61-3/2	SPC 0055 9403	1/22/01	0.054	Columbus Inst	
74-3	SPC 0055 9406	1/23/01	1.140	Columbus Inst	
75-3	SPC 0055 9408	1/23/01	1.650	Columbus Inst	
76-3/2	SPC 0055 9410	1/23/01	0.190	Columbus Inst	
77-3/2	SPC 0055 9412	1/23/01	0.090	Columbus Inst	
78-3/2/4	SPC 0055 9414	1/23/01	0.680	Columbus Inst	
185-2	SPC 0055 9416	1/23/01	6.810	Columbus Inst	
185-3	SPC 0055 9418	1/23/01	1.940	Columbus Inst	
186-3	SPC 0055 9420	1/23/01	7.760	Columbus Inst	
Observation Drift 1	SPC 0055 9394	1/22/01	0.040	Columbus Inst	
Observation Drift 2	SPC 0055 9422	1/23/01	0.040	Columbus Inst	
57-3/4	SPC 0055 9357	4/17/01	0.784	Li-Cor hi stds	
58-3	SPC 0055 9359	4/17/01	3.467	Li-Cor hi stds	
59-3	SPC 0055 9361	4/17/01	0.108	Li-Cor hi stds	
60-3/2/4/1	SPC 0055 9363	4/17/01	0.080	Li-Cor hi stds	
61-3/2/4	SPC 0055 9365	4/17/01	0.068	Li-Cor hi stds	
74-3	SPC 0055 9367	4/18/01	1.139	Li-Cor hi stds	
75-3	SPC 0055 9369	4/18/01	0.941	Li-Cor hi stds	
76-3/2	SPC 0055 9371	4/18/01	0.178	Li-Cor hi stds	
77-3/2	SPC 0055 9373	4/18/01	0.102	Li-Cor hi stds	
78-3/2/4/1	SPC 0055 9375	4/18/01	0.795	Li-Cor hi stds	
185-2	SPC 0055 9378	4/18/01	7.855	Li-Cor hi stds	

Table M-1. Standardization of CO₂ Concentrations (Continued)

Sample Interval (Borehole-Zone)	YMP Tracking Number	Date Sampled	CO ₂ ^(a) (v/v-percent)	Measurement Technique	High Conc Correction ^(b)
185-3	SPC 0055 9380	4/18/01	2.284	Li-Cor hi stds	
186-3	SPC 0055 9382	4/18/01	6.413	Li-Cor hi stds	
Heated Drift	SPC 0055 9384	4/18/01	0.046	Li-Cor hi stds	
Observation Drift	SPC 0055 9377	4/18/01	0.038	Li-Cor hi stds	
57-3/4	SPC 0055 9385	8/7/01	1.011	Li-Cor hi stds	
58-3	SPC 0055 9387	8/7/01	6.342	Li-Cor hi stds	
59-3/4	SPC 0055 9389	8/8/01	0.178	Li-Cor hi stds	
60-3/2/4/1	SPC 0055 9391	8/7/01	0.096	Li-Cor hi stds	
61-3/2/4	SPC 0055 9393	8/7/01	0.557	Li-Cor hi stds	
74-3	SPC 0055 9431	8/8/01	0.643	Li-Cor hi stds	
75-3	SPC 0055 9433	8/8/01	0.821	Li-Cor hi stds	
76-3/2	SPC 0055 9435	8/8/01	0.130	Li-Cor hi stds	
77-3	SPC 0055 9437	8/8/01	0.090	Li-Cor hi stds	
78-3/2/4	SPC 0055 9439	8/8/01	1.966	Li-Cor hi stds	
185-2	SPC 0055 9424	8/7/01	11.522	Li-Cor hi stds	
185-3	SPC 0055 9426	8/7/01	4.427	Li-Cor hi stds	
186-3	SPC 0055 9428	8/7/01	8.039	Li-Cor hi stds	
Heated Drift	SPC 0055 9356	8/7/01	0.039	Li-Cor hi stds	
Observation Drift	SPC 0055 9430	8/7/01	0.034	Li-Cor hi stds	
57-3/4	SPC 0101 6517	11/27/01	0.880	Columbus Inst	
58-3	SPC 0101 6519	11/27/01	2.500	Columbus Inst	
59-3/4	SPC 0101 6522	11/28/01	0.080	Columbus Inst	
61-3/2/4	SPC 0101 6524	11/28/01	0.270	Columbus Inst	
74-3	SPC 0101 6501	11/27/01	0.640	Columbus Inst	
75-3	SPC 0101 6504	11/27/01	0.850	Columbus Inst	
76-1	SPC 0101 6511	11/27/01	0.370	Columbus Inst	
76-3/2	SPC 0101 6509	11/27/01	0.920	Columbus Inst	
76-4	SPC 0101 6507	11/27/01	0.070	Columbus Inst	
77-3	SPC 0101 6513	11/27/01	0.060	Columbus Inst	
78-3/2/4	SPC 0101 6515	11/27/01	0.710	Columbus Inst	
185-1	SPC 0055 9448	11/26/01	0.690	Columbus Inst	
185-2	SPC 0055 9445	11/26/01	4.830	Columbus Inst	
185-3	SPC 0055 9443	11/26/01	2.900	Columbus Inst	
185-4	SPC 0055 9450	11/26/01	1.490	Columbus Inst	
186-3	SPC 0101 6526	11/28/01	7.700	Columbus Inst	
Heated Drift	SPC 0101 6528	11/26/01	0.060	Columbus Inst	
Observation Drift	SPC 0055 9452	11/26/01	0.070	Columbus Inst	
57-3/4	SPC 0101 6546	1/8/02	0.900	Columbus Inst	
59-3/4	SPC 0101 6400	1/8/02	0.150	Columbus Inst	
61-3/2/4	SPC 0101 6402	1/8/02	0.630	Columbus Inst	
74-3	SPC 0101 6538	1/7/02	1.080	Columbus Inst	
75-3	SPC 0101 6540	1/7/02	6.650	Columbus Inst	
76-3/2	SPC 0101 6542	1/7/02	0.770	Columbus Inst	
78-3/2/4	SPC 0101 6544	1/7/02	0.790	Columbus Inst	

Table M-1. Standardization of CO₂ Concentrations (Continued)

Sample Interval (Borehole-Zone)	YMP Tracking Number	Date Sampled	CO ₂ ^(a) (v/v-percent)	Measurement Technique	High Conc Correction ^(b)
185-2	SPC 0101 6532	1/7/02	7.500	Columbus Inst	
185-3	SPC 0101 6534	1/7/02	3.430	Columbus Inst	
186-3	SPC 0101 6536	1/7/02	3.450	Columbus Inst	
Heated Drift	SPC 0101 6531	1/7/02	0.050	Columbus Inst	
Observation Drift	SPC 0101 6530	1/7/02	0.060	Columbus Inst	
57-3/4	SPC 0101 6420	1/22/02	0.830	Columbus Inst	
58-3	SPC 0101 6422	1/23/02	3.870	Columbus Inst	
59-3/4	SPC 0101 6424	1/23/02	0.100	Columbus Inst	
61-3/2/4	SPC 0101 6426	1/23/02	0.510	Columbus Inst	
74-3	SPC 0101 6410	1/22/02	0.860	Columbus Inst	
75-3	SPC 0101 6412	1/22/02	4.920	Columbus Inst	
76-3/2	SPC 0101 6416	1/22/02	0.820	Columbus Inst	
78-3/2/4	SPC 0101 6418	1/22/02	1.220	Columbus Inst	
185-2	SPC 0101 6404	1/22/02	6.300	Columbus Inst	
185-3	SPC 0101 6406	1/22/02	2.450	Columbus Inst	
186-3	SPC 0101 6408	1/22/02	0.170	Columbus Inst	
Heated Drift	SPC 0101 6415	1/22/02	0.050	Columbus Inst	
Observation Drift	SPC 0101 6414	1/22/02	0.050	Columbus Inst	
57-3/4	SPC 0101 6444	2/19/02	0.970	Columbus Inst	
58-3	SPC 0101 6446	2/19/02	3.250	Columbus Inst	
59-3/4	SPC 0101 6448	2/19/02	0.070	Columbus Inst	
61-3/2/4	SPC 0101 6450	2/19/02	0.740	Columbus Inst	
74-3	SPC 0101 6440	2/19/02	0.560	Columbus Inst	
75-3/4	SPC 0101 6442	2/19/02	0.420	Columbus Inst	
76-3/2	SPC 0101 6436	2/19/02	0.120	Columbus Inst	
78-3/2/4	SPC 0101 6438	2/19/02	0.500	Columbus Inst	
185-2	SPC 0101 6430	2/19/02	6.090	Columbus Inst	
185-3	SPC 0101 6432	2/19/02	2.340	Columbus Inst	
186-3	SPC 0101 6434	2/19/02	6.730	Columbus Inst	
Heated Drift	SPC 0101 6429	2/19/02	0.040	Columbus Inst	
Observation Drift	SPC 0101 6428	2/19/02	0.050	Columbus Inst	
57-3/4	SPC 0101 6474	3/19/02	0.840	Columbus Inst	
58-3	SPC 0101 6476	3/19/02	1.570	Columbus Inst	
59-3/4	SPC 0101 6478	3/19/02	0.080	Columbus Inst	
61-3/2/4	SPC 0101 6480	3/19/02	0.120	Columbus Inst	
74-3	SPC 0101 6470	3/19/02	0.350	Columbus Inst	
75-3/4	SPC 0101 6472	3/19/02	0.270	Columbus Inst	
76-3/2	SPC 0101 6466	3/19/02	0.110	Columbus Inst	
78-3/2/4	SPC 0101 6468	3/19/02	0.190	Columbus Inst	
185-2	SPC 0101 6458	3/19/02	4.640	Columbus Inst	
185-3	SPC 0101 6460	3/19/02	1.820	Columbus Inst	
186-3	SPC 0101 6464	3/19/02	4.270	Columbus Inst	
Heated Drift	SPC 0101 6457	3/19/02	0.040	Columbus Inst	
Observation Drift	SPC 0101 6456	3/19/02	0.050	Columbus Inst	

Table M-1. Standardization of CO₂ Concentrations (Continued)

Sample Interval (Borehole-Zone)	YMP Tracking Number	Date Sampled	CO ₂ ^(a) (v/v-percent)	Measurement Technique	High Conc Correction ^(b)
57-3/4	SPC 0101 6482	4/16/02	0.830	Columbus Inst	
58-3	SPC 0101 6484	4/16/02	2.570	Columbus Inst	
59-3/4	SPC 0101 6486	4/16/02	0.070	Columbus Inst	
61-3/2/4	SPC 0101 6488	4/16/02	0.560	Columbus Inst	
74-3	SPC 0101 7202	4/16/02	0.330	Columbus Inst	
76-3/2	SPC 0101 6496	4/16/02	0.040	Columbus Inst	
78-3/2/4	SPC 0101 7200	4/16/02	0.270	Columbus Inst	
185-2	SPC 0101 6490	4/16/02	4.700	Columbus Inst	
185-3	SPC 0101 6492	4/16/02	2.420	Columbus Inst	
186-3	SPC 0101 6494	4/16/02	3.840	Columbus Inst	
Heated Drift	SPC 0101 6498	4/16/02	0.030	Columbus Inst	
Observation Drift	SPC 0101 6462	4/16/02	0.040	Columbus Inst	
57-3/4	SPC 0101 7221	5/14/02	1.130	Columbus Inst	
58-3	SPC 0101 7223	5/14/02	1.940	Columbus Inst	
59-3/4	SPC 0101 7225	5/14/02	0.060	Columbus Inst	
61-3/2/4	SPC 0101 7227	5/14/02	0.870	Columbus Inst	
74-3	SPC 0101 7207	5/14/02	0.410	Columbus Inst	
75-3/4	SPC 0101 7209	5/14/02	0.340	Columbus Inst	
76-3/2	SPC 0101 7211	5/14/02	0.150	Columbus Inst	
78-3/2/4	SPC 0101 7213	5/14/02	1.110	Columbus Inst	
185-2	SPC 0101 7215	5/14/02	6.500	Columbus Inst	
185-3	SPC 0101 7217	5/14/02	2.550	Columbus Inst	
186-3	SPC 0101 7219	5/14/02	3.940	Columbus Inst	
Heated Drift	SPC 0101 7206	5/14/02	0.050	Columbus Inst	
Observation Drift	SPC 0101 7206	5/14/02	0.040	Columbus Inst	
57-3/4	SPC 0101 7246	7/24/02	0.72	Columbus Inst	
58-3	SPC 0101 7248	7/24/02	0.48	Columbus Inst	
59-3/4	SPC 0101 7250	7/24/02	0.05	Columbus Inst	
61-3/2/4	SPC 0101 7252	7/24/02	0.36	Columbus Inst	
74-3	SPC 0101 7238	7/24/02	0.21	Columbus Inst	
75-3/4	SPC 0101 7240	7/24/02	0.18	Columbus Inst	
76-3/2	SPC 0101 7242	7/24/02	0.11	Columbus Inst	
78-3/2/4	SPC 0101 7244	7/24/02	0.12	Columbus Inst	
185-2	SPC 0101 7232	7/24/02	3.78	Columbus Inst	
185-3	SPC 0101 7234	7/24/02	1.46	Columbus Inst	
186-3	SPC 0101 7236	7/24/2002	2.72	Columbus Inst	186-3
Heated Drift	SPC 0101 7231	7/24/02	0.05	Columbus Inst	
Observation Drift	SPC 0101 7230	7/24/02	0.04	Columbus Inst	
57-3/4	SPC 0101 7270	12/4/02	0.642	Columbus Inst	
58-3	SPC 0101 7272	12/4/02	0.335	Columbus Inst	
59-3/4	SPC 0101 7274	12/4/02	0.093	Columbus Inst	
61-3/2/4	SPC 0101 7276	12/4/02	0.219	Columbus Inst	
74-3	SPC 0101 7262	12/4/02	0.306	Columbus Inst	
75-3/4	SPC 0101 7264	12/4/02	0.129	Columbus Inst	

Table M-1. Standardization of CO₂ Concentrations (Continued)

Sample Interval (Borehole-Zone)	YMP Tracking Number	Date Sampled	CO ₂ ^(a) (v/v-percent)	Measurement Technique	High Conc Correction ^(b)
76-3/2	SPC 0101 7266	12/4/02	0.073	Columbus Inst	
78-3/2/4	SPC 0101 7268	12/4/02	0.212	Columbus Inst	
185-2	SPC 0101 7256	12/4/02	1.503	Columbus Inst	
185-3	SPC 0101 7258	12/4/02	1.084	Columbus Inst	
186-3	SPC 0101 7260	12/4/02	1.927	Columbus Inst	
Heated Drift	SPC 0101 7254	12/4/02	0.048	Columbus Inst	
Observation Drift	SPC 0101 7255	12/4/02	0.054	Columbus Inst	
57-3/4	SPC 0101 7294	3/11/03	0.711	Columbus Inst	
58-3	SPC 0101 7296	3/11/03	0.401	Columbus Inst	
59-3/2	SPC 0101 7298	3/11/03	0.158	Columbus Inst	
61-3/2/4	SPC 0101 8800	3/11/03	0.469	Columbus Inst	
74-3	SPC 0101 7282	3/10/03	0.250	Columbus Inst	
75-3/4	SPC 0101 7284	3/10/03	0.097	Columbus Inst	
76-3/2	SPC 0101 7278	3/10/03	0.070	Columbus Inst	
78-3/2/4	SPC 0101 7280	3/10/03	0.178	Columbus Inst	
185-2	SPC 0101 7286	3/10/03	1.230	Columbus Inst	
185-3	SPC 0101 7288	3/10/03	0.934	Columbus Inst	
186-3	SPC 0101 7290	3/10/03	1.267	Columbus Inst	
Heated Drift	SPC 0101 7293	3/10/03	0.051	Columbus Inst	
Observation Drift	SPC 0101 7292	3/10/03	0.054	Columbus Inst	
57-3/4	SPC 0101 8804	7/15/03	0.614	Columbus Inst	
58-3	SPC 0101 8806	7/15/03	0.431	Columbus Inst	
59-3/4	SPC 0101 8808	7/15/03	0.171	Columbus Inst	
61-3/2/4	SPC 0101 8810	7/15/03	0.527	Columbus Inst	
74-3	SPC 0101 8812	7/15/03	0.235	Columbus Inst	
75-3/4	SPC 0101 8814	7/15/03	0.096	Columbus Inst	
76-3/2	SPC 0101 8816	7/15/03	0.090	Columbus Inst	
78-3/2/4	SPC 0101 8819	7/15/03	0.379	Columbus Inst	
185-2	SPC 0101 8821	7/15/03	1.235	Columbus Inst	
185-3	SPC 0101 8823	7/15/03	0.743	Columbus Inst	
186-3	SPC 0101 8825	7/15/03	1.512	Columbus Inst	
Heated Drift	SPC 0101 8827	7/15/03	0.051	Columbus Inst	
Observation Drift	SPC 0101 8803	7/15/03	0.051	Columbus Inst	
57-3/4	SPC 0101 8829	12/16/03	0.446	Columbus Inst	
58-3/2	SPC 0101 8831	12/16/03	0.192	Columbus Inst	
59-3/2	SPC 0101 8833	12/16/03	0.096	Columbus Inst	
61-3/2/4	SPC 0101 8835	12/16/03	0.185	Columbus Inst	
74-3/4	SPC 0101 8837	12/16/03	0.253	Columbus Inst	
75-3/4	SPC 0101 8839	12/16/03	0.122	Columbus Inst	
76-3/2/4	SPC 0101 8841	12/16/03	0.073	Columbus Inst	
78-3/2/4/1	SPC 0101 8843	12/16/03	0.109	Columbus Inst	
185-2	SPC 0101 8845	12/16/03	0.839	Columbus Inst	
185-3	SPC 0101 8847	12/16/03	0.504	Columbus Inst	
186-3/2	SPC 0101 8849	12/16/03	0.977	Columbus Inst	

Table M-1. Standardization of CO₂ Concentrations (Continued)

Sample Interval (Borehole-Zone)	YMP Tracking Number	Date Sampled	CO ₂ ^(a) (v/v-percent)	Measurement Technique	High Conc Correction ^(b)
Heated Drift	SPC 0101 8851	12/16/03	0.057	Columbus Inst	
Observation Drift	SPC 0101 8828	12/16/03	0.048	Columbus Inst	
57-3/4	SPC 0101 8860	4/19/04	0.458	Columbus Inst	
58-3/2	SPC 0101 8861	4/19/04	0.263	Li-Cor hi stds ^(c)	
59-3/2	SPC 0101 8862	4/19/04	0.106	Columbus Inst	
61-3/2/4	SPC 0101 8863	4/19/04	0.250	Columbus Inst	
74-3/4	SPC 0101 8852	4/19/04	0.236	Columbus Inst	
75-3/4	SPC 0101 8853	4/19/04	0.188	Columbus Inst	
76-3/2/4	SPC 0101 8854	4/19/04	0.119	Columbus Inst	
78-3/2/4	SPC 0101 8855	4/19/04	0.161	Columbus Inst	
185-2	SPC 0101 8856	4/19/04	0.87	Li-Cor hi stds ^(c)	
185-3	SPC 0101 8857	4/19/04	0.47	Columbus Inst	
186-3/2	SPC 0101 8858	4/19/04	0.87	Li-Cor hi stds ^(c)	
Heated Drift	SPC 0101 8869	4/19/04	0.045	Columbus Inst	
Observation Drift	SPC 0101 8859	4/19/04	0.042	Columbus Inst	
57-3/4	SPC 0101 8877	8/16/04	0.385	Li-Cor hi stds	
58-3/2	SPC 0101 8884	8/16/04	0.183	Li-Cor hi stds	
59-3/2	SPC 0101 8886	8/16/04	0.081	Li-Cor hi stds	
61-3/2/4	SPC 0101 8868	8/16/04	0.270	Li-Cor hi stds	
74-3/4	SPC 0101 8866	8/16/04	0.325	Li-Cor hi stds	
75-3/4	SPC 0101 8870	8/16/04	0.108	Li-Cor hi stds	
76-3/2/4	SPC 0101 8872	8/16/04	0.067	Li-Cor hi stds	
78-3/2/4	SPC 0101 8879	8/16/04	0.137	Li-Cor hi stds	
185-2	SPC 0101 8881	8/16/04	0.653	Li-Cor hi stds	
185-3	SPC 0101 8883	8/16/04	0.331	Li-Cor hi stds	
186-3/2	SPC 0101 8874	8/16/04	0.371	Li-Cor hi stds	
Heated Drift	SPC 0101 8865	8/16/04	0.049	Li-Cor hi stds	
Observation Drift	SPC 0101 8864	8/16/04	0.051	Li-Cor hi stds	
57-3/4	SPC 0103 4416	1/25/05	0.344	Li-Cor hi stds	
58-3/2/4	SPC 0103 4418	1/25/05	0.056	Li-Cor hi stds	
59-3/2	SPC 0103 4420	1/25/05	0.088	Li-Cor hi stds	
61-3/2/4	SPC 0103 4422	1/25/05	0.252	Li-Cor hi stds	
74-3/4	SPC 0103 4408	1/25/05	0.241	Li-Cor hi stds	
75-3/4	SPC 0103 4410	1/25/05	0.082	Li-Cor hi stds	
76-3/2/4	SPC 0103 4412	1/25/05	0.060	Li-Cor hi stds	
78-3/2/4	SPC 0103 4414	1/25/05	0.153	Li-Cor hi stds	
185-2	SPC 0103 4402	1/25/05	0.496	Li-Cor hi stds	
185-3	SPC 0103 4404	1/25/05	0.322	Li-Cor hi stds	
Heated Drift	SPC 0103 4401	1/25/05	0.040	Li-Cor hi stds	
Observation Drift	SPC 0103 4400	1/25/05	0.042	Li-Cor hi stds	
57-3/4	SPC 0103 4426	8/1/05	0.297	Li-Cor hi stds	
58-3/2/4	SPC 0103 4428	8/1/05	0.092	Li-Cor hi stds	
59-3/2	SPC 0103 4430	8/1/05	0.079	Li-Cor hi stds	
61-3/2/4	SPC 0103 4432	8/1/05	0.223	Li-Cor hi stds	

Table M-1. Standardization of CO₂ Concentrations (Continued)

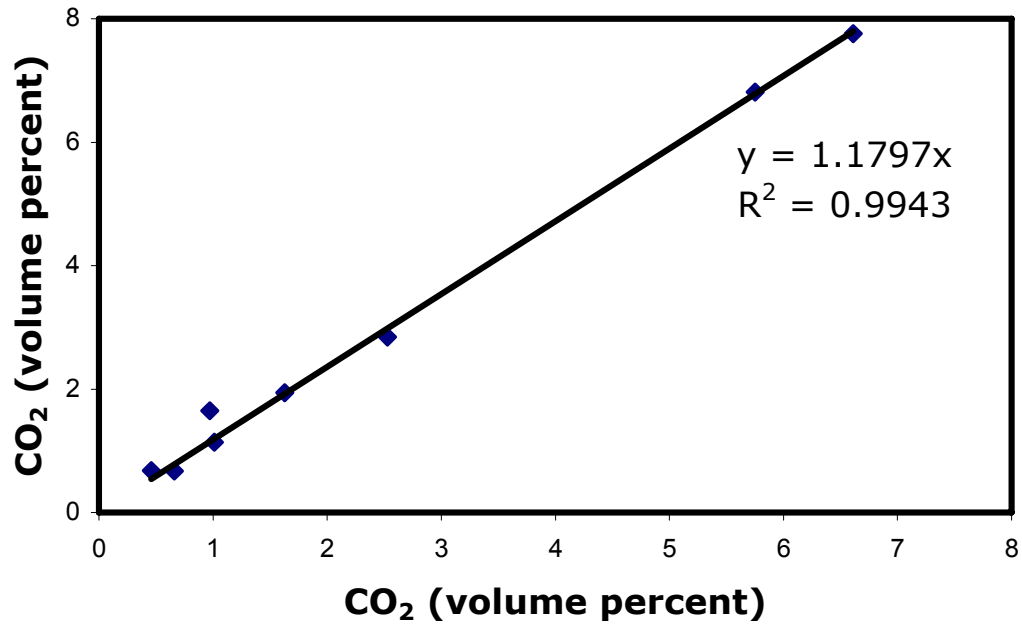
Sample Interval (Borehole-Zone)	YMP Tracking Number	Date Sampled	CO ₂ ^(a) (v/v-percent)	Measurement Technique	High Conc Correction ^(b)
74-3/4	SPC 0103 4434	8/1/05	0.292	Li-Cor hi stds	
75-3/4	SPC 0103 4436	8/1/05	0.063	Li-Cor hi stds	
76-3/2/4	SPC 0103 4438	8/1/05	0.065	Li-Cor hi stds	
78-3/2/4/1	SPC 0103 4440	8/1/05	0.146	Li-Cor hi stds	
185-2	SPC 0103 4442	8/2/05	0.367	Li-Cor hi stds	
185-3	SPC 0103 4444	8/2/05	0.293	Li-Cor hi stds	
Heated Drift	SPC 0103 4425	8/1/05	0.044	Li-Cor hi stds	
Observation Drift	SPC 0103 4424	8/1/05	0.041	Li-Cor hi stds	
57-3/4	SPC 0103 7564	11/29/05	0.245	Li-Cor hi stds	
58-3/2/4	SPC 0103 7566	11/29/05	0.095	Li-Cor hi stds	
59-3/2	SPC 0103 7568	11/29/05	0.034	Li-Cor hi stds	
61-3/2/4	SPC 0103 7570	11/29/05	0.167	Li-Cor hi stds	
74-3/4	SPC 0103 7556	11/29/05	0.147	Li-Cor hi stds	
75-3/4	SPC 0103 7558	11/29/05	0.101	Li-Cor hi stds	
76-3/2/4	SPC 0103 7560	11/29/05	0.063	Li-Cor hi stds	
78-3/2/4/1	SPC 0103 7562	11/29/05	0.086	Li-Cor hi stds	
185-2	SPC 0103 7550	11/29/05	0.287	Li-Cor hi stds	
185-3	SPC 0103 7552	11/29/05	0.170	Li-Cor hi stds	
186-3/2	SPC 0103 7554	11/29/05	0.104	Li-Cor hi stds	
Heated Drift	SPC 0103 7573	11/29/05	0.051	Li-Cor hi stds	
Observation Drift	SPC 0103 7572	11/29/05	0.042	Li-Cor hi stds	

Output DTN: LB0708DSTCO207.001.

^(a) Data from Table 6.3-28 of SNL 2007 [DIRS 177414].

^(b) The Li-Cor data were initially only based on a low concentration standard (400 ppm through 11/30/99 and 501 ppm from 4/18/00 through 8/22/00). This led to low measured concentrations for the higher concentration samples (>3,000 ppm or 0.3%). To correct for this, a standardization curve was constructed (Figure M-1) using a set of samples measured with the Li-Cor and with the Columbus Instruments analyzer at Yucca Mountain using appropriate standards (see 1/22/01 data set).

^(c) Hard disk for Columbus Instruments analyzer crashed before final three samples were analyzed.



Output DTN: LB0708DSTCO207.001.

Figure M-1. Standardization Curve for CO₂ Data

APPENDIX N
QUALIFICATION PLANS FOR INTENDED USE OF UNQUALIFIED DATA

INTENTIONALLY LEFT BLANK

N.1 QUALIFICATION PLAN FOR THE INTENDED USE OF HYDROLOGIC DATA FROM THE LITERATURE



Data Qualification Plan

Complete only applicable items.

QA: QA
Page 1 of 1

Section I. Organizational Information		
Qualification Title Qualification of intended use of hydrologic data for the report MDL-NBS-HS-000001 REV05.		
Requesting Organization Near-Field Environment		
Section II. Process Planning Requirements		
1. List of Unqualified Data to be Evaluated Tortuosities used for use with thermal and diffusive transport parameters of lithologic units from Penman [DIRS 109941], pgs. 441 and 461		
2. Type of Data Qualification Method(s) [Including rationale for selection of method(s) (Attachment 3) and qualification attributes (Attachment 4)] See Appendix O for the data qualification. SCI-PRO-001: Technical Assessment (Method 5). Rationale for method selection: a) The confidence in the data is in question because data collection procedures are unavailable for review, or the procedures used are not adequate; b) Documentation or proof of proper data acquisition is unavailable for review. Actions to be taken: b.) Determination that confidence in the data acquisition or developmental results is warranted. A discussion and justification that the data acquisition and/or subsequent data development (e.g., reduction or extrapolation) discussed in source documentation was appropriate for the type of data under consideration. This could include assurances that processes were conducted by qualified professionals; data were collected under proper environmental conditions; collected results and/or data development are appropriate, reasonable, and suitable for their intended use; etc. Attributes from Attachment 4 are stated below in Section 4 of this form.		
3. Data Qualification Team and Additional Support Staff Required Data Qualification Team: Nic Spycher (Chairperson), Eric Sonnenthal and Guoxiang Zhang Additional Support Staff: Wendy Mitcheltree and David Shields		
4. Data Evaluation Criteria Qualification Process Attributes Used: Attribute 1: Qualifications of personnel or organizations generating the data are comparable to qualification requirements of personnel generating similar data under an approved program that supports the YMP License Application process or post closure science. Attribute 2: The technical adequacy of equipment and procedures used to collect and analyze the data; Attribute 8: Prior peer or other professional reviews of the data and their results.		
5. Identification of Procedures Used SCI-PRO-001 REV04, Qualification of Unqualified Data SCI-PRO-006 REV05, Models		
6. Plan coordinated with the following known organizations providing input to or using the results of the data qualification This plan is internal to the Performance Assessment, Near-Field Environment Organization.		
Section III. Approval		
Qualification Chairperson Printed Name Nic Spycher	Qualification Chairperson Signature 	Date 9/27/07
Responsible Manager Printed Name Geoff Freeze	Responsible Manager Signature 	Date 9/27/07

SCI-PRO-001.1-R1

N.2 QUALIFICATION PLAN FOR THE INTENDED USE OF THERMODYNAMIC DATA FROM THE LITERATURE



Data Qualification Plan

Complete only applicable items.

QA: QA

Page 1 of 2

Section I. Organizational Information
Qualification Title Qualification for the intended use of thermodynamic data for the report MDL-NBS-HS-000001 REV05.
Requesting Organization Near-Field Environment
Section II. Process Planning Requirements
1. List of Unqualified Data to be Evaluated <ol style="list-style-type: none"> 1. Free energies of silicated oxides used for log K calculations from Chermak and Rimstidt (1989 [DIRS 105073], Table 2) 2. Input effective ionic radii for activity coefficient calculations from Helgeson et al. (1981 [DIRS 106024], Table 3) 3. Mordenite Molar Volume from Chipera and Apps (2001 [DIRS 171017], Table 3) 4. Development of input plagioclase log K values using regression coefficients from Arnorsson and Stefansson (1999 [DIRS 153329], pg. 173, Tables 4 and 6) 5. Amorphous silica log K values from Gunnarson and Arnorsson (2000 [DIRS 160465], pg. 2295) 6. Stellerite log K revised from data of Fridriksson et al. (2001 [DIRS 160460], Table 4) 7. Solubility of silica phase resembling beta-cristobalite from Fournier (1973 [DIRS 153464], Figure 1), used for opal-CT solubility alpha-cristobalite solubility from Fournier and Rowe (1962 [DIRS 124282], Table 1)
2. Type of Data Qualification Method(s) [Including rationale for selection of method(s) (Attachment 3) and qualification attributes (Attachment 4)] See Appendix C for the data qualification. SCI-PRO-001: Technical Assessment (Method 5). Rationale for method selection: a) The confidence in the data is in question because data collection procedures are unavailable for review, or the procedures used are not adequate; b) Documentation or proof of proper data acquisition is unavailable for review. Actions to be taken: b.) Determination that confidence in the data acquisition or developmental results is warranted. A discussion and justification that the data acquisition and/or subsequent data development (e.g., reduction or extrapolation) discussed in source documentation was appropriate for the type of data under consideration. This could include assurances that processes were conducted by qualified professionals; data were collected under proper environmental conditions; collected results and/or data development are appropriate, reasonable, and suitable for their intended use; etc. Attributes from Attachment 4 are stated below in Section 4 of this form.
3. Data Qualification Team and Additional Support Staff Required Data Qualification Team: Nic Spycher (Chairperson), Eric Sonnenthal and Guoxiang Zhang Additional Support Staff: Wendy Mitcheltree and David Shields
4. Data Evaluation Criteria Qualification Process Attributes Used: Attribute 1. Qualifications of personnel or organizations generating the data are comparable to qualification requirements of personnel generating similar data under an approved program that supports the YMP License Application process or post closure science. Attribute 2. The technical adequacy of equipment and procedures used to collect and analyze the data. Attribute 3. The extent to which the data demonstrate the properties of interest (e.g., physical, chemical, geologic, mechanical). Attribute 7: Prior uses of the data and associated verification processes; Attribute 8: Prior peer or other professional reviews of the data and their results; Note that one or more attributes can be used, not necessarily all for each data set listed above in Section 1.
5. Identification of Procedures Used

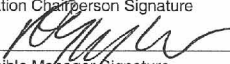

SCI-PRO-001.1-R1



Data Qualification Plan

Complete only applicable items.

QA: QA
Page 2 of 2

SCI-PRO-001 REV04, Qualification of Unqualified Data SCI-PRO-006 REV05, Models		
6. Plan coordinated with the following known organizations providing input to or using the results of the data qualification This plan is internal to the Performance Assessment, Near-Field Environment Organization.		
Section III. Approval		
Qualification Chairperson Printed Name Nic Spycher	Qualification Chairperson Signature 	Date 9/27/07
Responsible Manager Printed Name Geoff Freeze	Responsible Manager Signature 	Date 9/27/07

SCI-PRO-001.1-R1

N.3 QUALIFICATION PLAN FOR THE INTENDED USE OF KINETIC DATA FROM WHITE AND BRANTLEY 2003 [DIRS 1680880]



Data Qualification Plan

Complete only applicable items.

QA: QA

Page 1 of 2

<p>Section I. Organizational Information</p> <p>Qualification Title Qualification of the intended use of kinetic data from White and Brantley 2003 [DIRS 168088] for the report MDL-NBS-HS-000001 REV05.</p> <p>Requesting Organization Near-Field Environment</p>
<p>Section II. Process Planning Requirements</p> <p>1. List of Unqualified Data to be Evaluated</p> <p>Dissolution rate constants from White and Brantley 2003 [DIRS 168088] used as basis for lowering rate constants (i.e. field versus lab rates) for the following solids: Biotite (from pg. 497, Figure 9) Rhyolite Glass Sanidine (from pg. 488, Table 5 and pg. 495, Figure 7) Oligoclase (from pgs. 479, and 485, Table 4, and pg. 494, Figure 6)</p>
<p>2. Type of Data Qualification Method(s) [Including rationale for selection of method(s) (Attachment 3) and qualification attributes (Attachment 4)]</p> <p>See Appendix H for the data qualification. SCI-PRO-001: Technical Assessment (Method 5). Rationale for method selection: a) The confidence in the data is in question because data collection procedures are unavailable for review, or the procedures used are not adequate; b) Documentation or proof of proper data acquisition is unavailable for review. Actions to be taken: b.) Determination that confidence in the data acquisition or developmental results is warranted. A discussion and justification that the data acquisition and/or subsequent data development (e.g., reduction or extrapolation) discussed in source documentation was appropriate for the type of data under consideration. This could include assurances that processes were conducted by qualified professionals; data were collected under proper environmental conditions; collected results and/or data development are appropriate, reasonable, and suitable for their intended use; etc. Attributes from Attachment 4 are stated below in Section 4 of this form.</p>
<p>3. Data Qualification Team and Additional Support Staff Required</p> <p>Data Qualification Team: Nic Spycher (Chairperson) and Eric Sonnenthal Additional Support Staff: Wendy Mitcheltree and David Shields</p>
<p>4. Data Evaluation Criteria</p> <p>Qualification Process Attributes Used: Attribute 1. Qualifications of personnel or organizations generating the data are comparable to qualification requirements of personnel generating similar data under an approved program that supports the YMP License Application process or post closure science. Attribute 2. The technical adequacy of equipment and procedures used to collect and analyze the data. Attribute 3: The extent to which the data demonstrate the properties of interest (e.g., physical, chemical, geologic, mechanical). Attribute 4: The environmental conditions under which the data were obtained if germane to the quality of data. Attribute 8: Prior peer or other professional reviews of the data and their results;</p>
<p>5. Identification of Procedures Used</p> <p>SCI-PRO-001 REV04, Qualification of Unqualified Data SCI-PRO-006 REV05, Models</p>
<p>6. Plan coordinated with the following known organizations providing input to or using the results of the data qualification</p>

SCI-PRO-001.1-R1



Data Qualification Plan

Complete only applicable items.

QA: QA
Page 2 of 2

This plan is internal to the Performance Assessment, Near-Field Environment Organization.		
Section III. Approval		
Qualification Chairperson Printed Name Nic Spycher	Qualification Chairperson Signature <i>Nic Spycher</i>	Date 9/27/07
Responsible Manager Printed Name Geoff Freeze	Responsible Manager Signature <i>Geoff Freeze</i>	Date 9/27/07

SCI-PRO-001.1-R1

N.4 QUALIFICATION PLAN FOR THE INTENDED USE OF KINETIC DATA FROM THE LITERATURE



Data Qualification Plan

Complete only applicable items.

QA: QA

Page 1 of 2

Section I. Organizational Information
Qualification Title Qualification for the intended use of kinetic data for the report MDL-NBS-HS-000001 REV05.
Requesting Organization Near-Field Environment
Section II. Process Planning Requirements
1. List of Unqualified Data to be Evaluated <ol style="list-style-type: none"> 1. Quartz reaction rate constant (dissolution only) and activation energy from Tester et al 1994 [DIRS 101732], pg. 2415 2. Alpha-cristobalite reaction rate constant (dissolution only) and activation energy from Renders et al 1995 [DIRS 107088], pgs. 77, and 81 3. Amorphous silica reaction rate constant (precipitation only) and activation energy from Carroll et al 1998 [DIRS 124275], pgs. 1379 through 1389 4. Amorphous silica kinetic reaction rate constant (dissolution only) and activation energy from Rimstidt and Barnes (1980 [DIRS 101708], pgs. 1683 and 1690) 5. Clinoptilolite reaction rate constant and activation energy from Murphy et al 1996 [DIRS 142167], pg. 160 6. Heulandite dissolution rates from Ragnarsdottir 1993 [DIRS 126601], pgs. 2442, and 2447 7. Silica kinetic reaction rate constant and activation energy from Rimstidt and Barnes 1980 [DIRS 101708], pgs. 1683, and 1690 8. Oligoclase activation energy from Blum and Stillings 1995 [DIRS 126590], pg. 313, Table 2 9. Sanidine activation energy from Berger et al 2002 [DIRS 181221], pg. 669 10. Biotite reaction rate constant and activation energy from Malmstrom et al 1996 [DIRS 181209], pg. 208 11. Muscovite and illite reaction rate constant from Knauss and Wolery 1989 [DIRS 124300], pg. 1500 12. Kaolinite reaction rate constant from Brady and Walther 1989 [DIRS 110748], pg. 2826, Fig. 6 13. Kaolinite activation energy from Carroll and Walther 1990 [DIRS 160681], pg. 806, Table 2 14. Calcite dissolution rate constant from Svensson and Dreybrodt 1992 [DIRS 127978], pg. 129 15. Calcite activation energy from Inskeep and Bloom 1985 [DIRS 128129], pg. 2165 16. Fluorite reaction rate constant from Knowles-van Capellan et al 1997 [DIRS 124306], pg. 1873 17. Hematite reaction rate constant from Bruno et al 1992 [DIRS 160189] 18. Rhyolite glass reaction rate constant from Mazer et al 1992 [DIRS 124354], pg. 574 19. Hematite dissolution rate constant from Hersman et al. 1995 [DIRS 160190], pgs. 3327, and 3330
2. Type of Data Qualification Method(s) [Including rationale for selection of method(s) (Attachment 3) and qualification attributes (Attachment 4)] See Appendix H for the data qualification. SCI-PRO-001: Corroborating Data (Method 2) Rationale for method selection: a) Corroborating data are available for comparison with the unqualified data set(s). b) Inferences drawn to corroborate the unqualified data can be clearly identified, justified, and documented. SCI-PRO-001: Technical Assessment (Method 5). Rationale for method selection: a) The confidence in the data is in question because data collection procedures are unavailable for review, or the procedures used are not adequate; b) Documentation or proof of proper data acquisition is unavailable for review. Actions to be taken: b.) Determination that confidence in the data acquisition or developmental results is warranted. A discussion and justification that the data acquisition and/or subsequent data development (e.g., reduction or extrapolation) discussed in source documentation was appropriate for the type of data under consideration. This could include assurances that processes were conducted by qualified professionals; data were collected under proper environmental conditions; collected results and/or data development are appropriate, reasonable, and suitable for their intended use; etc. Attributes from Attachment 4 are stated below in Section 4 of this form.
3. Data Qualification Team and Additional Support Staff Required Data Qualification Team: Nic Spycher (Chairperson) and Eric Sonnenthal Additional Support Staff: Wendy Mitcheltree and David Shields

SCI-PRO-001.1-R1



Data Qualification Plan

Complete only applicable items.

QA: QA
Page 2 of 2

4. Data Evaluation Criteria Qualification Process Attributes Used: Attribute 1. Qualification of personnel or organizations that produced the data are comparable to qualification requirements of personnel generating similar data under an approved program that supports the YMP License Application process or post closure science. Attribute 2. Technical adequacy of equipment and procedures used to collect and analyze the data. Attribute 3. Extent to which the data demonstrate properties of interest. Attribute 4. Environmental conditions under which the data were obtained. Attribute 7. Prior uses of the data and associated verification processes. Attribute 8. Prior peer or professional reviews of the data and their results. Attribute 9. Extent and reliability of documentation associated with the data. Attribute 10. Extent and quality of corroborating data or confirmatory testing results Note that one or more attributes may be used, not necessarily all.		
5. Identification of Procedures Used SCI-PRO-001 REV04, Qualification of Unqualified Data SCI-PRO-006 REV05, Models		
6. Plan coordinated with the following known organizations providing input to or using the results of the data qualification This plan is internal to the Performance Assessment, Near-Field Environment Organization.		
Section III. Approval		
Qualification Chairperson Printed Name Nic Spycher	Qualification Chairperson Signature 	Date 9/27/07
Responsible Manager Printed Name Geoff Freeze	Responsible Manager Signature 	Date 9/27/07

SCI-PRO-001.1-R1

N.5 QUALIFICATION PLAN FOR THE INTENDED USE OF MINERALOGICAL DATA FROM THE LITERATURE



Data Qualification Plan

Complete only applicable items.

QA: QA
Page 1 of 2

Section I. Organizational Information
Qualification Title Qualification for the intended use of mineralogical data for the report MDL-NBS-HS-000001 REV05.
Requesting Organization Near-Field Environment
Section II. Process Planning Requirements
1. List of Unqualified Data to be Evaluated <ol style="list-style-type: none"> 1. Borehole SD-9 mineral abundances used for input rock mineralogy from Bish et al (2003 [DIRS 169638], Supplementary Data Table 1) as discussed in Section 6.2.2.3. 2. Molecular formula of stellerite, and molecular formula of clinoptilolite from Chipera and Apps 2001 [DIRS 171017] as discussed in Section 6.2.2.4 and Appendix C. 3. Smectite and rhyolite glass composition from Bish et al 1996 [DIRS 101430], Table 1 as discussed in Section 6.2.2.3 (13) and Appendix C. 4. Input plagioclase and biotite compositions for log K calculations from Johnson et al 1998 [DIRS 101630] as discussed in Section 6.2.2.4 and Appendix C. 5. Illite fraction in clay from Carey et al 1998 [DIRS 109051] pg. 18 as discussed in Section 6.2.2.3 (13) 6. Biotite phenocrysts composition analyses used in calculation of groundmass sanidine from Flood et al 1989 [DIRS 182723], Table 2.
2. Type of Data Qualification Method(s) [Including rationale for selection of method(s) (Attachment 3) and qualification attributes (Attachment 4)] See Appendix O for the data qualification. SCI-PRO-001: Corroborating Data (Method 2) Rationale for method selection: a) Corroborating data are available for comparison with the unqualified data set(s). b) Inferences drawn to corroborate the unqualified data can be clearly identified, justified, and documented. SCI-PRO-001: Technical Assessment (Method 5). Rationale for method selection: a) The confidence in the data is in question because data collection procedures are unavailable for review, or the procedures used are not adequate; b) Documentation or proof of proper data acquisition is unavailable for review. Actions to be taken: b.) Determination that confidence in the data acquisition or developmental results is warranted. A discussion and justification that the data acquisition and/or subsequent data development (e.g., reduction or extrapolation) discussed in source documentation was appropriate for the type of data under consideration. This could include assurances that processes were conducted by qualified professionals; data were collected under proper environmental conditions; collected results and/or data development are appropriate, reasonable, and suitable for their intended use; etc. Attributes from Attachment 4 are stated below in Section 4 of this form.
3. Data Qualification Team and Additional Support Staff Required Data Qualification Team: Nic Spycher (Chairperson) and Eric Sonnenthal Additional Support Staff: Wendy Mitcheltree and David Shields
4. Data Evaluation Criteria Qualification Process Attributes Used: Attribute 1: Qualifications of personnel or organizations generating the data are comparable to qualification requirements of personnel generating similar data under an approved program that supports the YMP License Application process or post closure science. Attribute 2: The technical adequacy of equipment and procedures used to collect and analyze the data. Attribute 3: The extent to which the data demonstrate the properties of interest. Attribute 8: Prior peer or other professional reviews of the data and their results. Attribute 10: Extent and quality of corroborating data or confirmatory testing results. Note that one or more attributes may be used for each dataset, not necessarily all.

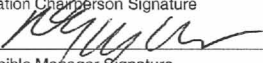
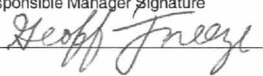
SCI-PRO-001.1-R1



Data Qualification Plan

Complete only applicable items.

QA: QA
Page 2 of 2

5. Identification of Procedures Used		
SCI-PRO-001 REV04, Qualification of Unqualified Data SCI-PRO-006 REV05, Models		
6. Plan coordinated with the following known organizations providing input to or using the results of the data qualification This plan is internal to the Performance Assessment, Near-Field Environment Organization.		
Section III. Approval		
Qualification Chairperson Printed Name Nic Spycher	Qualification Chairperson Signature 	Date 9/27/07
Responsible Manager Printed Name Geoff Freeze	Responsible Manager Signature 	Date 9/27/07

SCI-PRO-001.1-R1

N.6 QUALIFICATION PLAN FOR THE INTENDED USE OF UNQUALIFIED DTN LB990501233129.004 [DIRS 111475]



Data Qualification Plan

Complete only applicable items.

QA: QA

Page 1 of 2

Section I. Organizational Information
Qualification Title Qualification for the intended use of unqualified DTN LB990501233129.004 [DIRS 111475] for the report MDL-NBS-HS-000001 REV05.
Requesting Organization Near-Field Environment
Section II. Process Planning Requirements
1. List of Unqualified Data to be Evaluated Elevation of stratigraphic contacts from LB990501233129.004 [DIRS 111475] at the location of column 'j34'
2. Type of Data Qualification Method(s) [Including rationale for selection of method(s) (Attachment 3) and qualification attributes (Attachment 4)] See Appendix J for the data qualification. SCI-PRO-001: Corroborating Data (Method 2) Rationale for method selection: a) Corroborating data are available for comparison with the unqualified data set(s). b) Inferences drawn to corroborate the unqualified data can be clearly identified, justified, and documented. SCI-PRO-001: Technical Assessment (Method 5). Rationale for method selection: a) The confidence in the data is in question because data collection procedures are unavailable for review, or the procedures used are not adequate; b) Documentation or proof of proper data acquisition is unavailable for review. Actions to be taken: b.) Determination that confidence in the data acquisition or developmental results is warranted. A discussion and justification that the data acquisition and/or subsequent data development (e.g., reduction or extrapolation) discussed in source documentation was appropriate for the type of data under consideration. This could include assurances that processes were conducted by qualified professionals; data were collected under proper environmental conditions; collected results and/or data development are appropriate, reasonable, and suitable for their intended use; etc. Attributes from Attachment 4 are stated below in Section 4 of this form.
3. Data Qualification Team and Additional Support Staff Required Data Qualification Team: Nic Spycher (Chairperson), Eric Sonnenthal and Guoxiang Zhang Additional Support Staff: Wendy Mitcheltree and David Shields
4. Data Evaluation Criteria Qualification Process Attributes Used: Attribute 1: Qualifications of personnel or organizations generating the data are comparable to qualification requirements of personnel generating similar data under an approved program that supports the YMP License Application process or post closure science; Attribute 2: The technical adequacy of equipment and procedures used to collect and analyze the data; Attribute 3: The extent to which the data demonstrate the properties of interest (e.g., physical, chemical, geologic, mechanical); Attribute 10: Extent and quality of corroborating data or confirmatory testing results
5. Identification of Procedures Used SCI-PRO-001 REV04, Qualification of Unqualified Data SCI-PRO-006 REV05, Models
6. Plan coordinated with the following known organizations providing input to or using the results of the data qualification This plan is internal to the Performance Assessment, Near-Field Environment Organization.

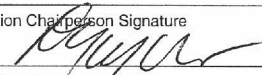

SCI-PRO-001.1-R1



Data Qualification Plan

Complete only applicable items.

QA: QA
Page 2 of 2

Section III. Approval		
Qualification Chairperson Printed Name Nic Spycher	Qualification Chairperson Signature 	Date 9/27/07
Responsible Manager Printed Name Geoff Freeze	Responsible Manager Signature 	Date 9/27/07

SCI-PRO-001.1-R1

INTENTIONALLY LEFT BLANK

APPENDIX O
**QUALIFICATION FOR INTENDED USE OF HYDROLOGIC
AND MINERALOGICAL DATA**

INTENTIONALLY LEFT BLANK

O.1 INTRODUCTION

This section presents documentation for the data qualification of unqualified hydrologic (Section O.2) and mineralogical (Section O.3) data used as direct input to this report. Data qualification is performed following the qualification plans:

- *Qualification Plan for the Intended Use of Hydrologic Data from the Literature* given in Appendix N (Section N.1)
- *Qualification Plan for the Intended Use of Mineralogical Data from the Literature* given in Appendix N (Section N.5).

O.2 QUALIFICATION OF HYDROLOGIC DATA

O.2.1 Data and Sources

The following data are qualified here for intended use:

- Fracture tortuosity data from Penman (1940 [DIRS 109941]) as discussed in Sections 4.1.1.1 and 6.4.6(15).

O.2.2 Qualification of the Tortuosity Data from Penman 1940 [DIRS 109941]

The data from Penman (1940 [DIRS 109941]) are qualified for intended use with Method 5 of SCI-PRO-001 (Technical Assessment). The rationale for method selection is: (a) The confidence in the data is in question because data collection procedures are unavailable for review, or the procedures used are not adequate; (b) Documentation or proof of proper data acquisition is unavailable for review. These data are considered qualified for intended use based on the following attributes (facts):

- Attribute 1: The first author of the data, Howard Latimer Penman (1909–1984), was a world-renowned scholar in soil sciences and a Fellow of the Royal Society, UK. Qualifications of this author are comparable to qualification requirements of personnel generating hydrology data under Yucca Mountain Project procedures that support the YMP license application process or postclosure science.
- Attribute 2: Penman (1940 [DIRS 109941], p. 461) presented an isotropic porous medium with a tortuosity of $\sqrt{2}^{-1}$ or ~ 0.707 as an estimate. The author also obtained an experimentally measured tortuosity value 0.66 (Penman 1940 [DIRS 109941], p. 461) based on steady-state vapor diffusion through soil material having porosities of up to 0.7, thus corroborating his own theoretical value. Supporting data are given by de Marsily (1986 [DIRS 100439], p. 233), who states that a tortuosity value of 0.7 is within the upper range for porous media. Its use in this model is based on the assumption that the ensemble of fractures in an unsaturated medium behaves as an isotropic porous medium, consistent with the assumption of laterally homogeneous rock properties (Section 6.4.6(15)).

- Attribute 8: The paper by Penman (1940 [DIRS 109941]) was published in *Journal of Agricultural Science*. This paper was carefully peer-reviewed by independent experts in the area, and the quality of the paper was assured.

O.3 QUALIFICATION OF MINERALOGICAL DATA FROM LITERATURE

O.3.1 Data and Sources

The following data are qualified here for intended use:

1. Borehole SD-9 mineral abundances used for input rock mineralogy from Bish et al. (2003 [DIRS 169638], Supplementary Data Table 1) as discussed in Section 6.2.2.3.
2. Chemical formula of stellerite and clinoptilolite from Chipera and Apps (2001 [DIRS 171017]) as discussed in Section 6.2.2.4.
3. Smectite and rhyolite glass composition from Bish et al. (1996 [DIRS 101430], Table 1) as discussed in Section 6.2.2.3(13).
4. Illite fraction in clay from Carey et al. (1998 [DIRS 109051], p. 18) as discussed in Section 6.2.2.3(13)
5. Input plagioclase and biotite compositions for log(K) calculations from Johnson et al. (1998 [DIRS 101630]) as discussed in Section 6.2.2.4.
6. Biotite phenocrysts composition, used in rock calculations of composition, from Flood et al. (1989 [DIRS 182723], Table 2) as discussed in Section 6.2.2.4.

O.3.2 Mineral Abundance (in Weight Percent) Data for Borehole SD-9 from Bish et al. (2003 [DIRS 169638], Supplementary Data Table 1)

The data from Bish et al. (2003 [DIRS 169638], Supplementary Data Table 1) are qualified for intended use with Method 2 (Corroborating Data) and Method 5 (Technical Assessment) of SCI-PRO-001, based on the following attributes:

- Attribute 1: The authors are part of the Yucca Mountain team of investigators, and have the qualifications of personnel generating similar data under an approved program that support the YMP license application process or postclosure science.
- Attributes 2, 3 and 10: Data from Bish et al. (2003 [DIRS 169638], Supplementary Data Table 1) for borehole USW SD-9 are essentially the same as the data for the same borehole submitted under qualified DTN: LA9908JC831321.001 [DIRS 113495]. Data from Bish et al. (2003 [DIRS 169638], Supplementary Data Table 1) (also in weight percent) were made on samples from borehole SD-9, for some individual layers (e.g., PTn), and for minor mineral phases. Their published data complements the data under DTN: SN0307T0510902.003 [DIRS 164196] and were collected with the same methodology, equipment, and qualification of personnel as the qualified data under DTN: LA9908JC831321.001 [DIRS 113495].

O.3.3 Chemical formula of Stellerite and Clinoptilolite from Chipera and Apps (2001 [DIRS 171017])

The zeolite chemical formulas from Chipera and Apps (2001 [DIRS 171017], Table 3), as shown in Table O.3.3-1 below, are qualified for intended use with Method 2 (Corroborating Data) and Method 5 (Technical Assessment) of SCI-PRO-001, based on the following attributes:

- Attribute 1: The authors of this paper, Steve J. Chipera and John A. Apps, are scientists from Los Alamos National Laboratory and Lawrence Berkeley National Laboratory, respectively. Both worked on mineralogy of the Yucca Mountain site for multiple years. Qualifications of these authors are comparable to the qualification requirements of personnel generating mineralogical data under Yucca Mountain Project procedures that support the YMP license application process or postclosure science.
- Attributes 2 and 3: The stellerite and clinoptilolite chemical formulae from Chipera and Apps (2001 [DIRS 171017], Table 3) are adequate for use because they were collected and developed using standard scientific practices, and are relevant to Yucca Mountain because they are based on samples from the site. Electron microprobe analyses were used to collect the raw compositional data on zeolites of the vitric Topopah Springs Tuff, and the zeolite chemical formulae were calculated from the compositional data.

Table O.3.3-1. YMP Zeolite Formulas and Molar Volume Qualified for Use

Zeolite	Formula or Molar Volume Qualified
Stellerite	$(Ca_{3.9}Na_{0.1})Al_{7.9}Si_{28.1}O_{72.0} \cdot 28H_2O$
Clinoptilolite	$(K_{0.8}Na_{0.4}Ca_{2.8})Al_{6.8}Si_{29.2}O_{72.0} \cdot 26H_2O$

Source: Chipera and Apps 2001 [DIRS 171017], Table 3, pp. 126 and 127.

Because zeolite minerals are strong cation-exchangers, and their compositions are highly variable and site- and process-specific, the reference formulas for these minerals are commonly quite general. These zeolite compositions in Table O.3.3-1 represent zeolites from Yucca Mountain borehole cores, and represent the properties of interest because zeolite compositions are site- and process-specific, so the use of site-specific data is highly desirable and ideal for use. The adequacy of the chemical formulae in Table O.3.3-1 is assessed by examining whether charge balance is maintained as follows:

$$\text{Net positive charge} = 144 = n_{Na} + n_K + (2 \times n_{Ca}) + (3 \times n_{Al}) + (4 \times n_{Si}) \quad (\text{Eq. O.3-1})$$

$$\text{Net negative charge} = -144 = (-2 \times n_O) \quad (\text{Eq. O.3-2})$$

where n_x represents the subscript on element x in the chemical formula. Application of these equations shows that the zeolite formulas for both stellerite and clinoptilolite are charge-balanced.

An assessment of the methods of data collection and development used by Chipera and Apps (2001 [DIRS 171017]) also provides confidence in the zeolite formulas presented in their paper.

- Attribute 8: The paper by Chipera and Apps (2001 [DIRS 171017]) is published in the well-known *Reviews in Mineralogy and Geochemistry*, and presents a scholarly investigation into the stability of zeolite minerals in Yucca Mountain pore waters. The paper was peer-reviewed before publication.

O.3.4 Smectite and Rhyolite Glass Composition Data from Bish et al. (1996 [DIRS 101430], Table 1)

The data from Bish et al. (1996 [DIRS 101430], Table 1) are qualified for intended use with Method 2 (Corroborating Data) and Method 5 (Technical Assessment), based on the following attributes:

- Attribute 1: The authors are part of the Yucca Mountain team of investigators, and have the qualifications of personnel generating similar data under an approved program that support the YMP license application process or postclosure science.
- Attributes 2, 3, and 10: Bish et al. (1996 [DIRS 101430], Table 1) present the results of electron probe microanalysis of a vitric sample collected from core from borehole USW GU-3, 30 ft below the top of the densely welded subzone of the vitric, crystal-poor member of the Topopah Spring Tuff (Ttpv3). These glass compositions are applied to the vitric materials throughout the modeled geologic column in this report (Sections 4.1.6 and 6.2.2.3). These data can be corroborated by data in DTN: LASL831322AN96.002 [DIRS 171957] (SEP Table S98444_002), which report glass analysis from YMP boreholes, measured by electron microprobe analysis. The data in DTN: LASL831322AN96.002 [DIRS 171957] consists of two to five repetitive measurements on seven samples collected from four different geologic units, from boreholes USW H-4 and USW H-5. The different samples include perlitic glass, pumice, and glass shards. Two of the measured samples, consisting of glass shards and shard rims, were from the Ttpv3 unit in borehole USW H-5. The corroborating data set provides opportunities to compare data from the same geologic unit (the Ttpv3), as well as to compare the data to measurements throughout the geologic column.

The data from Bish et al. (1996 [DIRS 101430], Table 1) were collected using the same methodology (by electron microprobe analysis), and measurements for the same oxide species as for the data in DTN: LASL831322AN96.002 [DIRS 171957] (SEP table S98444_002). These data demonstrate the properties of interest because they represent analyses of rhyolitic glass and other rocks from Yucca Mountain, thus yielding site-specific information.

Table O.3.4-1 shows the data of Bish et al. (1996 [DIRS 101430], Table 1) adopted in this report and data from DTN: LASL831322AN96.002 [DIRS 171957]. This comparison shows good agreement between both data sets. Note that comparing rhyolitic glass from various units in the geologic section is justified, because as stated above, the glass composition adopted in this report is applied to vitric zones throughout the entire geologic section.

Table O.3.4-1. Comparison of Glass Compositions

Glass Compositions from Bish et al. (1996 [DIRS 101430], Table 1) (Sample GU-3 1195C)										
	SiO ₂ (wt %)	Al ₂ O ₃ (wt %)	FeO (wt %)	MgO (wt %)	CaO (wt %)	Na ₂ O (wt %)	K ₂ O (wt %)			
	74.1	12.4	0.82	0.02	0.19	3.55	5.77			
Glass Compositions from DTN: LASL831322AN96.002 [DIRS 171957]										
Borehole	Depth (ft)	Unit	Sample Type	SiO ₂ (wt %)	Al ₂ O ₃ (wt %)	FeO (wt %)	MgO (wt %)	CaO (wt %)	Na ₂ O (wt %)	K ₂ O (wt %)
USW H-4	1,312	CH	Perilitic glass	74.0	12.3	0.77	—	0.45	3.38	4.96
USW H-4	1,312	CH	Perilitic glass	73.9	12	0.67	—	0.43	3.27	4.91
USW H-4	1,312	CH	Perilitic glass	74.3	12.1	0.83	—	0.41	3.29	5.09
USW H-4	1,312	CH	Pumice	73.4	12	0.86	—	0.43	3.03	5.39
USW H-4	1,312	CH	Pumice	74.0	12	0.83	—	0.49	3.28	5.37
USW H-4	1,312	CH	Pumice	74.0	12	0.73	—	0.43	3.16	5.25
USW H-5	420	TC	Glass shard cores	71.9	12.1	0.81	—	0.14	3.11	5.62
USW H-5	420	TC	Glass shard cores	71.3	11.9	0.75	—	0.07	3.29	5.18
USW H-5	420	TC	Shard rims	72.5	12.1	0.77	0.01	0.13	3.48	5.48
USW H-5	420	TC	Shard rims	72.6	12	0.73	0.02	0.1	3.5	5.37
USW H-5	450	TC	Glass shard cores	74.6	11.9	0.71	—	0.14	4.21	4.9
USW H-5	450	TC	Glass shard cores	73.6	11.8	0.77	—	0.18	4.28	4.66
USW H-5	450	TC	Glass shard cores	72.3	11.8	0.62	—	0.2	4.24	4.65
USW H-5	450	TC	Glass shard cores	73.7	11.6	0.83	0.01	0.2	4.34	4.64
USW H-5	1,610	TS	Brown glass shards	74.0	12	0.7	—	0.29	3.34	4.94
USW H-5	1,610	TS	Brown glass shards	72.6	12.1	0.69	—	0.3	3.33	4.85
USW H-5	1,610	TS	Brown glass shards	74.3	12	0.73	0.02	0.45	3.42	5.05
USW H-5	1,610	TS	Brown glass shards	72.7	12.2	0.71	—	0.26	3.39	5.16
USW H-5	1,610	TS	Colorless shard rims	74.5	12.2	0.08	—	0.23	3.35	5.09
USW H-5	1,610	TS	Colorless shard rims	71.5	12.2	0.18	—	0.27	3.26	5.07
USW H-5	1,610	TS	Colorless shard rims	73.1	12.3	0.07	—	0.27	3.41	4.91

Table O.3.4-1. Comparison of Glass Compositions (Continued)

Glass Compositions from DTN: LASL831322AN96.002 [DIRS 171957] (Continued)

Borehole	Depth (ft)	Unit	Sample Type	SiO2 (wt %)	Al2O3 (wt %)	FeO (wt %)	MgO (wt %)	CaO (wt %)	Na2O (wt %)	K2O (wt %)
USW H-5	1,610	TS	Colorless shard rims	74.0	12.3	0.16	—	0.2	3.56	5.05
USW H-5	1,762	CH	Glass shards	72.8	12	0.66	—	0.48	3.47	4.75
USW H-5	1,762	CH	Glass shards	73.0	12	0.71	—	0.45	3.41	4.9
USW H-5	1,762	CH	Glass shards	73.7	11.8	0.76	—	0.49	3.32	4.96
USW H-5	1,762	CH	Glass shards	73.7	11.7	0.64	—	0.48	3.52	4.96
USW H-5	1,800	CH	Perilitic glass fragments	74.4	11.8	0.69	—	0.53	3.3	5.13
USW H-5	1,800	CH	Perilitic glass fragments	74.6	11.7	0.47	—	0.52	3.48	5.18
USW H-5	1,800	CH	Perilitic glass fragments	74.1	11.7	0.36	—	0.49	3.26	5.11

O.3.5 Illite Fraction in Clay from Carey et al. (1998 [DIRS 109051], p. 18)

The illite fraction based on Carey et al. (1998 [DIRS 109051], p. 18) is qualified for intended use with Method 5 of SCI-PRO-001 (Technical Assessment), based on the following attributes:

- Attribute 1: The authors of this report are scientists from Los Alamos National Laboratory. These authors have worked for multiple years on the three-dimensional mineralogical model of Yucca Mountain site. Qualifications of these authors are comparable to, or exceed, the qualification requirements of personnel generating thermodynamic data under Yucca Mountain Project procedures that support the YMP license application process or postclosure science.
- Attribute 2: The report contains all available mineralogical data collected from drill holes. Minerals and mineral groups in the three-dimensional mineralogical model developed in the report include smectite + illite, sorptive zeolites (e.g., clinoptilite, mordenite, stellerite, chabazite, and erionite), tridymite, cristobalite + opal-CT, quartz, feldspar, volcanic glass, analcime, mica, and calcite. The mineral data are based on quantitative x-ray diffraction obtained on samples from the ground surface down to the Paleozoic basement in 24 drill holes. Mineral distributions have been obtained using a deterministic $1/r^2$ function. In addition, distributions have been characterized geostatistically, and kriged solutions with confidence intervals have been obtained.
- Attribute 8: The paper by Carey et al. (1998 [DIRS 109051], p. 18) was published by Los Alamos National Laboratory. This report was carefully review by independent experts such that the quality of the paper was assured.

O.3.6 Plagioclase Composition and Biotite Formula from Johnson et al. (1998 [DIRS 101630])

Plagioclase composition, $Or_{0.07}Ab_{0.76}An_{0.17}$, and Biotite formula from Johnson et al. (1998 [DIRS 101630]) are qualified for intended use with Method 5 of SCI-PRO-001 (Technical Assessment), based on the following attributes:

- Attribute 1: The authors of this paper are scientists from Lawrence Livermore National Laboratory. These authors have qualifications comparable to, or exceeding, qualification requirements of personnel generating thermodynamic data under Yucca Mountain Project procedures that support the YMP license application process or postclosure science.
- Attribute 2: Ideal representations of mineral formulas are published in reference books, such as mineralogic textbooks, encyclopedias, and geologic dictionaries that meet the YMP definition of “established fact.” However, plagioclase and biotite represent solid-solution series of variable compositions. The plagioclase and biotite compositions used by Johnson et al. (1998 [DIRS 101630]) are specific to the Yucca Mountain volcanic tuff, and can be considered to have been validated by the modeling work of these authors. In their paper, these authors compare the measured and modeled effluent concentrations from a plug-flow reactor experiment using tuff from Yucca Mountain.

Their modeling study provides confidence in the plagioclase and biotite compositions used in their work.

- Attribute 8: The paper by Johnson et al. (1998 [DIRS 101630]) was published in the *Journal of Hydrology*. This journal is considered one of the top peer-reviewed journals in the field. Papers published in this journal are typically reviewed by at least three independent experts, such that the quality of the paper is assured.

O.3.7 Biotite Phenocrysts Composition Data from Flood et al. (1989 [DIRS 182723], Table 2)

Biotite phenocrysts composition from Flood et al. (1989 [DIRS 182723], Table 2) are qualified for intended use with Method 5 of SCI-PRO-001 (Technical Assessment), based on the following attributes:

- Attribute 1: The authors of the data are from the Department of Geological Sciences, Michigan State University. The study has been supported by the Waste Isolation and Containment Programs at Lawrence Livermore National Laboratory. Qualifications of these authors are comparable to, or exceed, the qualification requirements of personnel generating data under Yucca Mountain Project procedures that supports the YMP license application process or postclosure science.
- Attribute 2: Chemical compositions of biotite, magnetite, and ilmenite separates were obtained from individual glassy pumice fragments that were collected from the unwelded tops and bottoms of the Topopah Spring and Pah Canyon ash-flow sheets that well-represent the tuff layers. The Topopah Spring Member is represented by 21 major- and trace-element analyses, and the Pah Canyon Member is represented by 15 major- and trace-element analyses. The estimated standard deviation by the authors is less than 2% for most components and 6.7% as the maximum. The average chemical compositions of the magnetites and the ilmenites were determined for 11 pumice fragments from the Topopah Spring Member and 12 pumice fragments from the Pah Canyon Member. The methods for the measurements and the analyses are considered adequate.
- Attribute 8: The paper by Flood et al. (1989 [DIRS 182723], Table 2) was published in *Journal of Volcanology and Geothermal Research*. This journal is considered one of the top peer-reviewed journals in its field. Papers published in this journal are typically reviewed by at least three independent experts, such that the quality of the paper is assured.

APPENDIX P
RESOLUTIONS OF CONDITION REPORTS

INTENTIONALLY LEFT BLANK

The following condition reports (CRs) have been addressed (or not) in this report revision. Where appropriate, text from the technical work plan (TWP) (SNL 2007 [DIRS 179287]) has been included for additional background. Descriptions of how the CRs have been addressed (or not) are presented in shaded text.

1. CR-5154: *Use of invert thermal and hydrologic properties that are not based on the ballast material description on the IED.*

This CR has been addressed by use of updated invert properties as described in Section 4.1.

2. CR-5383: *Use of DST waters affected by introduced materials in validation of the THC seepage model.* To address this CR, when the updated THC seepage model is re-validated, all sampled DST waters will be re-evaluated for use. Potential contamination of sample waters by introduced materials will be based on the determinations of “not affected,” “possibly affected,” or “affected” in *Thermal Testing Measurements Report* (SNL 2007 [DIRS 177414]), and will be noted in tables and figures in the validation section of the THC seepage report.

Also, in previous revisions of the THC seepage report, waters interpreted as probably being in-line condensate were excluded from the validation analysis. However, the excluded waters do not directly correlate to waters designated as condensate in *Thermal Testing Measurements Report* (SNL 2007 [DIRS 177414]). During re-validation, all waters designated as condensate in that report will be excluded, or will be clearly indicated on comparison plots as affected or possibly affected.

This CR has been addressed by re-evaluating for the DST waters for use in model validation in Section 7. Potential contamination of sample waters by introduced materials have been based on the determinations of “not affected,” “possibly affected,” or “affected” in *Thermal Testing Measurements Report* (SNL 2007 [DIRS 177414]), and have been noted in tables and figures in Section 7. In addition, during revalidation, all waters designated as condensate in that report have been clearly indicated on comparison plots. Appropriate discussions of measurement uncertainty have also been provided in Section 7.

3. CR-6334: *Errors and inconsistencies in simulation of new infiltration.* New average percolation flux values will be estimated using infiltration flux data obtained from the new infiltration model, documented in *Simulation of Net Infiltration for Present Day and Potential Future Climates* (SNL 2007 [DIRS 174294]) for use in all THC seepage model simulations and sensitivity analyses described here. The values used will be consistent with the average infiltration fluxes, and basis for estimating percolation from infiltration, as developed for revision of *Multiscale Thermohydrologic Model* (SNL 2007 [DIRS 181383]).

This CR has been addressed by use of updated average percolation flux values as described in Section 4.1. The values used are consistent with the average infiltration fluxes, and basis for estimating percolation from infiltration, as developed the *Multiscale Thermohydrologic Model* (SNL 2007 [DIRS 181383]).

4. CR-6342: *Errors and traceability for reactive surface area in THC models.* Errors in the calculation of the mineral reactive surface areas used by the THC seepage model have been identified, and traceability is lacking for the values used in the model (see BSC 2005 [DIRS 172862], Appendix B).

This CR has been addressed by additional description of calculations provided in Sections 6.2.2.3 and 6.4.3, and by filing of all new calculations under new specific DTNs as described in Appendix G.

5. CR-6344: *Database file not captured for SOLVEQ/CHILLER calculations.*

SOLVEQ/CHILLER calculations are no longer used in this report, and therefore this CR is no longer relevant.

6. CR-6489: *Sensitivity studies on the form of sepiolite used in ANL-EBS-MD-000074, Rev. 00.* The Mg-silicate phase(s) in the THC thermodynamic and kinetic databases will be selected and used in a manner consistent with associated changes in the in-drift precipitates/salts model, in response to this CR.

Sepiolite is no longer considered as a potential secondary mineral in this report, and an amorphous form of magnesium silicate is used instead as described in Section 6.2.2.2 (and as done in the in-drift precipitates/salts model), thus addressing this CR.

7. CR-6491: *Scientific Notebooks do not meet requirements.* In response to this CR, development work for the THC seepage model will be documented in the report itself, to the extent necessary to achieve transparency and traceability.

This CR was addressed by developing all work for the THC seepage model through documentation in the report itself, without recourse to Scientific Notebooks.

8. CR-6492: *Technical issues with Rev. 04 of Drift-Scale THC Seepage Model.* These include:

- The data qualification report for the THC thermodynamic database, Data Qualification for Thermodynamic Data Used to Support THC Calculations (BSC 2004 [DIRS 170268]), is not cited in the THC seepage report. References to the data qualification report will be added to the THC seepage report.

All thermodynamic data in this report were taken from qualified sources or were qualified in this report as described in Appendix C. This issue is therefore no longer relevant.

- Conclusions concerning model sensitivity to mineral dissolution rate constants are not adequately supported. A drift-scale THC simulation using mineral surface areas or dissolution rate constants varying by an order of magnitude from the base case will be run as a sensitivity analysis.

This issue has been addressed by new sensitivity analyses on reaction rates presented in Section 6.6.5.

- The process of selecting starting water compositions for the THC seepage model is not adequately documented. As stated earlier, the starting water compositions will be consistent with the selection documented in *Engineered Barrier System: Physical and Chemical Environment* (SNL 2007 [DIRS 177412]).

As described in Section 6.2.2.1, the selection of these waters is described in *Engineered Barrier System: Physical and Chemical Environment* (SNL 2007 [DIRS 177412]). The selected waters were then provided to the THC modeling team for input into the current THC seepage model, thus addressing this CR.

9. CR-6691: *Failure to maintain mass balance in THC normative salt precipitation calculations.* The THC seepage model uses a normative salt precipitation routine to precipitate out solutes when the prescribed liquid saturation limit or ionic strength limit are exceeded. However, some components may not be conserved during this dryout implementation, depending on the list of normative salts and the order in which they are applied.

This CR was addressed by selecting a new list of dryout minerals as described in Section 6.4.5 and conducting sensitivity analyses as well as evaluating mass balances as presented in Section 6.6.4. These evaluations confirm that the model results are not significantly affected by the normative salt precipitation procedure.

10. CR-7037: *New information available from THC sensitivity analyses (ANL-NBS-HS-000047 Rev. 00).* TOUGHREACT simulations at repository center and edge conditions were shown to have different bin histories in the THC sensitivity study (BSC 2006 [DIRS 174104]). A sensitivity analysis will be run to evaluate differences in composition of potential seepage waters at the repository edge. In addition, potential seepage water compositions will be selected from zones of higher liquid saturation, further away than the boiling/wetting front (e.g., from waters designated “HISAT” instead of those designated “FRONT,” as defined in BSC 2004 [DIRS 169858], Section 6.2.1.3).

This CR was addressed by including repository-edge simulations in this report in addition to repository-center simulations, as discussed in Section 6.5.1. In addition, predicted water compositions are now selected from model locations within condensation zones, as discussed in Section 6.4.8.

11. CR-7187: *Opportunity to improve THC model validation.* This CR suggests using results from a THC crushed tuff column test (Lowry 2001 [DIRS 157900]) as an additional validation test case. These data will be used during model development, to the extent practical, to evaluate and adjust the values of input parameters (e.g., mineral reactive surface areas).

This CR suggests further model validation against additional experimental data. However, the available experimental data suggested in this CR are poorly constrained, and therefore

are difficult to implement in a test case. The existing validation test cases are appropriate and sufficient.

12. CR-7193: *RIT action items associated with AMR MDL-NBS-HS-000001, Drift Scale Coupled Process Model.* Most of the action items carried forward in this CR will be addressed through the simulations in the THC sensitivity study or are being addressed by other CRs listed in this appendix; a complete list of the action items is presented here:

- *2-D simulations cause drift pressurization.* This effect will be evaluated by examining in-drift pressures predicted through time. Pressures will be extracted from THC seepage model outputs, and representative data will be reported in the THC seepage report.

Summary spreadsheets of model results submitted to the TDMS under DTNs listed in Appendix J include pressure as a function of time in rock directly at the drift wall. These model data show that between 50 and ~75 years, pressures in the rock matrix reach a maximum of about 2.5× atmospheric values. For all times thereafter, pressure remains at essentially atmospheric values in both fracture and matrix gridblocks. The inclusion of these results in outputs of this report address this issue.

- *Repository edge effects on seepage compositions.* This item is being addressed by the actions for CR-7037.

See CR-7037.

- *Justification that the DST-THC model, which does not include cool-down, validates the THC Seepage model.* This item is being addressed by including the DST cool-down data in the DST-THC model validation comparisons.

This issue was addressed by including the DST cool-down period in model validation as described in Section 7.1.3.

- *Improve integration of the THC and seepage models.* This item is being addressed by the THC sensitivity study workscope.

This issue is addressed in the report *THC Sensitivity Study of Heterogeneous Permeability and Capillarity Effects* (SNL 2007 [DIRS 177413]).

- *The 2-D THC model does not account for axial transport of vapor.* This item will be addressed in development of the near-field chemistry model.

This issue is addressed in the report *Engineered Barrier System: Physical and Chemical Environment* (BSC 2007 [DIRS 177412]).

- *Inadequate justification that flow focusing due to THC processes will not increase vertical fluxes at the drift crown.*

As discussed in Section 6.4.8, this issue is no longer relevant.

- *Plug flow reactor and fracture sealing experiment validation simulations were run with old model, and do not validate the current THC seepage model.* The plug flow reactor simulations will be re-run using updated inputs, and used for confidence building during model development. The fracture sealing experiment simulations will not be re-run. These experiments will not be used for model validation.

The plug-flow reactor experiment was not rerun in the current report. Rerunning simulations of these experiments was deemed non-essential for this report. However, the results of the older (historical) simulations of both the plug-flow and fracture sealing experiment were included in Sections 7.2 and 7.3, respectively, to provide added confidence in the conceptual model that is the basis of the THC seepage model, but not for model validation.

- Technical issues with the THC model:
 - *Justification for the ionic strength range for the Helgeson-Kirkham-Flowers model.*

Text was added in Section 6.4.1 pointing to Section A.H.1 of the *User Information Document for TOUGHREACT V3.1.1* (DOE 2007 [DIRS 182183]) for specific tests on the ionic strength range for the Helgeson-Kirkham-Flowers model.
 - *Mechanism for handling salt precipitation and redissolution.*

This is addressed by the actions for CR-6691.
 - *Minor corrections in discussion of $p\text{CO}_2$ values used in the model.*

The section discussing ambient CO_2 partial pressure (Section 6.2.2.1) was revised.
 - *Evaluate the importance of the processes of salt separation, deliquescence, and acid degassing, currently not included in the THC seepage model.*

A discussion pointing to the in-drift precipitates/salts model was added in Section 6.4.5.
 - *Clarify discussion of using 50% of a doubled fracture porosity as fracture minerals.*

The discussion in Section 6.4.6 (11) has been clarified.
 - *Discuss the effect of mineral precipitation in the fracture on matrix-fracture coupling.*

A discussion was added in Section 6.1.2.5 and in model approximation 8 in Section 6.4.6.
 - *Applicability of the ambient air-conductivity data.*

A new model approximation (number 26 in Section 6.4.6) was added to this effect.

- *Some missing data points on validation plots.*

This is addressed by the actions for CR-5383.

- *Basis for aqueous diffusion coefficients is not provided.*

A discussion was added to Section 4.1.1.1.

13. CR-7697: *Minor transparency and traceability issues in the THC model.* Three minor issues are included in this CR:

- *Calculation of activity coefficients for neutral species in solution, primarily $CO_2(aq)$ is incorrectly described in the current version of the THC Seepage model.*

The discussion was corrected in Section 6.4.1.

- *In Table 6.1-1 of Rev. 04 of the THC seepage report and its associated text, the starting water W5 is attributed to unit Tptpul, while it is actually in unit Tptpmn. The top of the borehole is in the Tptpul unit, but the interval from which the sample was collected was actually in the lower unit.*

New input water compositions have been selected for this report as shown on Table 6.2-1, making this issue no longer relevant.

- *The mineral sepiolite was not included in the initial mineral volume fraction and mineral reactive surface area summary tables in Appendices A and B or in the supporting spreadsheet.*

Appendices A and B have been updated to include data for all minerals considered in the simulations, including a new amorphous magnesium silicate replacing sepiolite (amorphous antigorite).

14. CR-7811: *Discrepancy between MDL-NBS-HS-000001 Rev. 04, Section 6.4.1, and the TOUGHREACT V3.0 description of activity coefficients for neutral species.* In Revision 05 of the THC seepage model report, the discussion will be changed to conform with the specific code features that are used to represent neutral species.

This CR was addressed by correcting the discussion in Section 6.4.1, as well as in the documentation of the new TOUGHREACT version used in this report.

15. CR-8009: *Capillary pressure function flag of 10 and Leverett scaling function in TOUGHREACT.*

This CR was addressed by the qualification of TOUGHREACT V3.1.1.

16. CR-8032: *THC time stepping effect unresolved (MDL-NBS-HS-000001)*. Model sensitivity to time steps will be evaluated by running several successive simulations, for both the DST validation case and the THC seepage model, with varying time stepping limits.

This CR was addressed by adding time-stepping analyses in Section 6.6.1 as well as in model validation simulations presented in Section 7.1.8.

17. CR-8316: *Pore-water chemistry analyses lack charge balance*. When measured pore-water compositions are re-evaluated for use as starting water compositions for the near-field chemistry model in *Engineered Barrier System: Physical and Chemical Environment* (SNL 2007 [DIRS 177412]), a discussion will be included of the potential causes of the lack of charge balances in many of the available repository-level pore-water chemical analyses.

This CR was addressed by citing in Section 6.2.2.1 of *Engineered Barrier System: Physical and Chemical Environment* (SNL 2007 [DIRS 177412]) as the source providing the rationale for the selection of water compositions used in the present report. The rationale includes good charge balance.

This revision of the THC seepage report also addresses the following Independent Validation Review Team comments documented by Booth (2006 [DIRS 176638]):

1. IDC-1: *Sensitivity to reaction rate constants—the sensitivity of the THC seepage model results to reaction rate constants must be evaluated*. The sensitivity study described above for CRs 6342 and 6492 will provide a response to this comment. It is anticipated that predicted water compositions will only be slightly sensitive to order-of-magnitude variation in the product of the intrinsic rate constant and the reactive surface area. If necessary, the THC seepage model uncertainty estimates will be modified to reflect additional uncertainty due to reaction rate constants.

This comment is addressed by sensitivity analyses provided in Section 6.6.5.

2. IDC-2: *Equal weighting of all five pore waters—the probability of a given starting water should be tied to the probability of occurrence of that water type*.

This comment is addressed in *Engineered Barrier System: Physical and Chemical Environment* (SNL 2007 [DIRS 177412]).

3. IDC-10: *Drift variability of water chemistries—use of time histories developed for repository-center THC simulations to represent repository edge water compositions is not appropriate*.

This comment is addressed by including specific repository edge simulations in the present report (Section 6.5.1).

INTENTIONALLY LEFT BLANK

APPENDIX Q
TOUGHREACT V3.1.1 AND CUTCHEM V2.0 EXECUTABLES INSTALLATION
INFORMATION

INTENTIONALLY LEFT BLANK

Q.1 TOUGHREACT V3.1.1 INSTALLATION ON LBNL MACHINE WORKHORSE (CAOS LINUX)

Q.1.1 Installation on Workhorse for Preliminary Modeling Prior to Qualification of TOUGHREACT V3.1.1.

Directory and file listings for TOUGHREACT V3.1.1 executables and installation tests on Lawrence Berkeley National Laboratory (LBNL) machine workhorse:

```
/home/ymp/tr3.1.1_X
```

```
total 20
```

```
drwxr-xr-x  2 jwong users 4096 Nov 15 23:08 executables
drwxr-xr-x  8 jwong users 4096 Dec  8 09:38 install_tests
drwxr-xr-x  2 jwong users 4096 Nov 15 22:39 source
drwxr-xr-x 25 jwong users 4096 Nov 15 22:43 test_problems_dec
drwxr-xr-x 25 jwong users 4096 Nov 15 22:37 test_problems_lin
```

```
/home/ymp/tr3.1.1_X/executables
```

```
total 8344
```

```
-r-xr-xr-x  1 jwong users 1267120 Nov 15 23:08 tr3.1.1e3_40k_dec
-r-xr--r--  1 jwong users 1571881 Nov 15 23:08 tr3.1.1e3_40k_lin
-r-xr-xr-x  1 jwong users 1277184 Nov 15 23:08 tr3.1.1e4_40k_dec
-r-xr--r--  1 jwong users 1583453 Nov 15 23:08 tr3.1.1e4_40k_lin
-r-xr-xr-x  1 jwong users 1256656 Nov 15 23:08 tr3.1.1e9_40k_dec
-r-xr--r--  1 jwong users 1556024 Nov 15 23:08 tr3.1.1e9_40k_lin
```

```
/home/ymp/tr3.1.1_X/install_tests
```

```
total 12
```

```
drwxr-xr-x  2 jwong users 4096 Nov 15 22:35 eos3
drwxr-xr-x  2 jwong users 4096 Nov 15 22:35 eos4
drwxr-xr-x  2 jwong users 4096 Nov 15 22:35 eos9
```

```
/home/ymp/tr3.1.1_X/install_tests/eos3
```

```
total 896
```

```
-r-xr--r--  1 jwong users 172953 Nov 15 22:35 GASOBS.DAT
-r-xr--r--  1 jwong users   91 Nov 15 22:35 GENER
-r-xr--r--  1 jwong users  149 Nov 15 22:35 INCON
-r-xr--r--  1 jwong users   0 Nov 15 22:35 LINEQ
-r-xr--r--  1 jwong users  9228 Nov 15 22:35 MESH
-r-xr--r--  1 jwong users  7518 Nov 15 22:35 SAVE
-r-xr--r--  1 jwong users   0 Nov 15 22:35 TABLE
-r-xr--r--  1 jwong users  6640 Nov 15 22:35 VERS
-r-xr--r--  1 jwong users  7049 Nov 15 22:35 chdump.out
-r-xr--r--  1 jwong users  5517 Nov 15 22:35 chemical.inp
-r-xr--r--  1 jwong users 14625 Nov 15 22:35 chemical.out
-r-xr--r--  1 jwong users  9711 Nov 15 22:35 flow.inp
-r-xr--r--  1 jwong users 228245 Nov 15 22:35 flow.out
```

```
-r-xr--r-- 1 jwong users 12001 Nov 15 22:35 iter.dat
-r-xr--r-- 1 jwong users 15528 Nov 15 22:35 mbalance.out
-r-xr--r-- 1 jwong users 31174 Nov 15 22:35 min_SI.out
-r-xr--r-- 1 jwong users 15277 Nov 15 22:35 runlog.out
-r-xr--r-- 1 jwong users 62613 Nov 15 22:35 savechem
-r-xr--r-- 1 jwong users 1646 Nov 15 22:35 solute.inp
-r-xr--r-- 1 jwong users 6209 Nov 15 22:35 solute.out
-r-xr--r-- 1 jwong users 33914 Nov 15 22:35 tec_conc.dat
-r-xr--r-- 1 jwong users 14089 Nov 15 22:35 tec_gas.dat
-r-xr--r-- 1 jwong users 48093 Nov 15 22:35 tec_min.dat
-r-xr--r-- 1 jwong users 88384 Nov 15 22:35 ther_dummy.dat
-r-xr--r-- 1 jwong users 60384 Nov 15 22:35 time.dat
```

/home/ymp/tr3.1.1_X/install_tests/eos4

total 896

```
-r-xr--r-- 1 jwong users 172557 Nov 15 22:35 GASOBS.DAT
-r-xr--r-- 1 jwong users 91 Nov 15 22:35 GENER
-r-xr--r-- 1 jwong users 149 Nov 15 22:35 INCON
-r-xr--r-- 1 jwong users 0 Nov 15 22:35 LINEQ
-r-xr--r-- 1 jwong users 9228 Nov 15 22:35 MESH
-r-xr--r-- 1 jwong users 7518 Nov 15 22:35 SAVE
-r-xr--r-- 1 jwong users 0 Nov 15 22:35 TABLE
-r-xr--r-- 1 jwong users 7047 Nov 15 22:35 VERS
-r-xr--r-- 1 jwong users 7049 Nov 15 22:35 chdump.out
-r-xr--r-- 1 jwong users 5517 Nov 15 22:35 chemical.inp
-r-xr--r-- 1 jwong users 14625 Nov 15 22:35 chemical.out
-r-xr--r-- 1 jwong users 9711 Nov 15 22:35 flow.inp
-r-xr--r-- 1 jwong users 227315 Nov 15 22:35 flow.out
-r-xr--r-- 1 jwong users 12001 Nov 15 22:35 iter.dat
-r-xr--r-- 1 jwong users 15528 Nov 15 22:35 mbalance.out
-r-xr--r-- 1 jwong users 31174 Nov 15 22:35 min_SI.out
-r-xr--r-- 1 jwong users 15277 Nov 15 22:35 runlog.out
-r-xr--r-- 1 jwong users 62613 Nov 15 22:35 savechem
-r-xr--r-- 1 jwong users 1646 Nov 15 22:35 solute.inp
-r-xr--r-- 1 jwong users 6209 Nov 15 22:35 solute.out
-r-xr--r-- 1 jwong users 33914 Nov 15 22:35 tec_conc.dat
-r-xr--r-- 1 jwong users 14089 Nov 15 22:35 tec_gas.dat
-r-xr--r-- 1 jwong users 48093 Nov 15 22:35 tec_min.dat
-r-xr--r-- 1 jwong users 88384 Nov 15 22:35 ther_dummy.dat
-r-xr--r-- 1 jwong users 60384 Nov 15 22:35 time.dat
```

/home/ymp/tr3.1.1_X/install_tests/eos9

total 200

```
-r-xr--r-- 1 jwong users 29403 Nov 15 22:35 GASOBS.DAT
-r-xr--r-- 1 jwong users 91 Nov 15 22:35 GENER
-r-xr--r-- 1 jwong users 7383 Nov 15 22:35 INCON
-r-xr--r-- 1 jwong users 0 Nov 15 22:35 LINEQ
```

```
-r-xr--r-- 1 jwong users 13967 Nov 15 22:35 MESH
-r-xr--r-- 1 jwong users 7491 Nov 15 22:35 SAVE
-r-xr--r-- 1 jwong users 0 Nov 15 22:35 TABLE
-r-xr--r-- 1 jwong users 3791 Nov 15 22:35 VERS
-r-xr--r-- 1 jwong users 41322 Nov 15 22:35 flow.inp
-r-xr--r-- 1 jwong users 79596 Nov 15 22:35 flow.out
```

/home/ymp/tr3.1.1_X/source

total 1312

```
-r-xr--r-- 1 jwong users 3081 Nov 15 22:34 T2_40K
-r-xr--r-- 1 jwong users 1839 Nov 15 22:34 chempar23_q311.inc
-r-xr--r-- 1 jwong users 3412 Nov 15 22:34 common23.inc
-r-xr--r-- 1 jwong users 46113 Nov 15 22:34 eos3.f
-r-xr--r-- 1 jwong users 60724 Nov 15 22:34 eos4.f
-r-xr--r-- 1 jwong users 32044 Nov 15 22:34 eos9.f
-r-xr--r-- 1 jwong users 204231 Nov 15 22:34 geochem.f
-r-xr--r-- 1 jwong users 97464 Nov 15 22:34 inichm.f
-r-xr--r-- 1 jwong users 1550 Nov 15 22:34 ma28abc.f
-r-xr--r-- 1 jwong users 1716 Nov 15 22:34 makefile_eos3q311_dec
-r-xr--r-- 1 jwong users 1894 Nov 15 22:34 makefile_eos3q311_linux
-r-xr--r-- 1 jwong users 1716 Nov 15 22:34 makefile_eos4q311_dec
-r-xr--r-- 1 jwong users 1894 Nov 15 22:34 makefile_eos4q311_linux
-r-xr--r-- 1 jwong users 1716 Nov 15 22:34 makefile_eos9q311_dec
-r-xr--r-- 1 jwong users 1894 Nov 15 22:34 makefile_eos9q311_linux
-r-xr--r-- 1 jwong users 41911 Nov 15 22:34 meshm.f
-r-xr--r-- 1 jwong users 141763 Nov 15 22:34 multi.f
-r-xr--r-- 1 jwong users 33584 Nov 15 22:34 newton.f
-r-xr--r-- 1 jwong users 507 Nov 15 22:34 perm23.inc
-r-xr--r-- 1 jwong users 17941 Nov 15 22:34 rctprop.f
-r-xr--r-- 1 jwong users 20523 Nov 15 22:34 readsolu.f
-r-xr--r-- 1 jwong users 827 Nov 15 22:34 second_dec.f
-r-xr--r-- 1 jwong users 73085 Nov 15 22:34 t2cg22.f
-r-xr--r-- 1 jwong users 165569 Nov 15 22:34 t2f.f
-r-xr--r-- 1 jwong users 73236 Nov 15 22:34 t2solv.f
-r-xr--r-- 1 jwong users 225993 Nov 15 22:34 treat.f
```

Q.1.2 Installation on Workhorse Using Qualified TOUGHREACT V 3.1.1 Media from Software Configuration Management

/home/jleem/tr3.1.1_X

total 20

```
drwxr-xr-x 2 jleem users 4096 2006-11-15 23:08:36.000000000 -0800 executables
drwxr-xr-x 5 jleem users 4096 2006-11-15 22:35:30.000000000 -0800 install_tests
drwxr-xr-x 2 jleem users 4096 2006-11-15 22:39:37.000000000 -0800 source
drwxr-xr-x 25 jleem users 4096 2006-11-15 22:43:01.000000000 -0800 test_problems_dec
drwxr-xr-x 25 jleem users 4096 2006-11-15 22:37:33.000000000 -0800 test_problems_lin
```

/home/jleem/tr3.1.1_X/executables

total 8344

```
-r-xr-xr-x 1 jleem users 1267120 2006-11-15 23:08:07.000000000 -0800 tr3.1.1e3_40k_dec
-r-xr--r-- 1 jleem users 1571881 2006-11-15 23:08:07.000000000 -0800 tr3.1.1e3_40k_lin
-r-xr-xr-x 1 jleem users 1277184 2006-11-15 23:08:07.000000000 -0800 tr3.1.1e4_40k_dec
-r-xr--r-- 1 jleem users 1583453 2006-11-15 23:08:06.000000000 -0800 tr3.1.1e4_40k_lin
-r-xr-xr-x 1 jleem users 1256656 2006-11-15 23:08:06.000000000 -0800 tr3.1.1e9_40k_dec
-r-xr--r-- 1 jleem users 1556024 2006-11-15 23:08:06.000000000 -0800 tr3.1.1e9_40k_lin
```

/home/jleem/tr3.1.1_X/install_tests

total 12

```
drwxr-xr-x 2 jleem users 4096 2006-11-15 22:35:30.000000000 -0800 eos3
drwxr-xr-x 2 jleem users 4096 2006-11-15 22:35:30.000000000 -0800 eos4
drwxr-xr-x 2 jleem users 4096 2006-11-15 22:35:30.000000000 -0800 eos9
```

/home/jleem/tr3.1.1_X/install_tests/eos3

total 896

```
-r-xr--r-- 1 jleem users 172953 2006-11-15 22:35:30.000000000 -0800 GASOBS.DAT
-r-xr--r-- 1 jleem users 91 2006-11-15 22:35:30.000000000 -0800 GENER
-r-xr--r-- 1 jleem users 149 2006-11-15 22:35:30.000000000 -0800 INCON
-r-xr--r-- 1 jleem users 0 2006-11-15 22:35:30.000000000 -0800 LINEQ
-r-xr--r-- 1 jleem users 9228 2006-11-15 22:35:30.000000000 -0800 MESH
-r-xr--r-- 1 jleem users 7518 2006-11-15 22:35:30.000000000 -0800 SAVE
-r-xr--r-- 1 jleem users 0 2006-11-15 22:35:30.000000000 -0800 TABLE
-r-xr--r-- 1 jleem users 6640 2006-11-15 22:35:30.000000000 -0800 VERS
-r-xr--r-- 1 jleem users 7049 2006-11-15 22:35:29.000000000 -0800 chdump.out
-r-xr--r-- 1 jleem users 5517 2006-11-15 22:35:29.000000000 -0800 chemical.inp
-r-xr--r-- 1 jleem users 14625 2006-11-15 22:35:29.000000000 -0800 chemical.out
-r-xr--r-- 1 jleem users 9711 2006-11-15 22:35:30.000000000 -0800 flow.inp
-r-xr--r-- 1 jleem users 228245 2006-11-15 22:35:30.000000000 -0800 flow.out
-r-xr--r-- 1 jleem users 12001 2006-11-15 22:35:30.000000000 -0800 iter.dat
-r-xr--r-- 1 jleem users 15528 2006-11-15 22:35:30.000000000 -0800 mbalance.out
-r-xr--r-- 1 jleem users 31174 2006-11-15 22:35:30.000000000 -0800 min_SI.out
-r-xr--r-- 1 jleem users 15277 2006-11-15 22:35:30.000000000 -0800 runlog.out
-r-xr--r-- 1 jleem users 62613 2006-11-15 22:35:30.000000000 -0800 savechem
-r-xr--r-- 1 jleem users 1646 2006-11-15 22:35:30.000000000 -0800 solute.inp
-r-xr--r-- 1 jleem users 6209 2006-11-15 22:35:30.000000000 -0800 solute.out
-r-xr--r-- 1 jleem users 33914 2006-11-15 22:35:30.000000000 -0800 tec_conc.dat
-r-xr--r-- 1 jleem users 14089 2006-11-15 22:35:30.000000000 -0800 tec_gas.dat
-r-xr--r-- 1 jleem users 48093 2006-11-15 22:35:30.000000000 -0800 tec_min.dat
-r-xr--r-- 1 jleem users 88384 2006-11-15 22:35:29.000000000 -0800 ther_dummy.dat
-r-xr--r-- 1 jleem users 60384 2006-11-15 22:35:30.000000000 -0800 time.dat
```

/home/jleem/tr3.1.1_X/install_tests/eos4

total 896

```
-r-xr--r-- 1 jleem users 172557 2006-11-15 22:35:30.000000000 -0800 GASOBS.DAT
-r-xr--r-- 1 jleem users 91 2006-11-15 22:35:30.000000000 -0800 GENER
```



```
-r-xr--r-- 1 jleem users 149 2006-11-15 22:35:30.000000000 -0800 INCON
-r-xr--r-- 1 jleem users 0 2006-11-15 22:35:30.000000000 -0800 LINEQ
-r-xr--r-- 1 jleem users 9228 2006-11-15 22:35:30.000000000 -0800 MESH
-r-xr--r-- 1 jleem users 7518 2006-11-15 22:35:30.000000000 -0800 SAVE
-r-xr--r-- 1 jleem users 0 2006-11-15 22:35:30.000000000 -0800 TABLE
-r-xr--r-- 1 jleem users 7047 2006-11-15 22:35:30.000000000 -0800 VERS
-r-xr--r-- 1 jleem users 7049 2006-11-15 22:35:30.000000000 -0800 chdump.out
-r-xr--r-- 1 jleem users 5517 2006-11-15 22:35:30.000000000 -0800 chemical.inp
-r-xr--r-- 1 jleem users 14625 2006-11-15 22:35:30.000000000 -0800 chemical.out
-r-xr--r-- 1 jleem users 9711 2006-11-15 22:35:30.000000000 -0800 flow.inp
-r-xr--r-- 1 jleem users 227315 2006-11-15 22:35:30.000000000 -0800 flow.out
-r-xr--r-- 1 jleem users 12001 2006-11-15 22:35:30.000000000 -0800 iter.dat
-r-xr--r-- 1 jleem users 15528 2006-11-15 22:35:30.000000000 -0800 mbalance.out
-r-xr--r-- 1 jleem users 31174 2006-11-15 22:35:30.000000000 -0800 min_SI.out
-r-xr--r-- 1 jleem users 15277 2006-11-15 22:35:30.000000000 -0800 runlog.out
-r-xr--r-- 1 jleem users 62613 2006-11-15 22:35:30.000000000 -0800 savechem
-r-xr--r-- 1 jleem users 1646 2006-11-15 22:35:30.000000000 -0800 solute.inp
-r-xr--r-- 1 jleem users 6209 2006-11-15 22:35:30.000000000 -0800 solute.out
-r-xr--r-- 1 jleem users 33914 2006-11-15 22:35:30.000000000 -0800 tec_conc.dat
-r-xr--r-- 1 jleem users 14089 2006-11-15 22:35:30.000000000 -0800 tec_gas.dat
-r-xr--r-- 1 jleem users 48093 2006-11-15 22:35:30.000000000 -0800 tec_min.dat
-r-xr--r-- 1 jleem users 88384 2006-11-15 22:35:30.000000000 -0800 ther_dummy.dat
-r-xr--r-- 1 jleem users 60384 2006-11-15 22:35:30.000000000 -0800 time.dat
```

/home/jleem/tr3.1.1_X/install_tests/eos9

total 200

```
-r-xr--r-- 1 jleem users 29403 2006-11-15 22:35:30.000000000 -0800 GASOBS.DAT
-r-xr--r-- 1 jleem users 91 2006-11-15 22:35:30.000000000 -0800 GENER
-r-xr--r-- 1 jleem users 7383 2006-11-15 22:35:30.000000000 -0800 INCON
-r-xr--r-- 1 jleem users 0 2006-11-15 22:35:30.000000000 -0800 LINEQ
-r-xr--r-- 1 jleem users 13967 2006-11-15 22:35:30.000000000 -0800 MESH
-r-xr--r-- 1 jleem users 7491 2006-11-15 22:35:30.000000000 -0800 SAVE
-r-xr--r-- 1 jleem users 0 2006-11-15 22:35:30.000000000 -0800 TABLE
-r-xr--r-- 1 jleem users 3791 2006-11-15 22:35:30.000000000 -0800 VERS
-r-xr--r-- 1 jleem users 41322 2006-11-15 22:35:30.000000000 -0800 flow.inp
-r-xr--r-- 1 jleem users 79596 2006-11-15 22:35:30.000000000 -0800 flow.out
```

/home/jleem/tr3.1.1_X/source

total 1312

```
-r-xr--r-- 1 jleem users 3081 2006-11-15 22:34:50.000000000 -0800 T2_40K
-r-xr--r-- 1 jleem users 1839 2006-11-15 22:34:50.000000000 -0800 chempar23_q311.inc
-r-xr--r-- 1 jleem users 3412 2006-11-15 22:34:50.000000000 -0800 common23.inc
-r-xr--r-- 1 jleem users 46113 2006-11-15 22:34:50.000000000 -0800 eos3.f
-r-xr--r-- 1 jleem users 60724 2006-11-15 22:34:50.000000000 -0800 eos4.f
-r-xr--r-- 1 jleem users 32044 2006-11-15 22:34:50.000000000 -0800 eos9.f
-r-xr--r-- 1 jleem users 204231 2006-11-15 22:34:50.000000000 -0800 geochem.f
-r-xr--r-- 1 jleem users 97464 2006-11-15 22:34:50.000000000 -0800 inichm.f
```

```

-r-xr--r-- 1 jleem users 1550 2006-11-15 22:34:50.000000000 -0800 ma28abc.f
-r-xr--r-- 1 jleem users 1716 2006-11-15 22:34:50.000000000 -0800 makefile_eos3q311_dec
-r-xr--r-- 1 jleem users 1894 2006-11-15 22:34:50.000000000 -0800 makefile_eos3q311_linux
-r-xr--r-- 1 jleem users 1716 2006-11-15 22:34:50.000000000 -0800 makefile_eos4q311_dec
-r-xr--r-- 1 jleem users 1894 2006-11-15 22:34:50.000000000 -0800 makefile_eos4q311_linux
-r-xr--r-- 1 jleem users 1716 2006-11-15 22:34:50.000000000 -0800 makefile_eos9q311_dec
-r-xr--r-- 1 jleem users 1894 2006-11-15 22:34:50.000000000 -0800 makefile_eos9q311_linux
-r-xr--r-- 1 jleem users 41911 2006-11-15 22:34:50.000000000 -0800 meshm.f
-r-xr--r-- 1 jleem users 141763 2006-11-15 22:34:50.000000000 -0800 multi.f
-r-xr--r-- 1 jleem users 33584 2006-11-15 22:34:50.000000000 -0800 newton.f
-r-xr--r-- 1 jleem users 507 2006-11-15 22:34:50.000000000 -0800 perm23.inc
-r-xr--r-- 1 jleem users 17941 2006-11-15 22:34:50.000000000 -0800 rctprop.f
-r-xr--r-- 1 jleem users 20523 2006-11-15 22:34:50.000000000 -0800 readsolu.f
-r-xr--r-- 1 jleem users 827 2006-11-15 22:34:50.000000000 -0800 second_dec.f
-r-xr--r-- 1 jleem users 73085 2006-11-15 22:34:50.000000000 -0800 t2cg22.f
-r-xr--r-- 1 jleem users 165569 2006-11-15 22:34:50.000000000 -0800 t2f.f
-r-xr--r-- 1 jleem users 73236 2006-11-15 22:34:50.000000000 -0800 t2solv.f
-r-xr--r-- 1 jleem users 225993 2006-11-15 22:34:50.000000000 -0800 treat.f

```

Q.2 TOUGHREACT V3.1.1 INSTALLATION ON LBNL MACHINE WORKHORSE2 (CAOS LINUX)

Q.2.1 Installation on Workhorse2 for Preliminary Modeling Prior to Qualification of TOUGHREACT V3.1.1

/home/ymp/tr3.1.1_X

total 20

```

drwxr-xr-x 2 jwong users 4096 Nov 15 23:08 executables
drwxr-xr-x 8 jwong users 4096 Dec 8 09:38 install_tests
drwxr-xr-x 2 jwong users 4096 Nov 15 22:39 source
drwxr-xr-x 25 jwong users 4096 Nov 15 22:43 test_problems_dec
drwxr-xr-x 25 jwong users 4096 Nov 15 22:37 test_problems_lin

```

/home/ymp/tr3.1.1_X/executables

total 8344

```

-r-xr-xr-x 1 jwong users 1267120 Nov 15 23:08 tr3.1.1e3_40k_dec
-r-xr--r-- 1 jwong users 1571881 Nov 15 23:08 tr3.1.1e3_40k_lin
-r-xr-xr-x 1 jwong users 1277184 Nov 15 23:08 tr3.1.1e4_40k_dec
-r-xr--r-- 1 jwong users 1583453 Nov 15 23:08 tr3.1.1e4_40k_lin
-r-xr-xr-x 1 jwong users 1256656 Nov 15 23:08 tr3.1.1e9_40k_dec
-r-xr--r-- 1 jwong users 1556024 Nov 15 23:08 tr3.1.1e9_40k_lin

```

/home/ymp/tr3.1.1_X/install_tests

total 12

```

drwxr-xr-x 2 jwong users 4096 Nov 15 22:35 eos3
drwxr-xr-x 2 jwong users 4096 Nov 15 22:35 eos4
drwxr-xr-x 2 jwong users 4096 Nov 15 22:35 eos9

```

/home/ymp/tr3.1.1_X/install_tests/eos3

total 896

```
-r-xr--r-- 1 jwong users 172953 Nov 15 22:35 GASOBS.DAT
-r-xr--r-- 1 jwong users   91 Nov 15 22:35 GENER
-r-xr--r-- 1 jwong users  149 Nov 15 22:35 INCON
-r-xr--r-- 1 jwong users   0 Nov 15 22:35 LINEQ
-r-xr--r-- 1 jwong users  9228 Nov 15 22:35 MESH
-r-xr--r-- 1 jwong users  7518 Nov 15 22:35 SAVE
-r-xr--r-- 1 jwong users   0 Nov 15 22:35 TABLE
-r-xr--r-- 1 jwong users  6640 Nov 15 22:35 VERS
-r-xr--r-- 1 jwong users  7049 Nov 15 22:35 chdump.out
-r-xr--r-- 1 jwong users  5517 Nov 15 22:35 chemical.inp
-r-xr--r-- 1 jwong users 14625 Nov 15 22:35 chemical.out
-r-xr--r-- 1 jwong users  9711 Nov 15 22:35 flow.inp
-r-xr--r-- 1 jwong users 228245 Nov 15 22:35 flow.out
-r-xr--r-- 1 jwong users 12001 Nov 15 22:35 iter.dat
-r-xr--r-- 1 jwong users 15528 Nov 15 22:35 mbalance.out
-r-xr--r-- 1 jwong users 31174 Nov 15 22:35 min_SI.out
-r-xr--r-- 1 jwong users 15277 Nov 15 22:35 runlog.out
-r-xr--r-- 1 jwong users 62613 Nov 15 22:35 savechem
-r-xr--r-- 1 jwong users  1646 Nov 15 22:35 solute.inp
-r-xr--r-- 1 jwong users  6209 Nov 15 22:35 solute.out
-r-xr--r-- 1 jwong users 33914 Nov 15 22:35 tec_conc.dat
-r-xr--r-- 1 jwong users 14089 Nov 15 22:35 tec_gas.dat
-r-xr--r-- 1 jwong users 48093 Nov 15 22:35 tec_min.dat
-r-xr--r-- 1 jwong users 88384 Nov 15 22:35 ther_dummy.dat
-r-xr--r-- 1 jwong users 60384 Nov 15 22:35 time.dat
```

/home/ymp/tr3.1.1_X/install_tests/eos4

total 896

```
-r-xr--r-- 1 jwong users 172557 Nov 15 22:35 GASOBS.DAT
-r-xr--r-- 1 jwong users   91 Nov 15 22:35 GENER
-r-xr--r-- 1 jwong users  149 Nov 15 22:35 INCON
-r-xr--r-- 1 jwong users   0 Nov 15 22:35 LINEQ
-r-xr--r-- 1 jwong users  9228 Nov 15 22:35 MESH
-r-xr--r-- 1 jwong users  7518 Nov 15 22:35 SAVE
-r-xr--r-- 1 jwong users   0 Nov 15 22:35 TABLE
-r-xr--r-- 1 jwong users  7047 Nov 15 22:35 VERS
-r-xr--r-- 1 jwong users  7049 Nov 15 22:35 chdump.out
-r-xr--r-- 1 jwong users  5517 Nov 15 22:35 chemical.inp
-r-xr--r-- 1 jwong users 14625 Nov 15 22:35 chemical.out
-r-xr--r-- 1 jwong users  9711 Nov 15 22:35 flow.inp
-r-xr--r-- 1 jwong users 227315 Nov 15 22:35 flow.out
-r-xr--r-- 1 jwong users 12001 Nov 15 22:35 iter.dat
-r-xr--r-- 1 jwong users 15528 Nov 15 22:35 mbalance.out
-r-xr--r-- 1 jwong users 31174 Nov 15 22:35 min_SI.out
-r-xr--r-- 1 jwong users 15277 Nov 15 22:35 runlog.out
```

```
-r-xr--r-- 1 jwong users 62613 Nov 15 22:35 savechem
-r-xr--r-- 1 jwong users 1646 Nov 15 22:35 solute.inp
-r-xr--r-- 1 jwong users 6209 Nov 15 22:35 solute.out
-r-xr--r-- 1 jwong users 33914 Nov 15 22:35 tec_conc.dat
-r-xr--r-- 1 jwong users 14089 Nov 15 22:35 tec_gas.dat
-r-xr--r-- 1 jwong users 48093 Nov 15 22:35 tec_min.dat
-r-xr--r-- 1 jwong users 88384 Nov 15 22:35 ther_dummy.dat
-r-xr--r-- 1 jwong users 60384 Nov 15 22:35 time.dat
```

/home/ymp/tr3.1.1_X/install_tests/eos9

total 200

```
-r-xr--r-- 1 jwong users 29403 Nov 15 22:35 GASOBS.DAT
-r-xr--r-- 1 jwong users 91 Nov 15 22:35 GENER
-r-xr--r-- 1 jwong users 7383 Nov 15 22:35 INCON
-r-xr--r-- 1 jwong users 0 Nov 15 22:35 LINEQ
-r-xr--r-- 1 jwong users 13967 Nov 15 22:35 MESH
-r-xr--r-- 1 jwong users 7491 Nov 15 22:35 SAVE
-r-xr--r-- 1 jwong users 0 Nov 15 22:35 TABLE
-r-xr--r-- 1 jwong users 3791 Nov 15 22:35 VERS
-r-xr--r-- 1 jwong users 41322 Nov 15 22:35 flow.inp
-r-xr--r-- 1 jwong users 79596 Nov 15 22:35 flow.out
```

/home/ymp/tr3.1.1_X/source

total 1312

```
-r-xr--r-- 1 jwong users 3081 Nov 15 22:34 T2_40K
-r-xr--r-- 1 jwong users 1839 Nov 15 22:34 chempar23_q311.inc
-r-xr--r-- 1 jwong users 3412 Nov 15 22:34 common23.inc
-r-xr--r-- 1 jwong users 46113 Nov 15 22:34 eos3.f
-r-xr--r-- 1 jwong users 60724 Nov 15 22:34 eos4.f
-r-xr--r-- 1 jwong users 32044 Nov 15 22:34 eos9.f
-r-xr--r-- 1 jwong users 204231 Nov 15 22:34 geochem.f
-r-xr--r-- 1 jwong users 97464 Nov 15 22:34 inichm.f
-r-xr--r-- 1 jwong users 1550 Nov 15 22:34 ma28abc.f
-r-xr--r-- 1 jwong users 1716 Nov 15 22:34 makefile_eos3q311_dec
-r-xr--r-- 1 jwong users 1894 Nov 15 22:34 makefile_eos3q311_linux
-r-xr--r-- 1 jwong users 1716 Nov 15 22:34 makefile_eos4q311_dec
-r-xr--r-- 1 jwong users 1894 Nov 15 22:34 makefile_eos4q311_linux
-r-xr--r-- 1 jwong users 1716 Nov 15 22:34 makefile_eos9q311_dec
-r-xr--r-- 1 jwong users 1894 Nov 15 22:34 makefile_eos9q311_linux
-r-xr--r-- 1 jwong users 41911 Nov 15 22:34 meshm.f
-r-xr--r-- 1 jwong users 141763 Nov 15 22:34 multi.f
-r-xr--r-- 1 jwong users 33584 Nov 15 22:34 newton.f
-r-xr--r-- 1 jwong users 507 Nov 15 22:34 perm23.inc
-r-xr--r-- 1 jwong users 17941 Nov 15 22:34 rctprop.f
-r-xr--r-- 1 jwong users 20523 Nov 15 22:34 readsolu.f
-r-xr--r-- 1 jwong users 827 Nov 15 22:34 second_dec.f
-r-xr--r-- 1 jwong users 73085 Nov 15 22:34 t2cg22.f
```

```
-r-xr--r-- 1 jwong users 165569 Nov 15 22:34 t2f.f
-r-xr--r-- 1 jwong users 73236 Nov 15 22:34 t2solv.f
-r-xr--r-- 1 jwong users 225993 Nov 15 22:34 treat.f
```

Q.2.2 Installation on Workhorse 2 Using Qualified TOUGHREACT V3.1.1 Media from Software Configuration Management

```
/home/jleem/tr3.1.1_X
```

```
total 20
```

```
drwxr-xr-x 2 jleem users 4096 2006-11-15 23:08:36.000000000 -0800 executables
drwxr-xr-x 5 jleem users 4096 2006-11-15 22:35:30.000000000 -0800 install_tests
drwxr-xr-x 2 jleem users 4096 2006-11-15 22:39:37.000000000 -0800 source
drwxr-xr-x 25 jleem users 4096 2006-11-15 22:43:01.000000000 -0800 test_problems_dec
drwxr-xr-x 25 jleem users 4096 2006-11-15 22:37:33.000000000 -0800 test_problems_lin
```

```
/home/jleem/tr3.1.1_X/executables
```

```
total 8344
```

```
-r-xr-xr-x 1 jleem users 1267120 2006-11-15 23:08:07.000000000 -0800 tr3.1.1e3_40k_dec
-r-xr--r-- 1 jleem users 1571881 2006-11-15 23:08:07.000000000 -0800 tr3.1.1e3_40k_lin
-r-xr-xr-x 1 jleem users 1277184 2006-11-15 23:08:07.000000000 -0800 tr3.1.1e4_40k_dec
-r-xr--r-- 1 jleem users 1583453 2006-11-15 23:08:06.000000000 -0800 tr3.1.1e4_40k_lin
-r-xr-xr-x 1 jleem users 1256656 2006-11-15 23:08:06.000000000 -0800 tr3.1.1e9_40k_dec
-r-xr--r-- 1 jleem users 1556024 2006-11-15 23:08:06.000000000 -0800 tr3.1.1e9_40k_lin
```

```
/home/jleem/tr3.1.1_X/install_tests
```

```
total 12
```

```
drwxr-xr-x 2 jleem users 4096 2006-11-15 22:35:30.000000000 -0800 eos3
drwxr-xr-x 2 jleem users 4096 2006-11-15 22:35:30.000000000 -0800 eos4
drwxr-xr-x 2 jleem users 4096 2006-11-15 22:35:30.000000000 -0800 eos9
```

```
/home/jleem/tr3.1.1_X/install_tests/eos3
```

```
total 896
```

```
-r-xr--r-- 1 jleem users 172953 2006-11-15 22:35:30.000000000 -0800 GASOBS.DAT
-r-xr--r-- 1 jleem users 91 2006-11-15 22:35:30.000000000 -0800 GENER
-r-xr--r-- 1 jleem users 149 2006-11-15 22:35:30.000000000 -0800 INCON
-r-xr--r-- 1 jleem users 0 2006-11-15 22:35:30.000000000 -0800 LINEQ
-r-xr--r-- 1 jleem users 9228 2006-11-15 22:35:30.000000000 -0800 MESH
-r-xr--r-- 1 jleem users 7518 2006-11-15 22:35:30.000000000 -0800 SAVE
-r-xr--r-- 1 jleem users 0 2006-11-15 22:35:30.000000000 -0800 TABLE
-r-xr--r-- 1 jleem users 6640 2006-11-15 22:35:30.000000000 -0800 VERS
-r-xr--r-- 1 jleem users 7049 2006-11-15 22:35:29.000000000 -0800 chdump.out
-r-xr--r-- 1 jleem users 5517 2006-11-15 22:35:29.000000000 -0800 chemical.inp
-r-xr--r-- 1 jleem users 14625 2006-11-15 22:35:29.000000000 -0800 chemical.out
-r-xr--r-- 1 jleem users 9711 2006-11-15 22:35:30.000000000 -0800 flow.inp
-r-xr--r-- 1 jleem users 228245 2006-11-15 22:35:30.000000000 -0800 flow.out
-r-xr--r-- 1 jleem users 12001 2006-11-15 22:35:30.000000000 -0800 iter.dat
-r-xr--r-- 1 jleem users 15528 2006-11-15 22:35:30.000000000 -0800 mbalance.out
```

```
-r-xr--r-- 1 jleem users 31174 2006-11-15 22:35:30.000000000 -0800 min_SI.out
-r-xr--r-- 1 jleem users 15277 2006-11-15 22:35:30.000000000 -0800 runlog.out
-r-xr--r-- 1 jleem users 62613 2006-11-15 22:35:30.000000000 -0800 savechem
-r-xr--r-- 1 jleem users 1646 2006-11-15 22:35:30.000000000 -0800 solute.inp
-r-xr--r-- 1 jleem users 6209 2006-11-15 22:35:30.000000000 -0800 solute.out
-r-xr--r-- 1 jleem users 33914 2006-11-15 22:35:30.000000000 -0800 tec_conc.dat
-r-xr--r-- 1 jleem users 14089 2006-11-15 22:35:30.000000000 -0800 tec_gas.dat
-r-xr--r-- 1 jleem users 48093 2006-11-15 22:35:30.000000000 -0800 tec_min.dat
-r-xr--r-- 1 jleem users 88384 2006-11-15 22:35:29.000000000 -0800 ther_dummy.dat
-r-xr--r-- 1 jleem users 60384 2006-11-15 22:35:30.000000000 -0800 time.dat
```

/home/jleem/tr3.1.1_X/install_tests/eos4

total 896

```
-r-xr--r-- 1 jleem users 172557 2006-11-15 22:35:30.000000000 -0800 GASOBS.DAT
-r-xr--r-- 1 jleem users 91 2006-11-15 22:35:30.000000000 -0800 GENER
-r-xr--r-- 1 jleem users 149 2006-11-15 22:35:30.000000000 -0800 INCON
-r-xr--r-- 1 jleem users 0 2006-11-15 22:35:30.000000000 -0800 LINEQ
-r-xr--r-- 1 jleem users 9228 2006-11-15 22:35:30.000000000 -0800 MESH
-r-xr--r-- 1 jleem users 7518 2006-11-15 22:35:30.000000000 -0800 SAVE
-r-xr--r-- 1 jleem users 0 2006-11-15 22:35:30.000000000 -0800 TABLE
-r-xr--r-- 1 jleem users 7047 2006-11-15 22:35:30.000000000 -0800 VERS
-r-xr--r-- 1 jleem users 7049 2006-11-15 22:35:30.000000000 -0800 chdump.out
-r-xr--r-- 1 jleem users 5517 2006-11-15 22:35:30.000000000 -0800 chemical.inp
-r-xr--r-- 1 jleem users 14625 2006-11-15 22:35:30.000000000 -0800 chemical.out
-r-xr--r-- 1 jleem users 9711 2006-11-15 22:35:30.000000000 -0800 flow.inp
-r-xr--r-- 1 jleem users 227315 2006-11-15 22:35:30.000000000 -0800 flow.out
-r-xr--r-- 1 jleem users 12001 2006-11-15 22:35:30.000000000 -0800 iter.dat
-r-xr--r-- 1 jleem users 15528 2006-11-15 22:35:30.000000000 -0800 mbalance.out
-r-xr--r-- 1 jleem users 31174 2006-11-15 22:35:30.000000000 -0800 min_SI.out
-r-xr--r-- 1 jleem users 15277 2006-11-15 22:35:30.000000000 -0800 runlog.out
-r-xr--r-- 1 jleem users 62613 2006-11-15 22:35:30.000000000 -0800 savechem
-r-xr--r-- 1 jleem users 1646 2006-11-15 22:35:30.000000000 -0800 solute.inp
-r-xr--r-- 1 jleem users 6209 2006-11-15 22:35:30.000000000 -0800 solute.out
-r-xr--r-- 1 jleem users 33914 2006-11-15 22:35:30.000000000 -0800 tec_conc.dat
-r-xr--r-- 1 jleem users 14089 2006-11-15 22:35:30.000000000 -0800 tec_gas.dat
-r-xr--r-- 1 jleem users 48093 2006-11-15 22:35:30.000000000 -0800 tec_min.dat
-r-xr--r-- 1 jleem users 88384 2006-11-15 22:35:30.000000000 -0800 ther_dummy.dat
-r-xr--r-- 1 jleem users 60384 2006-11-15 22:35:30.000000000 -0800 time.dat
```

/home/jleem/tr3.1.1_X/install_tests/eos9

total 200

```
-r-xr--r-- 1 jleem users 29403 2006-11-15 22:35:30.000000000 -0800 GASOBS.DAT
-r-xr--r-- 1 jleem users 91 2006-11-15 22:35:30.000000000 -0800 GENER
-r-xr--r-- 1 jleem users 7383 2006-11-15 22:35:30.000000000 -0800 INCON
-r-xr--r-- 1 jleem users 0 2006-11-15 22:35:30.000000000 -0800 LINEQ
-r-xr--r-- 1 jleem users 13967 2006-11-15 22:35:30.000000000 -0800 MESH
-r-xr--r-- 1 jleem users 7491 2006-11-15 22:35:30.000000000 -0800 SAVE
```

```
-r-xr--r-- 1 jleem users 0 2006-11-15 22:35:30.000000000 -0800 TABLE
-r-xr--r-- 1 jleem users 3791 2006-11-15 22:35:30.000000000 -0800 VERS
-r-xr--r-- 1 jleem users 41322 2006-11-15 22:35:30.000000000 -0800 flow.inp
-r-xr--r-- 1 jleem users 79596 2006-11-15 22:35:30.000000000 -0800 flow.out
```

/home/jleem/tr3.1.1_X/source

total 1312

```
-r-xr--r-- 1 jleem users 3081 2006-11-15 22:34:50.000000000 -0800 T2_40K
-r-xr--r-- 1 jleem users 1839 2006-11-15 22:34:50.000000000 -0800 chempar23_q311.inc
-r-xr--r-- 1 jleem users 3412 2006-11-15 22:34:50.000000000 -0800 common23.inc
-r-xr--r-- 1 jleem users 46113 2006-11-15 22:34:50.000000000 -0800 eos3.f
-r-xr--r-- 1 jleem users 60724 2006-11-15 22:34:50.000000000 -0800 eos4.f
-r-xr--r-- 1 jleem users 32044 2006-11-15 22:34:50.000000000 -0800 eos9.f
-r-xr--r-- 1 jleem users 204231 2006-11-15 22:34:50.000000000 -0800 geochem.f
-r-xr--r-- 1 jleem users 97464 2006-11-15 22:34:50.000000000 -0800 inichm.f
-r-xr--r-- 1 jleem users 1550 2006-11-15 22:34:50.000000000 -0800 ma28abc.f
-r-xr--r-- 1 jleem users 1716 2006-11-15 22:34:50.000000000 -0800 makefile_eos3q311_dec
-r-xr--r-- 1 jleem users 1894 2006-11-15 22:34:50.000000000 -0800 makefile_eos3q311_linux
-r-xr--r-- 1 jleem users 1716 2006-11-15 22:34:50.000000000 -0800 makefile_eos4q311_dec
-r-xr--r-- 1 jleem users 1894 2006-11-15 22:34:50.000000000 -0800 makefile_eos4q311_linux
-r-xr--r-- 1 jleem users 1716 2006-11-15 22:34:50.000000000 -0800 makefile_eos9q311_dec
-r-xr--r-- 1 jleem users 1894 2006-11-15 22:34:50.000000000 -0800 makefile_eos9q311_linux
-r-xr--r-- 1 jleem users 41911 2006-11-15 22:34:50.000000000 -0800 meshm.f
-r-xr--r-- 1 jleem users 141763 2006-11-15 22:34:50.000000000 -0800 multi.f
-r-xr--r-- 1 jleem users 33584 2006-11-15 22:34:50.000000000 -0800 newton.f
-r-xr--r-- 1 jleem users 507 2006-11-15 22:34:50.000000000 -0800 perm23.inc
-r-xr--r-- 1 jleem users 17941 2006-11-15 22:34:50.000000000 -0800 rctprop.f
-r-xr--r-- 1 jleem users 20523 2006-11-15 22:34:50.000000000 -0800 readsolu.f
-r-xr--r-- 1 jleem users 827 2006-11-15 22:34:50.000000000 -0800 second_dec.f
-r-xr--r-- 1 jleem users 73085 2006-11-15 22:34:50.000000000 -0800 t2cg22.f
-r-xr--r-- 1 jleem users 165569 2006-11-15 22:34:50.000000000 -0800 t2f.f
-r-xr--r-- 1 jleem users 73236 2006-11-15 22:34:50.000000000 -0800 t2solv.f
-r-xr--r-- 1 jleem users 225993 2006-11-15 22:34:50.000000000 -0800 treat.f
```

Q.3.1 CUTCHEM V2.0 Installation on PC

Q.3.1.1 Folders and Files of Installation (prior to qualification of CUTCHEM V2.0) on LBNL PC DOE #6574913 with Windows XP

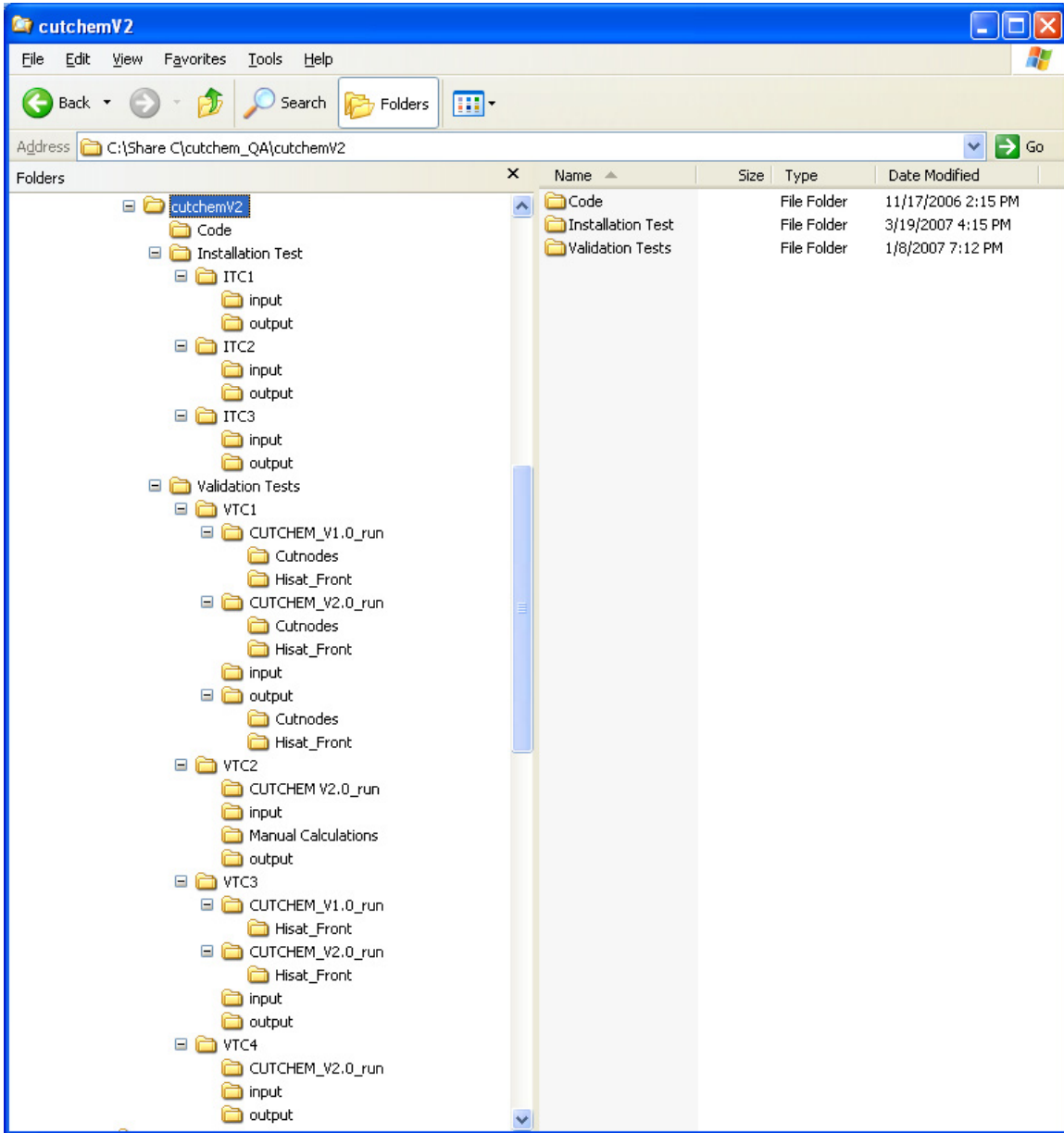
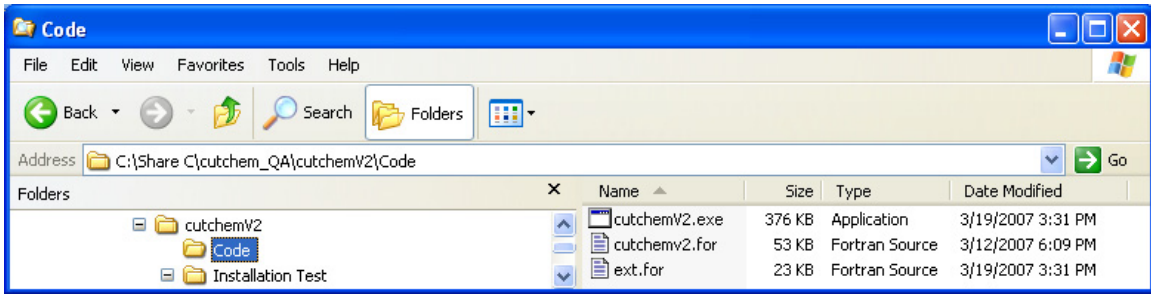


Figure Q-1. Folders of CUTCHEM on the LBNL PC DOE # 6574913



NOTE: The source codes (i.e., cutchemv2.for and ext.for) were removed in the qualified version of CUTCHEM.

Figure Q-2. List of Source Files and the Executable File in Subfolder \Code

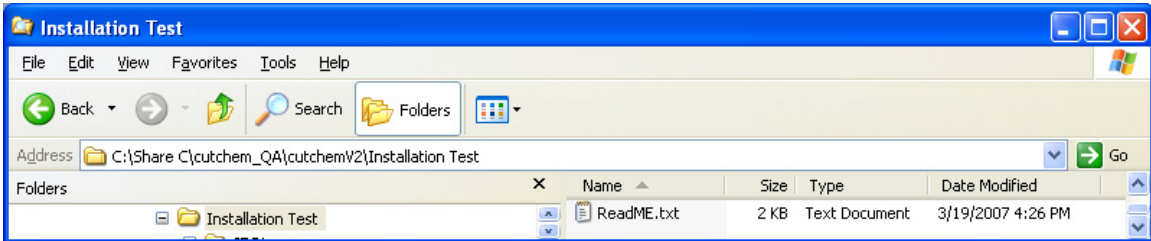


Figure Q-3. List of the ReadMe File of CUTCHEM V2.0 Installation Tests

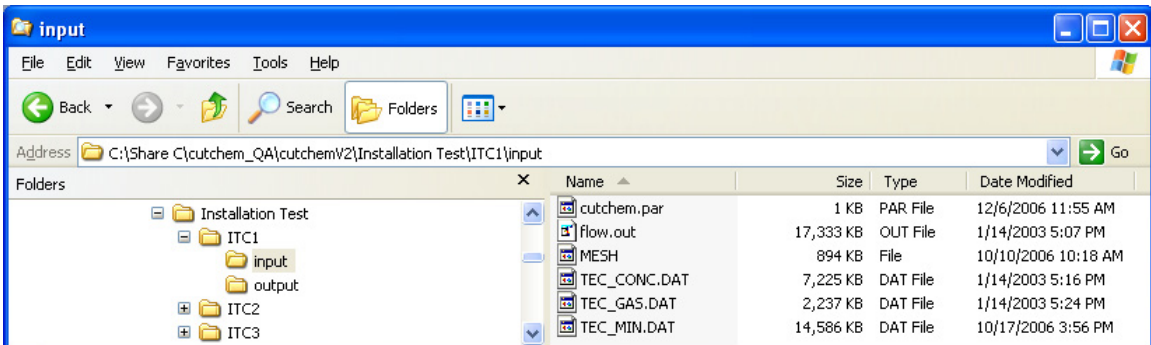


Figure Q-4. List of Files in Subfolder \Installation Test\ITC1\input

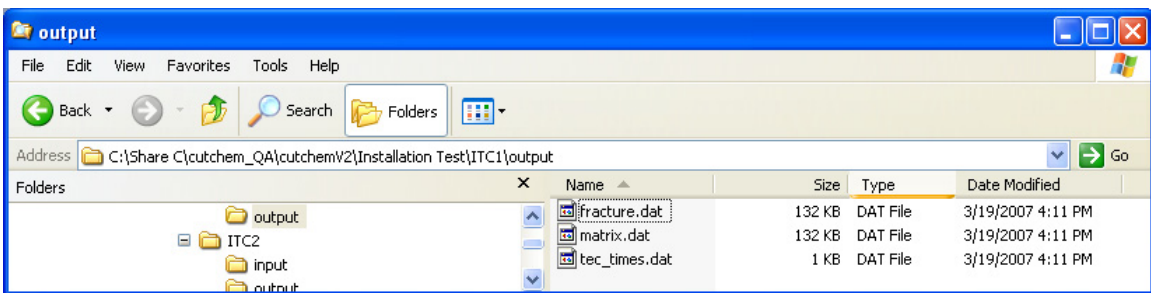


Figure Q-5. List of Files in Subfolder \Installation Test\ITC1\output

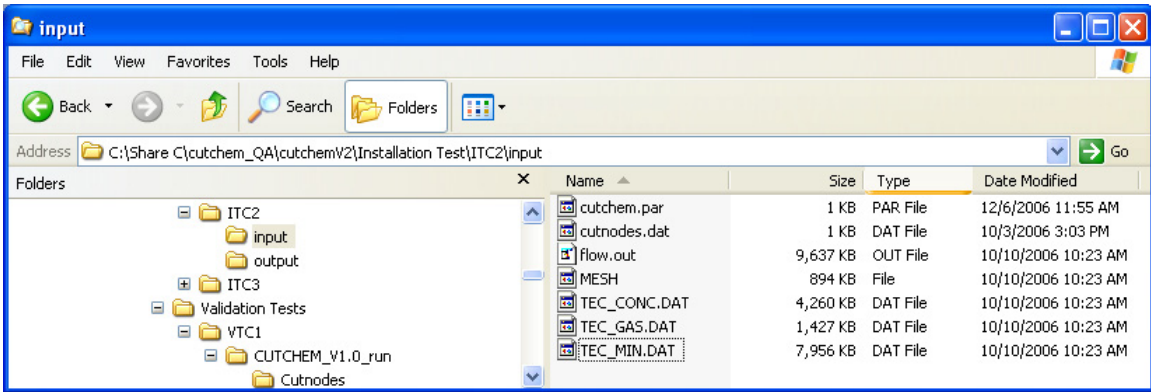


Figure Q-6. List of Files in Subfolder *Installation Test\ITC2\input*

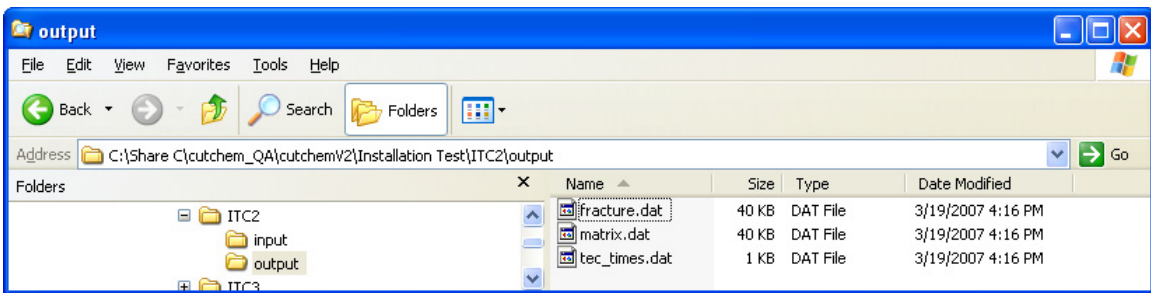


Figure Q-7. List of Files in Subfolder *Installation Test\ITC2\output*

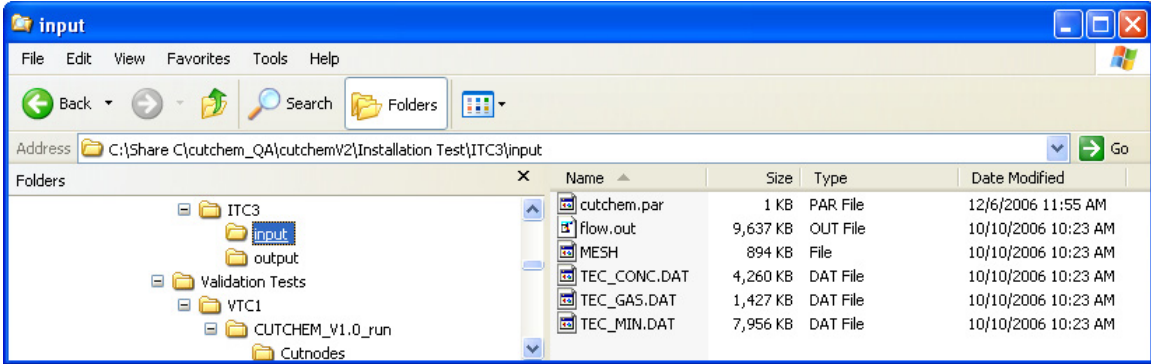


Figure Q-8. List of Files in Subfolder *Installation Test\ITC3\input*

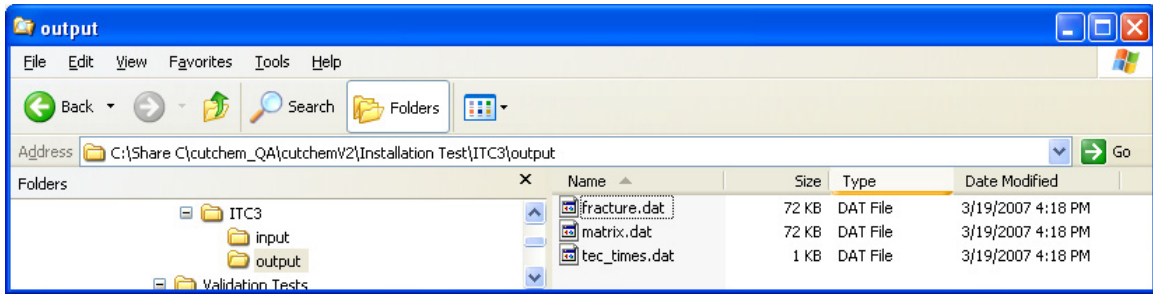


Figure Q-9. List of Files in Subfolder *Installation Test\ITC3\output*

Q.3.2 Folders and Files of Installation from the Qualified CUTCHEM V2 Media from Software Configuration Management on SNL PC S885719 with Windows XP

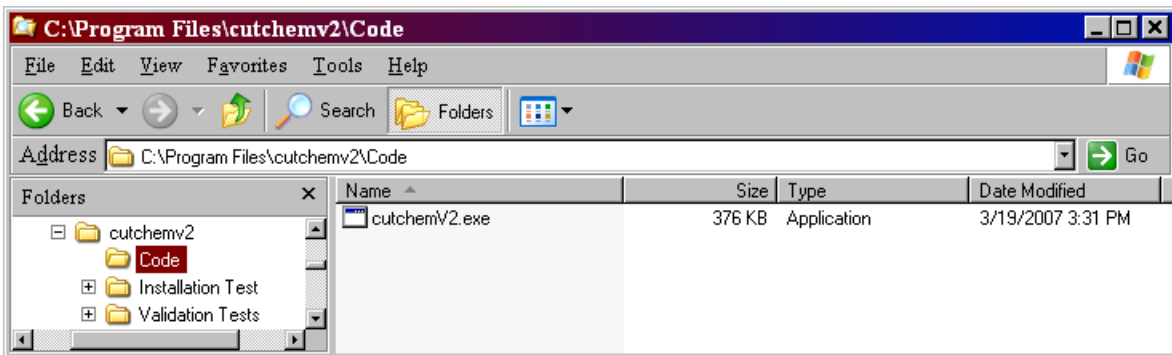


Figure Q-10. List of Source Files and the Executable File in Subfolder *\Code*

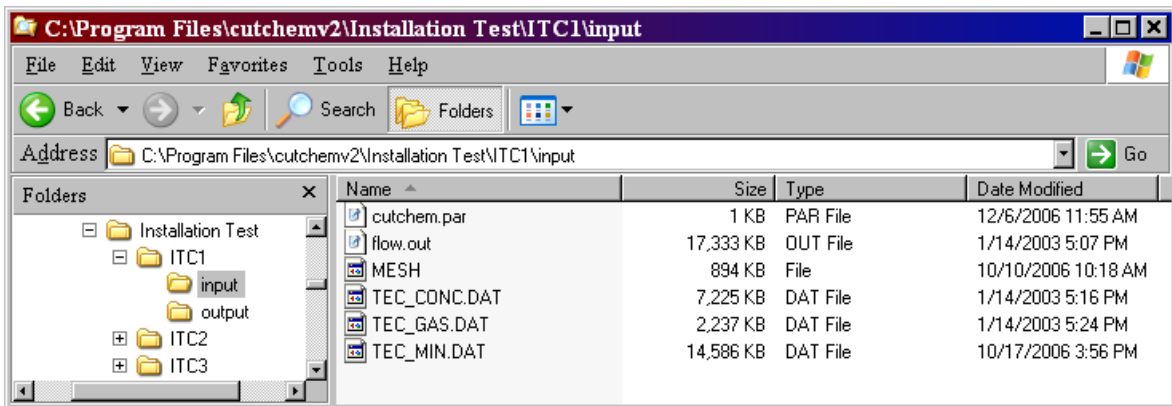


Figure Q-11. List of Files in Subfolder *Installation Test\ITC1\input*

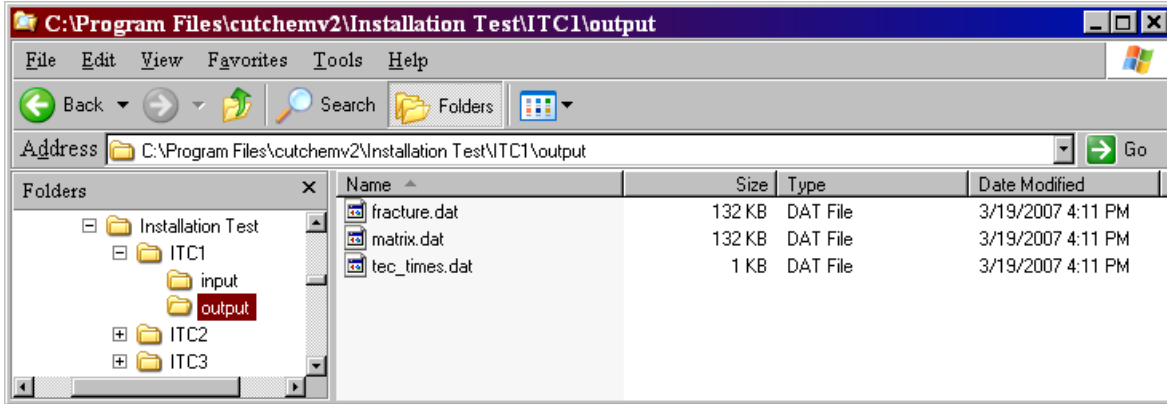


Figure Q-12. List of Files in Subfolder *Installation Test\ITC1\output*

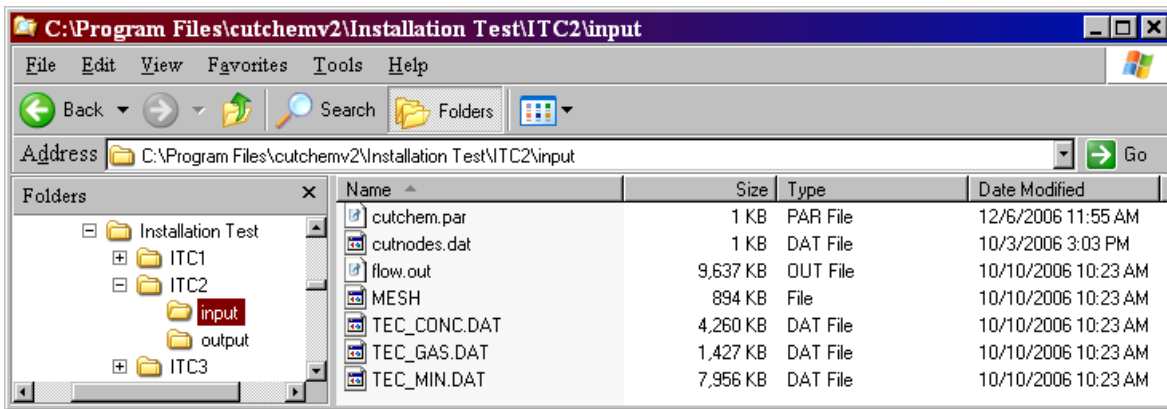


Figure Q-13. List of Files in Subfolder *Installation Test\ITC2\input*

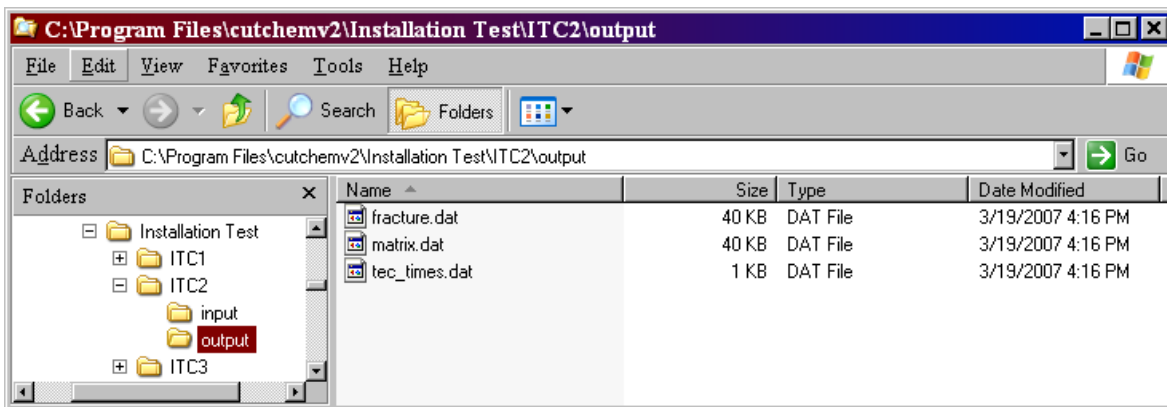


Figure Q-14. List of Files in Subfolder *Installation Test\ITC2\output*

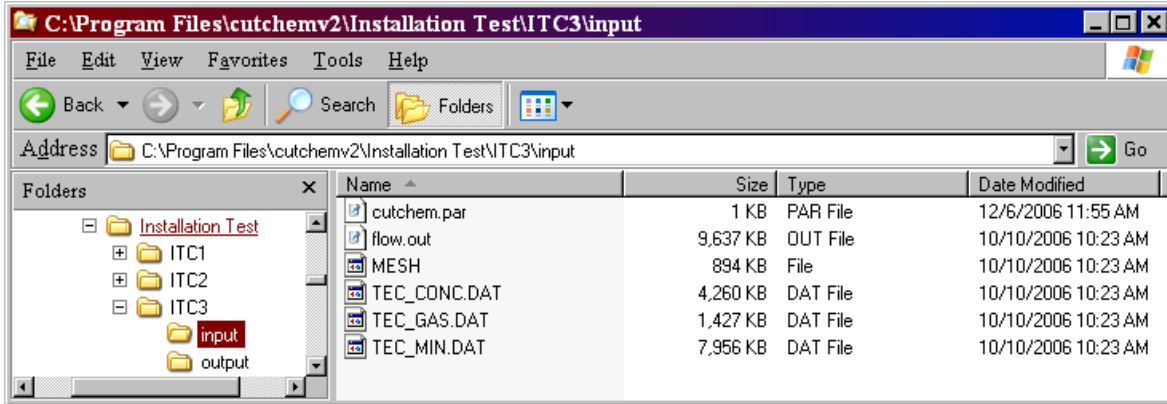


Figure Q-15. List of Files in Subfolder *Installation Test\ITC3\input*

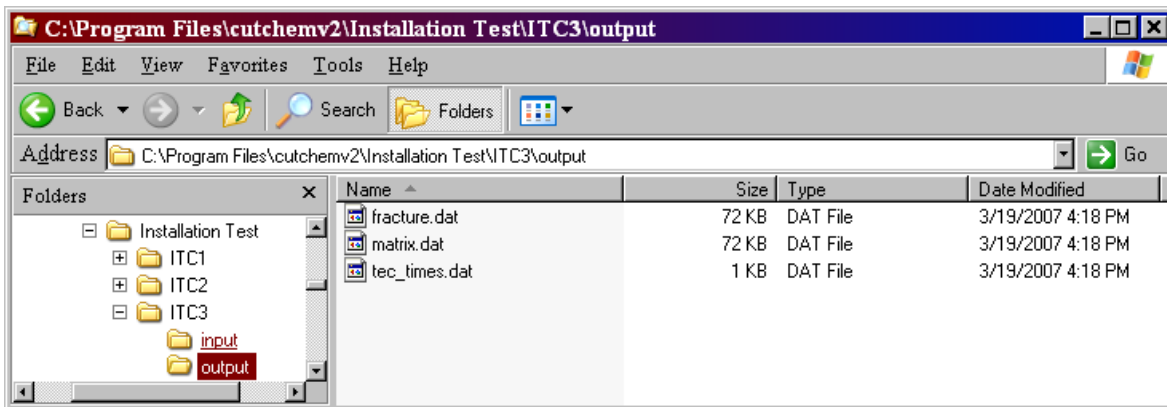


Figure Q-16. List of Files in Subfolder *Installation Test\ITC3\output*

INTENTIONALLY LEFT BLANK